

UNIVERSITE DE STRASBOURG

**Le magmatisme intra-plaque des marges passives :
mise en évidence des limites des modèles existants
par l'étude de deux cas concrets**

Mémoire présenté en vue de l'obtention de l'Habilitation à Diriger
des Recherches de l'Université de Strasbourg

RENAUD MERLE

Sommaire

Partie I : Parcours professionnel et scientifique	3
1. Curriculum Vitae	4
2. Thèmes de recherche	10
Partie II : Thématique de recherche principale : le magmatisme intra-plaque des marges passives (synthèse).	15
1. Problématique.....	16
1.1. Panaches mantelliques et extension continentale	16
1.2. Magmatisme intra-plaque des marges passives	18
1.3. Les limites des modèles existants	20
2. Etudes de cas : le magmatisme intraplaque sur les marges ouest-ibérique et ouest-australienne.....	21
2.1. Les marges conjuguées Ibérie-Terre Neuve.....	22
2.2. La marge ouest-sud-ouest de l'Australie occidentale.....	32
3. Les problèmes en suspens	40
4. Programme de recherche : approche méthodologique et analytique.....	41
5. Chantiers en cours et futurs développements	47
6. Conclusions	52
Références bibliographiques.....	53
Annexes.....	61
Annexe 1 : liste complète des publications et communications en congrés	61
Annexe 2 : Sélection d'articles (thématique de recherche principale)	67

Partie I : Parcours professionnel et scientifique

1. Curriculum Vitae

Renaud MERLE

Géologue-Géochimiste

Spécialiste en pétrologie des laves, géochimie isotopique et géochronologie U-Pb appliquées aux roches terrestres et extra-terrestres.

Nationalité française

Né le 20 Octobre 1976 à Talence (Gironde, France).

En couple, 1 enfant.

Langues: Français (langue maternelle), Anglais (courant), Italien (bon), Allemand (notions).

Adresse professionnelle :

School of Earth and Planetary Sciences, Kent Street, Bentley, Perth, Western Australia 6102, Australia.

E-mail: r.merle@curtin.edu.au

Parcours professionnel :

- Depuis Mars 2018 : Affiliated Research associate, School of Earth and Planetary Sciences, Curtin University (Perth, Australie).
- Décembre 2016-Mars 2018 : Affiliated Research associate, Research School of Earth Sciences, Australian National University (Canberra, Australie).
- Décembre 2015-Novembre 2016 : Research associate, Research School of Earth Sciences, Australian National University (Canberra, Australie). Superviseur : Yuri Amelin.
- 2012-2015 : Associated lecturer (temps partiel), Department of Applied Geology, Curtin University (Perth, Australie). Superviseur : Alexander Nemchin.
- 2011: Chercheur contractuel, Dipartimento di Geoscienze, Università di Padova (Padoue, Italie). Superviseur : Andrea Marzoli.
- Février-Août 2010 : Research associate, John De Laeter Centre of Mass Spectrometry, Department of Applied Physics, Curtin University (Perth, Australie).

- 2009 : Post-doctoral fellow, School of Earth and Environment, University of Western Australia (Perth, Australie). Superviseurs : Peter Cawood (UWA), Alexander Nemchin (Curtin University).
- 2006-2008 : Post-doctorant, Dipartimento di Geoscienze, Università di Padova, (Padoue, Italie). Superviseur : Andrea Marzoli.

Etudes supérieures :

2002-2006

Thèse de doctorat en pétrologie magmatique et géochimie isotopique (Université de Nantes en collaboration avec l'université de Nice-Sophia-Antipolis) : *Age et origine de la ride Tore-Madère : Début de l'accrétion de la dorsale atlantique ou trace d'un point chaud ?*

Directeur de thèse : Jacques Girardeau.

Superviseur : Urs Schärer (Université de Nice-Sophia-Antipolis).

2001-2002

DEA Géosciences Marines à l'université de Bretagne occidentale.

Mention bien, major de promotion.

Mémoire : *Modélisation géochimique d'une chambre magmatique réalimentée et cristallisant en continu : cas de la ride Est pacifique 17-19°S.*

Superviseur : Martial Caroff.

2000-2001

Maîtrise en Sciences de la Terre, Université de Clermont-Ferrand.

1999-2000

Licence en Sciences de la Terre, Université de Clermont-Ferrand.

Mention bien.

Compétences scientifiques :

- Géochronologie U-Pb sur matériaux terrestres (sphène et zircon) et extraterrestres (chondres) par dilution isotopique et spectrométrie de masse par thermo-ionisation (TIMS).
- Géochronologie U-Pb in-situ sur zircon, apatite et opale par sonde ionique (Sensitive High Resolution Ion Micro-Probe, SHRIMP).
- Traçage isotopique Sr-Nd-Pb sur minéraux séparés (isotopes du Sr et Pb sur plagioclase et feldspath alcalin par dilution isotopique, Hf sur zircon) et roches totales.
- Traçage isotopique Re-Os par dilution isotopique et TIMS sur basaltes.
- Mesure des isotopes du potassium par TIMS.

- Minéralogie, pétrologie, géochimie des éléments majeurs, mineurs et en traces des roches magmatiques.
- Modélisation numérique des processus magmatiques.

Production scientifique :

- 22 articles scientifiques publiés dans des journaux internationaux de rang A depuis 2005
- 9 articles publiés en tant que premier auteur
- Co-auteur d'un chapitre d'ouvrage collectif en 2017
- 4 articles soumis en 2018
- 298 citations, 74 en 2017, h-index = 10 (source : Scopus)
- Contribution à 15 communications en congrès internationaux depuis 2013.

Compétences techniques :

- Instrumentation :

Travail intensif avec :

- TIMS MAT Finnigan 262 (mesure des isotopes de l'Os, du K et datation U-Pb par dilution isotopique).
- TIMS Thomson 206 (mesure des isotopes des éléments Pb-U-Sr-Rb).
- Microsonde électronique CAMECA SX 50
- Microscopes électroniques à balayage Philips XL 30 et Zeiss Evo 40XVP.
- Sonde ionique SHRIMP II (mesure in-situ des rapports isotopiques des éléments U et Pb).

Travail occasionnel avec :

- Microsondes Electroniques JEOL 8530F et JEOL JXA-8200.
- Microscope électronique à balayage JEOL 5800.
- MC-ICP-MS VG plasma 54 (mesure des rapports isotopiques de l'Hf).
- LA-ICP-MS Elan DRC-E (analyse de la concentration des éléments en trace dans les clinopyroxènes).
- ICP-MS à quadripôle Perkin-Elmer Elan 6000 (mesure du Re).
- TIMS Thermo Triton (mesure des rapports isotopiques des éléments Sr-Nd-Pb et datation U-Pb).
- TIMS VG 354 (mesure des rapports isotopiques du Pb).
- TIMS VG Sector (mesure des rapports isotopiques du Sr et du Pb).
- Sonde ionique CAMECA ims1280 (mesure in-situ des rapports isotopes des éléments U, Pb, Si et O).

- Travail en laboratoire :

Travail intensif en salle blanche :

- Pesée d'échantillons et des traceurs isotopiques avec microbalances.
- Microchimie sur colonnes chromatographiques avec résines échangeuses d'ions.
- Préparation et distillation de solutions ultra-pures.

Préparation des échantillons :

Découpe en vue de la préparation de lames minces, analyses pétrographiques et texturales, broyage, séparations minérales par liqueurs denses et séparation magnétique, séparation finale sous loupe binoculaire.

Expériences de terrain :

- 2017 : Echantillonnage de la lithosphère océanique (basaltes et péridotites du manteau) de l'île Macquarie, Australie sub-antarctique (15 jours). Collaboration Australian Antarctic Division et Curtin University.
- 2014 : Echantillonnage des basaltes de la Newer Volcanic Province, western Victoria, Australie (1 semaine). Thèse Korien Oostingh (Curtin University).
- 2013 : Echantillonnage des affleurements du « Basalte de Bunbury » (point chaud des Kerguelen), Australie Occidentale (1 semaine). Thèse Hugo Olieroor (Curtin University).
- 2006 : Echantillonnage des massifs alcalins Crétacé du Portugal (8 jours). Thèse Marion Grange (Université de Nice).
- 2003 : Echantillonnage des massifs alcalins Crétacé du Portugal (12 jours). Thèse (Université de Nantes).
- 2001 : « Université flottante », campagne d'initiation à la géologie en mer (18 jours à bord du Marion Dufresne).
- Camp de terrain de DEA- Université de Bretagne Occidentale : Géologie de la croute océanique supérieure (1 jour), Péninsule de Crozon, Finistère.
- 2000-2001 : Camps de terrain de Maîtrise-Université de Clermont-Ferrand : Cartographie en terrain volcanique (1 semaine), Mont Dore, Puy de Dôme. Cartographie, métamorphisme de haute-température (1 semaine), Cap Creus, Espagne.
- 1999-2000 : Camps de terrain de Licence-Université de Clermont-Ferrand : Cartographie et géologie sédimentaire (1 semaine), Pic Saint-Loup, Hérault.

Cartographie, structures tectoniques superficielles (1 semaine), Chainon de Lagrasse, Aude.

Cartographie, analyse structurale des zones profondes (1 semaine), Ardèche.

Financements :

- Merle R., Bostock H., Jourdan F., Olierook H., *Age and origin of the magmatism along the transpressional Australian-Pacific plate boundary*, Australian Antarctic Science Program 2017, AUD 115005 (2017-2019).
- Jourdan F., Olierook H., Merle R., Coffin M., Whittaker J., Halpin J., *The Kerguelen Large Igneous Province: dynamics of a pulsating mantle plume*, Australian Antarctic Science Program 2017, AUD 75553 (2017-2020).
- Olierook H., Merle R., Jourdan F., Whittaker J., *Time constraints on the world's clearest oceanic curved fracture zone: implications for a global plate reorganisation in the Cretaceous*, Australian and New Zealand International Ocean Discovery Program Consortium grant 2016, AUD 10000 (2016-2018).
- Merle R., Jourdan F., Manatschal G., *Magmatism on the Iberia-Newfoundland passive margins since 200 Ma*, Australian and New Zealand International Ocean Discovery Program Consortium grant 2014, AUD 20000 (2014-2016).
- Merle R., Cawood P., Nemchin A., *Combined U-Pb, O and Hf isotope study of granites from New England Fold Belt (Eastern Australia): implications to growth of continental crust*, University of Western Australia Research and Development Award 2010, AUD 20350 (2010-2011).

Divers :

Reviewer régulier pour Lithos, Journal of Petrology, Geochimica Cosmochimica Acta, Journal of Geodynamics, projets NSF (US), Fond Mardsen (NZ).

Membre de la Geochemical Society depuis 2011.

Membre de la section australienne de NASA's Solar System Exploration Research Virtual Institute (SSERVI, www.sserviaustralia.org).

Enseignement et encadrement de projets de recherche :

Mes expériences professionnelles en enseignement m'ont amené à développer une approche qui consiste à être disponible pour les étudiants et d'écouter leurs questions, demandes spécifiques et commentaires sur le contenu de l'enseignement et la conception des cours et travaux pratiques pour permettre un transfert efficace du savoir

et une optimisation des méthodes d'acquisition. Cela implique de fournir des réponses précises en classe, d'organiser des rendez-vous avec les étudiants afin d'examiner plus en détails leurs questions et problèmes spécifiques et de fournir aux étudiants des commentaires détaillés après tests, travaux pratiques et examens.

Je m'efforce aussi de mieux préparer les étudiants à leur futur emploi en leur fournissant un matériel pédagogique et des informations qui pourront être directement utilisables dans leur environnement professionnel.

L'enseignement offre également la possibilité de repérer les étudiants les plus aptes à faire de la recherche et de les guider efficacement, s'ils veulent poursuivre une carrière académique.

Activités d'enseignement :

2012-2013 : « Associate Lecturer », Curtin University (192 heures par an).

- Travaux pratiques : géologie appliquée aux sciences de l'ingénieur - 10h par semaine (premier semestre) ; niveau première année.

- Travaux pratiques : géologie des ressources naturelles - 6h par semaine (second semestre) ; niveau première année.

- Camp de terrain (1 semaine) : géologie structurale et métamorphique ; niveau troisième année.

- Journée de terrain (1 jour) : découverte de la géologie de terrain ; niveau première année.

2009 : « Associate Lecturer », UWA.

- Camp de terrain (1 semaine) : géologie structurale et métamorphique ; niveau troisième année.

2004 : Vacataire, Université de Nantes (30 heures par an).

- Travaux pratiques : Hydrologie and hydrogéologie; niveau première année.

2003 : Vacataire, Université de Nantes (40 heures par an).

- Travaux pratiques : Géodynamique des bassins sédimentaires ; approche multidisciplinaire (bathymétrie, géophysique, géologie régionale, étude de lames minces); niveau première année.

- Travaux pratiques : Cartographie; niveau première année.

Co-encadrements de thèses de doctorat :

Au cours de ma carrière, j'ai été amené à travailler sur plusieurs projets impliquant des étudiants. Ce travail m'a permis d'acquérir de nouvelles compétences en encadrement de la recherche ainsi qu'en formation des étudiants. J'ai contribué à l'encadrement de trois thèses de doctorat. Ma participation a consisté à superviser le traitement, la mise en forme et l'interprétation des données pétrologiques et géochimiques (éléments majeurs et en trace ; rapports isotopiques Sr-Nd-Pb, modélisation numérique des processus magmatiques). J'ai aussi contribué à la rédaction des articles publiés par les doctorants. Ma contribution représente environ 30% du temps total de supervision.

Thèses co-supervisées :

- Bryant Ware, Curtin University : *Kalkarindji and Karoo-Ferrar Large Igneous Provinces: Contrasting Origins and Climatic Impacts*. Superviseur principal : F. Jourdan (Curtin University). Soutenue en Avril 2017.
- Korian Oostingh, Curtin University : *Geochronology and geochemistry of the Newer Victoria Province*. Superviseur principal : F. Jourdan (Curtin University). Soutenue en Septembre 2016.
- Hugo Olierook, Curtin University : *Geometry and geochronology of the Bunbury Basalt, Western Australia*. Superviseur principal : N. Timms (Curtin University). Soutenue en Février 2015.

2. Thèmes de recherche

Au cours de ma thèse, j'ai commencé à développer deux axes de recherche : (i) la pétrogénèse des laves intracontinentale incluant traçage isotopique des sources des magmas et (ii) la datation U-Pb sur une large variété de matériaux géologiques, par la technique de la dilution isotopique et analyse par spectrométrie de masse par thermionisation (TIMS). Au cours de mes dix ans d'expérience professionnelle en tant que chercheur en Italie puis en Australie, j'ai continué à travailler sur ces deux thématiques ce qui m'a amené à améliorer et étendre mes compétences analytiques et scientifiques en travaillant aux côtés de chercheurs renommés sur des projets variés et en utilisant des méthodes géochronologiques et géochimiques de pointe (système Re-Os ; datation U-Pb par la méthode d'abrasion chimique-dilution isotopique et TIMS ; datation U-Pb in-situ par SIMS). L'ensemble de ma recherche peut ainsi se regrouper en six thématiques :

A- Chronologie des processus de formation du système solaire primitif.

Ma recherche dans ce domaine consiste en la détermination de l'âge de formation des premiers objets du système solaire. Je suis actuellement impliqué dans deux projets sur cette thématique de recherche :

(1) Datation de très haute précision (erreur <0,02%) des chondres présents dans les météorites les plus primitives. Le but de ce projet est de déterminer la séquence temporelle de formation des objets les plus anciens du système solaire (chondres et inclusions réfractaires riches en Calcium-Aluminium connus sous l'acronyme CAI). Cette information est critique pour connaître la durée et les conditions physico-chimiques de l'accrétion des protoplanètes durant les premiers millions d'années du système solaire. Ce projet implique des datations ultra-précises et ultra-fiables par la méthode U-Pb par attaque acide par palier (« step-leaching »), dilution isotopique et analyse par TIMS. Ce projet implique aussi la détermination par MC-ICP-MS (Multi-Collection Induced Coupled Plasma Mass Spectrometry) des rapports isotopiques $^{235}\text{U}/^{238}\text{U}$ et systématique $^{26}\text{Al}-^{26}\text{Mg}$

dans le même chondre que celle datée par la méthode U-Pb. Cette approche est très peu répandue car jusqu'à récemment limitée par la précision requise pour produire des données précises et fiables et restreinte à des chondres dont la taille dépasse 5mm (« mégachondrules »). Une étude minéralogique et pétrographique préalable impliquant la détermination de la texture des chondres par microscope électronique à balayage et de la chimie des phases minérales par microsonde électronique, est essentielle pour pouvoir évaluer et interpréter les données géochimiques.

Les résultats et interprétations concernant un « mégachondrule » extrait de la météorite Allende (météorite de type CV) font l'objet d'un article dont la soumission (à Meteoritics and Planetary Sciences) est prévue dans les prochains mois. Collaboration avec : Y. Amelin et T. Ireland, ANU (Australie); Q.-Z. Yin, UC Davis (USA); K. Nagashima et A. Krot, Hawaii Institute of Geophysics and Planetology (USA). Un développement futur de ce projet sera de systématiquement pratiquer le même type d'étude (détermination sur le même chondre de l'âge U-Pb par step-leaching et ID-TIMS, des rapports $^{235}\text{U}/^{238}\text{U}$ et systématique $^{26}\text{Al}-^{26}\text{Mg}$) sur d'autres « mégachondriles » trouvés dans la météorite Allende et d'autres classes de météorites pour établir si, effectivement, ces objets sont aussi vieux que les CAIs comme notre étude semble indiquer.

(2) Géochronologie des cratères d'impact de la Lune primitive. Ce projet implique la datation in-situ des brèches d'impact de la Lune provenant des sites d'alunissage des missions Apollo 14 et 17. Collaboration avec A. Nemchin, R. Pidgeon, M. Grange (Curtin University) et M. Whitehouse (Museum d'Histoire Naturelle Suédois).

B- Evolution tectonique et thermique des orogènes précambrien et paléozoïque d'Ecosse et d'Australie au moyen de la datation par la méthode U-Pb.

(1) Géochronologie U-Pb par sonde ionique des roches des formations Moine et Dalradian d'Ecosse. Ce projet avait pour but d'identifier l'origine des blocs continentaux, composant actuellement la croûte continentale d'Ecosse, avant leur accrétion durant l'orogenèse calédonienne (~450 Ma). Les résultats obtenus au cours de ce projet et leur interprétation ont été publiés et ce projet est maintenant terminé.

Collaboration avec P. Cawood (Monash University, Australia) et A. Nemchin (Curtin University).

(2) Datation in-situ par la méthode U-Pb sur SHRIMP des granites de type I (précurseurs ignés) et S (précurseurs sédimentaires) de la province tectonique New England Fold Belt (Australie orientale). Ce projet a pour but de comparer l'âge des granites dans les successives ceintures orogéniques exposées dans cette province afin de déterminer si la croissance de la croûte continentale le long de la côte Est de l'Australie a été un processus continu ou plutôt sporadique. Ce projet est toujours en cours. Collaboration avec P. Cawood (Monash University, Australia) et A. Nemchin (Curtin University).

C- Modalités de formation des concrétions siliceuses.

Ce projet a pour but de déterminer la cinématique de formation de concrétions siliceuses comme les opales ou le bois silicifié par les méthodes de datation in-situ U-Pb et les

déséquilibres radioactifs des isotopes de la série de désintégration de l'U par SHRIMP et par la détermination des rapports isotopiques du Si et de l'O. Dans le cadre de ce projet, j'ai acquis les données géochronologiques et déterminé les rapports isotopiques du Si et O dans des bois silicifiés et des opales australiennes. Ce projet est actuellement dirigé par F. Tomaschek (Bonn University) en collaboration avec T. Geisler (Bonn University), M. Whitehouse (Museum d'Histoire Naturelle Suédois) et A. Nemchin (Curtin University).

D- Calibration croisée des méthodes Rb-Sr, U-Pb, K-Ca et ^{40}K - ^{39}Ar .

L'objectif de ce projet est de déterminer avec une très grande précision la constante de désintégration du Potassium 40 (^{40}K). Actuellement, la relative imprécision de cette constante ne permet pas une comparaison directe des âges des roches datées avec la méthode ^{40}Ar / ^{39}Ar et d'autres méthodes. Je suis activement impliqué dans ce projet notamment pour la détermination ultra-précise de la composition isotopique du K qui est un paramètre essentiel pour connaître la constante de désintégration du ^{40}K . Les futurs développements de ce projet permettront la détermination de la composition isotopique du K dans des minéraux communs des roches magmatiques et volcaniques en vue d'établir avec certitude si la composition isotopique du K est homogène sur terre. Collaboration avec Y. Amelin (ANU). Ce projet est développé dans le cadre de l'initiative internationale « Earth Time » visant à améliorer les calibrations croisées entre systèmes isotopiques et entre laboratoires.

E- Age et évolution géochimique du magmatisme le long de la limite de plaque convergente Australie-Pacifique.

Située à environ 1500 km au sud-est de la Tasmanie, l'île Macquarie est probablement le seul endroit sur terre où la lithosphère océanique (croûte et manteau) a été portée au-dessus de niveau de la mer par les mouvements des plaques tectoniques tout en étant non déformée et significativement préservée de toute modification chimique post-magmatique. L'île Macquarie est la seule partie émergée de la ride Macquarie qui est un complexe de reliefs et monts sous-marins dont l'âge de formation n'est pas bien connu. Ce complexe se situe le long de la limite de plaque Australie et Pacifique. Cette limite de plaque est le lieu de changements de régime tectonique relativement rapides depuis environ 40 millions d'années, évoluant d'un contexte de distension à celui de compression en passant par un stade de mouvement transformant.

Ces changements de mouvement de cinématique de plaque ont nécessairement laissé une trace géochimique dans les roches volcaniques et le manteau qui forment la ride Macquarie. Ce projet se concentre sur la nature et l'origine des roches exposées sur l'île Macquarie et du complexe sous-marin de la ride Macquarie afin d'identifier la trace géochimique laissée par ces mouvements tectoniques récents. Ces roches offrent l'occasion unique d'étudier des processus géologiques au tout début d'une subduction alors que l'enregistrement de ces processus a été partiellement ou totalement effacé au cours de l'évolution de la subduction et la collision continentale dans les autres contextes de convergence sur terre. En particulier, l'objectif de ce projet est de comprendre comment les changements rapides de cinématique des plaques auraient pu affecter la

production magmatique le long d'une zone de subduction en devenir et contribuer à créer des variations chimiques dans les sources de ces magmas.

Ce projet utilise la datation de haute-précision par la méthode $^{40}\text{Ar}/^{39}\text{Ar}$ des différentes générations de basaltes de l'île Macquarie et des monts sous-marins directement au nord de celle-ci et le traçage géochimique de ces roches (analyse des éléments majeurs et en trace, systématique Sr-Nd-Pb-Os). Ce projet est mené en collaboration avec F. Jourdan, H. Olieroos et K. Evans (Curtin University).

F- Pétrologie et géochimie, incluant la géochimie isotopique, des basaltes intraplaques océaniques (Ocean Island Basalts, OIBs) et continentaux (Continental Flood Basalts, CFBs).

Je m'intéresse en particulier à l'identification des sources mantelliques des magmas et des processus pétrogénétiques (degrés de fusion, processus de cristallisation, mélanges et contamination) les affectant par le biais des systèmes isotropiques Pb-Sr-Nd-Os. Sur cette thématique de recherche, je suis impliqué dans cinq projets :

(1) Identification des sources des basaltes continentaux de la province magmatique du Karoo. L'objectif de ce projet est de confirmer l'origine lithosphérique de la source des magmas en utilisant le système isotopique Re-Os. Ce projet est toujours en cours et implique des collaborations avec L. Reisberg (CRPG-Nancy), F. Jourdan (Curtin University), H. Bertrand (ENS Lyon) et A. Marzoli (Universita di Padova, Italie).

(2) Identification des sources mantelliques des basanites de la ligne du Cameroun. L'objectif principal de ce projet était de contraindre la proportion de manteau lithosphérique contribuant aux caractéristiques géochimiques des laves du mont Bambouto. Pour ce projet, j'ai effectué les analyses isotopiques des éléments Re et Os (microchimie et spectrométrie de masse). Ce projet, maintenant terminé a été mené en collaboration avec L. Reisberg (CRPG-Nancy), F. Jourdan (Curtin University) et A. Marzoli (Universita di Padova, Italie).

(3) Caractérisation des sources mantelliques des basaltes continentaux de la province magmatique de l'atlantique central (Central Atlantic Magmatic Province, CAMP) et identification du processus géodynamique à l'origine de cette province magmatique qui s'est mis en place vers 200 Ma pendant les tous premiers stades de la dislocation de la Pangée. Le but de ce projet est de déterminer la nature des sources (manteau profond et/ou lithosphérique) des laves, sills et dykes basaltiques provenant du Brésil, des USA, du Canada et du Maroc en utilisant les isotopes du Sr, Nd, Pb et Re et Os. La grande majorité des données que j'ai acquises au cours de la durée de ce projet sont maintenant publiées et mon rôle est maintenant secondaire.

Ce travail a été effectué en collaboration avec A. Marzoli (Universita di Padova, Italie), G. Bellieni (Universita di Padova, Italie), H. Bertrand (ENS Lyon, France), F. Jourdan (Curtin University), M. Chiaradia (Université de Genève, Suisse) et L. Reisberg (CRPG-Nancy, France).

(4) Géochronologie, évolution pétrogénétique et caractérisation isotopique des laves alcalines de la ride Tore-Madère (Atlantique nord-est, marge ibérique). L'objectif de ce projet est de déterminer si le volcanisme sous-marin de la ride Tore-Madère est lié à l'ouverture de l'océan Atlantique ou à l'activité d'un point chaud (potentiellement celui de Madère). Ce projet est la continuité de mes travaux de thèse. Les premiers résultats de cette étude, sur les roches différenciées, ont été publiés en 2006 dans *Geochimica Cosmochimica Acta*. Cette étude est maintenant orientée vers l'interprétation de données isotopiques Sr-Nd-Pb acquises sur des basaltes et des âges $^{40}\text{Ar}/^{39}\text{Ar}$ obtenus sur des roches qui n'avaient pas été étudiées jusqu'à présent, l'identification des sources des magmas de la ride Tore-Madère et les possibles liens génétiques entre cette ride, le magmatisme alcalin du sud-ouest du Portugal et l'archipel de Madère.

Cette étude inclut aussi un volet plus minéralogique et pétrogénétique qui se concentre sur les conditions de cristallisation (géobarométrie et géothermométrie), l'évolution chimique des laves au cours du temps et les processus dans la chambre magmatique (contamination, mélanges). Cette étude est toujours en cours et comporte l'analyse de la texture des roches, des éléments majeurs dans les principales phases minérales par microsonde électronique, des éléments en trace dans les pyroxènes et plagioclases par ICP-MS à ablation laser, l'analyse des roches totales et la modélisation géochimique des processus pétrogénétiques. Collaboration avec F. Jourdan (Curtin University), J. Girardeau (Université de Nantes, France), A. Marzoli (Universita di Padova, Italie), M. Chiaradia (Université de Genève, Suisse) et A. Zanetti (Universita di Pavia, Italie).

(5) Géochronologie et géochimie du magmatisme basaltique crétacé de la marge passive de l'Australie Occidentale. Le but de cette étude est de contraindre de manière précise l'âge et l'origine des basaltes par l'acquisition d'âges ultra-précis (0,1%) par la méthode $^{40}\text{Ar}/^{39}\text{Ar}$ et leur caractéristiques pétro-géochimiques. En effet, jusqu'en 2015, aucune donnée géochronologique fiable n'existe pour ce magmatisme et les relations entre celui-ci et l'activité du point chaud des Kerguelen et le rifting de la lithosphère continentale du Gondwana étaient spéculatives. Cette étude est l'extension de la thèse de H. Olierook (Curtin University).

Ce projet est mené en collaboration avec H. Olierook et F. Jourdan (Curtin University).

Partie II : Thématique de recherche principale : le magmatisme intra-plaque des marges passives (synthèse)

J'ai développé cette thématique de recherche à la suite de mes travaux de thèse sur le magmatisme intra-plaque de la ride Tore-Madère. Mes différentes expériences professionnelles suivantes m'ont permis de travailler sur le magmatisme de la CAMP et de la marge de l'Australie occidentale tout en continuant à étudier le magmatisme des marges conjuguées Ibérie-Terre Neuve. Grace à plus de dix ans de travail sur ces trois chantiers j'ai pu :

- (1) construire une vision synthétique du magmatisme intra-plaque des marges conjuguées Ibérie-Terre Neuve,
- (2) établir des similitudes entre les marges passives Ibérie-Terre Neuve et d'Australie occidentale en termes de magmatisme et d'évolution géodynamique,
- (3) acquérir une vision critique des modèles publiés concernant les relations entre le magmatisme intra-plaque et l'évolution géodynamique des marges passives et
- (4) par conséquent proposer un programme de recherche nouveau basé sur des données plus fiables.

Ces quatre points sont exposés et développés dans la synthèse qui suit.

1. Problématique

Comme la physique nucléaire au début du XX^e siècle avec la théorie de la relativité générale, la géologie est entrée dans une nouvelle ère avec la formulation de la théorie de la tectonique des plaques au milieu des années 1960 (par ex., Wilson, 1963a). Cette théorie a ainsi permis d'expliquer un grand nombre de processus géologiques, notamment le magmatisme intraplaque grâce au concept de panache mantellique profond (initié par Wilson, 1963b). Cependant, le développement des moyens analytiques (instruments plus précis, plus fiables, plus rapides en termes de temps d'acquisition, techniques chimiques plus efficaces et plus rapides) depuis environ 25 ans, a permis l'acquisition d'une énorme base de données géochimiques et géochronologiques dont certaines mettent en évidence des manifestations magmatiques dont la distribution spatiale ou temporelle ne peut s'expliquer facilement dans le cadre de la théorie des panaches mantelliques. Se pose alors la question de la fiabilité des modèles, mais aussi des données anciennes sur lesquelles sont bâtis la plupart des modèles existants.

Dans ce mémoire, la contribution des panaches mantelliques dans l'extension et la fracturation de la lithosphère continentale, processus majeur dans la tectonique des plaques, est débattu grâce à l'étude des caractéristiques chimiques et de la distribution spatiale et temporelle du magmatisme intraplaque associé à la formation des marges passives.

1.1. Panaches mantelliques et extension continentale

Dans le cadre de la théorie unificatrice de la tectonique des plaques, le modèle des panaches mantelliques profonds (conceptualisés par des remontées de matériel issu du manteau inférieur et plus chaud que le manteau environnant, qui perforent la lithosphère pour s'exprimer en surface sous la forme d'un volcan) a été universellement adoptée pour expliquer le magmatisme intra-plaque aussi bien continental qu'océanique (Wilson,

1963b ; Morgan, 1971, 1972). Le modèle actuel des panaches mantelliques a été en grande partie inspiré de l'étude de la chaîne volcanique partiellement immergée Hawaii-Empereur, dont les âges diminuent vers les volcans actifs de l'archipel hawaiien. Le volcan actif représentant l'expression en surface du panache mantellique est généralement nommé point chaud. Cet alignement est l'expression du mouvement de la plaque océanique du Pacifique passant au-dessus du panache mantellique (Wilson, 1963b). Selon le modèle actuel, les panaches mantelliques profonds ont une durée de vie de plus de 100 millions d'années (par ex. Steinberger, 2000) et un diamètre de tête de l'ordre de 1000 km (Campbell, 2007).

Depuis l'étude de Forsyth et Uyeda (1975) sur les forces susceptibles d'être responsable du mouvement des plaques tectoniques, il semble établi que la convection du manteau supérieur ne peut être le principal moteur de la tectonique des plaques. En d'autres termes, les forces exercées par la convection du manteau sur les plaques lithosphériques ne seraient pas suffisamment puissantes pour fracturer celles-ci. Pour expliquer la fragmentation continentale qui est l'élément majeur de la tectonique des plaques, le modèle de panache mantellique profond a donc été proposé : il explique la dislocation des super-continents par l'éirement de la lithosphère continentale qui conduit ultimement à la formation d'une nouvelle lithosphère océanique (modèle dit de rifting actif, Fig. 1a). Ce processus de dislocation des super-continents est expliqué par l'impact de la tête d'un panache mantellique profond, apportant à la base d'une lithosphère, la chaleur nécessaire pour l'affaiblir mécaniquement puis la fracturer par l'effet de la remontée de matière. Ceci est en accord avec la présence de magmatisme intra-plaque très abondant sur les marges de divergence (Courtillot et al., 1999). Néanmoins, ce modèle de rifting n'est pas complètement admis et des modèles alternatifs (par ex. Turcotte et Oxburg, 1976 ; White et McKenzie ; 1989 ; Anderson, 1994 ; Foulger, 2007) ont été proposés dans lesquels le panache mantellique n'a pas de rôle actif dans l'extension lithosphérique (modèle dit de rifting passif, Fig. 1b).

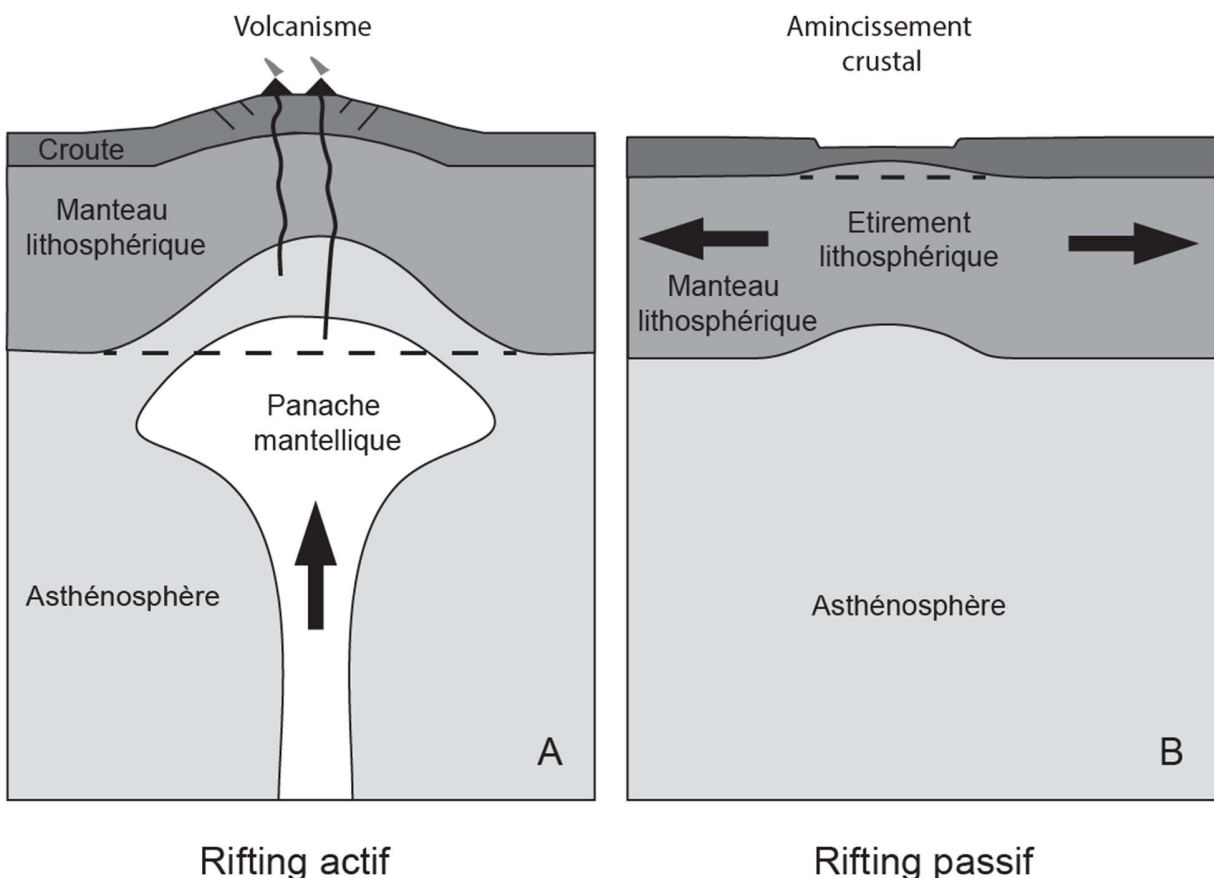


Figure 1 : Schémas illustrant les prémisses de l'amincissement de la lithosphère, continentale selon la présence ou non d'un panache mantellique (rifting actif : A ; rifting passif : B). Adapté d'après Merle, 2011.

1.2. Magmatisme intra-plaque des marges passives

Les deux modèles d'extension lithosphérique évoqués précédemment ont été établis sur la base d'interprétations expliquant l'abondance, la distribution spatiale et temporelle ainsi que les caractéristiques pétrologiques et géochimiques du magmatisme intra-plaque que l'on trouve sur certaines marges passives. Ils constituent donc la base théorique pour les modèles qui visent à expliquer la formation d'un certain nombre de marges passives actuelles et de leur classification en deux classes. En pratique, cette classification est essentiellement basée sur le volume du magmatisme présent sur la marge.

Dans un modèle d'extension lithosphérique impliquant un panache mantellique (rifting actif), l'étirement continental serait initié par l'impact de la tête du panache sous la lithosphère continentale. Dans ce cas, le modèle prédit l'émission d'importants volumes de produits basaltiques : mise en place sous la forme de successions de coulées de plusieurs centaines de mètres d'épaisseur, d'intrusions de plusieurs kilomètres de diamètre, et/ou de dykes de plusieurs dizaines de kilomètres de long. Ce phénomène se produirait dès les premiers stades de l'étirement de la lithosphère continentale. Les

magmas émis sont de type basaltique tholéïtique (tholéïites continentales) et constituent une grande province magmatique (ou LIP pour « Large Igneous Provinces » de type « Continental Flood Basalt » ou CFB).

L'émission de magmas est quasi continue pendant le processus d'étirement lithosphérique et se poursuit jusqu'à l'initiation de l'expansion océanique et la formation du plancher océanique, qui marque la fin du rifting continental. L'activité magmatique se poursuit par un magmatisme intra-plaque océanique caractérisé par la formation de petits groupes de monts sous-marins. Cette activité est mise en évidence par la présence d'une chaîne de monts sous-marins qui devrait en théorie avoir des âges décroissants depuis la grande province magmatique jusqu'à un volcan actif. Ceci se vérifie par exemple pour le point chaud de Tristan da Cunha (Fig. 2).

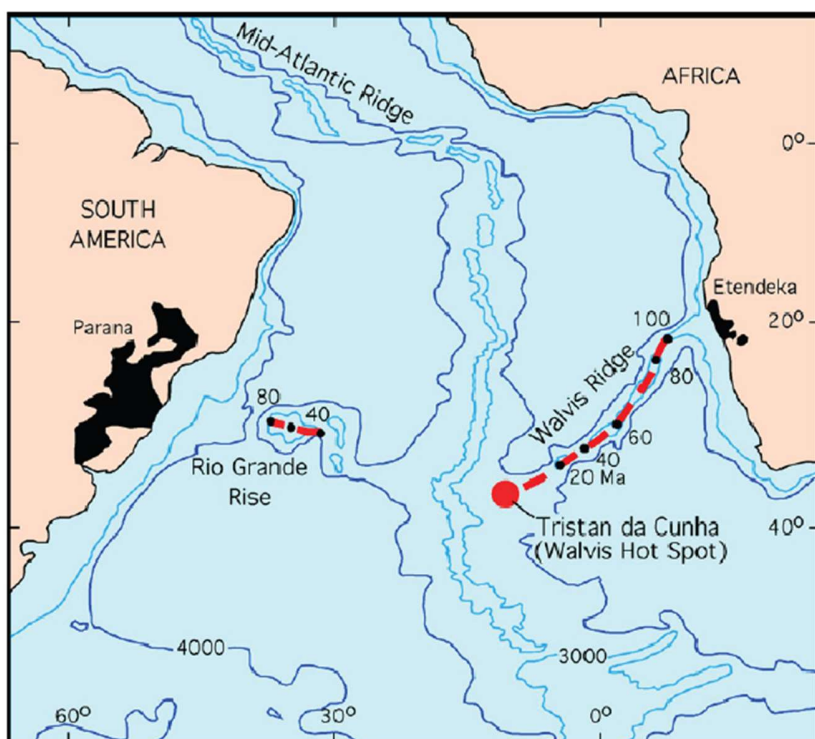


Figure 2 : Schéma montrant l'impact du panache de Tristan da Cunha sur les plaques africaines et sud-américaine. L'impact initial de la tête du panache au tout début du rifting forme le CFB “Parana-Etendeka”. La divergence océanique entraîne la fracturation du CFB en deux parties situées sur chaque plaque, la tige du panache formant des volcans sous-marins d'âge croissants depuis le CFB jusqu'au point chaud (actuel) de Walvis. D'après Campbell, 2007.

De ce fait, un continuum en termes de caractéristiques géochimiques, en particulier de compositions isotopiques Sr-Nd-Pb, devrait être observé depuis les compositions des tholéïites continentales du LIP jusqu'à des compositions de type OIB (pour Oceanic Island Basalts, désignant les magmas intraplaques issus de la fusion du matériel du panache) dans les laves de la chaîne de monts sous-marins et du point chaud.

Du fait que ces marges sont marquées par de très gros volumes de produits magmatiques (laves et roches intrusives), elles ont été dénommées marges passives volcaniques. Les exemples classiques de marges passives volcaniques sont par exemple les marges de l'est du Groenland et des îles Britanniques formant la province volcanique de l'Atlantique Nord qui est liée à l'activité du point chaud de l'Islande (Coffin et Eldholm, 1994). Ce sont aussi les marges du sud du Brésil et de la Namibie qui sont recouvertes par les basaltes de la grande province magmatique de Parana-Etendeka qui est reliée au point chaud de Tristan da Cunha par la dorsale de Walvis (Campbell, 2007). Un autre exemple est celui des marges de la Mer Rouge qui sont recouvertes par les basaltes tholéitiques de la grande province magmatique Ethiopie-Yemen liée au point chaud de l'Afar (Coffin et Eldholm, 1994).

L'autre catégorie de marge passive est au contraire caractérisée par un magmatisme peu abondant. Ce modèle de marge correspond aux marges dites amagmatiques ou non-volcaniques : le magmatisme associé à une « LIP » est absent et l'activité magmatique est limitée à la phase la plus intense d'amincissement lithosphérique (magmatisme syn-rift). Le magmatisme de la phase principale de rifting est volumétriquement faible, essentiellement représenté par des coulées de faible épaisseur et des intrusions n'excédant pas quelques kilomètres de diamètre. Ce magmatisme d'affinité alcaline se caractérise par une grande variété de types pétrographiques allant des basaltes alcalins aux trachytes et rhyolites et à leurs équivalents plutoniques (gabbros et granites). Vers la fin du rifting et juste avant l'initiation de l'expansion océanique, on peut observer une évolution des caractéristiques chimiques des magmas syn-rift vers des affinités de type MORB (pour Mid Ocean Ridge Basalt, basaltes issus de l'asthénosphère) qui est le magmatisme des dorsales océaniques (par ex. sur la marge ibérique ; Charpentier et al., 1998).

Sur ce type de marge, la présence d'un panache mantellique n'est pas requise pour générer le magmatisme pendant la phase d'amincissement lithosphérique. Cependant, un magmatisme intra-plaque peut se manifester soit sur la marge soit sur les domaines océaniques et continentaux adjacents après l'initiation de l'expansion océanique, ce magmatisme pouvant être l'expression d'un panache mantellique. D'après ce modèle, l'activité de ce panache mantellique est postérieure aux processus d'étirement lithosphérique, à son magmatisme associé (magmatisme syn-rift) et à l'initiation de l'expansion oceanique, et de fait sans connexion avec ceux-ci.

1.3. Les limites des modèles existants

Ces deux modèles de formation de marge passives ont été proposés il y a près de quarante ans à partir de l'étude d'exemples naturels (Coffin et Eldholm, 1994). Cependant, certaines de ces études sont basées sur un nombre limité d'échantillons, parfois analysés avec des méthodes et techniques qui sont désormais obsolètes (par ex. K/Ar, Verati et Jourdan, 2014). D'une manière générale, l'implication des panaches mantelliques dans le déclenchement de l'extension continentale et comme source du magmatisme des CFBs reste un sujet largement débattu par la communauté scientifique depuis plus de 30 ans (voir www.mantleplumes.org). De plus, les processus alternatifs

proposés pour expliquer le déclenchement du rifting continental sans recourir à un panache mantellique profond, comme les forces de tension aux frontières des plaques, ne peuvent expliquer la présence de grandes provinces magmatiques sur plusieurs marges passives.

Les études menées sur certaines marges au cours des vingt dernières années ont bénéficié de l'amélioration des techniques analytiques géochimiques et géochronologiques, permettant l'analyse, plus rapide et plus précise d'un plus grand nombre d'échantillons, ce qui a conduit à mettre en évidence les limites des modèles existants. Grâce à ces nouvelles données géochimiques et géochronologiques, l'examen attentif de l'âge et de la distribution spatiale du magmatisme sur de nombreuses marges passives révèle qu'elles divergent toutes plus ou moins sensiblement des définitions des marges passives volcaniques et des marges passives non-volcaniques. Ce fait va être illustré grâce à deux exemples de marges passives.

2. Etudes de cas : le magmatisme intraplaque sur les marges ouest-ibérique et ouest-australienne

Des études récentes font émerger une image complexe des marges divergentes non-magmatiques, notamment au vu du volume du magmatisme sur les marges conjuguées Ibérie-Terre Neuve. Ces marges conjuguées, situées le long des côtes du Portugal et du Maroc à l'est, des Etats-Unis et de Terre-Neuve à l'ouest, ont longtemps été considérées comme l'archétype des marges non-magmatiques. Elles sont cependant marquées par un magmatisme intra-plaque important, représenté par un « CFB » (par ex. Marzoli et al., 1999) et d'importants groupes de monts sous-marins (Merle et al., 2006, 2009).

Ces travaux tendent à montrer que les marges historiquement considérées comme pauvres en magmatisme ne le sont pas forcément, et ont constitué le point de départ de la réflexion de ce mémoire. Il était dès lors fondé de penser que l'occurrence d'un magmatisme abondant sur une marge de divergence n'était probablement pas unique et pourrait avoir d'autres équivalents. C'est effectivement le cas de la marge sud-ouest de l'Australie Occidentale (« Western Australia », WA). En effet, les marges Ibérie-Terre Neuve et WA partagent des similitudes en termes d'évolution structurale et d'activité magmatique :

(1) Un très faible volume de magmas produits au cours de la phase principale de rifting (par ex. Boillot et al., 1989 ; Beslier et al., 2004 ; Manatschal, 2004 ; Jagoutz et al., 2007 ; Gillard et al., 2015).

(2) Le rifting très lent de la lithosphère continentale entraînant l'exhumation du manteau sub-lithosphérique qui affleure aujourd'hui localement sous une couche de sédiments (par ex. Boillot et al., 1989 ; Beslier et al., 2004 ; Manatschal, 2004 ; Sutra et al., 2013 ; Nirrengarten et al., 2018).

(3) Une activité magmatique intra-plaque océanique initiée immédiatement après le début de l'expansion océanique (Merle 2006, 2009 ; Grange et al., 2010 ; Olierook et al, 2015a).

2.1. Les marges conjuguées Ibérie-Terre Neuve

Les marges conjuguées de l'Ibérie-Terre-Neuve se sont formées par étirement lithosphérique, suivi du rifting qui a conduit à la séparation des plaques Ibérie et Amérique du Nord (par ex. Féraud et al., 1988 ; Boillot et al., 1989 ; Manatschal, 2004 ; Fig. 3) durant le Crétacé (~ 200-125 Ma).

Historiquement, ces marges ont été considérées comme non-magmatiques car seul le magmatisme lié à la phase principale de rifting (magmatisme syn-rift) avait été documenté. Cependant, les travaux de Marzoli et al. (1999) ont montré que de nombreuses manifestations magmatiques sur la côte est des Etats Unis et au Portugal, considérés alors comme des manifestations magmatiques sans relation entre elles, faisaient partie d'une seule et même grande province magmatique (Central Atlantic Magmatic Province ou CAMP) mise en place vers 200 Ma donc au tout début de la dislocation de la Pangée.

Plus récemment, à partir de 2006, les travaux géochronologiques sur les monts sous-marins de la ride Tore-Madère ont mis en évidence une autre phase de magmatisme intra-plaque méconnue jusqu'alors et postérieure à l'initiation de l'expansion océanique (Geldmacher et al. 2006 ; Merle et al., 2006).

De fait, une synthèse des travaux menés depuis environ vingt ans sur le magmatisme intra-plaque de cette marge, permet de constater la présence de trois phases de magmatisme bien distinctes en termes d'âge et de caractéristiques géochimiques.

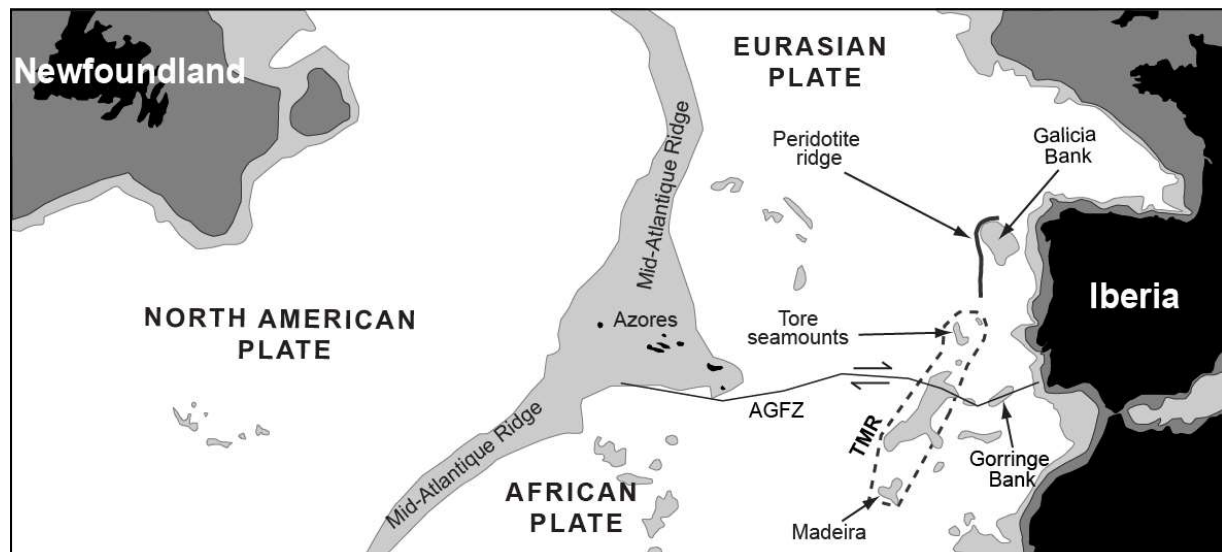


Figure 3 : Carte schématique de la partie nord de l'océan Atlantique montrant les marges conjuguées de l'Ibérie et de Terre-Neuve. Les principaux reliefs sous-marins sont aussi représentés. TMR : Tore-Madeira Rise (ride Tore-Madère). D'après Merle et al., 2012.

Première phase : ~201-190 Ma

La phase la plus ancienne datée à environ 201 Ma (Marzoli et al., 2011) est maintenant connue comme la Province Magmatique Centrale Atlantique (ou CAMP ; Marzoli et al., 1999 ; Fig. 4), qui s'est mise en place au cours d'un épisode magmatique relativement

bref avec une phase principale d'activité qui aurait duré environ un million d'années et dont les dernières manifestations seraient autour de 190 Ma (Marzoli et al., 2011; Blackburn et al., 2013; Davies et al., 2017). Cette phase magmatique est caractérisée par un énorme magmatisme basaltique tholéïtique (environ 10^6 km 3) mis en place sous forme de coulées épaisses, sills et dykes de plusieurs dizaines de kilomètres de long que l'on retrouve sur les marges en Nouvelle-Ecosse (Canada), aux US (Connecticut, New Jersey et Virginie), au Portugal et en France (par ex. Marzoli et al., 1999 ; McHone, 2003).

De nombreuses données géochronologiques ($^{40}\text{Ar}/^{39}\text{Ar}$, U-Pb) et une grande variété de données géochimiques (éléments majeurs et en trace, rapports isotopiques Sr-Nd-Pb-Os) ont été publiées sur les roches CAMP depuis plus de trente ans. Récemment, les âges, Ar/Ar en particulier, ont été revisités et filtrés avec attention (par ex. Jourdan et al., 2009), notamment pour répondre à des questions liées à la calibration des étages de l'échelle stratigraphique internationale et leur potentielle conjonction avec des épisodes d'extinction (par ex. Blackburn et al., 2013).

Les roches basaltiques de la CAMP présentent toutes les caractéristiques de tholéïites continentales c'est-à-dire : (1) des spectres d'éléments en trace incompatibles enrichis par rapport aux MORBs en éléments les plus incompatibles et les plus solubles (K, Rb, La, U, Ba, Ce) ; (2) des anomalies positives en Pb et négatives en Nb dans ces mêmes spectres élémentaires ; (3) des rapports Sr-Nd-Pb différents des MORBs avec des rapports $^{207}\text{Pb}/^{204}\text{Pb}$ et $^{208}\text{Pb}/^{204}\text{Pb}$ et $^{87}\text{Sr}/^{86}\text{Sr}$ élevés pour des rapports $^{206}\text{Pb}/^{204}\text{Pb}$ et $^{143}\text{Nd}/^{144}\text{Nd}$ faibles.

Ces caractéristiques ont été interprétées comme une preuve de la contamination de magmas issus d'un panache mantellique par la croûte continentale (par ex. Cebria et al., 2003) alors que d'autres travaux proposaient plutôt une signature de type lithosphère mantellique (par ex. Alibert, 1985 ; McHone, 2000). Les études récentes utilisant le système isotopique Re-Os (Callegaro et al., 2013 ; Merle et al., 2014) ont permis d'exclure toute contamination à grand échelle des magmas CAMP par la croûte continentale. De fait, l'implication d'un panache mantellique dans la genèse de la CAMP reste discutée (par ex. Merle et al., 2014).

Seconde phase : 148~112 Ma

La deuxième phase magmatique dans l'Atlantique Nord-Est s'est produite entre environ 148 et 121 Ma (Schärer et al., 2000 ; Grange et al., 2008 ; Mata et al., 2015) soit environ 50 millions d'années après l'événement CAMP. Ce magmatisme est lié à la principale phase de distension de la lithosphère continentale (magmatisme syn-rift). Cette phase s'est achevée vers 125 Ma avec le début de l'activité de la dorsale atlantique, selon les anomalies magnétiques les plus anciennes identifiées dans les bassins océaniques situés à l'ouest et au sud-ouest du Portugal (par ex. Olivet, 1996 ; Verhoef et al., 1996). Cependant il n'existe aucun consensus concernant le début de l'activité de la dorsale atlantique qui aurait pu également débuter vers 112 Ma (Jagoutz et al., 2007 ; Péron-Pinvidic et al., 2007 ; Tucholke et al., 2007 ; Nirrengarten et al., 2017).

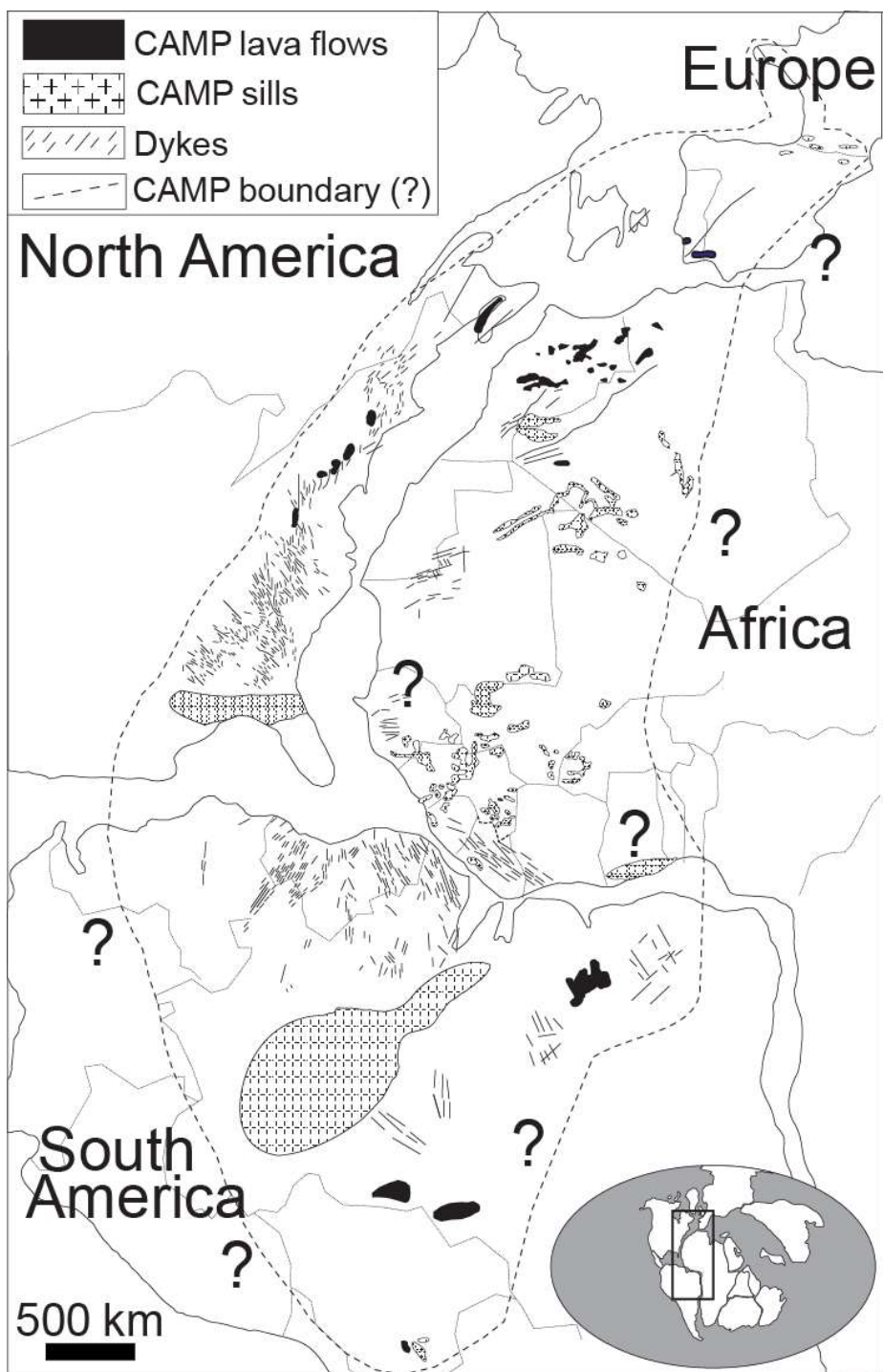


Figure 4 : Distribution spatiale des occurrences magmatiques de la CAMP (Central Atlantic Magmatic Province) vers 200 Ma. Dans l'hypothèse d'une origine liée à un panache mantellique profond, l'impact initial aurait eu lieu dans une zone située à la conjonction de la pointe de la Floride, du Guyana et de la Guinée. D'après Merle et al., 2014 et références incluses.

Cette phase se présente sous la forme de petits volumes de magmas, essentiellement des petites intrusions d'une grande variété de types pétrographiques (trachyandésites, dolérites, diorites), localisées dans le sud-ouest du Portugal et sur la partie submergée de la lithosphère amincie de l'Ibérie (Charpentier et al., 1998 ; Schärer et al., 2000 ; Grange et al., 2008 ; Miranda et al., 2009 ; Mata et al., 2015). Ces roches ont une affinité chimique allant d'alcaline à tholéïtique (Charpentier et al., 1998). L'âge de cette phase magmatique a longtemps été confondu avec celle de la CAMP (Pinheiro et al., 1996) en raison de données géochronologiques peu fiables obtenus par la méthode K-Ar sur roche totale (par exemple Ferreira et Macedo, 1983) ; méthode qui présente le désavantage de produire des âges potentiellement biaisés par les effets de l'altération des roches.

Les données géochimiques obtenues sur les roches de cette deuxième phase magmatique sont rares surtout pour les roches échantillonnées en domaine océaniques (comme par exemple les laves provenant du banc de Galice, Charpentier et al., 1998). De plus, les rapports isotopiques du Sr et surtout du Pb n'ont pas été systématiquement mesurés, ce qui complique les interprétations et les comparaisons entre les différentes phases magmatiques. Néanmoins, les rapports isotopiques Sr-Nd-Pb publiés suggèrent une interaction complexe entre différents composants de la croûte continentale, le manteau lithosphérique sous-continentale et l'asthénosphère (Charpentier et al., 1998 ; Grange et al., 2008 ; Mata et al., 2015).

Troisième phase : depuis 103 Ma

Cette phase correspond à la construction de la Ride Tore-Madère (Tore-Madeira Rise, TMR), de plusieurs monts sous-marins dans son voisinage (Seine, Ampère, Ormonde) et à la mise en place en domaine continental de petits volumes de roches effusives et intrusives alcalines au sud-ouest du Portugal (Geldmacher et al., 2006 ; Merle et al., 2006, 2009 ; Miranda et al., 2009 ; Grange et al., 2010). TMR représente probablement l'objet le plus important de cette phase magmatique. En effet, TMR est un haut fond océanique de plus de 1000 km de long et de 50 à 70 km de large, situé à 300 km au large des côtes atlantiques du Portugal et du Maroc. TMR est formé par une douzaine de monts sous-marins qui s'étalent depuis le complexe de Tore jusqu'à l'archipel de Madère et dont l'alignement franchit sans décalage visible la faille Açores-Gibraltar (Fig. 5) qui est considérée comme la frontière actuelle entre les plaques Afrique et Eurasie. Jusqu'à l'étude de Merle et al. (2006), la nature des roches formant TMR, et donc l'origine de ce relief, étaient inconnues.

Cette période magmatique aurait débuté vers 103 Ma (Merle et al., 2006, 2009 ; Fig. 5) c'est-à-dire après le début de l'extension océanique de la dorsale atlantique. Elle s'est ensuite poursuivie et continue encore aujourd'hui dans l'archipel de Madère à l'extrémité de TMR. L'extension temporelle et spatiale de cette phase magmatique n'a été identifiée que récemment avec la mise en évidence (i) d'un magmatisme alcalin post-océanisation formant TMR (Geldmacher et al., 2006 ; Merle et al., 2006) et (ii) d'un lien génétique entre TMR et le magmatisme du Portugal (Geldmacher et Hoernle, 2000 ; Geldmacher et al., 2000 ; Merle et al., 2009 ; Grange et al., 2010) qui était déjà en partie documenté (par ex. Rock, 1978).

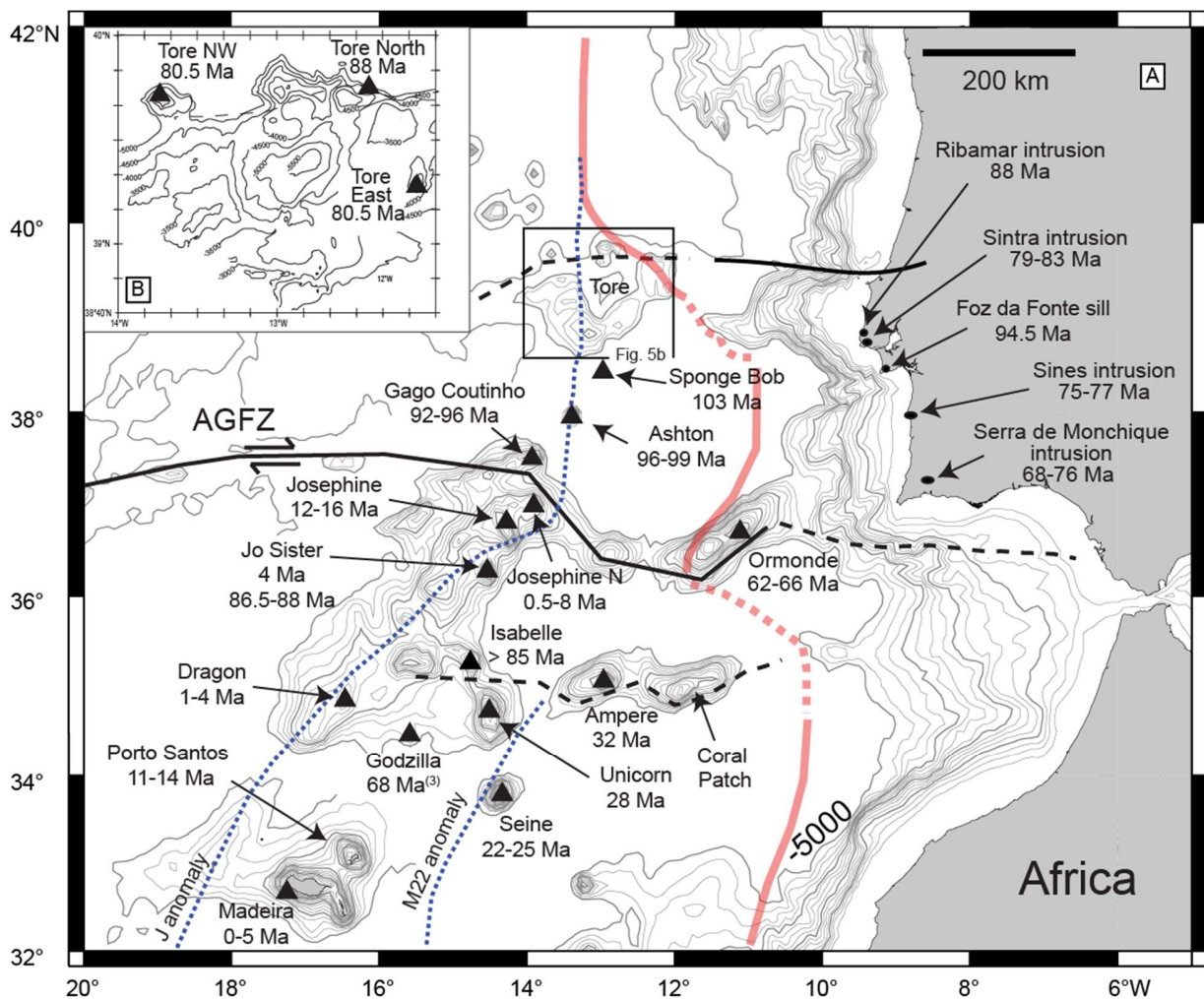


Figure 5 : Distribution spatiale et temporelle du magmatisme de la région de TMR et du Sud-Ouest du Portugal. (A) : carte bathymétrique de la région de TMR. Les principales structures de la marge (faille Açores-Gibraltar et autres failles lithosphériques), limite domaine océanique-domaine continental (ligne rouge) ainsi que les anomalies magnétiques sont représentées. Les âges obtenus sur les différents volcans sont aussi indiqués. (B) : détail de la bathymétrie du complexe de Tore avec les âges obtenus sur trois édifices. Ages d'après Merle et al., soumis et références incluses. Bathymétrie de Tore d'après Sanchez et al., en préparation.

Sur TMR et les monts sous-marins voisins, les roches volcaniques draguées ont une affinité modérément alcaline (roches saturées ou faiblement sous-saturées en silice). Les types pétrographiques vont des basaltes alcalins et basanites aux trachytes (Geldmacher et al., 2006 ; Merle et al., 2005 ; 2006 ; 2009). Au sud-ouest du Portugal, les roches liées à cette phase magmatique (roches volcaniques de semi-profondeur et intrusives) ont une affinité alcaline à fortement alcaline (roches sous-saturées en silice, comme les syénites néphéliniques du massif de Monchique). Les types pétrographiques vont des basaltes et

gabbros à trachytes, syénites et granites (Bernard-Griffiths, 1997 ; Grange et al., 2010 ; Miranda et al., 2009).

Depuis plus de trente ans, les monts sous-marins de TMR, Seine, Ampère, Ormonde et les manifestations magmatiques du Sud-Ouest du Portugal ont été datés par plusieurs méthodes sur roche totale (K-Ar, $^{40}\text{Ar}/^{39}\text{Ar}$ et Rb-Sr) et minéraux (K-Ar, $^{40}\text{Ar}/^{39}\text{Ar}$ et U-Pb). Cependant, jusqu'aux études géochronologiques de Geldmacher et al. (2006) et Merle et al. (2006), l'âge des roches de TMR était très mal défini, comprenant seulement quelques datations K-Ar sur roche totale, qui avait été effectuées sur des roches draguées, donc peu fiables, sur le mont Joséphine (Wendt et al., 1976). D'autre part, à l'échelle de cette province, de grandes variations d'âges, certains avec de larges incertitudes, existaient entre les données obtenues par des techniques différentes sur des roches provenant du même massif et pétrologiquement similaires. Par exemple, les datations K-Ar sur roche totale obtenues sur les gabbros de Sintra au Portugal sont plus jeunes de huit millions d'années ($74,9 \pm 1$ Ma ; Storetvedt et al., 1987) que celles obtenus par la méthode U-Pb sur zircon ($83,4 \pm 0,7$ Ma ; Grange et al., 2010). Ces analyses ont été compilées et filtrées par Merle et al. (2009) pour éliminer les données peu fiables. La base de données résultante montre une phase de magmatisme entre 88 Ma et 69 Ma au Portugal et trois phases sur TMR et les monts sous-marins voisins (103-80 Ma, 68-60 Ma et 32-0 Ma).

Certaines études géochronologiques ont suggéré la présence d'une progression d'âge depuis le continent (Serra de Monchique : 70-69 Ma) vers l'archipel de Madère (5-0 Ma) en passant par les monts sous-marins Ormonde (65-62 Ma), Ampère (~32 Ma) et Seine (Geldmacher et al., 2000 ; D'Oriano et al., 2010). Ces auteurs interprètent cet alignement volcanique comme le résultat du passage de la plaque ibérique au-dessus du panache de Madère, qui serait donc la source principale du magmatisme de TMR. Cependant cette interprétation ne tient pas compte du magmatisme au nord de la faille Açores-Gibraltar, c'est-à-dire des monts sous-marins de la partie nord de TMR et des manifestations magmatiques continentales situées au nord de Monchique (Fig. 5). Si ces derniers sont considérés, il n'y a plus vraiment de progression d'âge sur l'ensemble de la région mais seulement localement sur quelques petits alignements magmatiques d'environ 150 km de long (Merle et al., 2009).

Le magmatisme de TMR possède des caractéristiques géochimiques typiques du magmatisme océanique intraplaque (magmatisme de type OIB), c'est-à-dire (1) des spectres en éléments en trace incompatibles très enrichis par rapport aux MORBs, (2) des anomalies positives en Nd et négatives en Pb et (3) des rapports isotopiques Sr-Nd-Pb proches des compositions observées pour les archipels de Madère et des Canaries (Bernard-Griffith et al., 1997 ; Geldmacher et al., 2006).

Les roches de la Serra de Monchique au Portugal, des monts sous-marins Ormonde, Ampère et Seine seraient dérivées de la même source que l'archipel de Madère, mais contaminées par la lithosphère continentale (Geldmacher et Hoernle, 2000). Cette contamination serait plus importante à Monchique où la croûte continentale est la plus épaisse puis diminuerait progressivement à mesure que le point chaud de Madère se

déplace vers le sud-ouest sous une lithosphère continentale amincie puis sous la lithosphère océanique. Les rapports isotopiques mesurés sur des minéraux extraits de roches de TMR et du Portugal ont été interprétés comme résultants de la contamination par le manteau lithosphérique sous-continentale, de magmas issus d'une source de type panache mantellique (i.e. manteau enrichi par rapport à une source purement asthénosphérique) mais dont l'origine reste inconnue (Merle et al., 2006 ; Grange et al., 2010). Les roches de la partie sud de TMR mises en place au cours du Crétacé ont des signatures isotopiques proches de celles de l'archipel des Canaries alors que celles mises en place au cours du Tertiaire ont des signatures isotopiques proches des roches de l'archipel de Madère (Geldmacher et al., 2006).

L'origine du magmatisme de TMR et du sud-ouest du Portugal reste encore actuellement mal comprise. Les premières hypothèses sur la formation de TMR suggéraient soit (i) l'implication d'un point chaud (Pierce et Barton, 1991), soit (ii) l'accumulation de magmas sous la lithosphère continentale juste avant la rupture continentale. L'émission soudaine de ces magmas marquerait le véritable début de l'activité de la dorsale atlantique, TMR constituant ainsi la première croûte océanique formée par cette dorsale (Tucholke et Ludwig, 1982 ; Olivet, 1996 ; Girardeau et al., 1998), potentiellement en présence d'un panache mantellique (Tucholke et Ludwig, 1982 ; Pierce et Barton, 1991). Cependant aucune de ces hypothèses n'utilise des données géochronologiques ou géochimiques. Elles considéraient ce magmatisme comme un phénomène complètement dissocié de celui du Portugal, bien que ce dernier était interprété comme résultant du mouvement de la plaque Ibérique et de l'ouverture du golfe de Gascogne (Rock, 1978 ; Whitmarsh et al., 1986).

D'autres hypothèses existent, basées notamment sur les données géochimiques et géochronologiques. La première invoque le passage successif du panache des Canaries au Crétacé puis de celui de Madère au Tertiaire (Geldmacher et al., 2006), ce dernier expliquant aussi la progression d'âge depuis Monchique jusqu'à l'archipel de Madère (Geldmacher et al., 2006 ; D'Oriano et al., 2010). La seconde lie ce phénomène à un magmatisme alcalin mis en place au tout début du fonctionnement de la dorsale atlantique mais décalé de l'axe d'accrétion et antérieur à la production de magmas de type MORB (Jagoutz et al., 2007). Enfin, la troisième relie le magmatisme de TMR à une anomalie thermique active depuis 103 Ma qui aurait produit des pulses de magmas au cours du temps (Merle et al., 2009). L'interaction de cette anomalie thermique avec les mouvements de la plaque ibérique aurait induit cinq phases magmatiques sur TMR, les monts sous-marins Ormonde, Ampère et Seine et au sud-ouest du Portugal où alternent les phases avec une progression d'âge et celles avec une distribution spatiale aléatoire du magmatisme (Merle et al., 2009 ; Fig. 6).

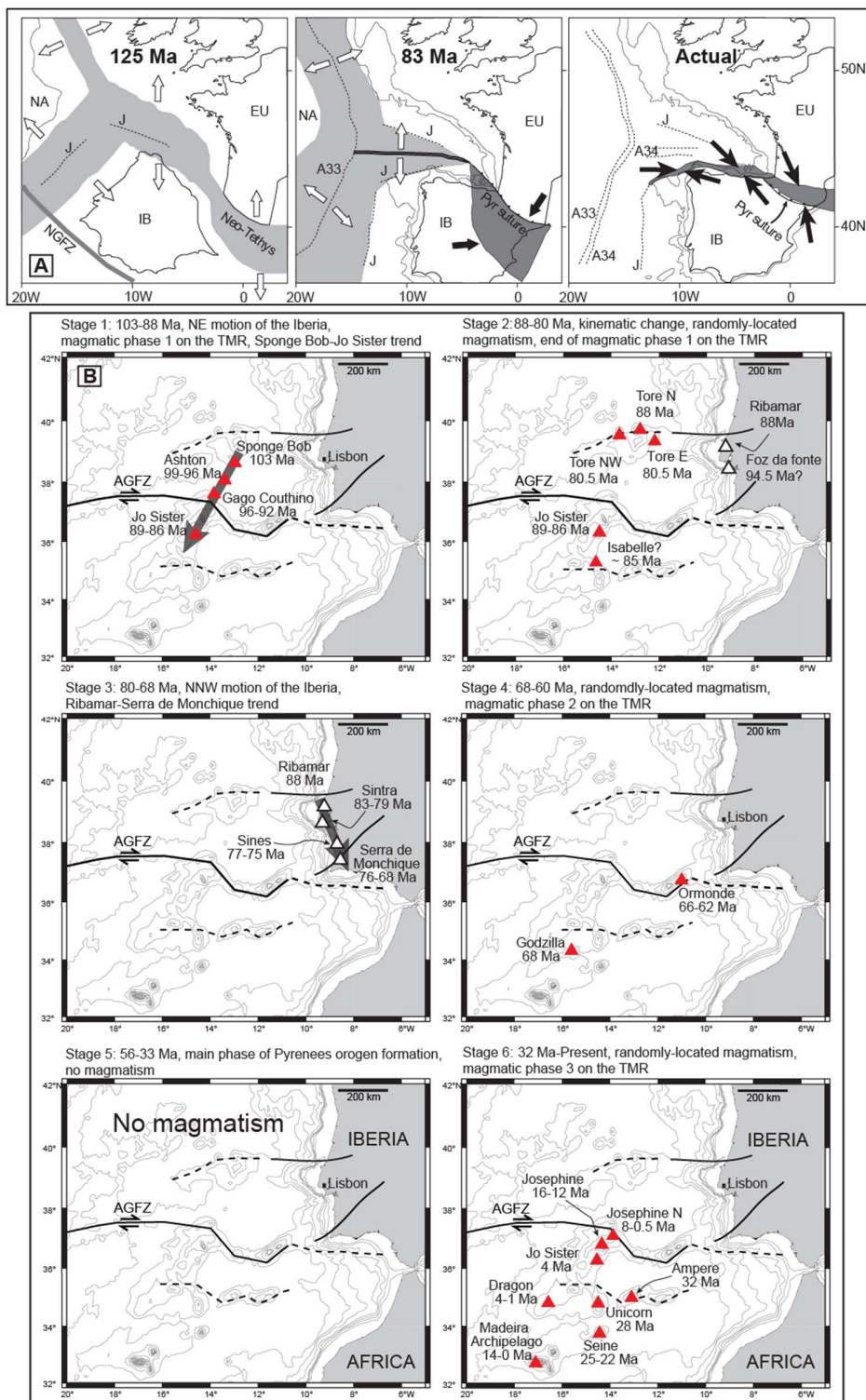


Figure 6 : Schémas montrant la corrélation entre les différentes phases magmatiques sur TMR, les monts sous-marins en périphérie et au SO du Portugal et les mouvements de la plaque ibérique entre 103 Ma et le présent. Ages d'après Merle et al., soumis et références incluses. Figure adaptée d'après Merle et al., 2009.

Chacune de ces hypothèses présente des faiblesses. L'hypothèse de l'action combinée des points chauds des Canaries puis de Madère au cours de deux phases magmatiques entre ~95 et 80 Ma puis entre 16 et 0.5 Ma (Geldmacher et al., 2006 ; D'Orano et al., 2010) ne tient compte ni des mouvements de la plaque ibérique depuis 120 Ma, ni du magmatisme au Nord de la faille Açores-Gibraltar. Cette hypothèse implique un déplacement de la plaque Ibérique vers le nord-ouest entre 68 Ma et l'actuel, ce qui est en contradiction avec les reconstructions géodynamiques de l'ouverture du Golfe de Gascogne et de la collision des Pyrénées (Sibuet et al., 2004 ; Fig. 6A). De plus, cette hypothèse omet la période magmatique qui a eu lieu vers 68-62 Ma (Merle et al., 2009 ; Merle et al., soumis ; Fig. 6B).

Concernant une origine de TMR liée à l'activité de la dorsale médio-atlantique (Jagoutz et al., 2007), on peut constater dans l'état actuel des connaissances, que le magmatisme le plus ancien sur TMR est postérieur d'au moins 10 millions d'années à la formation de la première lithosphère océanique typique (~125 Ma, anomalie J, Olivet, 1996). Néanmoins, la possibilité d'un magmatisme alcalin contemporain de l'initiation du magmatisme de la dorsale atlantique n'est pas irréaliste car seulement la partie la plus superficielle de TMR a été échantillonnée, ce qui rend plausible la présence de roches plus anciennes que 103 Ma dans les parties les plus internes des monts sous-marins. L'hypothèse d'une interaction entre les mouvements de la plaque ibérique et une anomalie thermique (Merle et al., 2009) reste la seule hypothèse capable d'expliquer la distribution spatiale et temporelle du magmatisme de TMR, des monts sous-marins avoisinant et du sud-ouest du Portugal. Cependant, cette hypothèse reste très dépendante des modèles géodynamiques contraignant les mouvements de la plaque ibérique.

La phase de magmatisme alcalin débutant à 103 Ma ne se limite pas à ces manifestations sur la marge ibérique. En effet, il existe plusieurs groupes de volcans sous-marins situés sur la marge de l'Amérique du Nord tels que les monts sous-marins de Nouvelle-Angleterre, Corner, Terre-Neuve, la ride de l'anomalie J et les intrusions alcalines forées par la campagne ODP 210 au site 1276 (Fig. 7).

Dans l'état actuel des données géochronologiques, tous ces groupes de volcans sous-marin ont débuté leur activité magmatique vers 100 Ma alors qu'ils se situaient à moins de 800 km de la ride Tore-Madère. Ceci suggère que ces groupes de volcans pourraient s'être formés au cours de la même phase magmatique que la ride TMR (Merle et al., 2009). Toutefois, la durée de la période d'activité des volcans sous-marins situés sur la plaque Amérique du Nord n'est pas bien connue en raison du petit nombre d'échantillons étudiés, mais surtout des faibles précisions et fiabilité des âges publiés dans la littérature. En effet, la plupart des échantillons ont été datés par la technique K-Ar sur roches draguées.

Sur la marge de Terre-Neuve, les manifestations magmatiques ont été interprétées comme étant les manifestations de plusieurs panaches mantelliques distincts (Duncan et al., 1984 ; Taras et Hart, 1987). Néanmoins, cette hypothèse repose uniquement sur quelques données géochimiques. Les données isotopiques publiées (Sr-Nd-Pb) sur ces roches magmatiques ne concernent que celles recueillies sur les monts de la Nouvelle-Angleterre (sept données, Taras et Hart, 1987) et sur les sills alcalins forés sur le site ODP 1276 au sud du cap Flemish (six données, Hart et Blusztajn, 2006).

Si l'hypothèse d'une même période d'activité magmatique devait être confirmée et en prenant en compte les caractéristiques chimiques similaires pour TMR et les manifestations magmatiques de la marge de Terre-Neuve, l'implication de plusieurs panaches mantelliques actifs pendant cette même période et situés dans un rayon de 800 km semble peu réaliste. Au vu des connaissances actuelles, il serait ainsi raisonnable d'envisager une origine commune pour les roches magmatiques à affinité alcaline situées de part et d'autre de la ride médio-atlantique.

Jusqu'à présent, chacune de ces trois phases magmatiques intra-plaques identifiées sur les marges conjuguées Ibérie-Terre Neuve avaient été considérées de manière indépendante. Dès lors, les possibles interactions entre ces différentes phases n'ont jamais été étudiées, comme par exemple, les effets de ré-enrichissements du manteau (asthénosphérique ou lithosphérique) au cours des successives phases magmatiques. Plus important, les processus géodynamiques à l'origine de chacune de ces périodes magmatiques ont toujours été envisagés indépendamment les uns des autres alors qu'il serait logique au contraire de proposer un lien tectonique/géodynamique dans l'éruption de ces magmas. .

Par conséquent, il n'existe aucun modèle géodynamique satisfaisant pour expliquer l'apparition de ce magmatisme intra-plaque au cours des derniers 200 millions d'années dans cette partie de l'océan Atlantique. En outre, la présence d'un (ou plusieurs) panache mantellique dans cette partie de l'océan Atlantique soulève de nombreuses questions :

(1) La première concerne sa contribution éventuelle à la formation de la CAMP. Cette hypothèse est contestée (par exemple McHone, 2000) en particulier du point de vue géochimique (Callegaro et al., 2013 ; Merle et al., 2014), d'autant plus qu'il n'existe aucune évidence de l'existence d'une évolution continue des rapports isotopiques entre les laves de CAMP et celles des manifestations intraplaques comme cela est prévu par les modèles de marges volcaniques.

(2) La seconde pose la question des relations entre ce panache mantellique et le processus de rifting.

(3) Enfin la troisième question concerne le sort du panache mantellique durant 50 millions d'années, période de calme magmatique entre l'événement CAMP et la phase magmatique syn-rift.

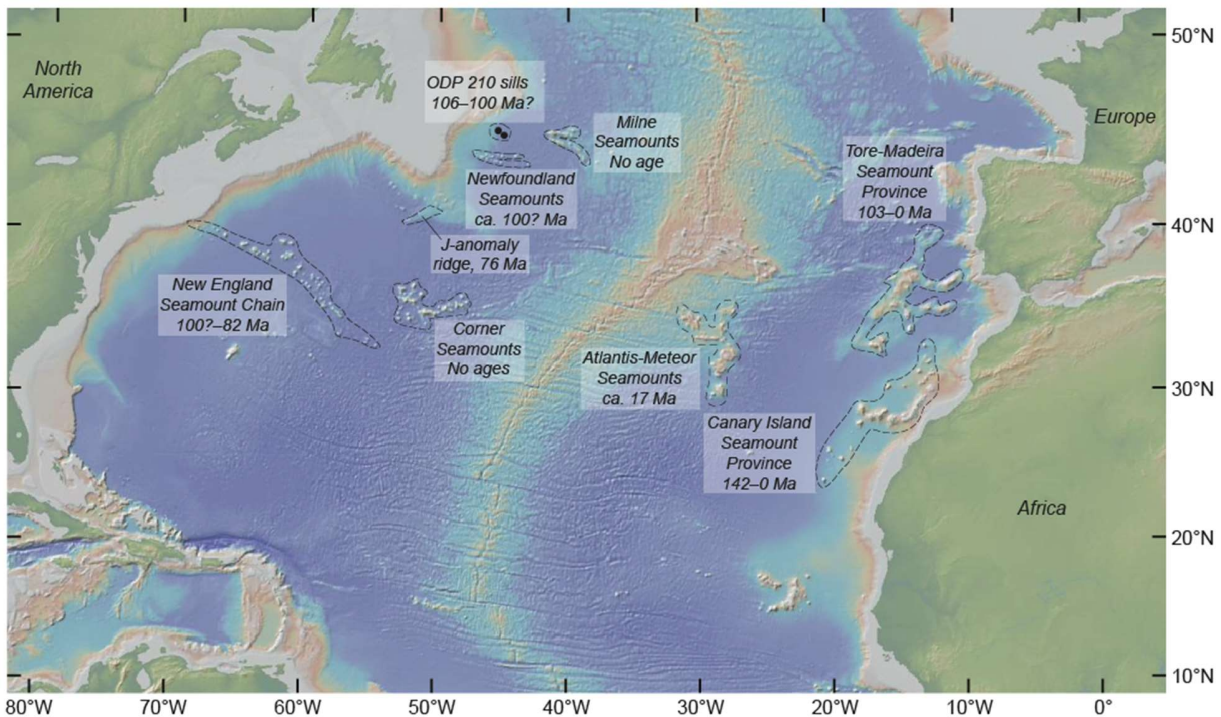


Figure 7 : Carte bathymétrique du nord de l'océan Atlantique central. Les groupes et chaînes de monts sous-marins d'âge Crétacé sont représentés avec leur période d'activité. Le groupe de monts sous-marins Atlantis-Meteor est représenté car suspecté de représenter la position du point chaud qui aurait formé la chaîne de Nouvelle-Angleterre. D'après Merle et al., en préparation.

2.2. La marge ouest-sud-ouest de l'Australie occidentale

Jusqu'à récemment, l'origine et la nature du magmatisme sur la marge de l'Australie occidentale (Western Australia ou WA, Fig. 8) était très peu connues et les données géochronologiques rares. Les études successives d'Olierook et al. (2015b ; 2016 ; 2017) ont permis de mieux contraindre la période d'activité de ce magmatisme et donc de mieux comprendre les processus géodynamiques qui pourraient être à l'origine de celui-ci.

Historiquement, cette marge est considérée comme une marge passive volcanique (Coffin et Eldholm, 1994; Goncharov et Nelson, 2012) sur la base de : (i) la présence de réflecteurs sismiques sur le plateau Wallaby (Fig. 8B), dont le pendage est orienté vers le bassin océanique (« seaward dipping reflectors » ou SDR) et qui pourraient représenter des coulées de lave intercalées entre les sédiments (par ex. Goncharov et Nelson, 2012) et (ii) l'échantillonnage de roches volcaniques sur le plateau Naturaliste (Fig. 8C). Les estimations du volume de roches volcaniques sur le plateau Wallaby ne sont pas bien contraintes, mais potentiellement de l'ordre de 10^4 - 10^5 km 3 (Goncharov et Nelson, 2012). Ces volumes restent néanmoins modestes en comparaison des volumes estimés pour les « véritables » marges passives volcaniques qui sont en général supérieur à 10 5 km 3 (Bryan et Ernst, 2008; Franke, 2013).

Les rares données géochimiques et géochronologiques suggèrent que cette phase de magmatisme est contemporaine de la dislocation du Gondwana oriental (bloc continental formé par l'Inde, l'Australie et l'Antarctique). Le rifting aurait débuté à environ ~160 Ma et l'initiation de l'extension océanique vers ~136 Ma (par ex., Gibbons et al., 2013). Toutefois, la rupture lithosphérique semble retardée dans la partie sud de la marge, au sud du plateau Naturaliste (Fig. 8D) où l'initiation de la propagation océanique aurait pu survenir seulement vers 83 Ma d'après l'identification de l'anomalie magnétique la plus ancienne (Veevers, 2012).

Sur cette section de la marge, le manteau lithosphérique a été exhumé au cours du très lent étirement lithosphérique et affleure sous une mince couche de sédiments (relief comparable à celui de la ride de péricotite sur la marge ibérique). En effet, des péricotites ont été draguées dans la zone de Diamantina, qui est une structure lithosphérique orientée E-W, constituée d'une succession de crêtes et de creux s'étendant vers le plateau Naturaliste (Fig. 8). L'origine de cette structure n'est pas encore bien comprise (Munschy, 1998 ; Beslier et al., 2004).

Des roches basaltiques ont été découvertes dans seulement quatre localités : sur le plateau de Wallaby, le plateau Naturaliste, la zone Diamantina et dans le bassin sédimentaire de Perth.

Le plateau Wallaby

Le plateau Wallaby est un plateau immergé d'une surface de 70000 km², situé à 500 km au large du nord-ouest de l'Australie occidentale (Fig. 8B). Les connaissances limitées de ce plateau ont été principalement déduites de l'interprétation des profiles sismiques et des anomalies magnétiques dans les plaines abyssales adjacentes (Mihut et Muller, 1998 ; Goncharov et Nelson, 2012).

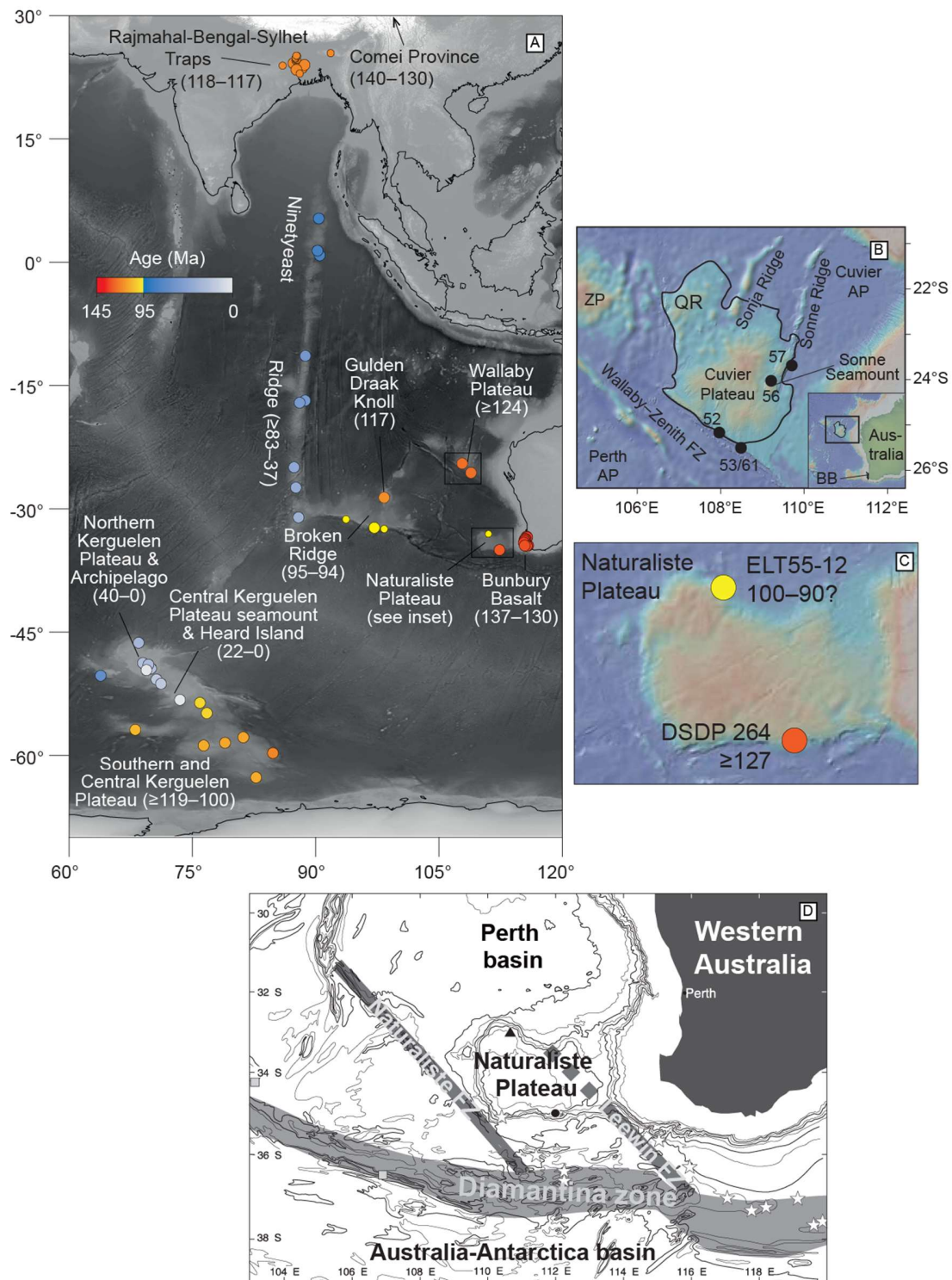


Figure 8 : Cartes de la grande province magmatique des Kerguelen. Les manifestations magmatiques dans l'océan Indien et circum-Gondwana oriental interprétées comme liées à l'activité du point chaud des Kerguelen sont aussi représentées. D'après Beslier et al. (2004) et Olieroor et al. (2016; 2017).

Le plateau Wallaby se situe sur la marge qui s'est formée, vers ~130-136 Ma, lors du rifting continental entre les blocs continentaux de l'Inde et de l'Australie (Gondwana oriental). Le plateau est formé par un haut-fond de croûte continentale recouvert par des épanchements volcaniques, eux-mêmes recouverts par des sédiments (par. ex. Stilwell et al., 2012).

Les quelques roches échantillonnées par dragage sur le plateau Wallaby et les domaines océaniques avoisinants sont des basaltes altérés et des roches légèrement différencierées d'affinité tholéïitique (Dadd et al., 2015).

Les premières données géochronologiques ont été obtenues récemment sur les roches basaltiques et volcano-clastiques provenant du flanc sud du plateau du Wallaby (Wallaby-Zenith Fracture Zone, Fig. 8B) et du flanc est (Sonne ridge, Fig. 8B) et indiquent une phase magmatique vers ~124 Ma, qui serait donc postérieure d'au moins 6 millions d'années à la première anomalie magnétique (Olierook et al., 2015b).

Une activité magmatique plus récente vers ~60 Ma, aussi sur le flanc est, aurait pu se produire (mont sous-marin Sonne, Fig. 8B) mais l'âge de cette phase magmatique est peu précis. En effet, l'analyse $^{40}\text{Ar}/^{39}\text{Ar}$ n'a pas pu produire de plateau de dégazage complet mais seulement un mini-plateau (Olierook et al., 2015b). Néanmoins, il est clair qu'une activité magmatique intraplaque a eu lieu sur le plateau Wallaby, peu de temps après le début de l'expansion océanique. Dans ce cas, le volcanisme sur le plateau Wallaby pourrait représenter un mini plateau océanique recouvrant un segment de croute continentale amincie durant le rifting (Olierook et al., 2015b).

Le Bassin de Perth (Bunbury trough)

Plus au sud, dans le bassin sédimentaire de Perth (« Bunbury trough », Fig. 9), les basaltes de Bunbury représentent de faibles volumes de magmas, limités à des coulées de laves basaltiques tholéïtiques et à quelques intrusions de semi-profondeur (Frey et al., 1996 ; Olierook et al., 2015a). Les coulées basaltiques affleurent uniquement à quatre localités (Fig. 9).

Jusqu'à récemment, peu de données géochronologiques (seulement cinq échantillons datés) avaient été publiées sur ces roches. Une grande partie de ces données géochronologiques étaient peu fiables car obtenues par la méthode $^{40}\text{Ar}/^{39}\text{Ar}$ sur des fractions minérales non triées donc susceptible d'inclure des minéraux altérés. Ces données suggéraient néanmoins que les basaltes de Bunbury avaient été émis au cours de deux phases magmatiques à 132 et 123 Ma.

Cette activité magmatique avait été alors attribuée à l'activité du panache mantellique qui aurait par la suite engendré le plateau et l'archipel des Kerguelen (par ex., Frey et al., 1996 ; Coffin et al., 2002). Des âges de meilleure précision, sur fractions minérales sélectionnées à la main sous loupe binoculaire, ont été récemment obtenus par la méthode $^{40}\text{Ar}/^{39}\text{Ar}$.

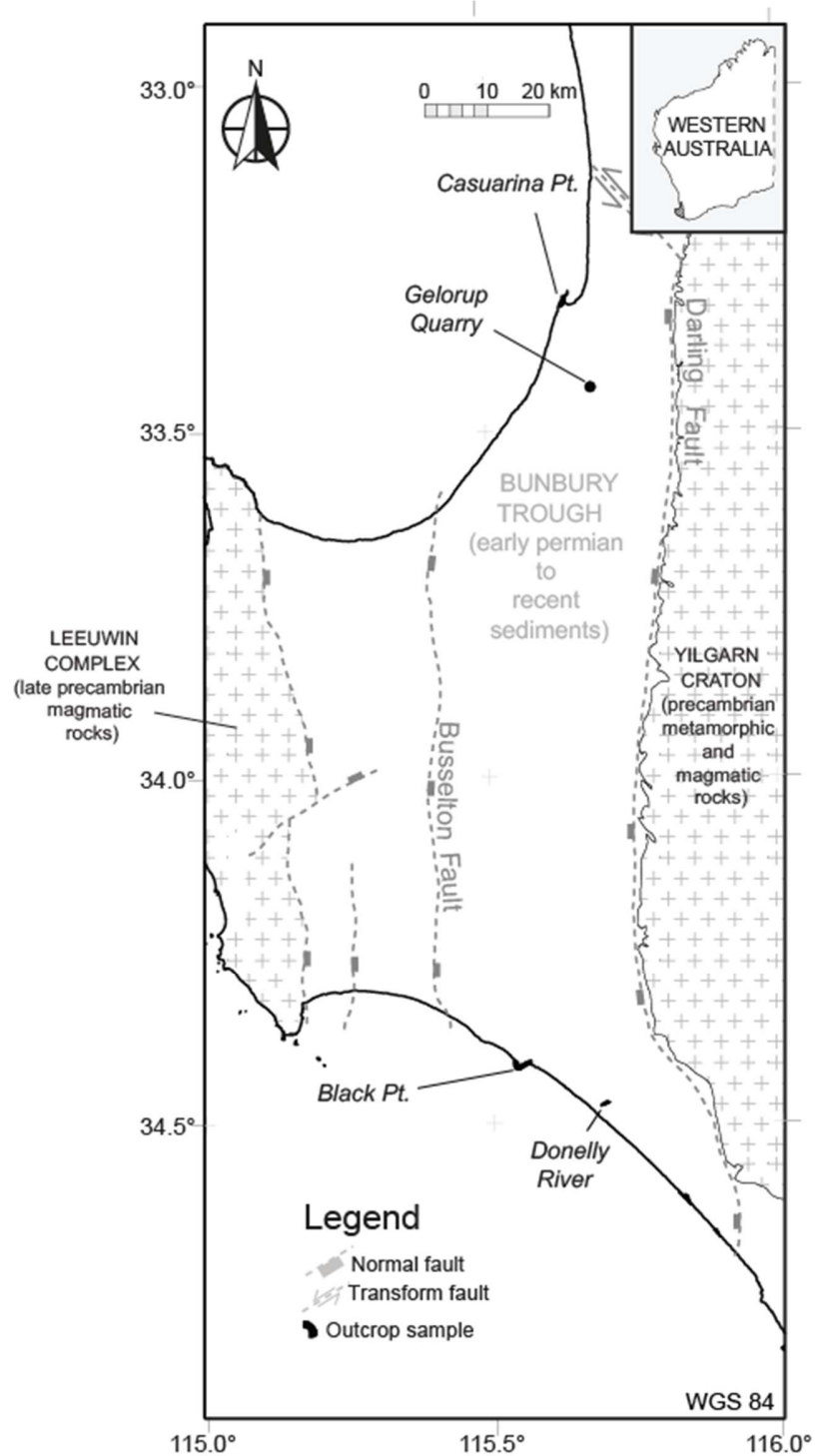


Figure 9 : Carte géologique schématique du bassin sédimentaire de Perth (Australie Occidentale). Les quatres zones d'affleurement du basalte de Bunbury sont indiquées en italique. D'après Olierook et al., 2016.

De plus, la grande précision de ces âges a permis d'identifier trois événements magmatiques distincts à 137, 132 et 130 Ma (Olierook et al., 2016). Ceci implique que la phase magmatique correspondant à l'extrusion des basaltes de Bunbury a eu lieu au cours de la phase principale d'extension continentale, et aussi qu'elle pourrait avoir perduré après le début de l'extension océanique. Comme le début attesté de l'activité magmatique sur le plateau oceanique des Kerguelen n'est pas plus ancienne que 119 Ma (par ex., Coffin et al., 2002), elle est donc postérieure d'au moins 18 millions d'années à la mise place des basaltes de Bunbury. En conséquence, l'hypothèse de l'implication du panache mantellique du point chaud des Kerguelen dans la genèse du magmatisme de la marge de WA semble être difficile à concilier avec les nouvelles données géochronologiques (Olierook et al., 2016).

Le plateau Naturaliste et la zone Diamantina

Le plateau Naturaliste et la zone Diamantina sont situés sur l'emplacement du point triple fossile entre l'Australie, l'Inde et l'Antarctique au début de la dislocation du Gondwana oriental. Jusqu'au milieu des années 1990, le magmatisme de cette zone de la marge était seulement connu grâce à une campagne de dragage en 1972 (« Eltanin campaign », dragage sur le flanc nord du plateau Naturaliste, site ELT55-12) et une campagne de forage DSDP en 1975 (flanc sud-est du plateau, site 264). Ces deux campagnes d'échantillonnage ont collecté de très faibles volumes de fragments de roches volcaniques très alterées et incorporées à des sédiments (Ford, 1975 ; Coleman et al., 1982). Deux campagnes de dragage en 1994 et 1998 (par le navire de recherche Marion Dufresne : campagnes MD 80 et M110) sur le flanc sud du plateau Naturaliste et le long de la zone Diamantina ont recueillies pour la première fois de grandes quantités de roches volcaniques (essentiellement des basaltes tholéïitiques) et les roches du manteau (Chatin et al., 1998 ; Beslier et al., 2004). Ces roches constituent aujourd'hui les seuls échantillonnages disponibles du magmatisme du plateau Naturaliste et de la zone Diamantina.

Jusqu'à l'étude d'Olierook et collaborateurs en 2017, une seule étude avait tenté de dater les basaltes de la drague ELT55-12 et du site DSDP 264 par la méthode $^{40}\text{Ar}/^{39}\text{Ar}$ (Pyle et al., 1995). Cependant, le résultat obtenu, sur roche totale, était assez imprécis. Cette datation reflète une altération en profondeur de la roche par l'eau de mer et suggère un âge d'éruption d'au moins 100 Ma. Dans l'étude récente d'Olierook et al. (2017), de nouvelles datations $^{40}\text{Ar}/^{39}\text{Ar}$ ont été effectuées sur séricite et la matrice de roches provenant des sites ELT55-12 et DSDP 264. Le but de ces datations est de dater l'altération par l'eau de mer en se basant sur le postulat que cette altération s'était produite peu de temps après la mise en place des roches magmatiques. Ces datations ont donné un âge de $127,6 \pm 0,6$ Ma, indiquant qu'un événement volcanique s'est produit il y a au moins 127 millions d'années, soit 25 millions d'années avant ce qui avait été précédemment envisagé (Olierook et al., 2017). Ceci suggère l'existence d'une activité magmatique juste avant le début de l'expansion océanique (estimée à environ 124 Ma dans cette zone, Olierook et al., 2017).

Sur la zone Diamantina, seul un basalte de la campagne MD80 a été daté à 93 ± 4 Ma par la méthode $^{40}\text{Ar}/^{39}\text{Ar}$ sur roche totale (Chatin et al., 1998). Cependant, il est possible que la chimie de la roche ait été modifiée par l'interaction avec l'eau de mer, ce qui peut perturber considérablement le chronomètre K-Ar (Verati et Jourdan, 2014). Jusqu'à présent, il n'y a pas d'âge pour les roches volcaniques recueillies au cours de la campagne MD110.

A l'échelle de la marge de WA, les données géochimiques disponibles, notamment les rapports isotopiques Sr-Nd-Pb, ne sont pas assez abondantes pour permettre d'établir des hypothèses solides quant à la source de ces magmas. Par exemple, seulement sept données Sr-Nd-Pb existent pour les roches volcaniques du plateau Naturaliste provenant des sites d'échantillonnages ETL55-12 et DSDP site 264 (Mahoney et al., 1995). Pour le plateau Wallaby, seulement deux roches ont été analysées pour obtenir des rapports isotopiques Sr-Nd-Pb (Dadd et al., 2015).

Sur la base de ces données géochimiques, certains auteurs ont constaté que les roches basaltiques provenant du plateau Naturaliste, les basaltes de Bunbury et les roches volcaniques du plateau Wallaby ont des caractéristiques chimiques assez similaires à des tholéïites continentales (Frey et al., 1996 ; Chatin et al., 1998 ; Beslier et al., 2004 ; Dadd et al., 2015).

Plusieurs auteurs ont attribué le magmatisme intraplaque le long de la marge sud-ouest australienne comme étant l'expression du panache mantellique actuellement situé sous l'archipel des Kerguelen (Frey et al., 1996 ; Ingle et al., 2002 ; 2004). D'autres exemples de manifestation magmatique intraplaque dans l'océan Indien oriental (par ex. Ninetyeast ridge, Broken ridge, Fig. 8) sont contemporains de l'activité magmatique de l'archipel des Kerguelen et ont été interprétés comme étant aussi la manifestation de ce même panache mantellique.

Les reconstructions géodynamiques les plus récentes qui contraintent les positions du panache mantellique au cours du temps et une compilation des données géochimiques et géochronologiques provenant de toutes les provinces magmatiques situées sur le pourtour du Gondwana oriental (ce qui inclus l'archipel des Kerguelen, le plateau sous-marin des Kerguelen, Broken ridge, Ninety-east ridge, et la marge sud-ouest australienne) suggèrent que les caractéristiques chimiques de chacune de ces provinces magmatiques proviennent de diverses contributions de l'asthénosphère, de la lithosphère continentale (manteau et croûte) et du panache mantellique Kerguelen (par ex. Frey et al., 1996 ; Ingle et al., 2002 ; 2004). Cependant, la contribution chimique provenant du panache mantellique des Kerguelen devient évidente seulement dans la composition des laves les plus jeunes (<100 Ma (Olieroor et al., 2017 ; Fig. 10).

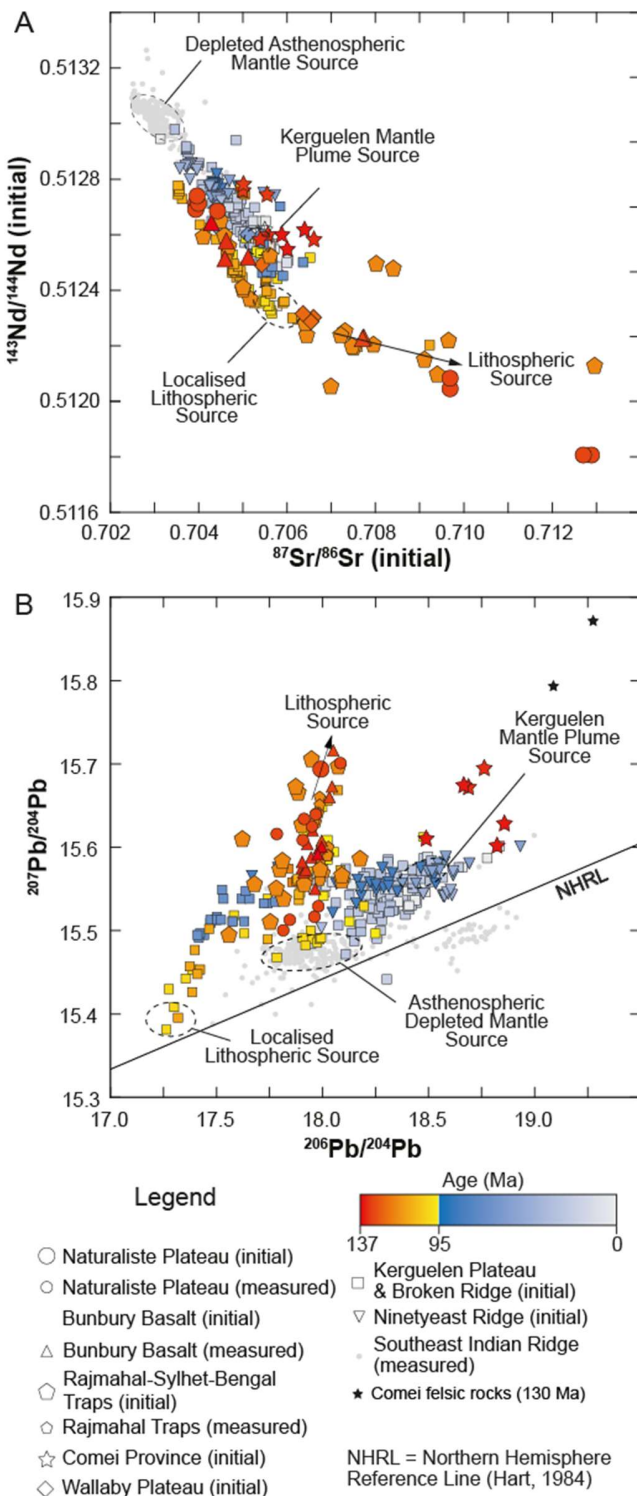


Figure 10 : Variations des rapports isotopiques mesurés et initiaux des roches des sous-provinces (symboles en légende) de la grande province magmatique des Kerguelen. Variation des rapports $^{144}\text{Nd}/^{143}\text{Nd}$ en fonction de $^{87}\text{Sr}/^{86}\text{Sr}$ (A) et $^{207}\text{Pb}/^{204}\text{Pb}$ en $^{206}\text{Pb}/^{204}\text{Pb}$ (B). D'après Olieroor et al., (2017). NB : même échelle de couleur que sur la Fig 8A.

3. Les problèmes en suspens

La distribution spatiale et temporelle du magmatisme sur les marges Ibérie-Terre-Neuve et les marges de l'Australie-occidentale révèlent que :

(1) bien qu'étant considérée comme l'archétype de marge passive pauvre en magma, la marge ibérique affiche un magmatisme intraplaque volumétriquement important pendant et après le début de l'extension océanique et distribué en trois phases.

(2) bien que la marge de WA soit considérée comme une marge passive volcanique, il n'existe pour l'instant aucune preuve irréfutable de la présence d'énormes volumes de magmas liés à sa formation. Au contraire elle montre des similarités avec la marge ibérique.

Ces deux exemples de marges passives suggèrent fortement que les modèles actuels de formation des marges de divergence et du magmatisme qui leur est associé ne sont pas satisfaisants. Les études récentes sur les marges de Ibérie-Terre Neuve et WA par Merle et al. (2006, 2009) et Olierook et al. (2015b, 2016, 2017) tendent à montrer qu'un modèle de panache mantellique classique ne parvient pas à fournir une explication satisfaisante pour l'âge et la distribution spatiale du magmatisme intraplaque sur ces deux marges. Dans l'état actuel des connaissances sur les marges Ibérie-Terre Neuve et WA, les questions suivantes sont toujours en suspens :

Un panache mantellique profond est-il nécessaire à la fracturation continentale, qui mènera au rifting et donc à la formation de marges océaniques ?

Si oui, quel est le devenir de ce panache mantellique pendant le rifting et lors de l'extension océanique ? Par conséquent, pourquoi certaines marges présentent de larges volumes de magmas et d'autres pas ?

Comment les diverses phases magmatiques observées sont-elles liées les unes aux autres, dans l'espace et le temps ?

Les marges conjuguées Ibérie-Terre Neuve et la marge d'Australie Occidentale offrent l'opportunité de répondre à ces questions. En effet, elles présentent à la fois des caractéristiques qui ont permis l'établissement des modèles de marges passives non-volcaniques (p. ex., Boillot et al., 1995) et à la fois des caractéristiques moins communes qui peuvent permettre de mieux comprendre l'origine du volcanisme associé au rifting (« LIP » peu exprimé en Australie, volcanisme intra-plaque précédent et postérieur à l'initiation de l'extension océanique). L'acquisition de nouvelles données géochimiques et géochronologiques, complètes et avec des techniques de pointe, constituent une nécessité pour une bonne compréhension de ce type de marge, et donc pour palier aux lacunes de compréhension sur une étape géodynamique fondamentale, le rifting au sens large.

4. Programme de recherche : approche méthodologique et analytique

La plupart des hypothèses et modèles proposés pour expliquer le magmatisme intraplaque sur les marges passives reposent sur (1) un faible nombre de données concernant le volume de roches magmatiques qui ont été documentées, (2) des jeux de données incomplets pour la géochimie des éléments majeurs, mineurs et en trace et (3) dans bien des cas des données isotopiques peu fiables. Sur ce dernier aspect, de nombreuses données ont été acquises au moyen de techniques géochronologiques et géochimiques qui sont maintenant considérées comme obsolètes (par exemple la méthode K-Ar pour dater des roches totales) ou qui n'étaient pas assez précises à l'époque pour distinguer différentes phases magmatiques espacées de quelques millions d'années comme cela a été montré pour les basaltes de Bunbury (Olierook et al., 2016). De plus, jusque dans les années 1990, de nombreuses données isotopiques Sr-Nd-Pb ont été publiées sans les concentrations de ces éléments, ce qui empêche le calcul du rapport isotopique initial. En conséquence, la base de données isotopiques est incomplète, ce qui exclut toute comparaison avec des roches dont les rapports isotopiques initiaux peuvent être calculés (voir par exemple, Olierook et al., 2017).

De fait, il est critique de procéder à un filtrage des données déjà publiées et d'acquérir de nouvelles données fiables et précises en utilisant les méthodes et techniques analytiques les plus avancées, mais aussi les plus adaptées aux roches échantillonnées.

4.1. Approche géochronologique

Pour obtenir des données fiables sur les âges, origine et distribution spatiale du magmatisme intraplaque des marges ibérique et ouest-australienne, une approche rigoureuse s'impose en termes de techniques analytiques. Il est donc nécessaire de combiner des techniques géochronologiques et géochimiques variées et adaptées à des échantillons océaniques d'une grande diversité chimique, disponibles en faible quantité (moins de 0,5 dm³) qui, de surcroit, ont probablement subit une altération due à l'interaction avec de l'eau de mer.

Cette altération des roches par l'eau de mer présente le principal défi pour dater des échantillons océaniques surtout lorsqu'ils ont été dragués. Dans ce type d'altération à basse température où le potassium est particulièrement mobile, les feldspaths sont les premiers minéraux à être affectés : ils sont transformés en séricite, ce qui rend impossible la détermination d'un âge de cristallisation.

Les minéraux ferro-magnésiens riches en potassium comme les amphiboles et les biotites ont aussi de grandes chances d'être affectés par l'interaction avec l'eau de mer et d'être partiellement ou totalement transformés en minéraux secondaires comme la chlorite. D'une manière générale, pour obtenir les meilleurs résultats et des âges fiables, les datations des roches doivent être effectuées sur des fractions minérales préalablement triées grains à grains sous loupe binoculaire, ce qui est aussi vrai pour les roches continentales qui peuvent aussi avoir été altérées.

Pour les roches basiques qui contiennent feldspaths, amphiboles ou ces deux types de minéral, la méthode privilégiée est la méthode ⁴⁰Ar/³⁹Ar car elle permet une évaluation

de la qualité de la datation (Verati et Jourdan, 2014). La dernière génération de spectromètres de masse multi-collection à gaz rares (comme le Thermo Fisher ARGUS VI) permet une amélioration significative en précision par rapport à la génération d'instrument précédente (Fig. 11). La précision atteinte est inférieure à $\pm 0,5\%$ (Olierook et al., 2016). L'avantage de la datation de très haute précision est la possibilité de distinguer différentes phases magmatiques espacées de seulement quelques centaines de milliers d'années (par ex. Olierook et al., 2016).

En outre, les récentes avancées techniques en spectrométrie de masse à gaz rares ont amélioré la sensibilité des instruments, ce qui permet maintenant d'utiliser de petites quantités de matériaux pour réaliser des mesures plus précises et plus fiables par rapport à celles effectuées par des instruments de générations antérieures. En effet, une petite quantité de matériel analysée permet un meilleur contrôle de la qualité des cristaux sélectionnés et donc, réduit le risque d'un possible biais des résultats dus à l'altération par l'eau de mer.

Les limites de la méthode $^{40}\text{Ar}/^{39}\text{Ar}$ (et par extension, de la méthode K-Ar) appliquée aux roches basiques sont (i) l'absence de minéraux riches en potassium (plagioclase, amphibole) et (ii) la fréquente altération de ces minéraux ou par des fluides mobilisant le potassium. Une méthode pour contourner cette difficulté est de déterminer l'âge de l'altération en datant les séricites en se basant sur le postulat que l'altération (par exemple par l'eau de mer pour les roches océaniques) a transformé les feldspaths magmatiques en séricite peu de temps après la mise en place des roches (par ex. Olierook et al., 2015). Cette approche ne fournit pas d'âge de cristallisation mais donne seulement une estimation minimale de l'âge de l'événement magmatique.

Pour les roches dépourvues de minéraux riches en potassium, deux approches sont possibles. La première consiste à dater la mésostase mais cette approche fournit des âges fiables seulement pour des roches complètement dépourvues de toute trace d'altération. Par conséquent, cette approche doit être le plus possible limitée aux roches échantillonnées en domaine continental. Pour des roches océaniques, la datation de la matrice ne peut jamais être considérée comme entièrement fiable et toute date obtenue doit être considérée comme une estimation minimale de l'âge de l'événement magmatique.

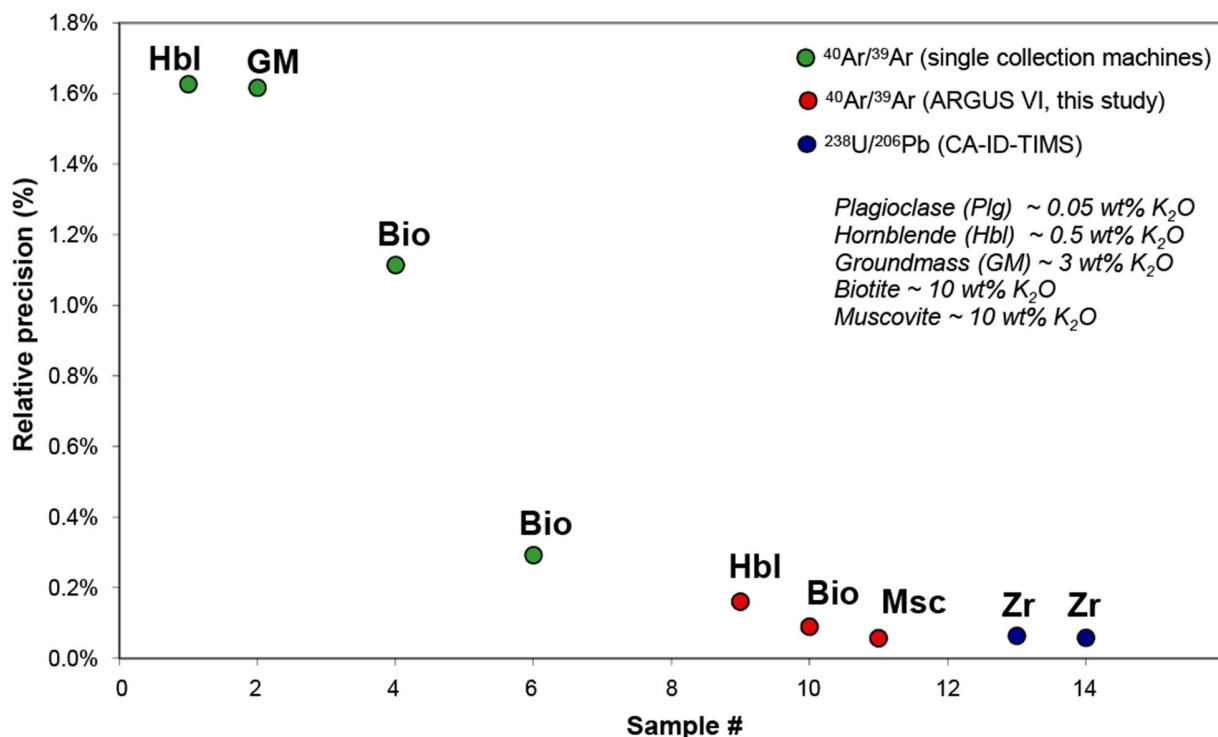


Figure 11 : Précision relative des âges obtenus sur différents minéraux par la méthode $^{40}\text{Ar}/^{39}\text{Ar}$ au moyen d'un instrument de type Argus VI (en rouge) et un spectromètre à gaz à mono-collection (en vert). Ces données sont comparées à celles obtenues par la méthode U-Pb par abrasion chimique, dilution isotopique et thermo-ionisation (CA-ID-TIMS U-Pb) qui constitue actuellement la méthode de datation des roches la plus précise. D'après Merle et al. accepté.

Une autre approche pour les roches ne contenant pas de minéraux riches en potassium est de dater les pyroxènes. Dater le pyroxène (au lieu du plagioclase et de l'amphibole) est extrêmement avantageux car (1) le pyroxène est très résistant à l'altération par l'eau de mer, ce qui permet de dater avec précision des roches pouvant être par ailleurs très altérées ; (2) le pyroxène est très commun dans certains basaltes (basanites, ankaramites) et dans les roches du manteau qui par ailleurs contiennent rarement des minéraux riches en potassium. Jusqu'à récemment, l'abondance du potassium dans les pyroxènes était trop faible pour espérer obtenir un âge significatif avec les générations précédentes de spectromètres de masse. Des études préliminaires sur la datation de cristaux de pyroxène en utilisant un ARGUS VI ont fourni les premiers âges valides (Ware et Jourdan, 2018 ; Fig. 12).

En datant le pyroxène dans les péridotites du manteau lithosphérique, il serait possible de dater le moment où le pyroxène s'est refroidi au-dessous de sa température de fermeture pour l'Ar, c'est-à-dire vers 600-700°C. Cela permet de contraindre dans le temps, soit (1) le moment où le manteau lithosphérique était à moins de 10 km sous le plancher océanique (Girardeau et al., 1988) au moment des dernières étapes de la distension soit (2) de dater l'âge de la dernière équilibration thermique après la fusion du manteau.

La datation des pyroxènes par la méthode $^{40}\text{Ar}/^{39}\text{Ar}$ dans les basaltes et les roches du manteau est toujours en cours de développement et constitue une méthode innovante et prometteuse pour le futur.

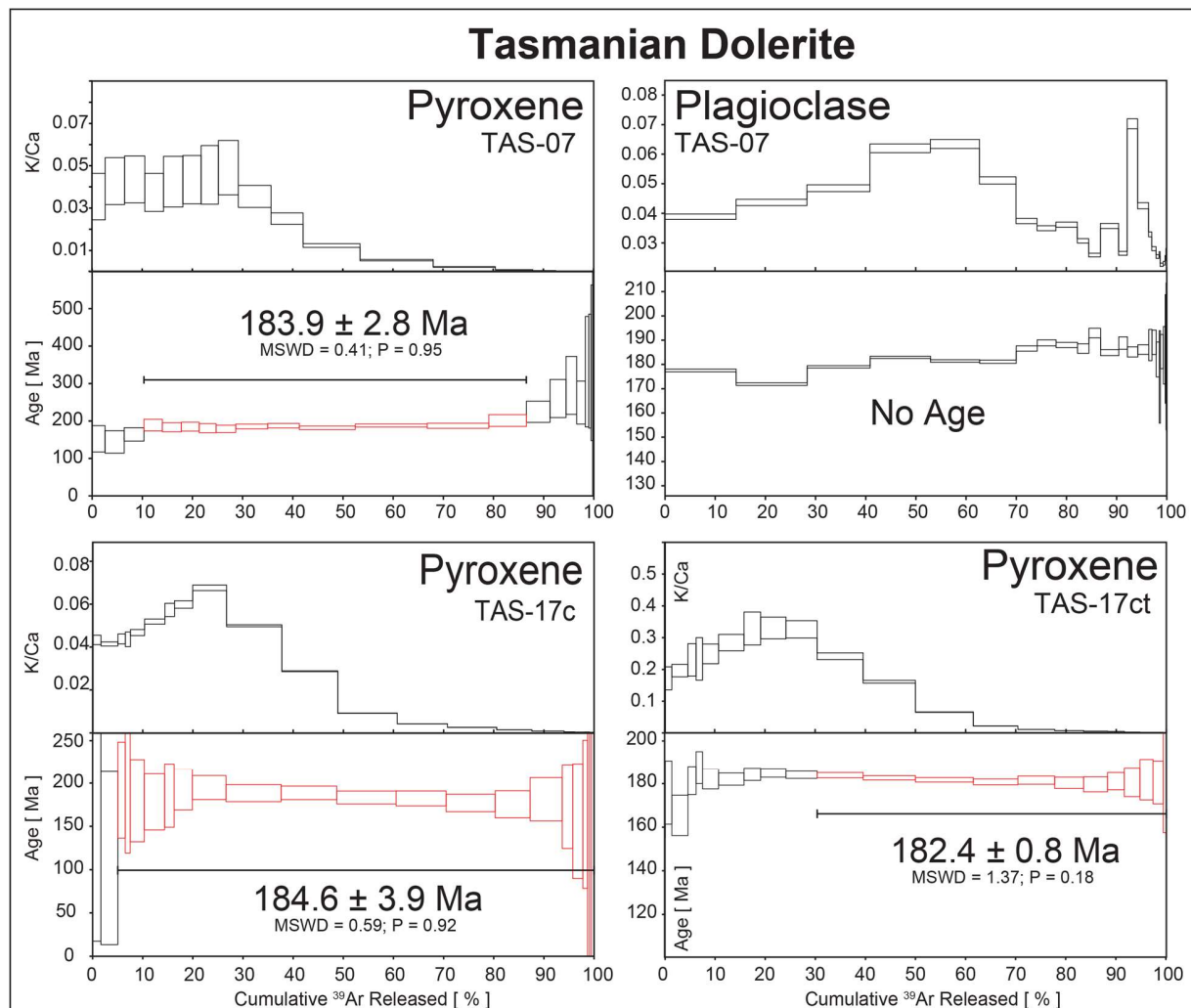


Figure 12 : Résultats de datation par la méthode $^{40}\text{Ar}/^{39}\text{Ar}$ d'une roche volcanique basique de Tasmanie (Ware et Jourdan, sous presse). Les analyses ont été faites avec un spectromètre multicollection à gaz rare de type ARGUS VI installé à Curtin University. Les pyroxènes analysés produisent des âges plateaux contrairement aux plagioclases.

Pour les roches acides (trachyandésites, trachytes, phonolites et rhyolites alcalines), la méthode $^{40}\text{Ar}/^{39}\text{Ar}$ est d'autant plus adaptée car ces roches contiennent généralement une grande variété de minéraux riches en potassium (feldspaths potassiques, amphiboles, biotites voire feldspathoides). L'altération des roches et minéraux reste la seule limitation de cette technique mais une solution alternative est la datation par U-Pb sur zircon qui a une précision inférieure à 0.1% (par ex. Wotzlaw et al., 2012). Ce type d'approche permet de dater des roches qui ont été affectées significativement par l'interaction avec l'eau de mer. Le zircon, minéral très commun dans les roches acides comme les trachytes, est au contraire, extrêmement résistant aux transformations

physico-chimiques de basse température comme c'est le cas pour l'altération des roches par l'eau de mer. En datant les zircons présents dans une roche magmatique, il est donc possible d'obtenir un âge magmatique fiable même pour une roche qui a été significativement altérée par l'eau de mer. Ce type d'approche a prouvé son efficacité avec les roches de TMR (Merle et al., 2006).

4.2. Approche géochimique

Pour définir les caractéristiques géochimiques des magmas intraplaque que l'on rencontre sur les marge passives et pour déterminer leur origine, c'est-à-dire la nature de leur source(s), il est nécessaire de combiner plusieurs systèmes isotopiques. Au préalable, l'analyse des teneurs en éléments majeurs et en traces dans les roches, est essentielle pour (1) évaluer le degré d'altération des échantillons, (2) déterminer leur affinité chimique (alcaline ou tholéitique) et (3) quantifier les effets des processus de fusion partielle et de cristallisation, ce qui constitue aussi la première étape vers la caractérisation chimique de la (ou des) source(s) mantellique(s) des magmas.

L'étude des CFBs a révélé que, seules, les données isotopiques Sr-Nd-Pb ne permettaient pas de distinguer entre un processus de contamination des magmas par la croûte continentale au cours de leur ascension vers la surface et une contamination de la source profonde par des composants avec une affinité continentale (recyclage de la croûte continentale dans le manteau). Par contre, le système isotopique Re-Os, grâce à ses propriétés chimiques, permet de distinguer entre ces deux phénomènes.

Du fait que les périclases du manteau contiennent entre 20 et 200 fois plus d'Os que les roches de la croûte continentale, une contamination d'une source périclastique par un composant crustal n'affectera pas les rapports isotopiques de l'Os. Les magmas issus de cette périclase contaminée auront donc un rapport isotopique de l'Os de type mantellique ($^{187}\text{Os}/^{188}\text{Os} < 0,15$). Par contre, les magmas issus de la fusion d'une source mantellique non contaminée auront initialement des rapports isotopiques de l'Os similaires à celui de leur source mais ils contiennent au mieux dix fois plus d'Os que la croûte continentale. Comme celle-ci a des rapports isotopiques $^{187}\text{Os}/^{188}\text{Os}$ de l'ordre de 0,8 à 1,2 (Peucker-Ehrenbrink et Jahn, 2001), les rapports isotopiques $^{187}\text{Os}/^{188}\text{Os}$ des magmas issus de la source mantellique seront significativement changés si une interaction se produit avec la croûte continentale au cours de leur ascension vers la surface. Les rapports isotopiques des magmas contaminés par un composant crustal seront typiquement supérieurs à 0,15 (Widom, 1997).

De plus le système Re-Os est le seul capable d'évaluer l'origine lithosphérique des périclases (Carlson, 2005), et donc de retracer une contribution éventuelle de ce type de manteau dans les caractéristiques chimiques des magmas comme cela a été démontré pour les basaltes de CAMP (par ex. Merle et al., 2014).

La combinaison des systèmes isotopiques Sr-Nd-Pb avec Re-Os constitue donc la base pour étudier les magmas intraplaques des marges passives. L'utilisation de nouvelles méthodes isotopiques, comme par exemple, la détermination des rapports des isotopes stables du Ti qui a le potentiel de tracer une contamination sédimentaire des magmas, permet de raffiner les informations sur les sources des magmas provenant des systèmes

Sr-Nd-Pb-Os. Ceci conduit à réinterpréter les données existantes et peut mettre en évidence des déviations subtiles mais significatives des modèles.

L'utilisation des nouvelles générations de spectromètre de masse de type MC-ICP-MS (Multi-Collection Inductively-Coupled Plasma Mass Spectrometer) comme le Thermo Fisher Neptune-plus (analyses des rapports isotopiques Nd et Pb) ou le MC-TIMS comme le Triton-plus (analyses des rapports isotopiques Sr et Os) constitue un réel avantage par rapport aux générations précédentes d'instruments. En effet, ses instruments modernes sont capables d'analyser dans un temps plus court (2h), un grand nombre d'échantillons avec une précision inférieure à 0.01 %. Une telle précision est nécessaire pour évaluer les changements minimes de compositions de source.

4.3. La nécessité de filtrer les données

Les analyses K-Ar (sur roche totale ou sur fraction minérale) ne permettent pas d'évaluer si l'âge obtenu est biaisé par effet d'une mobilisation du potassium (comme il est possible de le faire avec les analyses $^{40}\text{Ar}/^{39}\text{Ar}$ et le spectre du rapport Ca/K), les âges obtenus par la méthode K-Ar ne sont ainsi pas complètement fiables. En conséquence, ces âges doivent être considérés avec précaution et donc être plutôt utilisés comme des estimations de l'âge de l'événement magmatique. De même, les datations Rb-Sr sur roches totales (isochrone formée par une série de roches en se basant sur le postulat que ces roches sont co-magmatiques) peuvent être biaisées par l'altération, mais aussi par les processus magmatiques (mélange, contamination par les roches de l'encaissant) et doivent être aussi considérées comme des estimations de l'âge des roches. Les datations Rb-Sr sur fraction minérales peuvent fournir des données fiables mais doivent satisfaire les critères statistiques requis pour une isochrone valide : MSWD (pour « Mean Square Weighted Deviation » qui mesure la dispersion des données : plus le MSWD est élevé plus les données sont dispersées, moins l'isochrone est statistiquement significative) inférieur à 2 et P (pour « Probability of Fit » : évalue la probabilité que les points forment une droite) supérieur à 0,05 (par ex. Merle et al., 2009).

Pour les analyses $^{40}\text{Ar}/^{39}\text{Ar}$, les spectres de dégazage d'argon doivent comprendre au moins 70% du total de l'argon dégazé au cours de l'analyse pour former un plateau qui lui-même doit satisfaire à des critères statistiques stricts ($\text{MSWD} < 2$; $P > 0,05$) pour pouvoir fournir un âge significatif (Merle et al., 2009 ; Verati et Jourdan, 2015).

Pour les analyses U-Pb, les données valides doivent être concordantes (pourcentage de discordance inférieur à 5%, ellipses d'erreur recouvrant la courbe de concordance dans le diagramme exprimant la variation du rapport $^{206}\text{Pb}/^{236}\text{U}$ en fonction de la variation du rapport $^{207}\text{Pb}/^{235}\text{U}$). Les âges doivent être calculés par une moyenne pondérée comprenant au moins cinq analyses et le résultat doit pouvoir fournir des paramètres statistiques traduisant sa fiabilité ($\text{MSWD} < 2$; $P > 0,05$).

D'une manière générale, les âges ayant une incertitude supérieure à $\pm 5\%$ (incertitude donnée à $\pm 2\sigma$), doivent être considérées avec précaution.

En terme de géochimie, les analyses dont les rapports initiaux ne peuvent être calculés (concentration en élément père, en élément fils ou les deux sont manquant, rapport père-fils non fourni) ne peuvent être pris en compte. En effet, seuls les rapports initiaux traduisent la signature des sources des magmas. Même si la différence entre rapport mesuré et rapport initial (due à la désintégration in-situ du père) peut être faible pour des roches dont l'âge est inférieur à 100 Ma (les éléments considérés ont des temps de $\frac{1}{2}$ vie de plusieurs centaines de millions voire milliards d'années), la comparaison de rapports mesurés et initiaux n'est pas scientifiquement correcte. L'incertitude (à $\pm 2\sigma$) sur les rapports initiaux calculée par propagation d'erreur ne doit pas être supérieure à 0,5% pour les systèmes isotopiques Sr, Nd et Pb et de l'ordre de 5% pour les rapports de l'Os (par ex. Merle et al., 2014). Dans le cas contraire, les rapports initiaux sont trop imprécis pour être significatifs.

Ces critères de sélection permettent de constituer une base de données géochronologique et géochimique fiable pour bâtir des modèles géodynamiques solides.

5. Chantiers en cours et futurs développements

5.1. Marges conjuguées Ibérie-Terre Neuve

Sur ces marges conjuguées, deux questions majeures restent toujours sans réponse satisfaisantes : (1) quel est l'origine du magmatisme de TMR, des monts sous-marins avoisinants et du sud-ouest du Portugal et (2) quelles sont les possibles relations génétiques entre les manifestations magmatiques sur les plaques Ibérique et nord-américaine. Pour répondre à ces questions, quatre chantiers sont actuellement actifs et de futurs développements sont en cours d'étude :

Chantier A : Contraindre les caractéristiques des sources du magmatisme TMR et du SO Portugal.

Malgré les efforts pour étudier les roches provenant des volcans de TMR, peu de données isotopiques ont été publiées jusqu'à présent et de fait, les sources des magmas ne sont pas toujours bien définies. De nouvelles données Sr-Nd-Pb acquises sur des roches de TMR par Merle et al. (en préparation) sont en cours d'interprétation. Ces données suggèrent la présence d'au moins trois composants mantelliques contribuant aux caractéristiques géochimiques des laves de TMR (Fig. 13). Deux de ces composants ont une signature bien définie de type HIMU et de type asthénosphérique (« Depleted Mantle » ou DM). Le troisième a, par contre, une signature plus difficile à interpréter : ses caractéristiques isotopiques le rapprochent du pôle mantellique de type manteau enrichi I (« Enriched Mantle 1 » ou EMI) bien qu'il ait de de larges variations en terme de composition isotopique du Pb (Fig. 13).

Le composant EMI a depuis longtemps été associé au manteau lithosphérique (Zindler et Hart, 1986). Dans le cas des laves de TMR, cette interprétation pose un problème majeur car une signature clairement distincte de EMI et interprétée comme étant le manteau lithosphérique de la marge ibérique a déjà été identifiée dans les laves acides

de TMR (Merle et al., 2006). Un axe de recherche futur serait d'acquérir des données Re-Os sur les basaltes de TMR et du sud-ouest Portugal pour vérifier l'implication du manteau lithosphérique dans les caractéristiques géochimiques de ces roches.

Un autre axe de recherche future serait l'analyse systématique des rapports isotopiques Sr-Nd-Pb-Os des basaltes les moins altérés provenant du sud-ouest du Portugal. En effet, ces roches représentent potentiellement les liquides parentaux des roches différentiées. Les caractéristiques de ces dernières ont été interprétées comme résultant de la contamination par le manteau lithosphérique sous-continentale de magmas basaltiques issus d'une source sub-lithosphérique (Bernard-Griffith et al., 1997 ; Grange et al., 2010). La nature de cette source sub-lithosphérique n'est pas bien contrainte car en partie masquée par la contamination. Les roches basaltiques auraient plus de chance d'avoir conservé les caractéristiques de cette source mantellique. L'utilisation du système isotopique Re-Os pourrait ainsi contribuer à quantifier la contribution du manteau lithosphérique sous-continentale dans la source des roches du Portugal.

Chantier B : Confirmer la période d'activité magmatique de TMR et du sud-ouest Portugal et mettre à l'épreuve les hypothèses de formation de TMR.

L'hypothèse de formation de TMR formulée par Merle et al. (2009) reste la plus satisfaisante dans l'état actuel des connaissances, surtout en ce qui concerne les âges valides publiés. En effet, plusieurs monts de TMR n'ont toujours pas été datés de manière satisfaisante (Isabelle, Dragon, Lion, Fig. 6). Les derniers âges et estimations obtenus récemment sur les monts sous-marins de Tore Est et Isabelle (Merle et al., sous presse) semblent confirmer que TMR a connu une intense période d'activité magmatique vers 80 Ma y compris dans la partie sud de la ride (Fig. 6), ce qui n'est pas en contradiction avec l'hypothèse de Merle et al. (2009). Ces nouvelles données permettent de tester les hypothèses de formation de TMR et d'envisager d'autres modèles comme par exemple, la flexure de la lithosphère océanique en réponse à une hypothétique subduction sous l'arc de Gibraltar (Merle et al., sous presse).

Les futurs développements de ce chantier permettront notamment d'améliorer les estimations d'âge des monts Torillon, Lion, Isabelle et Dragon mais aussi des basaltes du sud-ouest du Portugal pour lesquels peu d'âges fiables sont disponibles.

Chantier C : Mise en évidence d'une grande province magmatique Crétacé sur les marges Ibérie-Terre Neuve et les bassins océaniques adjacents.

Ce chantier vise à confirmer par la géochronologie $^{40}\text{Ar}/^{39}\text{Ar}$ de précision et la géochimie isotopique l'hypothèse émise par Merle et al. (2009) suggérant que les manifestations magmatiques du Crétacé sur la plaque Amérique du Nord (chaîne de monts sous-marins de la Nouvelle-Angleterre, ride de l'anomalie J, monts sous-marins de Terre-Neuve) seraient liées génétiquement à la province regroupant TMR, les monts sous-marins Ormonde et Ampère et le sud-ouest du Portugal. Cette hypothèse se base sur une proximité géographique au moment de l'activité volcanique de ces manifestations. Les travaux récents ont eu pour but de confirmer cette hypothèse en produisant des âges

fiables à la fois sur les volcans de la chaîne de Nouvelle-Angleterre et de la ride de l'anomalie J pour laquelle il n'existe encore aucun âge. Les dernières datations confirment une activité autour de 80 Ma (Merle et al., en préparation).

En termes de géochimie isotopique, les derniers résultats suggèrent des similarités des rapports isotopiques Sr-Nd-Pb entre d'une part les roches de TMR, celles du Portugal, et des monts sous-marins Ormonde, Ampère, Seine et d'autre part celles de la chaîne de Nouvelle-Angleterre. La combinaison de ces deux ensembles de données montre clairement que le magmatisme de la fin du Crétacé sur les deux marges conjuguées est dû à l'activité de la même anomalie thermique centrée sur la partie nord de l'océan atlantique.

La faible quantité d'échantillons disponibles et leur degré avancé d'altération rendent les futurs développements de ce chantier difficiles à envisager dans un avenir proche. Seule une campagne de forage sur les volcans de la chaîne de Nouvelle-Angleterre, la ride de l'anomalie J et les monts sous-marins de Terre Neuve ouvrirait de nouvelles perspectives permettant la collecte de nouveaux échantillons.

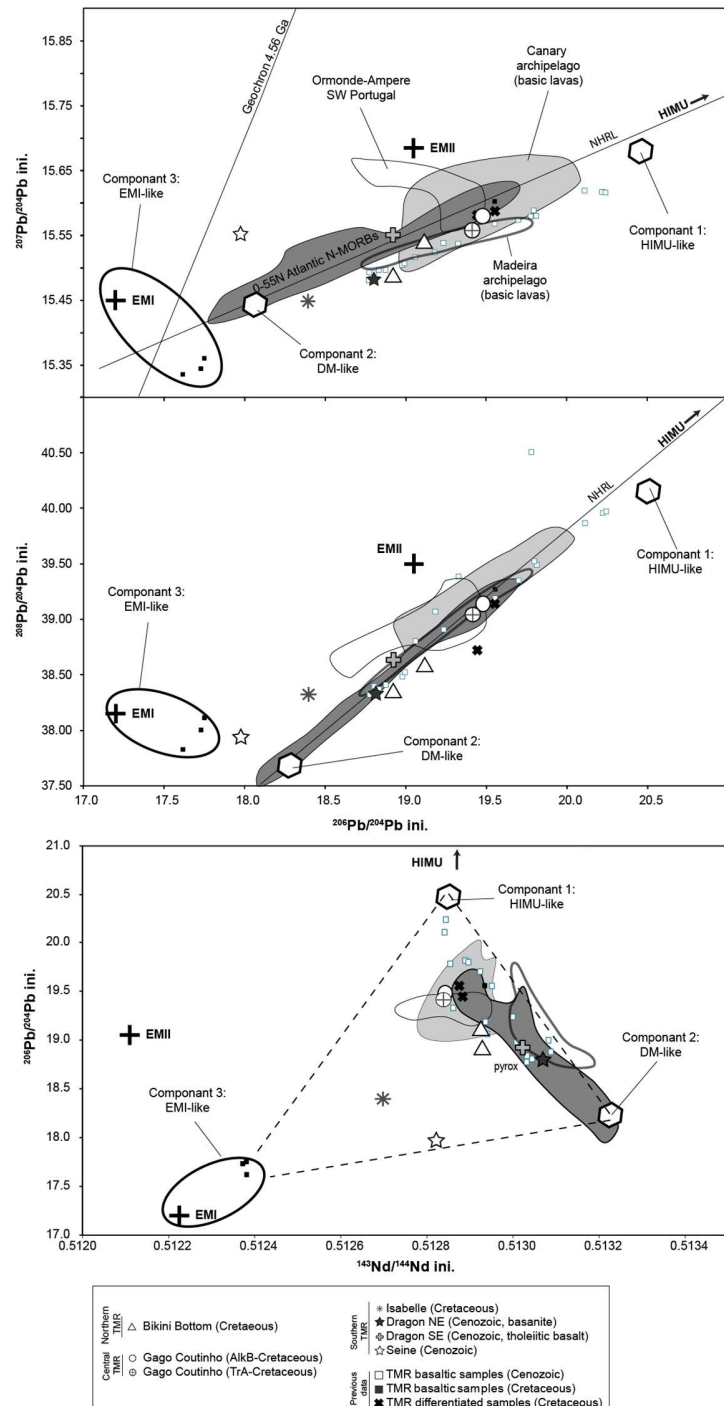


Figure 13: Diagrammes isotopiques Pb-Pb et Nd-Pb des roches de TMR montrant la contribution d'au moins trois composants. Données d'après Merle et al., en préparation. Données publiées sur les roches de TMR d'après Geldmacher et al. (2005, 2006, 2008). Champs des roches de Ormonde-Ampere, du sud-ouest du Portugal, de Madère, des Canaries et des N-MORBs de la ride médio-atlantique d'après Geldmacher et Hoernle, (2000); Geldmacher et al. (2006); Mata et al. (1998); Bernard-Griffith et al. (1997) et base de données Georoc.

Chantier D : Rôle des structures lithosphériques dans la localisation et la production du magmatisme.

Cet aspect du magmatisme a souvent été évoqué (par ex. Geldmacher et al., 2006 ; Merle et al., 2006 ; 2009 ; Grange et al., 2008) mais jamais vraiment étudié. L'étude des données bathymétriques pourrait contribuer à répondre à cette question (Sanchez et al., en préparation). En effet, l'analyse et l'interprétation des ces données semble indiquer que :

- (1) Les monts sous-marins de TMR présentent clairement des morphologies volcaniques. Des cônes éruptifs, des champs de coulées de lave, des fissures éruptives, des « rift zones » et des cicatrices d'effondrement de flancs ont été clairement identifiés sur les cartes bathymétriques produites récemment (Sanchez et al., en préparation).
- (2) Les édifices magmatiques et les rides volcaniques formés par les fissures éruptives sont systématiquement localisés soit sur, soit à proximité, des grandes structures lithosphériques, ce qui indique que les failles ont vraisemblablement servi de drains au cours de l'ascension des magmas à travers la lithosphère.
- (3) Les édifices et rides volcaniques ne montrent aucune évidence de décalage lié au fonctionnement des failles. Comme il est très probable que ces failles ont été actives depuis le Mésozoïque en connexion avec les mouvements de la plaque Ibérique et la collision des Pyrénées, il est possible que le magmatisme ait été contemporain de l'activité des failles, voire qu'il ait pu contribuer à étendre et développer le système de failles (Sanchez et al., en préparation).
- (4) Les structures volcaniques (« rift zones », fissures et rides éruptives) montrent une orientation préférentielle E-W et NNE-SSW pour ce qui est l'orientation dominante des structures lithosphériques de la marge. Aucune orientation N-S n'est observée au nord de la faille Açores-Gibraltar où au moins une partie de la ride TMR repose sur la lithosphère continentale étirée et donc où ces structures ont plus de chance d'être présentes. Néanmoins, les seules orientations N-S observées dans les formations volcaniques se trouvent sur les monts Lion et Unicorn situés au sud de faille Açores-Gibraltar sur une lithosphère océanique.

5.2. Marge de l'Australie occidentale et la grande province magmatique des Kerguelen

Ce chantier se focalise actuellement sur la datation de précision par la méthode $^{40}\text{Ar}/^{39}\text{Ar}$ des roches provenant de la grande province magmatique des Kerguelen. Sont en cours de datation des roches provenant du plateau océanique des Kerguelen et de la ride de 90° latitude Est (« Ninetyeast ridge »).

Plusieurs axes de développement de ce chantier sont en cours d'étude. Le premier concerne l'analyse des rapports isotopiques de l'Os dans les basaltes de Bunbury et des roches les plus fraîches du plateau Naturaliste, des Kerguelen et de la « Ninetyeast ridge ». En effet, peu de données fiables existent, notamment pour les basaltes de Bunbury pour lesquelles certains rapports isotopiques $^{187}\text{Os}/^{188}\text{Os}$ sont inférieurs à 0.1 (Ingle et al., 2004), ce qui est irréaliste pour des basaltes (Carlson, 2005). Ceci pourrait

résulter soit d'un problème analytique soit d'une perturbation du système Re-Os, ce qu'il faudrait vérifier.

Un développement majeur de ce chantier serait d'étudier les échantillons prélevés (lors des campagnes MD80 et MD110) sur le plateau Naturaliste et la zone Diamantina car ces roches présentent un intérêt majeur pour l'étude des marges passives :

(1) La collection disponible comprend une très grande quantité de roches magmatiques (basaltes) et mantelliques (péridotites), représentatives du versant sud de la zone Diamantina et du plateau Naturaliste où les forages et opérations de dragage antérieurs n'ont pu récupérer que de faibles quantités de roches souvent altérées par l'eau de mer.

(2) Ces échantillons sont a priori peu altérés ce qui est rare pour des échantillons océaniques et constitue une condition primordiale en préalable à toute étude géochimique et géochronologique fiable.

(3) Les échantillons n'ont été que très partiellement étudiés jusqu'à présent. Notamment, il n'y a pas d'étude isotopique sur les roches volcaniques : ni âge ni traçage de leurs sources mantelliques (systématiques Sr-Nd-Pb-Os).

Les objectifs de ce futur chantier permettraient de :

- (1) fournir une base de données géochronologiques complète et fiable des roches volcaniques (basaltes) et les roches ultramafiques (péridotites) sur le plateau Naturaliste et la zone Diamantina pour lesquelles seulement deux données existent.
- (2) déterminer les caractéristiques géochimiques (systématiques isotopiques Sr-Nd-Pb-Os) pour connaître la nature des sources mantelliques des basaltes afin de tester une contribution éventuelle d'un panache mantellique.
- (3) comparer l'activité magmatique de la marge de WA avec les marges conjuguées Ibérie-Terre-Neuve en termes de distribution spatiale et temporelle et de caractéristiques chimiques des sources des roches volcaniques.

6. Conclusions

Les modèles actuels de formation des marges passives ne semblent plus être adaptés pour décrire la distribution spatiale et temporelle du magmatisme qui leur est associé et pour décrire les liens génétiques entre ce magmatisme, la fracturation lithosphérique et les panaches mantelliques.

Les recherches menées depuis presque vingt ans sur le magmatisme intraplaque de la marge ibérique montrent clairement que cette marge n'est pas « non-volcanique » et ne peut plus être considérée comme l'archétype de ce type de marge. Le concept de marge non-volcanique sans l'implication d'un panache mantellique par opposition à celui de marge volcanique formée par l'action d'un panache profond ne traduit qu'une réalité géologique tronquée par le manque de données au moment de la formulation de ces concepts. Les marges passives devraient être plutôt classifiées en fonction de la présence ou non de trois phases magmatiques : (1) CFB (magmatisme tholéïtique) au

début de la fracturation ; (2) magmatisme alcalin au cours de la phase principale de rifting ; (3) magmatisme alcalin post-rifting et en fonction de la durée de ces phases.

Le problème essentiel concernant les modèles de formation des marges reste l'implication d'un panache mantellique à l'origine et au cours de l'évolution de la marge. Les modèles impliquant des panaches mantelliennes restent extrêmement populaires bien que leur implication dans la génèse des CFBs au tout début de la fracturation des supercontinents semble de plus en plus contestée. Plus largement, l'hypothèse de panaches mantelliennes comme origine du magmatisme intraplaque, reste un sujet très débattu au sein de la communauté scientifique.

Très clairement, si les modèles actuels doivent être remis en cause, voire rejetés, cela ne peut se faire que sur la base de nouvelles données représentatives et fiables, que je compte acquérir comme je viens de le proposer dans mon projet de recherche.

Références bibliographiques

- Alibert C., 1985. A Sr–Nd isotope and REE study of late Triassic dolerites from the Pyrénées (France) and the Messejana dyke (Spain and Portugal). *Earth and Planetary Sciences Letters*, 73, 81-90.
- Anderson D.L., 1994. The sublithospheric mantle as the source of subcontinental flood basalts; the case against the continental lithosphere and plume head reservoir. *Earth and Planetary Science Letters*, 123, 269-280.
- Bernard-Griffiths J., Gruau G., Cornen G., Azambre B., Macé J., 1997. Continental lithospheric contribution to alkaline magmatism: isotopic (Nd, Sr, Pb) and geochemical (REE) evidence from Serra de Monchique and Mount Ormonde Complexes. *Journal of Petrology*, 38, 115-132.
- Beslier M.-O., Royer J.-Y., Girardeau J., Hill P. J., Boeuf E., Buchanan C., Chatin, F., Jacovetti G., Moreau A., Munsch M., Partouche C., Robert U., Thomas S., 2004. A wide ocean-continent transition along the south-west Australian margin: First results of the MARGAU/MD110 cruise [Une large transition continent-océan en pied de marge sud-ouest australienne : Premiers résultats de la campagne MARGAU/MD110]. *Bulletin de la Société Géologique de France*, 175, 629-641.
- Blackburn T.J., Olsen P.E., Bowring S.A., Mclean N.M., Kent D.V., Puffer J., McHone G., Rasbury E.T., Et-Touhami M., 2013. Zircon U-Pb Geochronology Links the End-Triassic Extinction with the Central Atlantic Magmatic Province. *Science*, 340, 941–945.
- Boillot G., Féraud G., Recq M., Girardeau J., 1989. Undercrusting by serpentinite beneath rifted margins. *Nature*, 341, 523-525.

Bryan S.E., Ernst R.E., 2008. Revised Definition of Large Igneous Provinces (LIPs). *Earth-Science Reviews*, 86, 175–202.

Callegaro S., Marzoli A., Bertrand H., Chiaradia M., Reisberg L., Meyzen C., Bellieni G., Weems R.E., Merle R., 2013. Upper and lower crust recycling in the source of CAMP basaltic dykes from southeastern North America. *Earth and Planetary Science Letters*, 376, 186–199.

Campbell I.H., 2007. Testing the plume theory, *Chemical Geology*, 241, 153-17.

Carlson R.W., 2005. Application of the Pt–Re–Os isotopic systems to mantle geochemistry and geochronology. *Lithos*, 82, 249-272.

Cebria J.M., Lopez-Ruiz J., Doblas M., Martins L.T., Munha, J., 2003. Geochemistry of the Early Jurassic Messejana-Plasencia dyke (Portugal–Spain); implications on the origin of the Central Atlantic Magmatic Province. *Journal of Petrology*, 44, 547-568.

Charpentier S., Kornprobst J., Chazot G., Cornen G., Boillot G., 1998. Lithosphere–asthenosphere interaction during continental breakup: preliminary isotopic data on the passive Galicia margin (North-Atlantic). *Comptes Rendus de l'Académie des Sciences - Serie IIa: Sciences de la Terre et des Planètes*, 376, 757-762.

Chatin F., Robert U., Montigny R., Whitechurch H., 1998. The Diamantina rift zone (eastern Indian Ocean): petrological and geochemical approach [La zone Diamantine (océan Indien oriental), témoin de la séparation entre l'Australie et l'Antarctique: arguments pétrologiques et géochimiques]. *Comptes Rendus de l'Académie des Sciences - Série IIa: Sciences de la Terre et des Planètes*, 326, 839-845.

Coffin M.F., Eldholm O., 1994. Large igneous provinces: Crustal structure, dimensions, and external consequences. *Reviews of Geophysics*, 32, 1-36.

Coffin M.F., Pringle M.S., Duncan R.A., Gladzenko T.P., Storey M., Müller R.D., Gahagan L. A., 2002. Kerguelen hotspot magma output since 130 Ma. *Journal of Petrology*, 43, 1121-1139.

Coleman P.J., Michael, P.J. and Mutter, J.C., 1982. The origin of the Naturaliste Plateau, SE Indian Ocean: implications from dredged basalts. *Journal of Geological Society of Australia*, 29, 47-468.

Courtillot V.E., Jaupart C., Manighetti I., Tapponnier P., Besse J., 1999. On causal links between flood basalts and continental breakup. *Earth and Planetary Science Letters*, 166, 177-195.

Dadd K.A., Kellerson L., Borissova I., Nelson G. 2015. Multiple sources for volcanic rocks dredged from the Western Australian rifted margin. *Marine Geology*, 368, 42-57.

Davies J., Marzoli A., Bertrand H., Youbi N., Ernesto M., Schaltegger U., 2017. End-Triassic mass extinction started by intrusive CAMP activity. *Nature Communications*, DOI 10.1038/NCOMMS15596.

Ferreira M., Macedo C.R., 1983. Igneous rocks in the diapiric areas of the western Portuguese border: the K-Ar ages and settings of the Upper Jurassic suite. *Mem. Not. Univ. Coimbra Mus. Lab. Mineral. Geol.*, 96, 159–181.

Forsyth D., Uyeda S., 1975. On the relative importance of the driving forces of plate motion, *Geophysical Journal of the Royal Astronomical Society*, 43, 163-200.

Franke D., 2013. Rifting, lithosphere breakup and volcanism: Comparison of magma-poor and volcanic rifted margins. *Marine and Petroleum Geology*, 43, 63-87.

Frey F.A., McNaughton N.J., Nelson D.R., deLaeter J.R., Duncan R.A., 1996. Petrogenesis of the Bunbury Basalt, Western Australia: interaction between the Kerguelan plume and Gondwana lithosphere? *Earth and Planetary Science Letters*, 144, 1-2, 163-183.

Ford A.B., 1975. Volcanic rocks of Naturaliste Plateau, eastern Indian Ocean, Site 264, DSDP Leg 28. *Initial Report DSDP (Deep Sea Drilling Program)*, 28, 821-833.

Foulger G., 2007. The ‘Plate’ model for the genesis of melting anomalies. In: Foulger G., Jurdy D. (Eds.), The Origins of Melting Anomalies: Plumes, Plates, and Planetary Processes. *Geological Society of America Special Paper*, 430, 1–28.

Geldmacher J., Hoernle K., 2000. The 72 Ma geochemical evolution of the Madeira hotspot (eastern North Atlantic): recycling of Paleozoic (≤ 500 Ma) oceanic lithosphere. *Earth and Planetary Sciences Letters*, 183, 73-92.

Geldmacher J., Van der Bogaard P., Hoernle K., Schmincke H.-U. 2000. The $^{40}\text{Ar}/^{39}\text{Ar}$ age dating of the Madeira Archipelago and hotspot track (eastern North Atlantic). *Geochemistry Geophysics Geosystems*, 1, doi:10.1029/1999GC000018.

Geldmacher J., Hoernle K., Van den Bogaard P., Duggen S., Werner R., 2005. New $^{40}\text{Ar}/^{39}\text{Ar}$ age geochemical seamounts Canary and Madeira volcanic provinces: Support for the mantle plume hypothesis. *Earth and Planetary Sciences Letters*, 237, 85-101.

Geldmacher J., Hoernle K., Klügel A., Van den Bogaard P., Wombacher F., Berning B., 2006. Origin and geochemical evolution of the Tore-Madeira Rise (eastern North Atlantic). *Journal of Geophysical Research*, B09206. doi:10.1029/2005JB003931.

Geldmacher J., Hoernle K., Klügel A., Van der Bogaard P., Bindeman I., 2008. Geochemistry of a new enriched mantle type locality in the northern hemisphere: Implications for the origin of the EM-I source. *Earth and Planetary Sciences Letters*, 265, 167-182.

Gibbons A.D., Barckhausen U., Van Den Bogaard P., Hoernle K., Werner R., Whittaker J.M., Müller R.D., 2012. Constraining the Jurassic extent of Greater India: Tectonic evolution of the West Australian margin. *Geochemistry, Geophysics, Geosystems*, 13, Q05W13.

Gillard M., Autin J., Manatschal G., Sauter D., Munsch M., Schaming M., 2015. Tectonomagmatic evolution of the final stages of rifting along the deep conjugate Australian-Antarctic magma-poor rifted margins: Constraints from seismic observations. *Tectonics*, 34, 753-783.

Girardeau J., Evans C.A., Beslier M.-O., 1988. Structural analysis of plagioclase-bearing peridotites emplaced at the end of continental rifting: Hole 637A, ODP Leg 103 on the Galicia margin. *ODP Proceeding, scientific results, Leg 103, Galicia Margin*, 209-223.

Girardeau J., Cornen G., Beslier M. O., Le Gall B., Monnier C., Agrinier P., Dubuisson G., Pinheiro L., Ribeiro A., Whitechurch H., 1998. Extensional tectonics in the Gorringe Bank rocks, Eastern Atlantic Ocean: evidence of an oceanic ultra-slow mantelllic accreting center. *Terra Nova*, 10, 330-336.

Goncharov A., Nelson G., 2012. From two way time to depth and pressure for interpretation of seismic velocities offshore: Methodology and examples from the Wallaby Plateau on the West Australian margin. *Tectonophysics*, 572-573, 26-37.

Grange M., Schärer U., Cornen G., Girardeau J., 2008. First alkaline magmatism during Iberia-Newfoundland rifting, *Terra Nova*, 20, 494-503.

Ingle S., Weis D., Scoates J.S., Frey F.A., 2002. Relationship between the early Kerguelen plume and continental flood basalts of the paleo-Eastern Gondwanan margins. *Earth and Planetary Science Letters*, 197, 35-50.

Ingle S., Scoates J.S., Weis D., Brügmann G., Kent R.W., 2004. Origin of Cretaceous continental tholeiites in southwestern Australia and eastern India: insights from Hf and Os isotopes. *Chemical Geology*, 209, 83-106.

Jagoutz O., Müntener O., Manatschal G., Rubatto D., Péron-Pinvidic G., Turrin B.D., Villa I.M., 2007. The rift-to-drift transition in the North Atlantic: A suttering start of the MORB machine? *Geology*, 35, 1087-1090.

Jourdan F., Bertrand H., Schärer U., Blichert-Toft J., Féraud G., Kampunzu A.B., 2007. Major and Trace element and Sr, Nd, Hf and Pb isotope compositions of the Karoo Large Igneous Province, Botswana-Zimbabwe: lithosphere vs mantle plume contribution. *Journal of Petrology*, 48, 1043-1077.

Jourdan F., Marzoli A., Bertrand H., Cirilli S., Tanner L., Kontak D.J., McHone G., Renne P.R., Bellieni G., 2009. $^{40}\text{Ar}/^{39}\text{Ar}$ ages of CAMP in North America: implications for the Triassic-Jurassic boundary and the ^{40}K decay constant bias. *Lithos*, 110, 167-180.

Mahoney J.J., Jones W.B., Frey F.A., Salters V.J.M., Pyle D.G., Davies H.L., 1995. Geochemical characteristics of lavas from Broken Ridge, the Naturaliste Plateau and southernmost Kerguelen Plateau: Cretaceous plateau volcanism in the southeast Indian Ocean. *Chemical Geology*, 120, 315-345.

Manatschal G., 2004. New models for evolution of magma-poor rifted margins based on a review of data and concepts from West Iberia and the Alps. *International Journal of Earth Sciences*, 93, 432-466.

Marzoli A., Renne P.R., Piccirillo E.M., Ernesto M., Bellieni G., DeMin A., 1999. Extensive 200 million years old continental flood basalts from the Central Atlantic Magmatic Province. *Science*, 248, 616-618.

Marzoli A., Jourdan F., Puffer J.H., Cuppone T., Tanner L.H., Weems R.E., Bertrand H., Cirilli S., Bellieni G., De Min A., 2011. Timing and duration of the Central Atlantic magmatic province in the Newark and Culpeper basins, eastern U.S.A. *Lithos*, 122, 175-188.

Mata J., Kerrich R., MacRae N.D., Wu T.-W., 1998. Elemental and isotopic (Sr, Nd and Pb) characteristics of Madeira Island basalts: evidence for a composite HIMU-EMI plume fertilizing lithosphere. *Canadian Journal of Earth Sciences*, 35, 980-997.

Mata J., Alves C.F., Martins L., Miranda R., Madeira J., Pimentel N., Martins S., Azevedo M.R., Youbi N., De Min A., Almeida I.M., Bensalah M.K., Terrinha P., 2015. $^{40}\text{Ar}/^{39}\text{Ar}$ ages and petrogenesis of the West Iberian Margin onshore magmatism at the Jurassic-Cretaceous transition: Geodynamic implications and assessment of open-system processes involving saline materials. *Lithos*, 236-237, 156-172.

McHone J.G., 2000. Non-plume magmatism and rifting during the opening of the Central Atlantic Ocean. *Tectonophysics*, 316, 287-296.

McHone J.G., 2003. Volatile emissions of Central Atlantic Magmatic Province basalts: mass assumptions and environmental consequences, The Central Atlantic Magmatic Province, *AGU Geophysical Monograph*, 136, 241-254.

Merle O., 2011. A simple continental rift classification. *Tectonophysics*, 513, 88-95.

Merle R., Scharer U., Girardeau, J.; Cornen, G., 2006. Cretaceous seamounts along the ocean-continent of Iberian margin: U-Pb ages and Sr-Pb-Hf isotopes. *Geochimica et Cosmochimica Acta*, 70, 4950-4976.

Merle R., Jourdan F., Marzoli A., Renne P.R., Grange M., Girardeau J., 2009. Evidence of multi-phase Cretaceous to Quaternary alkaline magmatism on Tore-Madeira Rise and neighbouring seamounts from $^{40}\text{Ar}/^{39}\text{Ar}$ ages. *Journal of the Geological Society of London*, 166, 879-894.

Merle R., Marzoli A., Reisberg L., Bertrand H., Nemchin A., Chiaradia M., Callegaro S., Jourdan F., Bellieni G., Kontak D., Puffer J., McHone J.G., 2014. Sr, Nd, Pb and Os

Isotope Systematics of CAMP Tholeiites from Eastern North America (ENA): Evidence of a Subduction-enriched Mantle Source. *Journal of Petrology*, 55, 133-180.

Merle R., Jourdan F., Girardeau J., 2018. Geochronology of the Tore-Madeira Rise seamounts and surrounding areas: a review. Accepté à *Australian Journal of Earth Sciences*.

Mihut D., Muller D., 1998. Volcanic margin formation and Mesozoic rift propagators in the Cuvier Abyssal Plain off Western Australia. *Journal of Geophysical Research*, 103, 27135-27149.

Morgan W.J., 1972. Plate motions and deep mantle convection. *Memoir of the Geological Society of America*, 132, 7-22.

Morgan W.J., 1971. Convection plumes in the lower mantle. *Nature*, 230, 42-43.

Munsch M., 1998. The Diamantina Zone as the result of rifting between Australia and Antarctica: Geophysical constraints [La zone de Diamantine, témoin de la séparation de l'Australie et de l'Antarctique: Arguments géophysiques]. *Comptes Rendus de l'Académie des Sciences - Série IIa: Sciences de la Terre et des Planètes*, 327, 533-540.

Nirrengarten M., Manatschal G., Tugend J., Kusznir N.J., Sauter D., 2017. Nature and origin of the J-magnetic anomaly offshore Iberia–Newfoundland: implications for plate reconstructions. *Terra Nova*, 29, 20-28.

Nirrengarten M., Manatschal G., Tugend J., Kusznir N., Sauter D., 2018. Kinematic evolution of the southern North Atlantic: Implications for the formation of hyperextended rift systems. *Tectonics*, 37, 89-118.

Olieroor H.K.H., Timms N.E., Merle R.E., Jourdan F., Wilkes P.G., 2015a. Paleo-drainage and fault development in the southern Perth Basin, Western Australia during and after the breakup of Gondwana from 3D modelling of the Bunbury Basalt. *Australian Journal of Earth Sciences*, 62, 289-305.

Olieroor H.K.H., Merle R.E., Jourdan F., Sircombe K., Fraser G., Timms N.E., Nelson G., Dadd K.A., Kellerson L., Borissova I., 2015b. Age and geochemistry of magmatism on the oceanic Wallaby Plateau and implications for the opening of the Indian Ocean. *Geology*, 43, 971-974.

Olieroor H.K.H., Jourdan F., Merle R.E., Timms N.E., Kusznir N.J., Muhling J., 2016. Bunbury Basalt: Gondwana breakup products or earliest vestiges of the Kerguelen mantle plume? *Earth and Planetary Science Letters*, 440, 20-32.

Olieroor H.K.H., Merle R.E., Jourdan F., 2017. Toward a Greater Kerguelen large igneous province: Evolving mantle source contributions in and around the Indian Ocean. *Lithos*, 282-283, 163-172.

Olivet J.-L., 1996. La cinématique de la plaque Ibérique, Bulletin des Centres de Recherche et Exploration-Production Elf Aquitaine, 20, 131-195.

Peucker-Ehrenbrink B., Jahn B.-M., 2001. Rhenium-osmium isotope systematics and platinum group element concentrations: Loess and the upper continental crust. *Geochemistry Geophysics Geosystems*, 2001GC000172.

Pinheiro L.M., Wilson R.C.L., Pena dos Reis R., Whitmarsh R.B., Ribeiro A., 1996. The western Iberia margin: a geophysical and geological overview. In: Whitmarsh R.B., Sawyer D.S., Klaus A., Masson D.G., (eds.): *Proceedings of the Ocean Drilling Program, Scientific Results*, 149, 3–22.

Pyle D.G., Christe D.M., Mahoney J.J., Duncan R.A., 1995. Geochemistry and geochronology of ancient southeast Indian Ocean and southwest Pacific Ocean seafloor. *Journal of Geophysical Research*, B100, 22261-22282.

Rock N.M.S., 1978. Petrology and petrogenesis of the Monchique alkaline complex, southern Portugal. *Journal of Petrology*, 19, 171–214.

Schärer U., Girardeau J., Cornen G., Boillot G., 2000. 138-121 Ma asthenospheric magmatism prior to continental break-up in the North Atlantic and geodynamic implications. *Earth and Planetary Sciences Letters*, 181, 555-572.

Sibuet J.-C., Srivastava S., Spakman W. 2004. Pyrenean orogeny and plate kinematics. *Journal of Geophysical Research*, 108, B08104.

Steinberger B., 2000. Plumes in a convecting mantle: Models and observations for individual hotspots. *Journal of Geophysical Research: Solid Earth*, 105, 1999JB900398, 11127-11152.

Storetvedt K.M., Mogstad H., Abrançhes M.C., Mitchell J.G., Serralheiro A., 1987. Paleomagnetism and isotopic age data from Upper Cretaceous igneous rocks of W Portugal; geological correlation and plate tectonic aspects. *Geophysical Journal of Royal Astronomical Society*, 88, 241–263.

Stilwell J.D., Quilty P.G., Mantle D.J., 2012. Paleontology of Early Cretaceous deep-water samples dredged from the Wallaby Plateau: New perspectives of Gondwana break-up along the Western Australian margin. *Australian Journal of Earth Sciences*, 59, 29-49.

Sutra E., Manatschal G., Mohn G., Unternehr P., 2013. Quantification and restoration of extensional deformation along the Western Iberia and Newfoundland rifted margins. *Geochemistry, Geophysics, Geosystems*, 14, 2575-2597.

Tucholke B.E., Ludwig W.J., 1982. Structure and origin of the J Anomaly Ridge, Western North Atlantic Ocean. *Journal of Geophysical Research*, 87, 9389-9407.

Tucholke B.E., Sawyer D.S., Sibuet J.C., 2007. Breakup of the Newfoundland-Iberia rift. In: Karner, G.D., Manatschal G., and Pinheiro L.M., (eds.): Imaging, mapping and

modelling continental lithosphere extension and breakup. *Geological Society of London, Special Publication*, 282, 9-46.

Turcotte D.L., Oxburgh E.R., 1976. Stress accumulation in the lithosphere. *Tectonophysics*, 35, 183-199.

Veevers J.J., 2012. Reconstructions before rifting and drifting reveal the geological connections between Antarctica and its conjugates in Gondwanaland. *Earth-Science Reviews*, 111, 249-318.

Verati C., Jourdan F., 2014. Modelling effect of sericitization of plagioclase on the $^{40}\text{K}/^{40}\text{Ar}$ and $^{40}\text{Ar}/^{39}\text{Ar}$ chronometers: Implication for dating basaltic rocks and mineral deposits. In: Jourdan F., Mark D., Verati C., (eds.): Advances in $^{40}\text{Ar}/^{39}\text{Ar}$ Dating: from Archaeology to Planetary Sciences. *Geological Society of London, Special Publication*, 378, 155-174.

Verhoef J., Roest W.R., Macnab R., Arkani-Hamed J. and Members of the Project Team 1996. Magnetic anomalies of the Arctic and North Atlantic Oceans and Adjacent land areas, GSC Open file 3125. *Geological Survey of Canada*, 225.

Ware B., Jourdan F., 2018. $^{40}\text{Ar}/^{39}\text{Ar}$ Geochronology of Terrestrial Pyroxene. *Geochimica Cosmochimica Acta*, sous presse.

Wendt I., Kreuzer H., Muller P., Von Rad U., Raschka H., 1976. K-Ar age of basalts from Great Meteor and Josephine seamount (eastern North Atlantic). *Deep-Sea Research*, 23, 849-862.

Widom E., 1997. Sources of ocean island basalts: a review of the osmium isotope evidence. *Physica, A* 244, 484-496.

Wilson, J.T., 1963a. Continental drift. *Scientific American*, 208, 86-103.

Wilson J.T., 1963b. A possible origin of the Hawaiian Islands. *Canadian Journal of Physics*, 41, 863-870.

White R., McKenzie D., 1989. Magmatism at rift zones: the generation of volcanic continental margins and flood basalts. *Journal of Geophysical Research*, 94, 7685-7729.

Whitmarsh R.B., Avedik F., Saunders M.R., 1986. The seismic strucuture of thinned continental crust in the northern Bay of Biscay. *Geophysical Journal of the Royal Astronomical Society*, 86, 589-602.

Annexes

Annexe 1 : liste complète des publications et communications en congrès

Articles à comité de lecture

Soumis :

Sanchez G., **Merle R.**, Hinschberger F., Girardeau J. Post-seafloor spreading magmatism in the Atlantic Ocean : insight from submarine volcanoes of the Tore-Madeira Rise. Soumission prévu à *Marine Geology*.

Pidgeon R.T., **Merle R.E.**, Grange M.L., Nemchin A.A., Whitehouse M.J., Annealing history of zircons in three Apollo 14 impact breccias from around Cone Crater. Soumis à *Meteoritics and Planetary Science*.

Ware B., Jourdan F., **Merle R.**, Chiaradia M., Hodges K., Major, Trace, and Isotope Geochemistry of the Kalkarindji Large Igneous Province, Australia: Petrogenesis of the oldest province of the Phanerozoic. Accepté à *Journal of Petrology*.

Merle R., Jourdan F., Girardeau J., Geochronology of the Tore-Madeira Rise seamounts and surrounding areas: a review. Accepté à *Australian Journal of Earth Sciences*.

Chapitres de livre :

Marzoli A., Callegaro S., Dal Corso J., Davies J.H.F.L., Chiaradia M., Youbi N., Bertrand H., Reisberg L., **Merle R.**, Jourdan F., The Central Atlantic magmatic province: a review, in: Tanner L. (ed.), *The Late Triassic World: Earth in a Time of Transition, Topics in Geobiology*, Springer, 91-127, 2017.

Publications :

22- **Merle R.**, Marzoli A., Aka F.T., N'ni J., Chiaradia M., Castorina F., Reisberg R., Jourdan F., Renne P.R., Nyobe J.B., Mt Bambouto volcano, Cameroon Line: mantle source and differentiation of within-plate alkaline rocks, *Journal of Petrology*, 58, 933-962, 2017.

21- Olierook H.K.H., **Merle R.E.**, Jourdan F., Evolving mantle component contributions of the Greater Kerguelen Large Igneous Province, *Lithos*, 282-283, 163-172, 2017. 4 citations.

20- Marzoli A., Davies J., Youbi N., **Merle R.**, Dal Corso J., Dunkley D. J., Fioretti A.-M., Bellieni G., Medina F., Wotzlaw J.-F., McHone G., Font E., Bensalah M. K., Proterozoic

to Mesozoic evolution of North-West Africa and Peri-Gondwana microplates: detrital zircon ages from Morocco and Canada, *Lithos*, 278-281, 229-239, 2017. 1 citation.

19- **Merle R.**, Nemchin A.A., Whitehouse M.J., Pidgeon R.T., Grange M.L., Snape J.F., Thiessen F., Origin and transportation history of lunar breccia 14311, *Meteoritics and Planetary Science*, 52, 842-858, 2017. 1 citation.

18- Oostingh K.F., Jourdan F., **Merle R.**, Chiaradia M., Spatio-temporal geochemical evolution of the SE Australian upper mantle deciphered from Sr, Nd and Pb isotopes of Cainozoic intraplate volcanics, *Journal of Petrology*, 57, 1509-1530, 2016. 1 citation.

17- Olieroor H.K.H., Jourdan F., **Merle R.E.**, Timms N.E., Kusznir N., Muhling J.R., Bunbury Basalt: Gondwana break-up Products or earliest vestiges of the Kerguelen mantle plume? *Earth and Planetary Sciences Letters*, 440, 20-32, 2016. 9 citations.

16- Pidgeon R.T., **Merle R.**, Grange M.L., Nemchin A.A., Whitehouse M.J., Post formation annealing of radiation damage in zircons from Apollo 14 impact breccia 14311, *Meteoritics and Planetary science*, 51, 155-166, 2016. 2 citations.

15- Olieroor H.K.H., **Merle R.E.**, Jourdan F., Sircombe K., Fraser G., Timms N.E., Nelson G., Dadd K.A., Kellerson L., Borissova I., Age and geochemistry of magmatism on the oceanic Wallaby Plateau and implications for the opening of the Indian Ocean, *Geology*, 43, 971-974, 2015. 7 citations.

14- Olieroor H.K.H., Timms N.E., **Merle R.E.**, Jourdan F., Wilkes, P., Paleodrainage and fault development in the southern Perth Basin, Western Australia during and after the breakup of Gondwana from 3D modelling of the Bunbury Basalt, *Australian Journal of Earth Sciences*, 63, 289-305, 2015. 6 citations.

13- Marzoli A., Aka F.T., **Merle R.**, Callegaro S., N'ni J., Deep to shallow crustal differentiation of within-plate alkaline series, an example from Mt. Bambouto volcano, Cameroon Line, *Lithos*, 220-223, 272-288, 2015. 5 citations.

12- Cawood P.A., Strachan R.A., **Merle R.E.**, Millar I.L., Loewy S.L., Dalziel I.W.D., Kinny P.D., Jourdan F., Nemchin A.A., Connelly J.N., Neoproterozoic to early Paleozoic extensional and compressional history of East Laurentian margin sequences: the Moine Supergroup, Scottish Caledonides, *Geological Society of America Bulletin*, 127, 349-371, 2015. 13 citations.

11- **Merle R.**, Nemchin A., Grange M., Whitehouse M., Pidgeon R.T., High-resolution U-Pb Ca-phosphate ages in Apollo 14 breccias: implications for the age of the Imbrium impact, *Meteoritics and Planetary science*, 49, 2241-2251, 2014. 14 citations.

10- **Merle R.**, Marzoli A., Reisberg L., Bertrand H., Nemchin A., Chiaradia M., Callegaro S., Jourdan F., Bellieni G., Kontak D., Puffer J., McHone J.G., Sr, Nd, Pb and Os isotope systematics of CAMP tholeiites from Eastern North America (ENA): Evidence of a subduction-enriched mantle source, *Journal of Petrology*, 55, 133-180, 2014. 20 citations.

- 9- Callegaro S., Andrea Marzoli A., Bertrand H., Chiaradia M., Reisberg L., Meyzen C., Bellieni G., Weems R., **Merle R.**, Crustal recycling recorded in the geochemistry of CAMP basaltic dykes from south-eastern North America, *Earth and Planetary Sciences Letters*, 376, 186-199, 2013. 27 citations.
- 8- Cawood P.A., **Merle R.E.**, Strachan R.A., Tanner P.W.G., Provenance of the Highland Border Complex: constraints on Laurentian margin accretion in the Scottish Caledonides, *Journal of Geological Society of London*, 169, 575-586, 2012. 10 citations.
- 7- **Merle R.**, Kaczmarec M.-A., Tronche E., Girardeau J., Occurrence of inherited supra-subduction zone mantle in the oceanic lithosphere as inferred from mantle xenoliths and xenocrystals from Dragon and Lion seamounts (Southern Tore-Madeira Rise), *Journal of Geological Society of London*, 169, 251-267, 2012. 6 citations.
- 6- Cawood P.A., Leitch E.C., **Merle R.E.**, Nemchin A.A., Orogenesis without collision: Stabilizing the Terra Australis accretionary orogen, eastern Australia, *Geological Society of America Bulletin*, 123, 2240-2255, 2011. 70 citations.
- 5- **Merle R.**, Marzoli A., Verati C., Bertrand H., Reisberg L., Zimmermann C., Chiaradia M., Bellieni G., Ernesto M., $^{40}\text{Ar}/^{39}\text{Ar}$ ages and Sr-Nd-Pb-Os geochemistry of CAMP tholeiites from Western Maranhão basin (NE Brazil), *Lithos*, 122, 137-151, 2011. 28 citations.
- 4- Grange M., Schärer U., **Merle R.**, Girardeau J., Cornen G., Plume-Lithosphere interaction during migration of Cretaceous Alkaline Magmatism in SW Portugal: Evidence from U-Pb Ages and Pb-Sr-Hf Isotopes, *Journal of Petrology*, 51, 1143-1170, 2010. 18 citations.
- 3- **Merle R.**, Jourdan F., Marzoli A., Renne P.R., Grange M., Girardeau J., Evidence of multi-phase Cretaceous to Quaternary alkaline magmatism on Tore-Madeira Rise seamounts from $^{40}\text{Ar}/^{39}\text{Ar}$ ages, *Journal of Geological Society of London*, 266, 1-16, 2009. 18 citations.
- 2- **Merle R.**, Schärer U., Girardeau J., Cornen G., Cretaceous seamounts along the ocean-continent of Iberian margin: U-Pb ages and Sr-Pb-Hf isotopes, *Geochimica et Cosmochimica Acta*, 70, 4950-4976, 2006. 23 citations.
- 1- **Merle R.**, Caroff M., Girardeau J., Cotten J., Guivel C., Segregation vesicles, cylinders, and sheets in vapor-differentiated pillow lavas: examples from Tore-Madeira Rise and Chile Triple Junction, *Journal of Volcanology and Geothermal Research*, 141, 109-122, 2005. 7 citations.

Communications en congrés :

2017

- 27- **R. Merle**, Y. Amelin, K. Kossett, New Determination of ^{40}K Decay Constant: Preliminary Results, Goldschmidt conference, Paris, France, 13-18 August 2017.

26- H. Olierook, **R. Merle**, F. Jourdan, Cretaceous Magmatism along the Rifted Margin of Western Australia: Toward a Greater Kerguelen Large Igneous Province, Goldschmidt conference, Paris, France, 13-18 August 2017.

2016

25- **R. Merle**, Y. Amelin, Step leaching Pb-Pb isochron age of unradiogenic single chondrule from CV Allende chondrite, Annual Meeting of the Meteoritical Society, Berlin, Germany, 7-12 August 2016.

24- Y. Amelin, Q.-Z. Yin, P. Koefoed, **R. Merle**, M.H. Huyskens, T. Iizuka, Fractionation of radiogenic Pb induced by acid leaching: a pervasive phenomenon in Pb-isotopic dating meteorites, Goldschmidt conference, Yokohama, Japan, 26 June-1 July 2016.

23- M.H. Huyskens, Q.-Z. Yin, M.E. Sanborn, Y. Amelin, **R. Merle**, K. Yamashita, U isotopic composition of Allende chondrules and implications for Pb-Pb geochronology, Goldschmidt conference, Yokohama, Japan, 26 June-1 July 2016.

22- M.H. Huyskens, Q.-Z. Yin, M.E. Sanborn, Y. Amelin, **R. Merle**, K. Yamashita, Possible uranium isotopic heterogeneity in Allende chondrules, Lunar and Planetary Sciences Conference, 21-25 March 2016, The Woodlands, Texas, USA.

21- **R.E. Merle**, A.A. Nemchin, M.J. Whitehouse, M.L. Grange, R.T. Pidgeon, J.F. Snape and F. Thiessen, Origin and transportation history of lunar breccia 14311, Lunar and Planetary Sciences Conference, 21-25 March 2016, The Woodlands, Texas, USA.

2015

20- A. Marzoli, **R. Merle**, N. Youbi, D.J. Dunkley, J. Dal Corso, B. Andreucci, E. Font, G. Bellieni, A.M. Fioretti, Provenance Of Detrital Zircons From The High Atlas Of Morocco Deciphered By SHRIMP U-Pb Dating, XII international symposium on Antarctic Earth Sciences, 13-17 July 2015, Goa, India.

19- F. Tomaschek, A. Nemchin, T. Geisler, A. Heuser, **R. Merle**, U-Pb Geochronology of Hydrous Silica (Siebengebirge, Germany), EGU General Assembly, Vienna, 2015, 12-17 April 2015.

2014

18- F. Thiessen, A. Nemchin, M. Withehouse, J. Bellucci, J. Snape, R. Kielman, **R. Merle**, Annual Meeting of the Meteoritical Society, 08-13 September 2014, Casablanca, Morocco.

17- Y. Amelin, **R. Merle**, Q.Z. Yin, K. Yamashita, K. Nagashima, A.N. Krot, L.M. Heaman, The potential of multi-step dissolutionin Pb isotopic dating of individual chondrules, Lunar and Planetary Sciences Conference, 17-21 March 2014, The Woodlands, Texas, USA.

2013

16- **R. Merle**, A. Nemchin, S. Simons, F. Tomaschek, T. Geisler, Rates of Natural silica precipitation through time, Goldschmidt conference 2013, Florence, Italy, 25-30 August 2013.

15- M. Norman, A. Nemchin, M. Grange, R. Zeigler, M. Whitehouse, J. Muhling, **R. Merle**, U-Pb ages and compositions of Apollo 14 regolith glasses, Annual Meeting of the Meteoritical society 2013, Edmonton, Canada, 29 July-2 August 2013.

14- **R. Merle**, M. Grange, A. Nemchin, M. Whitehouse, Stratigraphy of the Fra Mauro Formation defined by U-Pb zircon ages of breccias samples from Apollo 14 landing site, Lunar and Planetary Sciences Conference, 18-22 March 2013, The Woodlands, Texas, USA.

13- M. Grange, A. Nemchin, R. Pidgeon, **R. Merle**, N. Timms, What Lunar zircon ages can tell? Lunar and Planetary Sciences Conference, 18-22 March 2013, The Woodlands, Texas, USA.

2012

12- **R. Merle**, M. Grange, A. Nemchin, R. Pidgeon, Comparison of zircon U-Pb ages of apollo 14 breccias, Annual Meeting of the Meteoritical society, August 2012, Cairns, Australia.

11- **R. Merle**, A. Marzoli, L. Reisberg, H. Bertrand, A. Nemchin, M. Chiaradia, S. Callegaro, F. Jourdan, G. Bellieni, New mantle source model for CAMP tholeiites of northeast America from Sr-Nd-Pb-Os isotopes, International Geological Congress 2012, Brisbane, Australia, August 2012.

10- **R. Merle**, M.-A. Kaczmarek, E. Tronche, J. Girardeau, Lithosphere as inferred from mantle xenoliths from Dragon Seamount (Southern Tore-Madeira Rise), International Geological Congress 2012, Brisbane, Australia, August 2012.

2004-2011

9- A. Marzoli, F.T. Aka, M. Chiaradia, L. Reisberg, **R. Merle**, Origin of Cameroon Line basanites from metasomatized lithosphere, Goldschmidt conference 2011, Prague, Czech Republic, 14-19 August 2011.

8- J. Girardeau, **R. Merle**, A. Marzoli, M. Chiaradia, Age and origin of alkaline lavas from Tore-Madeira Rise: interactions between complex lithosphere motion and multi-components source, Goldschmidt conference 2011, Prague, Czech Republic, 14-19 August 2011.

7- **R. Merle**, A. Marzoli, H. Bertrand, L. Reisberg, M. Chiaradia, G. Bellieni, Sr-Nd-Pb-Os isotopes of CAMP tholeiites from northeast America, Goldschmidt conference 2011, Prague, Czech Republic, 14-19 August 2011.

6- **R. Merle**, A. Marzoli, C. Verati, H. Bertrand, M. Chiaradia, L. Reisberg, G. Bellieni, M. Ernesto, $^{40}\text{Ar}/^{39}\text{Ar}$ ages and Sr-Nd-Pb-Os geochemistry of Maranhão CAMP tholeiites (Brazil): implications for low and high-Ti basalts sources, Geophysical research abstract, EGU General Assembly, Vienna, 2008.

5- **R. Merle**, F. Jourdan, J. Girardeau, A. Marzoli, P. Renne. Evidence of multi-phases alkaline magmatism on Tore-Madeira Rise seamounts from $^{40}\text{Ar}/^{39}\text{Ar}$ ages. Geophysical Research Abstract, EGU General Assembly, Vienna, 2008.

4- **R. Merle**, A. Marzoli, C. Verati, H. Bertrand, M. Chiaradia, G. Bellieni, M. Ernesto, $^{40}\text{Ar}/^{39}\text{Ar}$ ages and geochemistry of Maranhão CAMP tholeiites (Brazil): implications for low and high-Ti basalts sources, Goldschmidt conference 2007, Cologne, Germany, 19-24 August 2007.

3- **R. Merle**, M. Caroff, J. Girardeau, J. Cotten, C. Guivel, Segregation vesicles, cylinders and sheets in vapor-differentiated pillow lavas: examples from Tore-Madeira Rise and Chile Triple Junction, European Geosciences Union, General Assembly 2005, Vienna, Austria, 24-29 April 2005.

2- **R. Merle**, U. Schärer, G. Cornen, J. Girardeau, J. Cotten, Age and origin of the alkaline lavas from northern, Tore-Madeira Rise (Iberia margin): U-Pb ages, geochemistry and Pb-Sr isotopes, European Geosciences Union, General Assembly 2005, Vienna, Austria, 24-29 April 2005.

1- **R. Merle**, U. Schärer, G. Cornen, J. Girardeau, J. Cotten, Origin of Tore-Josephine seamounts from U-Pb ages, geochemistry and Pb isotopes, Joint Earth Sciences Meeting Société Géologique de France - Geologische Vereinigung, 20-25 September 2004, Strasbourg, France.

Annexe 2 : Sélection d'articles (thématique de recherche principale)

- 1- Sanchez G., **Merle R.**, Hinschberger F., Girardeau J. Post-seafloor spreading magmatism in the Atlantic Ocean : insight from submarine volcanoes of the Tore-Madeira Rise. Soumission prévu à *Marine Geology*.
- 2- **Merle R.**, Jourdan F., Girardeau J., Geochronology of the Tore-Madeira Rise seamounts and surrounding areas: a review. *Australian Journal of Earth Sciences*, accepté.
- 3- Olieroor H.K.H., **Merle R.E.**, Jourdan F., Sircombe K., Fraser G., Timms N.E., Nelson G., Dadd K.A., Kellerson L., Borissova I., Age and geochemistry of magmatism on the oceanic Wallaby Plateau and implications for the opening of the Indian Ocean, *Geology*, 43, 971-974, **2015**.
- 4- **Merle R.**, Marzoli A., Reisberg L., Bertrand H., Nemchin A., Chiaradia M., Callegaro S., Jourdan F., Bellieni G., Kontak D., Puffer J., McHone J.G., Sr, Nd, Pb and Os isotope systematics of CAMP tholeiites from Eastern North America (ENA): Evidence of a subduction-enriched mantle source, *Journal of Petrology*, 55, 133-180, **2014**.
- 5- Grange M., Schärer U., **Merle R.**, Girardeau J., Cornen G., Plume-Lithosphere interaction during migration of Cretaceous Alkaline Magmatism in SW Portugal: Evidence from U-Pb Ages and Pb-Sr-Hf Isotopes, *Journal of Petrology*, 51, 1143-1170, **2010**.
- 6- **Merle R.**, Jourdan F., Marzoli A., Renne P.R., Grange M., Girardeau J., Evidence of multi-phase Cretaceous to Quaternary alkaline magmatism on Tore-Madeira Rise seamounts from $^{40}\text{Ar}/^{39}\text{Ar}$ ages, *Journal of Geological Society of London*, 266, 1-16, **2009**.
- 7- **Merle R.**, Schärer U., Girardeau J., Cornen G., Cretaceous seamounts along the ocean-continent of Iberian margin: U-Pb ages and Sr-Pb-Hf isotopes, *Geochimica et Cosmochimica Acta*, 70, 4950-4976, **2006**.

1 Post-spreading deformation and associated magmatism along the Iberia-Morocco

2 **Atlantic margins: insight from submarine volcanoes of the Tore-Madeira Rise**

3 Guillaume Sanchez^{a*}, Renaud Merle^b, Florent Hinschberger^c, Isabelle Thinon ^d, Jacques

4 Girardeau^e,

5 ^aFrogtech Geoscience, Suite 17F, Level 1, 2 King Street, Deakin West, ACT 2600, Australia.

6 ^bResearch School of Earth and Planetary Sciences, Curtin University, GPO Box U1987,

7 Perth, WA 6845, Australia.

8 ^cLaboratoire de Géologie des Environnements Aquatiques Continentaux, Université de Tours,

9 UFR Sciences et Techniques, Parc de Grandmont, 37200 Tours, France.

10 ^dBRGM, Orléans, France.

11 ^eLaboratoire de Planétologie et Géodynamique, UMR-CNRS 6112, Université de Nantes, 2

12 rue de la Houssinière, 44322 Nantes cedex 3, France.

13 Corresponding author: gsanchezfr@gmail.com

14

15

16

17

18

19

20

21

22

23 **Abstract**

24 A new high-resolution bathymetric map combined with a regional DEM analysis reveal post-
25 spreading magmatism along the NNE-SSW oriented Tore-Madeira Rise (TMR) seamount
26 (1000×50 km) alignment associated with the activity of major fault systems including the
27 Estremadura Fault System (ESF) and the Azores-Gibraltar Fracture Zone (AGFZ).
28 Morphological and structural analysis of the bathymetric map were performed to map
29 volcanic features such as eruptive cones, vents and fissures together with faults along the
30 TMR to better understand the relationships between magmatism emplacement and
31 deformation. The new bathymetric map shows that the main NNW-SSE seamount alignment
32 is formed by three structurally distinct volcanic massifs, the Tore complex, the Josephine
33 complex and the southern group complex. The majority of the volcanoes within each group
34 emplaced within or along specific portion of pre-existing faults (ESF and AGFZ) including
35 splay fault, releasing bend, fault tips and interaction zones between different segments.
36 Magmas were channelled into sub-vertical pre-existing lithospheric faults that acted as
37 preferential pathways for the vertical magma ascent. The inferred NNE-SSW orientation of
38 the TMR is therefore not related to a N-S oriented sub-lithospheric thermal and
39 compositional anomaly source of the TMR magmas. Migration and final eruption of magma
40 are controlled by the local stress along the fault as well as the strong shear zone anisotropy as
41 suggested by the emplacement within localised areas of transtension. All these above-
42 mentioned results explain the limited structural connection between the three distinct
43 volcanic fields along a N-S transect of the TMR volcanoes. The term “Tore-Madeira Rise
44 magmatism” is thus misleading in such poly-phased tectono-magmatic context.

45 **Keywords**

46 **1. Introduction**

47 In oceanic basins, lithospheric discontinuities are likely able to control the geographical
48 distribution of intraplate magmatism and possibly its timing. The occurrence and more
49 importantly the influence of these structures on the localisation of the magmatism can be
50 diagnosed using the bathymetric data from seamounts chains and groups.

51 The Tore-Madeira Rise (TMR), a roughly NNE-SSW trending seamounts chain (Fig. 1),
52 represents one of the most significant magmatic features of the northern central Atlantic
53 Ocean. Many authors have suggested the involvement of the lithospheric discontinuities to
54 explain the localisation of the magmatic occurrences on TMR (Geldmacher et al., 2006;
55 Merle et al., 2006) but this aspect of TMR magmatism was never fully investigated. More
56 importantly, the morphology of TMR seamounts in particular, the volcanic features was
57 never investigated despite this might provide key evidences on the formation of TMR and an
58 insight of its origin.

59 In this study, we examined high resolution swath bathymetric data and global DEM dataset to
60 better understand the morphology of the Tore-Madeira volcanic features including volcanoes,
61 eruptive fissures and faults. Global DEM datasets with an increasing accuracy and spatial
62 resolution are now publicly available which allows better quantitative surface analysis. This
63 paper provides the first detailed map of the topography and major morpho-tectonic structures
64 of the TMR seamounts with the aim of deciphering the structural control on TMR formation
65 and provide new constrains on its origin.

66

67 **2. Geological Setting**

68 ***2.1. The western Iberia and north-west Morocco margin***

69 The West Iberia and the NW Morocco margins belong to the southern North Atlantic and
70 northern Central Atlantic Oceans which are separated by the Azores-Gibraltar Fracture Zone
71 (AGFZ; Fig. 1). These margins formed during several phases of continental rifting affecting

72 the Pangea Supercontinent from the Late Triassic until the Late Cretaceous (e.g. Tucholke et
73 al., 2007; Frizon de Lamotte et al., 2015; Peron-Pinvidic and Manatschal, 2009; Schettino
74 and Turco, 2009). These several rift events culminated in the final continental break-up,
75 mantle exhumation, oceanic seafloor spreading and subsequently to the separation of the
76 Iberia, NW Africa and North America plates (Fig. 2) from the Late Jurassic-Early Cretaceous
77 (e.g. Boillot et al., 1989; Bronner et al., 2011; Féraud et al., 1988; Kneller et al., 2012;
78 Nirrengarten et al., 2018; Sahabi et al., 2004; Srivastava et al., 2000; Schettino and Turco,
79 2009; Tucholke et al., 2007).

80 Following mantle exhumation around 143-122 Ma (Féraud et al., 1988; Scharer et al., 2000),
81 formation of the southern North Atlantic oceanic crust began between 125 and 112 Ma,
82 although this is highly debated depending on the J- magnetic anomaly interpretation (Fig. 2).
83 Indeed, this magnetic anomaly has been interpreted as the first magnetic anomaly created by
84 the mid-Atlantic ridge offshore Iberia ([Olivet, 1996](#)), as exhumed mantle ([Sibuet et al., 2007](#))
85 or a thickened crust or basement high related to syn- and post-spreading (i.e. TMR) magmatic
86 underplating ([Bronner et al., 2011](#); [Nirrengartner et al., 2017](#)). Mid-ocean ridge activity
87 started during the Late Jurassic-Early Cretaceous along the SW Iberia margin and migrated
88 northward with a final break-up on the NW Iberia-Newfoundland margin at Albian-Aptian
89 time (Fig. 2; [Bronner et al., 2011](#); [Nirrengartner et al., 2018](#); [Tucholke et al., 2007](#)).
90 Spreading was directed NE-SW during the Late Jurassic-Early Cretaceous and change
91 direction toward a E-W axis in relation to the clockwise rotation of Iberia and the opening of
92 the central segment of the North Atlantic (e.g. Barnett-Moore et al., 2018; [Hosseinpour et al.,](#)
93 [2018](#); [Nirrengartner et al., 2018](#); [Visser and Meijer, 2012](#)). In the meantime, left-lateral
94 oblique plate motion along the South Iberia margin resulted in segmented oceanic spreading
95 during the Late Jurassic connecting the Atlantic Ocean (i.e. AGFZ ; [Féraud et al., 1977](#)) to

96 the Alpine Tethys (Martinez-Loriente et al., 2014 ; Ramos et al., 2017 Sallares et al., 2011,
97 2013).

98 During the Cenozoic to present-day, the Iberia margin experienced widespread inversion due
99 to the northward convergence of Africa (Vergés et al., 2002). Rift migration resulted in
100 crustal segmentation and development of several sub-basins bounded by NNE-SSE to N-S
101 major faults with distinct tectonic and subsidence evolution along the West Iberia margin
102 (Alves et al., 2009; Pereira and Alves, 2011). This along-axis margin segmentation is
103 accommodated by major E-W and NE-SW transfer faults including the Nazare Fault Zone
104 and the Messejana-Plasencia Fault Zone (Fig. 1) which controlled basin geometry during the
105 three main periods of rifting from the Late Triassic to the late Early Cretaceous (Pereira and
106 Alves, 2012; Ramos et al., 2017). These faults likely correspond to reactivated pre-existing
107 crustal structures formed during the Late Variscan Orogeny (see Fig. 1). Although well
108 defined in the proximal domain of the margin (i.e. the Estremadura Fault System, ESF; Fig.
109 1; Fig. 2), the eastern continuity of these faults at the transition between the distal and oceanic
110 domains are, however, less clear due to recent inversion along these structures (Pereira et al.,
111 2016).

112 ***2.2. The TMR and surrounding seamounts***

113 TMR is defined as a NNE-SSW aligned seamounts chain, located at 300 km, West of Lisbon,
114 along the margins of Portugal and Morocco and straddling the AGFZ without visible offset
115 (Fig. 2). It extends over 1000km, between the Tore seamounts and Madeira Archipelago,
116 which forms the southernmost complex of the TMR. The main trend is formed by, from north
117 to south, Sponge bob, Ashton, Gago Coutinho, Josephine located close to the AGFZ, Jo
118 Sister, Lion, Dragon and Godzilla (Fig. 2). The northern end of the alignment is the Tore
119 complex which is characterised by an elliptic (120 km by 90 km), 5000 m deep depression
120 rimmed by ~2500 m high seamounts located at the western end of the Estremadura ridge. The

121 westernmost seamount is Torillon lying at around 100 km on the WSW of Tore. Note that a
122 group of three seamounts (Isabelle, Unicorn and Seine) is located slightly on the east of the
123 main alignment. This general NNE-SSW trend is parallel to the high amplitude curvilinear J-
124 magnetic anomaly extending from the Galicia margin to the Madeira archipelago (Fig. 2).
125 The magmatism on TMR is dated between 103 Ma to 0.5 Ma (Geldmacher et al. 2000, 2006;
126 Merle et al. 2006, 2009) represented by Oceanic Island basalt (OIB)-like alkaline lavas
127 ranging in term of petrological types from basalts to trachytes. The TMR magmatism has
128 been interpreted as (1) the first activity of the mid-Atlantic ridge (Tucholke and Ludwig,
129 1982; Pierce and Barton, 1991); (2) an accretion-related off-axis magmatic activity (Jagoutz
130 et al., 2007); (3) the 450km-wide Madeira hot-spot track imprint on the Iberia plate that is
131 based on the apparent decreasing age along a track spanning from Serra de Monchique to
132 Madeira archipelago through Seine, Unicorn, Ampere and Ormonde (Geldmacher et al.,
133 2000; 2001; D’Oriano et al. 2010); (4) the result of the combined effects of the Canary hot-
134 spot during Cretaceous times forming the basement of the rise which was capped by late
135 Tertiary to recent volcanics related to the Madeira hot-spot (Geldmacher et al., 2000; 2006;
136 D’Oriano et al. 2010); or (5) a large thermal anomaly located beneath the lithosphere and
137 emitting magma pulses, the geographical and timing of the magmatic occurrences being the
138 consequence of the interaction between these magma pulses and the complex motions of the
139 Iberia plate controlled by the Pyrenees Orogeny (Merle et al., 2009).

140

141 **3. Data and methods**

142 **3.1. Database**

143 Between September and October 2001, high resolution swath bathymetry was acquired using
144 a SIMRAD DUAL EM12 swath Multibeam Echo sounder system providing a high-resolution

145 bathymetry map of the Tore Seamount Complex and several seamounts of the TMR which
146 were identified as volcanic edifices (Fig. 2). The resulting bathymetric map was produced
147 with 8 different colours corresponding to 100m depth interval and 20m isobaths.

148 The regional EMODnet bathymetric grid of the North and Central Atlantic margins extracted
149 from the EMODnet Bathymetry portal (<http://www.emodnet-bathymetry.eu>) was also used to
150 give a continuous grid of the bathymetry at the regional scale and better understand structural
151 relationship between volcanic features (Fig. 2). This regional EMODnet grid combines high
152 resolution swath bathymetry acquired during the above-mentioned Tore-Madeira marine
153 survey with additional GEBCO DTM grids (For further explanation about processing the
154 reader is pleased to refer to the website). The grid was then re-processed and quality checked
155 to produce a regional digital bathymetric map at 1:230 000 scale (1/8-minute arc; Fig. 2).
156 Elevation contour lines were generated with the elevation interval chosen depending on the
157 DEM resolution. The interval should be approximately half the pixel size (e.g., a ~100m
158 interval for the 230 m DTM).

159 3.2. *Volcanic edifice morphology analyses*

160 To identify and quantify the morphometric parameters of volcanic features, we first analysed
161 the morphology of volcanic edifices, vents and eruptive fissures as well as lineaments on the
162 high-resolution swath bathymetric grid and derived slope distribution maps. We then used the
163 EMODnet bathymetric grid to obtain a regional map of the main volcanic and tectonic
164 structures. Shaded relief with illumination of N315 oblique to the main E-W, NE-SW and N-
165 S structures were processed to highlight lineaments. Given that the resolution of the
166 EMODnet grid is approximately 230m, we selected the features that have a length equal or
167 superior to ~250m which is below the documented average spacing between vents following
168 Applegate (2003) recommendations. To understand structural control on volcanism

169 distribution, we performed volcanic alignment analysis. We assume that vents alignments
170 form relatively straight lines along fissures and vents are subparallel to the overall trace
171 alignment and the subsurface feeder dykes (Tibaldi et al., 1995).

172 Volcanic vents were identified from bathymetric maps either interpolated grid images or
173 contours intervals each of which has intrinsic limitations. One of these is the impact of
174 destruction processes such as submarine landslides which enhance uncertainties in whether
175 the structure is related to gravitational processes or represent the location of a vent. We thus
176 mapped volcanic vents, eruptive fissures that are morphologically recognisable. The
177 alignments of three or more vents forming part of coalescent domes or one vent defining an
178 elliptical edifice were used to identify eruptive fissures. All this morphological information
179 was obtained using Qantum GIS. Stereograms of eruptive fissures and faults were drawn for
180 each area.

181

182 **4. Description of TMR submarine volcanoes morphology**

183 The bathymetric data allow for the first time the description of the topographic features in the
184 study area. From the maps (Fig. 2), it is clear that most of the seamounts are volcanoes and
185 display typical morphological features of volcanic edifices such as vents, lava flows, flank
186 collapse scars. The maximum depth of the seafloor along the Tore Madeira Rise ranges
187 between 3500m and 5000m. All the mapped seamounts have a height ranging between 2000
188 and 4000m above the surrounding seafloor. Summits of some of the volcanoes belonging to
189 the Tore Seamounts Complex are at 2500m above the seafloor while the highest seamounts
190 along the TMR such as Joséphine, Jo Sister, Lion, Unicorn and Seine are 4000m high and
191 less than 1000m below sea level.

192 The new bathymetric map (Fig. 2) shows clearly that TMR seamounts can be grouped into
193 three massifs: the northernmost Tore complex, the Joséphine Group in the central part in the
194 vicinity of the AGFZ and the southern group. The largest seamounts have a base diameter of
195 ~20 to ~50km (Bikini Bottom, Tore Northwest, Ashton, Gago Coutinho: 20-30 km, 48 km
196 for Seine). Such dimensions are comparable to the largest continental volcanoes (Mount
197 Etna: 47×38 km, 3350 m above sea level). Sponge Bob and Tore East seamounts are smaller
198 with a base diameter of ~10 km.

199 **4.1. Submarine volcanoes of the Tore Seamounts group**

200 The Tore Seamounts Group represents the largest volcanic complex of the TMR. It occurs at
201 the northern end of TMR, to the west of the Estremadura Spur and the West Iberian margin
202 (Fig. 2). High-resolution swath bathymetric map (Fig. 3) reveals a highly complex tore-like
203 shape morphology including several prominent topographic features such as (i) a deep basin
204 (Tore Depression) which lies in the central part of the area surrounded by uplifted plateaus
205 (Tore Plateaus) located at an average depth of ~3000m. This depression displays asymmetric
206 rhombohedra shape oriented NE-SW with a maximum subsidence of the seafloor of 5500m
207 to the NE. (ii) Several elongated topographic highs rise above the seafloor and are
208 unambiguously interpreted as submarine volcanoes. Volcanism occurs within a 350km long
209 and 100km wide ENE-WSW to E-W oriented ridge which separates the Iberian Abyssal Plain
210 (IAP) to the north and the Tagus Abyssal Plain (TAP) to the south. This ridge connects the
211 Tore Seamounts Complex to the major lithospheric structures of the Iberian Margin (Fig. 1)
212 suggesting that the shape of the Tore complex and thus, the locus of magmatism is strongly
213 controlled by pre-existing structures.

214 The North Tore and North-West Tore (NW Tore) volcanoes located at the northern edge of
215 the area at the transition with the IAP represent the largest volcanic edifices of the Tore
216 Seamount Complex with a total height of ~2600-2800m (Fig. 3, 4). The limits of the base of

217 the volcanoes are well defined and can be distinguished on the seafloor as shown on the slope
218 map (Fig. 3b). The NW Tore volcano has an elliptical shape oriented roughly E-W to NE-
219 SW. It is a large cone edifice, 60km long and 30km wide. Flanks are steep with average
220 values up to 25-30°. The summit has a narrow width (~2km) with a main elongation axis
221 along an E-W direction. The NW Tore shows on its eastern flank a NE-SW-oriented volcanic
222 cone connected to the main edifice by a NW-SE trending ridge. The general drainage pattern
223 is radial to the main volcano. Small scale humps surrounding the volcano on the seafloor are
224 interpreted as debris from flank collapse or volcanic projections. The southern flank is
225 however less clear as the North Tore volcanic edifice developed on the northern edge of the
226 Central Depression.

227 To the east of the Tore depression and the Northwest Tore and North Tore volcanoes, several
228 smaller volcanic edifices formed part of the East Tore Volcanic field located to the west of
229 the Estremadura Spur (Fig. 3, 4). They present a NE-SW oriented sub-elliptical conical shape
230 with one or two summits. The dimension of these volcanoes range between 1000m and
231 1400m high above seafloor. The East Tore volcano represents the largest edifice, 26km long
232 along the NNE-SSW direction and 14km wide along the NW-SE axis. Its flanks are relatively
233 steep to the south-west part of the edifice where the main cone is located while the slopes are
234 gently dipping to the northern and eastern side of the volcano.

235 Similarly, the Sponge Bob edifice located in the Tagus Abyssal Plain, south of the Tore
236 Complex represents a small elliptical edifice of 1600m high, 17km long in the WNW-ESE
237 direction and 10km in the NE-SW direction (Fig. 4). The volcano presents a broad
238 symmetrical shape along the WNW-ESE axis with a 6km long and 3.5km wide platform
239 localised at 800m above the seafloor on its SE flank. The conical summit of Sponge Bob is
240 800m above the platform.

241 ***4.2. Central group: Josephine massif***

242 The Josephine massif is located at the vicinity of the AGFZ, forming a NNE-SSW ridge of
243 250km long by 50km wide which comprises several main volcanoes such as Gago Coutinho,
244 Ashton, Josephine and Jo Sister Seamounts (Fig. 5).

245 *4.2.1. Gago Coutinho volcano*

246 The Gago Coutinho volcano represents the largest edifice of three submarine seamounts
247 aligned along a N80°E direction that connects the AGFZ to the Tagus Abyssal Plain
248 suggesting a strong structural control and a cogenetic emplacement. To the south, the Gago
249 Coutinho valley links to the main branch of the AGFZ and to an uplifted area on which the
250 Josephine submarine volcano formed (Fig. 5).

251 The transition between the volcanic complex and the surrounding seafloor is clearly defined
252 on the slopes map of the sea bottom topography except on its western side in which a series
253 of two other volcanic edifices developed (Fig. 6). The Gago Coutinho volcano is a complex
254 E-W elongated edifice of 3000m high and 26km wide in the N-S direction and roughly 36km
255 in the E-W direction and displays a high ellipticity according to the contour maps (Fig. 5).

256 The Gago Coutinho seamount shows a “tadpole-like” shape. Its geometric shape is
257 characterised by steep flanks with different slope domain from the summit to the seafloor and
258 a flat summit narrowing from 9km wide to the east to 3km wide to the western end
259 suggesting strong structural and gravitational control. The elliptical flat summit may result
260 either from subaerial or wave erosion during sea-level fluctuation and/or seafloor subsidence.

261 Flanks of the volcano reach the seafloor at 4500m to the east and the north while maximum
262 depth of the base of the volcano is at 3500m to the south giving an asymmetric shape to the
263 edifice (Fig. 6). The upper flank has sub-vertical slopes with a mid-slope break at 1800m
264 which give a distinct morphological front-bench slope. The general slope of the lower flank is
265 approximately 30°. The bathymetry map of the volcano along E-W and N-S directions reveals
266 a stair-case like topography with two or more steep slopes separated by an inclined plateau

267 (Fig. 6). The topographic profile perpendicular to the northern flank displays very steep
268 slopes forming a convex shape and a wide bulge at the bottom front. This feature is likely a
269 flank collapse scar (Fig. 6).

270 *4.2.2. Ashton submarine volcano*

271 The Ashton submarine volcano is a volcanic cone located at the vicinity of the AGFZ. As for
272 Gago Coutinho, it shows a “tadpole” shape, broadly symmetrical with respect to a NE-SW
273 axis (Fig. 5; Fig. 6). The volcano consists of a large edifice structurally linked to a NE-SW
274 oriented ridge to the SW. This ridge connects the main edifice to the nearby Gago Coutinho
275 volcano via a saddle located at around 4500m depth (Fig. 5; Fig. 6) indicating that the Ashton
276 volcano belongs to the Josephine Massif.

277 The bathymetry data shows that the summit of the volcanic cone has a minimum depth
278 beneath sea-level of ~1500m (Fig. 5; Fig. 6). The height and the diameter of the base of the
279 volcano are 2100m and up to 23km and the summit is 2km wide. Ashton volcano has
280 relatively irregular flank shapes but the main edifice to the NE is relatively circular while the
281 SW part forms an elongated relief (Ashton Ridge) following a NE-SW direction. Flanks to
282 the NE reach the seafloor on both side at a similar depth (c. 4400m) and an approximately
283 depth of 3500m to the SW part. The slopes of the edifice tend to be relatively steep close to
284 the base of the edifice with values ranging between 35-40° in average (Fig. 6). These high
285 slope values are rather localised along the Ashton ridge while slopes at the bottom of the
286 main edifice tend to be smoother. The upper flank range between 25-30° with a slope break at
287 ~1800m where slope values reach 35-40°. The summit is relatively flat with slope ranging
288 between 5 and 10° suggesting strong erosion processes. The general drainage pattern of the
289 SE and NW flank of the Ashton main edifice is radial with alternating ridges and gullies
290 extending from the summit to the sea bottom (Fig. 6).

291 One of the most prominent feature in the NE flank of the volcano is the Aston canyon, a
292 flat-bottomed, N80°E oriented erosional feature extending from the top to the bottom of the
293 volcano (Fig. 5). It is about 10km long, 2km wide and bounded by steep (more than 50°) and
294 straight scarps. A series of broad longitudinal N80°E depression and ridges are observed near
295 the base of the canyon. These volcanic ridges are also observed to the north in the same
296 direction suggesting that the present-day well-defined canyon scoured a broader and older
297 depression (i.e. dashed line).

298 The SW extension of the main edifice is characterised by two NE-SW and ENE-WSW
299 elongated ridges with average elevation of 1000m. The ridge is flanked by steep slope on its
300 SE side with hummocky features at the bottom on the ocean floor representing avalanche
301 debris. NE-SW elongated convex shape along the ridge observed in the profile curvature map
302 (Blue linear domain in Fig 6) continues along the same axis towards the main edifice which
303 suggests their structural link.

304 *4.2.3. Josephine and Joe Sister*

305 Josephine and Joe Sister Seamounts are located to the south-west of the AGFZ and are part of
306 large plateau with an average elevation of 2500m above the seafloor (Fig. 2; Fig 5). Multi-
307 beam high-resolution bathymetric data do not cover the entire edifices. Only 20% of
308 Josephine (southern flank) and 40% of Joe Sister (the northern flank) were fully imaged.
309 With respect to the large holes, the EMODnet regional bathymetric grid was used to fill the
310 gap (Fig. 5).

311 The Josephine seamount has an ellipsoidal shape with a NNW-SSE elongated axis,
312 structurally linked to the NE-SW to the AGFZ (Fig. 5). Bathymetric map shows a relatively
313 flat summit of 10km wide and 20km long while the entire seamount forms a 40km long ridge
314 connecting into the AGFZ to the north. No eruptive vents or cones are observed on the
315 summit suggesting a strong erosion imprint although some of the eruptive vents may be

316 undetectable due to the low resolution of the bathymetric map. The base of the edifice is
317 located at 3900m and 2400m beneath sea-level to the south and to the north, respectively
318 while the summit is only 200m below sea-level. Thus, the edifice dimension is 3700m high
319 above seafloor. The southern flank is well imaged and displays steep slopes with uneven
320 topographic surface interpreted as lava flows (Fig. 5). Two distinct ridges can be observed,
321 the first one along a NNW-SSE axis direction with a length of 14km and the other one with a
322 WNW-ESE orientation with a length of 17km. The southern flank of the volcanic edifice
323 displays a rough topography with a platform located at around 2700-2900m elevation and
324 sector collapse between the two ridges (Fig. 5). The eastern flank shows a smoother
325 topography.

326 Two volcanic features can be observed to the northwest of Josephine (VE1; VE2; Fig. 5).
327 Both are roughly NNW-SSE elongated conical edifices located along the AGFZ lying at a
328 depth of 1500m and 2600m while the summit is only 800m deep beneath sea-level. These
329 volcanic edifices are 700m and 1100m high above the Tagus Abyssal Plain. Faulting is
330 clearly evidenced by the steep slopes and vertical cliffs (Fig. 5).

331 Joe Sister seamount is located on the southern flank of the Josephine plateau (Fig. 5). This
332 edifice displays a square-like shape with NNE-SSW oriented steep flank to the east. The base
333 of the edifice lies on the seafloor at 2500m depth in the north and 4000m to the south in the
334 abyssal plain. The summit is also relatively flat with few eruptive vents observed on the
335 northern and western side.

336 **4.3. Southern TMR Volcanic Group**

337 This group has a crescent-like shape located in the vicinity of the southern branch of the
338 AGFZ (Fig. 7). The western branch is formed by a plateau-like relief oriented NNW-SSE and
339 capped by a volcanic edifice that is the Dragon seamount. The Lion seamount is located in
340 the central part of the crescent. The eastern branch is trending N-S and includes the Isabelle

341 and Unicorn seamounts. The Seine seamount is located at the tip of this branch yet separated
342 from the branch by a topographical gap (Fig. 2).

343 *4.3.1. Dragon*

344 The Dragon submarine volcano is located at the southwest end of the massif. It represents a
345 volcanic edifice that up-domed the seafloor with a maximum height of 1500m (Fig. 7). The
346 edifice lies on to an uplifted plateau that culminated at around 2500m above sea-bottom.
347 Maximum subsidence is observed in the abyssal plain to the south and west where the
348 seafloor reaches a depth of 4200m.

349 The volcanic edifice of Dragon shows a different morphology with a preferential elongation
350 along a N-S trend (Fig. 7). The base of the edifice has a length of 36km and a width of 19km
351 and lies at a depth of 2400m but deeper to the east (i.e. at about c. 2800m). The seafloor is
352 rugged and uneven with some circular features, possibly indicating the presence of lavas
353 cones and eruptive vents. The morphological asymmetry of Dragon between the eastern and
354 western side is evident on the slope maps where a well-defined ridge of 5km wide is observed
355 along a N-S direction. The western side is characterised by sub-horizontal platforms located
356 at around 1800-1900m above sea-bottom and are interpreted as related to a secondary N-S
357 ridge. Large sector collapses are present in the central and north-western part. A relative age
358 may be inferred as some vents occurred in the collapse area. Lava flows are clearly observed
359 in the NW flank. To the eastern flank, slopes exceed 40° in the upper part and decrease to few
360 degrees to reach the seafloor in the abyssal plain.

361 *4.3.2. Unicorn, Isabelle, Lion*

362 Unicorn represents the southern end-member of this group of volcanoes while Isabelle and
363 Lion are located in the northern part. Unicorn rises from seafloor which is 4300m deep with a
364 total height of the main volcanic edifice of 3500m (Fig. 7). Its summit reaches 800m below
365 sea level and shows a relatively flat area. As indicated by bathymetric contours, its flanks are

366 relative uneven suggesting that the edifice produced various flows and debris avalanche
367 deposits. Slopes are smoother with respect to those of Gago Coutinho or Aston in the North
368 ranging between 10° and 25°. This suggests that the construction processes occurred recently
369 (Fig. 7) confirming the geochronological data (28 Ma, Geldmacher et al., 2005). The edifice
370 elongation is oriented along a N-S to NW-SE axis near the Isabelle Seamount. The base of
371 the volcano is roughly 35km wide and 80km long while the summit is 30km long and 18km
372 wide. Three volcanic cones can be observed at the top (Fig. 7). This may suggest that
373 Unicorn formed during successive episodes occurring before and after a phase of erosion and
374 subsidence. Alternatively, the cones could represent a remnant of an older volcanic centre.
375 The volcanic summit was then eroded down to depth of 800m. Massive lava flows are present
376 along its flanks reaching the abyssal plain to the north-east and eastern part. Another volcanic
377 edifice can be observed, 1900m south-west of Unicorn. It is separated from the main edifice
378 by a saddle. Although it was not fully imaged during the Tore-Madeira marine survey in
379 2001, its average size can be defined with the global bathymetric grid. The entire edifice is
380 2400m high. Lava flows merge to a NW-SE oriented canyon (i.e. Unicorn Canyon) and go
381 toward the abyssal plain. The southern flank of the additional edifice is much steeper. The
382 transition from the abyssal plain and the volcanic centre is narrow and sharp.
383 Isabelle and Lion Seamounts are located to the north and northwest of Unicorn respectively.
384 High resolution bathymetry covers 40% of both volcanoes (Fig. 8). A tectonic horst of nearly
385 E-W direction with a summit at 600m depth below sea-level formed the Lion Seamount. Its
386 dimensions are 2400m high, 50km elongation and a 6km wide summit. Bathymetry map
387 shows that the ridge displays a series of WNW-ESE trending lineaments giving the ridge an
388 en-echelon like shape with average spacing of ~6km. The southern flank is nearly vertical
389 with an average slope value around 50°. Slope break and a 15km wide platform formed at the
390 bottom of the WNW-ESE northern edge at an average depth of 2000m can be observed on

391 the northern flank. Few isolated volcanic cones have also been mapped on both flanks of the
392 ridge. The platform to the north gives away to two ridges-oriented NW-SE and NNE-SSW.
393 The latter connects to the Isabelle Seamount. The platform and the orientation of these ridges
394 suggest that they may represent remnant of an older volcanic edifice on which the highest
395 ridge formed.

396 The Isabelle Seamount is located between Lion and Unicorn Seamounts emerging from
397 4400m depth at the seafloor and reaching a height of 1800m. Its elliptical morphology is
398 characterised by steep flanks and a 7km wide and 15km long flat summit. Its elongation is
399 oriented along a NNE-SSW to NE-SW turning to a E-W axis toward the NW near the Lion
400 Seamount. The Isabelle volcanic field extends to the east of the main edifice, as a linear
401 eruptive vent of different size on the seafloor. Most of these volcanic features are circular or
402 dome-shape although resolution of the bathymetry is poor which prevent any clear
403 interpretation. These eruptive vents are aligned along a NE-SW direction and connects the
404 Isabelle Seamount to Coral Patch Seamounts. The string of volcanic craters dies out into the
405 Horseshoe Abyssal Plain at 4000m depth.

406

407 **5. Analyses of the TMR volcano-structural features**

408 In order to better understand the structural control on volcanoes along the TMR as well as its
409 relationship with magma pathways in its ascent, we analysed eruptive vents and fissures
410 locations and distribution. Eruptive fissures have been identified or inferred from the
411 alignment of closely spaced vents, breaching direction or crater elongation if preserved
412 (Becerril et al., 2013; Tibaldi, 1995; Fig. 9).

413 ***5.1. The Tore Complex edifices***

414 A total of 113 eruptive fissures were identified across the Tore Complex volcanic area (Fig.
415 9a). The number of these eruptive fissures are likely to be underestimated due to the

416 resolution of the DEM. However, the large amount makes the estimation relatively
417 meaningful. The analysis of the main direction of these eruptive fissures shows
418 predominantly three strike families: N10-20°E, N80-90°E and N120-130°E. Timing of these
419 eruptive fissures cannot be given as stratigraphy or age is unknown in this area. These
420 directions coincide with the main continental margin related faults and their equivalent in the
421 oceanic crust as transform faults or rift related structures.

422 ***5.2. The Josephine Group volcanic edifices***

423 The analysis of vents alignments indicates a total of 30 eruptive fissures in the Josephine
424 Group Volcanic area (Fig. 9b). Across Gago Coutinho volcano, most of the eruptive fissures
425 have a NE-SW or ENE-WSW direction. To the west along the two smaller edifices, the
426 orientation of the eruptive fissures is N70°E defining a more narrow and localised volcanic
427 rift zone although the resolution of the bathymetric grid in this area do not allow a detailed
428 interpretation of the volcanic features. Eruptive vents were difficult to map in this area due to
429 gravitational and erosional processes combined with the resolution of the data. Nevertheless,
430 few eruptive vents were identified on the summit plateau and on the flanks, in particular in
431 the NE part of the edifice which is characterised by vent and fissure orientation along a NE-
432 SW direction at 2400m above seafloor. It is worth noting that on the eastern flank of Gago
433 Coutinho, eruptive fissures are mostly perpendicular to the contour line while on the northern
434 flank, fissures are oblique to the slopes. No vents were mapped on the southern steep flank.
435 Ashton volcanic edifice, eruptive fissures are mostly aligned along a N45°E direction,
436 defining a linear volcanic ridge zone (Fig. 9b). The south-western part of Ashton, the eruptive
437 fissures are oriented along two main directions N50-60°E and N20°E. In the southern part of
438 the ridge, fissures extend along a N-S direction down to the abyssal plain while to the south-
439 western part, elongated topographic feature on the seafloor can be observed along a NE-SW
440 direction in the prolongation of the Ashton ridge and seem to connect with Gago Coutinho.

441 Two major eruptive vents were identified on the summit plateau as well as along the ridge.
442 Vent alignment are oriented in a similar direction as the eruptive fissures along a NE-SW
443 direction.
444 The Ashton ridge is characterised by two main linear ridges down to 1200m above seafloor
445 oriented N80°E and N50°E (Fig. 9b). These linear lineaments present an en-echelon
446 morphology, and both connects to form one single ridge oriented along the same direction of
447 the main edifice elongation suggesting that the volcano is located along the same feeding
448 system as the ridge. 10 eruptive vents are visible along the flank and the summit of some of
449 the Josephine volcanic edifices (Fig. 9b). This allows to define 4 eruptive fissures with
450 WNW-ESE and NW-SE orientation similar to the cliffs localised to the NW and interpreted
451 as being the trace of the AGFZ.

452 ***5.3. Southern TMR Volcanic Group***

453 A total of 32 vents have been mapped across the Southern TMR Volcanic Group (including
454 the Dragon, Isabelle and Unicorn volcanic edifices; Fig. 9c). The resolution and the coverage
455 of the high-resolution DEM in this area is low and sparse preventing a detailed analysis of
456 eruptive fissures.
457 Nevertheless, 19 eruptive vents were recognisable along the Dragon volcanic edifice. They
458 are more abundant in the eastern part along the N-S oriented ridge, mainly forming part of the
459 rift volcanism edifice. Few eruptive centres have also been observed to the north-west along
460 the narrow en-echelon N-S ridge. The majority of the eruptive vents aligned along N-S
461 oriented eruptive fissures. The longest eruptive fissure was mapped to the East with a length
462 of several km. To the north-west and south-west, eruptive fissures have a similar N-S trend
463 but are shorter and separated by a large sector collapse suggesting that they might form part
464 of the same eruptive fissure. Although resolution does not allow identifying vents in the

465 surrounding area, it seems that eruptive centres are mostly located along a restricted N-S
466 ridge suggesting a strong structural control on magmatism development.

467 10 eruptive vents were identified along the Unicorn edifice, mostly on the platform to the
468 south and west of the summit. These vents define a clear NNW-SSE oriented fissure parallel
469 to the main elongation of the volcano, connecting to the Isabelle edifice to the north along
470 which 3 eruptive vents were identified. However, no clear alignment is observed due to the
471 few recognisable eruptive vents. In the Lion seamount, several eruptive vents aligned along a
472 WNW-ESE swarm of eruptive fissures similar to the bounded scarps can be identified at the
473 summit.

474

475 **6. Faults identification**

476 Criteria to define lineaments from bathymetry are mainly variations of the strike and offset of
477 morphologically distinct linear features such as ridges, scarps, cliffs. The lineament drawn by
478 following the bottom of the scarps were mapped and interpreted as related to fractures or
479 faults.

480 ***6.1. The Estremadura Fault System - The Tore Complex Volcanic Group***

481 Based on bathymetry analysis, the main lineaments were mapped in the Estremadura Ridge
482 (Fig. 10). The E-W faults of the Estremadura Fault System (EFS) vanishes to the west into
483 several en-echelon lineaments segments with a main N50°E direction and N10°E striking
484 lineaments. Bathymetry image show recent deformation on these structures although no
485 direct absolute or stratigraphic age are available. The westernmost part of the Estremadura
486 Fault and its splay faults have a clear bathymetric expression on the seafloor with a well-
487 developed rhomb-shaped basin along releasing step-overs suggesting a left-lateral strike-slip
488 component of the EFS (Fig. 10). Volcanoes of the Tore North and Tore North-West are
489 located to the northern segment of the EFS while the Tore East and Central Volcanic field

490 formed to the south of the northern segment of EFS along subordinate faults-oriented NE-SW
491 at a distance >20km. This suggests the Tore East volcano and central Volcanic field do not
492 have a clear connection with the main left lateral strike slip Estremadura Fault but rather
493 formed within splays and subordinate faults.

494 ***6.2. The Azores-Gibraltar Fracture Zone – Josephine Volcanic Group***

495 The Josephine Seamount Group lies along the central section of the AGFZ (Fig. 2). The
496 AGFZ is composed of several fault segments mostly striking N80-120°E (Fig. 1; Fig. 10). At
497 the vicinity of the Josephine Seamount Group, the AGFZ is oriented ~N110-120°E and splays
498 off eastward into two fault sets forming a horsetail geometry.

499 The main sub-vertical fault oriented N110-120°E has a length of 50km splitting into four
500 smaller steep secondary faults, 40km-60km long with an orientation ranging between N120°E
501 to N150°E. The splay faults are marked by a series of narrow valleys and cliffs along which
502 volcanic features of the Josephine Volcanic Group formed suggesting a strong structural
503 control of the AGFZ in this area. It is worth to note that the different volcanic edifices of the
504 Josephine Group are located either at the tip of the main fault or along the several splays of
505 oblique faults (Fig. 10; Fig. 12). To the south-east, several individual fault segments strike
506 N50°E similar to the orientation of the reactivated fault along the Gorringe Bank. At the
507 junction with the N130°E AGFZ system, these individual faults change their geometry along
508 a strip that is in south-eastward continuation of the AGFZ splay faults suggesting the possible
509 prolongation of the AGFZ to the southeast. These lineaments that have a different direction
510 define two linear corridors in the bathymetry where each individual segment displays a left-
511 lateral stepping geometry (Fig. 10; Fig. 12). These corridors are sub-parallel converging to a
512 small edifice of the Josephine Group located at the tip of one of the AGFZ splay fault. This
513 overall geometry is consistent with the development of a right lateral shear zone that connects
514 the AGFZ to the NE-oriented Gorringe Bank fault system (Fig. 2; Fig. 10).

515 The second set of faults is composed of several small segments of 20km long approximately
516 oriented N70-90°E displaying a staircase shape. The western termination of this fault
517 connects to the main branch of the AGFZ (Fig. 10). To the east, the fault is associated with
518 NE-striking, right lateral stepping cracks that merge to the northeast into a single NE oriented
519 single fault segment. Although the resolution of the bathymetric data is poor, we interpreted a
520 narrow-oriented NE-SW ridge in the south-western continuity of the main “volcanic tail” that
521 connects the structures related to the Ashton volcano to the ones oriented N80°E of the Gago
522 Coutinho volcanic edifice. This specific geometry defines a transtensional domain at the
523 intersection between the N70-80°E and N40°E faults. Gago Coutinho, one of the largest
524 volcanic edifices of the TMR developed within this domain at the eastern tip of the N80°E
525 fault while Ashton volcano formed at the tip of the N40°E fault. Other smaller and narrower
526 edifices developed along the N80°E segments that intersect the AGFZ to the west.

527 Steep slopes are observed across the summit and on the upper flank of the Gago-Coutinho
528 volcano. They define vertical cliffs that have an en-echelon like morphology oriented NE-SW
529 to the northern flank and NW-SE to the southern flank. These linear features have 30°
530 difference in orientation compared to the main edifice elongation and are interpreted as
531 vertical conjugate strike-slip faults although this interpretation needs to be confirmed. The
532 western part of the northern flank shows a well-defined NE-SW sharp edge, parallel to the
533 north-eastern edge of the volcano. The flank localised in between these two steep slopes
534 displays lobes structures and rounded shape scarp at the top with a flat bottom as well as a
535 bulge topography at the bottom suggesting that they are related to flank collapse.

536 **6.3. Southern TMR**

537 The Southern TMR lineaments have a length of 20-40km and cover an area of 40km wide
538 (Fig. 10). The fault system in the vicinity of the Dragon seamount is formed by two parallel
539 N-S faults branching to the north and south to roughly E-W transform faults. The strike of the

540 rift valley related normal fault are also N-S suggesting that the fractures observed on
541 bathymetry and along which the Dragon lavas formed are reactivated normal faults formed
542 during the oceanic spreading.

543 The Lion-Isabelle area consists of NW-SE right stepping en-echelon lineaments curving to
544 the east in the Lion volcano and to the west in the Isabelle edifice and connecting to an E-W
545 fault. The westernmost zone of this E-W segment connects to N-S structures of the Dragon
546 volcano suggesting that Lion E-W lineament represents an ancient transform fault. This latter
547 is well expressed in the bathymetry with a large vertical offset of the seafloor as shown on the
548 slope map (Fig. 10; Fig. 12). The Lion volcano lies to the north of the transform fault. To the
549 East, the transform fault is cross-cut by structures of Isabelle oriented NW-SE curving
550 westward to the north.

551

552 **7. Discussion**

553 **7.1. Morphostructures and spatial distribution of volcanic edifices along the Tore- 554 Madeira Ridge.**

555 TMR bathymetry analyses reveal several different volcanic morphologies including
556 elongated cone-shaped edifices, linear ridges, large massifs, isolated cones and lava flows.
557 The observed differences in morphology are likely related to magma supply rate and
558 composition, structural inheritance of the lithosphere on which the volcanoes are lying,
559 gravitational flank collapse and erosion processes. Most of the volcanoes within TMR have
560 an elongated shape and higher-gradient slope than common oceanic seamounts. Steep slopes
561 of most of the volcanoes are likely related to a combination of areal erosion processes,
562 formation of marine terraces during subsidence and flank collapse. Volcanoes of the Tore
563 Complex as well as the Aston and Dragon edifices seem to have better preserved their
564 original conical shape whatsoever the size of the edifice. In the Central and Southern

565 Volcanic groups, the volcanoes present various shapes with for most of them a wide flat
566 summit suggesting intense submarine and/or subaerial erosion by waves acting upon the
567 edifices. Although the exact initial morphology of the volcanoes is not known, the relative
568 preserved conical shape of the Tore Complex or Aston volcanoes may be explained by their
569 size, likely too small to reach sea-level and therefore were not subjected to subaerial erosive
570 processes. Their location in deep-water environment far away from the shelf may have also
571 prevented them from abrasion due to strong coastal currents as suggested for some oceanic
572 seamounts along the southern Australian margin ([Jackson, 2012](#)). On the other hand, the
573 evolution of the Central (Gago-Coutinho, Josephine) and the Southern Volcanic Groups
574 (Isabelle, Lyon, Unicorn) except Aston and Dragon edifices appears to be more subjected to
575 the strong interaction between constructive (i.e. volcanic) and destructive processes such as
576 marine erosion by waves and flank collapses. Several complex factors interplay to shape the
577 morphology of these volcanoes, among them the tectono-magmatic activity in particular
578 along the AGFZ. The Gago Coutinho volcano represents a good example that displays a
579 typical geometry controlled by horse-shoe shaped fault scarps suggesting large volume
580 gravitational mass-wasting events ([Mitchell et al., 2002](#)). Variation of the seafloor vertical
581 movement may have also a strong influence on volcano morphology in those areas. Long-
582 term subsidence is common for volcanoes due to flexural loading as well as plate cooling.
583 The detailed mapping of volcanic distribution together with structural analysis of the
584 bathymetry at the regional-scale show most of the volcanic fields (i.e. grey shaded area in
585 Fig. 13) distributed at the vicinity of major sub-vertical lithospheric structures such as
586 transfer faults of the margin, oceanic rift valley or oceanic transform faults (i.e. AGFZ, ESF;
587 Fig. 13). However, most of these volcanoes are located away from the major segments of the
588 regional faults (i.e. shaded grey area; Fig. 13) suggesting that a structural control on volcanic
589 emplacement is more complex than previously suspected ([Geldmacher et al, 2006; Merle et](#)

590 al., 2006; Nirrengartner et al., 2017). In addition, there is no visible offset on the volcanoes
591 by the AGFZ, ESF or other major subordinate faults. Instead, the volcanic edifices follow the
592 trend of the different fault segments.

593 The ellipticity of the volcanic edifices is variable across TMR and do not depend on whether
594 magmas intruded the oceanic crust, the continental margin or along the transform faults (Fig.
595 11). Likewise, the shape of these volcanoes highlights different types of volcanic
596 constructions such as circular seamounts related to point source volcanism and linear
597 volcanic ridges. Post-emplacement erosional processes as well as flank collapses may have
598 affected the ellipticity to some extent as illustrated by the Gago Coutinho volcano where both
599 the northern and southern flanks show large horse-shoe shape scars. However, assuming that
600 these destruction processes did not affect the entire edifice, the ellipticity reflects the primary
601 emplacement geometry of the volcanic edifices. This is also supported by the localisation
602 within the volcanic edifices of the eruptive fissures inferred from vent alignments as well as
603 their orientation, E-W or NE-SW, north of AGFZ and N-S south of AGFZ (Fig. 12). The
604 fractures which might represent dyke swarms also show the E-W, NE-SW and N-S
605 orientation to the north and south, respectively. Note that the main axis of the volcano
606 ellipticity of the Tore Complex and the Central Volcanic Group show an elongation
607 following a E-W to NE-SW trend which is the main direction of the former spreading centre
608 and rift transfer faults along the Iberia margin (Tucholke et al., 2007). Structural studies of
609 the Iberia margin evidenced pre-existing E-W and NE-SW fault systems formed long before
610 the beginning of the magmatic activity on the TMR during the Late Paleozoic Hercynian
611 Orogeny and the Early Mesozoic rifting event (Fig. 1; Alves et al., 2009; Ballevre et al.,
612 2014; Pereira et al., 2016). This clearly demonstrates the strong structural control on the
613 location of TMR magmatism as magmas used the pre-existing lithospheric structures as main
614 ascent pathways.

615 The absence of a major N-S oriented axis of the TMR volcanoes in the central and northern
616 part of the seamount chain contrasts with the inferred N-S to NNE-SSW orientation of the
617 overall TMR. Intrusives and volcanoes of similar age and composition as the Tore Complex
618 and Josephine Volcanic Group are also present 300km away from the TMR volcanoes in the
619 Tagus Abyssal Plain and onshore Portugal (Grange et al., 2010; Neres et al., 2012). These
620 intrusives have a preferred E-W to NE-SW orientation similar to the TMR edifices and were
621 emplaced in the vicinity of main lithospheric faults (Messejana and Nazaré faults). We thus
622 suggest that the spatial distribution of the TMR volcanoes reflects the channelling of magmas
623 into sub-vertical lithospheric faults rather than a N-S oriented sub-lithospheric thermal and
624 compositional anomaly source of the TMR magmas. This also explains the limited structural
625 connection along a N-S transect of the TMR volcanoes and the presence of three distinct
626 volcanic fields (i.e. Tore Complex, Josephine Volcanic Group and Southern Volcanic
627 Group). This demonstrates the misleading of the term “Tore-Madeira Rise magmatism” in
628 such poly-phased tectono-magmatic context.

629 **7.2. Mechanism of magma channelling and ascent**

630 Most of the volcanic edifices of the TMR formed along narrow areas of localised
631 deformation. Volcanic fissures are nearly concordant with the main regional and splay faults
632 suggesting that pre-existing faults are likely to control magma extraction and ascent to the
633 surface (Fig. 13). However, how these structures became preferential pathways for magma to
634 be transported has still to be identified and their role in the eruption of magma at the surface
635 is poorly known.

636 Transport of melt by fault zones greatly depends on fault-zone structure and permeability
637 within the damage zone (e.g. Gudmundsson et al., 2010). Indeed, structural and rheological
638 complexities of fault damage zones strongly perturb regional tectonic stresses along, across

639 and around the damage zone which favour the development of subdomains with different
640 deformation pattern, fault geometries and kinematics as well as stress regime (Ishii, 2016).
641 Thus, damage zones strongly influence fracture propagation, fault linkage and fault
642 permeability (Choi et al., 2016; Peacock et al., 2017). The development of damage zone also
643 results in strong rock anisotropy between the weaker and more permeable fault damage zone
644 and the surrounding host rocks. This strength contrast results in pressure gradient between the
645 fault zone and the host rock and may induce magma to ascent (Gudmundsson et al., 2014;
646 Reynolds et al., 2018). Alternatively, magma-assisted processes enhancing fracturation is
647 another process that may favour magma to flow (i.e. Hydrofracturation, Gudmundsson and
648 Brenner, 2011). This is particularly well documented along divergent plate boundary
649 (Sigmundson et al., 2014; Xu et al., 2015) but also in strike-slip setting where magma
650 pressure is sufficiently high to inject dyke to the surface creating local extension in the
651 shallow crust (Accola et al., 2014; Ruth et al., 2016). Considering the clear spatial connection
652 between volcanoes and faults, one would expect a direct control of the main fault activity on
653 volcanism with magma feeding fractures oriented in the same trend defined by the fault. The
654 ascending magmas could have used the existing faults as favoured pathways but could have
655 actively contributed to enhance and propagate the fault system. This would explain why none
656 of the TMR volcanoes does not show any offset by the activity of the faults (Fig. 12).

657 Faults along which volcanoes formed consist of several kilometric-scale sub-vertical
658 segments mainly oriented N0 in the southern part of TMR, N90°E or N120°E in the central
659 part along the AGFZ and in the Tore Seamounts Complex area (Fig. 10). Although some
660 volcanoes might have been buried beneath a thick sediment package and a large volume of
661 frozen melt bodies (i.e. magma underplating or sills) are present beneath the Iberia distal
662 margin or beneath the southern part of TMR in the north Central Atlantic (Peirce and Barton,
663 1991; Pereira et al., 2016), the fault related volcanoes appear to be spatially clustered and

represent only a small portion of the sub-vertical pre-existing fault (Fig. 12). Considering that the steep dip of the faults, the strong rock anisotropy within the deformation corridor may have enhanced fracturing parallel to the fault zone and favoured melt channelling. Indeed, schistosity and lithological boundaries between the deformed and host rocks as well as within the fault zone induce strong rheological contrast resulting in pressure gradient that exert a primary control on fracture localisation and melt flow between the fault and the stronger adjacent rocks. This may also explain the localisation of volcanic edifices within sub-vertical lithospheric faults such as oceanic transform or margin related transfer fault rather than gently dipping detachment faults within the exhumed mantle domain. The steep dip of the fault gives to the sub-lithospheric melts a direct access to the surface.

The majority of the volcanoes of the Tore and Josephine Complex studied here, did not develop directly on the major regional fault but rather along subordinate or splay faults suggesting a strong control of tectonic local stress in regard to fault geometry. Moreover, although the average strike of eruptive fissures and faults are nearly the same, the pattern of the eruptive fissure presents two or more preferential directions. In fact, most of the volcanoes of the TMR formed on a lithosphere with a complex structural geometry including, releasing bend zones defining transtensional domain within the interaction damage zone (Tore Complex), at the damage tip of the splay faults (Josephine Volcanic field, Gago Coutinho and Ashton Seamount), and at ancient spreading ridge interacting with transform fault (Lion, Isabelle). Based on these observations, we suggest that local stress reorganisation exerted a primary control on magma extraction at the surface and the site of emplacement of the TMR volcanoes. The complexity of the fault systems favoured the development of sub-domain between and at the tip of different fault segments that when optimally oriented to maximum horizontal stress will enhance magma ascent and allow eruption at the surface.

7.3. Control of the local stress field on TMR volcanism

689 The Tore Complex Volcanic group is located along the Estremadura Fault System (Fig. 12).
690 Based on our bathymetry analysis of the western tip of the EFS, we interpret this fault system
691 as being a left lateral strike slip fault zone that splay off to the west in several segments-
692 oriented NE-SW; the Tore basin formed along releasing step-overs (Fig. 12). This is in
693 agreement with the recent observations based on seismic data showing left lateral transcurrent
694 movement of the fault in the distal and proximal domain during continental rifting (Pereira et
695 al., 2016). Thus, we suggest that this fault zone is a pre-existing E-W margin related transfer
696 faults reactivated in a transtensional regime. Considering the likelihood of the syntectonic
697 emplacement of the Tore Complex volcanoes, the transtensional reactivation regime
698 occurred during the early Late Cretaceous similar to the age of magmatic activity in that area.

699 The striking aspect is that a large proportion of volcanoes that can be mapped on the
700 bathymetry developed within the transtensional domain of the ESF (shaded grey zone in Fig.
701 12). The main elongation E-W to ENE-WSW of Tore North and Tore North-West as well as
702 Torillon volcanoes is sub-parallel to the related fissures and faults of the main northern
703 segment of the ESF. Volcanoes intruded the Tore Plateau are also connected to the main E-W
704 segment of EFS via 100km NE-SW en-echelon faults that bordered the depression to the
705 south-east. Volcanoes of the East Tore Volcanic Field have an NE-SW elongation oblique to
706 the main northern segment of the ESF. Thus, this structural configuration of the Tore
707 Complex volcanoes indicate that magma transport and eruption are driven by subordinate or
708 splay faults. The transcurrent character interpreted along the ESF would favour a volcanic
709 emplacement in localised area of transtension (Fig. 12) rather than along a magmatic belt
710 such as those observed in extension settings. In that scenario, the NNE-SSW to NE-SW
711 oriented fractures may have opened to enhance volcanic eruptions. The NE-SW fractures
712 may be rooted to deep crustal level and to the Moho interface or they may be structurally
713 connected to the main E-W segment providing access to the main source of magma. We

714 speculate that the northern segment of the ESF played a major role in channelizing magma as
715 suggested by the larger size of the Tore North and Tore North-West volcanic edifices located
716 along the northern segment of ESF. Another explanation could be that magma extraction is
717 also enhanced by the development of the Tore depression however, this idea would require
718 further investigation.

719 The Josephine Volcanic group are located at the vicinity or along the eastern part of AGFZ.
720 This latter represent a roughly E-W transform plate boundary between the North and Central
721 Atlantic Oceanic plate changing to a more complex NE-SW and NW-SE oriented transform
722 margin toward the west between the Iberian and African plates (e.g. Jimenez-Munt et al.,
723 2001).

724 The Gago-Coutinho and Aston volcanic edifices were active at least 92-90Myrs ago while
725 the Josephine seamount seems younger (16-0.5Ma; Geldmacher et al., 2006; Fig. 2). The
726 Gago-Coutinho seamount represents the last volcano of a series of three seamounts aligned
727 along a E-W direction that connects to the AGFZ (GC2, GC3 in Fig. 5; Fig. 10). Although it
728 was affected by erosional processes such as sector collapse on its northern flank, Gago-
729 Coutinho is the largest volcanic edifice (Fig. 5; Fig. 6). The eruptive fissures as well as
730 fracture related lineaments follow a similar pattern with two preferential directions WNW-
731 ESE and NE-SW (Fig. 10), possibly reflecting the geometry of magma feeder dykes. This
732 specific pattern contrasts with the direction of the main elongation, volcanic alignment as
733 well as the main fault. In addition, the right-stepping pattern of the eruptive fissures linked by
734 E-W structure produces a zigzagged trace that suggests that the fault linkage created
735 dilatational jogs or pull-apart geometry in which volcanic edifices formed. In that
736 configuration, Gago Coutinho is located at the tip of the splay fault propagating toward the
737 east. The large volume of this edifice also indicates that the fault was reactivated by repeated
738 movement.

739 The Ashton volcano developed along a NE direction and present a ridge that potentially
740 connects to Gago-Coutinho at depth although it is not clearly observed on the bathymetry
741 (Fig. 5). The strike of the ridge and eruptive fissures are similar to the NE-oriented
742 interpreted fractures of the Gago-Coutinho Ridge that are interpreted as being extensive
743 fracture related dykes. The Ashton volcano shows dyke swarm tip-crack geometry as well as
744 en-echelon spatial distribution of eruptive fissures or dykes compatible with a right lateral
745 shear component during dyke propagation and volcanic building. We then suggest that the
746 Ashton volcano developed both along extension fractures formed earlier at the tip of the
747 AGFZ – Gago Coutinho splay fault segment that evolved as a right lateral shear fault once
748 interacting with Gago-Coutinho propagating faults. Thus, the large Ashton volcanic edifice
749 developed within the tip of this shear zone while Gago-Coutinho formed in the interaction
750 damage zone once the AGFZ splay segment connected to the Ashton Shear fault.

751 **7.4. Implications for the post-break-up deformation of the Iberian-Morocco**
752 **margin**

753 The proposed model of the TMR volcanism questions the localisation of the segmented N-S
754 to NNE-SSW oriented J magnetic anomaly that is laterally offset by transform faults
755 (Bronner et al., 2011). Indeed, the structural trend of post-spreading volcanoes differs
756 significantly from the inferred N-S trend of the J-anomaly (Fig. 13). Recently, Nirrengartner
757 et al. (2017) interpreted this anomaly as the result of polyphased syn- to post spreading
758 magmatic events emplaced in both the oceanic and exhumed mantle domains. We thus
759 speculate that this configuration may be related to relicts of underplated magma emplaced
760 along detachment faults and channelizing toward the major sub-vertical lithospheric faults
761 (Sauter et al., 2016). This also may suggest that migration and extraction of melt to the
762 surface is more efficient where steep lithospheric shear zones such as transfer or transform
763 zones associated with local stress variations are presents. However, although this may explain

764 the segmented and patchy high amplitude J-anomaly to the north of AGFZ, it does not clearly
765 justify the southern continuity in the northern Central Atlantic.

766 Post-breakup magmatism along the Iberia-Morocco margin is controlled by lithospheric
767 faults during the Late Cretaceous. These structures along which volcanoes emplaced formed
768 obliquely to the main NNE-SSW oriented seafloor oceanic fabric (Fig. 14). The direction of
769 principal stress at that time is inferred to be WNW-ESE to NE-SW in agreement with the ~E-
770 W direction of the flow lines obtained by reconstruction of the Iberia-Newfoundland margin
771 ([Hosseinpour et al., 2018](#); [Nirrengartner et al., 2018](#)). Three major fault zones can be mapped,
772 the ESF to the north, a pre-existing major transfer zone of the Iberia margin; (2) the AGFZ
773 restricted to the Gago-Coutinho and Josephine Volcanic alignment. This configuration shows
774 that the Iberia-Morocco margin experienced transtensional deformation during the Late
775 Cretaceous resulting in volcanic emplacement. In addition, deformation localised along these
776 major lithospheric deformation zones show large crustal thickness and thermal variations
777 inherited from the Late Variscan Orogeny and margin segmentation development ([Tesauro et](#)
778 [al., 2009](#); [Veludo et al., 2017](#)); These structures represent major crustal boundaries that
779 mostly reactivated inherited Late-Variscan basement boundaries and shear zones. These fault
780 zones likely act as boundaries accommodating the differential plate motion.

781

782 8. Conclusions

783 The new bathymetric map confirms that the oceanic seamounts of the TMR are volcanic
784 edifices as shown by the abundant morphological features such as lava flows, eruptive cones,
785 vents and fissures. The morphology and the size of these volcanic edifices greatly vary
786 depending on rock composition and age, tectonic control and erosive processes. A large
787 number of volcanoes reach up to 2000m height and a flat top creating steep cones strongly

788 influenced by subaerial erosion. The structural analysis reveals that the volcanoes of the
789 TMR may be grouped into three major massifs, the Tore complex, the Josephine complex and
790 the southern group complex that are not directly structurally connected to each other.
791 However, the individual volcanic edifices within the group are connected through elongated
792 ridges where eruptive vents and fissures are commonly observed.

793 The TMR volcanoes are spatially connected to the major regional faults such as ESF, AGFZ.
794 The systematic occurrence of volcanoes within the fault and the similar direction of faults and
795 elongation of volcanic edifices (i.e. the “tadpole” shape and subsidiary ridges) suggest that
796 the pre-existing crustal-scale shear zones acted as preferential pathways for the ascending
797 magmas. The direction of the elongation axis of the volcanoes and eruptive fissures show a
798 dominant E-W to NE-SW trend along the SW Iberia margin which is also the dominant
799 direction of the AGFZ and ESF fault system and a dominant N-S structural trend in the
800 Southern Volcanic Complex similar to the former ridge-transform system. The inherited
801 structures of the Mesozoic rift is not clearly expressed in the bathymetry of the volcanic
802 features offshore SW Iberia margin.

803 The presence of volcanoes along portion of the faults and the occurrence of volcanoes away
804 from the main fault segment may be explained by different processes in magma ascent and
805 eruptions. We suggest that this control is determined by several parameters including (i) the
806 steep dip of the faults that directly tap into the molten source, (ii) the rheological weakness of
807 the shear zones; these latter are likely reactivated pre-existing structures such as the Late
808 Variscan or Mesozoic faults as well as crustal boundaries, (iii) local stress reorganisation due
809 to complex fault geometry and fault segments interaction.

810 Magma transport and eruption are overall controlled by the local state of stress in the crust.
811 Fault kinematics vary along the different segments leading to contrasting stress direction and
812 magnitude. However, only specific portion of the faults including releasing bend, fault tips,

813 interaction zone between two segments are coated by large volcanoes. Therefore, magma
814 migration requires local stress reorganisation to erupt.

815 Development of a transtensional plate boundary during the Late Cretaceous likely resulting in
816 post-break magma emplacement in the southern part of the Iberia margin in relation to hot
817 spot activity. Distribution of TMR volcanoes are rather due to small-scale plate
818 reorganisation.

819

820 **Acknowledgements**

821 We thank the captain and the crew of the R/V *Atalante* for their professionalism during the
822 Tore-Madeira Rise cruise in 2001. For technical assistance we thank E. Boeuf, B. De Quillac
823 and H. Loyen.

824

825 **References**

826 Accola, V., 2014. Structural control on magmatism along divergent and convergent plate
827 boundaries: Overview, model, problems. *Earth-Science Reviews*, 136, 226-288

828 Alves, T. M., Moita, C., Cunha, T., Ullnaess, M., Myklebust, R., Monteiro, J. H.,
829 Manuppella, G., 2009, Diachronous evolution of Late Jurassic–Cretaceous continental rifting
830 in the northeast Atlantic (west Iberian margin). *Tectonics*, 28, TC4003,
831 doi:10.1029/2008TC002337.

832 Applegate, P., 2003. Detection of sinkholes developed on shaly Ordovician limestones,
833 Hamilton County, Ohio, using digital topographic data: Dependence of topographic
834 expression of sinkholes on scale, contour interval and slope. *Journal of Cave and Karst
835 Studies*, 65, 126-129.

- 836 Ballevre, M., Martínez Catalán, J.R., López-Carmona, A., Pitra, P., Abati, J., Díez Fernández,
837 R., Ducassou, C., Arenas, R., Bosse, V., Castiñeiras, P., Fernández-Suárez, J., Gómez
838 Barreiro, J., Paquette, J-L., Peucat, J-J., Poujol, M., Ruffet, G., Sánchez Martínez, S., 2014.
839 Correlation of the nappe stack in the Ibero-Armorican arc across the Bay of Biscay: a joint
840 French-Spanish project. In: Schulmann, K., Martínez Catalan, J. R., Lardeaux, J. M.,
841 Janousek, V. & Oggiano, G. (eds) 2014. The Variscan Orogeny: Extent, Timescale and the
842 Formation of the European Crust. *Geological Society, London, Special Publications*, 405, 77-
843 113. <http://dx.doi.org/10.1144/SP405.13>.
- 844 Becerril, L., Cappello, A., Galindo, I., Neri, M., Del Negro, C., 2013. Spatial probability
845 distribution of future volcanic eruptions at El Hierro Island (Canary Islands, Spain). *Journal*
846 *of Volcanology and Geothermal Research*, 257, 21-30.
- 847 Boillot, G., Féraud G., Recq M., & Girardeau J. 1989. Undercrusting by serpentinite beneath
848 rifted margins. *Nature*, 341, 523-525.
- 849 Bronner, A., Sauter, D., Manatschal, G., Péron-Pinvidic, G., & Munschy, M. (2011).
850 Magmatic breakup as an explanation for magnetic anomalies at magma-poor rifted margins.
851 *Nature Geosciences*, 4, 549-553.
- 852 Choi, J.H., Edwards, P., Ko, K., Kim, Y.S., 2016. Definition and classification of fault
853 damage zones: a review and a new methodological approach. *Earth-Sciences Review*, 152,
854 70-87.
- 855 D'Oriano, F., Angeletti, L., Capotondi, L., Laurenzi, M. A., López Correa, M., Taviani, M.,
856 Torelli, L., Trua, T., Vigliotti, L., & Zitellini, N., 2010. Coral Patch and Ormonde seamounts
857 as a product of the Madeira hotspot, Eastern Atlantic Ocean. *Terra Nova*, 22, 494-500.

- 858 Féraud, G., Bonin, J., Olivet, J.-L., Auzende, J.-M., Bougault, H., 1977. Sur quelques
859 datations du volcanisme alcalin de la ligne Açores-Gibraltar et leur contexte géodynamique.
860 *Comptes Rendus Academie des Sciences Paris*, 285, 1203-1206.
- 861 Féraud, G., Girardeau, J., Beslier, M.-O., Boillot, G., 1988. Datation $^{40}\text{Ar}/^{39}\text{Ar}$ de la mise en
862 place des peridotites bordant la marge de la Galice (Espagne). *Comptes Rendus Academie des*
863 *Sciences Paris*, 307, 49-55.
- 864 Frizon de Lamotte, D., Fourdan, B., Leleu, S., Leparmentier, F., de Clarens P., 2015. Style of
865 rifting and the stages of Pangea breakup. *Tectonics*, 34, 1009-1029.
- 866 Geldmacher, J., Van der Bogaard, P., Hoernle, K., Schmincke H.-U., 2000. The $^{40}\text{Ar}/^{39}\text{Ar}$ age
867 dating of the Madeira Archipelago and hotspot track (eastern North Atlantic). *Geochemistry*
868 *Geophysics Geosystems*, 1, doi:10.1029/1999GC000018.
- 869 Geldmacher, J., Hoernle, K., Van der Bogaard, P., Zankl, G., Garbe-Schönberg, D. 2001.
870 Earlier history of the $\geq 70\text{Ma}$ old Canary hotspot based on the temporal and geochemical
871 evolution of the Selvagen Archipelago and neighboring seamounts in the eastern North
872 Atlantic. *Journal of Volcanology and Geothermal Research*, 111, 55-87.
- 873 Geldmacher, J., Hoernle, K., Van den Bogaard P., Duggen, S., Werner, R., 2005. New
874 $^{40}\text{Ar}/^{39}\text{Ar}$ age geochemical seamounts Canary and Madeira volcanic provinces: Support for
875 the mantle plume hypothesis. *Earth and Planetary Sciences Letters*, 237, 85-101.
- 876 Geldmacher, J., Hoernle K., Klügel A., Van den Bogaard P., Wombacher F., Berning B.
877 2006. Origin and geochemical evolution of the Tore-Madeira Rise (eastern North Atlantic).
878 *Journal of Geophysal Research*, B09206, doi:10.1029/2005JB003931.

- 879 Grange, M., Scharer, U., Merle, R., Girardeau, J., Cornen, G., 2010. Plume–Lithosphere
880 Interaction during Migration of Cretaceous Alkaline Magmatism in SW Portugal: Evidence
881 from U–Pb Ages and Pb–Sr–Hf Isotopes. *Journal of Petrology*, 51, 1143–1170.
- 882 Gudmundsson, A. & Brenner, S.L. 2001. How hydrofractures become arrested. *Terra Nova*,
883 13, 456–462
- 884 Gudmundsson, A., Simmenes, T.H., Larsen, B., Philipp, S.L., 2010. Effects of internal
885 structure and local stresses on fracture propagation, deflection, and arrest in fault zones.
886 *Journal of Structural Geology*, 32, 1643–1655.
- 887 Gudmundsson, A., Lecoeur, N., Mohajeri, N., Thordarson, T., 2014. Dike emplacement at
888 Bardarbunga, Iceland, induces unusual stress changes, caldera deformation, and earthquakes.
889 *Bulletin of Volcanology*, 76, article 869.
- 890 Ishii, E., 2016. Far-field stress dependency of the failure mode of damage-zone fractures in
891 fault zones: results from laboratory tests and field observations of siliceous mudstone.
892 *Journal of Geophysical Research*, 121, 70–91.
- 893 Jagoutz, O., Müntener, O., Manatschal, G., Rubatto, D., Péron-Pinvidic, G., Turrin, B.D.,
894 Villa, I.M., 2007. The rift-to-drift transition in the North Atlantic: A stuttering start of the
895 MORB machine? *Geology*, 35, 1087–1090.
- 896 Jiménez-Munt, I., Fernandez, M., Torne, M., Bird, P., 2001. The transition from linear to
897 diffuse plate boundary in the Azores-Gibraltar region: results from a thin-sheet model. *Earth
898 and Planetary Sciences Letter*, 192, 175–189.
- 899 Kneller, E.A., Johnson, C.A., Karner, G.D., Einhorn, J., Queffelec, T.A., 2012. Inverse
900 methods for modeling non-rigid plate kinematics: Application to mesozoic plate
901 reconstructions of the Central Atlantic. *Computational Geosciences*, 49, 217–230.

- 902 Matthews, K.J., Seton, M., Muller, R.D., 2011. A global-scale plate reorganization event at
903 105-100 Ma. *Earth and Planetary Science Letters*, 355–356, 283-298.
- 904 Merle, R., Scharer U., Girardeau, J.; Cornen, G., 2006. Cretaceous seamounts along the
905 ocean-continent of Iberian margin: U-Pb ages and Sr-Pb-Hf isotopes. *Geochimica et*
906 *Cosmochimica Acta*, 70, 4950-4976.
- 907 Merle, R., Jourdan, F., Marzoli, A., Renne, P.R., Grange, M., Girardeau, J., 2009. Evidence
908 of multi-phase Cretaceous to Quaternary alkaline magmatism on Tore-Madeira Rise and
909 neighbouring seamounts from $^{40}\text{Ar}/^{39}\text{Ar}$ ages. *Journal of the Geological Society of London*,
910 166, 879-894.
- 911 Merle R., Jourdan F., Girardeau J., Geochronology of the Tore-Madeira Rise seamounts and
912 surrounding areas: a review. Submitted to *Australian Journal of Earth Sciences*.
- 913 Mitchell, N.C., Masson, D.G., Watts, A.B., Gee, M.J.R., Urgeles, R., 2002. The morphology
914 of the submarine flanks of volcanic ocean islands. A comparative study of the Canary and
915 Hawaiian hotspot islands. *Journal of Volcanology and Geothermal Research*, 115, 83-107.
- 916 Neres, M., Bouchez, J.L., Terrinha, P., Font, E., Moreira, M., Miranda, R., Launeau, P.,
917 Carvallo, C., 2014. Magnetic fabric in a Cretaceous sill (Foz da Fonte, Portugal): flow model
918 and implications for regional magmatism. *Geophysical Journal International*, 199, 78-101.
- 919 Nirrengarten, M., Manatschal, G., Tugend, J., Kusznir, N.J., Sauter, D., 2017. Nature and
920 origin of the J-magnetic anomaly offshore Iberia-Newfoundland: Implications for plate
921 reconstructions. *Terra Nova*, 29, 20-28.
- 922 Nirrengarten, M., Manatschal, G., Tugend, J., Kusznir, N., Sauter, D., 2018. Kinematic
923 evolution of the southern North Atlantic: Implications for the formation of hyperextended rift
924 systems. *Tectonics*, 37, <https://doi.org/10.1002/2017TC004495>

- 925 Olivet J.-L., 1996. La cinématique de la plaque Ibérique, *Bulletin Centres Recherches*
926 *Exploration-Prod. Elf Aquitaine*, 20, 131-195.
- 927 Peacock, D.C.P., Dimmen, V., Rotevatn, A., Sanderson, D.J., 2017. A broader classification
928 of damage zones. *Journal of Structural Geology*, 102, 179-192.
- 929 Peirce, C., Barton, P.J., 1991. Crustal structure of the Tore-Madeira Rise, Eastern North
930 Atlantic-results of a DOBS wide-angle and normal incidence seismic experiment in the
931 Josephine Seamount region. *Geophysical Journal International*, 106, 357-378.
- 932 Pereira, R., Alves, T.M., 2011. Margin segmentation prior to continental break-up: A
933 seismic-stratigraphic record of multiphased rifting in the North Atlantic. *Tectonophysics*, 505,
934 17-34.
- 935 Pereira, R., Alves, T.M., 2012. Tectono-stratigraphic signature of multiphased rifting on
936 divergent margins (deep-offshore southwest Iberia, North Atlantic). *Tectonics*, 31, TC4001,
937 doi:10.1029/2011TC003001.
- 938 Pereira, R., Alves, T.M. Mata, J., 2016. Alternating crustal architecture in West Iberia: a
939 review of its significance in the context of NE Atlantic rifting. *Journal of Geological Society*,
940 174, 522-540.
- 941 Péron-Pinvidic, G., Manatschal G., 2009. The final rifting evolution at deep magma-poor
942 passive margins from Iberia-Newfoundland: A new point of view. *International Journal of*
943 *Earth Sciences*, 98, 1581-1597.
- 944 Ramos, A., Fernández, O., Torne, M., Sánchez de la Muela, A., Muñoz, J.A., Terrinha, P.,
945 Manatschal, G., Salas, M.C., 2017. Crustal structure of the SW Iberian passive margin: The
946 westernmost remnant of the Ligurian Tethys? *Tectonics*, doi: 10.1016/j.tecto.2017.03.012.

- 947 Reynolds, P., Holford, S., Schofield N., Ross, A., 2018. The importance of subsurface
948 lithology in controlling magma storage vs. eruption: an example from offshore southern
949 Australia. *Journal of the Geological Society*, <https://doi.org/10.1144/jgs2017-109>.
- 950 Ruch, J., Vezzoli, L. De Rosa, R. Di Lorenzo, R., Acocella. V., 2016. Magmatic control
951 along a strike-slip volcanic arc: The central Aeolian arc (Italy). *Tectonics*, 35,
952 doi:10.1002/2015TC004060.
- 953 Sahabi, M., Aslanian, D., Olivet, J.-L., 2004. A new starting point for the history of the
954 central Atlantic. *Comptes Rendus Geosciences*, 336, 1041-1052.
- 955 Sallarès, V., Gailler, A., Gutscher, M.-A., Graindorge, D., Bartolomé, R., Gràcia, E., Zitellini,
956 N., 2011. Seismic evidence for the presence of Jurassic oceanic crust in the central Gulf of
957 Cadiz (SW Iberian margin). *Earth and Planetary Science Letters*, 311, 112-123.
- 958 Sallarès, V., Martínez-Loriente, S., Prada, M., Gràcia, E., Ranero, C., Gutscher, M.-A.,
959 Zitellini, N., 2013. Seismic evidence of exhumed mantle rock basement at the Gorringe Bank
960 and the adjacent Horseshoe and Tagus abyssal plains (SW Iberia). *Earth and Planetary
961 Science Letters*, 365, 120-131.
- 962 Schärer, U., Girardeau, J., Cornen, G., Boillot, G., 2000. 138-121 Ma asthenospheric
963 magmatism prior to continental break-up in the North Atlantic and geodynamic implications.
964 *Earth and Planetary Science Letters*, 181, 555-572.
- 965 Seton, M., Whittaker, J.M., Wessel, P., Müller, R.D., DeMets, C., Merkouriev, S., Williams,
966 S.E., 2014. Community infrastructure and repository for marine magnetic identifications.
967 *Geochemistry Geophysics Geosystems*, 15, 1629-1641.
- 968 Sibuet, J.C., Srivastava, S.P., Enachescu, M., Karner, G.D., 2007. Early Cretaceous motion of
969 Flemish Cap with respect to North America: Implications on the formation of Orphan Basin

- 970 and SE Flemish Cap–Galicia Bank conjugate margins. In: Karner, G.D., Manatschal, G.,
971 Pinheiro, L.M., (eds) Imaging, Mapping and Modelling Continental Lithosphere Extension
972 and Breakup. *Geological Society, London, Special Publications*, 282, 63-76.
- 973 Sigmundson, F., Hooper, A., Hreinsdottir, S., Vogfjord, K.S., Ofeigsson, B.G., Heimisson,
974 E.R., Dumont, S., Parks M., Spaans, K., Gudmundsson, G.B., Drouin, V., Arnadottir, T.,
975 Jonsdottir, K., Gudmundsson, M.T., Hognadottir, T., Fridriksdottir, H.M., Hensch, M.,
976 Einarsson, P., Magnusson, E., Samsonov, S., Brandsdottir, B., White, R.S., Agustsdottir, T.,
977 Greenfield, T., Green, R.G., Hjartardottir, A.R., Pedersen, R., Bennett, R.A., Geirsson, H., La
978 Femina, P.C., Bjornsson, H., Palsson, F., Sturkell, E., Bean, C.J., Mollhoff, M., Braiden,
979 A.K., Eibl, E.P.S., 2014. Segmented lateral dyke growth in a rifting event at Bardarbunga
980 volcanic system, Iceland. *Nature*, 517, 191-195.
- 981 Srivastava, S.P., Sibuet, J.-C., Cande, S., Roest, W.R., Reid, I.D., 2000. Magnetic evidence
982 for slow seafloor spreading during the formation of the Newfoundland and Iberian margins.
983 *Earth and Planetary Science Letters*, 182, 61-76.
- 984 Schettino, A., Turco, E., 2009. Breakup of Pangaea and plate kinematics of the central
985 Atlantic and Atlas regions. *Geophysical Journal International*, 178, 1078-1097.
- 986 Tesauro, M., Kaban, M.K., Cloetingh, S.A.P.L., 2009. A new thermal and rheological model
987 of the European lithosphere. *Tectonophysics*, 476, 478-495.
- 988 Tibaldi, A. 1995. Morphology of pyroclastic cones and tectonics. *Journal of geophysical
989 Research*, 100, B12, 24,521-24,535
- 990 Tucholke, B.E., Ludwig, W.J., 1982. Structure and origin of the J Anomaly Ridge, Western
991 North Atlantic Ocean. *J. Geophys. Res.* **87**, 9389-9407.
- 992 Tucholke, B.E., Sawyer, D.S., Sibuet, J.C., 2007. Breakup of the Newfoundland Iberia rift.
993 In: Karner, G.D., Manatschal, G. & Pinheiro, L.M. (eds) Imaging, Mapping and Modelling

994 Continental Lithosphere Extension and Breakup. *Geological Society, London, Special*
995 *Publication*, 282, 9-46.

996 Veludo, I., Dias, N.A., Fonseca, P.E., Matias, L., Carriho, F., Haberland, C., Villaseñor, A.,
997 2017. *Tectonophysics*, 717, 645-664.

998 Vergés, J., Fernàndez, M., Martínez, A., 2002. The Pyrenean orogen: Pre-, syn-, and post-
999 collisional evolution. *Journal of the Virtual Explorer*, 8, 55-74.

1000 Verhoef, J., Roest, W.R., Macnab, R., Arkani-Hamed, J., Members of the Project Team,
1001 1996. Magnetic anomalies of the Arctic and North Atlantic Oceans and Adjacent land areas,
1002 GSC Open file 3125. Geological Survey of Canada 225.

1003 Xu, W., Ruch, J., Jónsson, S., 2015. Birth of two volcanic islands in the southern Red Sea.
1004 Nature Communications 6, 7104, doi: 10.1038/ncomms8104.

1005

1006 **Figure Captions**

1007 **Figure 1.** Topography and bathymetric maps of the Iberia-Morocco margin within the
1008 southern North Atlantic and northern Central Atlantic showing the recent to present-day
1009 configuration of the plate boundary between the Iberia and NW Africa plates. Red dashed
1010 lines represent the Tore-Madeira Rise volcanic fields. AGFZ: Azores-Gibraltar Fracture
1011 Zone, IAP: Iberia Abyssal Plain, TAP: Tagus Abyssal Plain, SAP: Seine Abyssal Plain,
1012 MAR: Mid-Atlantic Ridge. Active volcanoes are represented in red triangles. Brown lines
1013 represent major inherited structures from the Late Cretaceous ([Ballevre et al., 2014](#)).

1014 **Figure 2.** Main volcanic edifices of the Tore-Madeira Rise and surroundings seamounts. The
1015 main volcanic groups with the names of the main volcanoes considered in this study are
1016 indicated with the black triangle. Ages of TMR seamounts, Ampere (Amp; 32Ma), Aston

1017 (A ; 99-96Ma), Gago Coutinho (GC ; 96-92Ma), Godzilla (G; 68Ma), Isabelle (I ; >85Ma),
1018 Joe Sister (JS; 86.5-88Ma), Josephine (J ; 16-12Ma and 8-0.5Ma), Madeira (M; 5-0Ma),
1019 Ormonde (O ; 66-62Ma), Porto Santo (PS; 11-14Ma), Seine (S; 25-22Ma), Sponge Bob (SB ;
1020 103Ma), Unicorn (U; 28Ma) from Féraud et al. (1981, 1982, 1986), Bernard-Griffiths et al.
1021 (1997), D'Oriano et al. (2010), Geldmacher et al. (2000, 2005, 2006, 2008), Merle et al.
1022 (2006, 2009). Ages of SW Portugal intrusions including Ribamar (R ; 88Ma), Sintra (Sin ;
1023 79-83Ma) ; Foz da Fonte (FdF; 94.5Ma), Sines (Si ; 77-75Ma) and Serra de Monchique
1024 (Mon ; 76-68Ma) from Grange et al. (2010) and Miranda et al. (2009). The white and black
1025 dashed line represents the location of the positive J- magnetic anomaly (Olivet, 1996;
1026 Bronner et al., 2011, Nirrengartner et al., 2017). Green dashed lines marked the crustal rift
1027 domain boundaries derived from published maps (Afilhado et al., 2008; Nirrengartner et al.,
1028 2017; Pereira et al., 2016; Ramos et al., 2017; Sallares et al., 2013). Inherited structures are
1029 modified from Alves et al. (2018) and Ballevre et al. (2014). Magnetic picks are extracted
1030 from the repository for magnetic anomaly (Seton et al., 2014). Thick white lines correspond
1031 to major fractures zone picked from public-domain databases (Matthews et al., 2011).
1032 Bathymetric contours (200m) are derived from the global DEM described in this study.
1033 Tracks of the Tore-Madeira cruise are shown in thin black lines. Upper left insert shows the
1034 coverage of the multibeam bathymetric survey (coloured by depth overlaid on the
1035 EMODNet).

1036 **Figure 3. a.** Swath bathymetric maps (using 100m isobaths) of the Tore Complex Volcanic
1037 Field localised to the north of Tore-Madeira Rise along the offshore Iberia margin. b. Slope
1038 distribution map of the Tore Complex Volcanic Field.

1039 **Figure 4.** Detailed swath bathymetric map (using 20m isobaths) of volcanic edifices of the
1040 Tore Complex Volcanic Group including (a) Tore North-West, (b) Tore North (c) Tore East,

1041 (d) Tore Central, (e) Tore South, (f) Sponge Bob. Colour code indicative of depth value is
1042 similar for maps.

1043 **Figure 5.** Slope distribution map of the Central Volcanic Group localised along the eastern
1044 branch of the Azores-Gibraltar Fracture Zone (AGFZ). AR, Ashton Ridge; GC2, GC3, Gago
1045 Coutinho Volcanic edifices; GCV, Gago Coutinho Valley; VE1, VE2, volcanic edifices.

1046 **Figure 6. (a)** Detailed swath bathymetric and **(b)** slope distribution maps of the Central
1047 Volcanic Group including Gago-Coutinho and Ashton volcanoes, north of AGFZ.

1048 **Figure 7.** a) Detailed swath bathymetric and (b) slope distribution maps of **(a)** Dragon and
1049 **(b)** Unicorn volcanic edifices located in the Southern Volcanic Group.

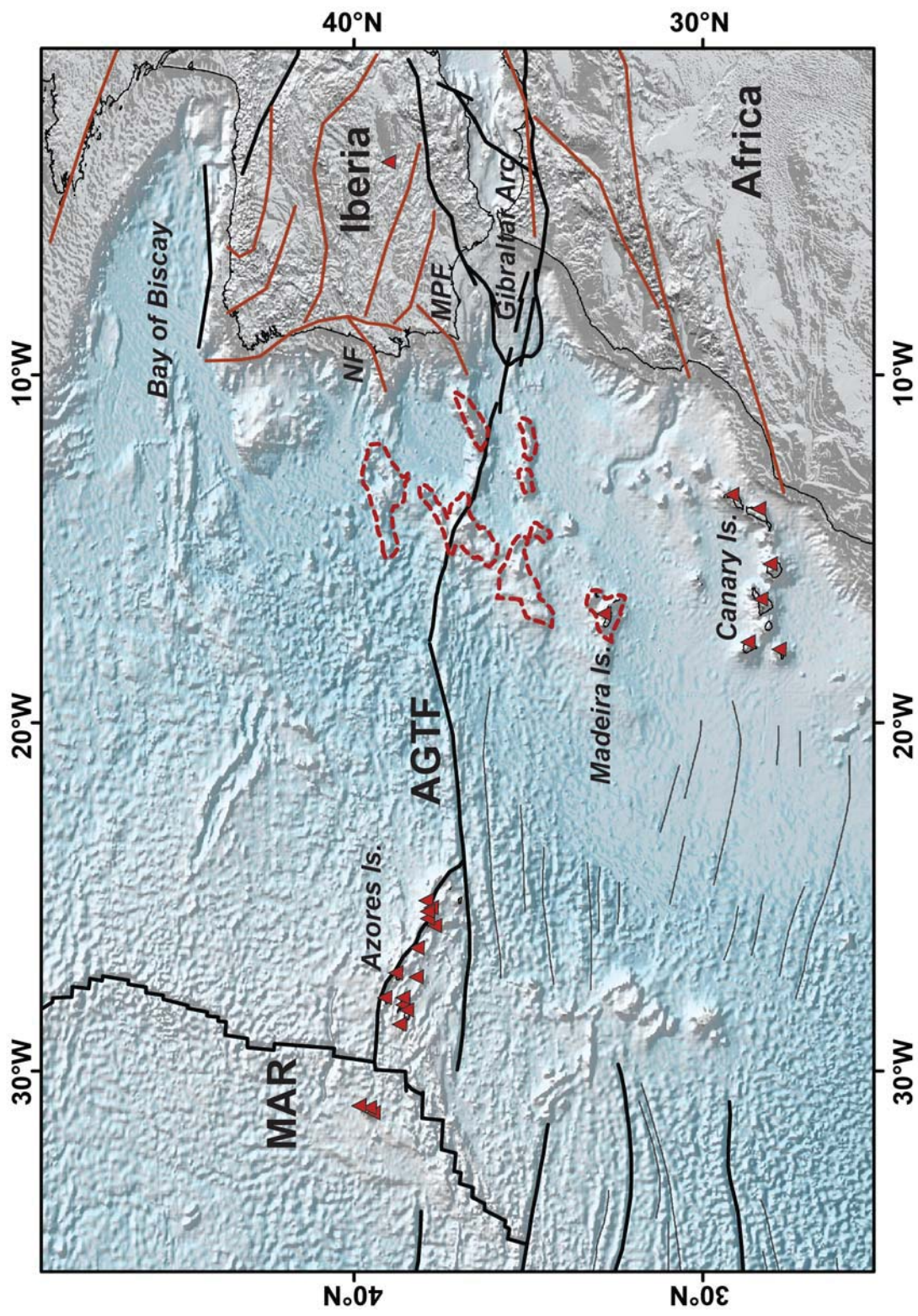
1050 **Figure 8.** Slope distribution map of the Lyon and Isabelle volcanic edifices in the Southern
1051 Volcanic Group.

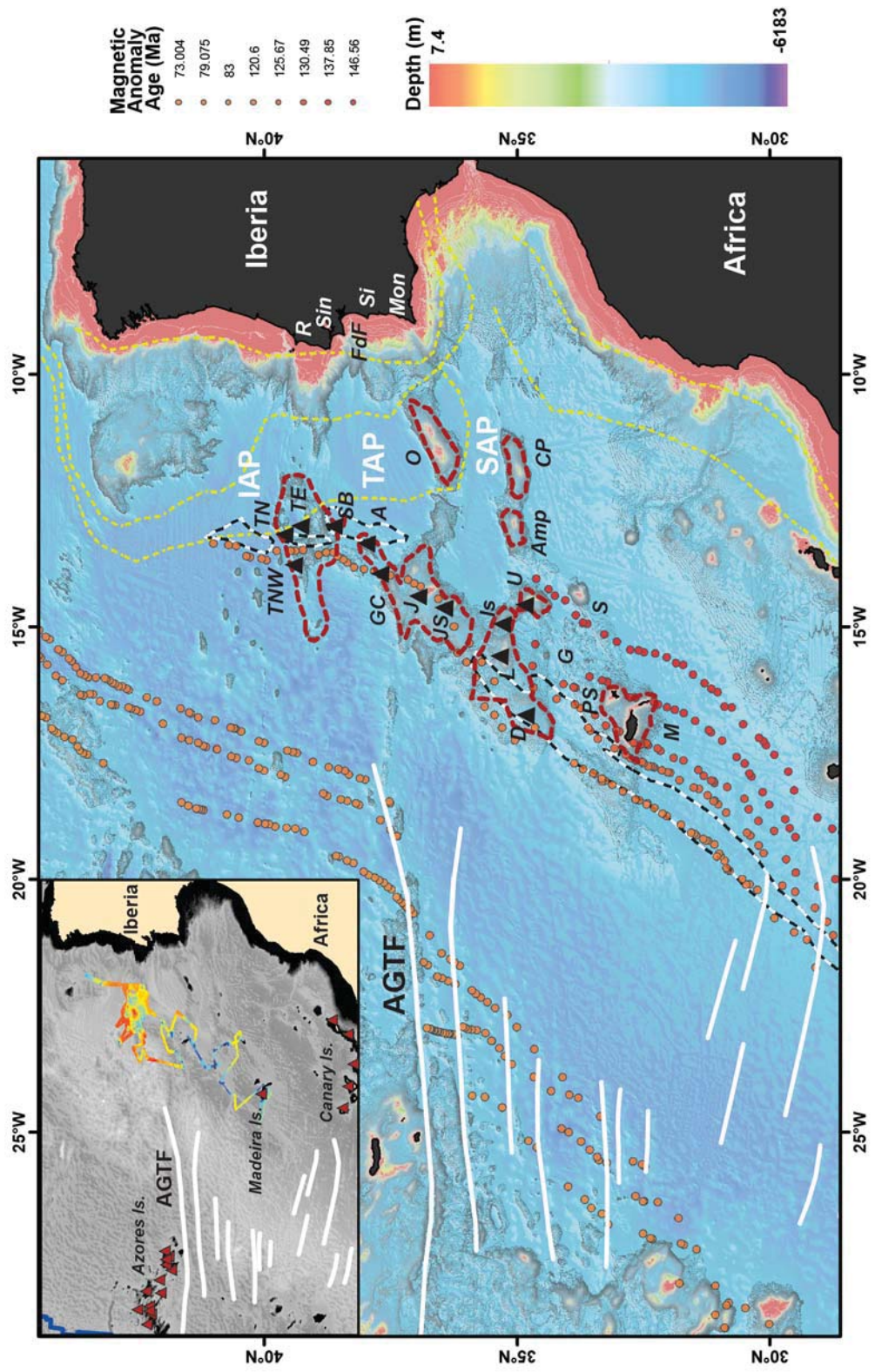
1052 **Figure 9.** Vents and interpreted volcanic eruptive fissures of the (a) Northern (Tore
1053 Complex), (b) Central (Jospehine Massif) and (c) Southern Volcanic Group. Insert: Rose
1054 diagram showing the azimuth frequency of eruptive fissures.

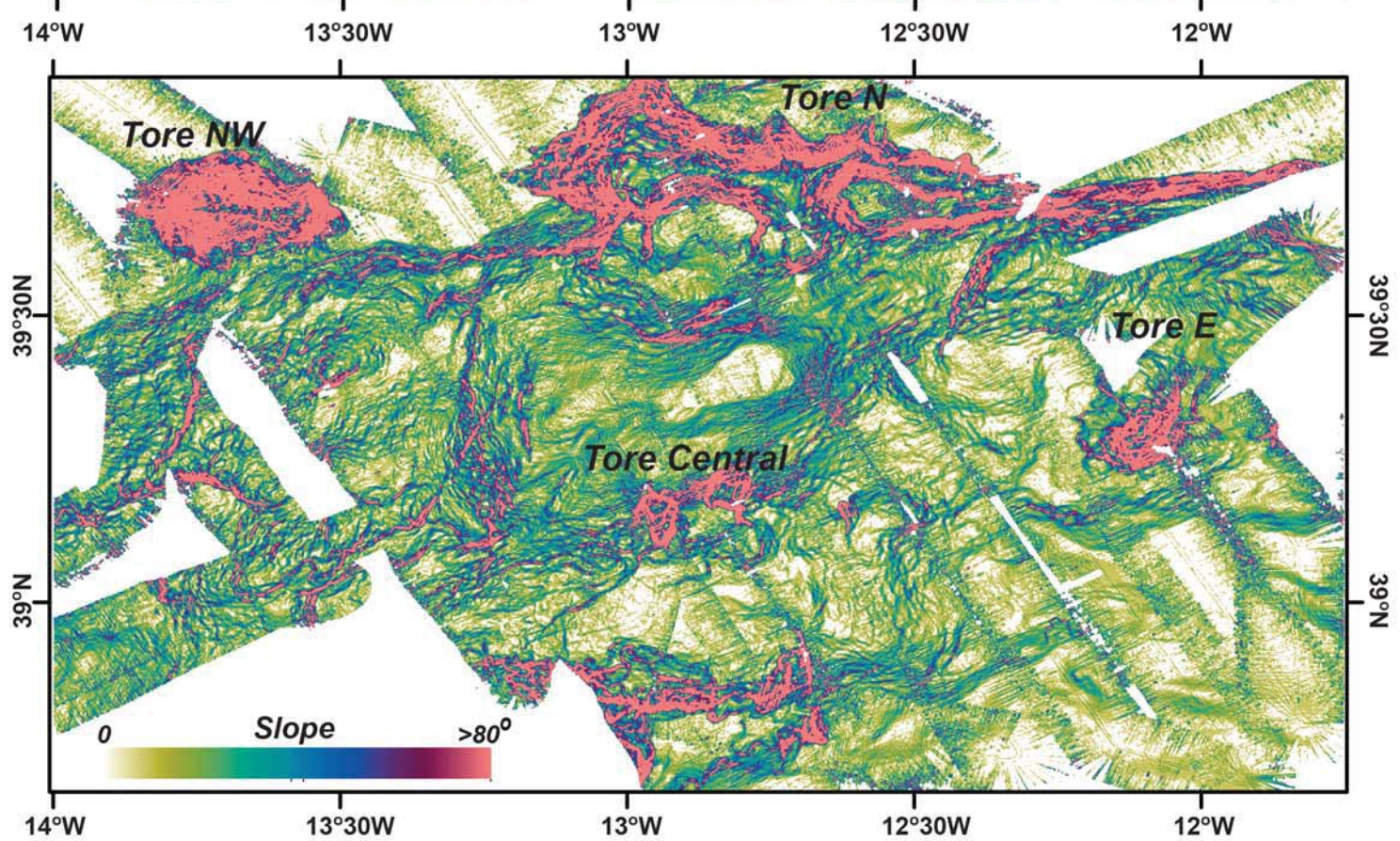
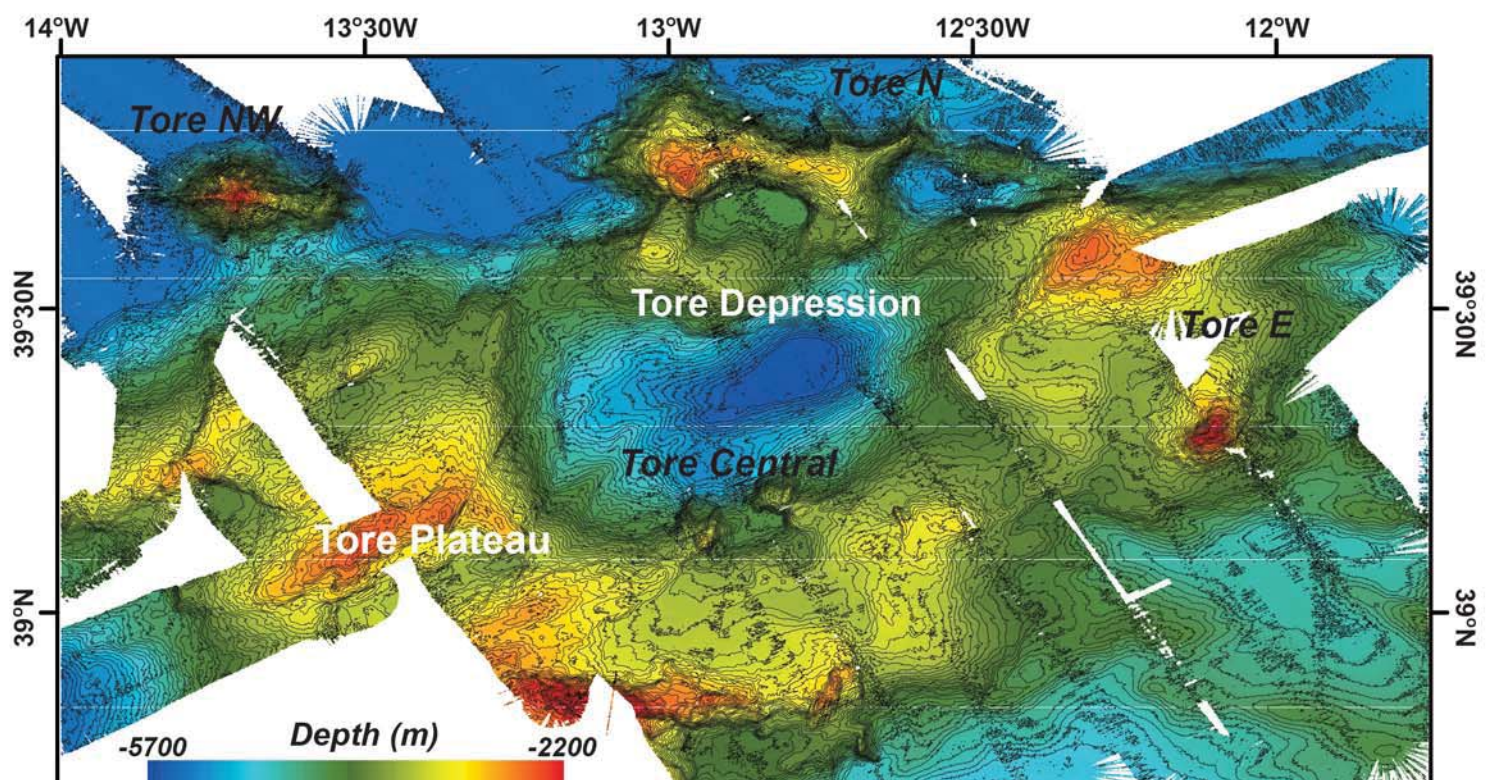
1055 **Figure 10.** DEM model of the (a) Northern (Tore Complex), (b) Central (Jospehine Massif)
1056 and (c) Southern Volcanic Group showing the main lineaments. Insert: Rose diagram
1057 showing the azimuth frequency of discrete lineaments.

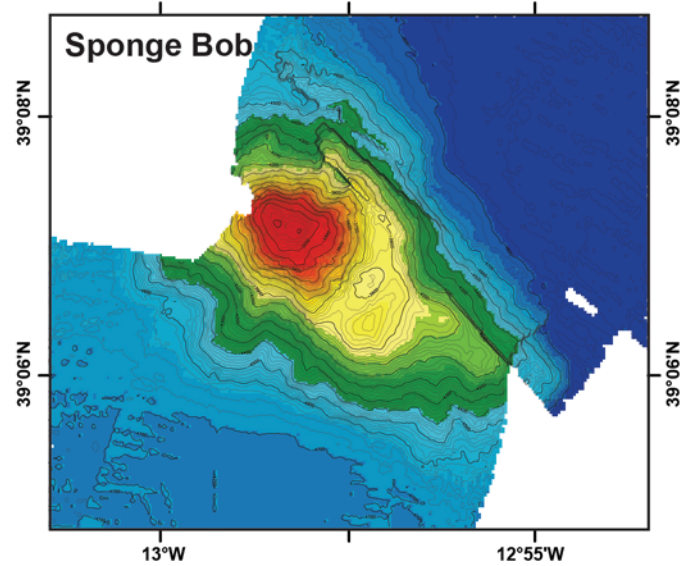
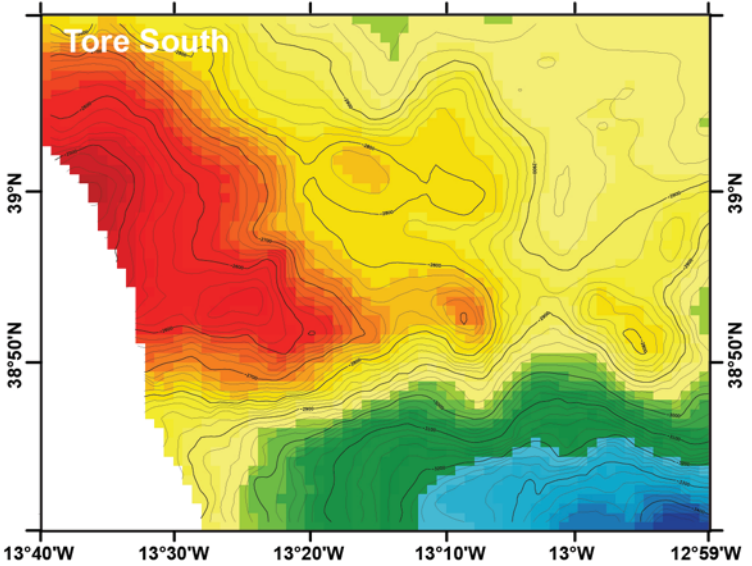
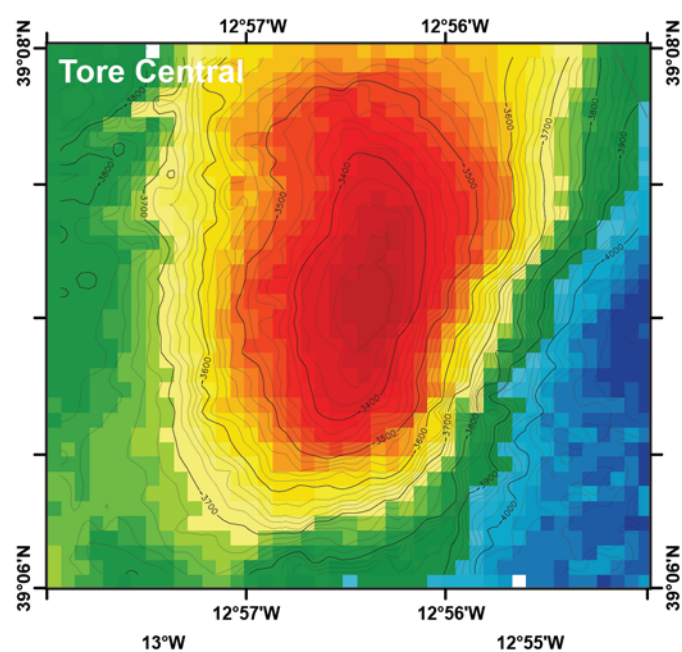
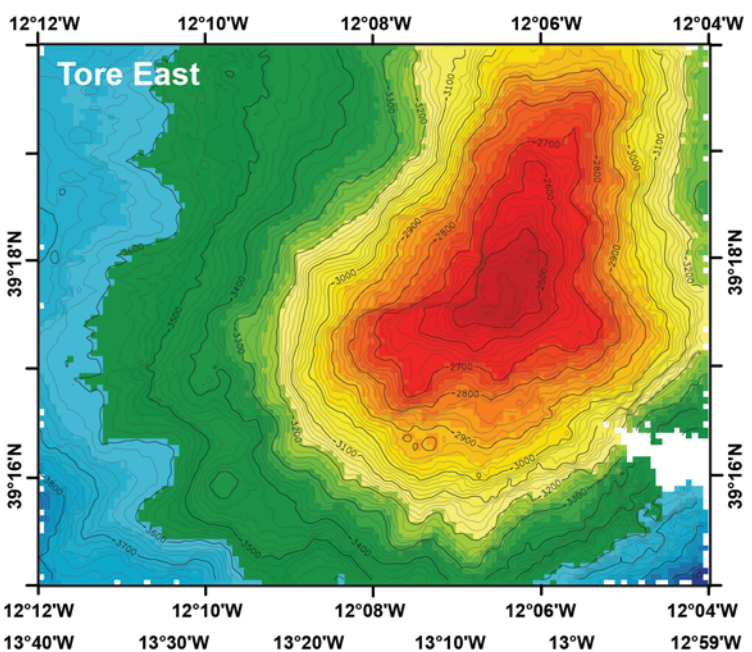
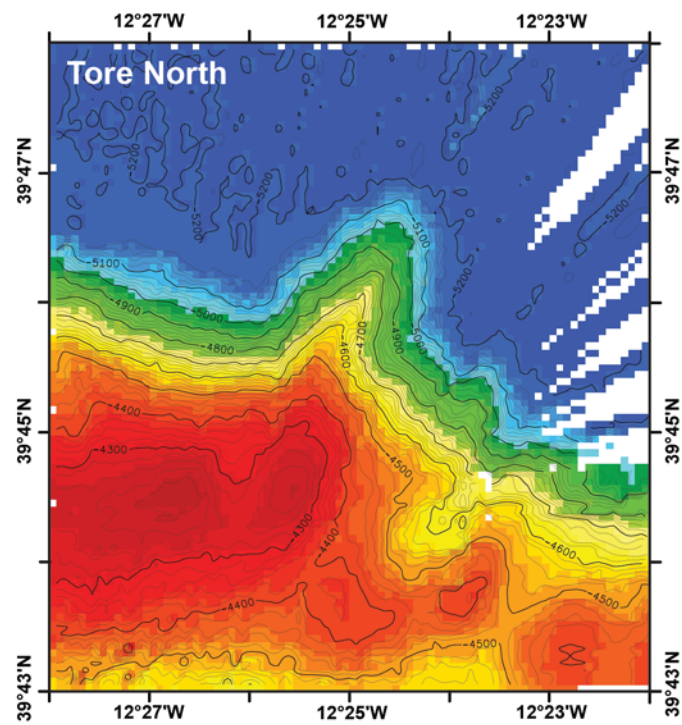
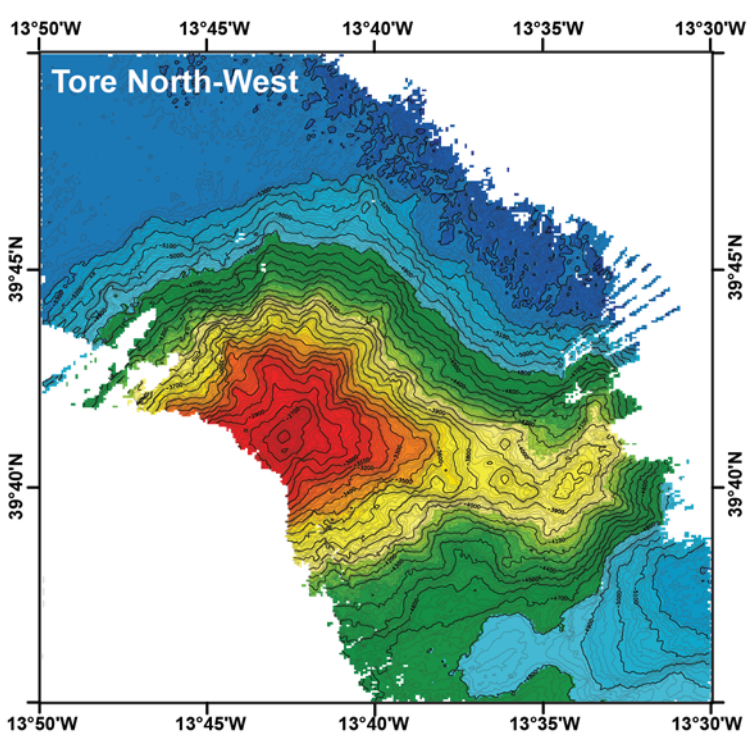
1058 **Figure 11.** Orientation of the elongation of the volcanoes (a) along the Tore-Madeira Rise
1059 and (b) per volcanic groups.

1060 **Figure 12.** Tectonic map with distribution of volcanoes









Depth (m)

<2200
-2200-2300
-2300-2400
-2400-2500
-2500-2600
-2600-2700

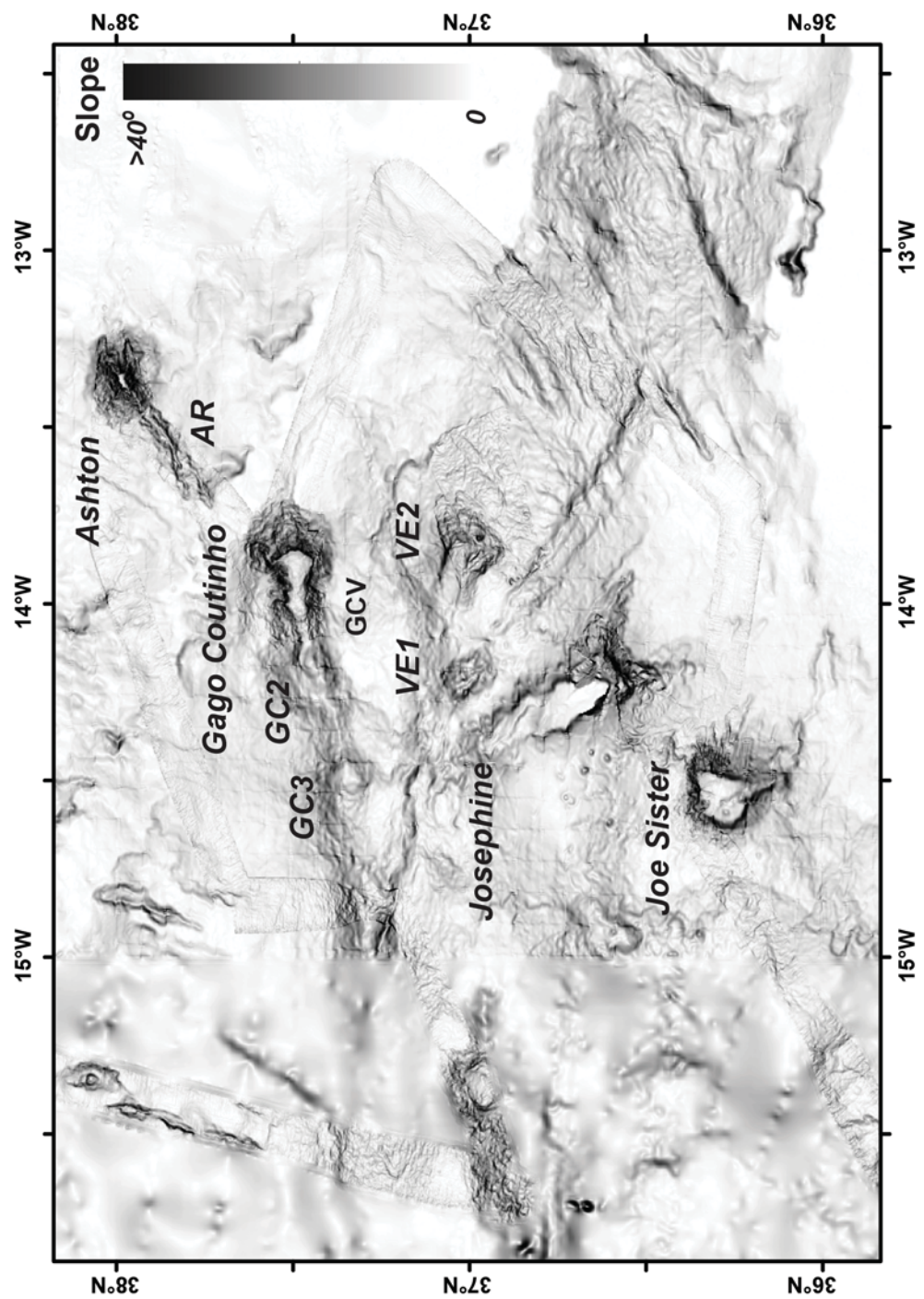
-2700-2800
-2800-2900
-2900-3000
-3000-3100
-3100-3200
-3200-3300

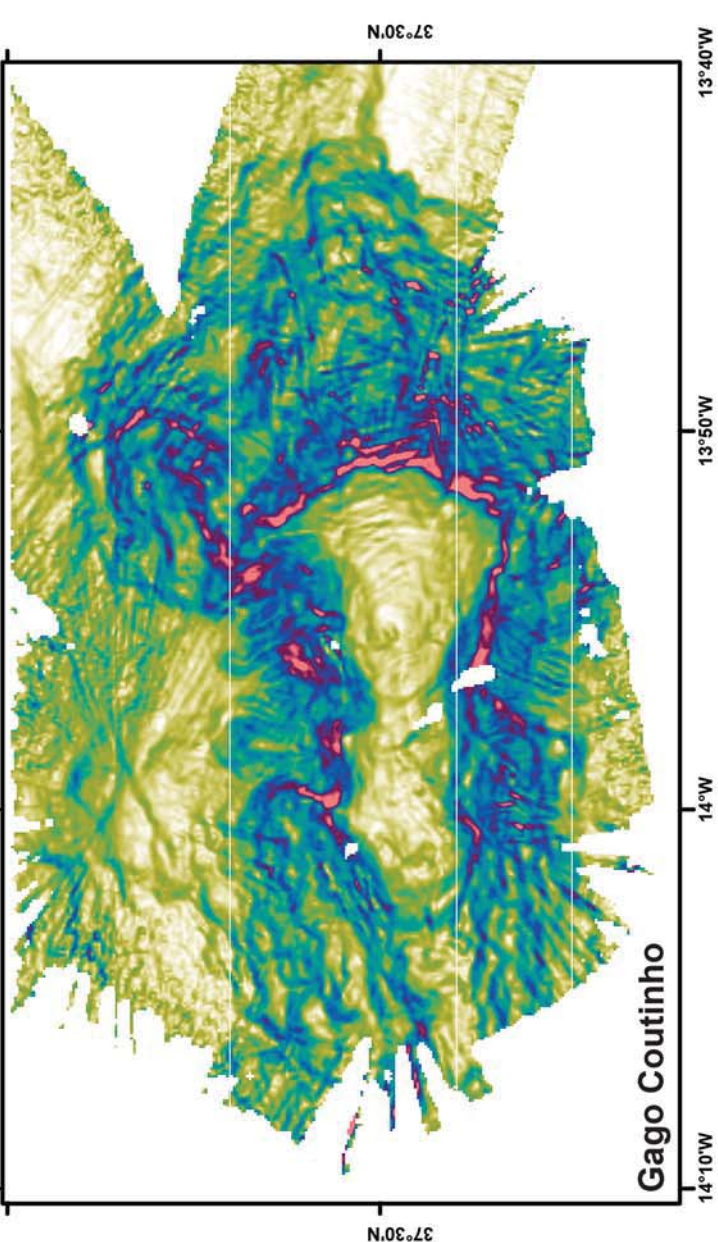
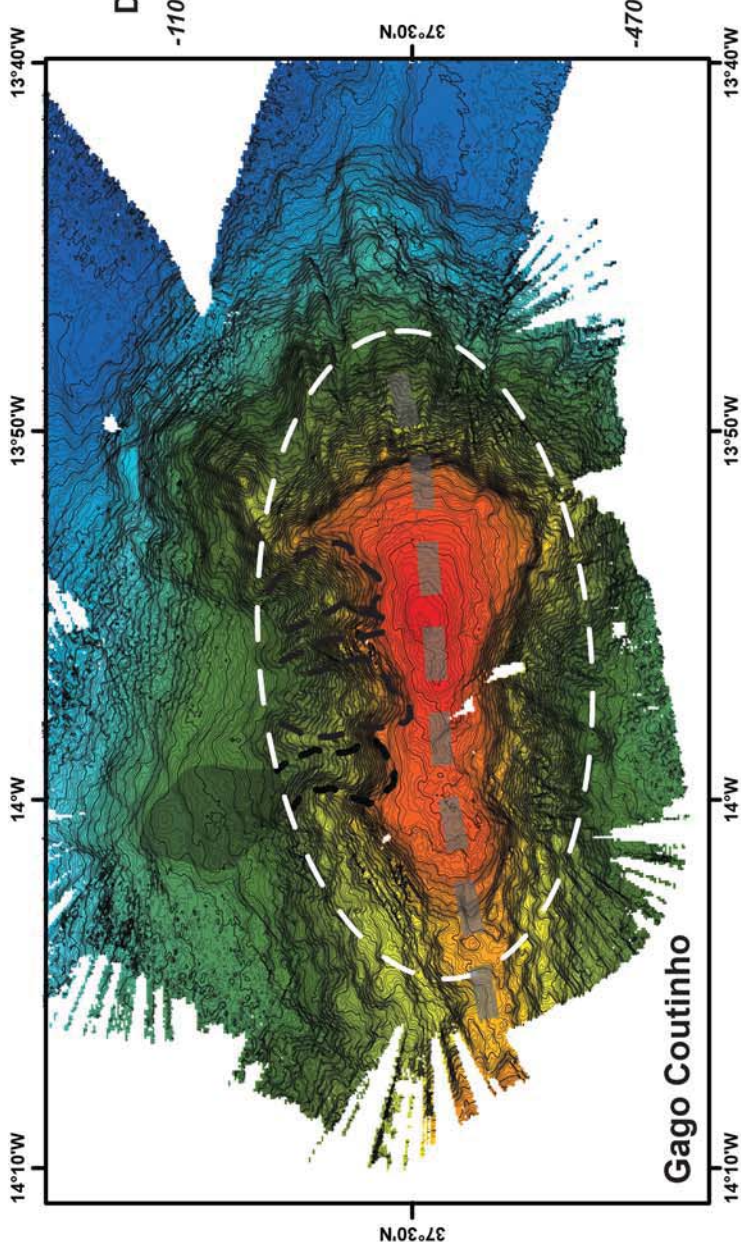
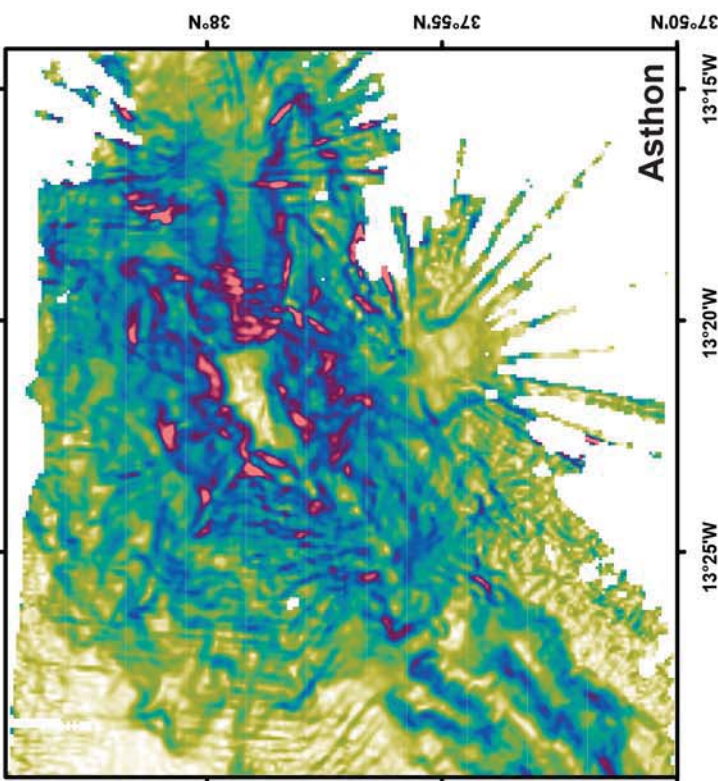
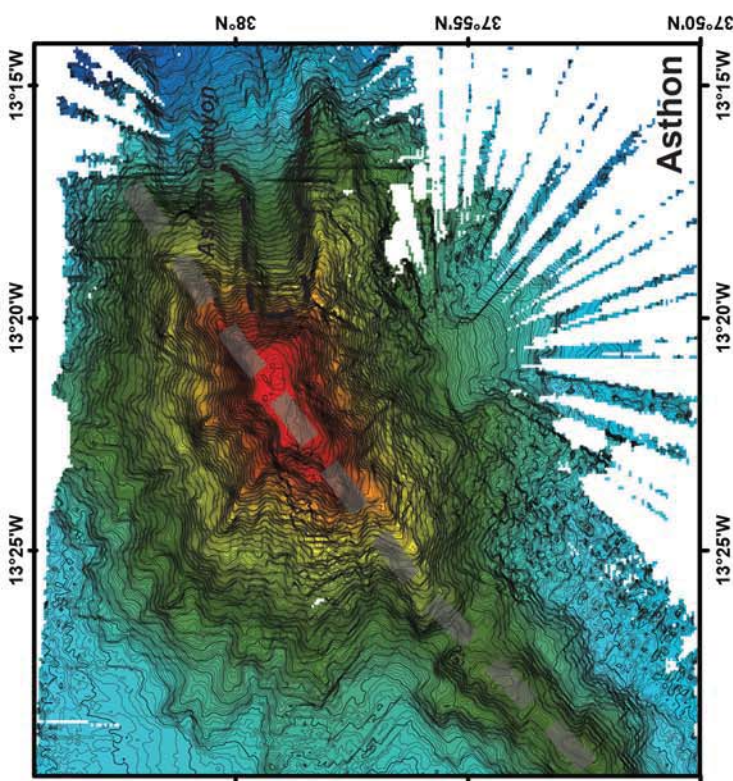
-3300-3400
-3400-3500
-3500-3600
-3600-3700
-3700-3800
-3800-3900

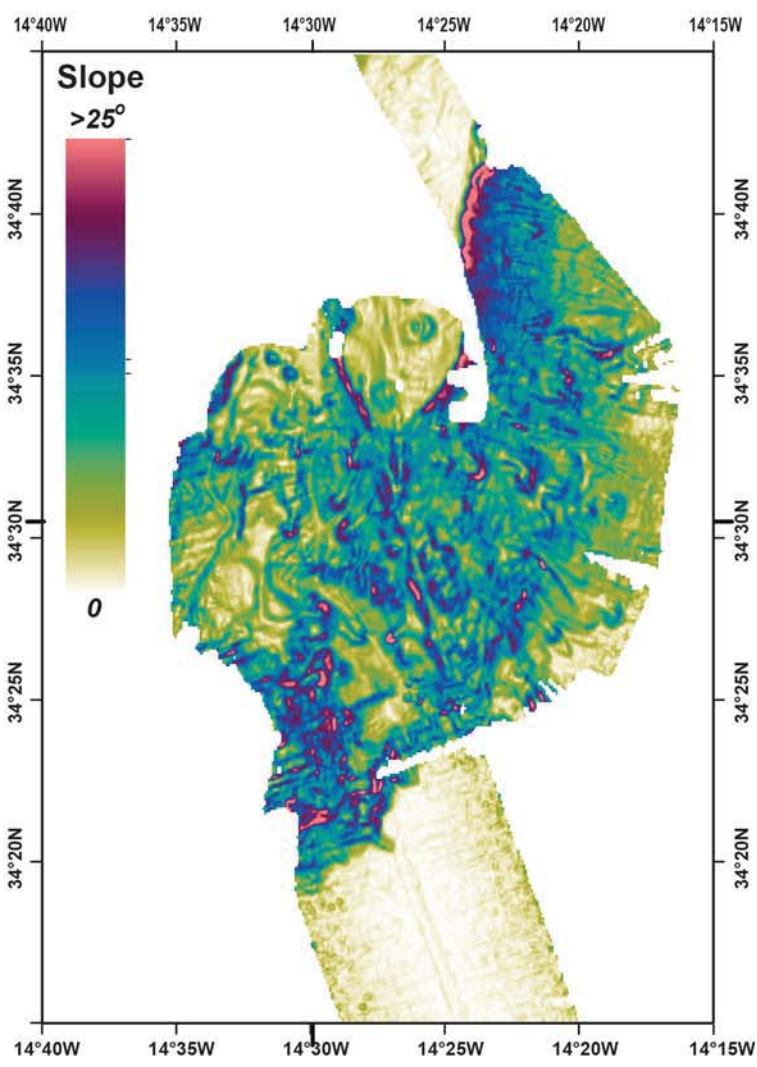
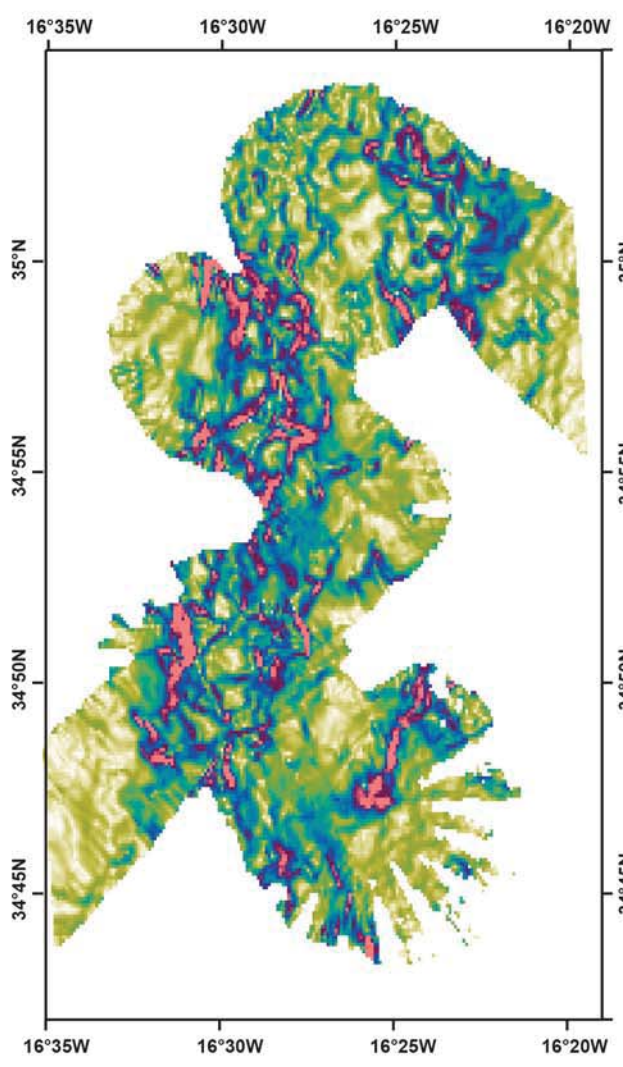
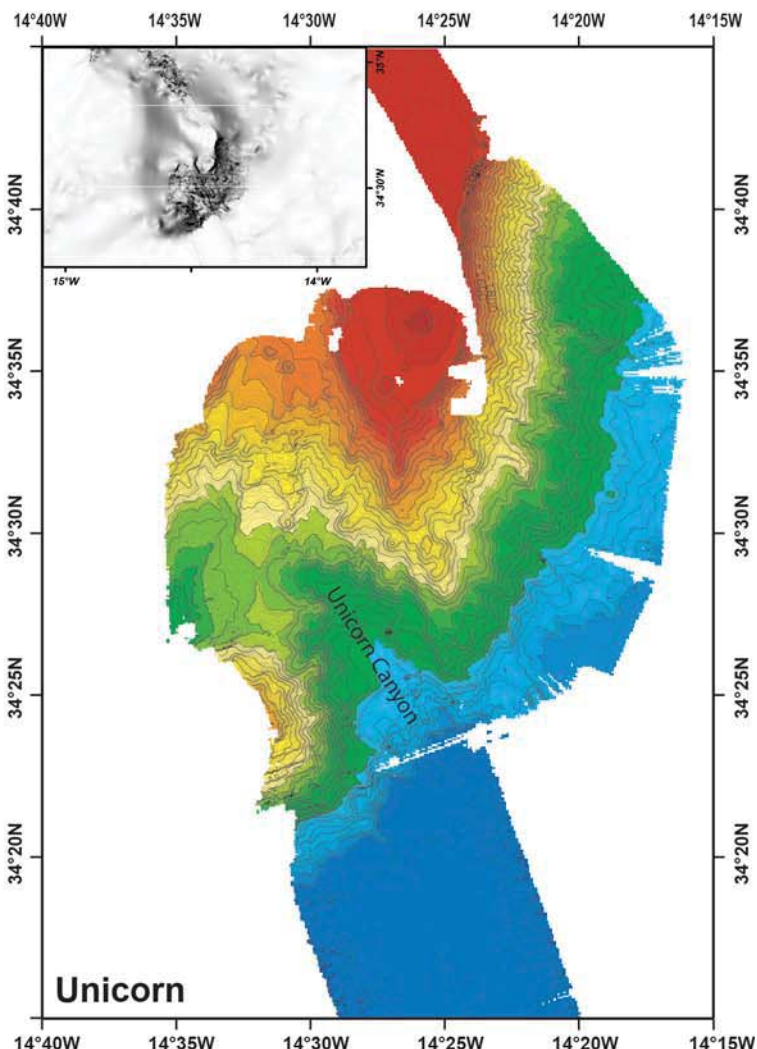
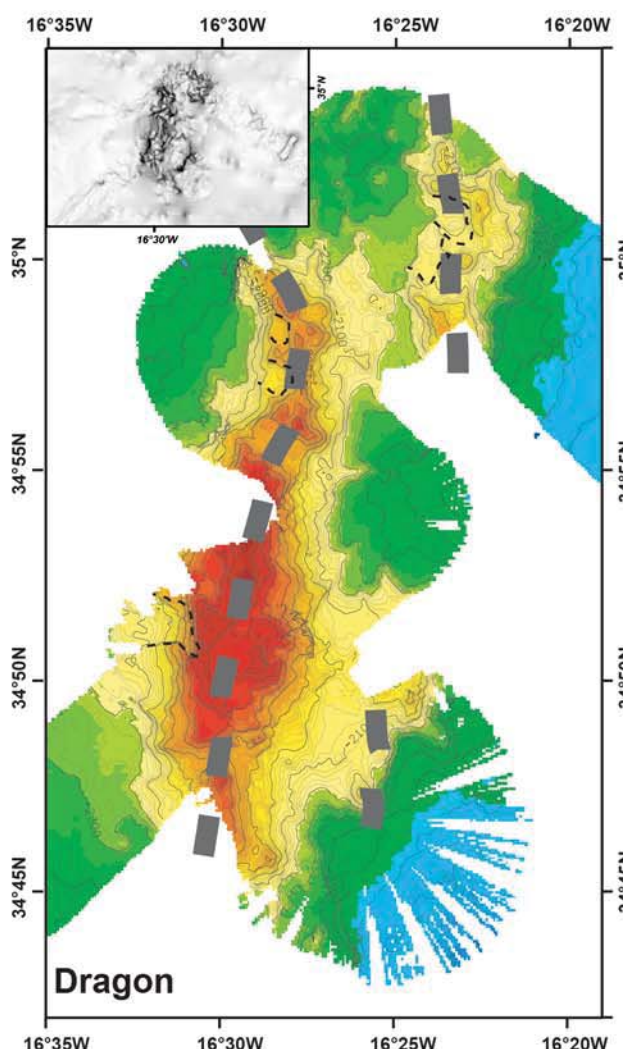
-3900-4000
-4000-4100
-4100-4200
-4200-4300
-4300-4400
-4400-4500

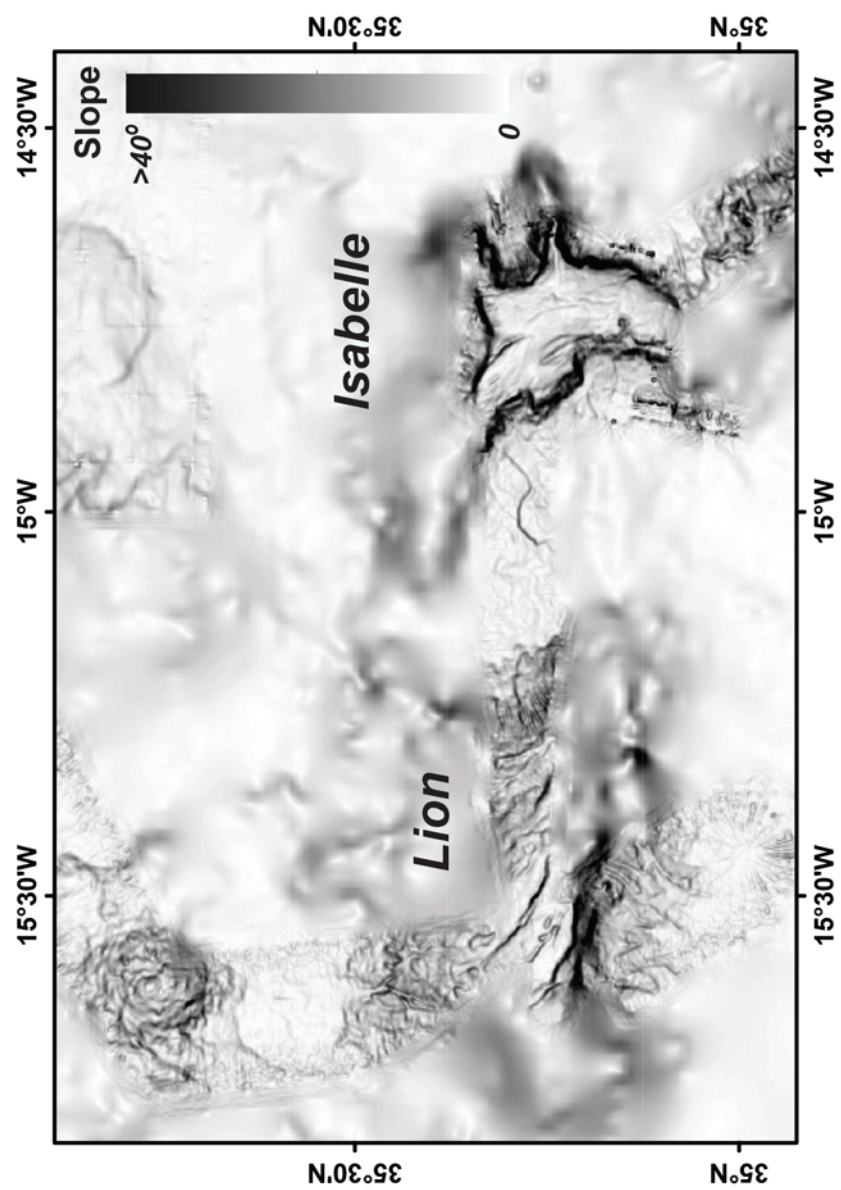
-4500-4600
-4600-4700
-4700-4800
-4800-4900
-4900-5000
-5000-5100

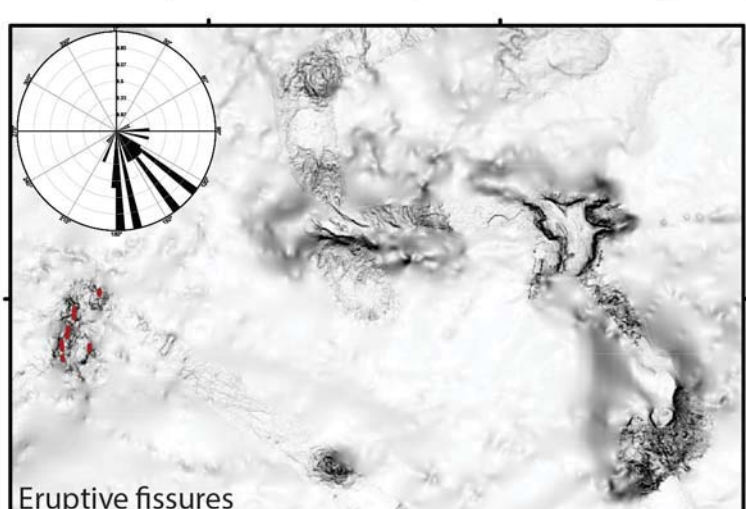
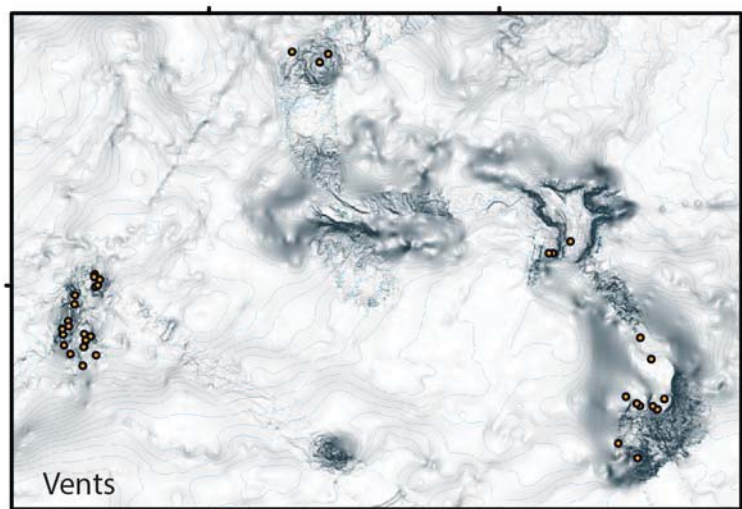
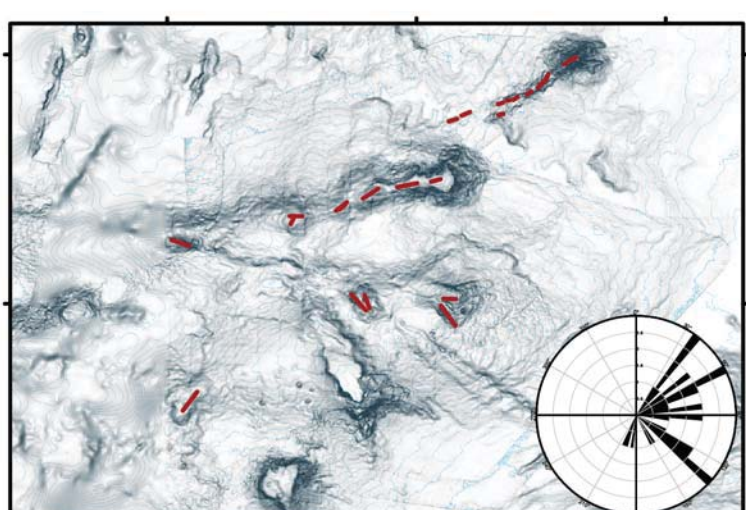
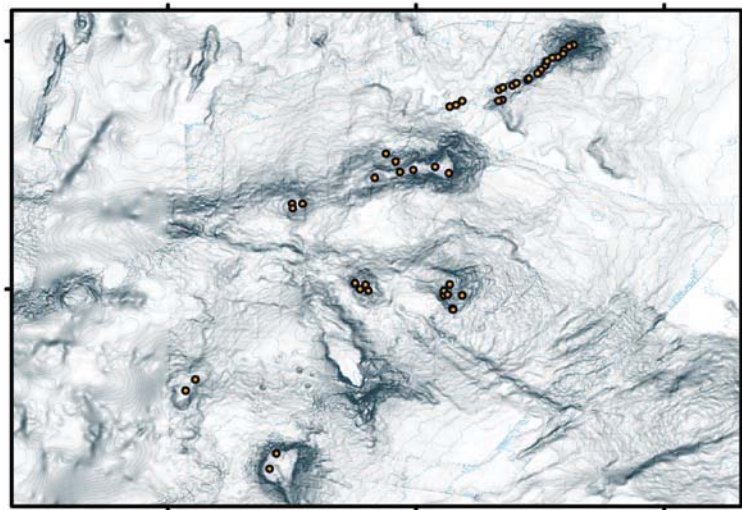
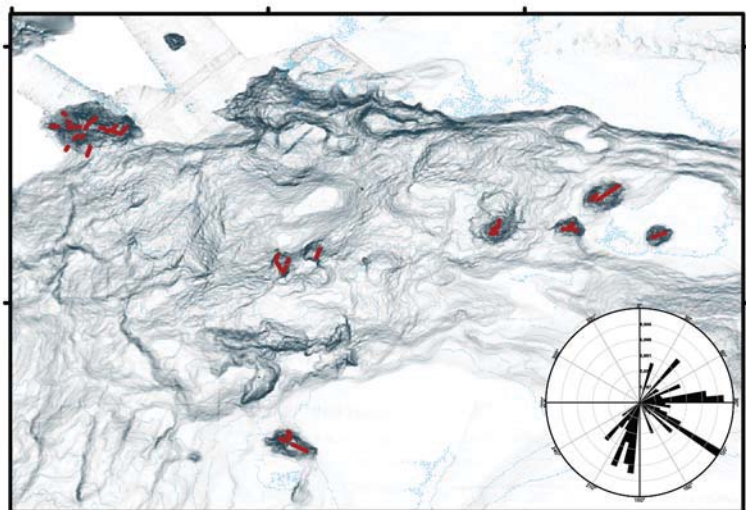
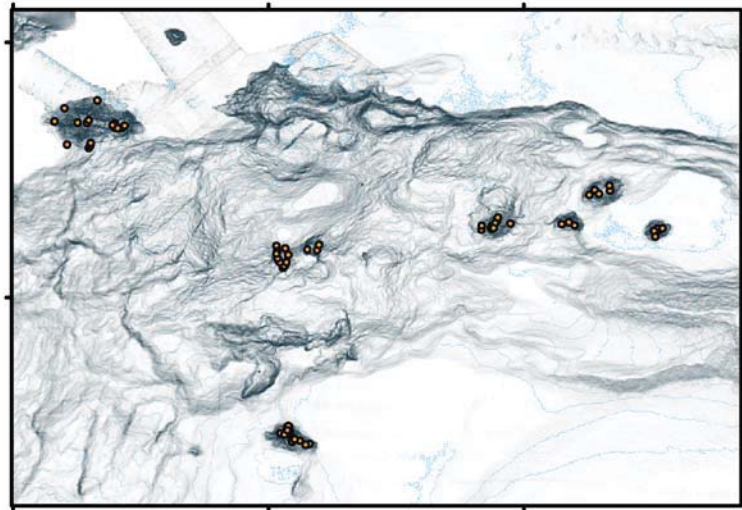
-5100-5200
-5200-5300
-5300-5400
-5400-5500
-5500-5600
-5600-5700





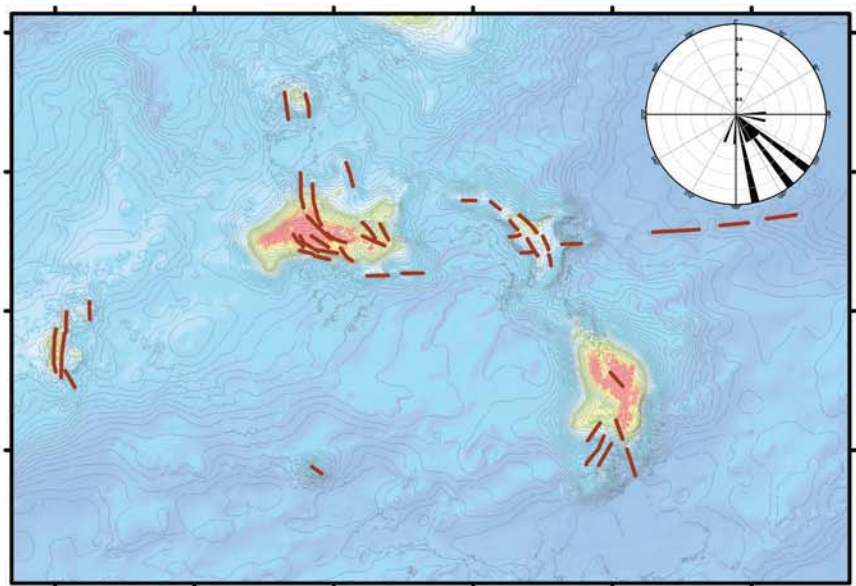
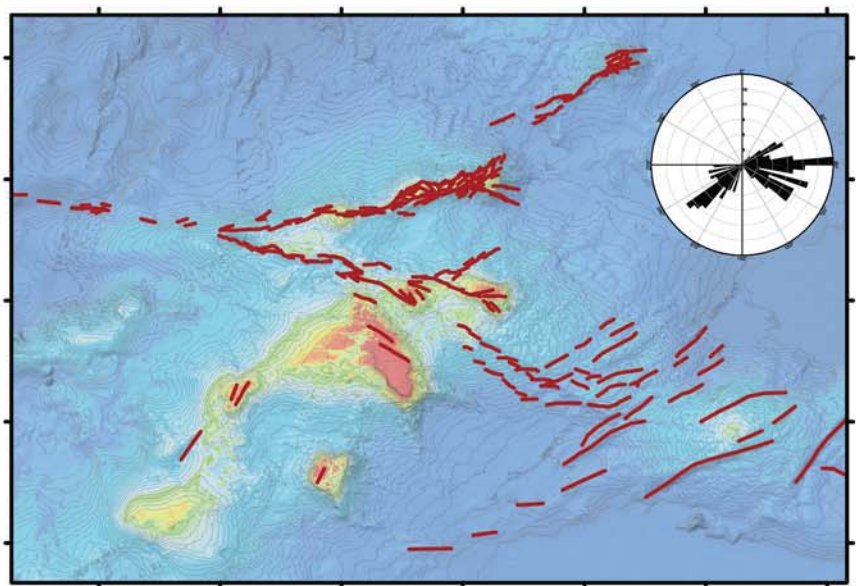
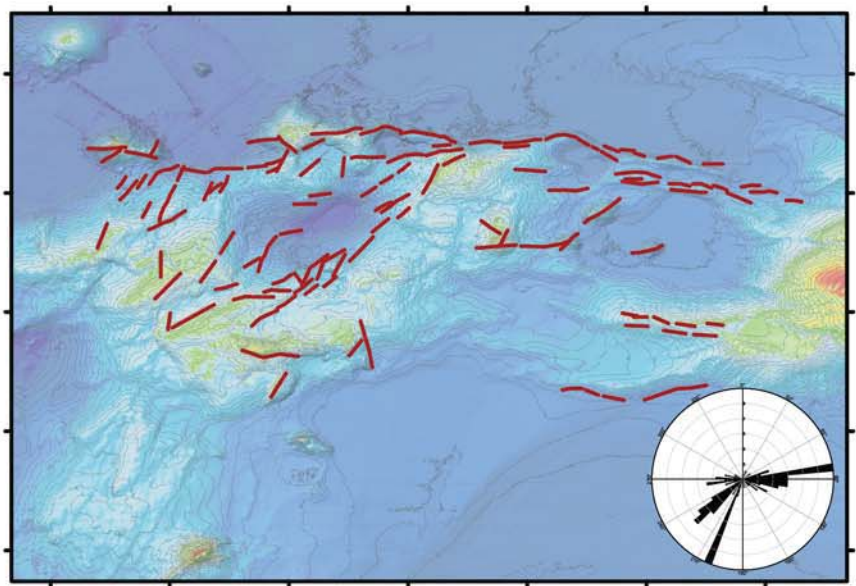


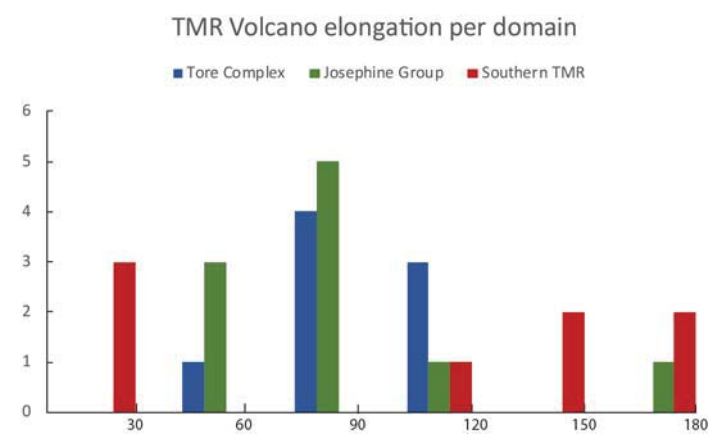
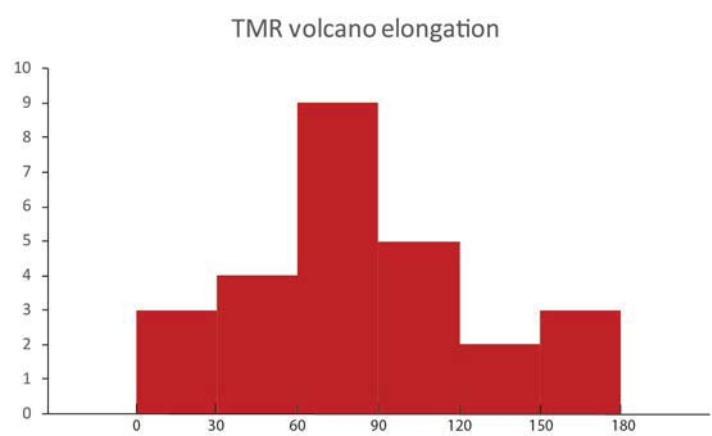


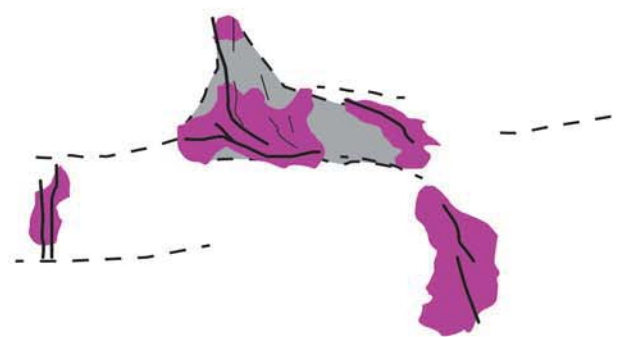
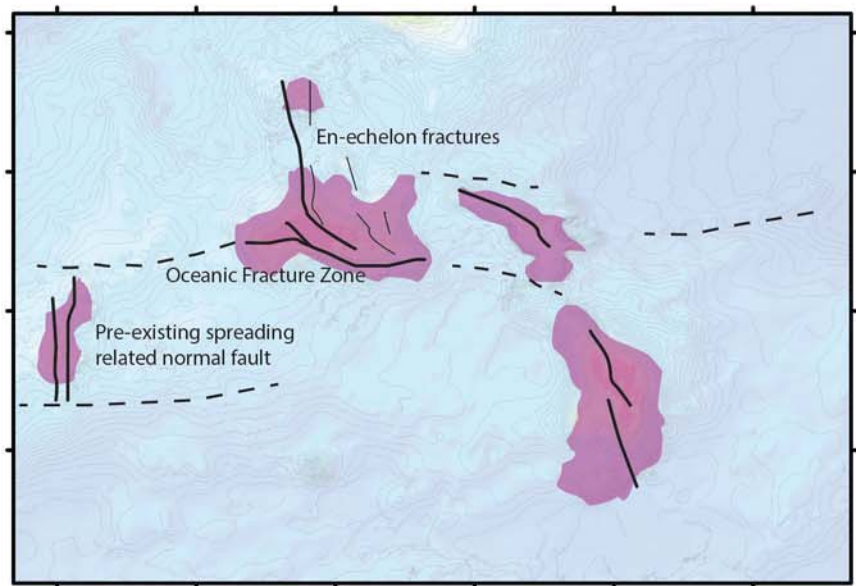
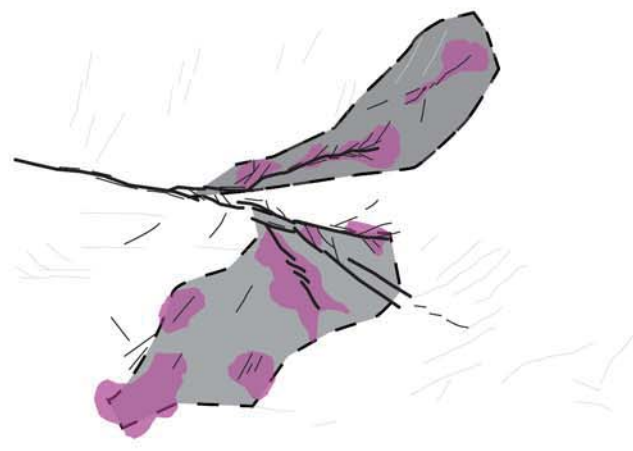
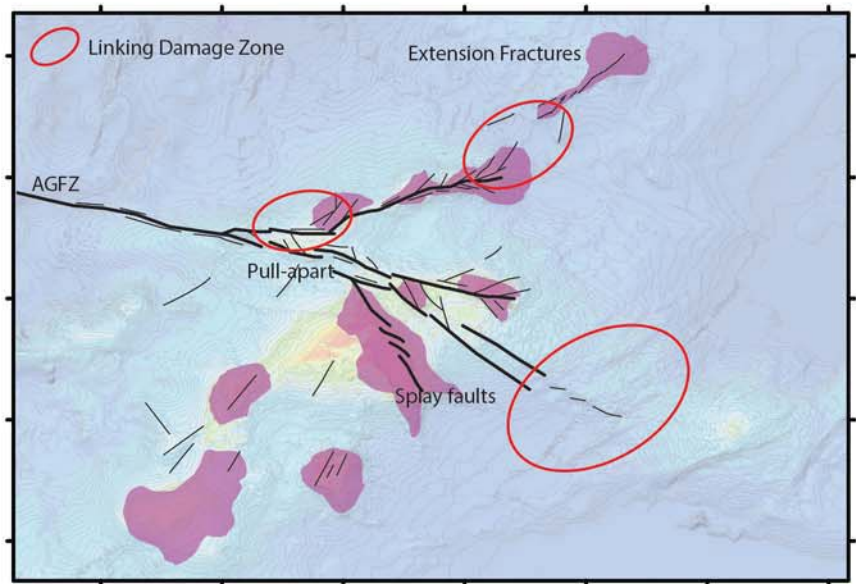
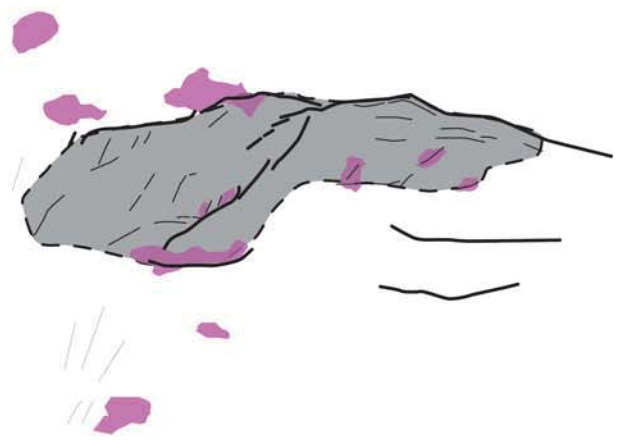
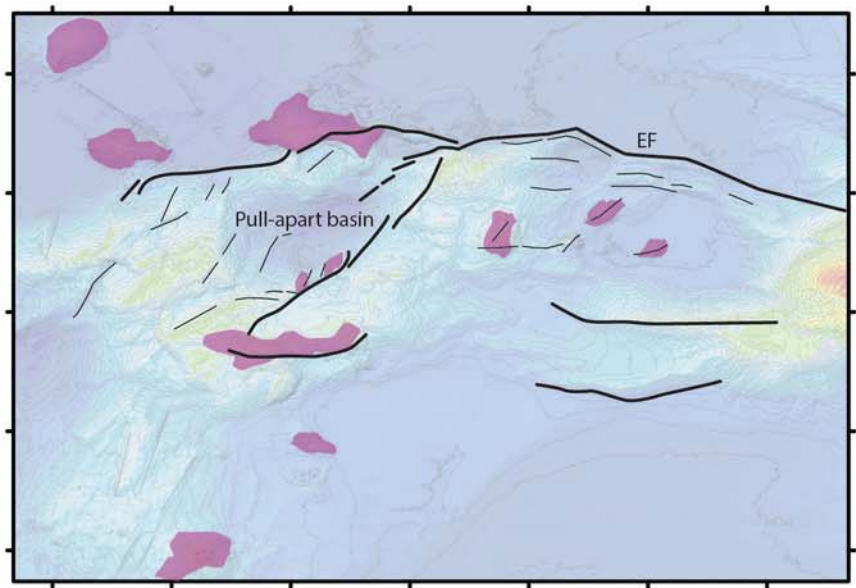


Vents

Eruptive fissures







Review paper

Geochronology of the Tore-Madeira Rise seamounts and surrounding areas: a review

R. Merle^{a,b,*}, F. Jourdan^{b,c}, and J. Girardeau^d

^a Research School of Earth Sciences, Australian National University, 142 Mills Road, Acton, ACT 0200, Australia; ^b School of Earth and Planetary Sciences, Curtin University, GPO Box U1987, Perth, WA 6845, Australia; ^c Western Australian Argon Isotope Facility & JdL Centre, Curtin University, GPO Box U1987, Perth, WA 6845, Australia; ^d Laboratoire de Planétologie et Géodynamique, UMR-CNRS 6112, Université de Nantes, 2 rue de la Houssinière, 44322 Nantes cedex 3, France.

*Corresponding author: r.merle@curtin.edu.au

Received 20 December 2017; accepted 12 April 2018

R.Merle: 0000-0001-9018-6862

F Jourdan: 0000-0001-5626-4521

Abstract

We present new $^{40}\text{Ar}/^{39}\text{Ar}$ data for two of the Tore Madeira Rise (TMR) volcanic seamounts. A sample from Tore East seamount on the northern part of the TMR yielded an ultra-precise age of 80.50 ± 0.13 Ma (2σ) that is similar within uncertainties to a published age obtained by U–Pb TIMS technique on titanites and zircons extracted from Tore NW seamount. Another sample from Isabelle seamount, located on the southern part of the TMR failed to produce a plateau age but yielded a minimum age estimate of > 85 Ma. We filtered the published ages available on the TMR, the surrounding seamounts and the massifs of southwest Portugal to better understand the origin of this magmatic province. Together with this dataset, our new data suggest that:

(1) An hypothetical Madeira hot-spot track spanning from Serra de Monchique on the continent to Madeira Archipelago is difficult to reconcile with the occurrence of several seamounts geographically located within or very close to this alleged hot-spot track yet being much older than the age predicted by the age trend.

(2) The geographical distribution and age pattern of the TMR and surrounding areas magmatism is still best explained by the interaction of a mantle melting anomaly emitting magma pulses and the different motion phases of the Iberia plate since 103 Ma.

Keywords: $^{40}\text{Ar}/^{39}\text{Ar}$ dating, Tore-Madeira Rise, seamounts, magmatism, Atlantic Ocean.

Introduction

The Tore-Madeira Rise (TMR) is a seamount chain, ~1000 km long by ~50 km wide, oriented NNE–SSW along the Atlantic coast of Portugal and Morocco (Figure 1). The estimated volume of TMR magmatic rocks ($\sim 10^5 \text{ km}^3$) is comparable to those of the other seamount groups and islands such as the Canary islands (Merle et al., 2009) that makes it one of the most significant features of the northern central Atlantic. In addition, it is located on a peculiar geodynamical setting: (1) it straddles without offset, the Azores-Gibraltar Fracture Zone (AGFZ), which is a dextral strike-slip fault representing a major lithospheric discontinuity since the Paleozoic, and the boundary between the Iberia and Africa plates since the Paleocene (Féraud, Bonnin, Olivet, Auzende, & Bougault, 1977; Jiménez-Munt, Fernández, Torne & Bird, 2001) and (2) the TMR partly overlaps the first magnetic anomaly created by the mid-Atlantic ridge (J anomaly, Figure 2). Therefore, the TMR is a key feature to understand the entire geodynamical evolution of the northern Atlantic Ocean since its birth. Nevertheless, until the last 15 years, the nature, the age and origin this magmatism were unknown, and thus models for the geodynamical process triggering the magmatism were highly speculative.

Since then, significant efforts have been underway to investigate the TMR magmatism and two oceanic campaigns in 2001 have dredged the flanks of the TMR seamounts. Geochronological analyses of the recovered rocks have shown that the TMR activity began at 105 Ma and lasted until the present (Geldmacher et al., 2006; Geldmacher, Hoernle, Klügel, Van der Bogaard, & Bindeman, 2008; Merle, Scharer, Girardeau, & Cornen, 2006; Merle et al., 2009). Two new, albeit different, models based on a series of isotopic geochemical analyses were proposed for the origin of the TMR (Geldmacher et al., 2006; Merle et al., 2009). Both studies proposed that the TMR magmatism might be attributed to a mantle plume (Geldmacher et al., 2006; Merle et al., 2006, 2009) but they differ in the role attributed to the mantle plume vs. plate processes. The first model involves two construction phases during the Cretaceous and late Cenozoic due to the successive activities of the Madeira then Canaries hot spots (Geldmacher et al., 2006). The second model proposes that the TMR magmatic activity and the surrounding areas, in particular, on SW Portugal could be distributed, geographically and timely, in three construction phases connected to the different motions of the Iberia plate during the Late Cretaceous and late Cenozoic (Merle et al., 2009). However, these two geodynamical models are based on a limited number of rocks and therefore, are hard to further evaluate.

In this contribution, we aimed to (1) provide an updated high-quality filtered age-data set of the TMR and surrounding areas (Merle et al., 2009) and (2) review and test the most recent geodynamical models proposed for the construction of the TMR. Specifically, we recalculated our 2009 filtered geochronological dataset using the recent revision of the ^{40}K decay constants proposed by Renne, Balco, Ludwig, Mundil and Min (2011) based on calibration against U–Pb ages, and critically assessed the most recently published ages (D’Oriano et al., 2010; Grange, Schärer, Merle, Girardeau, & Cornen, 2010; Miranda et al., 2009) using similar high-standard criteria as depicted by Merle et al. (2009).

In addition, we also included in the filtered database, two new $^{40}\text{Ar}/^{39}\text{Ar}$ measurements using an ARGUS VI multi collection mass spectrometer to assess the $^{40}\text{Ar}/^{39}\text{Ar}$ ages of two lavas dredged on the eastern flanks of the Tore and Isabelle seamounts. These two seamounts have been investigated in this study as they are key localities to understand the timing of formation of the TMR. In addition, the Tore seamounts are formed by a cluster of edifices that might have formed during several magmatic phases (Merle et al., 2006) but there are no solid time constraints on its construction. There are no ages for the volcanic rocks from the Isabelle seamount but knowing the age of this seamount is critical as it has been attributed to be one of the edifices of the Madeira hot spot track possibly formed around 30 Ma (D'Orario et al., 2010; Geldmacher, Van den Bogaard, Hoernle, & Schmincke, 2000).

This work aims to provide better constraints on the timing of the mechanisms and processes involved in the formation of the TMR.

Geological setting

The TMR is located on the western Iberia–Morocco margin formed during the Cretaceous by the drifting apart of the Iberia–North America plates (e.g., Boillot et al., 1980; Féraud, Girardeau, Beslier, & Boillot, 1988). The complex opening of the Atlantic ocean since at least 125 Ma led to complex movements of the Iberia plate, towards the northeast until approximately 80 Ma then toward the NNW until the Present (Figure 1b; Sibuet, Monti, Loubrieu, Mazé, & Srivastava, 2004a; Sibuet, Srivastava, & Spakman, 2004b; Zitellini et al., 2009). The dozen seamounts of the TMR form a $\sim 1000 \times \sim 50$ km seamount chain oriented NNE–SSW and stretching between the Tore complex, an elliptic (120×90 km), 5000 m deep depression rimmed by ~ 2500 m high seamounts and the Madeira Archipelago (Figure 1). The main alignment of seamounts is surrounded by scattered seamounts (Figure 2). From north to south this main trend is formed by: Tore, Sponge Bob, Ashton, Gago Coutinho (also been named Teresa by Geldmacher et al., 2006), Josephine, Jo Sister (also been named Erik by Geldmacher et al., 2006), Isabelle, Dragon and Godzilla (Figure 2). Most of these seamounts reach more than 3000 m above the seafloor (Figure 2).

The TMR straddles the Azores-Gibraltar Fracture Zone (AGFZ). This large dextral fault system, which is the main structural feature of the western Iberian margin, is a Mid-Atlantic Ridge transform fault constituting the limit between Eurasian and African plates (since 60–50 Ma; Féraud et al., 1977). Its eastern end seems to connect to three fault systems towards the Tore seamounts, Gorringe Bank, and Ampere-Coral Patch seamounts (Jiménez-Munt et al., 2001; Laughton, Roberts, & Graves, 1975; Figures 1 and 2). These three fault systems belong to the numerous crustal and lithospheric discontinuities on the western Iberian margin either inherited from the Hercynian basement, such as the Nazaré fault or formed since the Miocene due to the Europe–Africa convergence (Jiménez-Munt et al., 2001; Neves et al., 2009, 2016; Pereira, Tiago, Alves, & Mata, 2017; Zitellini et al., 2009). Many seamounts of the TMR and surrounding areas are located on lithospheric discontinuities (Figures 1 and 2) that were suspected to be preferential pathways for the magmas (D'Orario et al., 2010; Geldmacher et al., 2006; Merle et al., 2006, 2009). The AGFZ can also be seen as a marker to define three sections on the TMR: northern sector located north of the AGFZ (Tore to Ashton); central part located in the vicinity of the AGFZ (Gago Coutinho to Jo Sister) and southern sector located south of the AGFZ (Isabelle to Madeira archipelago).

According to the location of the western limit of the Ocean–Continent Transition (Figure 2) and the age of the magnetic anomalies identified on the Iberia–Morocco margin (J anomaly: 130–125 Ma, M22: 151 Ma; Gradstein, Ogg, & Smith, 2004), the TMR could be laying on an old oceanic lithosphere supporting the results of an early single geophysical investigation beneath the Josephine seamount (Pierce & Barton, 1991).

The TMR seamounts are built up by an OIB-type alkaline magmatism represented by lavas ranging in composition from basalt to trachyte (Geldmacher et al., 2006, 2008; Merle, Caroff, Girardeau, Cotton, & Guivel, 2005; Merle et al., 2006, 2009; Merle, Kaczmarec, Tronche, & Girardeau, 2012). The radiochronologic ages range from 103 Ma to the Present (Figure 2a; see review of the published ages in Merle et al., 2009 and in Table 1).

In the neighbouring area of the TMR (within <500 km; Figure 2a) and synchronous to its magmatic activity, alkaline magmatism occurs as scattered seamounts including Ormonde, which is the northeastern summit of the Gorringe bank (Figure 2a), Ampère-Coral Patch, Unicorn and Seine and as intrusions and massifs on southwest Portugal (Merle et al., 2009 and references included).

The geodynamic process leading to the construction of the TMR is still debated. Deep-rooted mantle plume possibly active coevally with mid-ocean ridge spreading (Bonner, Sauter, Manatschal, Péron-Pinvidic, & Munschy, 2011; Geldmacher et al., 2000, 2006; Merle et al., 2006, 2009; Pierce & Barton, 1991; Tucholke & Ludwig, 1982), early accretion off-axis magmatism (Jagoutz et al., 2007) or shallow mantle upwelling (Geldmacher et al., 2008) were considered as an origin for the TMR magmatic activity. These hypotheses present issues that are discussed in the light of the newly filtered age data set.

Geochronological overview

A filtered dataset of radiochronological ages from the TMR and the surrounding areas was published previously (Merle et al., 2009). In this work, we have updated the database by filtering and adding new upper Cretaceous ages published since then on the western-Iberian margin, concomitant to the TMR province (D’Oriano et al., 2010; Grange et al., 2010; Miranda et al., 2009), and updated the complete database for the new ^{40}K decay constant and latest standard calibration (Renne et al., 2011). As in our 2009 paper (Merle et al., 2009), the main aim was to provide a robust dataset in which all the data are statistically reliable and can be associated with crystallisation events rather than secondary processes (e.g., Verati & Jourdan, 2014). Therefore, the data have been screened on the basis of methodological and statistical criteria following the methodology described by Merle et al. (2009). Nevertheless, we outline here several criteria used for reviewing and filtering the dataset that can be used as guide lines for similar studies:

- 1) We have rejected ages that are not based on a concordia, age spectrum or isochron calculations as those ages are not statistically testable.
- 2) K–Ar and Rb–Sr ages on rocks suites (whole-rock isochrons) were rejected since they are likely biased by processes such as magma mixing and crustal contamination and alteration.
- 3) K–Ar ages on whole-rock or selected matrix or minerals were considered as potentially unreliable as the K–Ar method is unable to monitor post-emplacement alteration that is critical for rocks older than several million years (Verati & Jourdan, 2014).

4) The available U–Pb and $^{40}\text{Ar}/^{39}\text{Ar}$ ages were tested using statistical parameters of goodness of fit, Mean Squared Weighted Deviation (MSWD) and probability of fit (P), which must be equal or higher than 0.05 (the details concerning these parameters are given in e.g., Baksi, 2007; Jourdan, Renne, & Reimold, 2009 and references inside).

We have provided a list of semi-quantitative $^{40}\text{Ar}/^{39}\text{Ar}$ ages (e.g. >80 Ma) that suffered from obvious alteration effects but which could still be used to support robust ages or to rule out scenarios implying that the rock is much younger. Geochronological data for the newly investigated Tore East (robust age) and Isabelle (semi-quantitative age) seamounts have also been included in this compilation. The filtered dataset including the technique used and the type of material dated is shown in Table 1. All errors are given at the 2σ level in the following section. In this paper, we give significant uncertainties lower ± 0.5 Ma at two digits levels, at one digit level for uncertainties between 0.5 and 3.0 Ma and at the level of million years for uncertainties above ± 3 Ma (see Verati & Jourdan, 2014).

Geochronological data from the TMR seamounts

Full descriptions of the geochronological data of TMR are given in Merle et al. (2009). The evolved rocks collected from the northern TMR seamounts (Tore-Ashton section) were dated by isotopic dilution (ID) TIMS U–Pb method on titanite and zircon and step-heating $^{40}\text{Ar}/^{39}\text{Ar}$ technique on plagioclase and biotite (Merle et al., 2006, 2009). The ages range from 102.8 ± 0.7 Ma for Sponge Bob to 80.5 ± 0.9 Ma for Tore Northwest (Table 1; Figure 2).

Both evolved and basic rocks were collected on the central part of the TMR (Gago Coutinho to Jo Sister). The ages of the evolved rocks range from 95.8 ± 0.4 Ma to 86.5 ± 3.4 Ma using the ID TIMS U–Pb method on titanite and the step-heating $^{40}\text{Ar}/^{39}\text{Ar}$ technique on hornblende (Geldmacher et al., 2006; Merle et al., 2006). The ages of the basic rocks range from 16.3 ± 0.9 Ma to 0.5 ± 0.5 Ma using the $^{40}\text{Ar}/^{39}\text{Ar}$ method on glass and matrix (Geldmacher et al., 2006). Note that the Jo Sister seamount is the only location on the entire TMR and surrounding seamounts where both mafic and evolved samples were dated.

The southern TMR seamounts are located south of Jo Sister. So far, only basic rocks were collected in the southern section of TMR and their ages range from 68.4 ± 0.2 Ma to 1.1 ± 0.2 Ma using $^{40}\text{Ar}/^{39}\text{Ar}$ method on both matrix and biotite (Geldmacher et al., 2006, 2008). On Seine and Unicorn seamounts, the whole-rock and amphibole $^{40}\text{Ar}/^{39}\text{Ar}$ measurements yielded ages ranging from 22.2 ± 0.2 Ma and 24.6 ± 0.5 Ma on Seine and 28.1 ± 2.4 Ma on Unicorn (Geldmacher, Hoernle, Van den Bogaard, Duggen, & Werner, 2005; Merle et al., 2009).

The Madeira archipelago rocks were dated using the $^{40}\text{Ar}/^{39}\text{Ar}$ technique on whole rock and separated plagioclase crystals and the ages range from 14 Ma to the Present (Geldmacher et al., 2000 and references therein). The volcanic rocks from Porto Santo Island, located 45 km to the NE (Figures 1 and 2) have been dated by the same techniques and yielded ages ranging from 14 to 11 Ma while the age of Madeira Island is significantly younger with ages ranging from 5 Ma to the Present (Geldmacher et al., 2000) but could be as old as 7 Ma (Ramalho et al., 2015).

Cretaceous alkaline magmatism of Portugal

The petrography and petrology of these plutonic and intrusive rocks have been described in previous works (Grange et al., 2010; Miranda et al., 2009 and references included). The northernmost dated

intrusion is the Ribamar-Paco d'Ilhas dioritic monzogabbroic–monzonitic sill (Grange et al., 2010; Miranda et al., 2009). Only the age of 88.3 ± 0.5 Ma published by Grange et al. (2010) is retained after filtering.

A single attempt to date the Lisbon volcanic complex has been made by whole-rock K–Ar method leading to an apparent age of *ca* 73 Ma (Ferreira & Macedo, 1979). This age has questionable significance considering the limitations of the whole-rock K–Ar-dating method on rocks older than several million years (e.g. Jourdan & Verati, 2014). In addition, a recent paleomagnetic study on several intrusions in this area suggests that the Lisbon volcanic complex might be older (Neres et al., 2012).

No reliable ages were available for the Sintra massif until the recent study of Miranda et al. (2009), which gave an age of 79.3 ± 0.6 Ma (obtained by LA-ICP-MS U–Pb method on zircon from a granite). This age is similar within errors to the youngest ages from a series of analyses ranging from 80.1 ± 0.6 Ma to 83.4 ± 0.7 Ma obtained by ID-TIMS on zircon extracted for basic and differentiated lithologies (Grange et al., 2010).

The Foz da Fonte intrusion has been recently dated by $^{40}\text{Ar}/^{39}\text{Ar}$ step-heating method on amphibole separates from a tephritic sill (Miranda et al., 2009). The weighted mean plateau yielded an age at 95 ± 5 Ma. However, this age has been obtained using the LP-6 standard that has been shown to include two age populations and therefore cannot be compared to well-calibrated fluence monitors (Jourdan & Renne, 2007) used for the $^{40}\text{Ar}/^{39}\text{Ar}$ studies of TMR (Geldmacher et al., 2006; Merle et al., 2009; this study). Nevertheless, since the sample yielded a plateau age, thereby providing a qualitative estimate on the intrusion age, and as the resulting $^{40}\text{Ar}/^{39}\text{Ar}$ is associated with very large analytical uncertainties of ± 5 Ma in any case, this age is taken under (limited) consideration.

An alkali gabbro from the Sines complex yielded an ID-TIMS U–Pb zircon age of 77.2 ± 0.6 Ma (Grange et al., 2010), which is slightly older than the U–Pb age of 75.3 ± 0.5 Ma obtained by LA-ICP-MS from zircons extracted from a syenite (Miranda et al., 2009).

The main nepheline syenite body of the Monchique complex was dated at 68.5 ± 0.6 Ma by ID-TIMS on titanite (Grange et al., 2010). An ultramafic lamprophyre yielded a significantly older age of 76 ± 3 Ma obtained by $^{40}\text{Ar}/^{39}\text{Ar}$ dating of amphibole (Miranda et al., 2009). As for the Foz da Fonte sample, this age was obtained using the unreliable LP-6 fluence standard and thus must be considered with caution.

Sparse basaltic and lamprophyric dykes, between one to a few meters in width, occur in the Algarve region but represent significantly smaller magmatic volumes compared to the three main massifs. No reliable ages are available for this magmatism since the few attempts of dating were made using the K–Ar technique (Miranda et al., 2009).

Ampere, Coral Patch and Ormonde seamounts

Several attempts to date the rocks from Ormonde, Coral Patch and Ampere have been made on whole-rock and separated minerals using step-heating and total fusion $^{40}\text{Ar}/^{39}\text{Ar}$ techniques (D'Oriano et al., 2010; Féraud, Gastaud, Auzende, Olivet, & Cornen, 1982; Féraud et al., 1986; Geldmacher et al., 2000). The last attempt by D'Oriano et al. (2010) on biotite from Ormonde and Coral Patch samples fails to produce $^{40}\text{Ar}/^{39}\text{Ar}$ mini-plateau with more than 50% of ^{39}Ar released and is not considered as valid (Baksi, 1999; McDougall & Harrison, 1999). As a consequence, the only

reliable age for Ampere seamount is 32.0 ± 0.2 Ma (Geldmacher et al., 2000) and the age range for Ormonde seamount is 62–66 Ma (Féraud et al., 1982, 1986).

Samples and methodology

Studied samples

The studied samples were dredged during the Tore-Madeira cruise of the R/V *Atalante* in 2001. Two samples were selected from the Tore East seamount (sample TMD9-1) in the Tore complex and on the Isabelle seamount (sample TMD19-3) on the southern part of the TMR yet not belonging to the main alignment (Figure 2). Tore East is the easternmost of the main TMR trend (Figure 1b) and Isabelle is located along a branch of the AGFZ where both Late Cretaceous and Oligocene volcanism are present. Sample TMD9-1 (dredge coordinates: $39^{\circ}16.28' - 39^{\circ}16.97'$, $12^{\circ}09.33' - 12^{\circ}08.50'$; dredging depth: 3390–2830 m, Figure 2b) is a dark grey trachyandesite with high vesicularity containing phenocrystals of brown amphibole (2–5% modal), clinopyroxene (2–5% modal), rounded plagioclase due to partial dissolution (1% modal) and Fe–Ti oxide microphenocrystals. The rock shows evidence of alteration with carbonates and zeolites filling cracks and vesicles and clay minerals replacing the groundmass. Contrary to plagioclase, amphibole is, however, devoid of any alteration and fresh crystals were selected for $^{40}\text{Ar}/^{39}\text{Ar}$ dating. Sample TMD19-3 (dredge coordinates: $35^{\circ}16.52' - 35^{\circ}16.76'$, $14^{\circ}52.07' - 14^{\circ}49.94'$; dredging depth: 2478–1919 m) is a porphyric dark alkali basalt slightly vesicular and containing skeletal olivines (10% modal) and rare euhedral clinopyroxenes. The groundmass contains prismatic clinopyroxenes, euhedral Fe–Ti oxides, olivines and plagioclase microliths. The alteration is limited to iddingsitization of olivine and the few cracks and vesicles filled by clay minerals and carbonates. The plagioclase microliths are unaltered and were selected for $^{40}\text{Ar}/^{39}\text{Ar}$ dating.

Methodology

Plagioclases and amphiboles were separated from either the 150–215 μm or the 215–315 μm fractions using a Frantz isodynamic magnetic separator and were hand-picked grain-by-grain under the binocular stereomicroscope. Plagioclase and amphibole were further leached using diluted HF (2N) for 5 minutes and thoroughly rinsed in distilled water and loaded in two separated discs, along with unrelated samples. The disc containing the hornblende samples was irradiated for 40 hours and included a series of fully inter-calibrated biotite GA1550 (Renne et al., 1998) and muscovite WA1ms (Jourdan, Frew, Joly, Mayers, & Evans, 2014) standards, for which ages of 99.74 Ma ($\pm 0.10\%$; (Renne et al., 2011) and 2613 Ma ($\pm 0.09\%$; Jourdan et al., 2014) were used. The plagioclase sample was irradiated for 3 hours alongside FCs standards (Jourdan & Renne, 2007), for which an age of 28.294 Ma ($\pm 0.13\%$) was used (Renne et al., 2011). The discs were Cd-shielded (to minimise undesirable nuclear interference reactions) and irradiated in the Oregon State university nuclear reactor (USA) in central position. The mean J-values computed from standard grains within the small pits yielded values of 0.000854 ($\pm 0.10\%$) and 0.0111724 ($\pm 0.035\%$) for the plagioclase and hornblende samples, respectively. Mass discrimination was monitored regularly through the analysis using an automated air pipette and provided mean values of 0.99571 ($\pm 0.02\%$) and 0.99493 ($\pm 0.03\%$) per dalton (atomic mass unit) relative to an air ratio of 298.56 ± 0.31 (Lee et al., 2006). The correction factors for interfering isotopes were $(^{39}\text{Ar}/^{37}\text{Ar})_{\text{Ca}} = 7.6 \times 10^{-4}$ ($\pm 1.2\%$), $(^{36}\text{Ar}/^{37}\text{Ar})_{\text{Ca}} = 2.7 \times 10^{-4}$ ($\pm 0.7\%$) and $(^{40}\text{Ar}/^{39}\text{Ar})_{\text{K}} = 7.3 \times 10^{-4}$ ($\pm 10\%$). The $^{40}\text{Ar}/^{39}\text{Ar}$ analyses were performed at the Western Australian Argon Isotope Facility at Curtin University. Two plagioclase and hornblende crystal populations (5 mg

each) were step-heated using a continuous 100 W PhotonMachine© CO₂ (IR, 10.4 μm) laser fired on the crystals during 60 seconds. Each of the standard crystals was fused in a single step.

The gas was purified in an extra low-volume stainless steel extraction line of 240 cc and using one SAES AP10 and one GP50 getter. Ar isotopes were measured in static mode using a low volume (600 cc) ARGUS VI mass spectrometer from ThermoFisher© (Phillips & Matchan, 2013) set with a permanent resolution of ~200. Measurements were carried out in multi-collection mode using four faradays to measure mass 40 to 37 and a 0-background compact discrete dynode ion counter to measure mass 36. We measured the relative abundance of each mass simultaneously using 10 cycles of peak-hopping and 33 seconds of integration time for each mass. Detectors were calibrated to each other electronically and using air shot beam signals. The raw data were processed using the ArArCALC software (Koppers, 2002) and the ages have been calculated using the decay constants recommended by Renne et al. (2011). Blanks were monitored every 3 to 4 steps. All parameters and relative abundance values are provided in the Supplementary Papers (Appendix 1) and have been corrected for blank, mass discrimination and radioactive decay; individual errors are given at the 1σ level.

Our criteria for the determination of plateau are as follows: plateaus must include at least 70% of ³⁹Ar. The plateau should be distributed over a minimum of 3 consecutive steps agreeing at 95% confidence level and satisfying a probability of fit (P) of at least 0.05. Plateau ages are given at the 2σ level and are calculated using the mean of all the plateau steps, each weighted by the inverse variance of their individual analytical error. Uncertainties include analytical and J-value errors. Errors with all sources of uncertainties are indicated by a square bracket (e.g. [± 0.16 Ma]).

Results

A summary of the ⁴⁰Ar/³⁹Ar measurements data are presented in Table 2. The amphibole fractions extracted from sample TMD9-1 (Tore East) yielded a well-defined plateau age of 80.50 ± 0.13 Ma (MSWD = 0.86; P = 0.59), which include 88% of the total ³⁹Ar released (Figure 3). The K/Ca ratio is fairly homogenous with a value of 0.08 observed over more than 78% of the total ³⁹Ar released, and decrease to lower value of 0.02 in the high temperature steps, probably due to some Ca enrichment in the core of the amphibole crystals. The change in K/Ca ratio is not mimicked by the age spectrum. Including error on the decay constant following the Monte Carlo calculation approach of Renne, Mundil, Balco, Min and Ludwig (2010), yields a full uncertainty of [± 0.16 Ma], which is relevant only when comparing with U–Pb age data.

The plagioclase fraction from TMD 19-3 (Isabelle seamount) failed to yield any plateau age. The K/Ca spectrum is highly variable and show K/Ca values ranging from ~0.2 to 0.8 (Ca/K ~1.2 to 5), which likely indicates some contribution from sericite alteration not eliminated during picking (e.g., Verati & Jourdan, 2014). As a consequence, this age is most likely a minimum age. Although this sample did not give a firm age, it still provides qualitative constraints and suggests a minimum eruption age estimate of >85 Ma (Figure 3).

It should be noted that in this study, we improved the analytical precision for K-poor minerals from volcanic rocks with ages of *ca* 80 Ma, where we obtained a precision of ± 0.16 % [± 0.20% including all sources of uncertainties] on amphibole (K₂O ~1 wt% on the presently analysed phase). This is an increase of ~3 times compared to the most precise results previously obtained on other hornblende

phases ($\pm 0.43\%$; Geldmacher et al., 2006; see Supplementary Papers, Figure A2). A detailed discussion of the consequences of technical improvements on precision is given in the Supplementary Papers (Appendix 1).

Discussion

The construction of the Tore seamounts

So far, there is no satisfying model for the construction of the Tore complex and the timing of its magmatic activity. Considering its elliptic shape with a rim of ~ 2500 m high reliefs (some of them with a clear volcanic morphology) surrounding a $\sim 120 \times 90$ km depression, it is possible to consider the Tore complex as a large volcanic complex with a caldera. Calderas with similar dimensions or larger associated with complex volcanic edifices are not uncommon on Earth (e.g. Cole, Milner, & Spinks, 2005). Multiple episodes of caldera formation associated with the emission of evolved rocks (rhyolites, trachytes and phonolites) are widely documented on intraplate volcanoes during their life span. These episodes are usually separated by less than few million years (e.g. La Reunion Island; Deniel, Kieffer, & Lecointre, 1992). From the scarce geochronological constraints from the Tore seamounts, the dated evolved rocks (trachytes and trachyandesites) are related to two distinct magmatic phases occurring at approximately 88 and 80 Ma (Merle et al., 2006). Our new high-precision age of the Tore East seamount at 80.5 ± 0.1 Ma is similar within uncertainties to the age of 80.5 ± 0.9 Ma, using the TIMS U–Pb technique on the Tore NW seamount (Merle et al., 2006), suggesting a major phase of construction of Tore complex around 80 Ma. However, the age of 88 ± 3 Ma obtained by U–Pb TIMS on titanite (Merle et al., 2006) from the Tore N seamount is significantly older. It would imply a period of at least 8 Ma between two episodes of caldera formation but no pyroclastic rocks such as hyaloclastites or ignimbrites, which are typically associated with caldera formation events, have been identified on the TMR and on the Tore seamounts area. Although the hypothesis of caldera formation cannot be entirely properly tested due to the lack of geochronological data, it should be noted that such a long time gap has never been documented on a volcanic complex, making the caldera hypothesis suspicious, although not impossible.

An alternative model could involve the local lithospheric discontinuities (Figure 2), which have been proposed to be preferential pathways for the magmas (D’Oriano et al., 2010; Geldmacher et al., 2006; Merle et al., 2006, 2009). Indeed, the Tore seamounts are located on the western extension of the Nazare fault system (Figures 1 and 2). During the period of magmatic activity on the Tore complex (88–80 Ma), this region of the Iberian margin was dominantly under an extension regime (Sibuet et al., 2004b). The initially E–W strike-slip motion along the AGFZ could have changed to transtensional leading to the opening of small pull-apart basins of the order of several kilometres. This could facilitate the path of the magmas toward the surface.

A variant of this hypothesis involves a 350 km-long dyke-like feature stretching from the Foz da Fonte sill to the Tore seamount and emplaced along the fault systems on the Estremadura Spur (Neres et al., 2014). In this view, the Tore complex would be the westernmost end of a so-called “Tore-Sintra tecton-magmatic lineament” which includes several magmatic intrusions and seamounts identified on the Estremadura Spur and South of Sintra massif (Neres et al., 2014). Considering the present knowledge, this hypothesis cannot be ruled out but more reliable geochronological constraints are required on these magmatic occurrences in particular, the Foz da Fonte sill, to confirm or reject this hypothesis.

Testing the geodynamic models of the TMR and surrounding areas

Our new filtered and updated geochronological dataset provide new insight on the origin of the TMR and the time frame of its construction. Specifically, it allows us to test the models proposed for the origin of the TMR and surrounding area magmatism. In the following section, we discuss the different geodynamic processes that could have generated the TMR magmatism.

An early hypothesis about the origin of TMR suggests that TMR was the first oceanic crust formed by the Mid-Atlantic Ridge (Olivet, 1996; Tucholke & Ludwig, 1982). This hypothesis is based on the geophysical data suggesting that TMR in the vicinity of Josephine was formed on or near the Mid-Atlantic Ridge (Pierce & Barton, 1991) and the symmetry between the TMR and the J-anomaly ridge on the Newfoundland margin. In this model, both ridges formed as a single ridge during a huge and sudden episode of magmatism following immediately the break-up of the continental lithosphere where magmas from asthenospheric melting were released (Girardeau et al., 1998; Olivet, 1996). This initial ridge would have been split into two parallel aseismic ridges by the spreading of the Mid-Atlantic Ridge. In this view, the initial ridge would have been covered by a later magmatic event (Girardeau et al., 1998). However, this hypothesis presents two main issues: (1) the bathymetric data on the TMR show no evidence of an early basement of the volcanoes but that most of the volcanoes have volcano-like morphologies lying on the seafloor (Merle, 2006), and (2) there are no ages for the J-anomaly ridge sustaining a coeval formation these reliefs. In addition, the magmatism of the TMR has an alkaline affinity, enriched incompatible elements patterns and Sr–Nd–Pb isotope ratios rather typical of Island Ocean Basalts (Geldmacher et al., 2006; Merle et al., 2006, 2009) that is difficult to reconcile with the tholeiitic magmatism that commonly occurs at the axis of mid-ocean ridges.

Another mid-ocean ridge-related hypothesis is an accretion-related off-axis magmatic activity around 112 Ma that could have produced alkaline magmatism predating the final onset of MORB-like oceanic lithosphere formation after 112 Ma (Jagoutz et al., 2007). So far, the oldest TMR magmatic activity at 103 Ma postdates the postulated initial spreading of the Mid-Atlantic Ridge by more than 10 Ma (Merle et al., 2009). It is not impossible that the first magmatic rocks related to TMR could be older than 103 Ma assuming that the dredged rocks are possibly the most recent lavas. However, considering the sample set and the available geochronological data, it is impossible to establish a realistic stratigraphy of the volcanic activity. Therefore, there is no definitive evidence for the hypothesis of an off-axis accretion-related origin for TMR.

It should be noted that the timing of the initiation of the seafloor spreading is still debated and could have spanned from 112 Ma until 84 Ma (Bonner et al., 2011) implying a coeval magmatic activity of the TMR and the mid-Atlantic ridge as already suspected from the geochronological studies on the TMR rocks (Geldmacher et al., 2006; Merle et al., 2006). In such hypothesis, the oceanic spreading of the mid-Atlantic ridge could have been initiated or helped by a mantle plume hence those that could have generated the TMR magmas. This model for the origin of TMR is rather related to a classic mantle plume–mid-ocean-ridge interaction (Geldmacher et al., 2006; Pierce & Barton 1991) but the details of such an interaction are debated. In addition, the architecture of the Iberian margin revealed by the seismic data and drilling results suggest that oceanic spreading seems to have propagated northward (Tucholke, Sawyer, & Sibuet, 2007). The interaction with a fixed mantle plume should have resulted in a S–N age decreasing age trend that is in contradiction with a southward age decreasing trend observed from Sponge Bob to Jo Sister seamounts between 103 and 88 Ma (Merle et al., 2009).

Hereafter, we will discuss several variants of the mantle plume model, and in particular concerning the nature of the mantle plume.

A possible hypothesis for the origin of the TMR is a shallow mantle melting anomaly due to the presence of EMI-type metasomatised sub-continental lithospheric mantle (SCLM) in the asthenosphere (Geldmacher et al., 2008). A possible contribution of the SCLM of the Iberian margin in the chemical characteristics of the differentiated TMR lavas has been suggested (Merle et al., 2006) but this SCLM signature is clearly different from those of the EMI-type mantle end-member identified by Geldmacher et al. (2008). As this EMI component has been only documented on the 68 Ma-old Godzilla seamount (Geldmacher et al., 2008), this suggests rather a small chemical anomaly. In any case, the signature of the EMI mantle end-member is still poorly defined therefore its chemical characteristics cannot be considered as a proof for a deep or shallow mantle plume.

A similar model has been proposed to explain the Cretaceous to Eocene magmatism of the Christmas Island Seamount Province (CHRISP, Eastern Indian Ocean) but this model was directly connected to the activity of a mid-ocean ridge as a heat source (Hoernle et al., 2011). In the case of the TMR, the mid-Atlantic ridge could well trigger the melting of the ambient asthenosphere containing sections of EMI-type SCLM hence produce the Late Cretaceous magmatism but this model fails to explain the more recent magmatic activities. As a consequence, the model involving a shallow mantle melting anomaly triggered by the presence of a EMI-type component in the ambient asthenosphere as for the origin of the TMR magmatism presents the main issue of the lack of a heat source able to sustain the magmatism since 103 Ma.

The bending and uplift of the Atlantic oceanic lithosphere due to an eastward subduction located beneath the Gibraltar arc (Duarte et al., 2013; Gutscher et al., 2002) could trigger a forearc magmatism that could explain the >30 Ma volcanic activity on TMR. The bending and lifting of the lithosphere could create low-degree decompression melting in the asthenosphere and the faulting in the lithosphere could facilitate the migration of the generated melts toward the surface. Such a model has been suggested for volcanic provinces located on the back of subducted plates (Petit Spot seamounts, Hirano et al., 2006; Pliocene magmatism of Christmas Island, Hoernle et al., 2011). However, the presence of the eastward subduction beneath the Gibraltar arc has been highly criticised (Marques, 2014) and is in contradiction with the widely accepted N–S subduction of the neo-Thetis during the Pyrenees orogenesis (Sibuet et al., 2004b). In addition, the volume of magmatism on the Petit spot seamounts is significantly smaller than those of the TMR suggesting a small-scale melting anomaly. Therefore, in the present state of knowledge, a subduction-related melting anomaly as a the origin for the >30 Ma magmatism on TMR is very speculative.

The most conservative models involve deep-rooted mantle plumes. Two sub-types of models have been suggested. The first model involves a classic, Hawaiian-like fixed mantle plume located beneath the rotating Iberia plate. In this model, the Madeira hot-spot track imprints its path through the Iberia plate from Serra de Monchique (76–68 Ma) to Madeira (active) through Ormonde (66–62 Ma), Ampere (32 Ma), Unicorn (28 Ma), and Seine (22–25 Ma) then displaying a NE–SW age trend (D’Oriano et al., 2010; Geldmacher et al., 2000). Assuming a 450 km-wide hot-spot track, the TMR could have been formed by the Madeira mantle plume (Geldmacher, Hoernle, Van der Bogaard, Zankl, & Garbe-Schönberg, 2001). A variant of this model involves the successive activities of Canary and Madeira hot-spots (Geldmacher et al., 2006). In this hypothesis, the TMR was built up by two magmatic phases, the first one during Cretaceous times (>95–80 Ma), forming the basement of the

rise and related to the Canary hot-spot (Gelmacher et al., 2006). The second magmatic activity, which capped the Cretaceous volcanic basement, is represented by mid-Miocene to Pleistocene (16–0.5 Ma) volcanic rocks (Gelmacher et al., 2006). These rocks were related to: (1) decompression melting along extensional lithospheric fractures on the central part of the TMR in the Josephine area (the northern end for Geldmacher et al., 2006), and (2) to the Madeira hot-spot at the southern end and represented by a magmatism younger than 5 Ma occurring on Dragon and Jo Sister (Geldmacher et al., 2006). The activity of the Madeira hot-spot is believed to form the NE–SW trend spanning from Monchique to Madeira as expressed in the previous model. However, these models present some issues. In particular, they fail to explain the Upper Cretaceous onshore magmatic activity both on the north of the AGFZ and on the southwestern Portugal, north of Serra de Monchique complex (Figure 2). Furthermore, if we assume that the Madeira hot spot location were fixed through time, then the proposed Madeira hot-spot track is in contradiction with the NNW motion of Iberia and Africa plates since 80 Ma (e.g. Sibuet et al., 2004a, 2004b; Zitellini et al., 2009).

Despite these limitations, these models could be still valid south of the AGFZ. Indeed, Isabelle seamount is located less than 200 km from the Ampere (32 Ma)-Coral Patch, Unicorn (28 Ma) and Seine (25–22 Ma) seamounts (Figures 2 and 5). The formation of Isabelle seamount could be related to the postulated path of the Madeira hot-spot considering its close geographical proximity with these seamounts and that this hot-spot track would be between 200 and 450 km wide (Figure 4a; Geldmacher et al., 2000, 2001, 2005, 2006). According to its location related to Madeira and the postulated age progression, the expected age of Isabelle seamount should be between 32 and 22 Ma (Figure 4). However, our new minimum age estimate of approximately > 85 Ma implies that the age of Isabelle seamount does not fit in this trend (Figure 4). Similarly, the 68 Ma-old Godzilla seamount (Geldmacher et al., 2008) is also located within less than 150 km from Seine, Unicorn and Isabelle seamounts then potentially located within the hot-spot track yet its age does not fit with the expected age in this section of the trend (Figure 4). The occurrence of the Cretaceous Isabelle and Godzilla seamounts in the putative Cenozoic-only section of the postulated path of the Madeira hot-spot is difficult to reconcile with a unique hot-spot imprinting the Iberia plate and forming the NE–SW Monchique-Madeira age trend as proposed by Geldmacher et al. (2000) and D’Oriano et al. (2010).

The alternative model, suggested by Geldmacher et al. (2006) involving the imprint of the Canary hot-spot during the Cretaceous (>95–80 Ma) later capped by a Late Cenozoic volcanic (16–0.5 Ma) phase due to both decompression melting and the Madeira hot-spot activity, presents some issues south of the AGFZ. In this scenario, the entire Late Cretaceous magmatism on TMR was evolved in affinity and corresponds to the latest stage of the magmatic evolution of the volcanoes (Geldmacher et al., 2006). This hypothesis was based on a sample set representative from the central and southern TMR only and formed with a majority of basaltic rocks of Cenozoic age and few evolved rocks from the central part of the TMR (Geldmacher et al., 2006). The lava collected on the Isabelle seamount (*ca* 85 Ma) is, so far, the oldest basaltic rock sampled south of the AGFZ. This suggests that both basaltic and evolved lavas erupted on a large sector of the TMR straddling the AGFZ (Figures 2 and 6). As evolved alkaline rocks (phonolites and trachytes) are commonly associated with the end of a differentiation cycle in a magma chamber then possibly a waning magmatic phase, they can postdate the eruption of co-magmatic basaltic rocks. Therefore a basaltic magmatic activity older than 103 Ma cannot be ruled out.

When the magmatic activity on all the TMR and surrounding seamounts is considered three magmatic phases are recorded occurring at 103–80 Ma, 68–62 Ma and 32–0.5 Ma (Figures 2 and 6) shown by Merle et al. (2009). Regarding the spatial distribution of this last phase on the main alignment of TMR, the magmatic activity started at 16 Ma in the Josephine area (central TMR) close to the AGFZ, validating the hypothesis of magmatic production due to decompression melting in this area (Geldmacher et al., 2006). However, magmatic activity occurred at 4 Ma on Jo Sister and Dragon seamounts (central and southern TMR), while the hot-spot location was already further south beneath the position of the Madeira archipelago since 11 Ma as represented by the magmatism on Porto Santo (Figure 4). As Jo Sister and Dragon seamounts are located away from the alleged Madeira hot-spot track (Figure 2), the young (>5 Ma) magmatism on these seamounts is difficult to associate with the Madeira hot-spot unless considering a distal-off track manifestation of this mantle plume. Such a process is possible but its origin and modalities have not been discussed so far.

It is important to note that both Cretaceous and Cenozoic magmatic activities have been recorded together only on the Jo Sister seamount (Figures 2a and 6; Geldmacher et al., 2006; Merle et al., 2006). However, the Cenozoic age was obtained by performing $^{40}\text{Ar}/^{39}\text{Ar}$ dating on the matrix of a dredged sample (Geldmacher et al., 2006). Such an approach leads us to question the reliability of this age, as even $^{40}\text{Ar}/^{39}\text{Ar}$ ages obtained on relatively well-preserved groundmass from relatively old (few tens of Ma) continental basalts have been shown to be substantially inaccurate when compared to the much more reliable mineral separate ages (see discussions in Hofmann, Féraud, & Courtillot, 2000; Jourdan, Féraud, Bertrand, Watkeys, & Renne, 2007; Merle et al., 2009). As such, the Cenozoic $^{40}\text{Ar}/^{39}\text{Ar}$ age could in fact represent the age of a hydrothermal alteration event (Verati & Jourdan, 2014). This observation cripples the hypothesis of two successive magmatic phases related to the Canary and Madeira hot-spots as suggested by Geldmacher et al. (2006). However, as already stressed, the magmatic stratigraphy of the TMR seamounts is known only through dredged samples with two periods of volcanism occurring on the different seamounts cannot be ruled out. Proper sampling through drilling is required to investigate in details the construction phases of the TMR seamounts.

As a summary, the hypotheses involving the Madeira hot-spot track or the combination of the Canary and Madeira hot-spot tracks as an origin for the TMR south of the AGFZ (D’Oriano et al., 2010; Geldmacher et al., 2000, 2006) are not satisfactory to explain the age distribution of the seamounts.

Alternatively, the study published by Merle et al. (2009), based on a stringent filtering of all the published geochronological data, argues for five magmatic phases encompassing the TMR and the neighbouring seamounts and SW Portugal, all forming a single magmatic province. This model is based on the observation of a NE–SW decreasing-age trends on TMR between 103 and 88 Ma (Merle et al., 2006) and a NNW–SSE decreasing-age trend in SW Portugal between 80 and 70 Ma (Grange et al., 2010). This later age trend has been initially interpreted as a hot-spot track yet it was not mentioned whether this mantle plume was related to Madeira hot-spot (Grange et al., 2010). These two decreasing age trends match the motions of the Iberia plate according to the geodynamics reconstructions proposed by Sibuet et al. (2004a, 2004b). Therefore, this Late Cretaceous magmatism could be due to a mantle melting anomaly, and emitting magma pulses for the last 103 Ma; the time–space occurrence of magmatism being determined by the different phases of the Pyrenees orogenesis controlling the motion of the Iberia plate (Merle et al., 2009).

In this model, the nature of the mantle-melting anomaly is not clearly defined. The magmatism in this part of the Atlantic, in particular for the Madeira archipelago, could be the result of mantle upwellings (mantle plumes) originated from a large (2500 km × 4000 km, and extending to depths in excess of 500 km) mantle low-velocity anomaly (Hoernle, Zhang, & Graham, 1995; Mata, Kerrich, MacRae, & Wu, 1998). However, in the present knowledge, it is not possible to assess without any doubt the nature of the mantle melting anomaly involved in the model of Merle et al. (2009). In the frame of this model and following previous hypotheses (Geldmacher et al., 2006; Merle et al., 2006; Miranda et al., 2009; Neres et al., 2014), the lithospheric discontinuities may have facilitated the magma ascent through the lithosphere.

Considering the Tore East seamount being distant of less than 200 km from Tore NW and Tore N seamounts (Figure 2) and its age (80.5 ± 0.1 Ma, this study), the volcanic activity recorded by the analysed sample from this seamount could be related to the 88–80 Ma phase of randomly-located magmatism in the TMR region and associated with a kinematic change in the Iberia plate motion (stage 2 of the geodynamical model of Merle et al., 2009). Despite the uncertainty of the data, the qualitative age estimate of >85 Ma from the Isabelle seamount could be also related to the same magmatic phase, or be in fact older by few Ma to few tens of Ma.

A possible limitation of this model is the Foz da Fonte intrusion (95 ± 5 Ma; Miranda et al., 2009) that does not fit the 88–68 Ma age trend (stages 2 and 3 of the model proposed by Merle et al., 2009) and would represent an early continental magmatic event (Figure 2). However, this age would be quite isolated compared to the 88–68 Ma semi-continuous magmatic activity observed on the western Iberian margin. In addition to the issue related to the use of the unreliable standard, the age of the Foz da Fonte intrusion overlaps within error with the age of Jo Sister seamount (89.3 ± 2.3 Ma; Merle et al., 2006). Considering its location, it is then plausible that the Foz da Fonte intrusion was emplaced during the same randomly-located phase as the Jo Sister seamount (stage 2: 88–80 Ma).

As a consequence, our data support the geodynamic model for the construction of the TMR proposed by Merle et al. (2009).

Conclusions

The new updated and reviewed age dataset suggests that: (1) a hypothetical Madeira hot-spot track spanning from the 76–68 Ma Serra de Monchique on the continent to Madeira through Ormonde (66–62 Ma), Ampere (32 Ma) and Seine (25–22 Ma) would fail to explain the occurrence of several seamounts geographically located within or very close to this hot-spot track yet being much older than the age predicted by the age trend; and (2) rather, the geographical distribution and age pattern of the TMR and surrounding areas magmatism is still best explained by involving five magmatic phases due to the interaction of a mantle melt anomaly emitting magma pulses and the different motion phases of the Iberia plate since 103 Ma.

Acknowledgements

We thank the captain and the crew of the R/V *Atalante*. For thin sections and technical assistance we thank E. Boeuf, B. De Quillac and H. Loyen. C. Mayers and A. Frew are thanked for their technical assistance in the $^{40}\text{Ar}/^{39}\text{Ar}$ laboratory. Drs Youbi and Mata are thanked for their constructive comments, which helped to improve the manuscript.

Funding

Supplementary papers

Appendix 1. Consequences of the new technical improvements

Appendix 2. Details of Ar analytical results.

References

- Baksi, A. K. (1999). Re-evaluation of plate motion models based on hotspot tracks in the Atlantic and Indian Oceans. *Journal of Geology*, 107, 13–26.
- Baksi, A. K. (2007). A quantitative tool for detecting alteration in undisturbed rocks and minerals—I: Water, chemical weathering, and atmospheric argon. Special Paper 430: Plates, Plumes and Planetary Processes, 285–303.
- Boillot, G., Grimaud, S., Mauffret, A., Mougenot, D., Kornprobst, J., Mergoil-Daniel, J., & Torrent, G. (1980). Ocean–continent boundary of the Iberian margin: a serpentinite diapir west of the Galicia Bank. *Earth Planetary Sciences Letters*, 48, 23–34.
- Bonner, A., Sauter, D., Manatschal, G., Péron-Pinvidic, G., & Munschy, M. (2011). Magmatic breakup as an explanation for magnetic anomalies at magma-poor rifted margins. *Nature Geosciences*, 4, 549–553.
- Cole, J. W., Milner, D. M., & Spinks, K. D. (2005). Calderas and caldera structures: A review. *Earth-Science Reviews*, 69, 1–26.
- Deniel, C., Kieffer, G., & Lecointre, J. (1992). New ^{230}Th – ^{238}U and ^{14}C age determinations from Piton des Neiges volcano, Reunion – A revised chronology for the differentiated series. *Journal of Volcanology and Geothermal Research*, 51, 253–267.
- D'Oriano, F., Angeletti, L., Capotondi, L., Laurenzi, M. A., López Correa, M., Taviani, M., Torelli, L., Trua, T., Vigliotti, L., & Zitellini, N. (2010). Coral Patch and Ormonde seamounts as a product of the Madeira hotspot, Eastern Atlantic Ocean. *Terra Nova*, 22, 494–500.
- Duarte, J. C., Rosas, F. M., Terrinha, P., Schellart, W. P., Boutelier, D., Gutscher, M. A., & Ribeiro, A. (2013). Are subduction zones invading the Atlantic? Evidence from the southwest Iberia margin. *Geology*, 41, 839–842.
- Féraud, G., Bonnin, J., Olivet, J. L., Auzende, J. M., & Bougault, H. (1977). Sur quelques datations du volcanisme alcalin de la ligne Açore-Gibraltar et leur contexte géodynamique. *Comptes Rendus Académie des Sciences Paris*, 285, 1203–1206.
- Féraud, G., Gastaud, J., Auzende, J. M., Olivet, J. L., & Cornen, G. (1982). $^{40}\text{Ar}/^{39}\text{Ar}$ ages for the alkaline volcanism and basement of Gorringe Bank, North Atlantic Ocean. *Earth and Planetary Sciences Letters*, 57, 211–226.

- Féraud, G., York, D., Mevel, C., Cornen, G., Hall, C. M., & Auzende, J. M. (1986). Additional $^{40}\text{Ar}/^{39}\text{Ar}$ dating of the basement and the alkaline volcanism of Gorringe Bank (Atlantic Ocean). *Earth and Planetary Sciences Letters*, 79, 255–269.
- Féraud, G., Girardeau, J., Beslier, M. O., & Boillot, G. (1988). Datation $^{40}\text{Ar}/^{39}\text{Ar}$ de la mise en place des peridotites bordant la marge de la Galice (Espagne). *Comptes Rendus Academie des Sciences Paris*, 307, 49–55.
- Ferreira, M. R. P., & Macedo, C. R. (1979). K–Ar Ages of the Permian–Mesozoic Basaltic Activity in Portugal. Abstracts VI. European Col. Geochronology, Cosmochronology and Isotope Geology, Norway, 26–27.
- Geldmacher, J., Hoernle, K., Van der Bogaard, P., Zankl, G., & Garbe-Schönberg, D. (2001). Earlier history of the ≥ 70 Ma old Canary hotspot based on the temporal and geochemical evolution of the Selvagen Archipelago and neighboring seamounts in the eastern North Atlantic. *Journal of Volcanology and Geothermal Research*, 111, 55–87.
- Geldmacher, J., Hoernle, K., Van den Bogaard, P., Duggen, S., & Werner, R. (2005). New $^{40}\text{Ar}/^{39}\text{Ar}$ age geochemical seamounts Canary and Madeira volcanic provinces: Support for the mantle plume hypothesis. *Earth and Planetary Sciences Letters*, 237, 85–101.
- Geldmacher, J., Hoernle, K., Klügel, A., Van den Bogaard, P., Wombacher, F., & Berning, B. (2006). Origin and geochemical evolution of the Tore-Madeira Rise (eastern North Atlantic). *Journal of Geophysical Research*, B09206, doi:10.1029/2005JB003931.
- Geldmacher, J., Hoernle, K., Klügel, A., Van der Bogaard, P., & Bindeman, I. (2008). Geochemistry of a new enriched mantle type locality in the northern hemisphere: Implications for the origin of the EM-I source. *Earth and Planetary Sciences Letters*, 265, 167–182.
- Geldmacher, J., Van den Bogaard, P., Hoernle, K., & Schmincke, H. U. (2000). The $^{40}\text{Ar}/^{39}\text{Ar}$ age dating of the Madeira Archipelago and hotspot track (eastern North Atlantic). *Geochemistry Geophysics Geosystems*, 1, doi: 10.1029/1999GC000018.
- Girardeau, J., Cornen, G., Beslier, M. O., Le Gall, B., Monnier, C., Agrinier, P., Dubuisson, G., Pinheiro, L., Ribeiro, A., & Whitechurch, H. (1998) Extensional tectonics in the Gorringe Bank rocks, Eastern Atlantic Ocean: evidence of an oceanic ultra-slow mantellic accreting center. *Terra Nova*, 10, 330–336.
- Gradstein, F. M., Ogg, J. G., & Smith, A. G. (2004). *A geological time scale*. Cambridge UK: Cambridge University Press.
- Grange, M., Schärer, U., Merle, R., Girardeau, J., & Cornen, G. (2010). Plume–lithosphere interaction during migration of Cretaceous alkaline magmatism in SW Portugal: Evidence from U–Pb ages and Pb–Sr–Hf isotopes. *Journal of Petrology*, 51, 1143–1170.
- Gutscher, M. A., Malod, J., Rehault, J. P., Contrucci, I., Klingelhofer, F., Mendes-Victor, L., & Spakman, W. (2002). Evidence for active subduction beneath Gibraltar. *Geology*, 30, 1071–1074.

- Hirano, N., Takahashi, E., Yamamoto, J., Abe, W., Ingle, S. P., Kaneoka, I., Hirata, T., Kimura, J. I., Ishii, T., Ogawa, Y., Machida, S., & Suyehiro, K. (2006). Volcanism in response to plate flexure. *Science*, 313, 1426–1428.
- Hoernle, K., Zhang, Y. S., & Graham, D. (1995). Seismic and geochemical evidence for large-scale mantle upwelling beneath the eastern Atlantic and western and central Europe. *Nature*, 374, 34–39.
- Hoernle, K., Hauff, F., Werner, R., Van Den Bogaard, P., Gibbons, A. D., Conrad, S., & Müller, R. D. (2011). Origin of Indian Ocean Seamount Province by shallow recycling of continental lithosphere. *Nature Geosciences*, 4, 883–887.
- Hofmann, C., Féraud, G., & Courtillot, V. (2000). $^{40}\text{Ar}/^{39}\text{Ar}$ dating of mineral separates and whole rocks from the Western Ghats lava pile: further constraints on duration and age of the Deccan traps. *Earth and Planetary Sciences Letters*, 180, 13–27.
- Jagoutz, O., Müntener, O., Manatschal, G., Rubatto, D., Péron-Pinvidic, G., Turrin, B. D., & Villa, I. M. (2007). The rift-to-drift transition in the North Atlantic: A suttering start of the MORB machine? *Geology*, 35, 1087–1090.
- Jiménez-Munt, I., Fernández, M., Torne, M., & Bird, P. (2001). The transition from linear to diffuse plate boundary in the Azore-Gibraltar region: results from a thin-sheet model. *Earth and Planetary Sciences Letters*, 192, 175–189.
- Jourdan, F., & Renne, P. R. (2007). Age calibration of the Fish Canyon sanidine $^{40}\text{Ar}/^{39}\text{Ar}$ dating standard using primary K–Ar standards. *Geochimica Cosmochimica Acta*, 71, 387–402.
- Jourdan, F., Féraud, G., Bertrand, H., Watkeys, M. K., & Renne, P. R. (2007). Distinct brief major events in the Karoo large igneous province clarified by new $^{40}\text{Ar}/^{39}\text{Ar}$ ages on the Lesotho basalts. *Lithos*, 98, 195–209.
- Jourdan, F., Frew, A., Joly, A., Mayers, C., & Evans, N. J. (2014). WA1ms: A ~ 2.61 Ga muscovite standard for $^{40}\text{Ar}/^{39}\text{Ar}$ dating. *Geochimica Cosmochimica Acta*, 141, 113–126.
- Jourdan, F., Renne, P. R., & Reimold, W. U. (2009). An appraisal of the ages of terrestrial impact structures. *Earth and Planetary Sciences Letters*, 286, 1–13.
- Koppers, A. A. P. (2002). ArArCALC – software for $^{40}\text{Ar}/^{39}\text{Ar}$ age calculations. *Computers and Geosciences*, 28, 605–619.
- Laughton, A. V., Roberts, D. G., & Graves, R. (1975). Bathymetry of the northeast Atlantic: mid-Atlantic ridge to southwest Europe. *Deep Sea Research*, 22, 791–810.
- Lee, J. Y., Marti, K., Severinghaus, J. P., Kawamura, K., Yoo, H. S., Lee, J. B., & Kim, J. S. (2006). A redetermination of the isotopic abundances of atmospheric Ar. *Geochimica Cosmochimica Acta*, 70, 4507–4512.
- Marques, F. O. (2014). Are subduction zones invading the Atlantic? Evidence from the southwest Iberia margin: Comment. *Geology*, e327–e328, doi:10.1130/G34100C.

- Mata, J., Kerrich, R., MacRae, N. D., & Wu, T.-W. (1998). Elemental and isotopic (Sr, Nd, and Pb) characteristics of Madeira Island basalts: Evidence for a composite HIMU–EM I plume fertilizing lithosphere. *Canadian Journal of Earth Sciences*, 35, 980–997.
- McDougall, I., & Harrison, T. M. (1999) *Geochronology and thermochronology by the $^{40}\text{Ar}/^{39}\text{Ar}$ Method*. Oxford UK: Oxford University Press.
- Merle, R. (2006). *Age and origin of Tore-Madeira Rise: Beginning of Atlantic Ocean spreading or hotspot track. Petrology, Geochemistry, U–Pb Geochronology and Pb–Sr–Hf isotopes*. PhD thesis. Nantes France: University of Nantes.
- Merle, R., Caroff, M., Girardeau, J., Cotton, J., & Guivel, C. (2005). Segregation vesicles, cylinders, and sheets in vapor-differentiated pillow lavas: examples from Tore-Madeira Rise and Chile Triple Junction. *Journal of Volcanology and Geothermal Research*, 141, 109–122.
- Merle, R., Jourdan, F., Marzoli, A., Renne, P. R., Grange, M., & Girardeau, J. (2009). Evidence of multi-phase Cretaceous to Quaternary alkaline magmatism on Tore-Madeira Rise and neighbouring seamounts from $^{40}\text{Ar}/^{39}\text{Ar}$ ages. *Journal of Geological Society of London*, 166, 879–894.
- Merle, R., Kaczmarec, M. A., Tronche, E., & Girardeau, J. (2012). Occurrence of inherited supra-subduction zone mantle in the oceanic lithosphere as inferred from mantle xenoliths and xenocrystals from Dragon and Lion seamounts (Southern Tore-Madeira Rise). *Journal of Geological Society of London*, 169, 251–267.
- Merle, R., Scharer, U., Girardeau, J., & Cornen, G. (2006). Cretaceous seamounts along the ocean-continent of Iberian margin: U–Pb ages and Sr–Pb–Hf isotopes. *Geochimica Cosmochimica Acta*, 70, 4950–4976.
- Miranda, R., Valadares, V., Terrinha, P., Mata, J., Do Rosario Azevedo, M., Gaspar, M., Kullberg, J. C., & Ribeiro, C. (2009). Age constraints on the Late Cretaceous alkaline magmatism on the West Iberian Margin. *Cretaceous Research*, 30, 575–586.
- Neres, M., Font, E., Miranda, J. M., Camps, P., Terrinha, P., & Miro, J. (2012). Reconciling Cretaceous paleomagnetic and marine magnetic data for Iberia: New Iberian paleomagnetic poles. *Journal of Geophysical Research: Solid Earth*, 117, B06102.
- Neres, M., Bouchez, J.-L., Terrinha, P., Font, E., Moreira, M., Miranda, R., Launeau, P., & Carvalho, C. (2014). Magnetic fabric in a Cretaceous sill (Foz da Fonte, Portugal): flow model and implications for regional magmatism. *Geophysical Journal International*, 199, 78–101.
- Neres, M., Carafa, M. M. C., Fernandes, R. M. S., Matias, L., Duarte, J. C., Barba, S., & Terrinha, P. (2016). Lithospheric deformation in the Africa–Iberia plate boundary: Improved neotectonic modeling testing a basal-driven Alboran plate. *Journal of Geophysical Research: Solid Earth*, 121, 6566–6596.
- Neves, M. C., Terrinha, P., Afilhado, A., Moulin, M., Matias, L., & Rosas, F. (2009). Response of a multi-domain continental margin to compression: study from seismic reflection-refraction and numerical modelling in the Tagus Abyssal Plain. *Tectonophysics*, 468, 113–130.

- Olivet, J. L. (1996). La cinématique de la plaque Ibérique. *Bulletin des Centres Recherches Exploration-Production Elf Aquitaine*, 20, 131–195.
- Pierce, C., & Barton, P. J. (1991). Crustal structure of the Tore-Madeira Rise, Eastern North Atlantic – results of a DOBS wide-angle and normal incidence seismic experiment in the Josephine Seamount region. *Geophysical Journal International*, 106, 357–378.
- Pereira, R., Tiago, M., Alves, T. M., & Mata, J. (2017). Alternating crustal architecture in West Iberia: a review of its significance in the context of NE Atlantic rifting. *Journal of the Geological Society*, 174, 522–540.
- Phillips, D., & Matchan, E. L. (2013). Ultra-high precision $^{40}\text{Ar}/^{39}\text{Ar}$ ages for Fish Canyon Tuff and Alder Creek Rhyolite sanidine: New dating standards required? *Geochimica Cosmochimica Acta*, 121, 229–239.
- Ramalho, R. S., Brum Da Silveira, A., Fonseca, P. E., Madeira, J., Cosca, M., Cachão, M., Fonseca, M. M., & Prada, S. N. (2015). The emergence of volcanic oceanic islands on a slow-moving plate: The example of Madeira Island, NE Atlantic. *Geochemistry Geophysics Geosystems*, 16, 522–537.
- Renne, P. R., Balco, G., Ludwig, K. R., Mundil, R., & Min, K. (2011). Response to the comment by W. H. Schwarz et al. on "Joint determination of K-40 decay constants and Ar-40*/K-40 for the Fish Canyon sanidine standard, and improved accuracy for Ar-40/Ar-39 geochronology" by P. R. Renne et al. (2010). *Geochimica Cosmochimica Acta*, 75, 5097–5100.
- Renne, P. R., Mundil, R., Balco, G., Min, K., & Ludwig, K. R. (2010). Joint determination of ^{40}K decay constants and $^{40}\text{Ar}^*/^{40}\text{K}$ for the Fish Canyon sanidine standard, and improved accuracy for $^{40}\text{Ar}/^{39}\text{Ar}$ geochronology. *Geochimica Cosmochimica Acta*, 74, 5349–5367.
- Renne, P. R., Swisher, C. C., Deino, A. L., Karner, D. B., Owens, T. L., & DePaolo, D. J. (1998). Intercalibration of standards, absolute ages and uncertainties in $^{40}\text{Ar}/^{39}\text{Ar}$ dating. *Chemical Geology*, 145, 117–152.
- Rovere, M., Ranero, C. R., Sartori, R., Torelli, L., & Zitellini, N. (2004). Seismic images and magnetic signature of the Late Jurassic to Early Cretaceous Africa–Eurasia plate boundary off SW Iberia. *Geophysical Journal International*, 158, 554–568.
- Sibuet, J. C., Monti, S., Loubrieu, B., Mazé, J. P., & Srivastava, S. (2004a). Carte bathymétrique de l'Atlantique nord-est et du golfe de Gascogne: implications géodynamiques. *Bulletin de la Société Géologique de France*, 175, 429–442.
- Sibuet, J.-C., Srivastava, S., & Spakman, W. (2004b). Pyrenean orogeny and plate kinematics. *Journal of Geophysical Research*, 108, B08104.
- Tucholke, B. E., & Ludwig, W. J. (1982). Structure and origin of the J Anomaly Ridge, Western North Atlantic Ocean. *Journal of Geophysical Research*, 87, 9389–9407.
- Tucholke, B. E., Sawyer, D. S., & Sibuet, J.-C. (2007). Breakup of the Newfoundland–Iberia rift. In G. D. Karner, G. Manatschal & L. M. Pinheiro (Eds.), *Imaging, mapping and modelling continental*

lithosphere extension and breakup (pp. 9–46). London UK: Geological Society of London, Special Publications, No. 282.

Verati, C., & Jourdan, F. (2014). Modelling effect of sericitization of plagioclase on the $^{40}\text{K}/^{40}\text{Ar}$ and $^{40}\text{K}/^{39}\text{Ar}$ chronometers: Implication for dating basaltic rocks and mineral deposits. In: F. Jourdan, D. Mark & C. Verati (Eds.) *Advances in $^{40}\text{Ar}/^{39}\text{Ar}$ Dating: from Archaeology to Planetary Sciences* (pp. 155–174). London UK: Geological Society of London, Special Publication, No. 378

Verhoef, J., Roest, W. R., Macnab, R., Arkani-Hamed, J. & Members of the Project Team (1996). *Magnetic anomalies of the Arctic and North Atlantic Oceans and Adjacent land areas*. GSC Open file 3125. Ottawa CA: Geological Survey of Canada 225.

Welford, J. K., Smith, J. A., Hall, J., Deemer, S., Srivastava, S. P., & Sibuet, J. C. (2010). Structure and rifting evolution of the Northern Newfoundland Basin from Erable multichannel seismic reflection profiles across the southeastern margin of Flemish Cape. *Geophysical Journal International*, 180, 976–998.

Zitellini, N., Gràcia, E., Matias, L., Terrinha, P., Abreu, M. A., DeAlteriis, G., Henriet, J. P., Dañobeitia, J. J., Masson, D. G., Mulder, T., Ramella, R., Somoza, L., & Diez, S. (2009). The quest for the Africa–Eurasia plate boundary west of the Strait of Gibraltar. *Earth and Planetary Sciences Letters*, 280, 13–50.

Figure and table captions

Figure 1. Geological setting of the Iberia margin and the TMR. (a) Bathymetric map of the East northern central Atlantic (from Sibuet et al., 2004a) and geological setting of the TMR. Solid lines represent faults, and dashed lines inferred faults. AGFZ, Azores-Gibraltar Fracture Zone; ES, Estremadura Spur. (b) Sketch showing the movements of the Iberia plate since 125 Ma. Europe is considered as fixed. The light grey domains are areas in extension and dark grey domains are areas under compression. The nascent Atlantic spreading centre is show as double lines in the Bay of Biscay at 83 Ma. Also shown the magnetic anomalies J, A33 and A34. Black arrows, directions of convergence; white arrows, directions of extension; EU, Europe plate; IB, Iberian plate; NA, North America plate; Pyr suture, Pyrenees suture. Adapted from Sibuet et al. (2004b).

Figure 2. (a) Bathymetric map of the TMR and surroundings seamounts. Red triangles indicate the TMR seamounts investigated in this study and black triangles are seamounts investigated by Geldmacher et al. (2006, 2008) and Merle et al. (2006, 2009). Location of the J anomaly after Olivet (1996) and M22 after Verhoef et al. (1996). Thick pink line, Ocean–Continent boundary (after Rovere et al., 2004; Welford et al., 2010; Verhoef et al., 1996). Ages of TMR seamounts, Ormonde (Gorringe Bank), Ampere, Madeira, Porto Santo, Desertas Islands, Unicorn, Seine and Godzilla from D’Oriano et al. (2010), Féraud et al. (1982, 1986), Geldmacher et al. (2000, 2005, 2006, 2008), Merle et al. (2006, 2009) and Ramalho et al. (2015). Ages of southwestern Portugal intrusions from Grange et al. (2010) and Miranda et al. (2009). (b) Simplified bathymetry of the Tore seamounts after Hirschberger (unpublished data). Ages from Merle et al. (2006) and this study.

Figure 3. Amphibole and plagioclase $^{40}\text{Ar}/^{39}\text{Ar}$ apparent age and related K/Ca ratio for the samples from Tore East (TMD9-1) and Isabelle seamounts (TMD19-3). Errors on plateau ($>70\%$ ^{39}Ar

released) ages are quoted at 2σ and do not include systematic errors (i.e. uncertainties on the age of the monitor and on the decay constant). MSWD and probability are indicated.

Figure 4. Location of the postulated NE–SW Madeira hot-spot track and the age progression through the seamounts involved in this trend as proposed by D’Oriano et al. (2010) and Geldmacher et al. (2000). (a) Proposed Madeira hot-spot track (modified after D’Oriano et al., 2010; Geldmacher et al., 2000, 2005). Ages of the different seamounts are those shown in Figure 1. (b) Age versus distance from Madeira plot showing the age trend formed by the hot-spot path. The age trend line assumes a plate velocity of 12 km/Ma deduced from the ages of Ormonde, Ampere and Seine seamounts and Madeira archipelago proposed by Geldmacher et al. (2000).

Figure 5. Age vs latitude plot for the TMR and surrounding seamounts and southwestern Portugal magmatism showing three magmatic phases. Error bars are given at 2σ level and are usually smaller than the symbols. Age references same as Figure 1.

Table 1. Filtered geochronological database of the TMR and surrounding areas.

Table 2. $^{40}\text{Ar}/^{39}\text{Ar}$ results.

Table 1. Filtered geochronological database of the TMR and surrounding areas.

Reference	Sample name	Location	Rock type	Technique ^a	Phase dated ^b	Age (Ma)	2σ error (Ma)	MSWD	P
Tore-Madeira rise									
Northern TMR									
Merle et al., 2006	TMD10c-1	Tore N	trachyte	U-Pb (ID-TIMS)	titanite	88.3	3.3	0.34	0.89
Merle et al., 2006	TMD10c-2	Tore N	trachyte	U-Pb (ID-TIMS)	titanite	88.3	3.8	1.01	0.39
Merle et al., 2006	TMD3b-2	Tore NW	trachyte	U-Pb (ID-TIMS)	titanite+zrc	80.5	0.9	0.86	0.54
<i>this work</i>	TMD9-1	Tore East	trachyandesite	$MC\ ^{40}Ar/^{39}Ar$ (StH)	hbl	80.5	0.1	0.86	0.59
Merle et al., 2006	TMD4-3	Sponge Bob	trachyte	U-Pb (ID-TIMS)	titanite+zrc	102.8	0.7	0.38	0.91
Merle et al., 2006	TMD14-9	Ashton	trachyte	$U-Pb$ (ID-TIMS)	titanite+zrc	96.3	1.0	0.60	0.81
Merle et al., 2009	TMD14-9	Ashton	trachyte	$^{40}Ar/^{39}Ar$ (StH)	biot	98.3	1.2	1.20	0.28
Merle et al., 2009	TMD14-9	Ashton	trachyte	$^{40}Ar/^{39}Ar$ (StH)	biot	98.7	1.1	0.80	0.71
Central TMR									
Merle et al., 2006	TMD15-5	Gago Coutinho/ Teresa	trachyte	U-Pb (ID-TIMS)	titanite	92.3	3.7	0.25	0.91
Geldmacher et al., 2006	403 DR-5	Gago Coutinho/ Teresa	trachyte	$^{40}Ar/^{39}Ar$ (StH)	hbl	95.8	0.4	2.00	0.05
Geldmacher et al., 2006	399 DR-1	Josephine N (Pico Pia)	basalt	$^{40}Ar/^{39}Ar$ (StH)	mtrx	0.5	0.5	0.60	0.83
Geldmacher et al., 2006	406 DR-7	Josephine N (Toblerone Ridge)	basalt	$^{40}Ar/^{39}Ar$ (StH)	gls	1.4	0.6	0.70	0.74
Geldmacher et al., 2006	406 DR-7	Josephine N (Toblerone Ridge)	basalt	$^{40}Ar/^{39}Ar$ (StH)	mtrx	0.5	0.1	1.50	0.07
Geldmacher et al., 2006	407 DR-4	Josephine N (Pico Julia)	basalt	$^{40}Ar/^{39}Ar$ (StH)	mtrx	7.2	0.7	0.70	0.74
Geldmacher et al., 2006	407 DR-4	Josephine N (Pico Julia)	basalt	$^{40}Ar/^{39}Ar$ (StH)	mtrx	7.6	0.5	0.60	0.80
Geldmacher et al., 2006	408 DR-2	Josephine	basalt	$^{40}Ar/^{39}Ar$ (StH)	mtrx	16.3	0.9	1.00	0.45
Geldmacher et al., 2006	408 DR-2	Josephine	basalt	$^{40}Ar/^{39}Ar$ (StH)	mtrx	13.9	0.7	1.40	0.14
Geldmacher et al., 2006	409 DR-1	Josephine	basalt	$^{40}Ar/^{39}Ar$ (StH)	mtrx	11.9	0.7	1.30	0.22
Geldmacher et al., 2006	409 DR-1	Josephine	basalt	$^{40}Ar/^{39}Ar$ (StH)	mtrx	11.7	0.7	0.50	0.89
Geldmacher et al., 2006	410 DR-4	Josephine	basalt	$^{40}Ar/^{39}Ar$ (StH)	mtrx	13.5	0.6	0.70	0.78

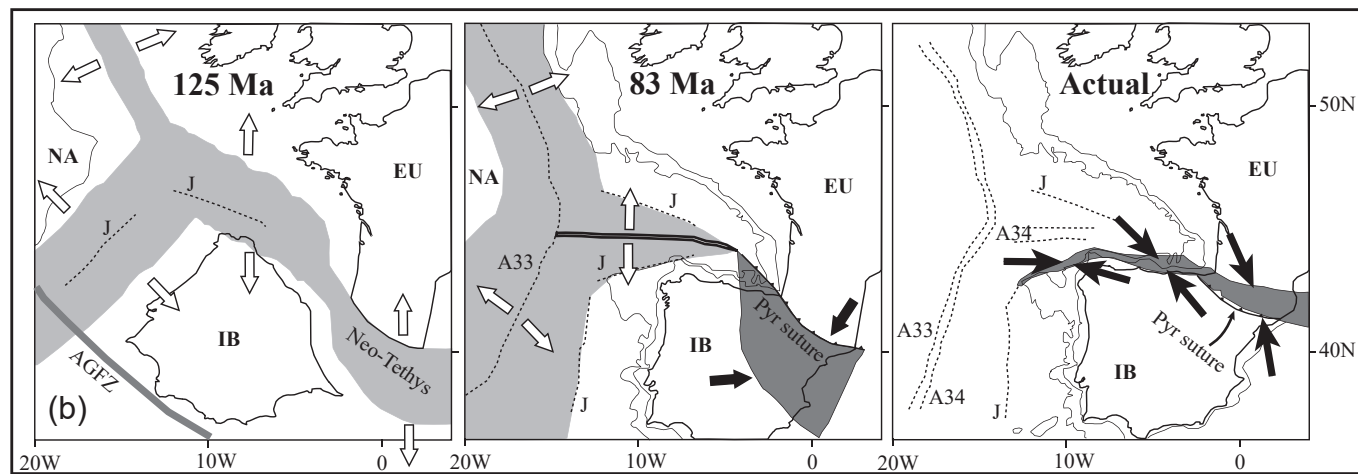
2006	Geldmacher et al., 2006	410 DR-4	Josephine	basalt	$^{40}\text{Ar}/^{39}\text{Ar}$ (StH)	mtrx	13.2	0.3	1.60	0.07
Merle et al., 2006	TMD16-1	Jo Sister/Erik	trachyte	U-Pb (ID-TIMS)	titanite	86.5	3.4	0.13	0.97	
Merle et al., 2006	TMD16-2	Jo Sister/Erik	trachyte	U-Pb (ID-TIMS)	titanite	89.3	2.3	0.76	0.64	
Geldmacher et al., 2006	412 DR-2	Jo Sister/Erik	basalt	$^{40}\text{Ar}/^{39}\text{Ar}$ (StH)	mtrx	3.7	0.3	1.70	0.07	
Southern TMR										
<i>this work</i>		TMD19-3	<i>Isabelle</i>	<i>basalt</i>	$MC\ ^{40}\text{Ar}/^{39}\text{Ar}$ (StH)	<i>plag</i>	~85	0.4	0.90	0.57
Geldmacher et al., 2006	429 DR-1	Dragon	basalt	$^{40}\text{Ar}/^{39}\text{Ar}$ (StH)	mtrx	1.5	0.4			
Geldmacher et al., 2006	429 DR-1	Dragon	basalt	$^{40}\text{Ar}/^{39}\text{Ar}$ (StH)	mtrx	1.1	0.2	0.60	0.73	
Geldmacher et al., 2006	431 DR-1	Dragon	basalt	$^{40}\text{Ar}/^{39}\text{Ar}$ (StH)	mtrx	4	0.3	1.30	0.19	
Geldmacher et al., 2008	428 DR-1	Godzilla	trachyandesite	$^{40}\text{Ar}/^{39}\text{Ar}$ (StH)	biot	68.4	0.2	2.10	0.05	
Seine-Unicorn										
Geldmacher et al., 2005	423 DR-1	Unicorn	basalt	$^{40}\text{Ar}/^{39}\text{Ar}$ (StH)	mtrx	28.1	2.4	0.70	0.73	
Geldmacher et al., 2005	426 DR-1	Seine	basalt	$^{40}\text{Ar}/^{39}\text{Ar}$ (StH)	mtrx	22.2	0.2	1.20	0.29	
Merle et al., 2009	TMD21-1	Seine	basalt	$^{40}\text{Ar}/^{39}\text{Ar}$ (StH)	hbl	24.6	0.4	0.30	0.98	
Merle et al., 2009	TMD21-1	Seine	basalt	$^{40}\text{Ar}/^{39}\text{Ar}$ (StH)	hbl	24.6	0.5	1.20	0.26	
Ampere-Ormonde										
Geldmacher et al., 2000	DS-797-1	Ampere	basalt	$^{40}\text{Ar}/^{39}\text{Ar}$ (TF)	mtrx	32.0	0.2	1.33	0.19	
Féraud et al., 1982	DR-06-03	Ormonde	basic lamprophyre (monchiquite)	$^{40}\text{Ar}/^{39}\text{Ar}$ (StH)	biot	64.9	1.1	0.65	0.74	
Féraud et al., 1982	DR-06-18	Ormonde	trachyte	$^{40}\text{Ar}/^{39}\text{Ar}$ (StH)	mtrx	62.2	2.4	0.26	0.91	
Féraud et al., 1986	CY14-2	Ormonde	basic lamprophyre (monchiquite)	$^{40}\text{Ar}/^{39}\text{Ar}$ (StH)	biot	65.7	0.7	1.30	0.25	
Southwest Portugal										
Grange et al., 2010	PT2-A	Ribamar	alkali diorite	U-Pb (ID-TIMS)	zrc	88.3	0.5	0.90	0.48	
Grange et al., 2010	PT5-A	Sintra	micro-granite	U-Pb (ID-TIMS)	zrc	82.2	0.8	0.39	0.81	
Grange et al., 2010	PT6-A	Sintra	alkali gabbro	U-Pb (ID-TIMS)	zrc	83.4	0.7	0.64	0.67	
Grange et al., 2010	PT7-A	Sintra	syenite	U-Pb (ID-TIMS)	zrc	80.1	0.6	2.00	0.08	

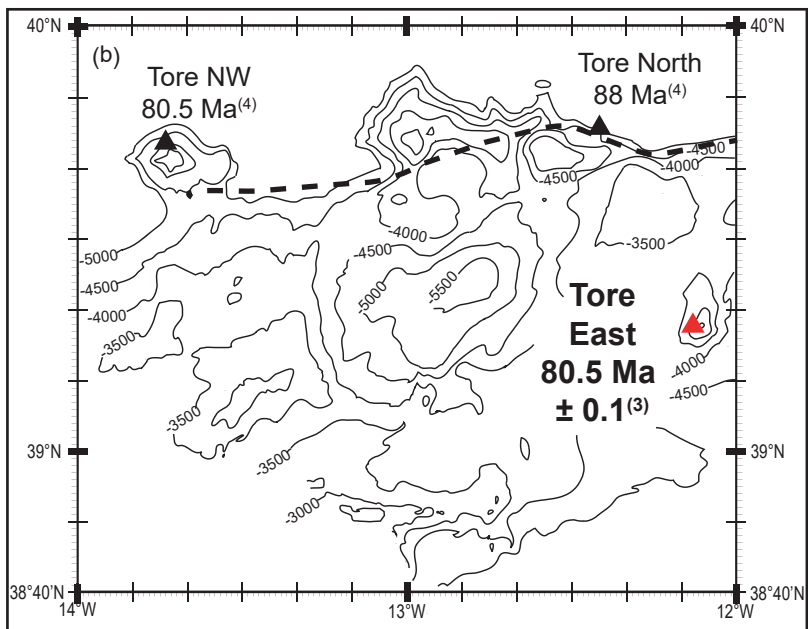
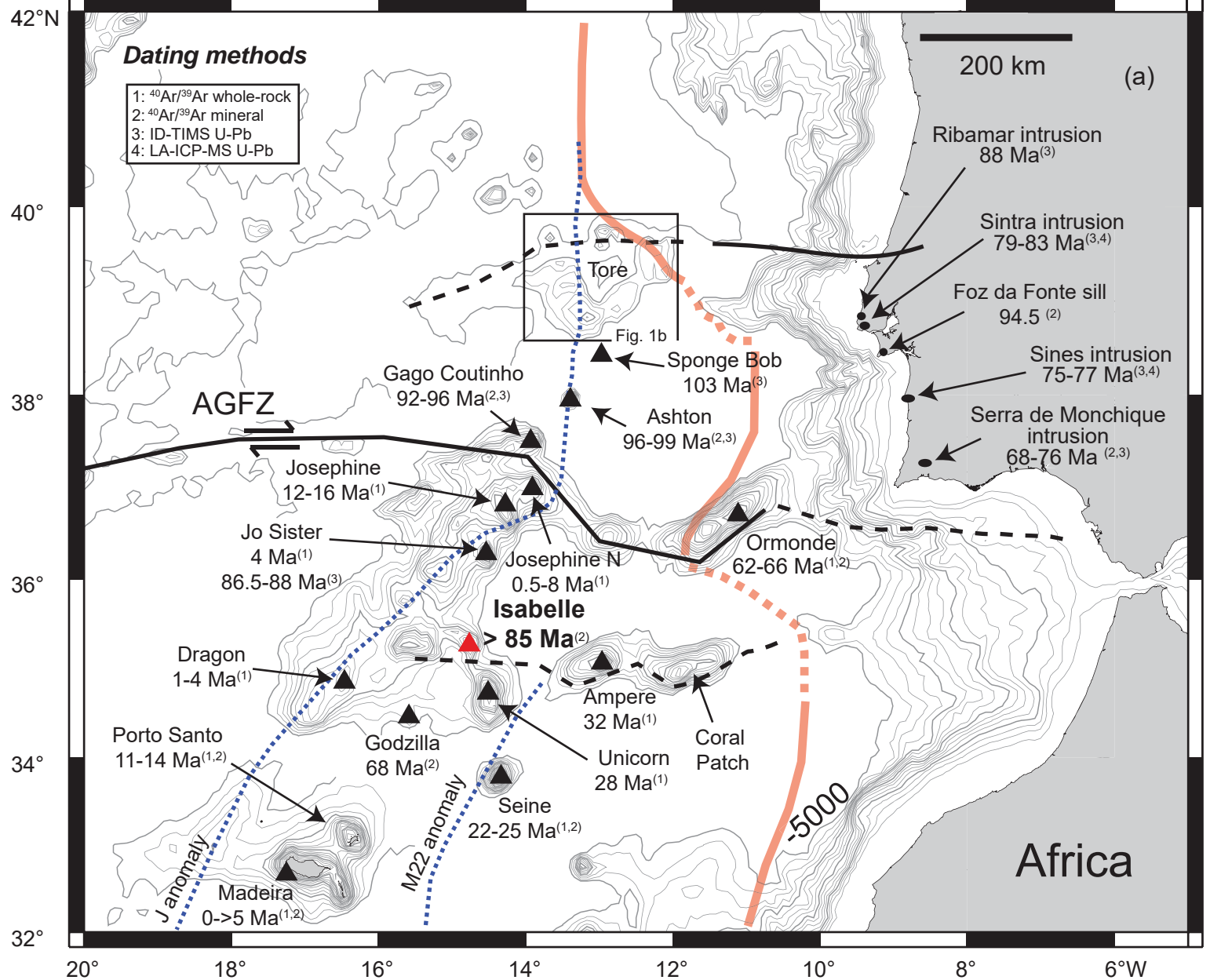
Grange et al., 2010	PT9-A	Sintra	alkali granite	U-Pb (ID-TIMS)	zrc	81.7	0.4	0.96	0.46
Miranda et al., 2009	?	Sintra	granite	U-Pb (LA-ICP-MS) $^{40}\text{Ar}/^{39}\text{Ar}$ (StH)	zrc	79.3	0.6	1.00	0.45
Miranda et al., 2009	?	Foz da fonte	tephrite	$^{40}\text{Ar}/^{39}\text{Ar}$ (StH)	hbl	94.5	4.8	0.17	0.97
Grange et al., 2010	PT16-A	Sines	alkali gabbro	U-Pb (ID-TIMS)	zrc	77.2	0.6	0.19	0.94
Grange et al., 2010	PT17-A	Sines	alkali gabbro	U-Pb (ID-TIMS)	zrc	77.2	0.4	0.49	0.86
Miranda et al., 2009	?	Sines	syenite	U-Pb (LA-ICP-MS)	zrc	75.3	0.5	1.30	0.15
Grange et al., 2010	PT20-A	Monchique	nepheline syenite	U-Pb (ID-TIMS)	titanite	68.5	0.6	1.30	0.24
Miranda et al., 2009	?	Monchique	basic lamprophyre	$^{40}\text{Ar}/^{39}\text{Ar}$ (StH)	hbl	76.1	2.9	1.03	0.40

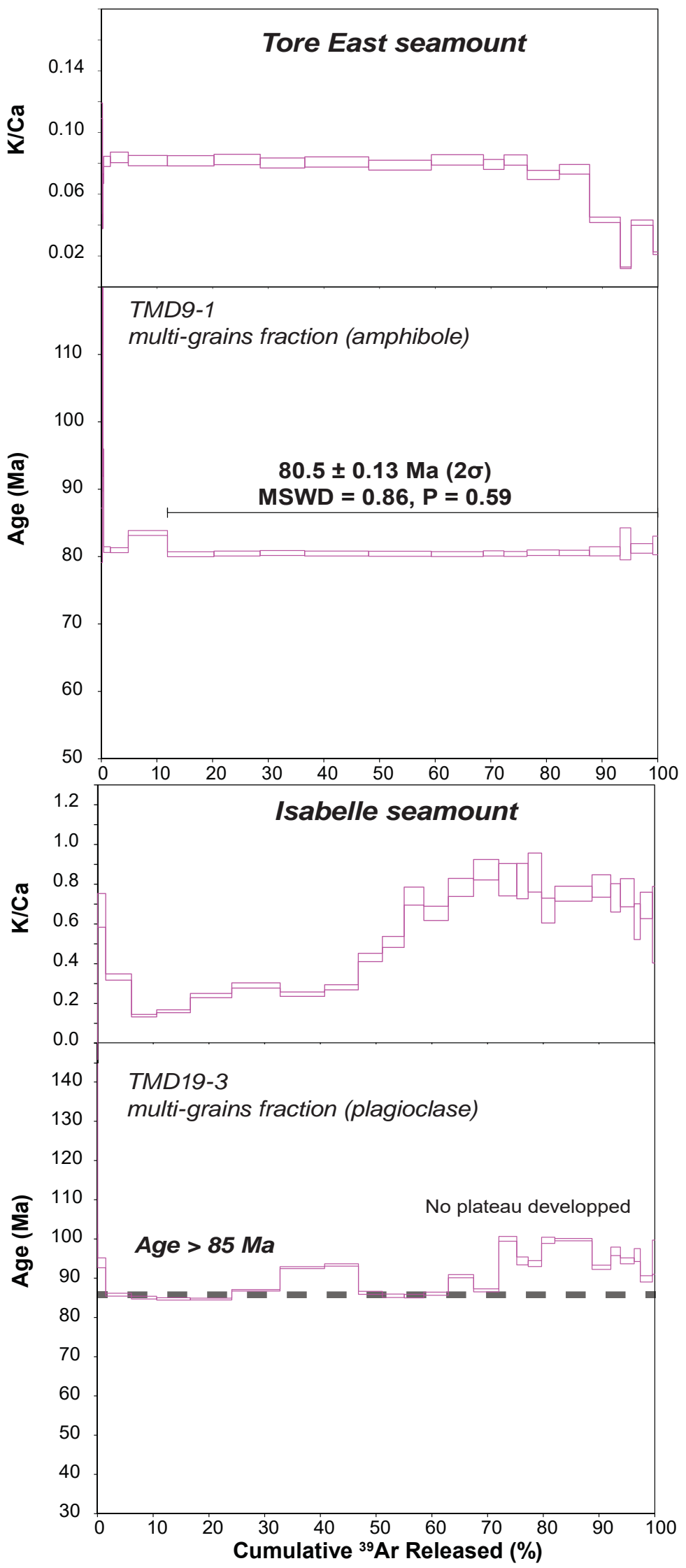
^a ID, isotopic dilution; TF, total fusion; StH, step heating, MC, multi-collection. ^b zrc, zircon, biot, biotite, hbl, hornblend, gls, glass, matrix, plag, plagioclase.

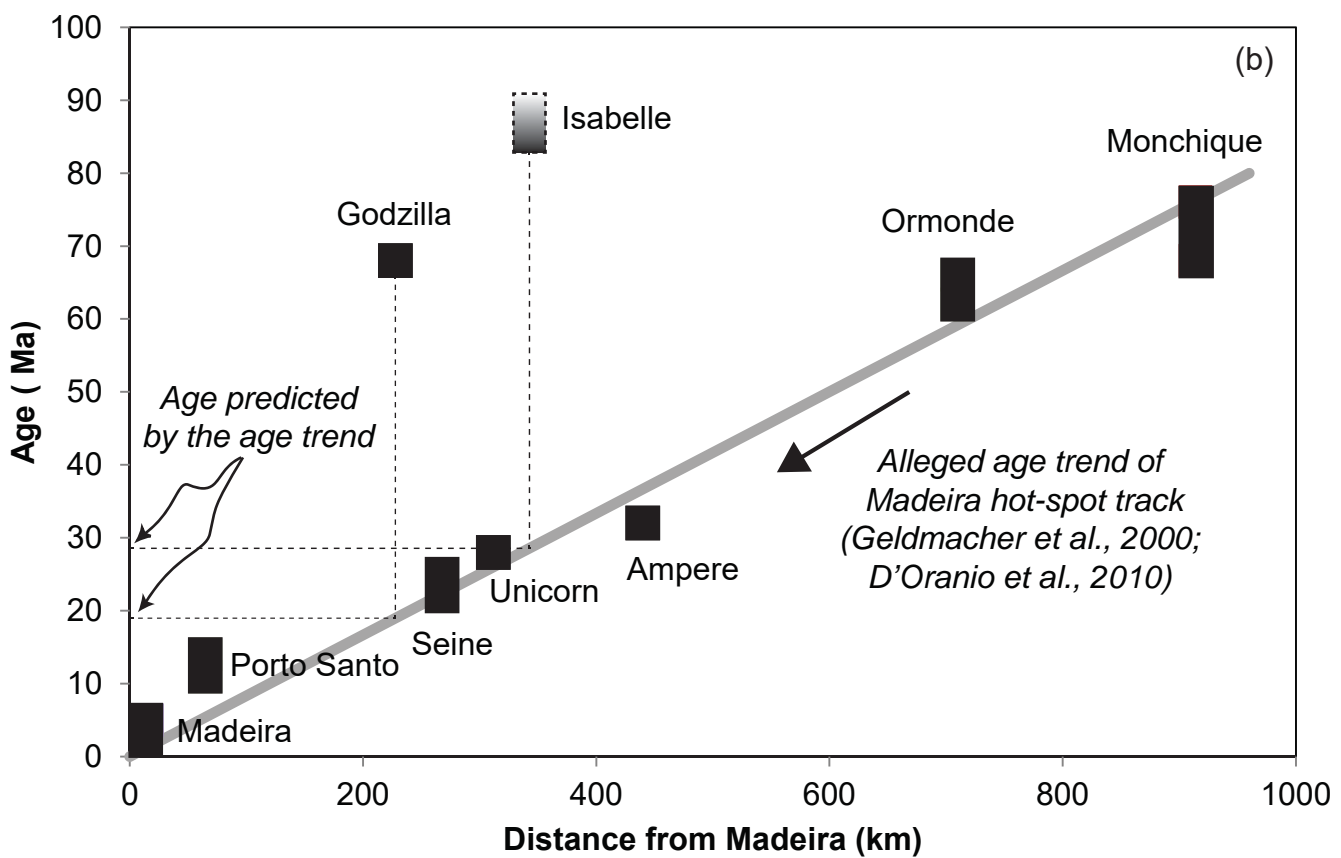
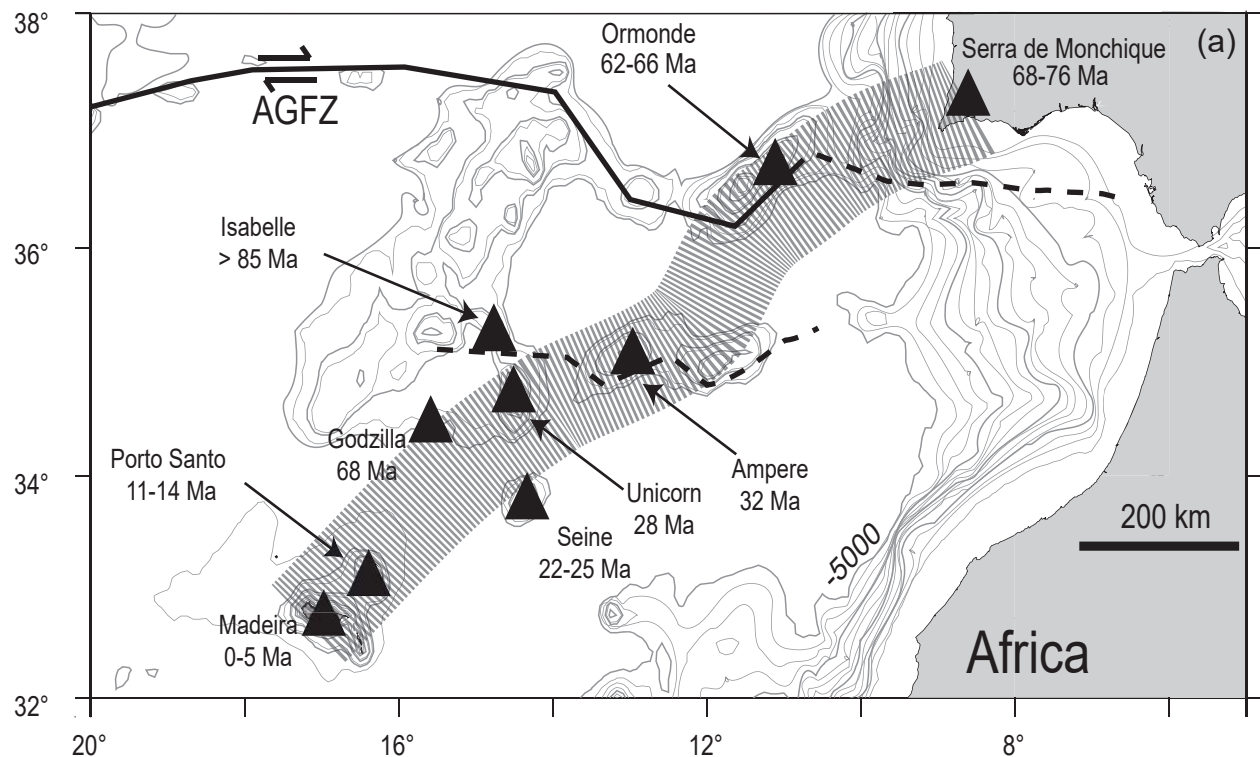
Table 2. ${}^{40}\text{Ar}/{}^{39}\text{Ar}$ results.

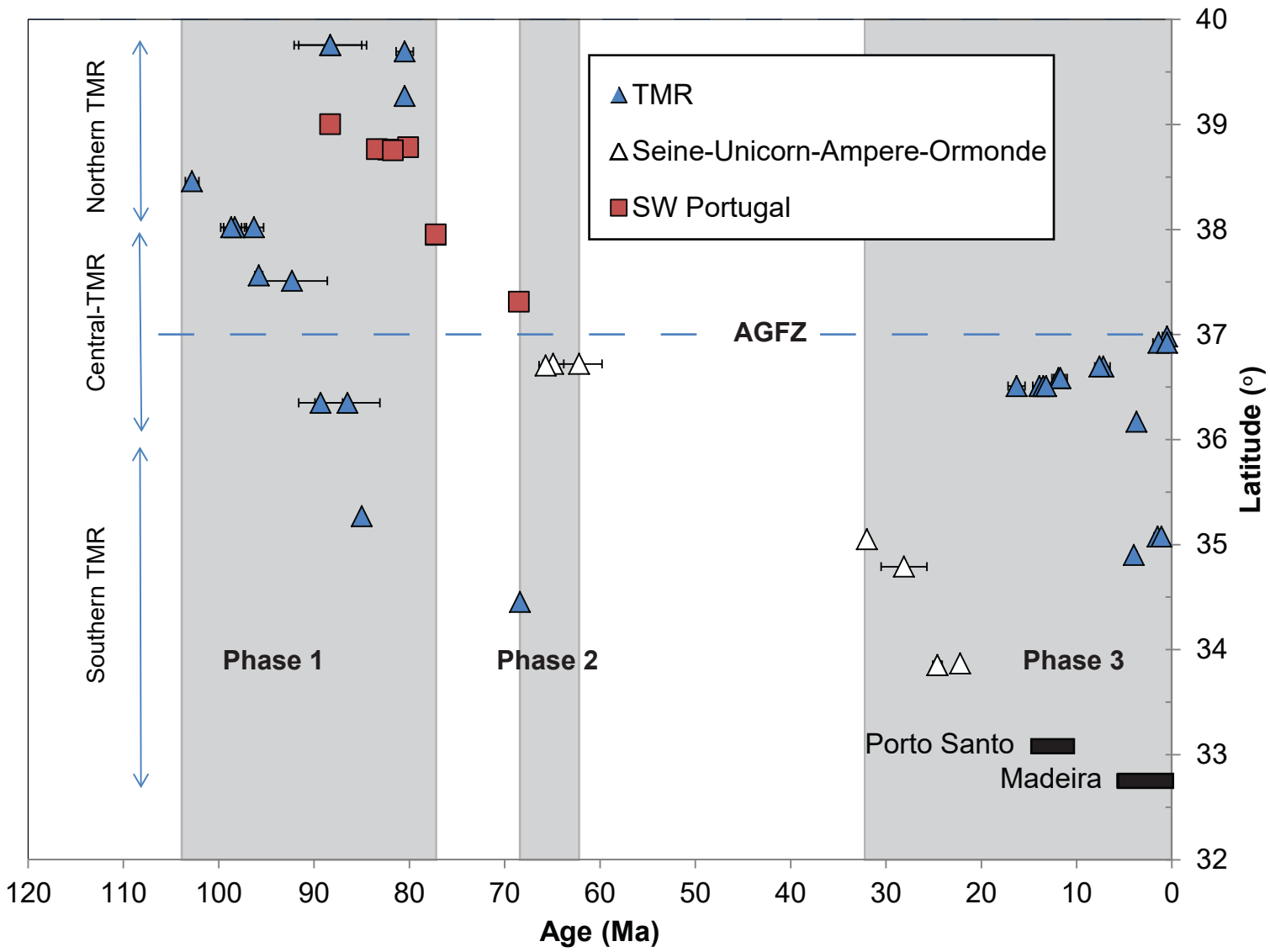
Summary table indicating plateau and isochron ages for the TMR samples. MSWD for plateau and isochron, percentage of ^{39}Ar degassed used in the plateau calculation, number of analysis included in the isochron, and $^{40}\text{Ar}/^{36}\text{Ar}$ intercept are indicated. Plateau age calculated using trapped $^{40}\text{Ar}/^{36}\text{Ar}$ is indicated. Analytical uncertainties on the ages are quoted at 2 sigma (2σ) confidence levels and at 2σ for the $^{40}\text{Ar}/^{36}\text{Ar}$ intercept.











Supplementary papers

Appendix 1: Consequences of the new technical improvements

Our new $^{40}\text{Ar}/^{39}\text{Ar}$ data were obtained using state-of-the-art multi-collection noble gas mass spectrometry and provide new perspectives for resolving problems in volcanology such as distinguishing different magmatic phases occurring within intervals of less than few hundred thousands of years, several tens or hundreds of million years ago.

New generation of $^{40}\text{Ar}/^{39}\text{Ar}$ instrumentation, and in particular the ARGUS VI™ multi-collection noble gas mass spectrometer, allows to obtain an unprecedented $^{40}\text{Ar}/^{39}\text{Ar}$ analytical precision that in turn, allows us to date event at the permil, to even sub-permil level of precision, depending on the K_2O concentration of the crystals analyzed. The gain of precision is due to the improved stability of the faraday cups equipped with $10^{12} \Omega$ (or more recently $10^{13} \Omega$) resistors located under vacuum, and the ultra-precise ion counter detector that can precisely measure ion beams with measurable values below few fA or tenth of fA, usually where faraday measurement capacity degrades. Phillips and Matchan (2013) and Matchan and Phillips (2014) have illustrated the clear advantage of the ARGUS VI instrument when dating young to very young eruptions (several tens to hundreds of ka) and when measuring standards.

In this study, we show that the improvement of precision extend to K-poor minerals from volcanic rocks with ages of ca. 80 Ma, where we obtained a precision of $\pm 0.16\%$ [$\pm 0.20\%$ including all sources of uncertainties] on amphibole ($\text{K}_2\text{O} \sim 1\%$ on the presently analysed phase). This is an increase of ca. 3 times compared to the most precise results previously obtained on other hornblende phases ($\pm 0.43\%$; Fig. A2; Geldmacher et al. 2006). Such an increase of precision shows that the $^{40}\text{Ar}/^{39}\text{Ar}$ technique can now approach the precision offered by the CA-ID-TIMS U-Pb dating technique obtained on zircon. For example, state-of-the-art $^{238}\text{U}/^{206}\text{Pb}$ zircon ages of 139.55 ± 0.09 [± 0.18] Ma (Vennari et al. 2014) corresponding to relative precision of $\pm 0.07\%$ [$\pm 0.13\%$], and 55.838 ± 0.032 [0.064] Ma (Wotzlaw et al. 2012) corresponding to a relative precision of $\pm 0.06\%$ [$\pm 0.11\%$] were recently published. Hornblende is a phase that contains relatively low level of K_2O . A better comparison to zircon is given by K-rich phases like muscovite and biotite. For such comparison, we used the results obtained on the GA1550 biotite and WA1ms muscovite standards measured for this study (Fig. A1), which when pooled together, yielded a precision on the J-value of $\pm 0.07\%$ (2σ). Of course, this series of mica have been used as a fluence monitors, but if an age where to be derived from them, and including an additional J-value uncertainty of $\pm 0.07\%$ on top of the analytical uncertainties, one would obtain an age of 99.74 ± 0.10 Ma for GA1550, corresponding to a relative precision of $\pm 0.09\%$, and an age of 2613.0 ± 1.5 Ma for WA1ms corresponding to a relative precision of $\pm 0.06\%$, the latter precision being indistinguishable with the precision obtained by U/Pb dating of zircon (Fig. A2). Although our plagioclase sample did not yield any plateau age, we can still use the data to

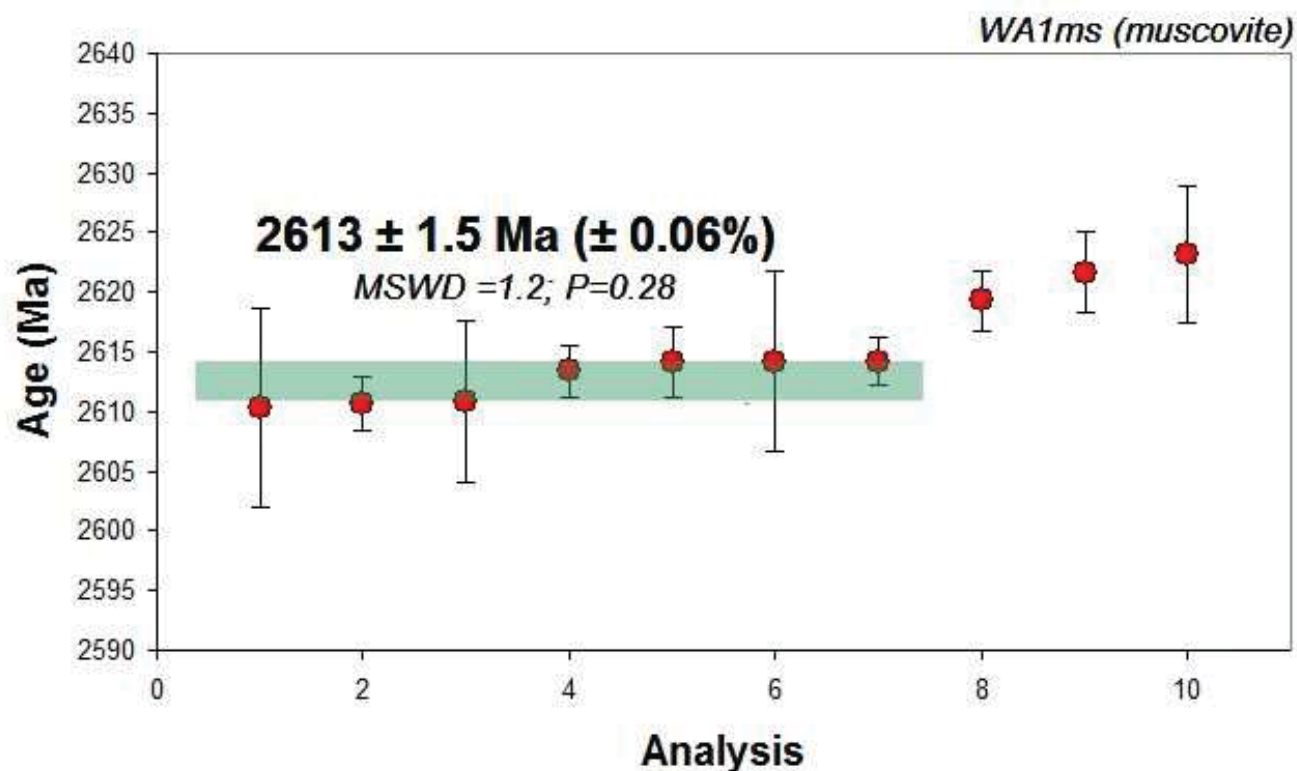
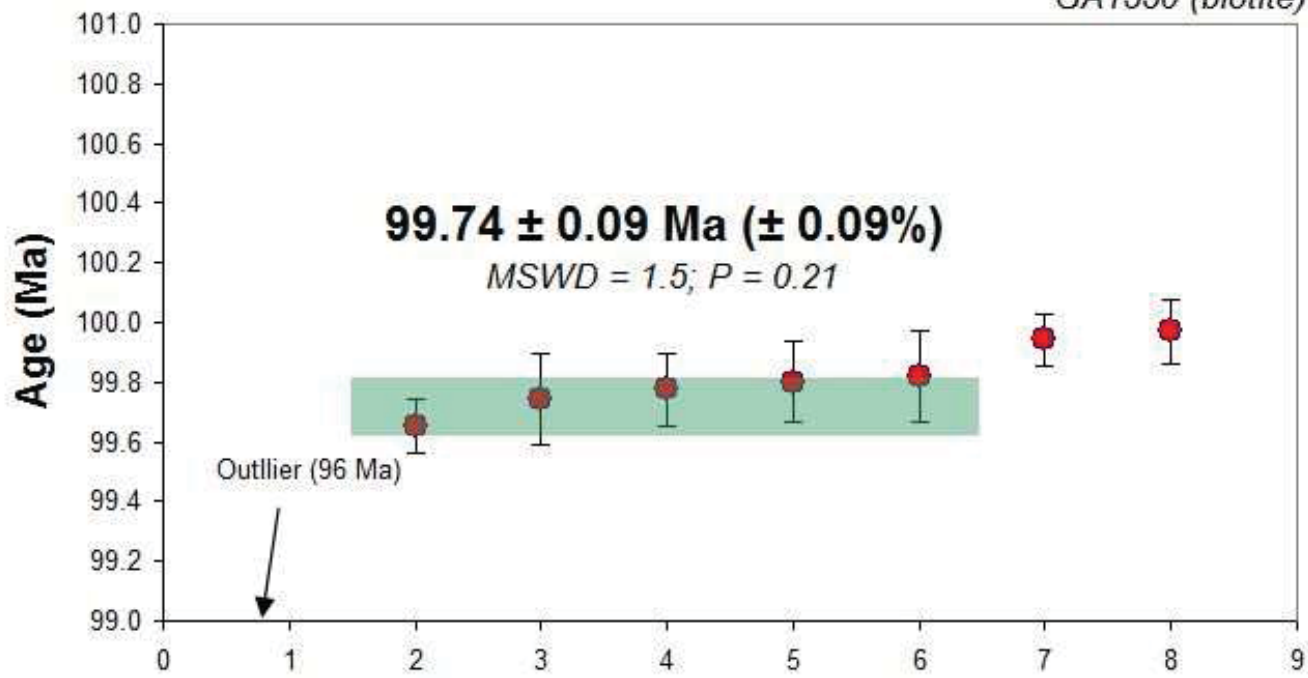
estimate the relative precision that would have been obtained by such an ultra-low K phase (ca. 0.05%; Verati and Jourdan 2014). To this instance, the total fusion age obtained on plagioclase, although having no geological meaning, yielded an error age of 90.14 ± 0.20 [0.23] Ma which corresponds to a relative precision of $\pm 0.22\%$ [$\pm 0.26\%$]. This should be however tempered by the fact that the plagioclase has been enriched by additional K during the alteration phase, and thus the present plagioclase tends toward the K-rich end member of the plagioclase solution, rather than an average value (cf. discussion in Verati and Jourdan 2014). Plagioclase is the most abundant phase in basalts, so it is expected that it will play an increasing dominant role in high-precision geochronology of Phanerozoic basalts, devoid of U-rich and K₂O rich crystals. ⁴⁰Ar/³⁹Ar dating of plagioclase extracted from flows and intrusions of large igneous provinces tends to show relative precisions ranging from $\pm 1\%$ to $\pm 0.6\%$ depending on the K/Ca ratio and K₂O concentration and when measured on a single-collector machine (e.g., Verati and Jourdan 2014 and references inside). Such a temporal resolution is sufficient in some cases to assess duration of the global magmatic activity (Jourdan et al. 2008; Sell et al. 2014) or episodic events with duration of more than 1 Ma, but is not sufficient to differentiate events that are several hundreds of ka apart (Jourdan et al. 2007). Our data show that the new generation of multi-collection noble gas instruments will provide a step-change in our understanding of mafic event, especially since most of the rocks, provided that they are fresh, will be accessible for ⁴⁰Ar/³⁹Ar geochronological investigations (i.e., as they contain K₂O). In addition, since the new generation of mass spectrometers have a much reduced volume and when coupled with a low-volume extraction line as used in this study, the relative sensitivity of the instrument increase drastically. As a consequence, this allows the analysis of a significantly lower volume of material (here we used 5 mg of crystals in both case), which is particularly useful when dredge rocks or thin continental flows have a limited amount of fresh material available.

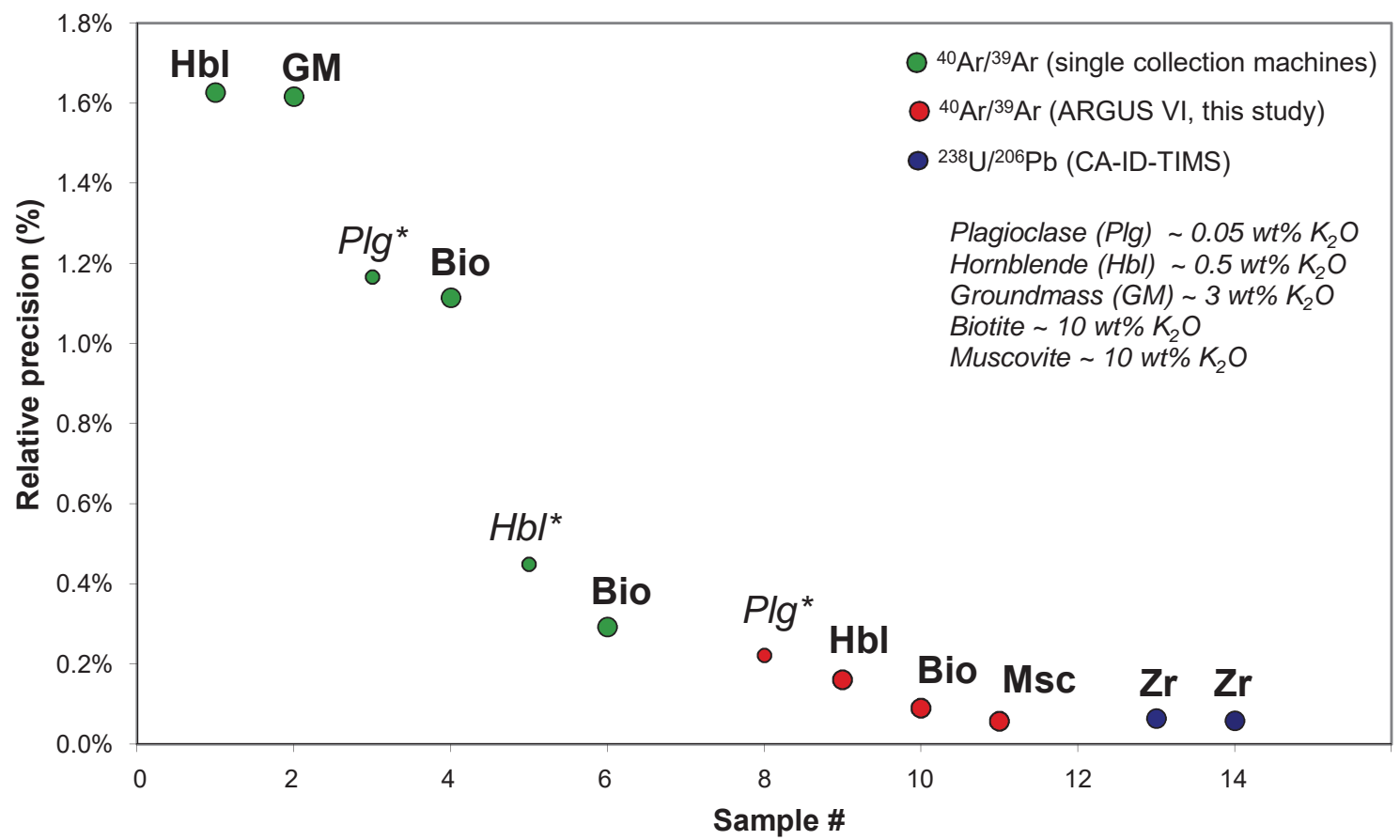
Figure A1: Single grain total fusion analyses of standards GA1550 (biotite) and WA1ms (muscovite) using the Argus VI instrument. An error of $\pm 0.07\%$ (2σ) on the J-value calculated by pooling the GA150 and WA1ms standards, is included on the calculated ages. The data have been ranked by increasing apparent age for a given J-value. The data not included in the calculation illustrate the neutron-fluence gradient in the analysed disc that is now apparent with the new generation of machine. The calculated age have no significance since these analyses are from two standards with known age and are used to calculate the J-value (McDougall and Harrison 1999) rather than any sample age, but this exercise illustrates rather well the capability of the ARGUS VI to obtain sub-permil precision on K₂O rich crystals.

Figure A2: Comparison of the relative age precision obtained with a single-collection vs. a multi-collection Argus VI instrument, using different materials. Also shown is the precision given by the chemical-abrasion isotopic dilution U-Pb technique (CA-ID-TIMS) on zircon. Selected single-collection ⁴⁰Ar/³⁹Ar data from table 1 and after Geldmacher et al. (2006) and Merle et al. (2009). Argus VI multi-collection ⁴⁰Ar/³⁹Ar data on plagioclase, amphibole, biotite and muscovite from this study. CA-ID-TIMS zircon (Zr) data from Wotzlaw et al. (2012) and Vennari et al. (2014) and have been both obtained using Earthtime spikes. Smaller circle, italic font and *, altogether indicate that the datum did not yield any plateau age and the uncertainty is derived from the equivalent total fusion (geologically meaningless) age.

References:

- Jourdan F, Féraud G, Bertrand H, Watkeys MK, Renne PR (2007) Distinct brief major events in the Karoo large igneous province clarified by new $^{40}\text{Ar}/^{39}\text{Ar}$ ages on the Lesotho basalts. *Lithos* 98:195-209.
- Jourdan F, Féraud G, Bertrand H, Watkeys MK, Renne PR (2008) The $^{40}\text{Ar}/^{39}\text{Ar}$ ages of the sill complex of the Karoo large igneous province: Implications for the Pliensbachian-Toarcian climate change. *Geochem Geophys Geosyst* 9:Q06009.
- Geldmacher J, Hoernle, K, Klügel A, Van den Bogaard P, Wombacher F, Berning B. (2006) Origin and geochemical evolution of the Tore-Madeira Rise (eastern North Atlantic). *J Geophys Res* B09206. doi:10.1029/2005JB003931.
- Matchan EL, Phillips D (2014) High precision multi-collector $^{40}\text{Ar}/^{39}\text{Ar}$ dating of young basalts: Mount Rouse volcano (SE Australia) revisited. *Quat Geochronol* 22:57-64.
- McDougall I, Harrison TM (1999) *Geochronology and Thermochronology by the $^{40}\text{Ar}/^{39}\text{Ar}$ Method*. Oxford University Press, Oxford.
- Merle R, Jourdan F, Marzoli A, Renne PR, Grange M, Girardeau J. (2009) Evidence of multi-phase Cretaceous to Quaternary alkaline magmatism on Tore-Madeira Rise and neighbouring seamounts from $^{40}\text{Ar}/^{39}\text{Ar}$ ages. *J Geol Soc London* 166:879-894.
- Phillips D, Matchan EL (2013) Ultra-high precision $^{40}\text{Ar}/^{39}\text{Ar}$ ages for Fish Canyon Tuff and Alder Creek Rhyolite sanidine: New dating standards required? *Geochim Cosmochim Acta* 121:229-239.
- Sell B, Ovtcharova M, Guex J, Bartolini A, Jourdan F, Spangenberg JE, Vicente JC, Schaltegger U (2014) Evaluating the temporal link between the Karoo LIP and climatic-biologic events of the Toarcian Stage with high-precision U-Pb geochronology. *Earth Planet Sci Lett* 408:48-56.
- Vennari VV, Lescano M, Naipauer M, Aguirre-Urreta B, Concheyro A, Schaltegger U, Armstrong R, Pimentel M, Ramos VA (2014) New constraints on the Jurassic-Cretaceous boundary in the High Andes using high-precision U-Pb data. *Gondwana Res* 26: 374-385.
- Verati C, Jourdan F (2014) Modelling effect of sericitization of plagioclase on the $^{40}\text{K}/^{40}\text{Ar}$ and $^{40}\text{K}/^{39}\text{Ar}$ chronometers: Implication for dating basaltic rocks and mineral deposits. In: Jourdan F, Mark D, Verati C, (eds) *Advances in $^{40}\text{Ar}/^{39}\text{Ar}$ Dating: from Archaeology to Planetary Sciences, vol 378*. Geological Society of London, pp 155-174 (Spec Publ).
- Wotzlaw JF, Bindeman IN, Schaltegger U, Brooks CK, Naslund HR (2012) High-resolution insights into episodes of crystallization, hydrothermal alteration and remelting in the Skaergaard intrusive complex. *Earth Planet Sci Lett* 355-356:199-212.





Age and geochemistry of magmatism on the oceanic Wallaby Plateau and implications for the opening of the Indian Ocean

Hugo K.H. Olierook^{1*}, Renaud E. Merle¹, Fred Jourdan^{1,2}, Keith Sircombe³, Geoff Fraser³, Nicholas E. Timms¹, Gabriel Nelson^{3,4}, Kelsie A. Dadd⁵, Laurent Kellerson⁵, and Irina Borissova³

¹Department of Applied Geology, Curtin University, GPO Box U1987, Perth, WA 6845, Australia

²Western Australian Argon Isotope Facility and John de Laeter Centre, Curtin University, GPO Box U1987, Perth, WA 6845, Australia

³Geoscience Australia, GPO Box 378, Canberra, ACT 2601, Australia

⁴FROGTECH, Suite 17F, Level 1, 2 King Street, Deakin West, ACT 2600, Australia

⁵Department of Earth and Planetary Sciences, Macquarie University, Sydney, NSW 2109, Australia

ABSTRACT

The temporal relationship between tectonic and volcanic activity on passive continental margins immediately before and after the initiation of mid-ocean ridge spreading is poorly understood because of the scarcity of volcanic samples on which to perform isotope geochronology. We present the first accurate geochronological constraints from a suite of volcanic and volcanioclastic rocks dredged from the 70,000 km² submerged Wallaby Plateau situated on the Western Australian passive margin. Plagioclase ⁴⁰Ar/³⁹Ar and zircon U-Pb sensitive high-resolution ion microprobe ages indicate that a portion of the plateau formed at ca. 124 Ma. These ages are at least 6 m.y. younger than the oldest oceanic crust in adjacent abyssal plains (minimum = 130 Ma). Geochemical data indicate that the Wallaby Plateau volcanic samples are enriched tholeiitic basalt, similar to continental flood basalts, including the spatially and temporally proximal Bunbury Basalt in southwestern Australia. Thus, the Wallaby Plateau volcanism could be regarded as a (small) flood basalt event on the order of 10⁴–10⁵ km³. We suggest that magma could not erupt prior to 124 Ma because of the lack of space adjacent to the plateau. Eruption was made possible at 124 Ma via the opening of the Indian Ocean during the breakup of Greater India and Australia along the Wallaby-Zenith Fracture Zone. The scale of volcanism and the temporal proximity to breakup challenges the prevailing theory that the Western Australian margin formed as a volcanic passive margin. Given that the volume of volcanism is too small for typical flood basalts associated with volcanic passive margins, we suggest that the two end members, magma-poor and volcanic passive margins, should rather be treated as a continuum.

INTRODUCTION

Passive margins are the locus of complex tectonic and magmatic processes leading from continental rifting to oceanic spreading. Understanding these processes is critical to deciphering how the continental lithosphere eventually breaks up and how the first oceanic lithosphere is generated by the mid-ocean ridge. Specifically, the tectonic and chronological mechanisms that drive the switch from rifting to spreading and how associated magmatism is generated are still not well constrained. Relatively little has been published on many of the known passive margins, in part due to the prohibitive cost associated with offshore sample recovery expeditions, including on the Western Australian passive margin that formed during the breakup of Greater India and Australia. The relict northeastern junction between Greater India and Australia is enigmatic. Evidence of seaward-dipping reflectors and high-velocity lower crust led researchers to consider this margin as a volcanic passive margin (Coffin and Eldholm, 1994; Goncharov and Nelson, 2012; Symonds et al., 1998). Esti-

mations of the volume of volcanic rocks are not well constrained, but such volume is probably on the order of 10⁴–10⁵ km³ (Goncharov and Nelson, 2012), which is not as voluminous as “true” volcanic passive margins (Courtillot et al., 1999; Franke, 2013). However, no high-quality geochronological data exist for offshore volcanic rocks along the Western Australian margin, and so the timing between breakup and magmatism remains poorly understood (Ludden, 1992; von Stackelberg et al., 1980). In this contribution, we present radioisotopic data on a set of volcanic and volcano-detrital rocks dredged from the Wallaby Plateau, a continental fragment that was once situated along the relict northeastern junction between Greater India and Australia prior to the breakup of eastern Gondwana. The data provide the first constraints on the timing of volcanism and new constraints on the geochemical composition of the Wallaby Plateau volcanic rocks associated with the continental breakup on the northeasternmost conjugate paleo-Greater Indian and paleo-Australian margins.

GEOLOGICAL SETTING

The Wallaby Plateau is a large bathymetric high with an areal extent of ~70,000 km², ~500 km off the northwest coast of Australia (Fig. 1)

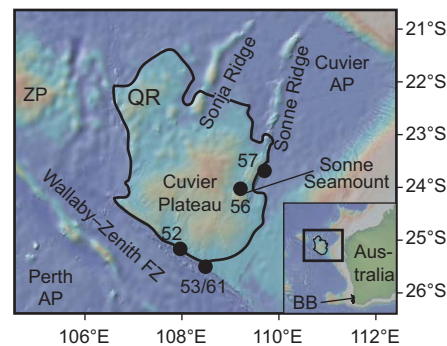


Figure 1. Bathymetric map of Wallaby Plateau (off northwest Australia) with geomorphic features and numbered sample sites (Daniell et al., 2009). BB—Bunbury Basalt; FZ—fracture zone; QR—Quokka Rise; AP—Abyssal Plain; ZP—Zenith Plateau.

(Daniell et al., 2009). The current understanding of the nature and evolution of the Wallaby Plateau is based largely on interpretations of seafloor-spreading magnetic anomalies (e.g., Gibbons et al., 2012; Mihut and Müller, 1998; Robb et al., 2005), seismic reflection profiles (e.g., Goncharov and Nelson, 2012; Rey et al., 2008), and dredge sampling data (Colwell et al., 1994; Daniell et al., 2009; von Stackelberg et al., 1980). These studies have indicated that the Wallaby Plateau is probably composed of continental crust thinned during lithospheric rifting, which is buried beneath a volcanic sequence, which is in turn overlain by a sedimentary capace (Daniell et al., 2009). Geochemical and paleontological studies of dredged rocks indicate a continental origin for the Wallaby Plateau, and the plateau is therefore interpreted as a continental fragment (Colwell et al., 1994; Stilwell et al., 2012; von Stackelberg et al., 1980).

The thick volcanic sequence overlying the continental basement is thought to have formed during a magmatic event located along the adjoining northwest-southeast-trending Wallaby-Zenith Fracture Zone (WZFF) (Mihut and Müller, 1998). Seaward-dipping reflectors interpreted on two-dimensional seismic reflection images indicate 320,000 km³ of volcanic flows interspersed with sedimentary strata (Goncharov and Nelson, 2012; Symonds et al., 1998). Volcanic rocks are estimated to comprise ~10%–90% of the total

*Current address: Department of Earth, Ocean and Ecological Sciences, University of Liverpool, 4 Brownlow Street, Liverpool L69 3GP, UK; E-mail: h.olierook@liverpool.ac.uk.

volume, which approximates to 10^4 – 10^5 km 3 . Interpretations from seafloor-spreading anomalies imply that this volcanism could either be rift related and coeval with breakup (Robb et al., 2005) or be pseudo-intraplate and postdate breakup by ~20–30 m.y. (Mihut and Müller, 1998). As there are no accurate ages for these volcanic rocks, it remains unknown whether the Wallaby Plateau volcanism occurred relatively quickly during breakup or during a prolonged and/or episodic period of volcanism after breakup.

RESULTS

Samples dredged from the seafloor on the Wallaby Plateau during the marine reconnaissance survey GA2746 in 2009 (Daniell et al., 2009) provide an opportunity to improve temporal constraints on magmatic activity along the rifted margin of northwest Australia. Zircons from three volcaniclastic samples were dated by the sensitive high-resolution ion microprobe (SHRIMP) U-Pb method, and plagioclase separates from three basaltic samples were dated by the $^{40}\text{Ar}/^{39}\text{Ar}$ method. Four samples were analyzed for major and trace element geochemistry.

SHRIMP U-Pb Geochronology of Detrital Zircons from the WZFZ

Three volcaniclastic samples from two dredge sites (sites 53 and 61; see Fig. 1; see Table DR1 in the GSA Data Repository¹ for full sample names) along the WZFZ <1 km apart were dated using zircon U-Pb SHRIMP. Zircons were separated using conventional techniques (see the Data Repository for analytical techniques).

The three samples display age clusters at ca. 124 Ma and scattered ages ranging from Paleozoic to Archean (Fig. 2). Zircon grains from volcaniclastic samples 53-1 and 53-2 from dredge site 53 yielded weighted average $^{206}\text{Pb}/^{238}\text{U}$ ages of 123.9 ± 1.0 Ma (mean square of weighted deviates [MSWD] = 1.0; P = 0.42) and 123.9 ± 1.3 Ma (MSWD = 1.8; P = 0.10), respectively (Fig. 2). The sample from dredge site 61 produced a similar apparent age range, with individual spot $^{206}\text{Pb}/^{238}\text{U}$ ages ranging from 118 to 134 Ma, but the MSWD and P-value of 4.9 and <0.001 indicate that the data are scattered beyond statistical expectation for a single population and thus a reliable weighted mean age could not be calculated.

In the three samples, the 14 analyses yielding Paleozoic, Proterozoic, and Archean ages indicate that the grains were derived from older continental sources, either directly available to sedimentary transport at the time of deposition or via recycling from preexisting sedimentary units.

¹GSA Data Repository item 2015328, tabulated U-Pb SHRIMP, $^{40}\text{Ar}/^{39}\text{Ar}$, and geochemistry results, zircon photomicrographs, and detailed analytical techniques, is available online at www.geosociety.org/pubs/ft2015.htm, or on request from editing@geosociety.org or Documents Secretary, GSA, P.O. Box 9140, Boulder, CO 80301, USA.

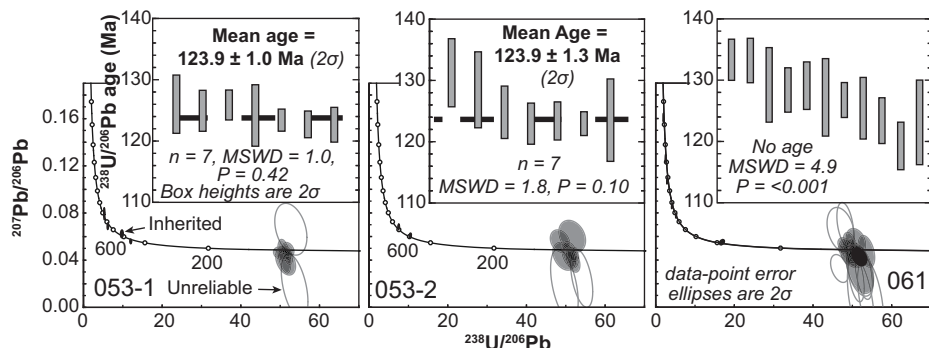


Figure 2. Tera-Wasserburg inverse concordia plots for zircon populations, where ages are in Ma. Insets show weighted average ages based on $^{206}\text{Pb}/^{238}\text{U}$ for zircons younger than 140 Ma. MSWD—mean square of weighted deviates.

$^{40}\text{Ar}/^{39}\text{Ar}$ Plagioclase Ages from the WZFZ, Sonne Ridge, and Sonne Seamount

Three plagioclase separates from basaltic samples of the Wallaby Plateau yielded statistically reliable $^{40}\text{Ar}/^{39}\text{Ar}$ plateau ages (Fig. 3; Table DR2; see the Data Repository). The first sample was collected along the WZFZ (46B from dredge site 52; Fig. 1). Two aliquots of plagioclase from this sample yielded plateau ages of 125.12 ± 0.90 Ma (MSWD = 0.99; P = 0.45) and 123.8 ± 1.0 Ma (MSWD = 1.80 P = 0.09) with at least 97% of the total ^{39}Ar released included

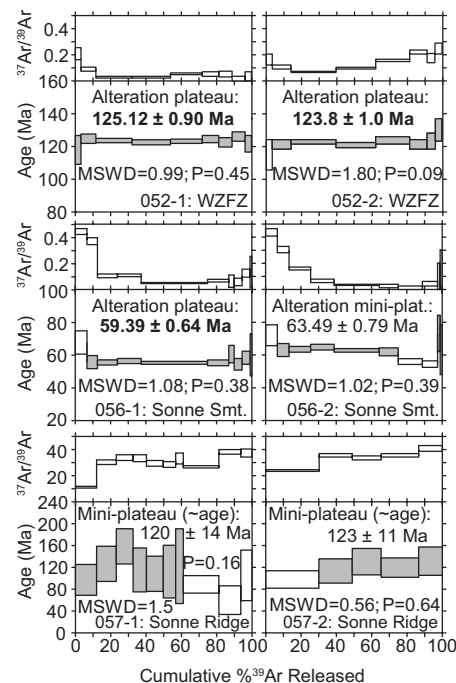


Figure 3. $^{40}\text{Ar}/^{39}\text{Ar}$ apparent age and related $^{37}\text{Ar}/^{39}\text{Ar}$ ratio spectra of plagioclase separates versus cumulative percentage of ^{39}Ar released. Steps included in plateau (>70% ^{39}Ar released) and mini-plateau (50%–70% ^{39}Ar released) age calculation are shaded gray. Errors on plateau and mini-plateau ages are quoted at 2σ . WZFZ—Wallaby-Zenith Fracture Zone; Smt.—Seamount; plat.—plateau; MSWD—mean square of weighted deviates.

in the plateau calculation (Fig. 3). A weighted mean age between the two aliquots yields an age of 124.53 ± 0.54 Ma for this sample. The $^{37}\text{Ar}/^{39}\text{Ar}$ ratio, a proxy for Ca/K, was abnormally low (~0.1; Fig. 3), which is incompatible with pure plagioclase and illustrates the quasi-complete sericitization of the crystals, a process commonly observed for altered basaltic samples (Verati and Jourdan, 2014). Therefore, this age is interpreted as the age of the alteration process (Verati and Jourdan, 2014) and thus provides a minimum age for the eruption of the basalt.

The second sample was collected on the Sonne Seamount (49B from dredge site 56; Fig. 1). Two aliquots of plagioclase from this sample yielded plateau and mini-plateau ages of 59.39 ± 0.64 Ma (MSWD = 1.08; P = 0.38) and 63.49 ± 0.79 Ma (MSWD = 1.02; P = 0.39), respectively, which include 94% and 69% of ^{39}Ar , respectively (Fig. 3). Similar to the previous sample, the $^{37}\text{Ar}/^{39}\text{Ar}$ ratio was abnormally low (~0.1; Fig. 3), which is interpreted to result from sericitic replacement of plagioclase, and thus these ages represent the age of the alteration event(s) and provide minimum ages for the timing of the eruption of the host basalt.

The third sample was recovered from the Sonne Ridge (51A from dredge site 57; Fig. 1). Two aliquots of plagioclase yielded imprecise mini-plateau apparent ages of 120 ± 14 Ma and 123 ± 11 Ma (Fig. 3) indicating an Early Cretaceous age for the Sonne Ridge samples, but the relatively poor resolution of the age spectra prevent detailed age comparison (Fig. 3).

Major and Trace Element Geochemistry from the WZFZ, Sonne Ridge, and Sonne Seamount

Two samples from the WZFZ (52 and 61), one sample from the Sonne Ridge (57), and one sample from the Sonne Seamount (56) were analyzed for major and trace elements (Table DR2; see the Data Repository). All samples are basaltic or slightly differentiated as shown by their low Mg content. Three of the samples show negative Nb and positive Pb anomalies,

which are characteristic of many continental flood basalts. Incompatible and rare earth element (REE) patterns are similar to those of enriched tholeiitic basalts such as enriched mid-oceanic ridge basalts (Fig. 4; Dadd et al., 2015). They are remarkably similar to that of the ca. 132 Ma Bunbury Basalt in southwestern Australia (Fig. 4) (Coffin et al., 2002; Frey et al., 1996). The sample from the Sonne Seamount presents a stronger light REE (LREE) enrichment relative to heavy REE (HREE) compared to the other samples, and shows positive Nb and negative Pb anomalies.

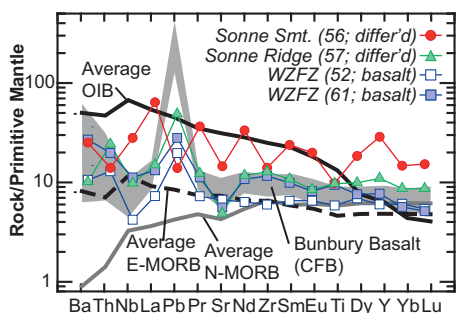


Figure 4. Primitive mantle–normalized incompatible element patterns. Primitive mantle normalization, average ocean island basalt (OIB), enriched mid-oceanic ridge basalt (E-MORB), and normal MORB (N-MORB) values from Sun and McDonough (1989). Bunbury Basalt data are from Frey et al. (1996). Smt.—Seamount; WZFZ—Wallaby-Zenith fracture zone; differ'd—differentiated; CFB—continental flood basalt.

DISCUSSION

The chronology of volcanism on the Wallaby Plateau as indicated by zircon and sericite/plagioclase isotopic ages provides new constraints on the duration of magmatism as Greater India drifted away from Australia. The concordant U-Pb ages from volcaniclastic detrital zircon indicate that an episode of volcanism occurred along the WZFZ at ca. 124 Ma on the edge of the Wallaby Plateau. The sericite minimum $^{40}\text{Ar}/^{39}\text{Ar}$ age of ≥ 124 Ma further west along the WZFZ confirms the importance of this volcanic phase along the WZFZ. Despite the sericitization age being very similar to the age recorded by the zircon and thus indicating strong hydrothermal activity at the time, we note that the true age of the basaltic eruption could range from being synchronous with the alteration process (cf. Jourdan et al., 2009) to up to a few million years older (Verati and Jourdan, 2014). Therefore, we can say with certainty that some of the Wallaby Plateau volcanic rocks formed at ca. 124 Ma, but the total duration of volcanism remains uncertain. The sericite $^{40}\text{Ar}/^{39}\text{Ar}$ age from the Sonne Seamount has indicated a much younger age of alteration of ≥ 60 Ma. As a result, the true age of the eruption remains elusive. The

Sonne Seamount sample could be related to the rest of the Wallaby Plateau volcanism at ca. 124 Ma and have been severely altered at ca. 60 Ma. However, the geochemistry of the Sonne Seamount is more typical of an ocean island basalt (Fig. 4). Alternatively, we note that the closest magmatic occurrences of ca. 60 Ma are located in the Christmas Island Seamount Province (CHRISP; Hoernle et al., 2011), which was, at the time, only a few hundred kilometers away from the Sonne Seamount, suggesting a possible connection between the two. In any case, the difference in age and chemistry points to a distinct origin for the Sonne Seamount relative to the rest of the Wallaby Plateau.

The age of the bordering oceanic crust in adjacent abyssal plains is significantly older than that of the 124 Ma Wallaby Plateau volcanic rocks, taking into account the uncertainties associated with the ages of the magnetic anomalies. Although most authors agree that the oldest magnetic anomalies adjacent to the Wallaby Plateau are M11 (Perth Abyssal Plain) and M10 (Cuvier Abyssal Plain), in the absence of isotopic ages, there is current debate about the absolute ages of these chronos, ranging from 136 to 132 Ma (M11) and 134 to 130 Ma (M10) (cf. Heine et al., 2013). In any case, some portion of the volcanic rocks on the Wallaby Plateau erupted at least 6 m.y. after the onset of oceanic spreading, although the initiation of the volcanism on the plateau could have happened a few million years earlier.

Furthermore, we showed that the Wallaby Plateau has rocks with enriched compositions similar to that of continental tholeiitic basalt (Fig. 4). Such geochemical signatures clearly point to the involvement of continental material during the melt generation for the Wallaby Plateau volcanic rocks, either by contamination of the basaltic melts ascending through the continental lithosphere or by derivation from a fertile subcontinental lithospheric mantle. Temporally and spatially, the closest known basalt with similar geochemical signatures is the ca. 132 Ma Bunbury Basalt in southwestern Australia (Fig. 4) (Coffin et al., 2002), although it only has a volume of $\sim 10^2 \text{ km}^3$ (Oliver et al., 2015). The Bunbury Basalt and volcanism on the Wallaby Plateau have a similar composition despite an

8 m.y. gap, suggesting that both eruptive processes share some affinities. Nevertheless, the volumetric approximations for the Wallaby Plateau volcanism are two to three orders of magnitude greater than for the Bunbury Basalt flood basalt (Goncharov and Nelson, 2012). Plate reconstruction models indicate that the position of the dredge samples along the WZFZ coincide with the opening of the Indian Ocean along this major lithospheric discontinuity (Gibbons et al., 2012; Hall et al., 2013) (Fig. 5). This would imply that while the Bunbury Basalt volcanism was restricted to southwest Australia at ca. 132 Ma, the Wallaby Plateau could have initiated only when space opened sufficiently at ca. 124 Ma that could allow basaltic lavas to flow freely along the WZFZ and over the Wallaby Plateau. The sericite age of 124 Ma could be explained by intense hydrothermal activity associated with the magmatism along the WZFZ.

Incubation of a mantle plume head underneath the lithosphere could provide an origin for the Wallaby Plateau volcanism that is consistent with the volcanic rock geochemistry (e.g., Xu et al., 2014). Upwelling plume material is stored at the base of the thick continental lithosphere below its solidus before continental breakup. This plume can only rise after breakup, crossing its solidus and melting by decompression. This provides an alternative mechanism to generate plume-type magmatism after continental breakup and is probably the direct consequence of mantle melting caused by plate breakup.

Despite $10^4\text{--}10^5 \text{ km}^3$ of basalt on the Wallaby Plateau, these contiguous margins are still like neither magma-poor (e.g., Iberia-Newfoundland, $<10^3 \text{ km}^3$) nor volcanic passive margins (e.g., East Greenland, $10^6\text{--}10^7 \text{ km}^3$) (Courtillot et al., 1999; Eldholm and Grue, 1994). We suggest that magma-poor and volcanic passive margins are only “end members” of a continuous spectrum for continental breakup. The age, geochemistry, and volume of the Wallaby Plateau volcanic rocks indicate that intermediate levels of volcanism exist within what we suggest should be a continuum between the two end members.

CONCLUSIONS

New zircon U-Pb and $^{40}\text{Ar}/^{39}\text{Ar}$ ages of volcaniclastic and volcanic rocks at 124 Ma along

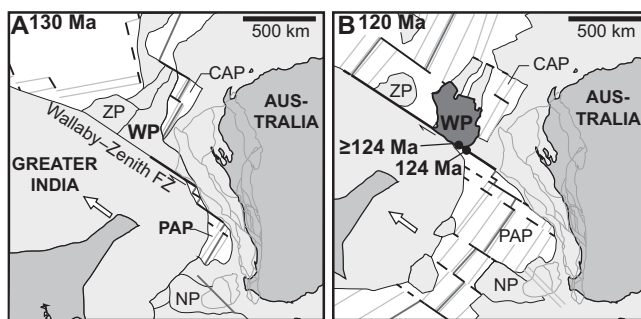


Figure 5. Plate reconstructions during breakup of Greater India from Austral-Antarctic portion of Gondwana, modified from Gibbons et al. (2012) and Hall et al. (2013). CAP—Cuvier Abyssal Plain; PAP—Perth Abyssal Plain; ZP—Zenith Plateau; WP—Wallaby Plateau; NP—Naturaliste Plateau; FZ—fracture zone.

the WZFZ indicate a significant magmatic event shortly after the onset of seafloor spreading. Geochemical and volume constraints indicate that the Wallaby Plateau volcanic rocks are part of a small continental flood basalt province with a volume of 10^4 – 10^5 km 3 . Known plate reconstruction constraints imply that this volcanism occurred when space was generated as the northeastern Indian Ocean opened adjacent to the Wallaby Plateau, potentially by means of an incubating plume. These intermediary volumes of continental flood basalts related to continental breakup challenge the prevailing theory that passive margins are either magma poor or volcanic. We suggest that a continuum between these end members is far more suitable.

ACKNOWLEDGMENTS

We would like to thank the shipboard crew from Geoscience Australia marine reconnaissance survey GA2476 aboard the RV *Sonne* that dredged the rocks used in this study, and the German Ministry of Education and Research for funding the RV *Sonne*. This is contribution 633 of the ARC Centre of Excellence for Core to Crust Fluid Systems (www.ccfs.mq.edu.au) and 1014 of the GEMOC Key Centre (www.gemoc.mq.edu.au). The analytical data were obtained using instrumentation funded by DEST Systemic Infrastructure Grants, ARC LIEF, NCRIS, industry partners, Macquarie University, and Curtin University. We also thank S. Planke, J. O’Conner, and three anonymous reviewers for significantly improving the manuscript.

REFERENCES CITED

- Coffin, M.F., and Eldholm, O., 1994, Large igneous provinces: Crustal structure, dimensions, and external consequences: *Reviews of Geophysics*, v. 32, p. 1–36, doi:10.1029/93RG02508.
- Coffin, M.F., Pringle, M.S., Duncan, R.A., Gladzenko, T.P., Storey, M., Müller, R.D., and Gaghan, L.A., 2002, Kerguelan hotspot magma output since 130 Ma: *Journal of Petrology*, v. 43, p. 1121–1137, doi:10.1093/petrology/43.7.1121.
- Colwell, J.B., Symonds, P.A., and Crawford, A.J., 1994, The nature of the Wallaby (Cuvier) Plateau and other igneous provinces of the west Australian margin: *AGSO Journal of Australian Geology & Geophysics*, v. 15, p. 137–156.
- Courtillot, V.E., Jaupart, C., Manighetti, I., Tapponnier, P., and Besse, J., 1999, On causal links between flood basalts and continental breakup: *Earth and Planetary Science Letters*, v. 166, p. 177–195, doi:10.1016/S0012-821X(98)00282-9.
- Dadd, K.A., Kellerson, L., Borissova, I., and Nelson, G., 2015, Multiple sources for volcanic rocks dredged from the Western Australian rifted margin: *Marine Geology*, v. 368, p. 42–52, doi:10.1016/j.margeo.2015.07.001.
- Daniell, J., et al., 2009, Frontier basins of the west Australian continental margin: Post-survey report of marine reconnaissance and geological sampling survey GA2476: *Geoscience Australia Record* 2009/38, 229 p.
- Eldholm, O., and Grue, K., 1994, North Atlantic volcanic margins: Dimensions and production rates: *Journal of Geophysical Research*, v. 99, p. 2955–2968, doi:10.1029/93JB02879.
- Franke, D., 2013, Rifting, lithosphere breakup and volcanism: Comparison of magma-poor and volcanic rifted margins: *Marine and Petroleum Geology*, v. 43, p. 63–87, doi:10.1016/j.marpetgeo.2012.11.003.
- Frey, F.A., McNaughton, N.J., Nelson, D.R., deLáeter, J.R., and Duncan, R.A., 1996, Petrogenesis of the Bunbury Basalt, Western Australia: Interaction between the Kerguelan plume and Gondwana lithosphere?: *Earth and Planetary Science Letters*, v. 144, p. 163–183, doi:10.1016/0012-821X(96)00150-1.
- Gibbons, A.D., Barckhausen, U., van den Bogaard, P., Hoernle, K., Werner, R., Whittaker, J.M., and Müller, R.D., 2012, Constraining the Jurassic extent of Greater India: Tectonic evolution of the West Australian margin: *Geochemistry Geophysics Geosystems*, v. 13, Q05W13, doi:10.1029/2011GC003919.
- Goncharov, A., and Nelson, G., 2012, From two way time to depth and pressure for interpretation of seismic velocities offshore: Methodology and examples from the Wallaby Plateau on the West Australian margin: *Tectonophysics*, v. 572–573, p. 26–37, doi:10.1016/j.tecto.2012.06.037.
- Hall, L.S., Gibbons, A.D., Bernardel, G., Whittaker, J.M., Nicholson, C., Rollet, N., and Müller, R.D., 2013, Structural architecture of Australia’s southwest continental margin and implications for Early Cretaceous basin evolution, in *Proceedings, West Australian Basin Symposium 2013*, Perth, Australia, 18–21 August: 22 p., http://www.earthbyte.org/Resources/Pdf/Hall_etal_WABS2013.pdf.
- Heine, C., Zoethout, J., and Müller, R.D., 2013, Kinematics of the South Atlantic rift: Solid Earth Discussions, v. 5, p. 41–116, doi:10.5194/sed-5-41-2013.
- Hoernle, K., Hauff, F., Werner, R., van den Bogaard, P., Gibbons, A.D., Conrad, S., and Müller, R.D., 2011, Origin of Indian Ocean Seamount Province by shallow recycling of continental lithosphere: *Nature Geoscience*, v. 4, p. 883–887, doi:10.1038/ngeo1331.
- Jourdan, F., Marzoli, A., Bertrand, H., Cirilli, S., Tanner, L.H., Kontak, D.J., McHone, G., Renne, P.R., and Bellieni, G., 2009, $^{40}\text{Ar}/^{39}\text{Ar}$ ages of CAMP in North America: Implications for the Triassic-Jurassic boundary and the ^{40}K decay constant bias: *Lithos*, v. 110, p. 167–180, doi:10.1016/j.lithos.2008.12.011.
- Ludden, J.N., 1992, Radiometric age determinations for basement from sites 765 and 766, Argo Abyssal Plain and northwestern Australian margin, in Gradstein, F.M., and Ludden, J.N., eds., *Proceedings of Ocean Drilling Program, Scientific Results, Volume 123: College Station, Texas, Ocean Drilling Program*, p. 557–559, doi:10.2973/odp.proc.sr.123.162.1992.
- Mihut, D., and Müller, R.D., 1998, Volcanic margin formation and Mesozoic rift propagators in the Cuvier Abyssal Plain off Western Australia: *Journal of Geophysical Research*, v. 103, p. 27,135–27,149, doi:10.1029/97JB02672.
- Olierook, H.K.H., Timms, N.E., Merle, R.E., Jourdan, F., and Wilkes, P.G., 2015, Paleo-drainage and fault development in the southern Perth Basin, Western Australia during and after the breakup of Gondwana from 3D modelling of the Bunbury Basalt: *Australian Journal of Earth Sciences*, v. 62, p. 289–305, doi:10.1080/08120099.2015.1030774.
- Rey, S.S., Planke, S., Symonds, P.A., and Faleide, J.I., 2008, Seismic volcanostratigraphy of the Gascoyne margin, Western Australia: *Journal of Volcanology and Geothermal Research*, v. 172, p. 112–131, doi:10.1016/j.jvolgeores.2006.11.013.
- Robb, M.S., Taylor, B., and Goodliffe, A.M., 2005, Re-examination of the magnetic lineations of the Gascoyne and Cuvier Abyssal Plains, off NW Australia: *Geophysical Journal International*, v. 163, p. 42–55, doi:10.1111/j.1365-246X.2005.02727.x.
- Stilwell, J.D., Quilty, P.G., and Mantle, D.J., 2012, Paleontology of Early Cretaceous deep-water samples dredged from the Wallaby Plateau: New perspectives of Gondwana break-up along the Western Australian margin: *Australian Journal of Earth Sciences*, v. 59, p. 29–49, doi:10.1080/08120099.2011.615864.
- Sun, S.-s., and McDonough, W.F., 1989, Chemical and isotopic systematics of oceanic basalts: Implications for mantle composition and processes, in Saunders, A.D., and Norry, M.J., eds., *Magma in the Ocean Basins: Geological Society of London Special Publication 42*, p. 313–345, doi:10.1144/GSL.SP.1989.042.01.19.
- Symonds, P.A., Planke, S., Frey, Ø., and Skogseid, J., 1998, Volcanic evolution of the western Australian continental margin and its implications for basin development, in Purcell, P.G., and Purcell, R.R., eds., *The Sedimentary Basins of Western Australia 2: Proceedings of Petroleum Exploration Society of Australia Symposium*: Perth, Petroleum Exploration Society of Australia, p. 33–54.
- Verati, C., and Jourdan, F., 2014, Modelling effect of sericitization of plagioclase on the $^{40}\text{K}/^{40}\text{Ar}$ and $^{40}\text{K}/^{39}\text{Ar}$ chronometers: Implication for dating basaltic rocks and mineral deposits, in Jourdan, F., et al., eds., *Advances in $^{40}\text{Ar}/^{39}\text{Ar}$ Dating: From Archaeology to Planetary Sciences: Geological Society of London Special Publication 378*, p. 155–174, doi:10.1144/SP378.14.
- von Stackelberg, U., Exon, N.F., von Rad, U., Quilty, P., Shafuk, S., Beiersdorf, H., Seibertz, E., and Veevers, J.J., 1980, Geology of the Exmouth and Wallaby Plateaus off northwest Australia: Sampling of seismic consequences: *AGSO Journal of Australian Geology & Geophysics*, v. 5, p. 113–140.
- Xu, Y.-G., Wei, X., Luo, Z.-Y., Liu, H.-Q., and Cao, J., 2014, The Early Permian Tarim Large Igneous Province: Main characteristics and a plume incubation model: *Lithos*, v. 204, p. 20–35, doi:10.1016/j.lithos.2014.02.015.

Manuscript received 5 June 2015

Revised manuscript received 25 August 2015

Manuscript accepted 26 August 2015

Printed in USA

Sr, Nd, Pb and Os Isotope Systematics of CAMP Tholeiites from Eastern North America (ENA): Evidence of a Subduction-enriched Mantle Source

RENAUD MERLE¹*, ANDREA MARZOLI¹, LAURIE REISBERG², HERVÉ BERTRAND³, ALEXANDER NEMCHIN⁴, MASSIMO CHIARADIA⁵, SARA CALLEGARO¹, FRED JOURDAN⁴, GIULIANO BELLINI¹, DAN KONTAK⁶, JOHN PUFFER⁷ AND J. GREGORY McHONE⁸

¹DIPARTIMENTO DI GEOSCIENZE, UNIVERSITÀ DI PADOVA, IGG-CNR PADOVA, VIA GRADENIGO 6, 35100 PADOVA, ITALY

²CENTRE DE RECHERCHES PETROGRAPHIQUES ET GEOCHIMIQUES (CRPG/CNRS), BP 20, 54501 VANDOEUVRE-LES-NANCY CEDEX, FRANCE

³LABORATOIRE DE GEOLOGIE DE LYON, UMR-CNRS 5276, UNIVERSITE DE LYON 1 AND ENS LYON, 46 ALLEE D'ITALIE, 69364 LYON CEDEX 07, FRANCE

⁴DEPARTMENT OF APPLIED GEOLOGY, CURTIN UNIVERSITY, GPO BOX U1987, PERTH, WA 6845, AUSTRALIA

⁵SECTION DES SCIENCES DE LA TERRE, UNIVERSITÉ DE GENÈVE, 13 RUE DES MARAÎCHERS, 1201 GENÈVE, SWITZERLAND

⁶DEPARTMENT OF EARTH SCIENCES, LAURENTIAN UNIVERSITY, 935 RAMSEY LAKE ROAD, SUDBURY, ON, CANADA

⁷DEPARTMENT OF EARTH AND ENVIRONMENTAL SCIENCES, RUTGERS UNIVERSITY, SMITH HALL, NEWARK, NJ 07102, USA

⁸9 DEXTERS LANE, GRAND MANAN, NB E5G 3A6, CANADA

**RECEIVED JUNE 4, 2012; ACCEPTED SEPTEMBER 30, 2013
ADVANCE ACCESS PUBLICATION NOVEMBER 21, 2013**

The Central Atlantic Magmatic Province (CAMP) is one of the largest igneous provinces on Earth, with an areal extent exceeding 10^7 km^2 . Here we document the geochemical characteristics of CAMP basalts from Triassic–Jurassic basins in northeastern USA and Nova Scotia (Canada). The CAMP rocks occur as lava flows, sills and dykes. All of our analysed samples show chemical characteristics typical of CAMP basalts with low titanium content, which include enrichment in the most incompatible elements and negative Nb anomalies. All the basalts also show enriched Sr–Nd–Pb initial

($t = 201 \text{ Ma}$) isotopic compositions ($^{206}\text{Pb}/^{204}\text{Pb}_{\text{ini}} = 18.155$ – 18.691 , $^{207}\text{Pb}/^{204}\text{Pb}_{\text{ini}} = 15.616$ – 15.668 , $^{208}\text{Pb}/^{204}\text{Pb}_{\text{ini}} = 38.160$ – 38.616 , $^{143}\text{Nd}/^{144}\text{Nd}_{\text{ini}} = 0.512169$ – 0.512499). On the basis of stratigraphy, rare earth element (REE) chemistry and Sr–Nd–Pb isotope composition, three chemical groups are defined. The Hook Mountain group, with the lowest La/Yb ratios, initial $^{206}\text{Pb}/^{204}\text{Pb}_{\text{ini}} > 18.5$ and $^{143}\text{Nd}/^{144}\text{Nd}_{\text{ini}} > 0.51238$, comprises all the lastest and upper stratigraphic units. The Preakness group, with intermediate La/Yb ratios, $^{206}\text{Pb}/^{204}\text{Pb}_{\text{ini}} > 18.5$ and

*Corresponding author. Present address: Department of Applied Geology, Curtin University, GPO Box U1987, Perth, WA 6845, Australia. E-mail: r.merle@curtin.edu.au

© The Author 2013. Published by Oxford University Press. All rights reserved. For Permissions, please e-mail: journals.permissions@oup.com

$0.51233 > {}^{143}\text{Nd}/{}^{144}\text{Nd}_{\text{ini}} > 0.51225$, comprises the intermediate units. The Orange Mountain group has the highest La/Yb ratios and ${}^{143}\text{Nd}/{}^{144}\text{Nd}_{\text{ini}} < 0.51235$ and involves all the earliest and stratigraphically lowest units, including the entire North Mountain basalts from Nova Scotia. In this last group, three sub-groups may be distinguished: the Rapidan sill, which has ${}^{206}\text{Pb}/{}^{204}\text{Pb}_{\text{ini}}$ higher than 18.5, the Shelburne sub-group, which has ${}^{143}\text{Nd}/{}^{144}\text{Nd}_{\text{ini}} < 0.51225$, and the remaining Orange Mt samples. With the exception of one sample, the Eastern North America (ENA) CAMP basalts display initial ${}^{187}\text{Os}/{}^{188}\text{Os}$ ratios in the range of mantle-derived magmas (< 0.15). Simple modelling shows that the composition of the ENA CAMP basalts cannot plausibly be explained solely by crustal contamination of oceanic island basalt (OIB), mid-ocean ridge basalt (MORB) or oceanic plateau basalt (OPB) magmas. Mixing of such magma compositions with sub-continental lithospheric mantle (SCLM)-derived melts followed by crustal contamination, by either assimilation-fractional crystallization (AFC) or assimilation through turbulent ascent (ATA) processes is somewhat more successful. However, this latter scenario does not reproduce the REE and isotopic composition of the ENA CAMP in a fully satisfactory manner. Alternatively, we propose a model in which asthenospheric mantle overlying a subducted slab (i.e. mantle wedge) was enriched during Cambrian to Devonian subduction by sedimentary material, isotopically equivalent to Proterozoic-Lower Paleozoic crustal rocks. Subsequently, after subduction ceased, the isotopic composition of this mantle evolved by radioactive decay for another 170 Myr until the CAMP magmatic event. Varying amounts and compositions of the incorporated sedimentary component coupled with radiogenic ingrowth over time can account for the main geochemical characteristics of the ENA CAMP (enriched incompatible element patterns, negative Nb anomalies, enriched Sr-Nd-Pb isotopic composition) and the differences between the three chemical groups.

KEY WORDS: flood basalt; subcontinental lithospheric mantle; Re-Os isotopes

INTRODUCTION

The Central Atlantic Magmatic Province (CAMP, Marzoli *et al.*, 1999) is one of the largest continental flood basalt (CFB) provinces on Earth. The CAMP extends for more than 7500 km from north to south, exceeds 10^7 km^2 and is distributed over four continents on both sides of the central Atlantic Ocean (Fig. 1; Marzoli *et al.*, 1999; McHone, 2003). The CAMP is dominated by low-titanium (low-Ti, with TiO_2 contents lower than 2%), and rare high-titanium (high-Ti), basaltic dykes, sills and remnants of more extensive lava flows that are now preserved in Triassic-Jurassic basins (Olsen *et al.*, 2003). This magmatic event mainly occurred at the Triassic-Jurassic boundary at ~ 201 Ma, as constrained mostly by ${}^{40}\text{Ar}/{}^{39}\text{Ar}$ ages [recalibrated using the decay constants proposed by Renne *et al.* (2010); see Marzoli *et al.* (2011)]. However,

magmatism may also have occurred in distinct pulses spaced over a few million years, with the latest volcanic activity lasting until ~ 190 Ma (Sebai *et al.*, 1991; Deckart *et al.*, 1997; Marzoli *et al.*, 1999, 2004, 2011; Knight *et al.*, 2004; Nomade *et al.*, 2007; Verati *et al.*, 2007; Jourdan *et al.*, 2009). The CAMP event is linked to the break-up of Pangaea, which resulted in incipient opening of the Central Atlantic Ocean in the Florida-Guyana-Guinea area, pre-dating by ~ 10 Myr the opening of the ocean between the Morocco-Mauritania and Nova Scotia-northern USA conjugate margins (Sahabi *et al.*, 2004).

The genesis of CAMP magmatism remains controversial (e.g. Bertrand *et al.*, 1982; Alibert, 1985; Dupuy *et al.*, 1988; Pegram, 1990; Bertrand, 1991; Sebai *et al.*, 1991; Deckart *et al.*, 1997; Marzoli *et al.*, 1999; Hames *et al.*, 2000; McHone, 2000; Cebria *et al.*, 2003; De Min *et al.*, 2003; Jourdan *et al.*, 2003; Verati *et al.*, 2005; Nomade *et al.*, 2007) as is true for many other CFB provinces. It has been proposed that CAMP magmatism may have been induced either by a plume head under the continental lithosphere (May, 1971; Morgan, 1983; White & McKenzie, 1989; Hill, 1991; Wilson, 1997; Courtillot *et al.*, 1999; Ernst & Buchan, 2002; Cebria *et al.*, 2003) or by heat incubation under thick continental lithosphere, possibly coupled with edge-driven convection generated by the thickness contrast of different lithospheric domains (McHone, 2000; De Min *et al.*, 2003; Puffer, 2003; McHone *et al.*, 2005; Verati *et al.*, 2005; Coltice *et al.*, 2007).

Understanding the genetic relationship of the CAMP magmatism with continental rifting and possibly with mantle plume impingement requires identification of its source(s), notably through the use of isotopic tracers. A recent Sr-Nd-Pb-Os isotopic study of Brazilian CAMP basalts from the western part of the Maranhão basin failed to identify a clear plume source component, but instead suggested that the low-Ti basaltic melts were derived mainly from a shallow mantle source with the geochemical characteristics of subduction-metasomatized sub-continental lithospheric mantle (SCLM; Merle *et al.*, 2011). This study raises the question of whether the specific geological setting of the Maranhão basin, in which small volumes of magma erupted over 700 km from the Atlantic margin and 2000 km from the first Pangaea break-up site, promoted the local melting of the most fusible portions of the SCLM or whether a shallow SCLM-like source can be identified on a large (supercontinent) scale.

To further evaluate the mechanism of basalt magma generation and its source, in particular where the volume is substantial, we selected CAMP basalts occurring in the Triassic-Jurassic Eastern North American (ENA) basins. They are situated along 1000 km of the Atlantic margin. This sampling represents a transect across a large area of the CAMP providing a large range of chemical types. The study area includes Connecticut, Massachusetts, New

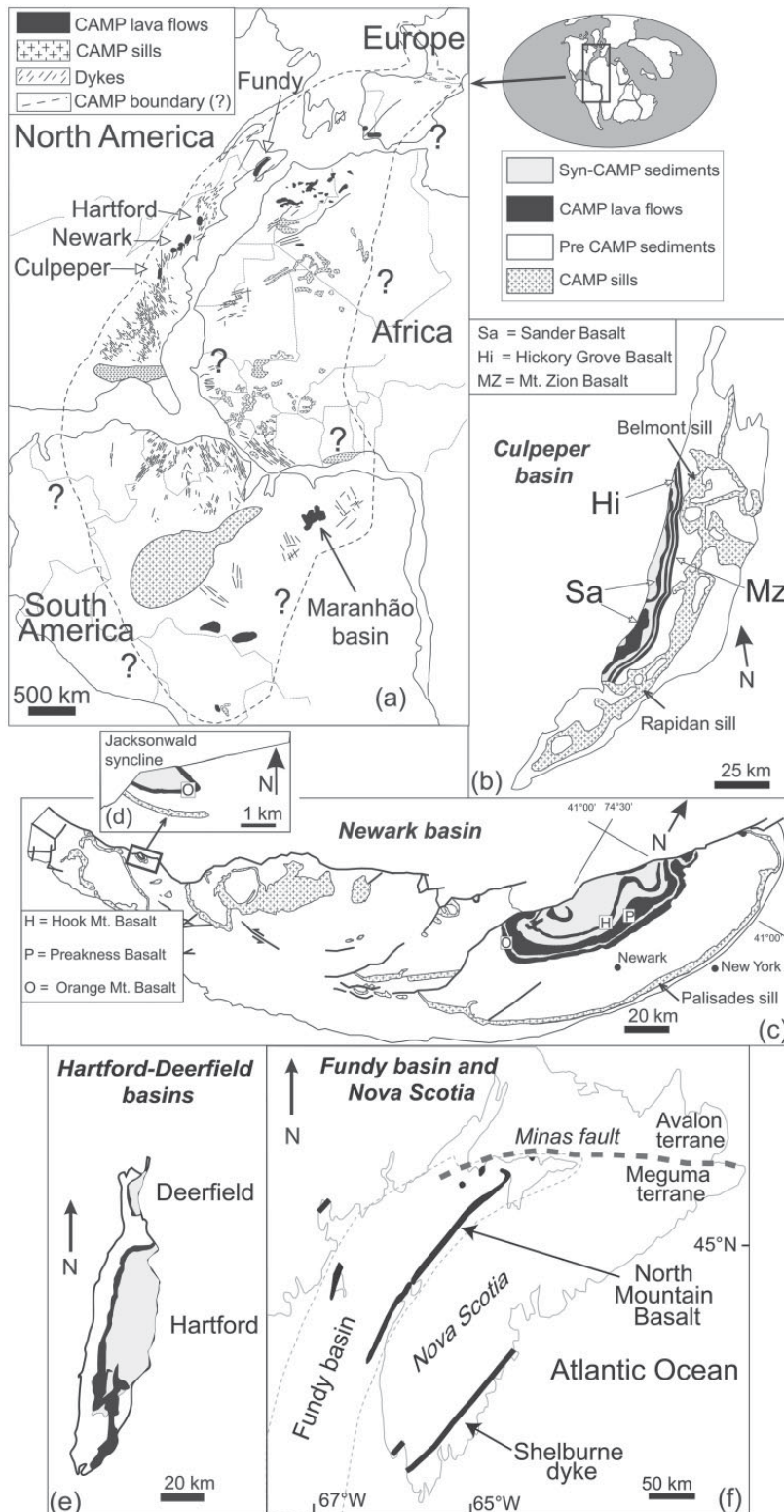


Fig. 1. (a) General map of the circum-Atlantic region at the time of CAMP emplacement and Pangea break-up [~200 Ma; modified after Deckart *et al.* (2005)]. Schematic maps of the Culpeper (b), Newark (c), and Hartford-Deerfield (e) basins of the eastern USA. Inset (d) shows the Jacksonwald syncline where Orange Mountain basalt (NEW133) was sampled. (f) Schematic map of the Fundy basin of Nova Scotia showing extent of the North Mountain Basalt and dykes (e.g. Shelburne).

Jersey and Virginia in the eastern USA and Nova Scotia in eastern Canada. In these areas, the basalts occur as three successive lava flow units with associated sills and feeder dykes, separated by thick layers of sedimentary rocks of latest Triassic to earliest Jurassic age (e.g. Webster *et al.*, 2006; Kontak, 2008; Cirilli *et al.*, 2009; Marzoli *et al.*, 2011). The few Sr–Nd–Pb isotopic studies on the ENA CAMP basalts have suggested derivation from an SCLM-type source (Pegram, 1990; Puffer, 1992; Heatherington & Mueller, 1999; Murphy *et al.*, 2011). However, these studies were provincial in extent and, therefore, did not provide an assessment of the possibility of chemical variation along the entire ENA. Moreover, these studies did not investigate the time-related isotopic variations between the various flow units and their potential sources [SCLM-like source, asthenosphere, ocean island basalt (OIB)-type mantle].

This study presents a comprehensive Sr–Nd–Pb–Os isotopic investigation of the entire ENA CAMP sub-province, which includes the first Pb isotopic data for the Nova Scotian CAMP basalts and the first Os isotopic data for any basalts in the North American CAMP.

Geological setting and previous results

The ENA CAMP basaltic rocks sampled occur onshore in Triassic–Jurassic rifted basins from Nova Scotia (Canada) to Virginia (USA). They include, from south to north, the Culpeper, Newark and Hartford basins in the USA, and the Fundy basin in Nova Scotia (Figs 1 and 2). These basins formed during the early stages of extensional activity preceding the breakup of Pangaea during the late Triassic–early Jurassic and are filled with fluvial–lacustrine sedimentary rocks of Late Triassic to Early Jurassic age (e.g. Olsen *et al.*, 2003).

The local continental crust

The Triassic–Jurassic rifting event affected a very complex continental crust that was assembled during the Grenvillian (\sim 1300–1000 Ma) and Appalachian–Ouachita orogenies (\sim 500–270 Ma). This crust was formed by the successive accretion of parallel slivers during the Late Precambrian to the Palaeozoic (e.g. Thomas, 2004, for an overview). The most landward terranes, of Grenvillian age, formed the Laurentia margin during the Appalachian–Ouachita orogeny. This orogeny involved successive, diachronous Taconic (\sim 485–420 Ma), Acadian (\sim 420–320 Ma) and Alleghanian (\sim 320–270 Ma) phases culminating in closure of the Iapetus and Rheic Oceans and Pangaea assembly (e.g. Drake *et al.*, 1989; Hatcher *et al.*, 1989; Osberg *et al.*, 1989; Van Staal *et al.*, 1998; Hibbard *et al.*, 2002). These phases are related to the accretion of peri-Laurentian and peri-Gondwanan ribbon-shaped micro-continental masses (including magmatic arcs) to the Laurentian margin, which are now found from Cape Breton Island and Newfoundland to Alabama (e.g. Murphy & Nance, 2002; Hibbard *et al.*, 2007; Van Staal

et al., 2009). All of these terranes are formed of highly diverse Mesoproterozoic to Late Palaeozoic lithologies, which include reworked Grenvillian meta-igneous and metasedimentary rocks. They are intruded by several generations of mafic and calc-alkaline felsic magmatic suites formed during Palaeozoic extensional and subduction-related magmatic phases (e.g. Ayuso & Bevier, 1991; Barr & Hegner, 1992; Whalen *et al.*, 1994; Samson *et al.*, 1995; Murphy & Keppe, 1998; Pe-Piper & Piper, 1998; Pe-Piper & Jansa, 1999; Moench & Aleinikoff, 2002; Tomascak *et al.*, 2005). In Nova Scotia, and the northeastern USA, the CAMP basalts occur within the peri-Gondwanan Meguma, Avalonia, Gander and Carolina terranes and several segments of the Laurentian margin or peri-Laurentian terranes (Piedmont and Blue Ridge terranes; e.g. Hibbard *et al.*, 2007). The Meguma, Avalonia and Carolina terranes were the last to be accreted to the Laurentia margin in Canada and the northern USA during the Appalachian orogenesis (e.g. Pollock *et al.*, 2012). Gander, Avalonia and Carolina were once located together along the northern margin of Gondwana and share a Neoproterozoic magmatic arc-related basement (e.g. Nance & Murphy, 1996; Murphy *et al.*, 2004; Hibbard *et al.*, 2007; Schultz *et al.*, 2008; Pollock & Hibbard, 2010).

Previous geological, geochronological and chemical data for the CAMP in eastern North America

The CAMP basalts occur as lava flow sequences up to 450 m thick, and also as dykes and sills. In the Triassic–Jurassic basins, the lava piles consist of a maximum of three main units, each unit comprising multiple flows. In the USA basins, the ENA basalt units are interlayered with latest Triassic and possibly earliest Jurassic sedimentary rocks. In the Culpeper basin (Virginia, USA; Fig. 2), the CAMP lava flows comprise three main units, which, from bottom to top, are the Mt Zion Church, the Hickory Grove and the Sander basalts. In the Newark basin (New Jersey and Pennsylvania, USA; Fig. 2), the CAMP lava flow units are the Orange Mountain, Preakness and Hook Mountain basalts (e.g. Puffer & Student, 1992). In the Hartford basin and its northernmost extension (Connecticut and Massachusetts, USA), the units, which are up to 400 m thick, include, from bottom to top, the Talcott, Holyoke (named Deerfield basalt in the Deerfield basin) and Hampden units. These units are fed by the Higganum or Fairhaven, Buttress and Bridgeport dykes, respectively (Philpotts & Martello, 1986; Philpotts *et al.*, 1996; Philpotts, 1998). In the Fundy basin, located on the western side of Nova Scotia and \sim 500 km north of the Hartford basin, the CAMP basaltic flows occur as the North Mountain Basalt (NMB) and comprise three units (from bottom to top: East Ferry, Margaretville and Brier Island members; Kontak, 2008), which we will refer to, respectively, as the lower, intermediate and upper NMB. These units have an aggregate thickness of up to 500 m.

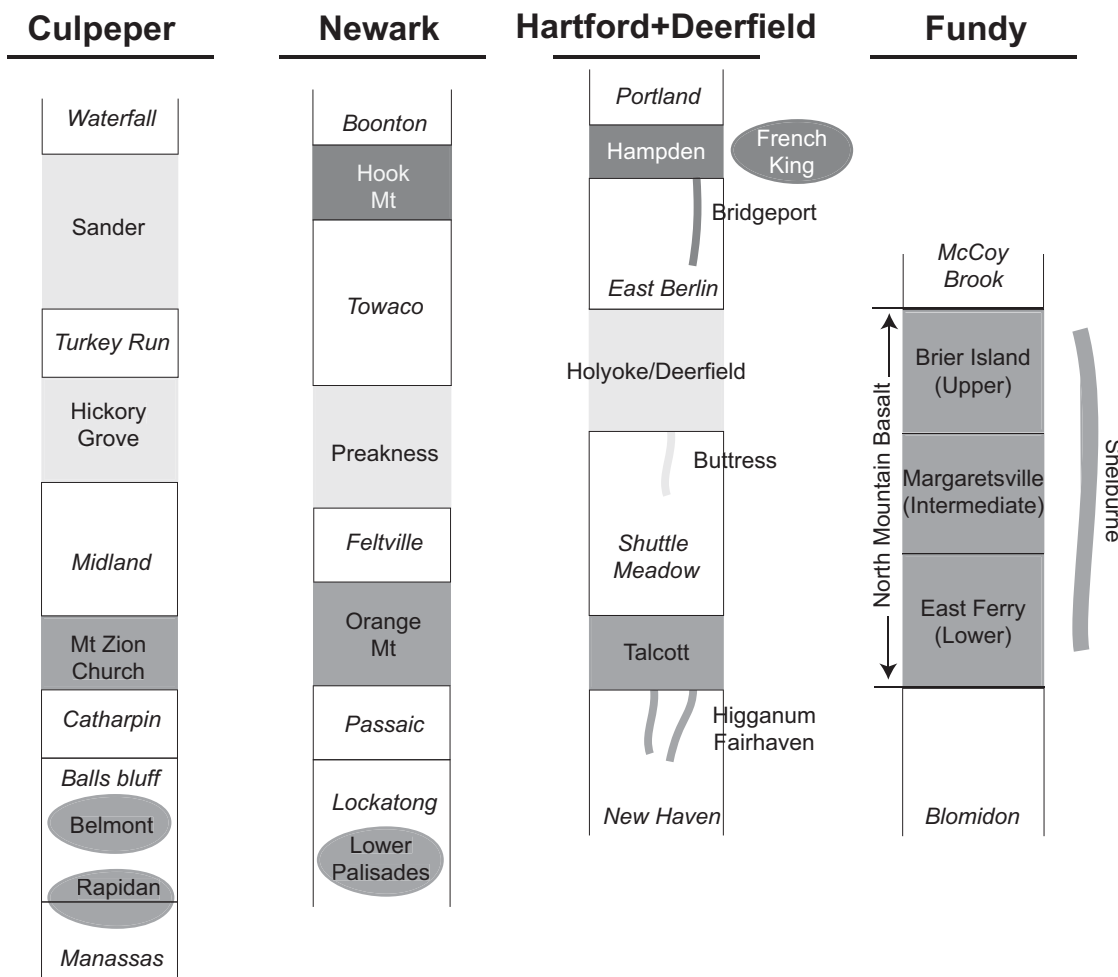


Fig. 2. Stratigraphic correlations between the CAMP units (sills, flows and dykes) within the Culpeper, Newark, Hartford, and Fundy basins and adjacent areas. Thick lines, dykes; grey rectangles, flows; ovals, sills. The stratigraphic (for the flows) and chemical correlations between the CAMP units are represented by similar shades of grey. Units located within the basins are represented in the schematic stratigraphic logs. Sedimentary formations are represented as white rectangles. Not to scale.

Shallow intrusive mafic rocks also occur in the ENA basins as thick sills and dykes, such as the Rapidan and Belmont sills in the Culpeper basin (Woodruff *et al.*, 1995), the Palisades sill in the Newark basin, the French King sill in the Hartford basin, and the Shelburne dyke in Nova Scotia. The Palisades and Rapidan sills reach a thickness of up to 350 m.

Reliable, high-quality $^{40}\text{Ar}/^{39}\text{Ar}$ plateau ages (selection criteria discussed by Nomade *et al.*, 2007) for the Culpeper and Newark sills and flows give a weighted mean age of 201.8 ± 0.7 Ma (2σ ; Marzoli *et al.*, 2011), which is similar within error to the age of the basalts from the nearby Hartford basin in the USA and the NMB (201.6 ± 1.1 Ma) in Nova Scotia (Jourdan *et al.*, 2009; recalculated by Marzoli *et al.*, 2011). By combining the ages of the USA and Nova Scotia basins, the peak activity of the CAMP event in ENA occurred at 201.5 ± 0.9 Ma. This age is

similar to those obtained by thermal ionization mass spectrometry (TIMS) U–Pb dating for the NMB and for the Triassic–Jurassic boundary (201.4 ± 0.4 Ma and 201.3 ± 0.4 Ma, respectively; Schoene *et al.*, 2010). It should be noted that the Hook Mt basalt (uppermost flows) yielded a slightly younger, but statistically indistinguishable age of 200.3 ± 0.9 Ma (Marzoli *et al.*, 2011).

The ENA CAMP basalts are quartz- and olivine-normative, low-Ti tholeiites ($\text{TiO}_2 < 2$ wt %) (Weigand & Ragland, 1970; McHone, 2000; Heatherington & Mueller, 2003). To differentiate the high-Mg, olivine normative tholeiites with very low Ti contents found in the southeastern USA, some researchers divide the low-Ti group into low-Ti basalts ($\text{TiO}_2 < 1$ wt %) and intermediate-Ti basalts ($\text{TiO}_2 \approx 1$ wt %; McHone, 2000; Salters *et al.*, 2003). The ENA CAMP basalts contain calcic plagioclase, augitic and pigeonitic clinopyroxene and occasional

orthopyroxene (mainly in the intrusive rocks). Olivine microphenocrysts are rare, but can be locally abundant in cumulus layers of the thick Rapidan and Palisades sills (Hush, 1990; Philpotts *et al.*, 1996). The major element and compatible trace element trends for the lava flows and sills can be related to fractional crystallization, mineral accumulation, and post-emplacement differentiation processes such as compaction and gas-filter pressing (Woodruff *et al.*, 1995; Philpotts *et al.*, 1996; Kontak, 2008). These latter processes are thought to generate differentiated pegmatitic or granophytic layers, which are commonly observed in the thick ENA flows and sills (Puffer & Hörter, 1993; Philpotts, 1998; Kontak, 2008). The most significant geochemical trends occurring from base to top within each sill are a decrease of MgO and Cr (e.g. Walker, 1969; Shirley, 1987; Gorring & Naslund, 1995; Woodruff *et al.*, 1995; Puffer *et al.*, 2009). Re-injection of variably differentiated magmas has been also suggested to explain the observed geochemical trends (Hush, 1990; Marzoli *et al.*, 2011). Nevertheless, overall geochemical similarities exist between the lower part of the Palisades sill and the Orange Mountain basalt, and between the upper half of the sill and the Preakness basalt (Puffer *et al.*, 2009). As is also true for CAMP basalts from other locations, there are no picrites or other primitive rocks in the ENA in contrast to what is observed in other continental or oceanic large igneous provinces (LIPs).

Based on detailed field observations, biostratigraphic data, and major- (TiO_2) and trace-element chemistry (e.g. La/Yb ratios), and despite the large variety of petrogenetic processes that may have influenced the generation of the ENA CAMP basalts (polybaric fractional crystallization, post-magmatic differentiation, melting rate variation, upper crust assimilation and alteration), correlations can be established between the various units within the US basins (Fig. 2; Weigand & Ragland, 1970; Tollo & Gottfried, 1992; Fowell & Olsen, 1993; Olsen *et al.*, 2003; Puffer *et al.*, 2009; Marzoli *et al.*, 2011). The Mt Zion Church unit is equivalent to the Orange Mountain and Talcott basalts (lower units), and the Hickory Grove and Sander units of the Culpeper basin (separated locally by more than 100 m of sediments of the Turkey Run formation) are equivalent to the Preakness and Holyoke basalts (e.g. Tollo & Gottfried, 1992; Marzoli *et al.*, 2011). The Hook Mountain basalt from the Newark basin is equivalent to the Hampden basalt from the Hartford basin (upper units), whereas a geochemically and stratigraphically equivalent basaltic flow does not occur in the Culpeper basin. The NMB from Nova Scotia show the same biostratigraphic markers and paleomagnetic intervals as the Orange Mt basalt group flows (Kent & Olsen, 2000; Cirilli *et al.*, 2009), yet until now no clear geochemical correlation has been established between the flows in the USA and Nova Scotia basins.

Compared with normal mid-ocean ridge basalts (N-MORB, basalts from mid-ocean ridges derived from the depleted asthenosphere), the ENA CAMP basalts show moderate enrichment in large ion lithophile elements (LILE; e.g. Rb, Cs, Ba), systematic negative Nb anomalies, and slightly sloped to flat heavy rare earth element (HREE) patterns (Dostal & Dupuy, 1984; Pegram, 1990; Dostal & Greenough, 1992; Heatherington & Mueller, 1999; Murphy *et al.*, 2011).

The few existing Sr–Nd–Pb isotope data available for the CAMP tholeiites from Connecticut to Florida ($^{87}\text{Sr}/^{86}\text{Sr} = 0.70583\text{--}0.71083$, $^{143}\text{Nd}/^{144}\text{Nd} = 0.51207\text{--}0.51247$, $^{206}\text{Pb}/^{204}\text{Pb} = 18.26\text{--}18.63$, $^{207}\text{Pb}/^{204}\text{Pb} = 15.57\text{--}15.65$, $^{208}\text{Pb}/^{204}\text{Pb} = 38.16\text{--}38.31$; initial ratios recalculated at 201 Ma), have been interpreted as arguing against significant involvement of MORB or OIB mantle components, but may indicate derivation from (or substantial contamination by) the SCLM and/or variable contamination by the upper crust (Pegram, 1990; Puffer, 1992, 2001; Heatherington & Mueller, 1999). Based on Pb–Pb mantle isochrons and Nd model ages, it has been proposed that this SCLM might be derived from a ~ 1 Ga, sediment-contaminated, sub-arc mantle related to the Carolina and Suwannee (Avalonian) terranes that was later incorporated into the Laurentian lithosphere (Pegram, 1990; Heatherington & Mueller, 1999).

In Nova Scotia, only a few initial Sr and Nd isotopic ratios ($^{87}\text{Sr}/^{86}\text{Sr} = 0.70443\text{--}0.71285$, $^{143}\text{Nd}/^{144}\text{Nd} = 0.51203\text{--}0.51256$) are available for the CAMP tholeiites (Greenough *et al.*, 1989; Dostal & Durning, 1998; Murphy *et al.*, 2011). As for the USA CAMP basalts, the Nd model ages argue for derivation from an SCLM source underneath the Avalonia–Meguma terranes that was enriched by Neoproterozoic subduction (Murphy & Dostal, 2007; Murphy *et al.*, 2011). The CAMP magmas derived from this source were eventually contaminated by the Meguma terrane crust (Murphy *et al.*, 2011). Prior to the formation of the CAMP, the Avalonia and Meguma terranes experienced successive rift-related, tholeiitic magmatic episodes of Neoproterozoic to Devonian age. It has been suggested that all of these magmatic episodes, including CAMP, were derived from the same Avalonia–Meguma SCLM (Murphy & Dostal, 2007; Murphy *et al.*, 2011). Whereas this might be expected to lead to progressive SCLM depletion, the initial ϵ_{Nd} values of these basalts indicate progressive enrichment of their source (see Murphy *et al.*, 2011). We note, however, that contamination by the continental crust might invalidate the Nd model ages (e.g. Arndt & Goldstein, 1987) and thus weaken this argument favouring an SCLM origin for the ENA CAMP basalts.

SAMPLE SELECTION

After discarding the rocks that show obvious evidence of alteration in thin section (large amounts of sericite and chlorite replacing plagioclase and pyroxene, and clay

minerals replacing the microcrystalline matrix), 132 samples of flows, sills, and dykes were selected for major and compatible trace element analysis by X-ray fluorescence (XRF). This set includes, from south to north, 22 samples from the Culpeper basin, 30 samples from the Newark basin, 29 samples from the Hartford–Deerfield basin, and 51 samples from the Fundy basin (Nova Scotia). The Nova Scotia samples include four Shelburne dyke samples and 25 drill-hole samples (hole GAV-77-3; Kent & Olsen, 2000) from the North Mountain Basalt.

A subset of samples with low loss on ignition ($\text{LOI} < 3.5 \text{ wt \%}$) and negligible optical alteration was selected for REE and incompatible trace element analysis by inductively coupled plasma mass spectrometry (ICP-MS; 55 samples) and Sr–Nd–Pb isotopic analysis (43 samples). A subset of 20 of the least differentiated samples was also selected for Re–Os analysis.

The detailed analytical procedures, major and trace element analyses, and the geographic coordinates of the samples are given in Supplementary Data Tables A1 and A2 (supplementary data are available for downloading at <http://www.petrology.oxfordjournals.org>). The Sr–Nd–Pb isotope data are reported in Table 1 and the Re–Os data in Table 2. All the isotopic ratios discussed in the following sections are back-calculated to 201 Ma (Jourdan *et al.*, 2009; Marzoli *et al.*, 2011) using the incompatible element contents measured by ICP-MS for the Sr–Nd–Pb isotopic ratios and the Re and Os contents measured by isotopic dilution for the Os isotope ratios.

RESULTS

Major and trace elements

All the samples analysed for major and compatible and incompatible trace elements are fairly fresh or slightly altered and have LOI values lower than 3.5 wt %. Samples with LOI higher than 3.5% are not considered further.

The primary mineralogy of the ENA rocks consists of augite, plagioclase, and Fe–Ti oxides, and, in some samples, olivine and/or pigeonite. Orthopyroxene is common in the Rapidan and Palisades Sills.

Bulk-rock compositions, recast to anhydrous values, range from basalt to basaltic andesite (Fig. 3a) and all samples can be classified as low-Ti with $\text{TiO}_2 < 2 \text{ wt \%}$ (Fig. 3b). The four samples with TiO_2 close to or higher than 2 wt % are evolved pyroxene-rich rocks with MgO contents lower than 4 wt % (NS19, NS23, NS24 and CUL67A). Most samples are moderately evolved with MgO contents between 5 and 8 wt %. Sixteen samples are less evolved with more than 8 wt % MgO , but have Ni and Co contents lower than 234 ppm and 57 ppm, respectively, thus indicating early olivine fractionation (Fig. 3c and d). Four samples from the Palisades Sills have MgO between 15 and 19 wt %, together with high Ni, Cr

and Co contents, owing to olivine and pyroxene accumulation, as confirmed from thin-section observations.

As discussed above, field observations and geochemical considerations allow units from the various basins to be correlated. Three groups of effusive and intrusive samples can be defined based on both stratigraphic position (Fig. 2) and incompatible element composition, as best illustrated by the La/Yb vs TiO_2 plot (Fig. 4). The stratigraphically uppermost group has the highest TiO_2 ($\sim 1.3\text{--}1.5 \text{ wt \%}$) and the lowest La/Yb (~ 2), and encompasses the Hampden and Hook Mt flow units, their feeder dyke (Bridgeport dyke), and the French King sill. This group is referred to hereafter as the Hook Mt group. The group with $\text{TiO}_2 \sim 0.7\text{--}1.1 \text{ wt \%}$ and $\text{La/Yb} \sim 2.5\text{--}3.5$ encompasses the Holyoke, Preakness, Sander and Hickory Grove flow units and their feeder dyke (Buttress dyke) and is referred to as the Preakness group in the following sections. The stratigraphically lowest group, with the largest TiO_2 variation (0.5–1.3 wt %) and the highest La/Yb ($\sim 4\text{--}6$), includes the Talcott, Orange Mountain and Mt Zion Church flow units and their feeder dyke (Higganum–Fairhaven dyke) and all Nova Scotian samples, both the NMB and Shelburne dyke. In addition, the lower part of the Palisades sill and the Culpeper basin sills (including the Rapidan sill) belong to this group. This group is referred to as the Orange Mt group.

In primitive mantle-normalized multi-element diagrams all the samples display moderate enrichment of the most incompatible elements with respect to the least incompatible ones, as well as prominent positive Pb and negative Nb anomalies (Fig. 5). The samples are all enriched in LILE and light REE (LREE) with $\text{La/Sm}_N = 1.38\text{--}2.71$. It should be noted that the most enriched samples, which have $\text{La/Sm}_N > 2.5$, are evolved rocks (NS19 and NS23). The parallel chondrite-normalized REE patterns (Fig. 6) observed within a given flow unit are probably related to fractional crystallization (e.g. the Sander unit in the Culpeper basin).

The REE patterns of the Hook Mt group are similar to those of the Preakness group, but distinct from those of the Orange Mt group. Whereas the Hook Mt group shows the least LREE enrichment ($\text{La/Sm}_N = 1.38\text{--}1.46$) and flat HREE patterns ($\text{Dy/Yb}_N = 1.05\text{--}1.10$), the Preakness group shows slightly more enriched LREE patterns ($\text{La/Sm}_N = 1.66\text{--}1.88$), but similar flat HREE patterns ($\text{Dy/Yb}_N = 1.04\text{--}1.11$). The Orange Mt group shows the most LREE-enriched patterns ($\text{La/Sm}_N = 1.76\text{--}2.45$; excluding the differentiated samples) and sloped HREE patterns ($\text{Dy/Yb}_N = 1.15\text{--}1.36$). It should be noted that among these samples, the NMB upper and intermediate flow units and the Shelburne dyke (hereafter the Shelburne sub-group) show slightly lower Dy/Yb_N (1.15–1.30), but slightly higher La/Sm_N (1.90–2.45) values than the remaining samples of the Orange Mt group.

Table 1: Sr–Nd–Pb isotope data for the ENa CAMP basalts

Unit	Sample	$(^{87}\text{Sr}/^{86}\text{Sr})_{\text{mass.}}$	$\pm 1\sigma$	$^{87}\text{Rb}/^{88}\text{Sr}$	$(^{87}\text{Sr}/^{86}\text{Sr})_{\text{ini.}}$	$\pm 1\sigma$	$(^{143}\text{Nd}/^{144}\text{Nd})_{\text{mass.}}$	$\pm 1\sigma$	$^{147}\text{Sm}/^{148}\text{Nd}$	$(^{143}\text{Nd}/^{144}\text{Nd})_{\text{ini.}}$	$\pm 1\sigma$	$\varepsilon\text{Nd}_{\text{ini.}}$	
Talcott flow	HB64	0.706744	0.000002	0.151	0.706311	0.000031	0.512532	0.00004	0.153	0.512330	0.000009	-0.95	
Higginan Dike	HB87	0.706627	0.000003	0.243	0.705933	0.000041	0.512537	0.00005	0.155	0.512333	0.000010	-0.91	
Holyoke flow	HB56	0.707274	0.000004	0.353	0.706266	0.000060	0.512509	0.000017	0.164	0.512293	0.000019	-1.68	
Buttress dike	HB102	0.706690	0.000002	0.185	0.706160	0.000031	0.512545	0.00004	0.169	0.512323	0.000010	-1.11	
Hampden flow	HB29	0.710390	0.000006	0.307	0.709511	0.000052	0.512530	0.000012	0.184	0.512388	0.000016	0.16	
Bridgeport Dike	HB88	0.707298	0.000002	0.406	0.706137	0.000069	0.512740	0.000016	0.183	0.512489	0.000019	2.33	
NMB lower flow	NS1	0.707118	0.000007	0.425	0.705801	0.000072	0.512522	0.000007	0.161	0.512309	0.000011	-1.36	
NMB lower flow	NS6	0.707418	0.000009	0.348	0.706342	0.000060	0.512495	0.000004	0.159	0.512296	0.000010	-1.62	
NMB lower flow	NS19	0.707148	0.000003	0.494	0.705600	0.000084	n.d.	n.d.	n.d.	n.d.	n.d.	n.d.	
NMB lower flow	NS23	0.706436	0.000005	0.388	0.705007	0.000066	0.512540	0.000005	0.158	0.512343	0.000010	-0.70	
NMB Middle flow	NS7	0.708609	0.000008	0.146	0.708224	0.000026	0.512412	0.000005	0.154	0.512207	0.000010	-3.36	
NMB Middle flow	NS12	0.708407	0.000006	0.318	0.707631	0.000054	0.512413	0.000007	0.153	0.512202	0.000011	-3.45	
NMB Upper flow	NS8	0.707241	0.000002	0.079	0.707014	0.000014	0.512378	0.000004	0.157	0.512169	0.000010	-4.10	
NMB Upper flow	NS9	0.707416	0.000002	0.116	0.707085	0.000020	0.512395	0.000004	0.153	0.512203	0.000009	-3.45	
NMB Upper flow	NS13	0.707417	0.000003	0.243	0.706783	0.000041	0.512392	0.000005	0.156	0.512192	0.000010	-3.66	
NMB Upper flow	NS15	0.707415	0.000002	0.181	0.706924	0.000031	0.512362	0.000005	0.155	0.512169	0.000010	-4.10	
NMB Upper flow	NS21	0.707414	0.000003	0.275	0.706739	0.000047	0.512393	0.000003	0.152	0.512197	0.000009	-3.56	
GAV Middle flow	GA1/81	0.706575	0.000008	0.302	0.705726	0.000052	0.512522	0.000006	0.149	0.512325	0.000010	-1.05	
GAV Lower flow	GAV162	0.706743	0.000009	0.223	0.706104	0.000039	0.512490	0.000004	0.150	0.512283	0.000009	-1.68	
GAV Lower flow	GAV174	0.706778	0.000007	0.149	0.706353	0.000026	0.512512	0.000003	0.145	0.512322	0.000009	-1.13	
GAV Lower flow	GAV181	0.706561	0.000008	0.163	0.706095	0.000029	0.512500	0.000005	0.151	0.512301	0.000010	-1.52	
GAV Lower flow	GAV193	0.706504	0.000002	0.175	0.706004	0.000030	0.512536	0.000007	0.148	0.512341	0.000011	-0.75	
Shalburne dyke	NS27	0.707357	0.000003	0.221	0.706724	0.000038	0.512414	0.000006	0.154	0.512211	0.000010	-3.28	
Shalburne dyke	NS28	0.708018	0.000002	0.359	0.706891	0.000061	0.512392	0.000003	0.155	0.512189	0.000009	-3.72	
Palisades sill	NEW3	0.707903	0.000009	0.395	0.706773	0.000068	0.512335	0.000006	0.152	0.512335	0.000010	-0.87	
Palisades sill	NEW/36C	0.706674	0.000012	0.219	0.706047	0.000039	0.512516	0.000013	0.161	0.512305	0.000016	-1.46	
Palisades sill	NEW16	0.707911	0.000003	0.338	0.706362	0.000057	0.512520	0.000004	0.156	0.512318	0.000010	-1.28	
Palisades sill	NEW17	0.706829	0.000007	0.338	0.705880	0.000058	0.512530	0.000006	0.156	0.512328	0.000011	-1.08	
Palisades sill	NEW18	0.706879	0.000008	0.322	0.705886	0.000055	0.512517	0.000004	0.156	0.512318	0.000010	-1.34	
Orange Mt	NEW69	0.706695	0.000004	0.135	0.706309	0.000023	0.512526	0.000007	0.158	0.512318	0.000011	-1.20	
Orange Mt	NEW/33	0.708305	0.000002	0.029	0.708221	0.000005	0.512552	0.000007	0.156	0.512347	0.000011	-0.63	
Preakness	NEW52	0.707285	0.000004	0.294	0.706445	0.000050	0.512486	0.000005	0.163	0.512271	0.000010	-2.11	
Preakness	NEW68	0.706377	0.000002	0.230	0.705719	0.000039	0.512531	0.000007	0.170	0.512307	0.000012	-1.41	
Hook Mt	NEW73	0.708134	0.000002	0.466	0.706802	0.000079	0.512549	0.000003	0.184	0.512407	0.000011	0.54	
Hook Mt	NEW74	0.707088	0.000002	0.513	0.705621	0.000087	0.512581	0.000002	0.183	0.512440	0.000010	1.19	
Hickory Grove	CUL6	0.707413	0.000002	0.041	0.707296	0.000087	0.512539	0.000003	0.156	0.512333	0.000009	-0.90	
Sander	CUL25	0.707872	0.000009	0.178	0.706122	0.000034	0.512551	0.000017	0.170	0.512327	0.000019	-1.02	
Sander	CUL28	0.707514	0.000003	0.316	0.706612	0.000054	0.512534	0.000003	0.161	0.512260	0.000009	-2.33	
Rapidan sill	CUL8	0.706617	0.000006	0.309	0.705735	0.000053	0.512491	0.000003	0.159	0.512282	0.000009	-1.90	
Rapidan sill	CUL9	0.706469	0.000003	0.135	0.706073	0.000023	0.512516	0.000005	0.164	0.512300	0.000010	-1.55	
Belmont Sill	CUL67	0	0.707107	0.000002	0.357	0.706086	0.000061	0.512478	0.000003	0.155	0.512274	0.000009	-2.05

(continued)

Table 1. *Continued*

Sample	$(^{208}\text{Pb}/^{204}\text{Pb})_{\text{meas.}}$	$\pm 1\sigma$	$^{238}\text{U}/^{204}\text{Pb}$	$(^{207}\text{Pb}/^{204}\text{Pb})_{\text{meas.}}$	$\pm 1\sigma$	$^{235}\text{U}/^{204}\text{Pb}$	$(^{208}\text{Pb}/^{204}\text{Pb})_{\text{meas.}}$	$\pm 1\sigma$	$^{232}\text{Th}/^{204}\text{Pb}$	$(^{206}\text{Pb}/^{204}\text{Pb})_{\text{ini.}}$	$\pm 1\sigma$	$(^{208}\text{Pb}/^{204}\text{Pb})_{\text{ini.}}$	$\pm 1\sigma$	$(^{208}\text{Pb}/^{204}\text{Pb})_{\text{ini.}}$	$\pm 1\sigma$
HB64	18-650	0.001	6.6	15.648	0.000	0.049	38.668	0.001	24.24	18.440	0.025	15.637	0.001	38.424	0.028
HB87	18-586	0.001	7.6	15.656	0.001	0.056	38.726	0.001	30.17	18.346	0.029	15.644	0.002	38.422	0.035
HB56	18-849	0.001	9.2	15.644	0.000	0.068	38.741	0.001	31.72	18.557	0.035	15.629	0.002	38.421	0.037
HB102	18-880	0.001	7.2	15.669	0.001	0.053	38.850	0.001	23.21	18.652	0.027	15.658	0.001	38.616	0.027
HB29	n.d.	n.d.	n.d.	n.d.	n.d.	n.d.	n.d.	n.d.	n.d.	n.d.	n.d.	n.d.	n.d.	n.d.	n.d.
HB98	18-719	0.000	4.9	15.640	0.000	0.036	38.611	0.001	12.03	18.562	0.019	15.632	0.001	38.490	0.014
NS1	18-541	0.001	7.1	15.628	0.001	0.052	38.642	0.002	31.97	18.315	0.027	15.616	0.002	38.320	0.037
NS6	18-651	0.001	9.9	15.640	0.001	0.073	38.760	0.003	42.08	18.337	0.037	15.624	0.002	38.336	0.049
NS19	18-676	0.001	10.0	15.656	0.001	0.073	38.823	0.002	44.35	18.559	0.038	15.640	0.002	38.376	0.052
NS23	18-594	0.002	9.4	15.633	0.002	0.069	38.688	0.005	41.76	18.295	0.036	15.618	0.003	38.267	0.049
NS7	18-681	0.001	11.4	15.642	0.001	0.084	38.808	0.003	45.08	18.318	0.043	15.624	0.002	38.353	0.063
NS12	18-442	0.001	7.8	15.629	0.001	0.058	38.556	0.001	35.31	18.193	0.030	15.616	0.002	38.200	0.041
NS8	18-490	0.001	7.2	15.640	0.001	0.053	38.648	0.002	34.73	18.263	0.027	15.628	0.002	38.298	0.041
NS9	18-490	0.005	8.9	15.631	0.004	0.066	38.639	0.010	40.80	18.206	0.034	15.617	0.005	38.228	0.049
NS13	18-500	0.002	7.5	15.641	0.001	0.055	38.672	0.003	30.67	18.262	0.028	15.629	0.002	38.363	0.036
NS15	18-446	0.007	7.5	n.d.	0.055	38.528	0.014	36.47	18.206	0.029	n.d.	n.d.	n.d.	n.d.	0.045
NS21	n.d.	n.d.	n.d.	n.d.	n.d.	n.d.	n.d.	n.d.	n.d.	n.d.	n.d.	n.d.	n.d.	n.d.	n.d.
GAV81	18-661	0.005	9.0	15.646	0.004	0.066	38.808	0.010	38.67	18.376	0.034	15.632	0.004	38.418	0.046
GAV162	18-613	0.001	6.8	15.635	0.001	0.050	38.711	0.002	29.19	18.396	0.026	15.624	0.001	38.417	0.034
GAV174	18-640	0.002	9.0	15.639	0.002	0.066	38.765	0.004	30.85	18.353	0.034	15.624	0.002	38.454	0.036
GAV181	18-684	0.001	8.5	15.651	0.001	0.062	38.824	0.003	32.08	18.414	0.032	15.637	0.002	38.500	0.038
GAV193	18-694	0.000	11.5	15.641	0.000	0.084	38.837	0.001	50.34	18.329	0.044	15.623	0.002	38.330	0.059
NS27	18-436	0.004	8.2	15.635	0.003	0.060	38.597	0.007	35.06	18.176	0.031	15.622	0.003	38.243	0.042
NS28	18-539	0.002	10.0	15.642	0.002	0.074	38.776	0.005	44.91	18.221	0.038	15.625	0.003	38.323	0.053
NEW3	18-589	0.008	9.1	15.644	0.006	0.067	38.707	0.016	34.80	18.301	0.035	15.629	0.007	38.356	0.044
NEW36C	18-550	0.020	8.3	15.634	0.017	0.061	38.623	0.042	34.60	18.288	0.037	15.621	0.017	38.275	0.059
NEW16	18-567	0.001	8.8	15.638	0.001	0.064	38.692	0.001	34.21	18.294	0.033	15.624	0.002	38.354	0.040
NEW17	18-567	0.001	8.8	15.646	0.001	0.064	38.660	0.001	34.20	18.289	0.033	15.632	0.002	38.315	0.040
NEW18	18-576	0.000	8.0	15.663	0.000	0.059	38.746	0.001	35.15	18.329	0.030	15.650	0.002	38.402	0.044
NEW69	18-618	0.000	9.6	15.658	0.001	0.077	38.777	0.002	33.94	18.315	0.036	15.642	0.002	38.435	0.040
NEW136C	18-678	0.002	16.5	15.656	0.002	0.121	38.718	0.004	18.91	18.155	0.062	15.629	0.004	38.528	0.022
NEW52	18-923	0.001	11.1	15.653	0.001	0.082	38.820	0.003	34.77	18.569	0.042	15.635	0.002	38.470	0.041
NEW68	18-887	0.001	10.3	15.659	0.001	0.076	38.816	0.002	35.63	18.561	0.039	15.643	0.002	38.466	0.042
NEW73	19-015	0.001	11.7	15.663	0.001	0.086	38.939	0.003	37.55	18.642	0.044	15.644	0.002	38.561	0.044
NEW74	18-961	0.001	11.6	15.661	0.001	0.086	38.904	0.003	42.53	18.591	0.044	15.642	0.003	38.475	0.050
NEW13	18-887	0.001	11.6	15.659	0.001	0.085	38.816	0.002	42.43	18.519	0.044	15.640	0.002	38.388	0.050
CUL6	18-547	0.001	9.0	15.645	0.001	0.066	38.644	0.002	26.48	18.261	0.034	15.631	0.002	38.377	0.031
CUL13	18-606	0.001	9.3	15.652	0.001	0.069	38.757	0.003	23.57	18.310	0.035	15.637	0.002	38.519	0.028
CUL25	18-581	0.002	11.4	15.675	0.001	0.084	38.768	0.004	31.30	18.219	0.043	15.657	0.003	38.452	0.037
CUL28	18-883	0.002	10.6	15.663	0.001	0.078	38.804	0.003	33.54	18.518	0.040	15.646	0.002	38.466	0.039
CUL8	18-961	0.001	9.1	15.661	0.001	0.067	38.904	0.003	41.69	18.671	0.035	15.646	0.002	38.483	0.049
CUL9	18-949	0.001	8.1	15.640	0.001	0.060	38.834	0.002	34.95	18.691	0.031	15.627	0.002	38.482	0.041
CUL7	18-681	0.003	9.5	15.682	0.003	0.070	38.902	0.007	35.93	18.380	0.036	15.667	0.003	38.540	0.043

Nd_{ini} calculated at 201 Ma using the present-day values for CHUR: ($^{143}\text{Nd}/^{144}\text{Nd}_{\text{CHUR}} = 0.512638$, $^{147}\text{Sm}/^{144}\text{Nd} = 0.1967$) (Jacobsen & Wasserburg, 1990).

Table 2: Re–Os isotope data for the ENA CAMP basalts

Unit	Sample	Group	MgO	[Os] (ppt)	[Re] (ppt)	^{188}Os (mol g $^{-1}$)	$(^{187}\text{Os}/^{188}\text{Os})_{\text{meas.}}$	$\pm 2\sigma$	$^{187}\text{Re}/^{188}\text{Os}$	$(^{187}\text{Os}/^{188}\text{Os})_{\text{ini.}}$	$\pm 2\sigma$	Error (%)
<i>Fundy</i>												
NMB Lower flow	NS6	Orange Mt	6.64	23	495	1.50E-14	0.51197	0.00270	111	0.1387	0.0065	4.7
NMB Upper flow	NS21	Orange Mt	8.90	69	326	4.74E-14	0.22522	0.00101	23.2	0.1474	0.0015	1.0
GAV Middle flow	GAV81	Orange Mt	6.49	22	457	1.50E-14	0.49063	0.00423	103	0.1451	0.0068	4.7
GAV Lower flow	GAV181	Orange Mt	6.18	16	462	1.08E-14	0.58827	0.01076	144	0.1058	0.0141	13.4
Shelburne dyke	NS27	Orange Mt	8.46	440	458	3.06E-13	0.14695	0.00067	5.0	0.1300	0.0007	0.6
Shelburne dyke	NS28	Orange Mt	6.80	85	641	5.87E-14	0.25660	0.00120	36.9	0.1329	0.0021	1.6
<i>Newark</i>												
Palisades sill	NEW3	Orange Mt	6.86	82	393	5.66E-14	0.21440	0.00128	23.3	0.1362	0.0020	1.5
Palisades sill	NEW136C	Orange Mt	16.82	1670	236	1.16E-12	0.13139	0.00057	0.7	0.1291	0.0006	0.4
Palisades sill	NEW17	Orange Mt	12.91	744	386	5.18E-13	0.13698	0.00063	2.5	0.1286	0.0007	0.5
Orange Mt	NEW69	Orange Mt	7.91	50	566	3.41E-14	0.32170	0.00156	55.8	0.1346	0.0037	2.8
Orange Mt	NEW133	Orange Mt	8.20	56	599	3.82E-14	0.31357	0.00157	52.7	0.1368	0.0032	2.4
Preakness	NEW68	Preakness	7.33	7.7	568	4.47E-15	1.62717	0.02042	427	0.1935	0.0319	16.5
Hook Mt	NEW73	Hook Mt	5.60	5.9	1008	2.61E-15	4.52975	0.11504	1300	0.1701	0.1335	78.5
Hook Mt	NEW74	Hook Mt	5.66	18	1098	1.06E-14	1.31229	0.00915	348	0.1459	0.0218	15.0
<i>Culpeper</i>												
Mt Zion Church	CUL6	Orange Mt	7.65	56	522	3.82E-14	0.28173	0.00148	45.9	0.1276	0.0029	2.3
Hickory Grove	CUL13	Preakness	7.78	14	496	9.28E-15	0.79020	0.00613	180	0.1874	0.0123	6.6
Sander	CUL25	Preakness	5.62	3.5	620	1.49E-15	4.94438	0.21833	1397	0.2600	0.2332	89.7
Rapidan sill	CUL8	Orange Mt	11.75	369	245	2.57E-13	0.14344	0.00094	3.2	0.1327	0.0010	0.7

Os isotopic ratios were normalized to $^{192}\text{Os}/^{188}\text{Os} = 3.08271$. Uncertainties for the measured $^{187}\text{Os}/^{188}\text{Os}$ ratios include in-run 2SE, long-term 2 σ reproducibility of the liquid standard ($\sim 0.2\%$) and uncertainties on blanks (isotopic composition and quantity). All data are blank corrected, using blank values given in the Supplementary Data. Uncertainties on initial ratios include in-run errors and uncertainties on blank corrections and on $^{187}\text{Re}/^{188}\text{Os}$ ratios and ages used for radiogenic corrections (all 2 σ). Initial ratios were calculated using a decay constant $\lambda = 1.666 \times 10\text{E}-11$ (Smoliar *et al.*, 1996).

(Dy/Yb_N = 1.20–1.36; La/Sm_N = 1.76–2.21; hereafter the lower NMB sub-group).

Sr–Nd–Pb isotopes

All data plot within the field of previously analysed CAMP low-Ti basalts in the Sr–Nd and Pb–Pb isotope diagrams (Figs 7–10).

In the $^{208}\text{Pb}/^{204}\text{Pb}$ and $^{207}\text{Pb}/^{204}\text{Pb}$ vs $^{206}\text{Pb}/^{204}\text{Pb}$ diagrams (Fig. 7), the data plot well above the Northern Hemisphere Reference Line (NHRL) with relatively high $^{207}\text{Pb}/^{204}\text{Pb}$ and $^{208}\text{Pb}/^{204}\text{Pb}$ at low to moderate $^{206}\text{Pb}/^{204}\text{Pb}$. The ENA samples can be distinguished on the basis of whether their $^{206}\text{Pb}/^{204}\text{Pb}$ values are higher or lower than 18.5. With the exception of the Rapidan sill, all the samples of the Orange Mt group have Pb isotopic compositions typical of low-Ti CAMP basalts ($^{206}\text{Pb}/^{204}\text{Pb} = 18.155\text{--}18.440$; $^{207}\text{Pb}/^{204}\text{Pb} = 15.616\text{--}15.667$;

$^{208}\text{Pb}/^{204}\text{Pb} = 38.160\text{--}38.540$) and form a rough trend parallel to the NHRL. This range of Pb isotope compositions corresponds approximately to the average Pb isotopic composition of low-Ti basalts from other CFBs (see Carlson, 1991). In contrast, with the exception of CUL25 (Sander basalt) and CUL13 (Hickory basalt), all samples of the upper units (Hook Mt and Preakness groups), have $^{206}\text{Pb}/^{204}\text{Pb} > 18.5$ and seem to be shifted towards the NHRL (Fig. 7). Unlike the first group, these samples have both $\Delta 7/4$ less than 15 and $\Delta 8/4$ less than 50 (Fig. 8), where Δ values represent the relative vertical deviation in $^{207}\text{Pb}/^{204}\text{Pb}$ or $^{208}\text{Pb}/^{204}\text{Pb}$ from the NHRL.

In a Sr–Nd isotope diagram (Fig. 9), the ENA samples can be subdivided into three clusters, according to their Nd isotope composition. Samples of the Hook Mt group have the highest Nd initial ratios ($^{143}\text{Nd}/^{144}\text{Nd} = 0.512388\text{--}0.512499$), but similar Sr initial ratios to those

observed in the other samples ($^{87}\text{Sr}/^{88}\text{Sr} \sim 0.7054\text{--}0.7073$). The second isotopic cluster, which has lower Nd initial ratios ($^{143}\text{Nd}/^{144}\text{Nd} = 0.512260\text{--}0.512347$), includes all the units of the Preakness group and the units of the Orange Mt group in the USA. It also contains samples of the lower unit of the NMB and the intermediate unit of the GAV drill hole in the Fundy basin. In contrast, the Shelburne sub-group, including the upper and intermediate units of the NMB flows and the Shelburne dyke, compose the third isotopic cluster, which has the lowest $^{143}\text{Nd}/^{144}\text{Nd}$ ($0.512169\text{--}0.512211$) and relatively high $^{87}\text{Sr}/^{86}\text{Sr}$ ($0.7067\text{--}0.7082$). Within each group, the trend to

high $^{87}\text{Sr}/^{86}\text{Sr}$ (>0.708) at nearly constant $^{143}\text{Nd}/^{144}\text{Nd}$ (HB29, NS7 and NEW133) suggests that the $^{87}\text{Sr}/^{86}\text{Sr}$ composition of a few samples might have been affected by post-emplacement alteration.

In a $^{143}\text{Nd}/^{144}\text{Nd}$ vs $^{206}\text{Pb}/^{204}\text{Pb}$ diagram (Fig. 10), the same groups can be distinguished as in the Sr–Nd isotope diagram. Overall, the four groups define a positive correlation between Nd and Pb isotopic ratios, from the Shelburne sub-group with the lowest Pb and Nd isotopic ratios, which plots at the extremity of the field of the Meguma terrane basement rocks, towards the Hook Mt group with the highest Pb and Nd isotopic ratios. The

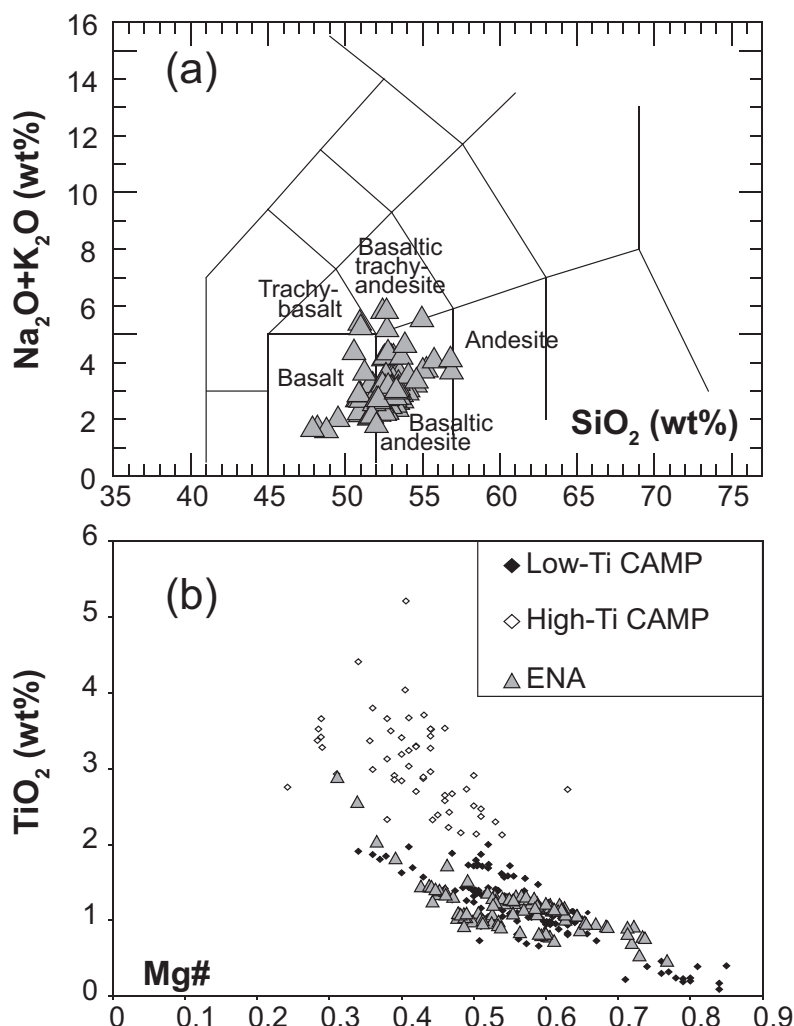


Fig. 3. (a) Total alkalies–silica (TAS) diagram. The abundances of major elements have been recalculated on a volatile-free basis (Le Maitre *et al.*, 2002). (b) TiO_2 vs $\text{Mg}\#$ diagram for the ENA CAMP basalts. CAMP data are from the GEOROC website. Data for low-Ti and high-Ti CAMP tholeiites are from Dupuy *et al.* (1988), Nomade *et al.* (2002), De Min *et al.* (2003), Jourdan *et al.* (2003), Deckart *et al.* (2005), Verati *et al.* (2005) and Merle *et al.* (2011). The data have been recalculated to 100% on a volatile-free basis; cumulative rocks have been excluded. $\text{Mg}\# = \text{Mg}^{2+}/(\text{Mg}^{2+} + \text{Fe}^{2+})$. (c, d) MgO vs Co and MgO vs Ni diagrams. Range expected for magmas in equilibrium with their mantle source: $\text{Ni} = 200\text{--}500$ ppm, $\text{Co} = 50\text{--}70$ ppm (Allégre *et al.*, 1977).

(continued)

cluster with intermediate $^{143}\text{Nd}/^{144}\text{Nd}$ values (Preakness group and part of the Orange Mt group) shows decreasing $^{206}\text{Pb}/^{204}\text{Pb}$ at constant or very slightly increasing $^{143}\text{Nd}/^{144}\text{Nd}$ trending through the field of the Meguma terrane rocks. However, samples from the Preakness group do not plot in the latter field; except for the two samples from the Sander–Hickory Grove units (CUL13 and CUL25) with $^{206}\text{Pb}/^{204}\text{Pb}$ lower than 18.5. The Hook Mt group also shows a very approximate trend with decreasing Pb and increasing Nd isotopic ratios.

Os isotopes and Re and Os concentrations

Os concentrations range from 4 to 1670 ppt, whereas Re concentrations vary from 236 to 1098 ppt. An approximate positive correlation is observed between Os and MgO, whereas an approximate negative relationship exists between Re concentration and MgO (Fig. 11), consistent

with the compatible and incompatible behaviours of Os and Re, respectively, during fractional crystallization–accumulation processes. Measured $^{187}\text{Os}/^{188}\text{Os}$ ratios range from 0.1314 to 4.9444 and the initial ratios from 0.1058 to 0.2600. Five samples (GAV181, NEW68, NEW73, NEW74 and CUL25) have very low Os concentrations (3.5–17.6 ppt) and $^{187}\text{Re}/^{188}\text{Os}$ higher than 140, which leads to uncertainties higher than 10% on the calculated initial ratios owing to the error propagation related to the blank and age corrections. As a consequence, these data are not considered precise enough and are not considered further (Fig. 12). A sixth sample (CUL13, Hickory Grove) also has a low Os concentration (14.4 ppt) coupled with a more reliable elevated initial $^{187}\text{Os}/^{188}\text{Os}$ ratio (0.1874 ± 0.0123). Such characteristics are observed in basalts that have experienced differentiation accompanied by contamination with material from the continental crust

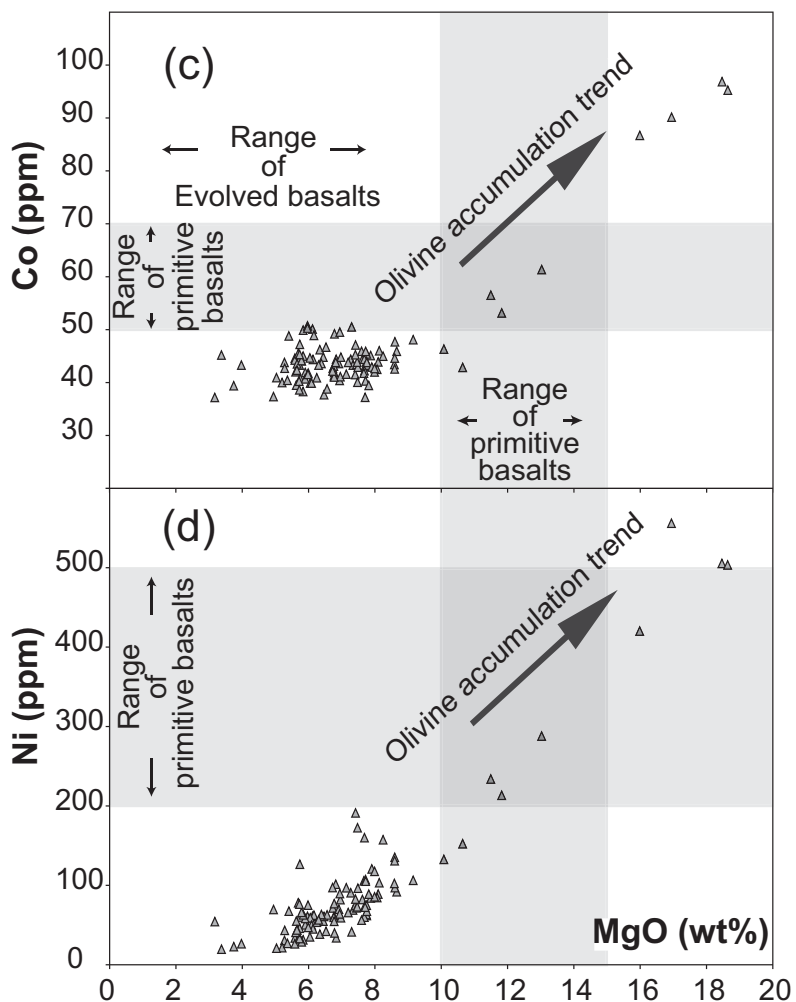


Fig. 3. Continued.

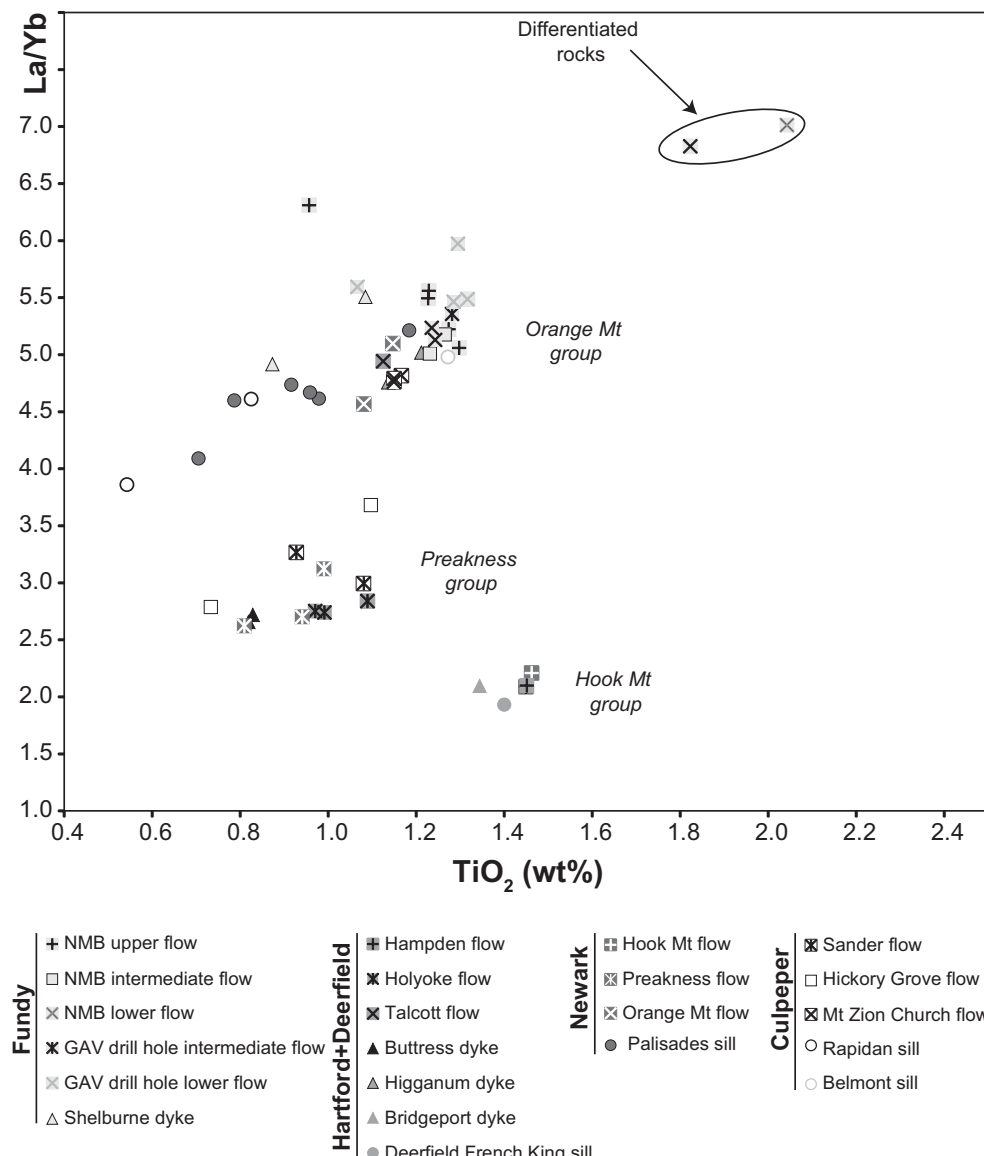


Fig. 4. Variation of TiO_2 vs La/Yb showing the chemical groups of the ENA CAMP basalts.

(Fig. 13). Indeed, this sample plots in the field expected for basalts contaminated by the upper continental crust (Fig. 13).

The remaining 12 samples have initial $^{187}\text{Os}/^{188}\text{Os}$ lower than 0.150, which are characteristic of mantle-derived magmas, coupled with Os concentrations ranging from 22.5 to 1670 ppt; these samples all belong to the Orange Mountain group. The isotopic compositions of three samples (CUL6, NEWI36C and NEWI7) overlap with the Primitive Upper Mantle (PUM) value at 201 Ma (0.1281 ± 0.0008 , based on the present-day value of PUM of 0.1296; Meisel *et al.*, 2001; Fig. 13). Samples with Os

concentrations higher than 300 ppt have initial $^{187}\text{Os}/^{188}\text{Os}$ in the restricted range of 0.1286–0.1327 (Fig. 13) and all are intrusive (sills or dykes: NS27, CUL8, NEWI7 and NEWI36C) with MgO contents higher than 8 wt % reflecting olivine and pyroxene accumulation.

There are no obvious correlations between the initial isotopic ratios of Os and those of Pb and Nd (Fig. 14). However, in the $^{187}\text{Os}/^{188}\text{Os}$ vs $^{143}\text{Nd}/^{144}\text{Nd}$ plot (Fig. 14), the ENA samples plot close to the field of the low-Ti CAMP basalts from Maranhão basin (Merle *et al.*, 2011) and do not show any trend toward the modern OIB.

DISCUSSION

The possible mantle sources of the CAMP

The CAMP basalts are clearly mantle-derived magmas as shown by their unradiogenic Os isotopic compositions, which are characteristic of mantle melts. Nevertheless, they have negative Nb and positive Pb anomalies in

normalized trace element patterns and Sr–Nd–Pb isotopic ratios approaching those typically found in crustal rocks. Regardless of the geodynamic process that generated their parental magmas, several hypotheses could explain this enigma, including the following: (i) direct derivation from a mantle plume with the trace element and isotopic characteristics described above (Wilson, 1997);

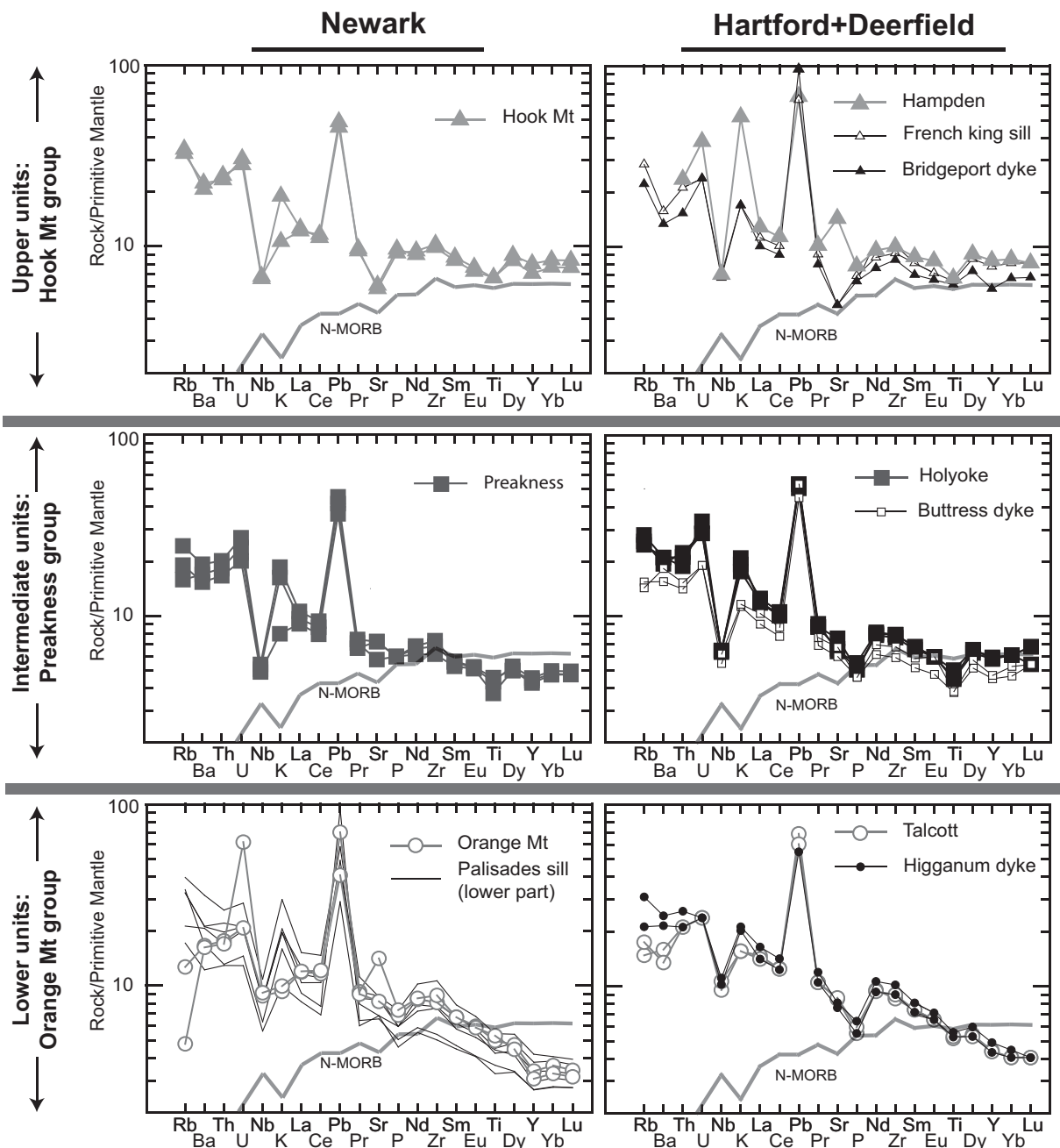
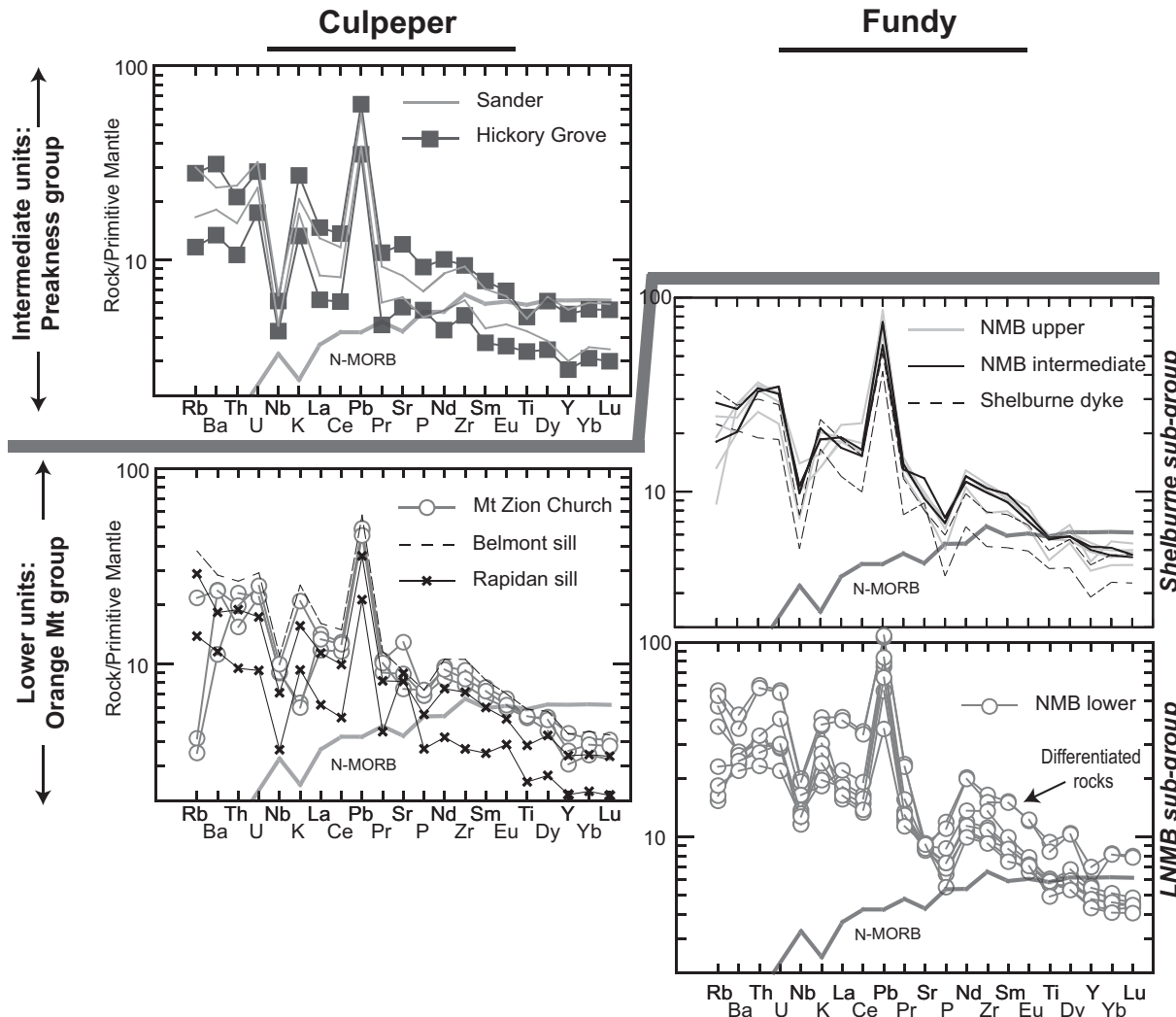


Fig. 5. Multi-element patterns of the Newark, Hartford–Deerfield, Culpeper and Fundy basin samples. Primitive mantle normalization values are from Sun & McDonough (1989).

(continued)

**Fig. 5.** Continued.

(ii) contamination of magmas derived from a mantle plume by continental crust (Arndt *et al.*, 1993); (iii) mixing between OIB or asthenospheric melts and ultra-alkaline mafic melts, such as lamproite, kimberlite, and kamafrugite-type liquids assumed to be derived from metasomatized SCLM (Arndt & Christensen, 1992; Gibson *et al.*, 2006; Heinonen *et al.*, 2010), possibly followed by crustal contamination; (iv) derivation from oceanic plateau basalt (OPB)-type melts (e.g. Kerr & Mahoney, 2007); (v) ternary mixing between OIB, MORB and SCLM-related melts, possibly followed by crustal contamination; (vi) direct melting of a shallow source enriched in incompatible elements such as metasomatized SCLM or the mantle wedge above subduction zones (Puffer, 2001; De Min *et al.*, 2003; Deckart *et al.* 2005; Dorais & Tubrett, 2008). We will examine each of these models in turn to see which one is

most compatible with the geological and geochemical constraints placed by the CAMP volcanism, and in particular, the ENA sub-province.

Plume-related origin without crustal contamination (hypothesis i)

It has commonly been proposed that CFB are derived from mantle plumes as the latter can provide large amounts of heat capable of producing large volumes of melt. Plumes may include a significant proportion of recycled crust and/or sediment (e.g. Zindler & Hart, 1986) and it is possible that these may contribute to the enriched Sr–Nd–Pb isotopic characteristics observed in the CAMP basalts. However, as previously noted by Merle *et al.* (2011) in their study of the Brazilian CAMP, plume-related (OIB) lavas with the required isotopic characteristics are lacking in

the Atlantic region. Generally, there are no OIB displaying $^{187}\text{Os}/^{188}\text{Os}$ values in the range of the ENA CAMP basalts with $^{143}\text{Nd}/^{144}\text{Nd}$ as low as found in the CAMP basalts (Fig. 14). The Sava'i'i lavas from Samoa, representing an extreme end-member EM-II mantle component, are the

only OIB free of any shallow contamination by the continental crust but with the required negative Nb anomalies (Jackson *et al.*, 2007). Whereas these OIB lavas have $^{187}\text{Os}/^{188}\text{Os}$ ratios of 0.1270–0.1353 (Workman *et al.*, 2004) similar to the CAMP basalts, they show significantly

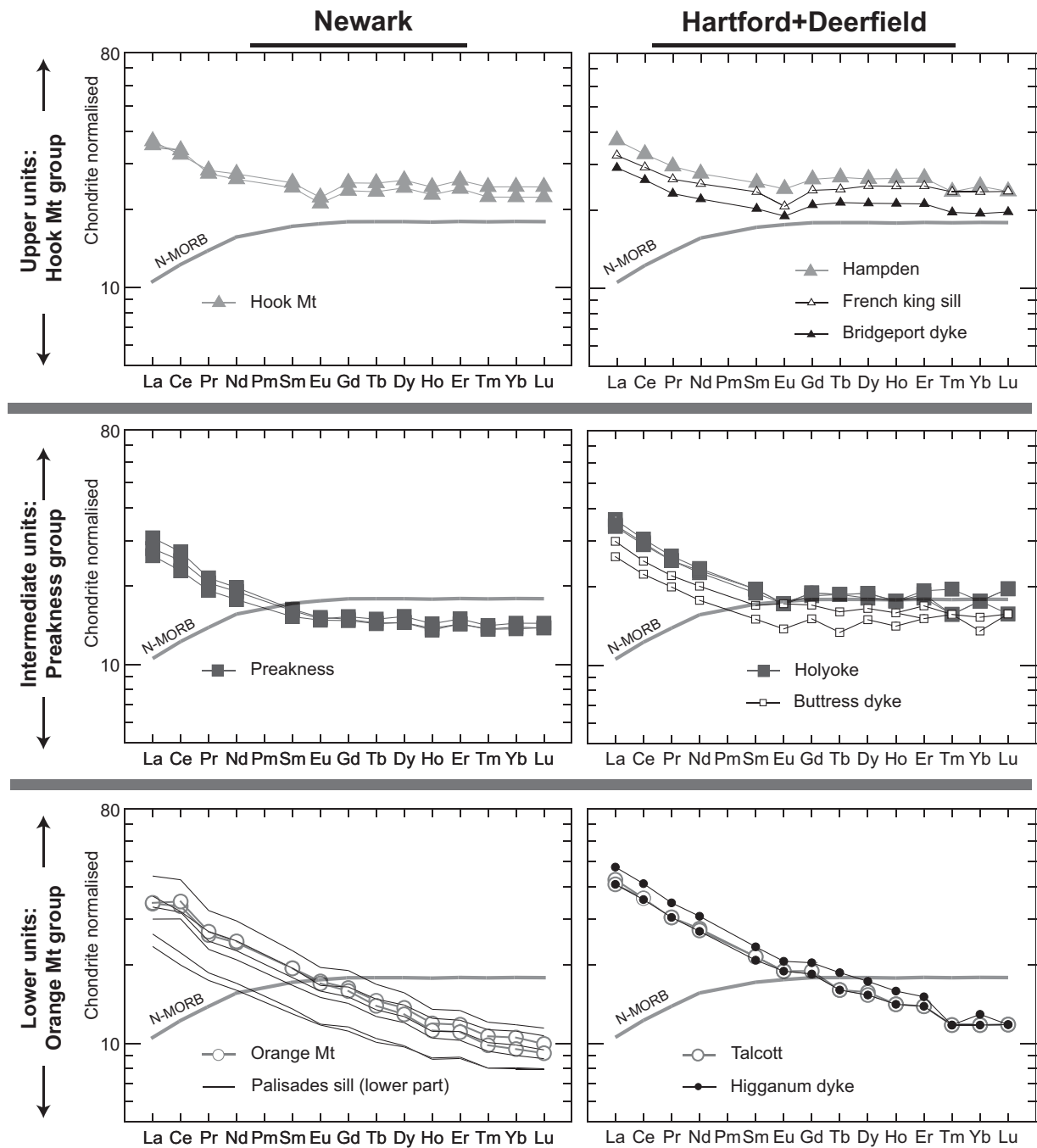


Fig. 6. Rare earth elements patterns of the Newark, Hartford–Deerfield, Culpeper and Fundy basin samples. Chondrite normalization values and average value for N-MORB are from Sun & McDonough (1989).

(continued)

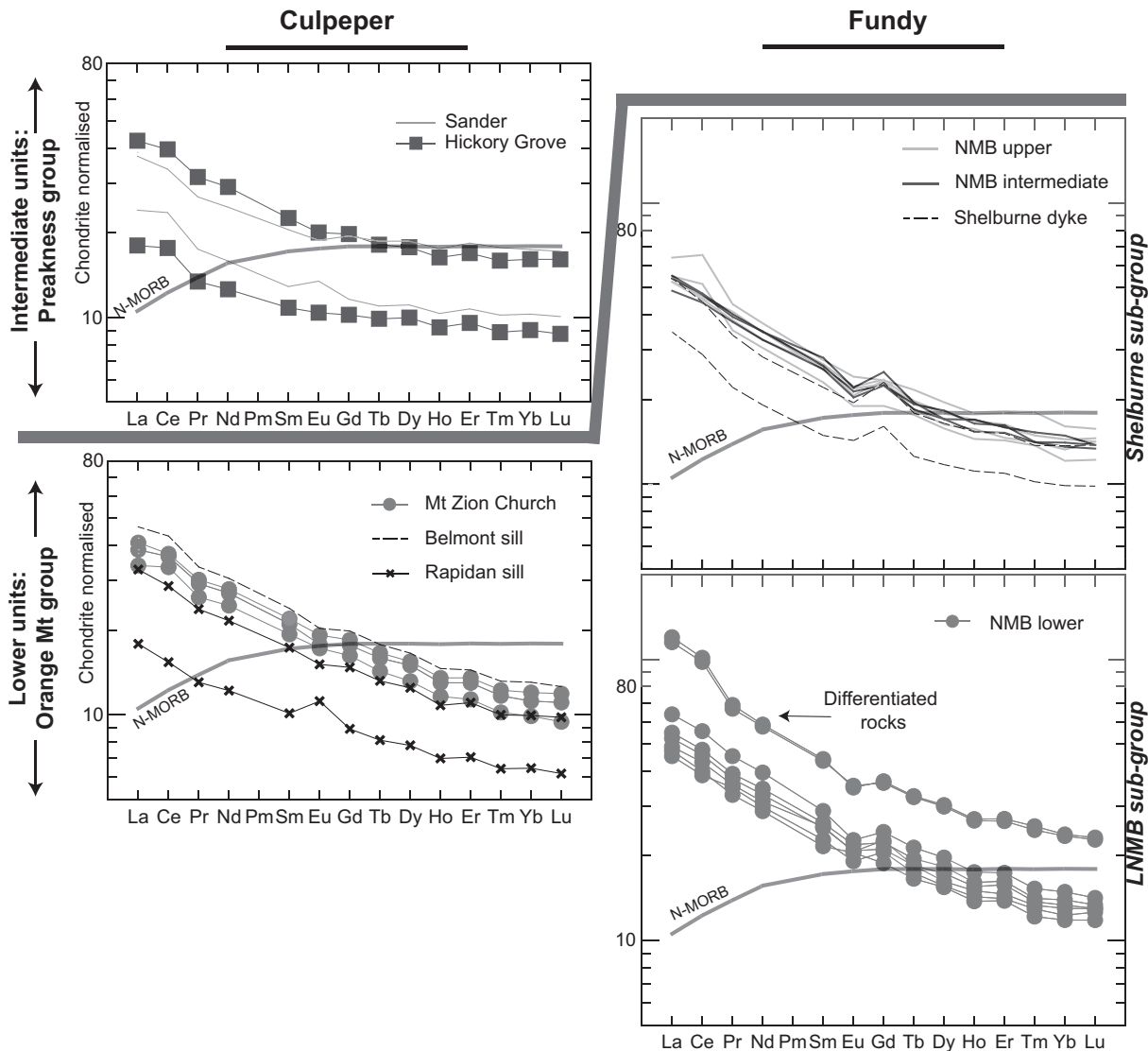


Fig. 6. Continued.

higher $^{143}\text{Nd}/^{144}\text{Nd}$, $^{206}\text{Pb}/^{204}\text{Pb}$ and $^{208}\text{Pb}/^{204}\text{Pb}$ than the CAMP basalts. Moreover, these extreme EM-II OIB are rare and it is difficult to imagine that a plume of this composition could have affected the entire Central Atlantic region at 200 Ma with no trace of it remaining today.

Plume-related origin with involvement of crustal contamination (hypothesis ii)

The CAMP basalts could be derived from a mantle plume with a composition close to those of central Atlantic OIB (i.e. Cape Verde, Fernando de Noronha, Ascension, Canaries), with their enriched continental crust-like character acquired through contamination by the continental crust. Considering that Atlantic OIB have higher

$^{206}\text{Pb}/^{204}\text{Pb}$ and $^{143}\text{Nd}/^{144}\text{Nd}$ and lower $^{207}\text{Pb}/^{204}\text{Pb}$ than the CAMP basalts (e.g. Zindler & Hart, 1986; Halliday *et al.*, 1992), a large amount of crustal contamination would be required to produce the observed isotopic compositions. In this case, a simple assimilation-fractional crystallization (AFC) process would be expected to produce trends of decreasing differentiation indices (such as MgO content) with decreasing $^{143}\text{Nd}/^{144}\text{Nd}$ among samples of each group of ENA CAMP basalts or even a part of the dataset. However, there is no such correlation for the dataset but instead a decrease of $^{143}\text{Nd}/^{144}\text{Nd}$ at constant MgO content is observed between and within the groups (Fig. 15). This observation argues against extensive crustal contamination by AFC processes. Another

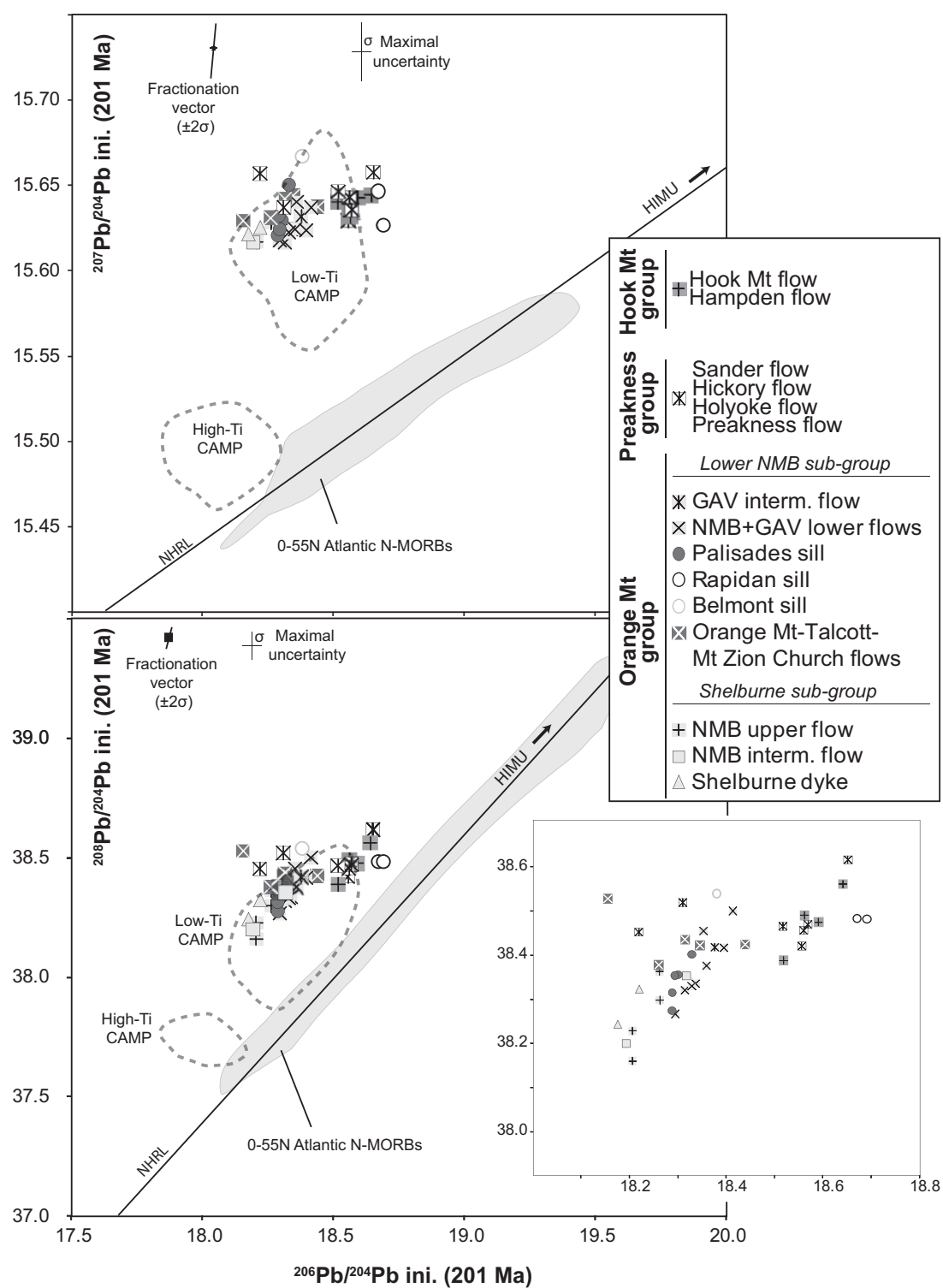


Fig. 7. Variation of $^{207}\text{Pb}/^{204}\text{Pb}$ and $^{208}\text{Pb}/^{204}\text{Pb}$ vs $^{206}\text{Pb}/^{204}\text{Pb}$ for samples of ENA CAMP basalts, all back-calculated to 201 Ma. Fields for CAMP low- and high-Ti tholeites are based on data from Dupuy *et al.* (1988), Cebria *et al.* (2003), Jourdan *et al.* (2003), Deckart *et al.* (2005) and Merle *et al.* (2011). Trajectories of mass fractionation and maximal analytical error (calculated based on error propagation with analytical errors of U and Pb and measured isotopic ratios) are shown.

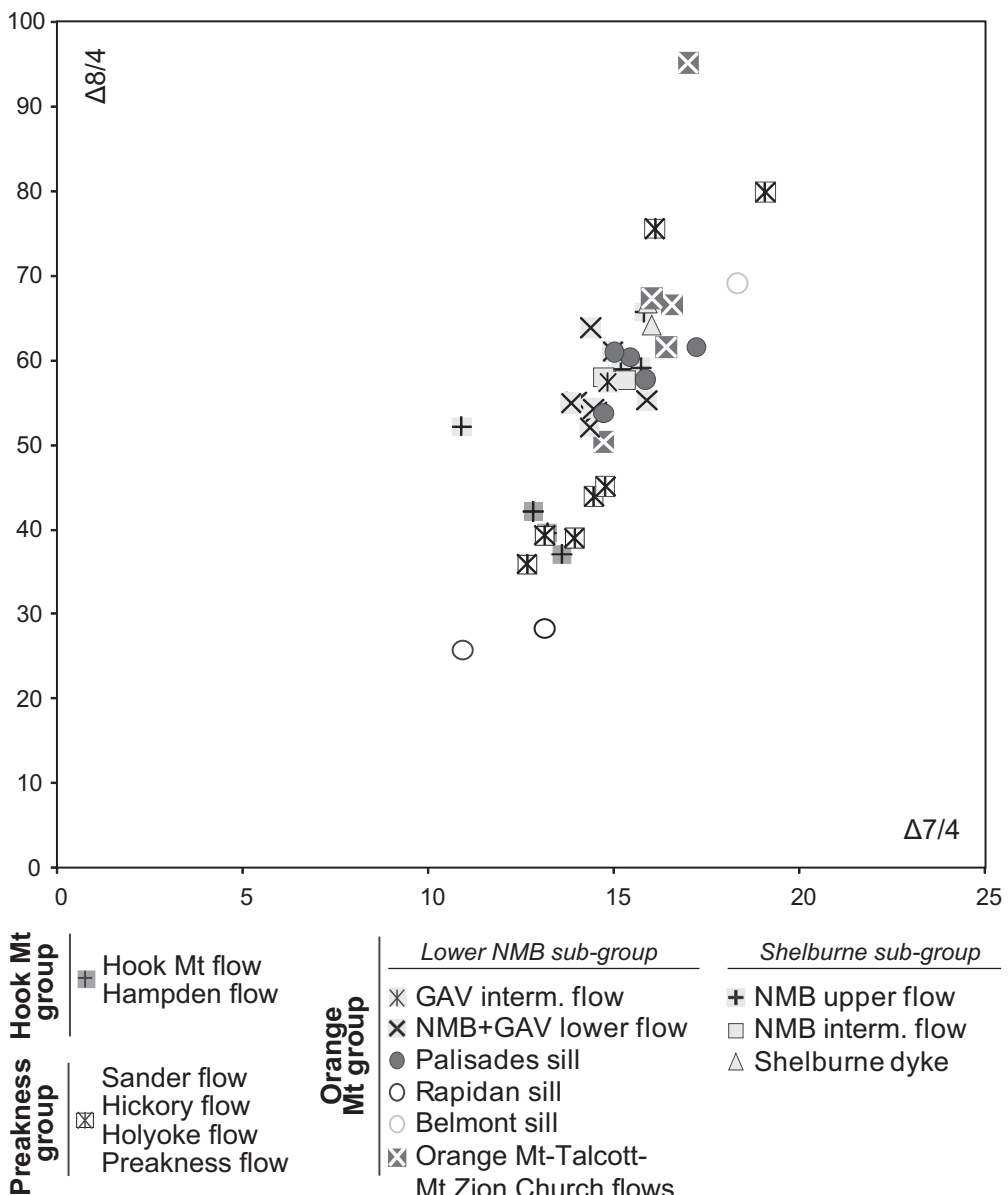


Fig. 8. $\Delta_{7/4}$ vs $\Delta_{8/4}$ for the ENA CAMP basalts.

argument against AFC is that this process would result in high incompatible element contents (Aitcheson & Forrest, 1994), which are never observed for the CAMP basalts. Perhaps the most compelling argument is that extensive crustal contamination by AFC is not compatible with the mantle-like Os isotopic ratios of the ENA CAMP samples. Magmas significantly contaminated by the crust should have initial $^{187}\text{Os}/^{188}\text{Os}$ ratios higher than 0.15 at Os concentrations lower than 50 ppt (e.g. Widom, 1997). Indeed, Os is a compatible trace element, so basalts are generated with relatively low Os concentrations that decrease rapidly

during fractional crystallization. As continental crust has much more radiogenic Os isotopic compositions than the mantle ($^{187}\text{Os}/^{188}\text{Os}$ \sim 1–15 for the crust; \sim 0.1100–0.1500 for the mantle), Os isotopic ratios would be rapidly modified during AFC processes as basaltic Os concentration decreases. There are no trends in the Os–Pb or Os–Nd diagrams from any OIB components toward crustal compositions through the CAMP basalts that may be interpreted as reflecting crustal contamination (Fig. 14).

Nevertheless, more complex models of differentiation coupled with contamination might be considered. For

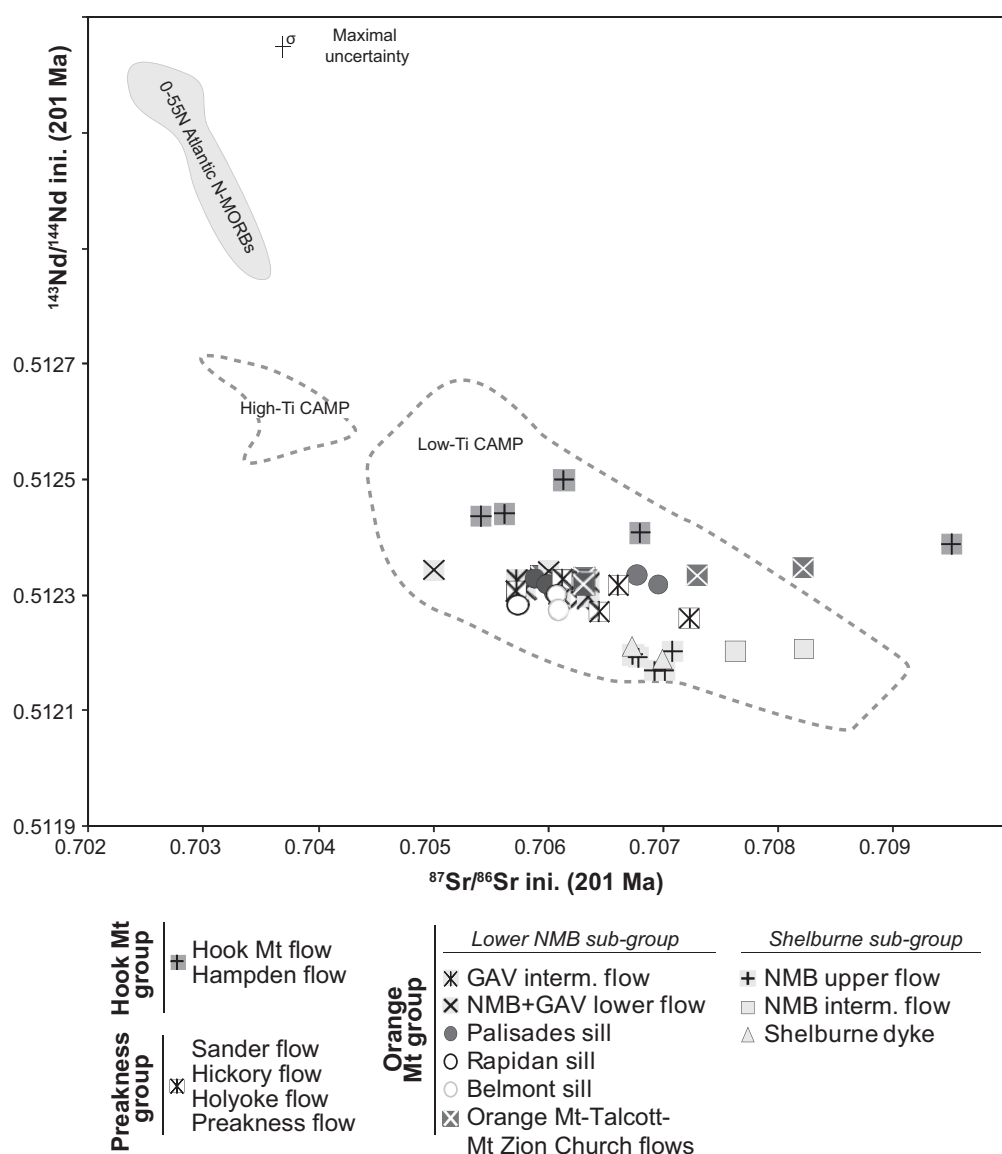


Fig. 9. Variation of $^{143}\text{Nd}/^{144}\text{Nd}$ vs $^{87}\text{Sr}/^{86}\text{Sr}$ in ENA CAMP basalts back-calculated to 201 Ma. Fields for CAMP low- and high-Ti tholeiites are based on data from Dupuy *et al.* (1988), Cebria *et al.* (2003), Jourdan *et al.* (2003), Deckart *et al.* (2005), Verati *et al.* (2005) and Merle *et al.* (2011).

instance, models of crystallizing magma chambers periodically refilled with primitive magma such as picritic liquids cannot be fully excluded [for discussion, see Molzahn *et al.* (1996)]. However, such models were designed for CFBs in which picritic magma types are common. This model could not be applied to the CAMP as no related picrites or primitive basalts have been identified so far. Moreover, picritic melts are not consistent with the relatively low mantle potential temperatures calculated for the CAMP ($<1500^\circ\text{C}$; Herzberg & Gazel, 2009).

Alternatively, large amounts of assimilation of continental crust by hot and primitive mafic magmas flowing

turbulently through conduits with very limited crystallization [assimilation through turbulent ascent (ATA); Huppert & Sparks, 1985] suggest that the more primitive samples should show greater evidence of crustal contamination (e.g. Kerr *et al.*, 1995a). It should be noted that ATA is mathematically equivalent to simple bimodal mixing between primitive melts and the continental crust (Kerr *et al.*, 1995a). In this case, different isotopic compositions should be expected between the more primitive (more contaminated) and the more evolved samples (less contaminated). However, this is never observed for the ENA CAMP basalts (Fig. 15).

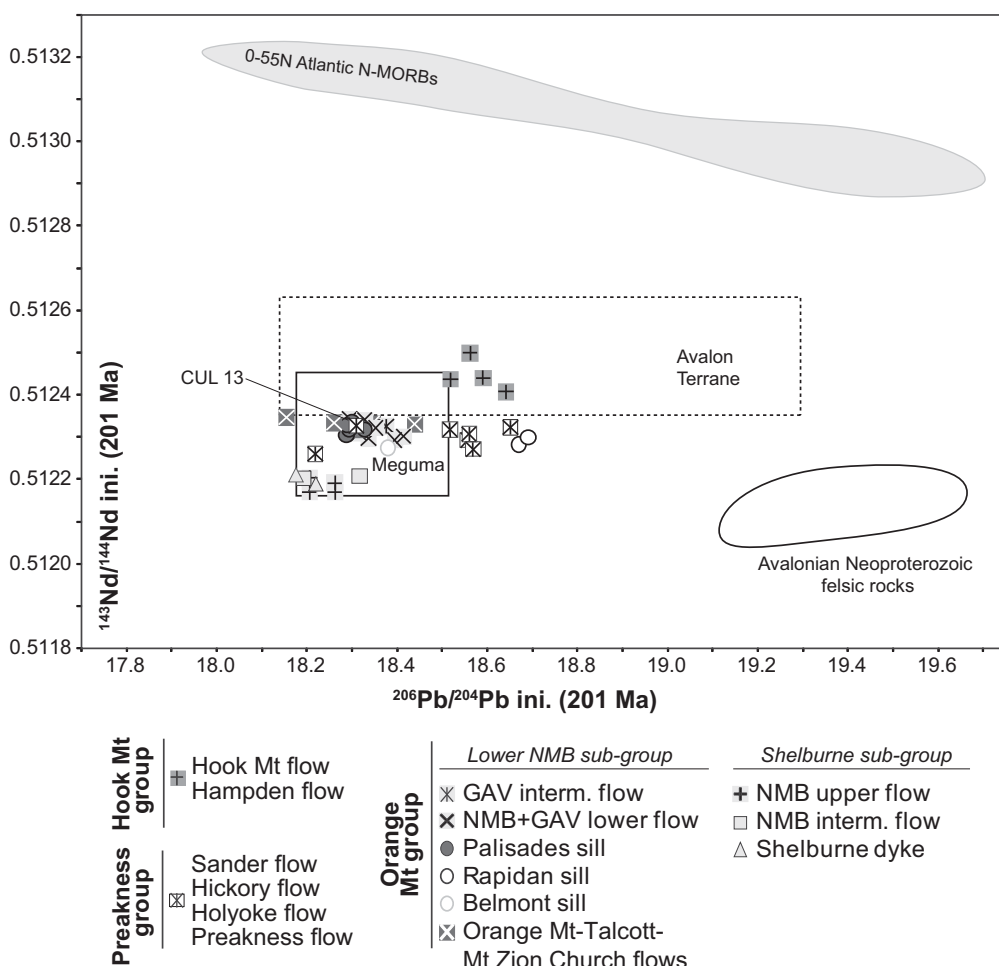


Fig. 10. Variation of initial isotopic ratios (back-calculated at 201 Ma) of $^{143}\text{Nd}/^{144}\text{Nd}$ vs. $^{206}\text{Pb}/^{204}\text{Pb}$ for samples from ENA CAMP basalts. The fields for the local continental crust have been compiled from published data combining Pb and Nd and back-calculated to 201 Ma. Initial Pb isotopic ratios measured on feldspars have been included. Data for the Avalon terrane and Avalonian Neoproterozoic felsic rocks (Bass River block) are from Pe-Piper & Piper (1998); data for the Meguma terrane are from Currie *et al.* (1998) and Pe-Piper & Jansa (1999).

For all of the reasons stated above, the chemical characteristics of the CAMP basalts and in particular the enriched signature seem unlikely to be related to substantial crustal contamination of OIB- or MORB-type parental magmas.

Mixing between OIB or asthenospheric melts and ultra-alkaline mafic melts (*hypothesis iii*)

An alternative mechanism for generating enriched Sr–Nd–Pb isotopic compositions in tholeiitic basalts would be to mix asthenospheric or OIB-type melts with ultra-alkaline melts derived from metasomatized SCLM (Arndt & Christensen, 1992; Gibson *et al.*, 2006; Heinonen *et al.*, 2010), followed by contamination by the continental crust. This hypothesis is essentially based on the occurrence of SCLM-derived ultra-alkaline mafic rocks (lamproites, kimberlites or carbonatites) that are associated with

tholeiitic magmatism in some flood basalt provinces such as the Parana–Etendeka province (Gibson *et al.*, 2006). However, no such compositions are known to be related (spatially or temporally) with the CAMP event. Nevertheless, this process has been modelled to see whether it might provide a feasible explanation for the isotopic compositions of the ENA CAMP basalts. A two-step process is assumed: (1) simple mixing between OIB- or MORB-type melts and SCLM-related melts; (2) subsequent contamination involving components of the local continental crust. For the contamination process, both AFC (DePaolo, 1981) and ATA (Huppert & Sparks, 1985) have been modeled.

Because ultra-alkaline SCLM-derived rocks are not associated with the CAMP, we used the composition of such rocks associated with the Mesozoic Paraná LIP. Our choice is driven by the geodynamic similarity of the

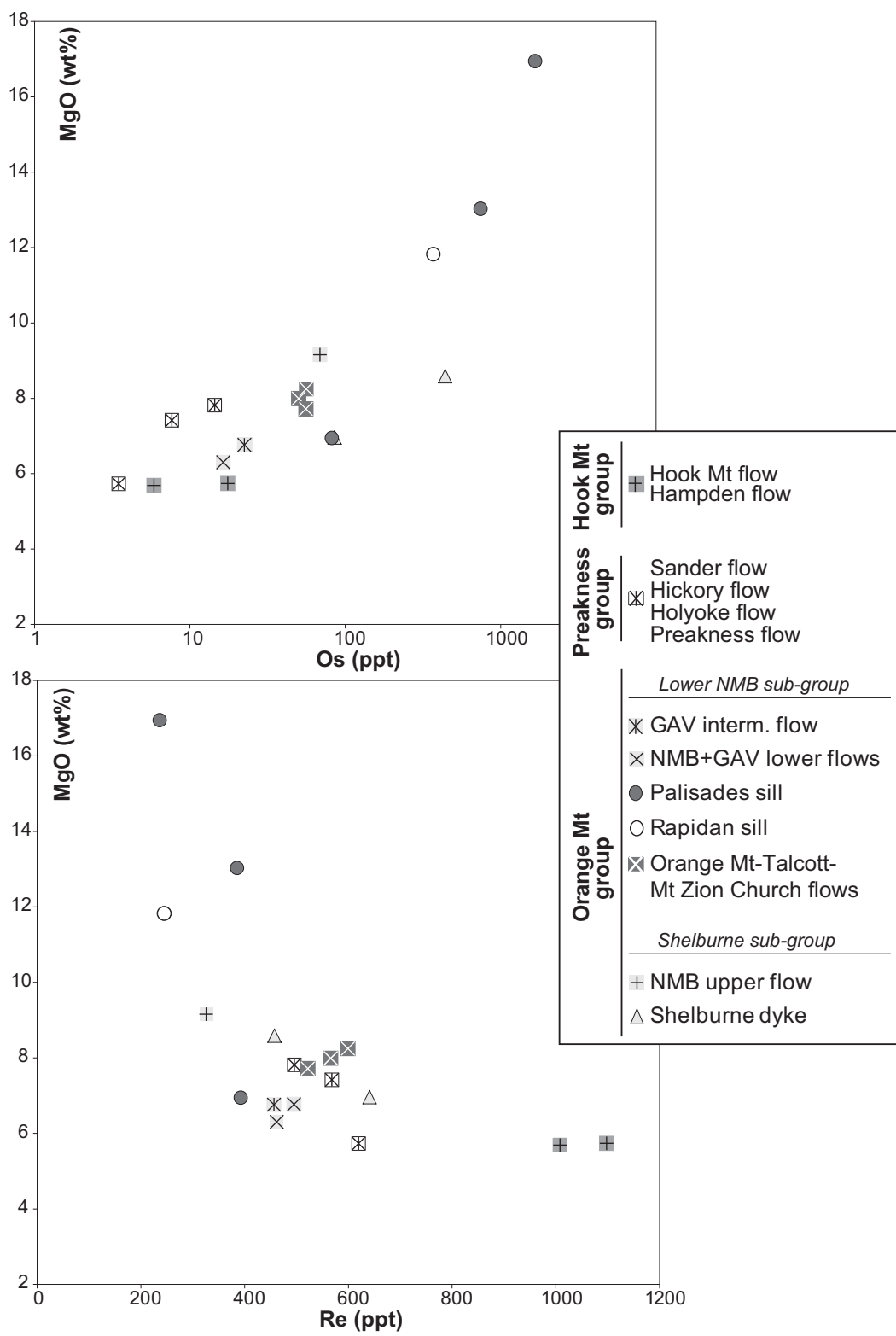


Fig. 11. Variation of Re and Os (ppt) vs MgO (wt %).

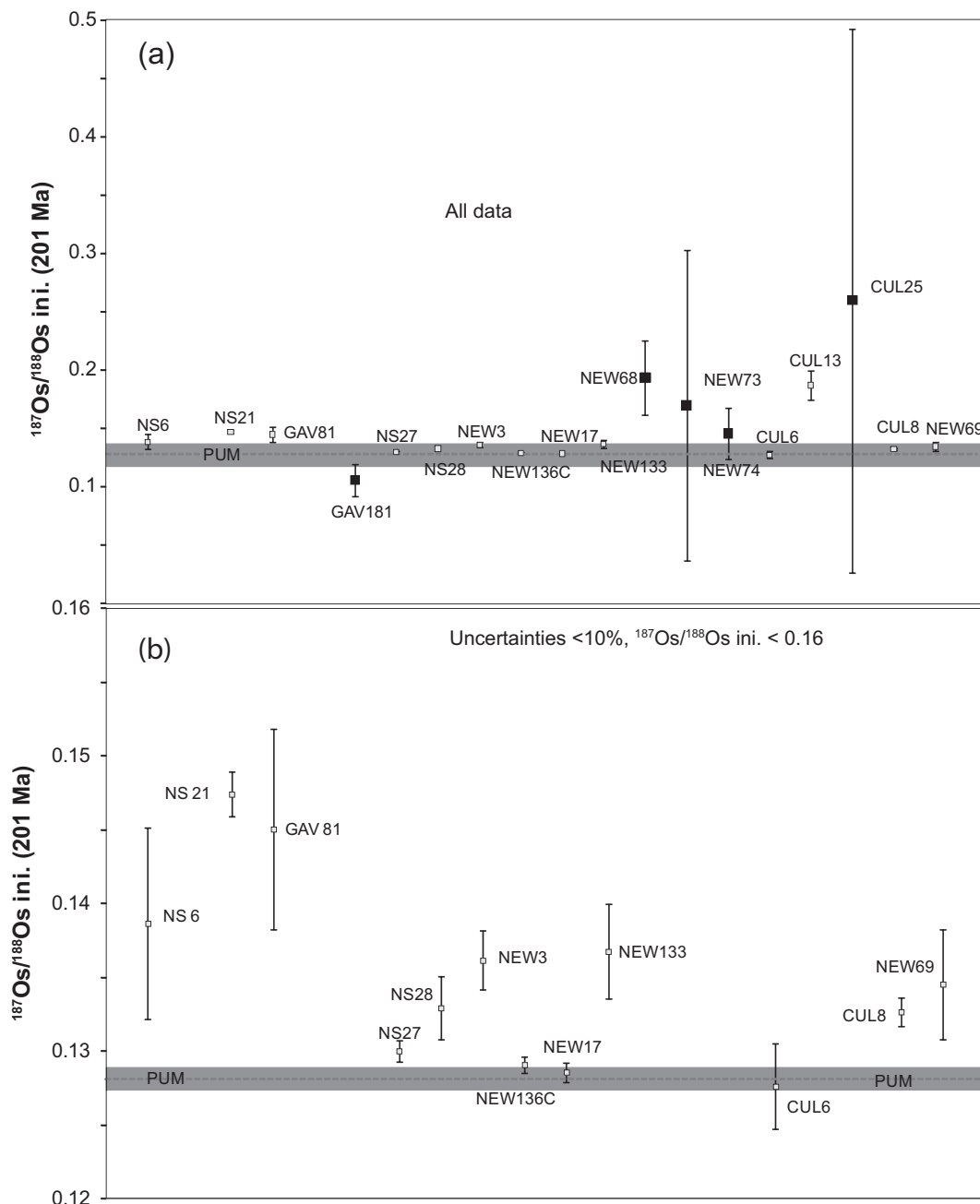


Fig. 12. Initial $^{187}\text{Os}/^{188}\text{Os}$ (back-calculated to 201 Ma) with uncertainties. Error bars are given at the 2σ level. (a) All data shown. Filled black rectangles, data with uncertainties higher than 10%; open rectangles, data with uncertainties lower than 10%. (b) Samples with $^{187}\text{Os}/^{188}\text{Os} < 0.16$ and uncertainties lower than 10%. Value of the Primitive Upper Mantle (PUM) back-calculated to 201 Ma (present-day PUM values: $^{187}\text{Os}/^{188}\text{Os} = 0.1296 \pm 0.0008$, $^{187}\text{Re}/^{188}\text{Os} = 0.4353$; Meisel *et al.*, 2001).

CAMP and Paraná, both LIPs being associated with the opening of the Atlantic Ocean. Because there is no modern equivalent of the hypothetical CAMP mantle plume, the composition of the OIB end-member is poorly constrained. Considering the large range of OIB compositions worldwide and the fact that the results are strongly dependent

on this parameter, the best proxy needs to be constrained by the geology of the CAMP. As a consequence, we assumed an average OIB composition close to that of Atlantic OIB (i.e. Cape Verde, Fernando de Noronha, Ascension, Canaries). For the assimilation model, we considered several components of the local

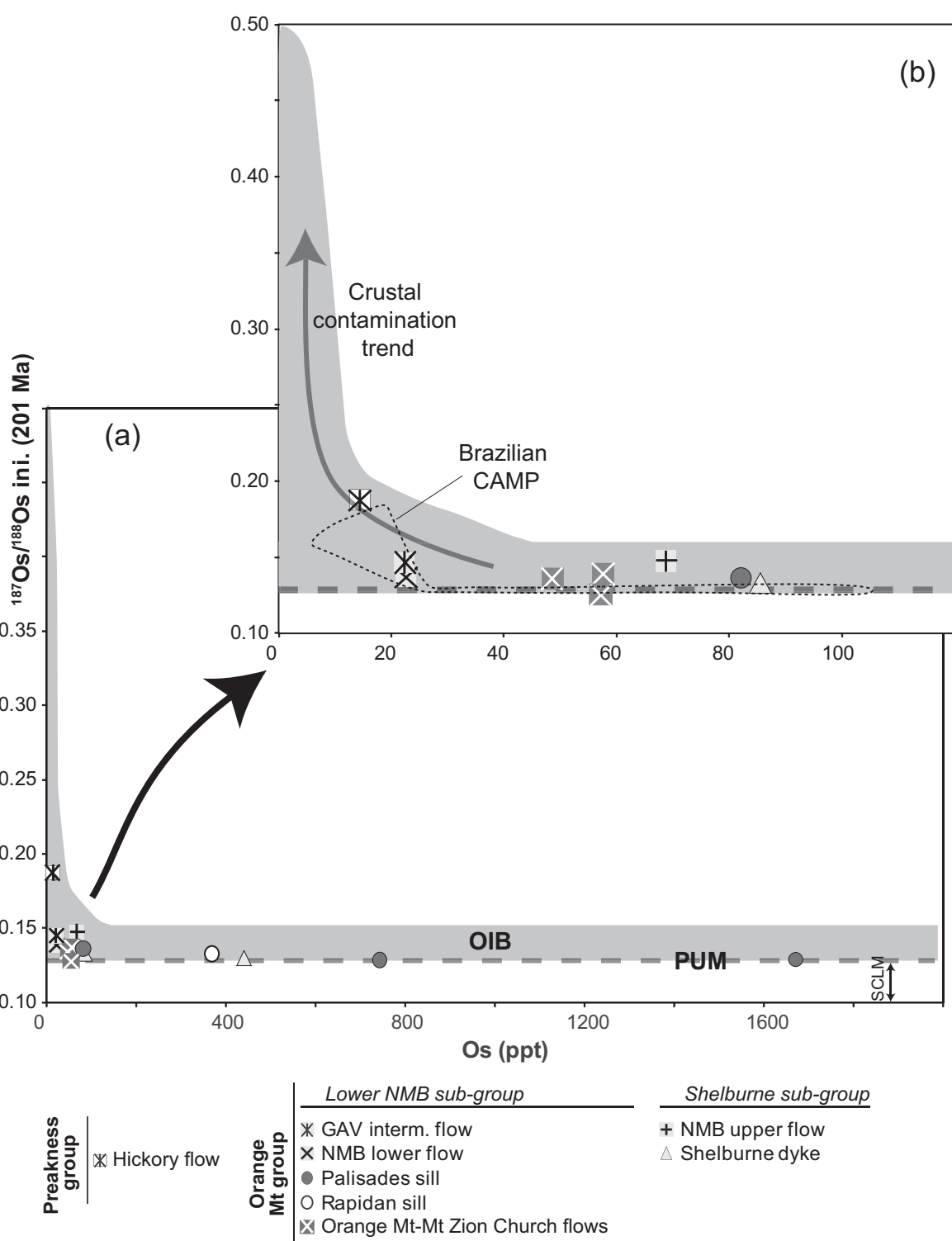


Fig. 13. Variation of initial $^{187}\text{Os}/^{188}\text{Os}$ (back-calculated to 201 Ma) vs Os concentration. (a) All ENA data represented. (b) Samples with Os contents lower than 120 ppt. The general crustal contamination trend is based on upper continental crust with low [Os] and high $^{187}\text{Os}/^{188}\text{Os}$. The grey field corresponds to worldwide occurrences of OIB. The value of the Primitive Upper Mantle (PUM) has been back-calculated to 201 Ma (present-day PUM values: $^{187}\text{Os}/^{188}\text{Os} = 0.1296 \pm 0.0008$; $^{187}\text{Re}/^{188}\text{Os} = 0.4353$; Meisel *et al.*, 2001). Field for Brazilian CAMP is from Merle *et al.* (2011).

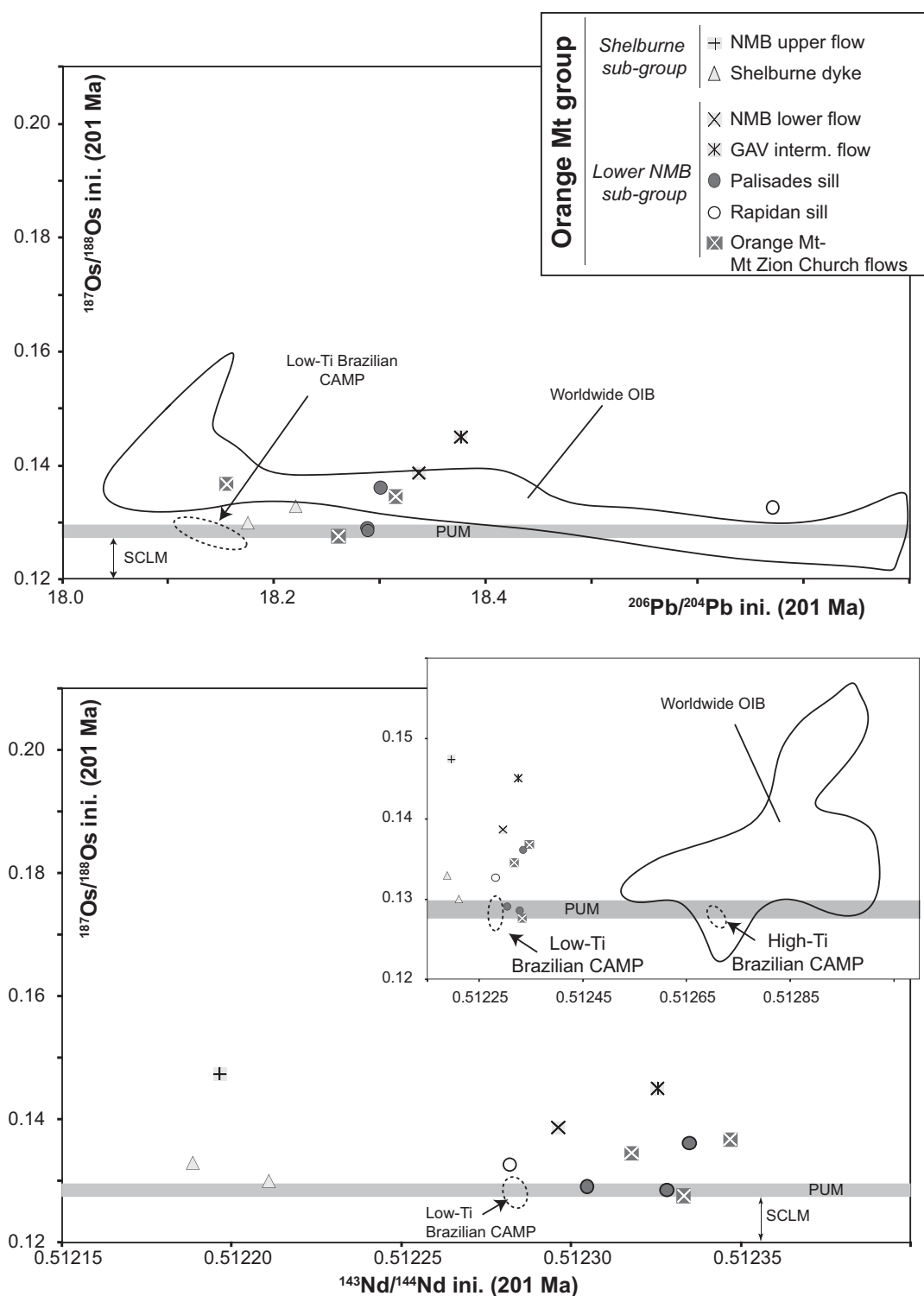


Fig. 14. Variation of initial $^{187}\text{Os}/^{188}\text{Os}$ vs $^{143}\text{Nd}/^{144}\text{Nd}$ and $^{206}\text{Pb}/^{204}\text{Pb}$ for ENA CAMP basalts (data back-calculated to 201 Ma). Primitive upper mantle (PUM) value is from Meisel *et al.* (2001), back-calculated to 201 Ma. Field for modern worldwide OIB is based on data from the Georoc database. The OIB data have been filtered for lithosphere contamination: samples with $[\text{Os}] < 30 \text{ ppt}$ and $^{187}\text{Os}/^{188}\text{Os} > 0.16$ have been discarded. It should be noted that sample CUL13 (Hickory Grove), which shows characteristics of contamination by the continental crust, is not plotted. The fields for Brazilian CAMP basalts are from Merle *et al.* (2011).

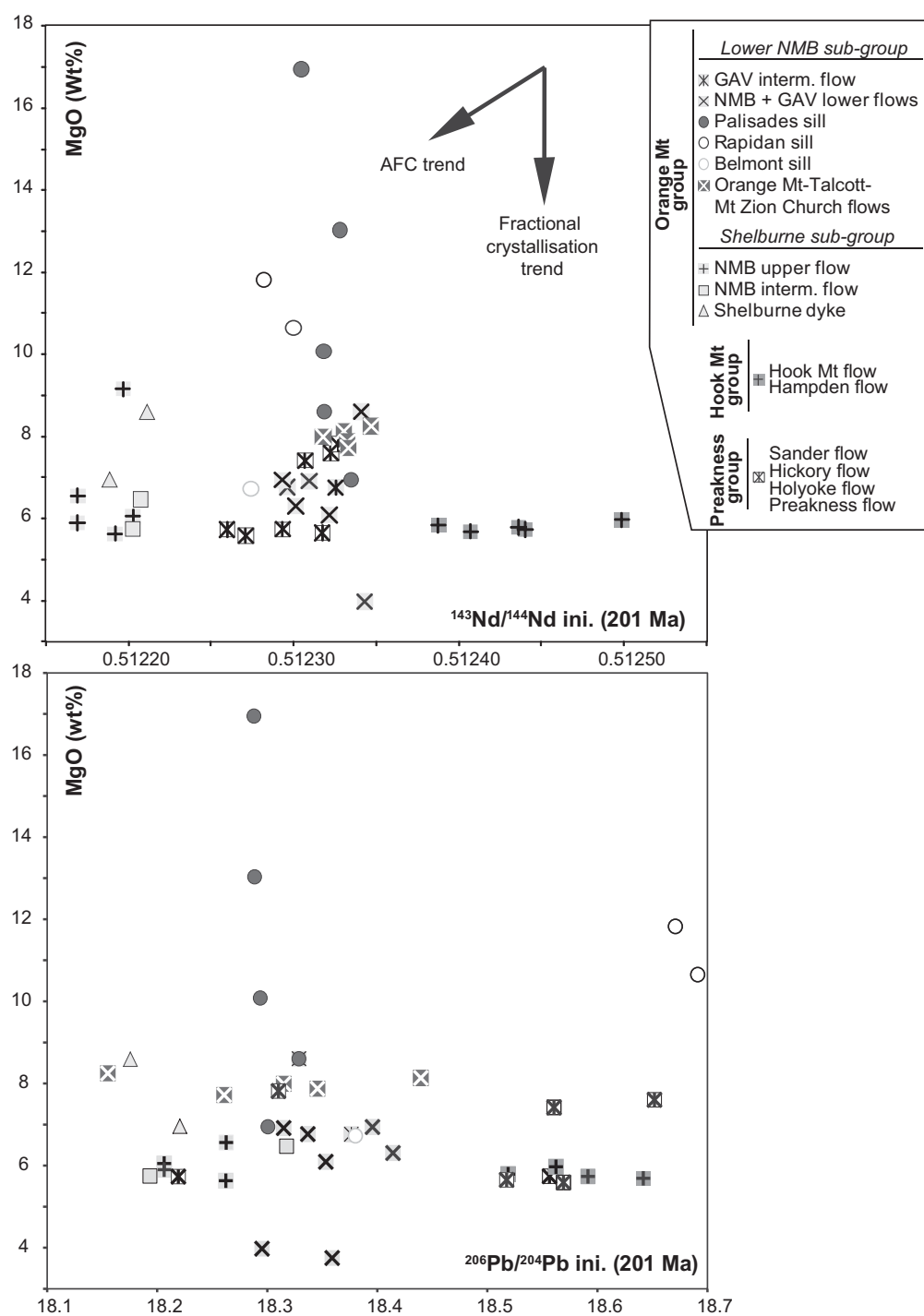


Fig. 15. Variation of initial $^{143}\text{Nd}/^{144}\text{Nd}$ and $^{206}\text{Pb}/^{204}\text{Pb}$ vs MgO for the ENA CAMP basalts. The AFC trend indicates the general evolution of the chemistry of the basalts when contaminated by average upper continental crust with a low MgO content and low $^{143}\text{Nd}/^{144}\text{Nd}$.

crust. The chemical characteristics of the ENA CAMP basalts were best reproduced using the composition of Avalonian Neoproterozoic felsic crust (Pe-Piper & Piper, 1998).

According to the numerical modelling, mixing involving either OIB or MORB-like parental melts followed by crustal contamination partially reproduces the compositions of the three chemical ENA CAMP groups (Figs 16–19;

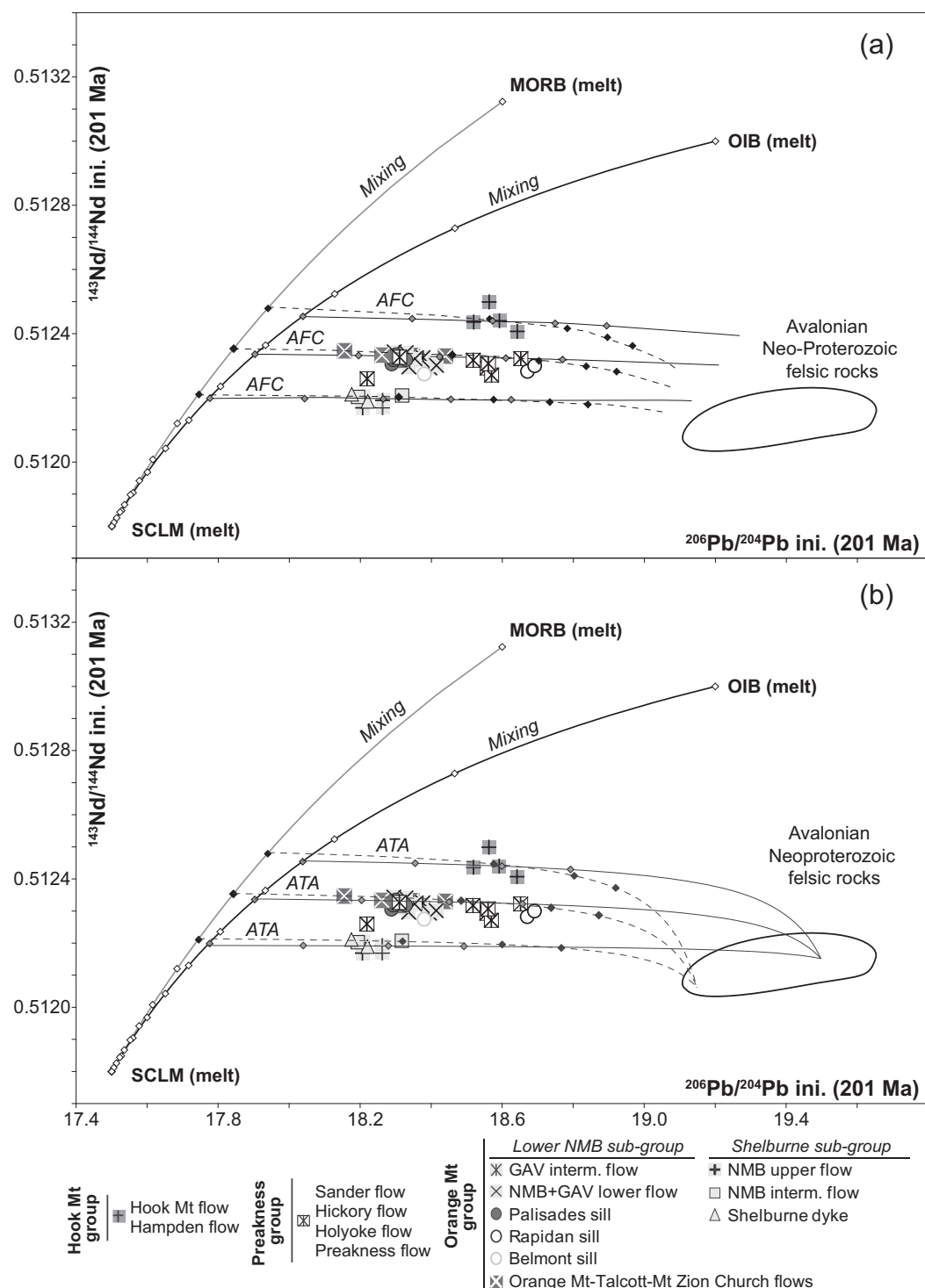


Fig. 16. Models combining mixing of OIB or MORB compositions with SCLM-derived melts followed by crustal contamination. (a) $^{143}\text{Nd}/^{144}\text{Nd}$ vs $^{206}\text{Pb}/^{204}\text{Pb}$ assuming an AFC contamination process. (b) $^{143}\text{Nd}/^{144}\text{Nd}$ vs $^{206}\text{Pb}/^{204}\text{Pb}$ assuming an ATA contamination process. The lozenges on the mixing and AFC or ATA lines represent 10% increments. Composition of Avalonian Neoproterozoic felsic rocks is from Pe-Piper & Piper (1998). All model parameters are given in Supplementary Data Tables A4 and A5.

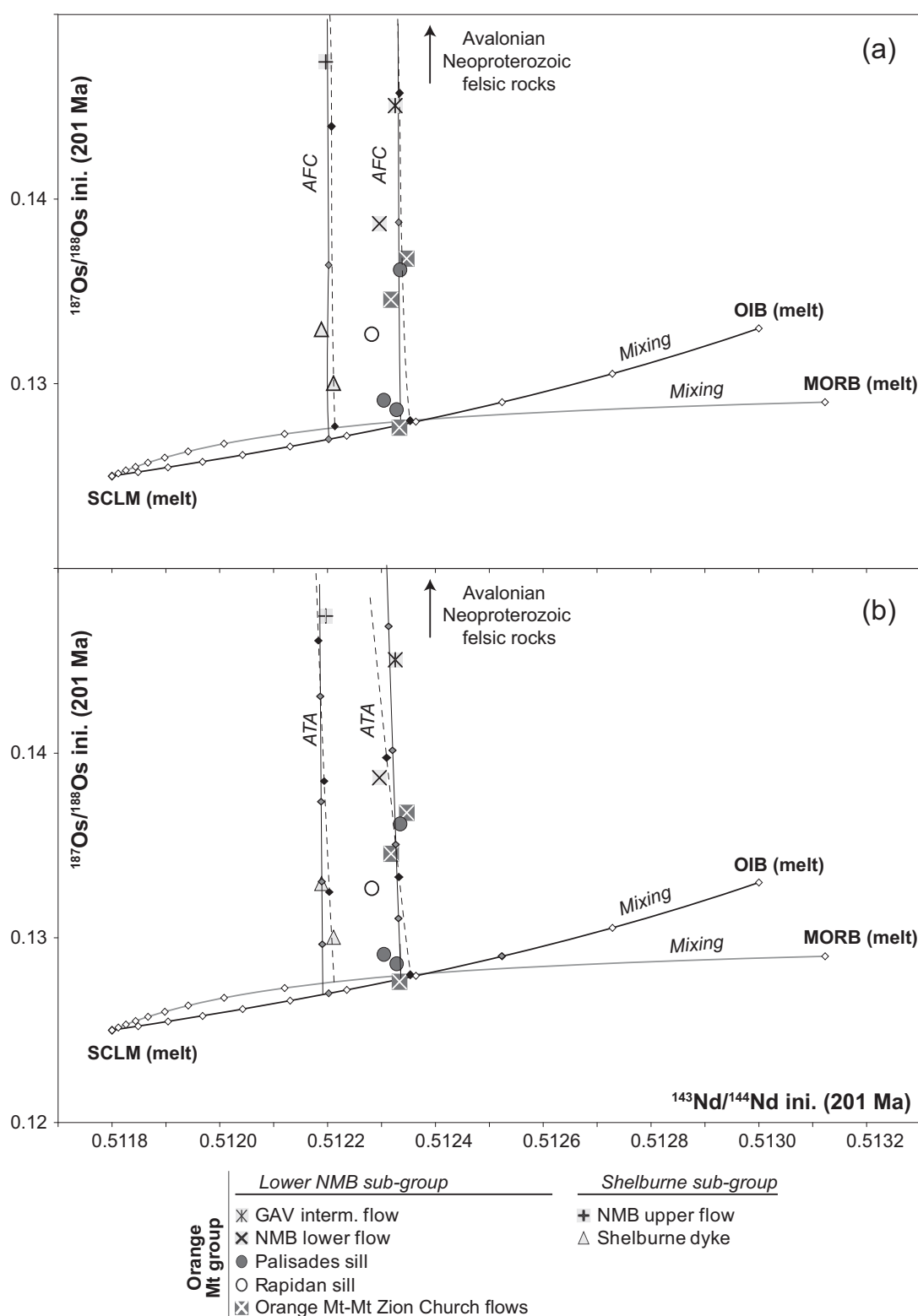


Fig. 17. Models combining mixing of OIB or MORB compositions with SCLM-derived melts followed by crustal contamination. (a) $^{143}\text{Nd}/^{144}\text{Nd}$ vs $^{187}\text{Os}/^{188}\text{Os}$ assuming an AFC contamination process. (b) $^{143}\text{Nd}/^{144}\text{Nd}$ vs $^{187}\text{Os}/^{188}\text{Os}$ assuming an ATA contamination process. The lozenges on the mixing and AFC or ATA lines represent 10% increments. Composition of the Avalonian Neoproterozoic felsic rocks is from Pe-Piper & Piper (1998). All model parameters are given in Supplementary Data Tables A4 and A5.

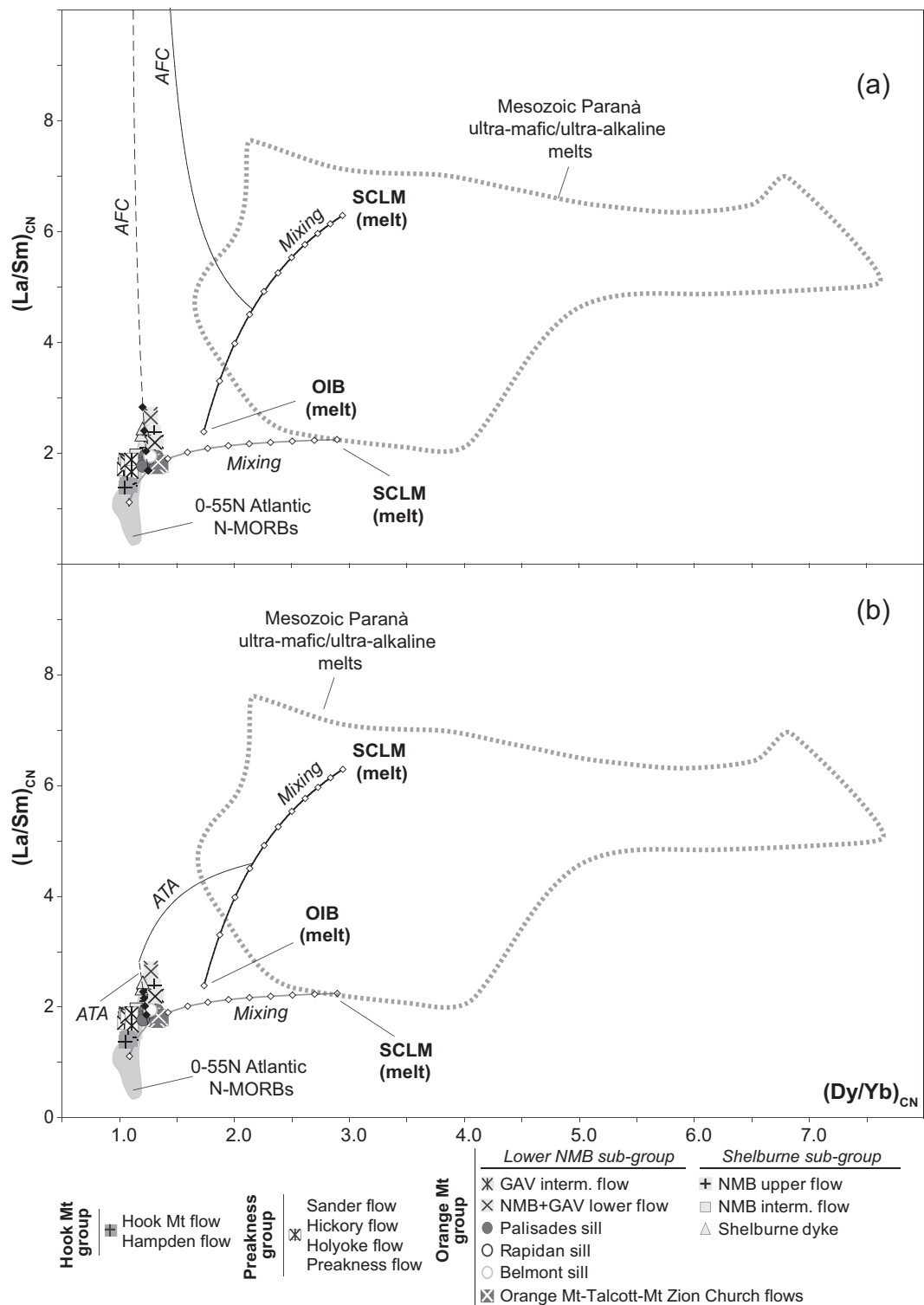


Fig. 18. Models combining mixing of OIB or MORB compositions with SCLM-derived melts followed by crustal contamination. (a) $\text{La}/\text{Sm}_{\text{CN}}$ vs $\text{Dy}/\text{Yb}_{\text{CN}}$ assuming an AFC contamination process. (b) $\text{La}/\text{Sm}_{\text{CN}}$ vs $\text{Dy}/\text{Yb}_{\text{CN}}$ assuming an ATA contamination process. The lozenges on the mixing and AFC or ATA lines represent 10% increments. All model parameters are given in Supplementary Data Tables A4 and A5. Composition of Mesozoic ultramafic or ultra-alkaline rocks of the Paraná LIP are from the Georoc database. CN, chondrite normalization values from Sun & McDonough (1989).

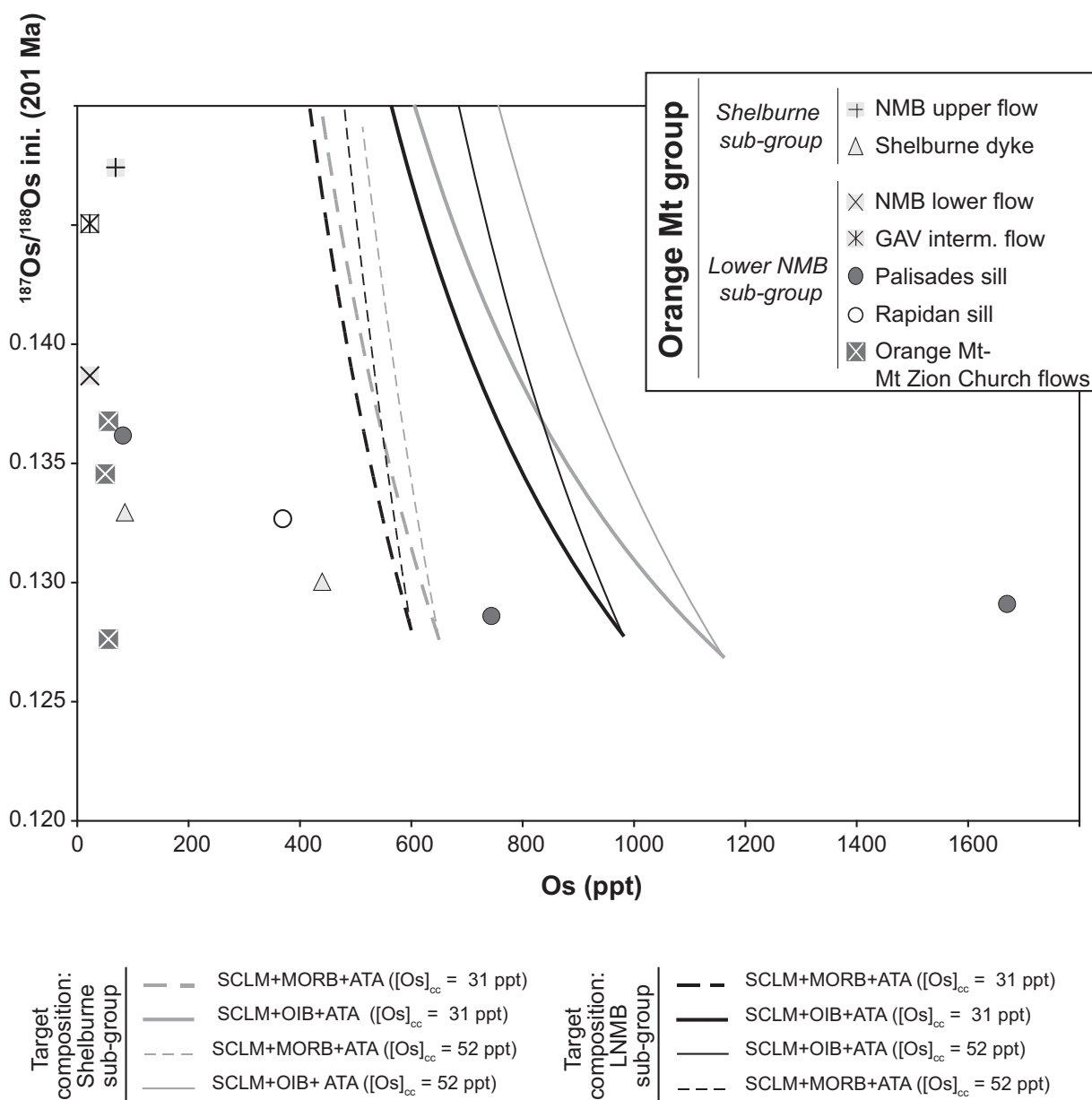


Fig. 19. Variation of Os concentration in ppt vs initial $^{187}\text{Os}/^{188}\text{Os}$ (at 201 Ma) showing models of mixing between OIB or MORB melts and SCLM-derived melts followed by ATA involving different compositions of continental crust. (See further explanation in the text.)

parameters and results are given in Supplementary Data Tables A4 and A5). In the case of mixing of OIB with SCLM-related melts, the isotopic composition of the ENA CAMP basalts can be modelled by mixing with 24% (Hook Mt group) and 44% (Shelburne sub-group) of SCLM-related melts followed by very large amounts of assimilation of continental crust, regardless of the process of assimilation (AFC: 13–35%; ATA: 12–32%; Figs 16–18). However, this model presents some problems. First, the Nd–Pb–Os isotopic compositions of the ENA CAMP

basalts can be matched only for very high Os and very low Nd contents (2000 ppt and 100 ppm, respectively) in the primary SCLM-related melt (Fig. 16). Second, and, more significantly, the main problem of this modelling concerns the incompatible elements and in particular the REE ratios of the resulting melts. Whereas the large majority of OIB and Paraná SCLM-related melts have $\text{La}/\text{Sm}_N > 2$ (Sun & McDonough, 1989; Gibson *et al.*, 1999), most of the ENA CAMP basalts have $\text{La}/\text{Sm} < 2$ (Fig. 18). An AFC or ATA process following the mixing would

result in more enriched REE contents that would never match the compositions of the ENA CAMP basalts regardless of the composition of the continental crust (Fig. 18). Moreover, the trends observed in the Nd–Pb and Os–Nd isotopic diagrams require up to 35% of contamination by the local continental crust (Figs 16–18). Such high degrees of assimilation should have been observed in the MgO vs $^{143}\text{Nd}/^{144}\text{Nd}$ and MgO vs $^{206}\text{Pb}/^{204}\text{Pb}$ diagrams as trends for an AFC process or as significant differences between more primitive and more evolved samples for an ATA process (Fig. 15). In addition, assimilation of more than 20% of continental crust is thermodynamically unrealistic (Spera & Bohrson, 2001). Consequently, the hypothesis of a magma originating from mixing between OIB and SCLM-related melts and further contaminated by the continental crust is unlikely.

When MORB and SCLM-related melts mix, the Nd–Pb–Os isotopic compositions of the ENA CAMP basalts could be matched by between 15% (Shelburne sub-group) and 7% (Hook Mt group) of SCLM-related melts and by assimilation of 5–20% of the local continental crust through an AFC process and by 5–18% through an ATA process (Figs 16–18). As for mixing between OIB- and SCLM-related melts, the compositions of the ENA CAMP basalts can be obtained only for very low Nd contents (<100 ppm) in the SCLM-related melt. As for the OIB–SCLM model, the main flaw concerns the REE ratios, as the ENA CAMP basalt compositions can be matched only by involving depleted compositions of N-MORB and extreme compositions (lowest La/Sm and Dy/Yb observed for the ultra-alkaline melts) of the SCLM-related melts.

In the case of an AFC process, the trends observed in the Nd–Pb and Nd–Os isotopic variations of the ENA CAMP basalts can be matched only if a very low Pb content (5 ppm) is assumed for the local continental crust. The main problem with this scenario concerns the discrepancy between the amount of assimilation required to match the isotopic (*c.* 20%) and the REE (*c.* 30%) compositions of the ENA tholeiites (Fig. 17). This issue is not resolved when ATA is considered instead of AFC and the same composition of continental crust is assumed. Indeed, the Nd–Pb isotopic compositions require smaller amounts of assimilation (less than 20%) than suggested by the Os isotopic compositions (up to 30%) or the REE contents (up to 50%).

This discrepancy could be eliminated by considering a continental crust component with a slightly atypical composition ([La] = 39 ppm, [Sm] = 3.1 ppm, [Dy] = 3.6 ppm, [Yb] = 2 ppm), which would match the CAMP compositions for approximately 20% crustal contamination (both AFC and ATA considered). In the case of the AFC process, the composition of the lower NMB sub-group is modelled by assuming a crust with a very low Os concentration ([Os] = 2.6 ppt). Such low Os contents are rare in the

continental crust, and similar concentrations have been found only in lower crustal plagioclase-rich cumulates (Saal *et al.*, 1998). However, the latter rocks have higher initial Os and Nd isotopic ratios and lower initial Pb isotopic ratios than the composition of the crust required to model the ENA CAMP basalts (Saal *et al.*, 1998, and references included). Moreover, this kind of plagioclase cumulate has not been documented in the NE USA. In the case of an ATA process, crust with an Os concentration up to 52 ppt is required. Nevertheless, this process cannot produce the Os concentrations of the ENA CAMP basalts (Fig. 19).

In conclusion, mixing between OIB and SCLM-related melts seems rather unrealistic and can be ruled out. The MORB–SCLM-related model seems more plausible but also has some limitations.

Derivation from OPB-type melts (hypothesis iv)

Because most OIB compositions are extreme end-members that result from small degrees of partial melting of the mantle, they might not be representative of the composition produced by the large-scale melting proposed for generation of LIPs. Moreover, for continental LIP magmas, even the least evolved, crustal contamination cannot be entirely ruled out. High-MgO OPB compositions might, therefore, be a better proxy for the primary melts derived from a deep mantle source (Kerr *et al.*, 1995b). In addition, many continental flood basalts show evidence for depleted (MORB-like) components in their sources that are not related to a shallow contamination by the asthenosphere (entrainment of the asthenosphere by a rising plume) but are genuinely deep mantle components (Kerr *et al.*, 1995b). As a consequence, the uncontaminated magmas share characteristics of both MORB and OIB (Kerr *et al.*, 1995b).

We therefore tested the possibility that the ENA CAMP basalts were derived from magmas analogous to OPB melts that experienced crustal contamination, possibly preceded by mixing with SCLM-derived melts. For the primitive parental magma composition, we used the average compositions of primitive melts (i.e. tholeiitic, picritic and komatiitic compositions with MgO > 8%) from both the Caribbean and the Ontong–Java plateaux (e.g. Kerr & Mahoney, 2007). Considering that no Os data are available for the latter, we used the average $^{187}\text{Os}/^{188}\text{Os}$ initial ratio and Os concentration of the Caribbean plateau basalts. Because OPBs are clearly distinct from the CAMP basalts, continental crustal contamination is required to achieve the enriched signature observed in the latter. However, simple crustal contamination of OPB-type primitive melts by either ATA or AFC mechanisms fails to reproduce the chemical characteristics of the ENA CAMP basalts (Fig. 20). A slightly better fit is achieved if the OPB melts are first mixed with SCLM-derived melts and then contaminated by the continental crust; nevertheless, in this case also, only part of ENA CAMP compositions can be reproduced, in particular the REE compositions of the

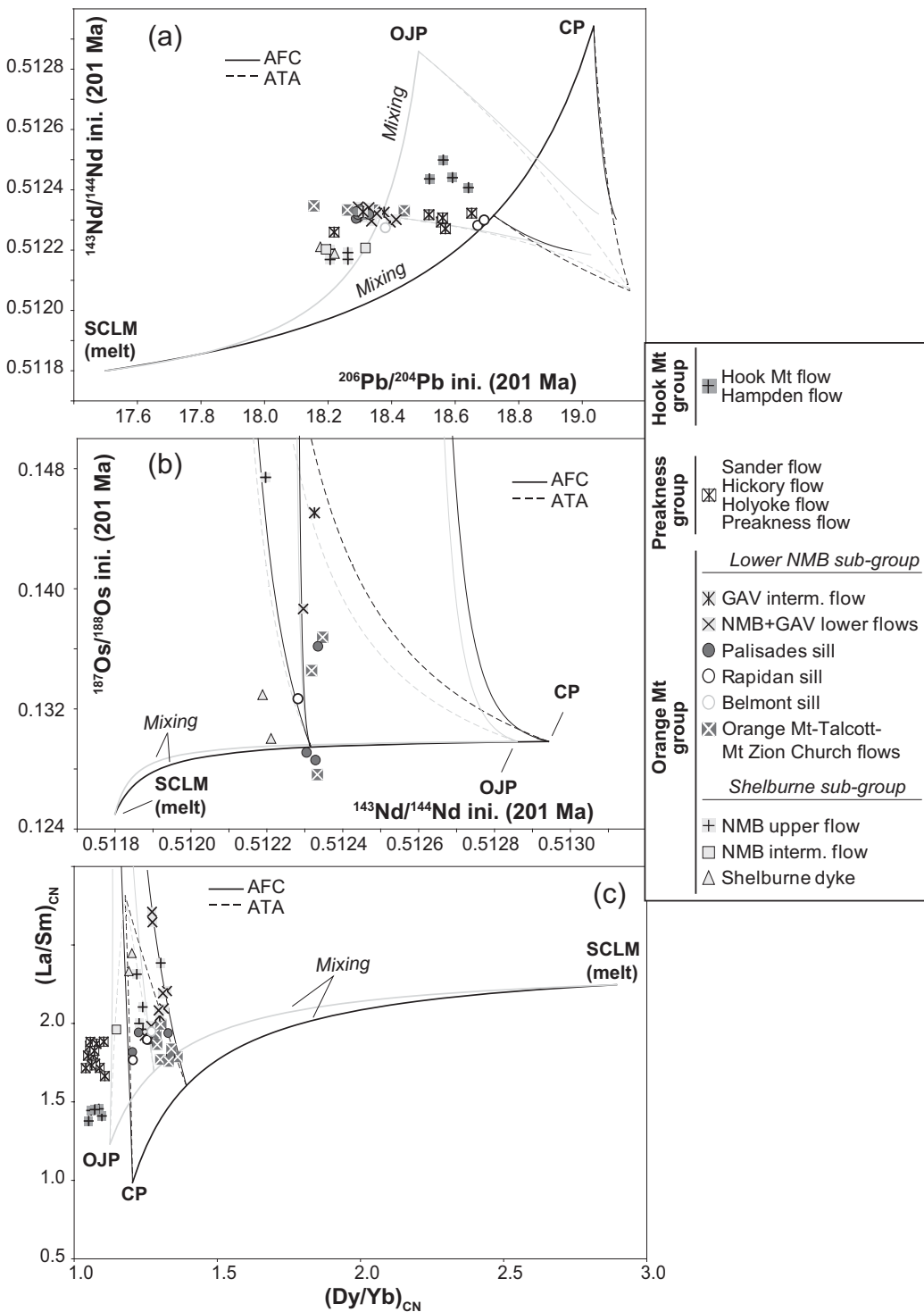


Fig. 20. Variation of (a) $^{143}\text{Nd}/^{144}\text{Nd}$ vs $^{206}\text{Pb}/^{204}\text{Pb}$, (b) $^{143}\text{Nd}/^{144}\text{Nd}$ vs $^{187}\text{Os}/^{188}\text{Os}$ and (c) La/Sr_{CN} vs Dy/Yb_{CN} showing combined models of mixing + AFC and ATA between Ontong-Java Plateau (OJP) or Caribbean Plateau (CP) melts and SCLM-derived melts. Average composition of OJP and CP primitive basalts is from the Georoc database. All model parameters are given in Supplementary Data Table A6.

Hook Mt and Preakness groups and the Pb–Nd isotopic compositions of the Orange Mt group (Fig. 20). It should be noted that the composition of the SCLM end-member is similar to that used in the previous modeling, and hence presents the same problems. Nevertheless, it is the only composition able to partly reproduce the composition of the CAMP basalts.

Because the OPB compositions used in this modeling are averages it could be argued that they are not representative of the oceanic plateau and different compositions could perhaps match the ENA CAMP basalts. Nevertheless, extreme compositions are more rare and less representative of large-scale mantle melting. Moreover, tholeiitic OPB compositions are close to those of MORB, leading to the same problems as encountered for mixing between MORB and SCLM melts. Conversely, more enriched OPB compositions tend to display the same problems as observed for mixing between OIB and SCLM melts.

As a consequence, although this model can plausibly reproduce the compositions of the ENA CAMP basalts it still presents some limitations.

Ternary mixing between OIB or asthenospheric melts and ultra-alkaline mafic melts (hypothesis v)

The chemical characteristics of the ENA CAMP basalts could result from ternary mixing between OIB, MORB and SCLM compositions, possibly followed by crustal assimilation (AFC or ATA). In this model the compositions for OIB, MORB and SCLM melts are the same as for the binary mixing models of hypothesis iii (parameters are given in Supplementary Data Tables A4 and A5) and the composition of the continental crust is similar to that used in the models of MORB–SCLM mixing (see parameters in Supplementary Data Tables A4 and A5). The isotopic composition of the lower NMB sub-group and Preakness group can be modeled by mixing 69% MORB, 15% OIB and 16% SCLM melt followed by approximately 4% crustal contamination (both by ATA or AFC; Fig. 21). The Hook Mt group isotopic composition can be reproduced by mixing 73% MORB, 16% OIB and 11% SCLM, followed by 8% crustal contamination (ATA or AFC). The isotopic composition of the Shelburne sub-group can be reproduced with 63% MORB, 14% OIB and 23% SCLM melt, followed by approximately 7% crustal contamination (ATA or AFC). In this model, the proportion of the MORB end-member is dominant, with very limited crustal contamination. However, this model fails to reproduce the REE and Os contents of the lower NMB sub-group (Fig. 22).

Melting of a metasomatized SCLM-type source (hypothesis vi)

In this scenario, the continental crust-like isotopic characteristics of the ENA CAMP basalts (e.g. high Sr and low

Nd initial isotopic ratios; negative Nb and positive Pb anomalies) reflect the composition of the SCLM source, without the need for significant crustal assimilation. Indeed, except for one sample with high initial $^{187}\text{Os}/^{188}\text{Os}$ (CUL13: $^{187}\text{Os}/^{188}\text{Os} = 0.1874$), all the ENA CAMP samples have initial $^{187}\text{Os}/^{188}\text{Os} < 0.1500$, which is compatible with them being virtually uncontaminated mantle-derived magmas. As noted above, even small amounts of crustal contamination by AFC or ATA processes very rapidly drive the Os isotopic composition outside the mantle field. Considering the intensive sampling of the ENA province, in particular the lava units in the Triassic–Jurassic basins, the dataset is expected to encompass chemical and isotopic variations related to possible crustal contamination. The lack of correlations between MgO and the Nd, Os, or Pb isotopic ratios between or within the groups (Fig. 15) precludes significant assimilation of crustal rocks through an AFC process. Moreover, most of the samples with the highest MgO (8–11 wt %) and compatible trace element contents (Co = 43–53 ppm, Ni = 102–213 ppm, Cr = 358–850 ppm), display Sr, Pb and Nd isotopic compositions comparable with those of the more evolved rocks. These observations argue against extensive contamination by the continental crust by either AFC or ATA processes and favour a mantle source with a low $^{187}\text{Os}/^{188}\text{Os}$. Hence, the continental crust-like characteristics of the ENA CAMP rocks may directly reflect the characteristics of their mantle source(s). Recent studies have suggested that such contrasting chemical characteristics may be derived from a metasomatized SCLM-type source (e.g. Brauns *et al.*, 2000). Regardless of the nature of the source, the uncontaminated magmas need an initial $^{187}\text{Os}/^{188}\text{Os}$ that is lower than or similar to ~ 0.1276 (Fig. 7), which is the lowest value for the ENA samples. In this case, the Os isotopic composition of the source is within the range of $^{187}\text{Os}/^{188}\text{Os}$ of off-cratonic SCLM (0.1180–0.1290; Carlson, 2005).

We next consider the process that may have enriched a shallow section of the asthenospheric mantle beneath eastern North America. The mantle at present underlying this region experienced several subduction events during the Palaeozoic related to the accretion of peri-Laurentia and peri-Gondwana terranes such as Avalonia and Meguma (e.g. Van Staal *et al.*, 2009; Nance *et al.*, 2010). As a consequence, this mantle may not have been refractory during the CAMP event. This suggestion is supported by evidence of several episodes of tholeiitic mafic magmatism in the Avalonia–Meguma terranes since the Late Neoproterozoic. These mafic magmas are suspected to have originated in the SCLM (Pe-Piper & Piper, 1999; Puffer, 2001, 2003; Murphy *et al.*, 2008, 2011) and show a progressive time-related decrease in their initial ϵNd that could reflect a progressive enrichment of their source (Murphy *et al.*, 2011). The similarities between these rocks and the ENA

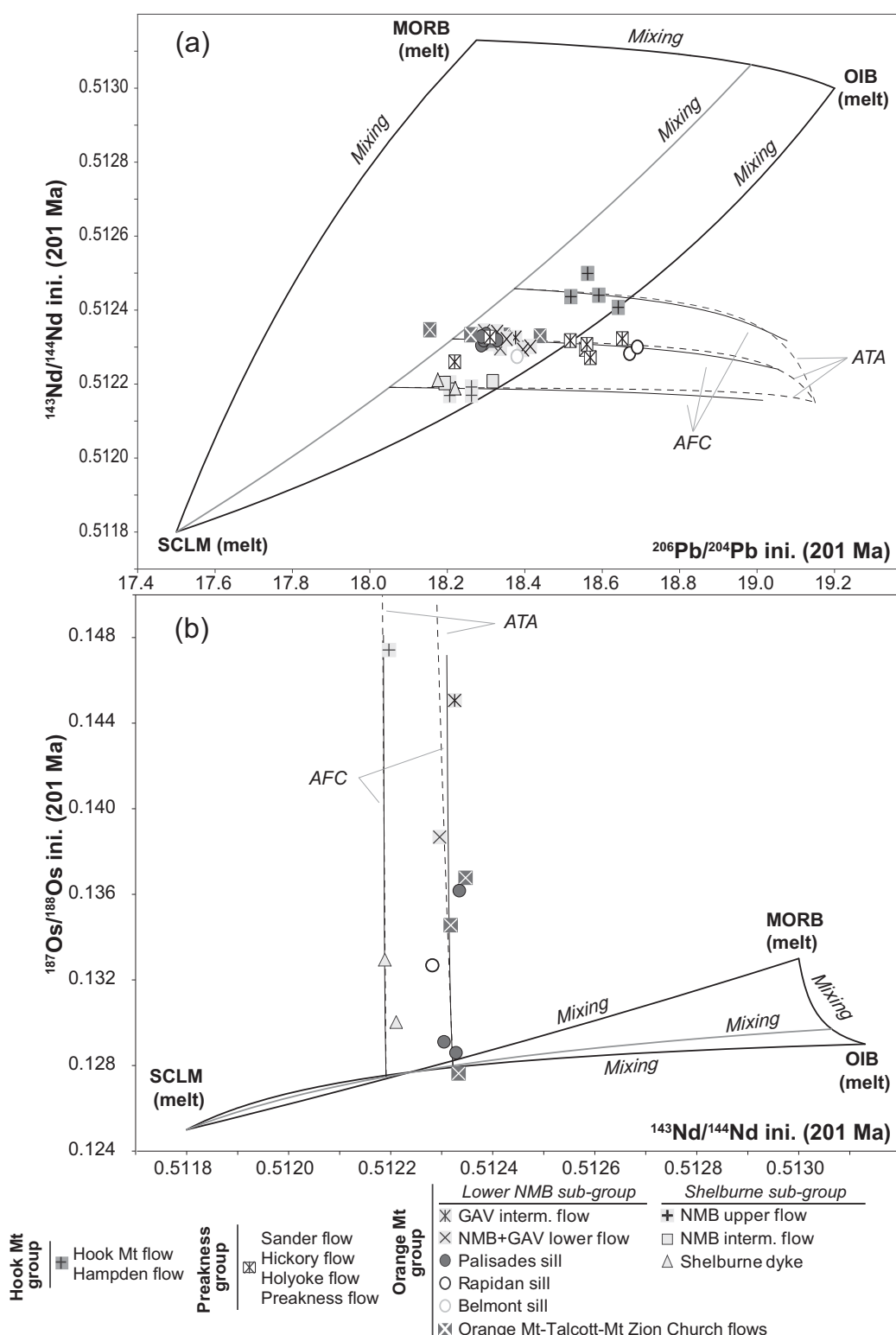


Fig. 21. Variation of (a) $^{143}\text{Nd}/^{144}\text{Nd}$ vs $^{206}\text{Pb}/^{204}\text{Pb}$ and (b) $^{143}\text{Nd}/^{144}\text{Nd}$ vs $^{187}\text{Os}/^{188}\text{Os}$ showing combined models of ternary mixing between OIB, MORB and SCLM-derived compositions followed by AFC or ATA.

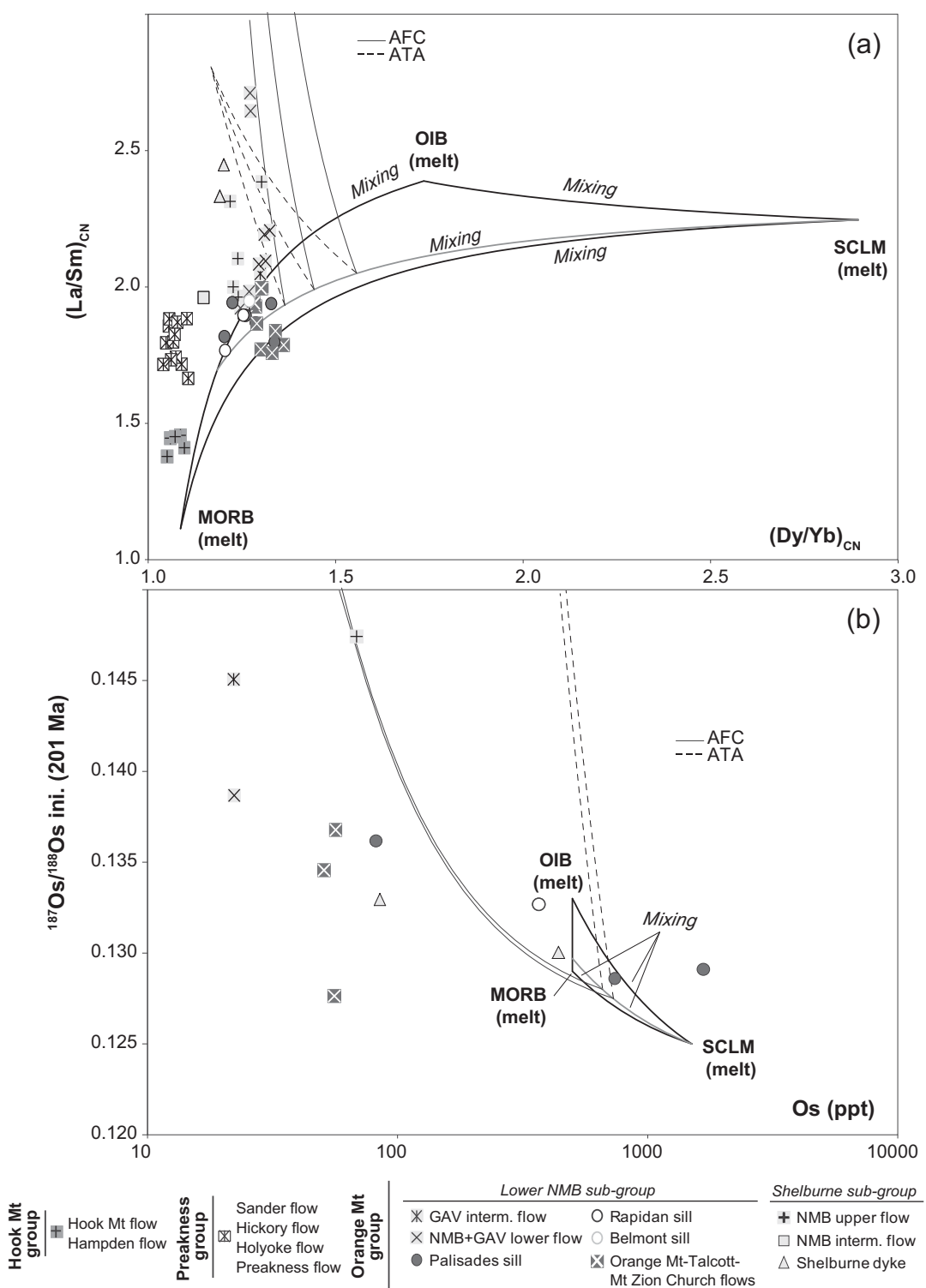


Fig. 22. Variation of (a) $\text{La}/\text{Sm}_{\text{CN}}$ vs $\text{Dy}/\text{Yb}_{\text{CN}}$ and (b) Os concentration vs initial $^{187}\text{Os}/^{188}\text{Os}$ showing combined models of ternary mixing between OIB, MORB and SCLM-derived compositions followed by AFC or ATA. Models use the same compositions for OIB, MORB, SCLM and continental crust as in the binary mixing models (Figs 16 and 17). All parameters are reported in Supplementary Data Tables A4 and A5.

CAMP basalts in terms of Nd–Pb isotopic compositions might suggest that the ENA basalts were derived from the same SCLM-like source, which acquired its crustal-like enrichment during episodes of Palaeozoic subduction (Puffer, 2003) when the accretion of the Avalonia–Meguma terranes to the Laurentia margin occurred.

Involvement of subduction-related sediments and fluids is suggested by the isotopic and trace element characteristics of the ENA CAMP basalts. Among the various groups, a broadly negative correlation exists between incompatible element ratios (IE), such as La/Sm and Th/Yb, and initial $^{143}\text{Nd}/^{144}\text{Nd}$ (Fig. 23). The highest incompatible element ratios and lowest initial $^{143}\text{Nd}/^{144}\text{Nd}$ are found in the Shelburne sub-group, whereas the lowest incompatible element ratios and highest $^{143}\text{Nd}/^{144}\text{Nd}$ belong to the Hook Mt group; the other Orange Mt samples and Preakness group samples plot between these groups. Increasing Th/Yb coupled with decreasing initial $^{143}\text{Nd}/^{144}\text{Nd}$ has also been documented in present-day arc-related lavas and suggests variable enrichment of the mantle source by subduction of sediments. In contrast, a decrease of initial $^{143}\text{Nd}/^{144}\text{Nd}$ at constant Th/Yb argues for enrichment through slab-derived fluids (Woodhead *et al.*, 2001). Correlations between Th/Yb and $^{143}\text{Nd}/^{144}\text{Nd}$ have been used successfully to distinguish between fluid and sediment input in the source (SCLM-like source) of the Karoo CFB (Jourdan *et al.*, 2007). Because a similar correlation is observed between initial Nd isotopic composition and La/Sm, the LREE enrichment within the ENA CAMP basalts may also be related to the progressive increase of a sedimentary contribution from the Hook Mountain group to the Shelburne sub-group. In this scenario, the sources of the lower NMB sub-group and those of the Preakness group would have experienced similar extents of sediment input, and the variation of Th/Yb and La/Sm at constant initial $^{143}\text{Nd}/^{144}\text{Nd}$ (Fig. 23) would reflect a decreasing degree of melting from the Preakness to the Orange group. The Shelburne sub-group has a lower initial $^{143}\text{Nd}/^{144}\text{Nd}$ but similar Th/Yb to the lower NMB sub-group (Fig. 23) that suggests source enrichment by an increasing fluid contribution from the latter towards the former.

An alternative source model for the CAMP magmas

As demonstrated above, crustal contamination by AFC or ATA processes of typical mantle-derived magmas (MORB, OIB, OPB) is very unlikely to produce the geochemical characteristics of the ENA CAMP basalts. Mixing of such magmas (particularly MORB or OPB) with lithosphere-derived melts, possibly followed by limited amounts of crustal contamination, is somewhat more successful, but nevertheless does not produce fully satisfactory results, assuming probable end-member compositions. We therefore examine the alternative possibility that the

ENA CAMP basalts were derived from a mantle source enriched in incompatible elements, more specifically, an SCLM-like source that has been metasomatized by subduction-related processes. This suggestion is supported by the fact that the ENA region underwent successive episodes of subduction during the Paleozoic Era. The presumably highly refractory nature of the lithospheric mantle has been used to argue that this reservoir could not produce massive volumes of basaltic volcanism (Arndt *et al.*, 1993). However, significant metasomatic enrichment events, such as earlier subduction, may facilitate melting of the SCLM (e.g. Gallagher & Hawkesworth, 1992). Several geochemical studies of CFBs, including the CAMP (Pegram, 1990; Puffer, 2001, 2003; De Min *et al.*, 2003; Deckart *et al.*, 2005; Merle *et al.*, 2011; Murphy *et al.*, 2011) have suggested a dominant contribution from a mantle source with geochemical characteristics similar to metasomatized SCLM. An alternative source might be the so-called ‘Perisphere’, which has been defined as the less refractory, enriched and hydrated uppermost part of the asthenosphere that is isolated from the convecting mantle under the continents and which may share the chemical characteristics of the SCLM (Anderson, 1994).

To determine whether such a mantle source would be able to produce the ENA CAMP basalts we modelled the geochemical effects of long-lasting subduction on the sub-arc mantle, assuming a starting composition similar to that of the depleted asthenosphere.

Modelling the effects of subduction-related metasomatism on a section of sub-arc mantle

Geodynamic reconstructions suggest that the Avalonia–Meguma terranes were rifted away from the Gondwana margin and accreted to the Laurentia margin during a complex succession of subduction episodes. However, there is no general consensus for the timing of these events. Nevertheless, the most recent studies suggest that the Avalonia–Meguma terranes were separated from Gondwana and accreted to Laurentia during one or several events from c. 540 until c. 370 Ma (e.g. Puffer, 2003; Van Staal *et al.*, 2009; Nance *et al.*, 2010). This suggests that the asthenospheric (DMM-like) sub-arc mantle underneath the terranes underwent progressive enrichment owing to continuous injection of sediments, melts and fluids between 540 Ma and 370 Ma. At c. 370 Ma, the continental collision between Gondwana and Laurentia occurred with cessation of subduction and isolation of the former sub-arc mantle from more injection of material (e.g. Murphy *et al.*, 2006; Van Staal *et al.*, 2009). Considering these geodynamic reconstructions, we infer that the source of the ENA CAMP basalts was originally MORB-source depleted mantle (DMM) into which subduction-derived melts or fluids were continuously injected between 540 and 370 Ma. This metasomatized mantle-wedge was then isolated from further sedimentary input

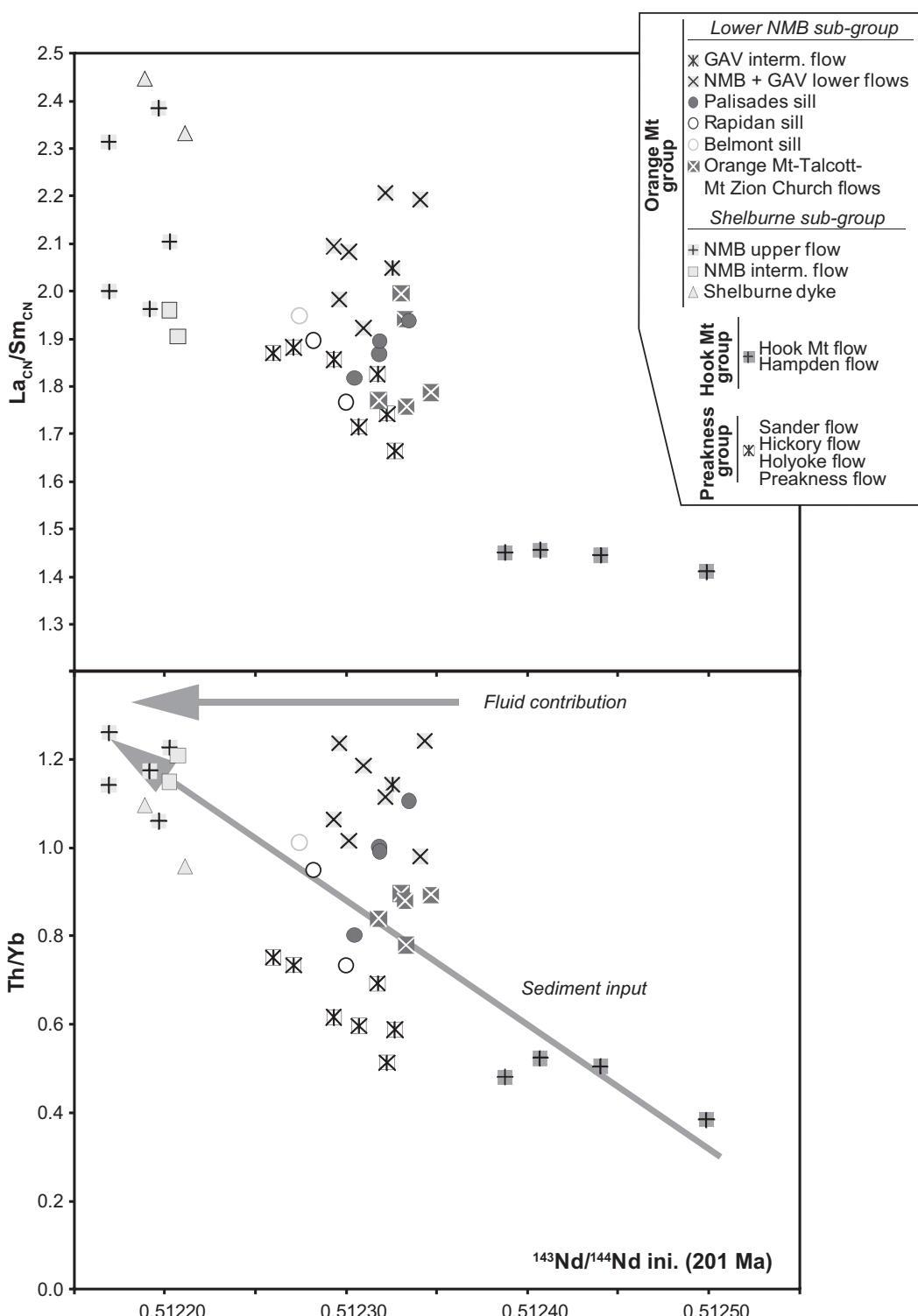


Fig. 23. Variation of La/Sm_N and Th/Yb vs $^{143}\text{Nd}/^{144}\text{Nd}$ initial (at 201 Ma). The trends (grey arrows) represent sediment input and slab-derived fluid contribution as discussed by Woodhead *et al.* (2001). The Nd isotopic data have been back-calculated to 201 Ma.

from 370 Ma until 201 Ma when the CAMP event occurred; during this period the evolution of the Sr–Nd–Pb–Os isotopic ratios would be due to only radioactive decay.

Based on these considerations, we designed a mathematical mantle evolution model to evaluate the time-dependent change of the Nd–Pb–Os isotopic composition of this mantle region. The model assumes a period of 170 Myr (540–370 Ma) during which sediments were progressively incorporated into the depleted mantle wedge through a mixing process (open-system behaviour). In terms of the evolution of the isotopic composition during this period, the effects of sediment addition must be integrated with the effects of radioactive decay. The period of open-system behaviour was followed by a period of c. 170 Myr (370–201 Ma) of closed-system behaviour during which the isotopic composition of the sediment-contaminated mantle was modified only by radioactive decay. The open-system period model is approximated by a mass-balanced flux box model. The mathematical development of the model is presented in the Supplementary Material.

For the open-system period, we start with a sub-arc mantle with a composition close to the average value of the present-day DMM (see parameters in Supplementary Data Table A5). The Nd–Pb–Os isotopic composition of this mantle is back-calculated to the period between 540 and 370 Ma in increments of 10 Ma. The composition of the subducted sediment is considered to be equivalent to the present-day local continental crust (see parameters in Supplementary Data Table A5) and its Nd–Pb–Os isotopic composition is also back-calculated to the period between 540 and 370 Ma, again in increments of 10 Ma. All the Pb isotopic compositions of the sediments involved in the modelling are in the range of the values of the upper continental crust and close to those for mature arc sediments (Zartman & Doe, 1981), which are expected for a subduction system lasting 170 Myr.

The equations translating the evolution of the isotopic composition resemble the classic binary mixing equation, but the mixing parameter F is a function of time, sediment input rate, and the ratio of the number of moles per unit volume of the non-radiogenic isotope of a given element in the depleted mantle and the sediments at 540 Ma (see details in Supplementary Material). The calculated percentages of sediment represent the mass of sediment accumulated over a period of 170 Myr in a given volume of depleted mantle. We stress that the mantle segments into which sediments have been incorporated are also those that are most likely to melt (e.g. Merle *et al.*, 2011).

According to the model, the Nd–Pb–Os isotopic composition of the Hook Mountain group can be reproduced by incorporating into the depleted mantle ~3% sediment with a composition identical to that of the present-day Avalonian Neoproterozoic felsic crust (Figs 24 and 25).

The isotopic composition of the Preakness group and the Rapidan sill can be modelled by incorporating 5% of two slightly different sediment components derived from the Avalonian Neoproterozoic felsic crust close to that involved in the source of the Hook Mt group (see Supplementary Data Table A5). The lower NMB sub-group can be modelled by incorporating 5% sediment, which would have a present-day composition equivalent to the Meguma terrane felsic rocks. The isotopic composition of the Shelburne sub-group can be modelled by incorporating 10% sediment with a present-day composition slightly different from that involved in the lower NMB sub-group, yet still within the range of the Meguma terrane rocks. The contaminant incorporated in the Shelburne sub-group source has a lower $^{143}\text{Nd}/^{144}\text{Nd}$ ratio and Nd content than that which influenced the lower NMB sub-group, perhaps reflecting the involvement of fluids or more hydrated sediments in the source of the Shelburne sub-group.

It is worth noting that the percentages of sediment calculated for the source of the ENA CAMP basalts are not too different from those assumed for recycled sediments in EMII-type OIB (e.g. 3–8% in Samoa–Society; Eiler *et al.*, 1997) or continental arc lavas (2–6%; Plank, 2005). In the case of the source of the ENA CAMP basalts, the percentage of sediment input is related to a specific section of depleted mantle. These percentages are not inconsistent with the production of basaltic magmas.

As stated above, all of the reliable (uncertainty <10%) initial $^{187}\text{Os}/^{188}\text{Os}$ ratios but one (CUL13) are less than 0.1500 and were obtained only for the Orange Mt group (see Fig. 24). Nevertheless, the percentage range of sediment input in the sources of the different groups would be unable to produce very large variations of the initial $^{187}\text{Os}/^{188}\text{Os}$ ratio (Fig. 24). As has been often shown (e.g. Chesley *et al.*, 2004), the low Os concentrations of most sediments are unable to substantially modify the $^{187}\text{Os}/^{188}\text{Os}$ ratios of mantle peridotites, which typically have high Os concentrations. The differences in initial Os isotopic composition observed between samples of the Orange Mt group could reflect heterogeneity of the mantle source rocks prior to sediment incorporation and variations of the Os concentration and/or isotopic composition of the incorporated sediments. In particular, sediments rich in ancient mafic material or black shales could add non-negligible amounts of radiogenic Os. Because most of the ENA CAMP basalts have low Os concentrations, very small amounts (2–3%) of shallow contamination by the upper continental crust could also lead to minor variation of the $^{187}\text{Os}/^{188}\text{Os}$ ratio (Merle *et al.*, 2011) without significantly affecting the other isotope systems. Minor shallow contamination could, in particular, explain the high initial $^{187}\text{Os}/^{188}\text{Os}$ ratio of sample CUL13, given the very low Os concentration of this sample.

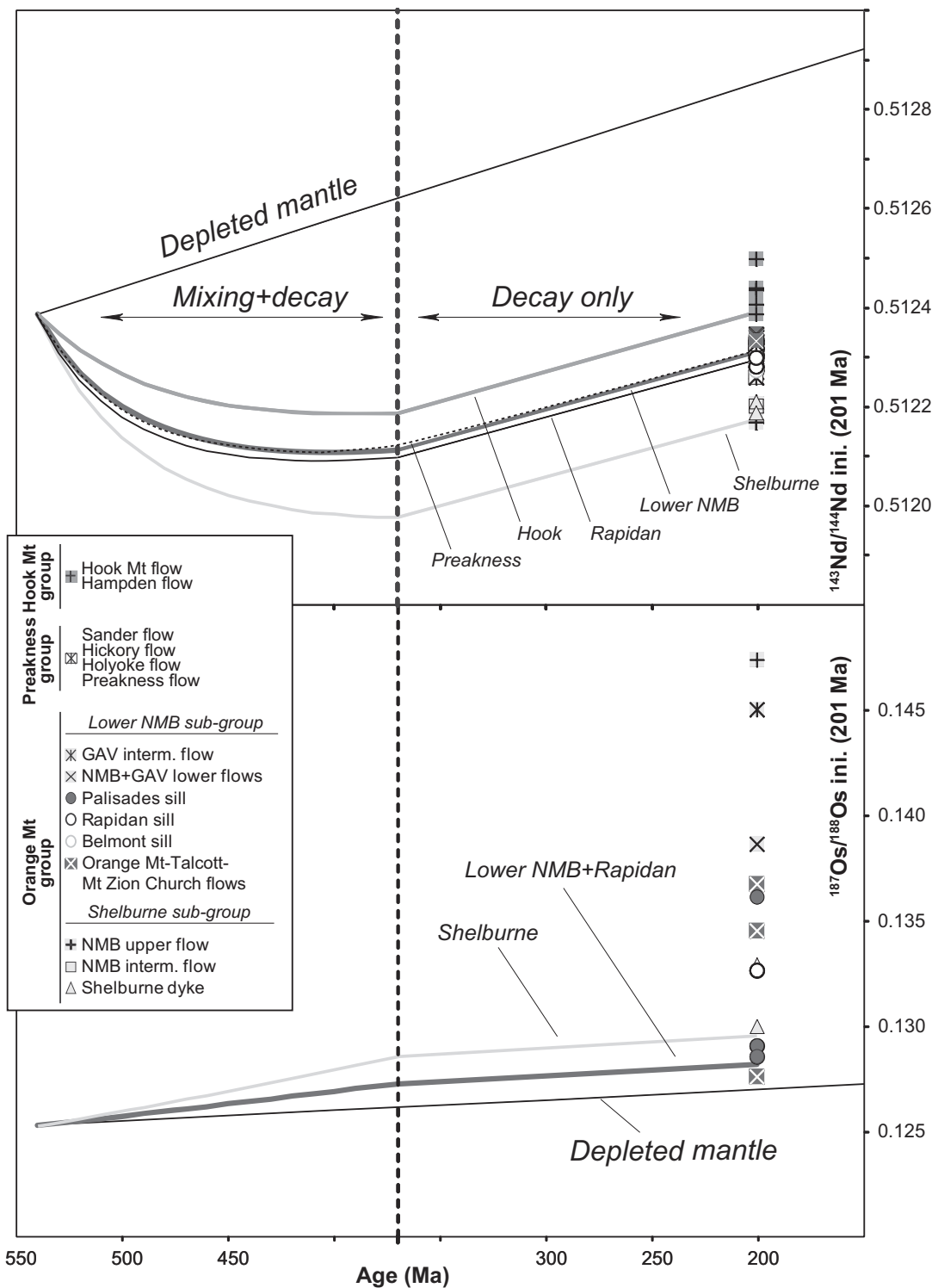


Fig. 24. Time evolution of $^{143}\text{Nd}/^{144}\text{Nd}$ and $^{187}\text{Os}/^{188}\text{Os}$ for an asthenospheric sub-arc mantle wedge undergoing continuous input of subducted sediment over 170 Myr (open-system behaviour) and evolving by isotopic decay (closed-system behaviour) during the following 170 Myr until the CAMP magmatic event. Model details are given in the text and in the Supplementary Material.

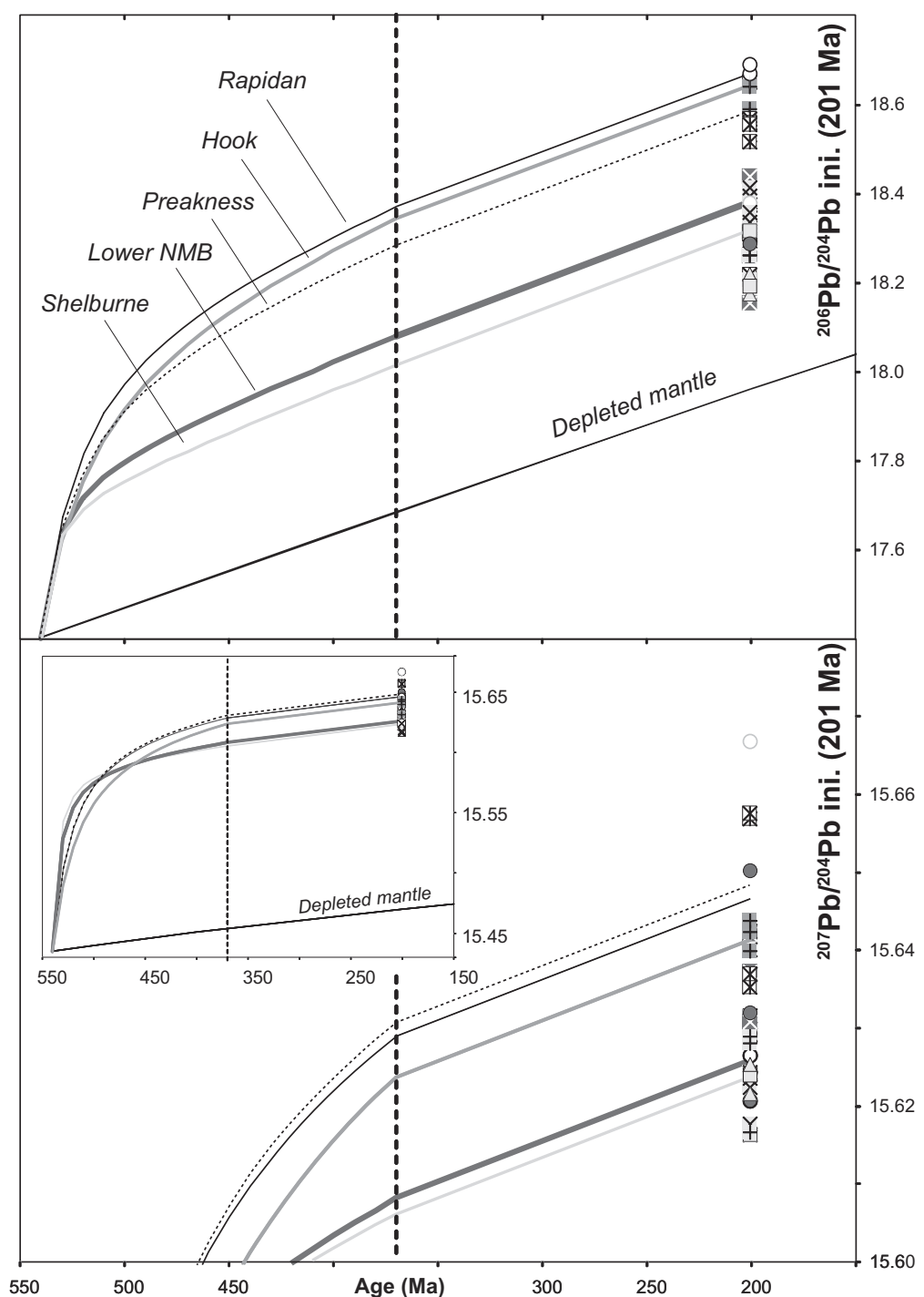


Fig. 25. Time evolution of $^{206}\text{Pb}/^{204}\text{Pb}$ and $^{207}\text{Pb}/^{204}\text{Pb}$ for an asthenospheric sub-arc mantle wedge undergoing continuous input of subducted sediment over 170 Myr (open-system behaviour) and evolving by isotopic decay (closed-system behaviour) during the following 170 Myr until the CAMP magmatic event. The symbols representing the ENA CAMP basalts are identical to those of Fig. 24. Model details are given in the text and in the Supplementary Material.

Consequences for the CAMP

According to our model, the isotope composition of the CAMP basalts might originate from progressive incorporation of subducted sediments derived from the local continental crust into a depleted sub-arc mantle wedge above a subduction zone. The age and duration of the enrichment process during subduction (open-system phase), as well as the duration of the subsequent isolation (radioactive decay phase), might vary throughout the CAMP province. For instance, by changing these parameters in the model in a manner consistent with the geological constraints from the Maranhão basin in Brazil (subduction between 660 and 575 Ma then isolation phase until 201 Ma), the isotopic characteristics of the Brazilian CAMP basalts can be modelled assuming the same starting mantle composition as the ENA CAMP basalts. As the isotopic composition of the local Brazilian crust is not well constrained [for details about the geological setting of the Maranhão basin see Merle *et al.* (2011)], we assumed the present-day composition of mature-arc sediments ($^{143}\text{Nd}/^{144}\text{Nd} = 0.51185$, $^{206}\text{Pb}/^{204}\text{Pb} = 18.520$, $^{207}\text{Pb}/^{204}\text{Pb} = 15.640$, $^{208}\text{Pb}/^{204}\text{Pb} = 38.75$, $^{187}\text{Os}/^{188}\text{Os} = 2$, Nd = 38 ppm, Pb = 12 ppm, Os = 50 ppt; Ben Othman *et al.*, 1989; Esser & Turekian, 1993; Fig. 26).

It should be noted that the isotopic characteristics of the CAMP basalts in the Maranhão basin are similar to those of the majority of the CAMP basalts including those from ENA. As a consequence, this model can be applied to all of the CAMP sub-provinces studied to date and is probably able to yield the isotopic compositions of the CAMP basalts in any given area using the same parameters as for the Maranhão CAMP basalts. Nevertheless, such modelling may be more accurate and geologically meaningful by applying the correct geodynamic constraints (duration of the subduction, length of isolation after continental collision for a specific area) and composition of the local crust as a proxy for the subducted sediments.

Both the modalities of sediment incorporation into the sub-arc mantle and the fate of the modified mantle wedge after collision stops subduction are currently highly speculative. However, this mantle segment could have been incorporated into the lithosphere and might form an enriched portion of the SCLM. Alternatively, it could have remained on top of the depleted asthenosphere as an enriched layer (i.e. Perisphere). In either case this mantle would probably have been hydrated and would include very fusible portions that could melt in response to an increase in the ambient temperature (e.g. Coltice *et al.*, 2007, 2009).

The case of CUL13

Samples CUL13 and CUL25 plot away from the other Preakness group samples yet close to those of the Orange

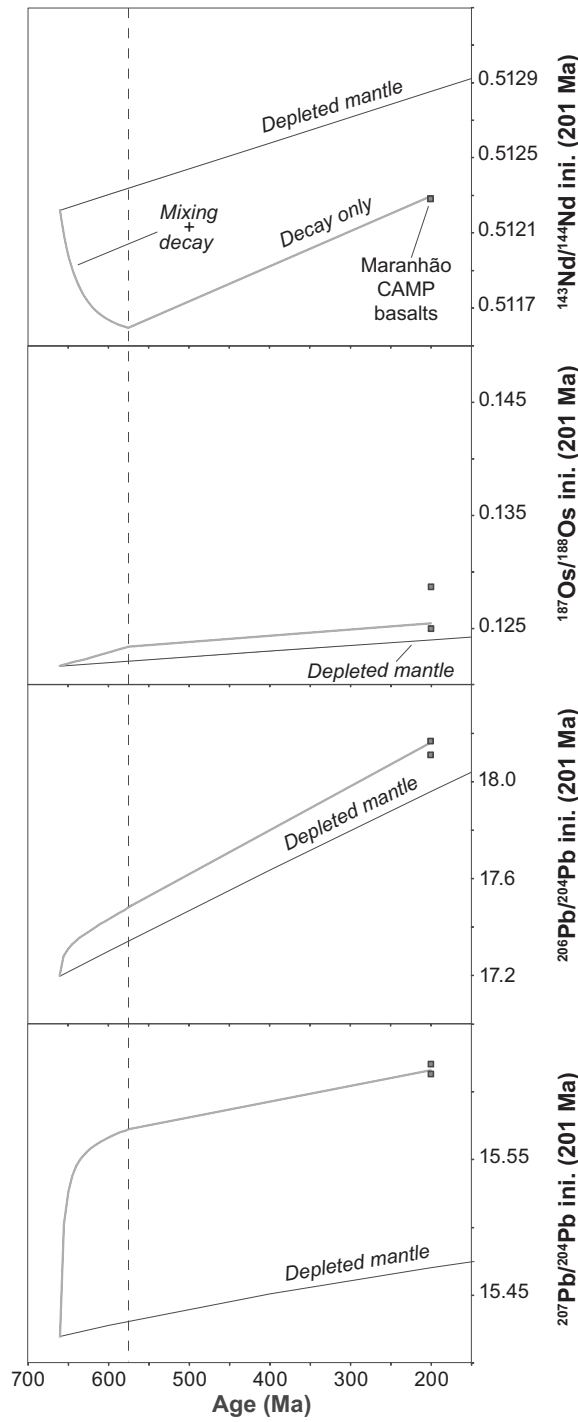


Fig. 26. Modelling of the source of the CAMP basalts in the Maranhão basin, showing the time evolution of $^{143}\text{Nd}/^{144}\text{Nd}$, $^{187}\text{Os}/^{188}\text{Os}$, $^{206}\text{Pb}/^{204}\text{Pb}$ and $^{207}\text{Pb}/^{204}\text{Pb}$ for an asthenospheric sub-arc mantle wedge undergoing continuous input of subducted sediment from 660 Ma until 575 Ma (open-system behaviour) and evolving by isotopic decay (closed-system behaviour) until the CAMP magmatic event. Data for CAMP Maranhão basalts are from Merle *et al.* (2011).

Mt in the Pb–Pb and initial $^{206}\text{Pb}/^{204}\text{Pb}$ vs initial $^{143}\text{Nd}/^{144}\text{Nd}$ diagrams (Figs 7 and 10). In contrast to sample CUL25, CUL13 has a reliable high initial Os ratio ($^{187}\text{Os}/^{188}\text{Os} = 0.1874 \pm 0.0123$) and low Os content ($[\text{Os}] = 14.4 \text{ ppt}$), which may be accounted for by shallow-level contamination by the upper continental crust. We assume that the other samples of the Preakness group represent uncontaminated or very slightly contaminated magmas, based on the previous discussion. None of these samples are primitive and considering that the contamination occurred in the upper crust, we consider the least evolved of the Preakness group basalts (the Buttress dyke sample HBL02) as the parental magma composition. We also assumed an isotopic composition of $^{187}\text{Os}/^{188}\text{Os} = 0.1282$ for the uncontaminated magma, which is that calculated at 201 Ma by our sediment-enriched mantle model for the Preakness group. Based on these parameters, we modelled the $^{143}\text{Nd}/^{144}\text{Nd}$ and $^{206}\text{Pb}/^{204}\text{Pb}$ initial ratios of sample CUL13 through an AFC process (Fig. 14). The modelling failed to reach the isotopic composition of CUL13 using a contaminant composition similar to that of the felsic rocks of the Meguma terrane. However, the composition of CUL13 can be reached through an AFC process by involving c. 10% of a contaminant with an isotopic and IE composition close to that of Devonian plutonic rocks in New Hampshire and Western Maine (Tomascak *et al.*, 2005). This modelling may also explain the slight variation in the isotopic compositions observed within the Preakness group samples, as outlined above, by less than 4% of shallow contamination by the local crust. The isotopic composition of sample CUL25 can be explained by more than 10% contaminant (Fig. 27).

Further remarks about the CAMP

Many features of the CAMP suggest that it might be different from other LIPs and that the common models for LIP generation may not be applicable. Indeed, the tectonic context of the CAMP is difficult to reconcile with the classic mantle plume hypothesis (e.g. Campbell, 2007). CAMP lacks geological evidence (e.g. hotspot track with decreasing age toward an active volcano, radiating dyke pattern, lithospheric uplift preceding basalt eruption, high-temperature melts such as picrites and ultramafic and ultra-alkaline liquids) for the involvement of a mantle plume (McHone, 2000; Coltice *et al.*, 2009). Moreover, the mantle potential temperatures calculated for CAMP are substantially lower than those calculated for the Deccan or Siberian Traps (Herzberg & Gazel, 2009).

In terms of chemistry, the CAMP basalts are also distinct from other LIP basalts. Whereas several LIPs such as Parana–Etendeka, North Atlantic or Deccan have experienced crustal contamination by ATA (Devey & Cox, 1987; Kerr *et al.*, 1995a; Peate & Hawkesworth, 1996), this process probably did not significantly affect the

CAMP basalts. The large majority of the CAMP basalts show rather homogeneous REE contents at the scale of the whole province. Indeed, they have flat HREE patterns, which have been modelled as resulting from the melting of a spinel-bearing source (e.g. Bellieni *et al.*, 1990; Jourdan *et al.*, 2003; Verati *et al.*, 2005) and are thus indicative of a shallow melting zone. However, plume models predict that as the plume head impinges on the base of the lithosphere the initial average depth of melting is relatively deep but decreases as the degree of melting increases (White & McKenzie, 1995). This should produce compositional trends that are inconsistent with the homogeneity of the CAMP basalts (Salters *et al.*, 2003).

The high abundance of evolved basalts and the lack of picritic rocks might be related to the composition of the mantle source. Indeed, during subduction recycled crustal material might form garnet-pyroxenitic veins or layers in the shallow mantle. Melts of these garnet-pyroxenites may react with the ambient depleted mantle to produce fertile spinel lherzolite that has a lower MgO content than average lherzolite and retains the signature of recycled crustal material (Marchesi *et al.*, 2013).

Although metasomatic or refertilization processes may promote melting of the SCLM or the perisphere by lowering the solidus, a source of heat is still needed to initiate magma generation. Physical models suggest that large-scale mantle warming under supercontinents such as Pangaea, resulting from accumulation of internal heat beneath the insulating lithosphere, can lead to an increase in temperature of up to 100°C that might be sufficient to melt metasomatized SCLM (Coltice *et al.*, 2007, 2009). However, the timescales of melting of the SCLM by heat conduction from the underlying convecting mantle may be far too long to be consistent with the rapid timescales of eruption of CFB-type magmas (Gibson *et al.*, 2006). As a consequence, the involvement of one or more deep-rooted mantle plumes as heat suppliers cannot be ruled out, and may contribute to the melting of an SCLM source.

CONCLUSIONS

New data for the ENA CAMP sills, dykes, and lava flows define three groups (Orange Mt, Preakness and Hook Mt groups) based on the stratigraphy and chemistry of the units. Geochemical and Sr–Nd–Pb–Os isotopic data for selected samples allow the following conclusions to be reached.

- (1) The continental crust-like characteristics of the CAMP basalts probably do not result from extensive contamination by the upper continental crust or plume-derived or other asthenospheric melts. Furthermore, derivation from a plume source with an unusual isotopic composition is also unlikely.
- (2) Numerical modelling shows that mixing between two enriched melts, such as OIB-type and SCLM-related

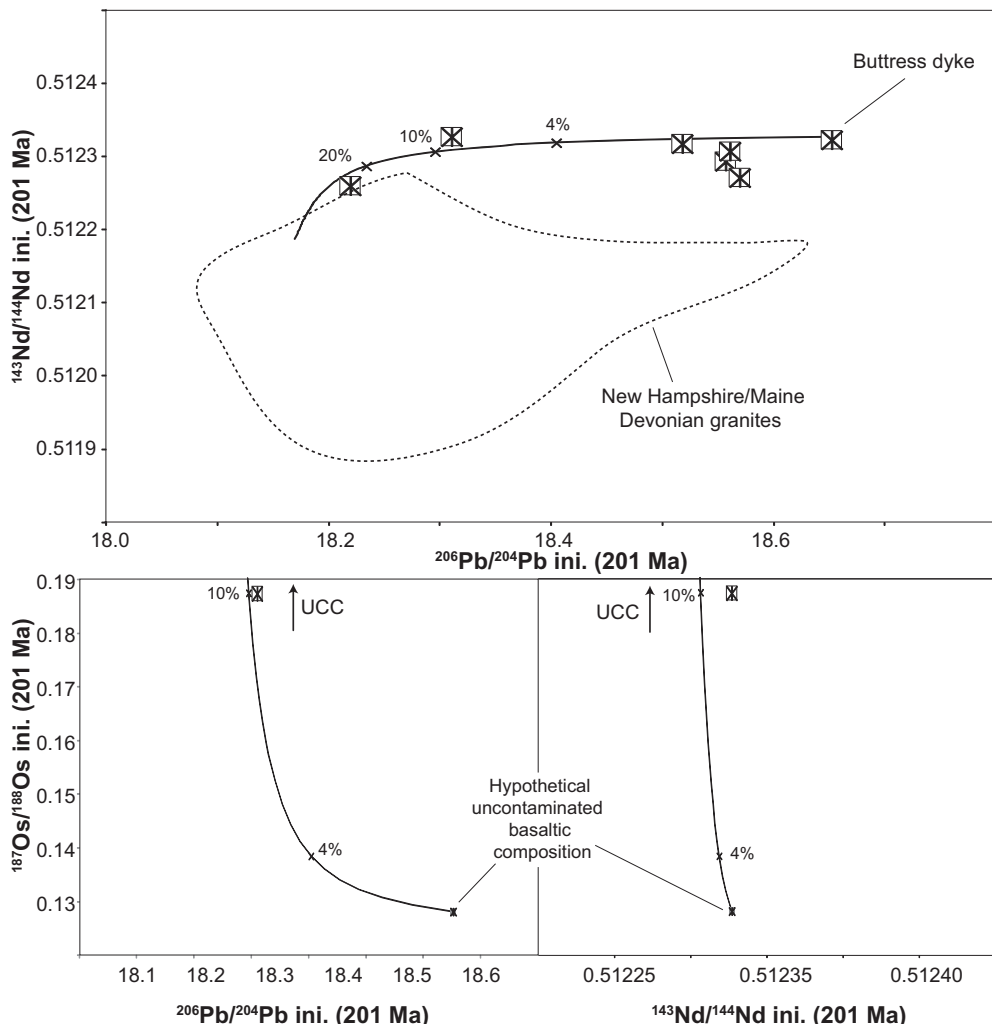


Fig. 27. AFC modelling of the composition of the Preakness samples. Uncontaminated basaltic magma composition: [Nd] = 9 ppm, [Pb] = 2 ppm, [Os] = 300 ppt, $^{143}\text{Nd}/^{144}\text{Nd} = 0.512327$, $^{187}\text{Os}/^{188}\text{Os} = 0.1282$, $^{206}\text{Pb}/^{204}\text{Pb} = 18.65$; continental crust contaminant: [Nd] = 5 ppm, [Pb] = 49 ppm, [Os] = 31 ppt, $^{143}\text{Nd}/^{144}\text{Nd} = 0.51195$, $^{187}\text{Os}/^{188}\text{Os} = 1.7$, $^{206}\text{Pb}/^{204}\text{Pb} = 18.16$ (Esser & Turekian, 1993; Tomascak *et al.*, 2005). AFC parameters: $K_D(\text{Nd}) = 0.25$, $K_D(\text{Pb}) = 0.5$, $K_D(\text{Os}) = 8.5$, $r = 0.4$. (See text for details.)

- melts (ultra-alkaline–ultramafic liquids), possibly followed by limited contamination by the upper continental crust, is unlikely to produce the composition of the ENA CAMP basalts.
- (3) The mixing of MORB-like or OPB-like magmas with melts derived from the SCLM is more plausible; however, the REE contents of the ENA CAMP basalts require extreme compositions of such SCLM-derived melts and up to 30% assimilation of upper continental crust, which is rather unrealistic.
 - (4) Our numerical model shows that incorporation of subducted sediments into an asthenospheric mantle wedge during episodes of Paleozoic subduction can reconcile the paradoxical coexistence of continental crust-like isotopic and trace element signatures (i.e. high $^{87}\text{Sr}/^{86}\text{Sr}$,

high $^{207}\text{Pb}/^{204}\text{Pb}$ for moderate $^{206}\text{Pb}/^{204}\text{Pb}$, low $^{143}\text{Nd}/^{144}\text{Nd}$, higher LILE contents than MORB, specific Nb and Pb anomalies) with low, SCLM-like, $^{187}\text{Os}/^{188}\text{Os}$ ratios. The small range of initial $^{187}\text{Os}/^{188}\text{Os}$ (0.128–0.15) observed in the ENA CAMP basalts could reflect initial heterogeneity in the asthenospheric mantle, variations in the nature and/or the amount of subducted sediment incorporated, and a limited amount of shallow contamination by the local crust.

ACKNOWLEDGEMENTS

Angelo De Min, Robert Weems, Larry Tanner, Simonetta Cirilli and Paolo Podestà, as well as Paul Olsen,

participated in the field trip to the ENA CAMP and they are all thanked for their contributions. Sampling of the drill hole that penetrated the North Mountain Basalt was made possible by the Nova Scotia Department of Natural Resources and the Department of Geology, Acadia University, Wolfville, Nova Scotia. Finally, we thank C. Zimmerman, C. Keller, C. Douchet and P. Capiez for their capable laboratory assistance. Drs A. Kerr, B. Murphy and two anonymous reviewers are thanked for their comments on the earlier versions of this paper. J. Gamble is thanked for editorial handling of this paper.

FUNDING

Financial assistance for the project came from grants CARIPARO 2008 and PRIN-2008 (to A.M.) and from the GDR Marges CNRS-INSU program (to H.B.).

SUPPLEMENTARY DATA

Supplementary data for this paper are available at *Journal of Petrology* online.

REFERENCES

- Aitchison, S. J. & Forrest, A. H. (1994). Quantification of crustal contamination in open magmatic systems. *Journal of Petrology* **35**, 461–488.
- Alibert, C. (1985). A Sr–Nd isotope and REE study of late Triassic dolerites from the Pyrénées (France) and the Messejana dyke (Spain and Portugal). *Earth and Planetary Science Letters* **73**, 81–90.
- Allègre, C. J., Treuil, M., Minster, J. F., Minster, B. & Albarède, F. (1977). Systematic use of trace elements in igneous processes: part I. Fractional crystallisation processes in volcanic suites. *Contributions to Mineralogy and Petrology* **60**, 57–75.
- Anderson, D. L. (1994). The sublithospheric mantle as the source of subcontinental flood basalts; the case against the continental lithosphere and plume head reservoir. *Earth and Planetary Science Letters* **123**, 269–280.
- Arndt, N. & Christensen, U. (1992). The role of lithospheric mantle in continental flood volcanism; thermal and geochemical constraints. *Journal of Geophysical Research* **97**, 10967–10981.
- Arndt, N. T. & Goldstein, S. L. (1987). Use and abuse of crust formation ages. *Geology* **15**, 893–895.
- Arndt, N. T., Czamanske, G. K., Wooden, J. L. & Fedorenko, V. A. (1993). Mantle and crustal contributions to continental flood volcanism. *Tectonophysics* **223**, 39–52.
- Ayuso, R. A. & Bevier, M. L. (1991). Regional differences in Pb isotopic compositions of feldspars in plutonic rocks of the northern Appalachian Mountains, USA, Canada: A geochemical method of terrane correlation. *Tectonics* **10**, 191–212.
- Barr, S. M. & Hegner, E. (1992). Nd isotopic compositions of felsic igneous rocks in Cape Breton Island, Nova Scotia. *Canadian Journal of Earth Sciences* **29**, 650–657.
- Bellieni, G., Piccirillo, E. M., Cavazzini, G., Petrini, R., Comin-Chiaromonti, P., Nardy, A. J. R., Civetta, L., Melfi, A. J. & Zantedeschi, P. (1990). Low- and high TiO₂ Mesozoic tholeiitic magmatism of the Maranhão basin (NE Brazil): K–Ar age, geochemistry, petrology, isotope characteristics and relationships with Mesozoic low- and high-TiO₂ flood basalts of the Paraná Basin (SE Brazil). *Neues Jahrbuch für Mineralogie, Abhandlungen* **162**, 1–33.
- Ben Othman, D., White, W. M. & Patchett, J. (1989). The geochemistry of marine sediments, island arc magma genesis, and crust–mantle recycling. *Earth and Planetary Science Letters* **94**, doi: 10.1016/0012-821X(89)90079-4.
- Bertrand, H. (1991). The Mesozoic Tholeiitic Province of Northwest Africa: a volcano-tectonic record of the early opening of Central Atlantic. In: Kampunzu, A. B. & Lubala, R. T. (eds) *Magmatism in Extensional Structural Settings. The Phanerozoic African Plate*. Springer, pp. 147–188.
- Bertrand, H., Dostal, J. & Dupuy, C. (1982). Geochemistry of early Mesozoic tholeiites from Morocco. *Earth and Planetary Science Letters* **58**, 225–239.
- Brauns, C. M., Hergt, J. M., Woodhead, J. D. & Maas, R. (2000). Os isotopes and the origin of the Tasmanian dolerites. *Journal of Petrology* **41**, 905–918.
- Campbell, I. H. (2007). Testing the plume theory. *Chemical Geology* **241**, 153–176.
- Carlson, R. W. (1991). Physical and chemical evidence on the cause and source characteristics of flood basalt volcanism. *Australian Journal of Earth Sciences* **38**, 525–544.
- Carlson, R. W. (2005). Application of the Pt–Re–Os isotopic systems to mantle geochemistry and geochronology. *Lithos* **82**, 249–272.
- Cebria, J. M., Lopez-Ruiz, J., Doblas, M., Martins, L. T. & Munha, J. (2003). Geochemistry of the Early Jurassic Messejana–Plasencia dyke (Portugal–Spain); implications on the origin of the Central Atlantic Magmatic Province. *Journal of Petrology* **44**, 547–568.
- Chesley, J., Righter, K. & Ruiz, J. (2004). Large-scale mantle metasomatism: a Re–Os perspective. *Earth and Planetary Science Letters* **219**, 49–60.
- Cirilli, S., Marzoli, A., Tanner, L., Bertrand, H., Buratti, N., Jourdan, F., Bellieni, G., Kontak, D. & Renne, P. R. (2009). Latest Triassic onset of the Central Atlantic magmatic province (CAMP) volcanism in the Fundy basin (Nova Scotia): new stratigraphic constraints. *Earth and Planetary Science Letters* **286**, 514–525.
- Coltice, N., Phillips, B. R., Bertrand, H., Ricard, Y. & Rey, P. (2007). Global warming of the mantle at the origin of flood basalts over supercontinents. *Geology* **35**, 391–394.
- Coltice, N., Bertrand, H., Rey, P., Jourdan, F., Phillips, B. R. & Ricard, Y. (2009). Global warming of the mantle beneath continents back to the Archean. *Gondwana Research* **15**, 254–266.
- Courtillot, V., Jaupart, C., Manighetti, I., Tapponnier, P. & Besse, J. (1999). On causal links between flood basalts and continental breakup. *Earth and Planetary Science Letters* **166**, 177–195.
- Currie, K. L., Whalen, J. B., Davis, W. J., Longstaffe, F. J. & Cousens, B. L. (1998). Geochemical evolution of peraluminous plutons in southern Nova Scotia, Canada—a pegmatite-poor suite. *Lithos* **44**, 117–140.
- Deckart, K., Féraud, G. & Bertrand, H. (1997). Age of Jurassic continental tholeiites of French Guyana, Surinam and Guinea: implications for the initial opening of the Central Atlantic Ocean. *Earth and Planetary Science Letters* **150**, 205–220.
- Deckart, K., Bertrand, H. & Liegeois, J.-P. (2005). Geochemistry and Sr, Nd, Pb isotopic composition of the Central Atlantic Magmatic Province (CAMP) in Guyana and Guinea. *Lithos* **82**, 289–314.
- De Min, A., Piccirillo, E. M., Marzoli, A., Bellieni, G., Renne, P. R., Ernesto, M. & Marques, L. (2003). The Central Atlantic Magmatic Province (CAMP) in Brazil: Petrology, Geochemistry, ⁴⁰Ar/³⁹Ar ages, paleomagnetism and geodynamic implications. In: Hames, W. E., McHone, J. G., Renne, P. R. & Ruppel, C. (eds) *The Central Atlantic Magmatic Province: Insights from Fragments of*

- Pangea. *Geophysical Monograph, American Geophysical Union* **136**, 209–226.
- DePaolo, D. J. (1981). Trace element and isotopic effects of combined wall rock assimilation and fractional crystallization. *Earth and Planetary Science Letters* **53**, 189–202.
- Devey, C. W. & Cox, K. G. (1987). Relationships between crustal contamination and crystallisation in continental flood basalt magmas with special reference to the Deccan Traps of the Western Ghats, India. *Earth and Planetary Science Letters* **84**, 59–68.
- Dorais, M. J. & Tubrett, M. (2008). Identification of a subduction zone component in the Higganum dyke, Central Atlantic Magmatic province: a LA-ICP-MS study of clinopyroxenes with implication for flood basalt petrogenesis. *Geochemistry, Geophysics, Geosystems* **9**, doi:10.1029/2008GC002079.
- Dostal, J. & Dupuy, C. (1984). Geochemistry of the North Mountain Basalts (Nova Scotia, Canada). *Chemical Geology* **45**, 245–261.
- Dostal, J. & Durning, M. (1998). Geochemical constraints on the origin and evolution of early Mesozoic dykes in Atlantic Canada. *European Journal of Mineralogy* **10**, 79–93.
- Dostal, J. & Greenough, J. D. (1992). Geochemistry and petrogenesis of the early Mesozoic North Mountain basalts of Nova Scotia, Canada. In: Puffer, J. H. & Ragland, P. C. (eds) *Eastern North American Mesozoic Magmatism*. Geological Society of America, Special Papers **268**, 149–159.
- Drake, A. A., Jr, Sinha, A. K., Laird, J. & Guy, R. E. (1989). The Taconic orogen. In: Hatcher, R. D., Jr, Thomas, W. A. & Viele, G. W. (eds) *The Appalachian–Ouachita Orogen in the United States*. Geological Society of America, *The Geology of North America* **F-2**, 101–177.
- Dupuy, C., Marsh, J., Dostal, J., Michard, A. & Testa, S. (1988). Asthenospheric and lithospheric sources for Mesozoic dolerites from Liberia (Africa): trace element and isotopic evidence. *Earth and Planetary Science Letters* **87**, 100–110.
- Eiler, J. M., Farley, K. A., Valley, J. W., Hauri, E., Craig, H., Hart, S. R. & Stolper, E. (1997). Oxygen isotope variations in ocean island basalt phenocrysts. *Geochimica et Cosmochimica Acta* **61**, 2281–2293.
- Ernst, R. E. & Buchan, K. L. (2002). Maximum size and distribution in time and space of mantle plumes: evidence from large igneous provinces. *Journal of Geodynamics* **31**, 309–342.
- Esser, B. K. & Turekian, K. K. (1993). The osmium isotopic composition of the continental crust. *Geochimica et Cosmochimica Acta* **57**, 3093–3104.
- Fowell, S. J. & Olsen, P. E. (1993). Time calibration of Triassic–Jurassic microfloral turnover, eastern North America. *Tectonophysics* **222**, 361–369.
- Gallagher, K. & Hawkesworth, C. (1992). Dehydration melting and generation of continental flood basalts. *Nature* **358**, 57–59.
- Gibson, S. A., Thompson, R. N., Leonardos, O. H., Dickin, A. P. & Mitchell, J. G. (1999). The limited extent of plume–lithosphere interactions during continental flood-basalt genesis: geochemical evidence from Cretaceous magmatism in southern Brazil. *Contributions to Mineralogy and Petrology* **137**, 147–169.
- Gibson, S. A., Thompson, R. N. & Day, J. A. (2006). Timescales and mechanisms of plume–lithosphere interactions: $^{40}\text{Ar}/^{39}\text{Ar}$ geochronology and geochemistry of alkaline igneous rocks from the Paraná–Etendeka large igneous province. *Earth and Planetary Science Letters* **251**, 1–17.
- Gorring, M. L. & Naslund, H. R. (1995). Geochemical reversals within the lower 100 m of the Palisades sill, New Jersey. *Contributions to Mineralogy and Petrology* **119**, 263–276.
- Greenough, J. D., Jones, L. M. & Mossman, D. J. (1989). Petrochemical and stratigraphic aspects of North Mountain Basalt from the north shore of the Bay of Fundy, Nova Scotia, Canada. *Canadian Journal of Earth Sciences* **26**, 2710–2717.
- Halliday, A. N., Davies, G. R., Lee, D. C., Tommasini, S., Paslick, C. R., Fitton, J. G. & James, D. E. (1992). Lead isotopic evidence for young trace element enrichment in the oceanic upper mantle. *Nature* **359**, 623–627, [correction (1993) *Nature* **362**, 184].
- Hames, W. E., Renne, P. R. & Ruppel, C. (2000). New evidence for geologically instantaneous emplacement of earliest Jurassic Central Atlantic magmatic province basalts on the North American margin. *Geology* **28**, 859–862.
- Hart, S. R., Hauri, E. H., Oschmann, L. A. & Whitehead, J. A. (1992). Mantle plumes and entrainment: isotopic evidence. *Science* **256**, 517–520.
- Hatcher, R. D., Jr, Thomas, W. A., Geiser, P. A., Snee, A. W., Mosher, S. & Wiltschko, D. V. (1989). Alleghanian orogen. In: Hatcher, R. D., Jr, Thomas, W. A. & Viele, G. W. (eds) *The Appalachian–Ouachita Orogen in the United States*. Geological Society of America, *The Geology of North America* **F-2**, 233–318.
- Heatherington, A. L. & Mueller, P. A. (1999). Lithospheric sources of North Florida, USA tholeites and implications for the origin of the Suwannee terrain. *Lithos* **46**, 215–233.
- Heatherington, A. L. & Mueller, P. A. (2003). Mesozoic igneous activity in the Suwannee Terrane, Southeastern USA: petrogenesis and Gondwanan affinities. *Gondwana Research* **2**, 296–311.
- Heinonen, J. S., Carlson, R. W. & Luttinen, A. V. (2010). Isotopic (Sr, Nd, Pb, and Os) composition of highly magnesian dykes of Vestfjella, western Dronning Maud Land, Antarctica: A key to the origins of the Jurassic Karoo large igneous province? *Chemical Geology* **277**, 227–244.
- Herzberg, C. & Gazel, E. (2009). Petrological evidence for secular cooling in mantle plumes. *Nature* **458**, 619–623.
- Hibbard, J. P., Stoddard, E. F., Secor, D. T. & Dennis, A. J. (2002). The Carolina Zone: Overview of Neoproterozoic to early Paleozoic peri-Gondwanan terranes along the eastern flank of the southern Appalachians. *Earth-Science Reviews* **57**, 299–339.
- Hibbard, J. P., van Staal, C. R. & Rankin, D. W. (2007). Links among Carolinia, Avalonia, and Ganderia in the Appalachian peri-Gondwanan realm. In: Sears, J. W., Harms, C. A. & Evenchick, C. A. (eds) *Whence the Mountains? Inquiries into the Evolution of Orogenic Systems*. Geological Society of America, Special Papers **433**, 291–311.
- Hill, R. I. (1991). Starting plumes and continental break-up. *Earth and Planetary Science Letters* **104**, 398–416.
- Huppert, H. E. & Sparks, R. S. J. (1985). Cooling and contamination of mafic and ultramafic magmas during ascent through continental crust. *Earth and Planetary Science Letters* **74**, 371–386.
- Hush, J. (1990). Palisades sill: origin of the olivine zone by separate magmatic injection rather than gravity settling. *Geology* **18**, 699–702.
- Jackson, M. G., Hart, S. R., Koppers, A. A. P., Staudigel, H., Konter, J., Blusztajn, J., Kurz, M. & Russell, J. A. (2007). The return of subducted continental crust in Samoan lavas. *Nature* **448**, 684–687.
- Jacobsen, S. B. & Wasserburg, G. J. (1980). Sm–Nd isotopic evolution of chondrites. *Earth and Planetary Science Letters* **50**, 139–155.
- Jourdan, F., Marzoli, A., Bertrand, H., Cosca, M. & Fontignie, D. (2003). The northernmost CAMP: $^{40}\text{Ar}/^{39}\text{Ar}$ age, petrology and Sr–Nd–Pb isotope geochemistry of the Kerforne dyke, Brittany, France. In: Hames, W. E., McHone, J. G., Renne, P. R. & Ruppel, C. (eds) *The Central Atlantic Magmatic Province: Insights from Fragments of Pangea*. *Geophysical Monograph, American Geophysical Union* **136**, 209–226.
- Jourdan, F., Bertrand, H., Schärer, U., Blichert-Toft, J., Féraud, G. & Kampunzu, A. B. (2007). Major and trace element and Sr, Nd, Hf and Pb isotope compositions of the Karoo Large Igneous

- Province, Botswana–Zimbabwe: lithosphere vs mantle plume contribution. *Journal of Petrology* **48**, 1043–1077.
- Jourdan, F., Marzoli, A., Bertrand, H., Cirilli, S., Tanner, L., Kontak, D. J., McHone, G., Renne, P. R. & Bellieni, G. (2009). $^{40}\text{Ar}/^{39}\text{Ar}$ ages of CAMP in North America: implications for the Triassic–Jurassic boundary and the ^{40}K decay constant bias. *Lithos* **110**, 167–180.
- Kent, D. V. & Olsen, P. E. (2000). Magnetic polarity stratigraphy and paleolatitude of the Triassic–Jurassic Blomidon Formation in the Fundy Basin (Canada): implications for early Mesozoic tropical climate gradients. *Earth and Planetary Science Letters* **179**, 311–324.
- Kerr, A. C. & Mahoney, J. J. (2007). Oceanic plateau: problematic plumes, potential paradigms. *Chemical Geology* **241**, 332–353.
- Kerr, A. C., Kempton, P. D. & Thompson, R. N. (1995a). Crustal assimilation during turbulent magma ascent (ATA): new isotopic evidence from the Mull Tertiary lava succession, N. W. Scotland. *Contributions to Mineralogy and Petrology* **119**, 142–154.
- Kerr, A. C., Saunders, A. D., Tarney, J., Berry, N. H. & Hards, V. L. (1995b). Depleted mantle-plume geochemical signatures: no paradox for plume theories. *Geology* **23**, 843–846.
- Knight, K. B., Nomade, S., Renne, P. R., Marzoli, A., Bertrand, H. & Youbi, N. (2004). The Central Atlantic Magmatic Province at the Triassic–Jurassic boundary: paleomagnetic and $^{40}\text{Ar}/^{39}\text{Ar}$ evidence from Morocco for brief, episodic volcanism. *Earth and Planetary Science Letters* **228**, 143–160.
- Kontak, D. J. (2008). On the edge of CAMP: Geology and volcanology of the Jurassic North Mountain Basalt, Nova Scotia. *Lithos* **101**, 74–101.
- Le Maitre, R. W. (2002). *Igneous Rocks: A Classification and Glossary of Terms: Recommendations of the International Union of Geological Sciences Subcommission on the Systematics of Igneous Rocks*. Cambridge University Press, 240 p.
- Marchesi, C., Garrido, C. J., Bosch, D., Bodinier, J.-L., Gerville, F. & Hidas, K. (2013). Mantle refertilization by melts of crustal-derived garnet pyroxenite: Evidence from the Ronda peridotite massif, southern Spain. *Earth and Planetary Science Letters* **362**, 66–75.
- Marzoli, A., Renne, P. R., Picirillo, E. M., Ernesto, M. & De Min, A. (1999). Extensive 200-million-year-old continental flood basalts of the Central Atlantic Magmatic Province. *Science* **284**, 616–618.
- Marzoli, A., Bertrand, H., Knight, K., Cirilli, S., Buratti, N., Verati, C., Nomade, S., Renne, P. R., Youbi, N., Martini, R., Allenbach, K., Neuwerth, R., Rapaille, C., Zaninetti, L. & Bellieni, G. (2004). Synchrony of the Central Atlantic magmatic province and the Triassic–Jurassic boundary climatic and biotic crisis. *Geology* **32**, 376–973.
- Marzoli, A., Jourdan, F., Puffer, J. H., Cuppone, T., Tanner, L. H., Weems, R. E., Bertrand, H., Cirilli, S., Bellieni, G. & De Min, A. (2011). Timing and duration of the Central Atlantic magmatic province in the Newark and Culpeper basins, eastern USA. *Lithos* **122**, 175–188.
- May, P. R. (1971). Pattern of Triassic diabase dykes around the North Atlantic in the context of predrift position of the continents. *Geological Society of America Bulletin* **82**, 1285–1292.
- McHone, J. G. (2000). Non-plume magmatism and rifting during the opening of the Central Atlantic Ocean. *Tectonophysics* **316**, 287–296.
- McHone, J. G. (2003). Volatile emissions of Central Atlantic Magmatic Province basalts: mass assumptions and environmental consequences. In: Hames, W. E., McHone, J. G., Renne, P. R. & Ruppel, C. (eds) *The Central Atlantic Magmatic Province: Insights from Fragments of Pangea. Geophysical Monograph, American Geophysical Union* **136**, 241–254.
- McHone, J. G., Anderson, D. L., Beutel, E. K. & Fialko, Y. A. (2005). Giant dikes, rifts, flood basalts, and plate tectonics: A contention of mantle models. In: Foulger, G. R., Natlund, J. H., Presnall, D. C. & Anderson, D. L. (eds) In: *Plates, Plumes, and Paradigms, Geological Society of America, Special Paper* **388**, 401–420.
- Meisel, T., Walker, R. J., Irving, A. J. & Lorand, J.-P. (2001). Osmium isotopic compositions of mantle xenoliths: A global perspective. *Geochimica et Cosmochimica Acta* **65**, 1311–1323.
- Merle, R., Marzoli, A., Bertrand, H., Reisberg, L., Verati, C., Zimmermann, C., Chiaradia, M., Bellieni, G. & Ernesto, M. (2011). $^{40}\text{Ar}/^{39}\text{Ar}$ ages and Sr–Nd–Pb–Os geochemistry of CAMP tholeiites from the western Maranhão basin (NE Brazil). *Lithos* **122**, 137–151.
- Moench, R. H. & Aleinikoff, J. N. (2002). Stratigraphy, geochronology, and accretionary terrane settings of two Bronson Hill arc sequences, northern New England. *Physics and Chemistry of the Earth* **27**, 47–95.
- Molzahn, M., Reisberg, L. & Wörner, G. (1996). Os, Sr, Nd, Pb and O isotope data from the Ferrar flood basalts, Antarctica: Evidence for an enriched subcontinental lithospheric source. *Earth and Planetary Science Letters* **144**, 529–546.
- Morgan, W. J. (1983). Hotspot tracks and the early rifting of the Atlantic. *Tectonophysics* **94**, 123–139.
- Murphy, J. B. & Dostal, J. (2007). Continental mafic magmatism of different ages in the same terrane: constraints on the evolution of an enriched mantle source. *Geology* **35**, 335–338.
- Murphy, J. B. & Keppie, J. D. (1998). Late Devonian palinspastic reconstruction of the Avalon–Meguma terrane boundary: Implications for terrane accretion and basin development in the Appalachian orogen. *Tectonophysics* **284**, 221–231.
- Murphy, J. B. & Nance, R. D. (2002). Sm–Nd isotopic systematics as tectonic tracers: an example from West Avalonia in the Canadian Appalachians. *Earth-Science Reviews* **59**, 77–100.
- Murphy, J. B., Pisarevsky, S. A., Nance, R. D. & Keppie, J. D. (2004). Neoproterozoic–early Paleozoic configuration of peri-Gondwanan terranes: Implications for Laurentia–Gondwanan connections. *International Journal of Earth Sciences* **93**, 659–682.
- Murphy, J. B., Gutierrez-Alonso, G., Damian Nance, R. D., Fernandez-Suarez, J., Keppie, J. D., Quesada, C., Strachan, R. A. & Dostal, J. (2006). Origin of the Rheic Ocean: Rifting along a Neoproterozoic suture? *Geology* **34**, 325–328.
- Murphy, J. B., Dostal, J. & Keppie, J. D. (2008). Neoproterozoic–Early Devonian magmatism in the Antigonish Highlands, Avalon terrane, Nova Scotia: tracking the evolution of the mantle and crustal sources during the evolution of the Rheic Ocean. *Tectonophysics* **461**, 181–201.
- Murphy, J. B., Dostal, J., Gutierrez-Alonso, G. & Keppie, J. D. (2011). Early Jurassic magmatism on the northern margin of CAMP: Derivation from a Proterozoic sub-continental lithospheric mantle. *Lithos* **123**, 158–164.
- Nance, R. D. & Murphy, J. B. (1996). Basement isotopic signatures and Neoproterozoic paleogeography of Avalonian–Cadomian and related terranes in the circum North Atlantic. In: Nance, R. D. & Thompson, M. D. (eds) *Avalonian and Related Peri-Gondwanan Terranes of the Circum North Atlantic. Geological Society of America, Special Papers* **304**, 333–346.
- Nance, R. D., Gutierrez-Alonso, G., Keppie, J. D., Linnemann, U., Murphy, J. B., Quesada, C., Strachan, R. A. & Woodcock, N. H. (2010). Evolution of the Rheic Ocean. *Gondwana Research* **17**, 194–222.
- Nomade, S., Pouclet, A. & Chen, Y. (2002). The French Guyana doleritic dykes: geochemical evidence of three populations and new data for the Jurassic Central Atlantic Magmatic Province. *Journal of Geodynamics* **34**, 595–614.
- Nomade, S., Knight, K. B., Beutel, E., Renne, P. R., Verati, C., Féraud, G., Marzoli, A., Youbi, N. & Bertrand, H. (2007).

- Chronology of the Central Atlantic Magmatic Province: Implications for the Central Atlantic rifting processes and the Triassic–Jurassic biotic crisis. *Palaeogeography Palaeoclimatology Palaeoecology* **244**, 326–344.
- Olsen, P. E., Kent, D. V., Et-Touhami, M. & Puffer, J. H. (2003). Cyclo-, magneto-, and biostratigraphic constraints on the duration of the CAMP event and its relationship to the Triassic–Jurassic boundary. In: Hames, W. E., McHone, J. G., Renne, P. R. & Ruppel, C. (eds) *The Central Atlantic Magmatic Province: Insights from Fragments of Pangea*. *Geophysical Monograph, American Geophysical Union* **136**, 7–32.
- Osberg, P. H., Tull, J. F., Robinson, P., Hon, R. & Butler, J. R. (1989). The Acadian orogen. In: Hatcher, R. D., Jr, Thomas, W. A. & Viele, G. W. (eds) *The Appalachian–Ouachita Orogen in the United States*. *Geological Society of America, The Geology of North America* **F-2**, 179–232.
- Peate, D. W. & Hawkesworth, C. J. (1996). Lithospheric to asthenospheric transition in Low-Ti flood basalts from the southern Paraná, Brazil. *Chemical Geology* **127**, 1–24.
- Pegram, W. J. (1990). Development of continental lithospheric mantle as reflected in the chemistry of the Mesozoic Appalachian tholeites, USA. *Earth and Planetary Science Letters* **97**, 316–331.
- Pe-Piper, G. & Jansa, L. F. (1999). Pre-Mesozoic basement rocks offshore Nova Scotia, Canada: New constraints on the origin and Paleozoic accretionary history of the Meguma terrane. *Geological Society of America Bulletin* **111**, 1773–1791.
- Pe-Piper, G. & Piper, D. J. W. (1998). Geochemical evolution of Devonian–Carboniferous igneous rocks of the Magdalen basin, eastern Canada: Pb and Nd isotope evidence for mantle and lower crustal sources. *Canadian Journal of Earth Sciences* **35**, 201–221.
- Philpotts, A. R. (1998). Nature of flood-basalt-magma reservoir based on the compositional variation in a single flood-basalt flow and its feeder dyke in the Mesozoic Hartford basin, Connecticut. *Contributions to Mineralogy and Petrology* **133**, 69–82.
- Philpotts, A. R. & Martello, A. (1986). Diabase feeder dykes for the Mesozoic basalts in southern New England. *American Journal of Science* **286**, 105–126.
- Philpotts, A. R., Carroll, M. & Hill, J. M. (1996). Crystal-mush compaction and the origin of pegmatitic segregation sheets in a thick flood-basalt flow in the Mesozoic Hartford Basin, Connecticut. *Journal of Petrology* **37**, 811–836.
- Plank, T. (2005). Constraints from thorium/lanthanum on sediment recycling at subduction zones and the evolution of the continents. *Journal of Petrology* **46**, 921–944.
- Pollock, J. C. & Hibbard, J. P. (2010). Geochemistry and tectonic significance of the Stony Mountain gabbro, North Carolina: Implications for the Early Paleozoic evolution of Carolina. *Gondwana Research* **17**, 500–515.
- Pollock, J. C., Hibbard, J. P. & Van Staal, C. R. (2012). A paleogeographical review of the peri-Gondwanan realm of the Appalachian orogeny. *Canadian Journal of Earth Sciences* **49**, 259–288.
- Puffer, J. H. (1992). Eastern North American flood basalts in the context of the incipient breakup of Pangea. In: Puffer, J. H. & Ragland, P. C. (eds) *Eastern North American Mesozoic Magmatism*. *Geological Society of America, Special Papers* **268**, 95–119.
- Puffer, J. H. (2001). Contrasting HFSE contents of plume sourced and reactivated arc-sourced continental flood basalts. *Geology* **29**, 675–678.
- Puffer, J. H. (2003). A reactivated back-arc source for CAMP magma. In: Hames, W. E., McHone, J. G., Renne, P. R. & Ruppel, C. (eds) *The Central Atlantic Magmatic Province: Insights from Fragments of Pangea*. *Geophysical Monograph, American Geophysical Union* **136**, 151–162.
- Puffer, J. H. & Horter, D. L. (1993). Origin of the pegmatitic segregation veins within flood basalts. *Geological Society of America Bulletin* **105**, 738–748.
- Puffer, J. H. & Student, J. J. (1992). Volcanic structures, eruptive style, and posteruptive deformation and chemical alteration of the Watchung flood basalts, New Jersey. *Special Paper of the Geological Society of America* **268**, 261–277.
- Puffer, J. H., Block, K. A. & Steiner, J. C. (2009). Transmission of flood basalts through a shallow crustal sill and the correlation of sill layers with extrusive flows: the Palisades Intrusive System and the basalts of the Newark Basin, New Jersey, U.S.A. *Journal of Geology* **117**, 139–155.
- Renne, P. R., Mundil, R., Balco, G., Min, K. & Ludwig, K. R. (2010). Joint determination of ^{40}K decay constants and $^{40}\text{Ar}^*/^{40}\text{K}$ for the Fish Canyon sanidine standard, and improved accuracy for $^{40}\text{Ar}/^{39}\text{Ar}$ geochronology. *Geochimica et Cosmochimica Acta* **74**, 5349–5367.
- Saal, A. E., Runick, R. L., Ravizza, G. E. & Hart, S. R. (1998). Re–Os isotope evidence for the composition, formation and age of the lower continental crust. *Nature* **393**, 58–61.
- Sahabi, M., Aslanian, D. & Olivet, J.-L. (2004). A new starting point for the history of the central Atlantic. *Comptes Rendus Géosciences* **336**, 1041–1052.
- Salter, V. J. M., Ragland, P. C., Hames, W. E., Milla, K. & Ruppel, C. (2003). Temporal chemical variations within lowermost Jurassic tholeiitic magmas of the Central Atlantic Magmatic Province. In: Hames, W. E., McHone, J. G., Renne, P. R. & Ruppel, C. (eds) *The Central Atlantic Magmatic Province: Insights from Fragments of Pangea*. *Geophysical Monograph, American Geophysical Union* **136**, 163–177.
- Samson, S. D., Coler, D. G. & Speer, J. A. (1995). Geochemical and Nd–Sr–Pb isotopic composition of Alleghanian granites of the southern Appalachians: Origin, tectonic setting, and source characterization. *Earth and Planetary Science Letters* **134**, 359–376.
- Schoene, B., Guex, J., Bartolini, A., Schaltegger, U. & Blackburn, T. J. (2010). Correlating the end-Triassic mass extinction and flood basalt volcanism at the 100 ka level. *Geology* **38**, 387–390.
- Schultz, K. J., Stewart, D. B., Tucker, R. D., Pollock, J. C. & Ayuso, R. A. (2008). The Ellsworth terrane, coastal Maine: Geochronology, geochemistry, and Nd–Pb isotopic composition—Implications for the rifting of Ganderia. *Geological Society of America Bulletin* **120**, 1134–1158.
- Sebai, A., Féraud, G., Bertrand, H. & Hanes, J. (1991). $^{40}\text{Ar}/^{39}\text{Ar}$ dating and geochemistry of tholeiitic magmatism related to the early opening of the Central Atlantic rift. *Earth and Planetary Science Letters* **104**, 455–472.
- Shirley, D. N. (1987). Differentiation and compaction in the Palisades sill, New Jersey. *Journal of Petrology* **28**, 835–865.
- Smoliar, M. I., Walker, R. J. & Morgan, J. W. (1996). Re–Os, isotope constraints on the age of Group IIA, IIIA, IVA, and IVB iron meteorites. *Science* **271**, 1099–1102.
- Spera, F. J. & Bohrson, W. A. (2001). Energy-constrained open-system magmatic processes I: general model and energy-constrained assimilation and fractional crystallization (EC-AFC) Formulation. *Journal of Petrology* **42**, 999–1018.
- Sun, S. S. & McDonough, W. F. (1989). Chemical and isotopic systematics of oceanic basalts: implication for mantle composition and processes. In: Saunders, A. D. & Norry, M. J. (eds) *Magmatism in the Ocean Basins*. *Geological Society, London, Special Publications* **42**, 313–345.
- Thomas, W. A. (2004). Genetic relationship of rift-stage crustal structure, terrane accretion, and foreland tectonics along the southern Appalachian–Ouachita orogen. *Journal of Geodynamics* **37**, 549–563.

- Thomas, W. A. (2006). Tectonic inheritance at a continental margin. *GSA Today* **16**, 4–11.
- Tollo, R. P. & Gottfried, D. (1992). Petrochemistry of Jurassic basalt from eight cores, Newark basin, New Jersey. In: Puffer, J. H. & Ragland, P. C. (eds) *Eastern North American Mesozoic Magmatism*. Geological Society of America, Special Papers **268**, 233–260.
- Tomascak, P. B., Brown, M., Solar, G. S., Becker, H. J., Centorbi, T. L. & Tian, J. (2005). Source contributions to Devonian granite magmatism near the Laurentian border, New Hampshire and Western Maine, USA. *Lithos* **80**, 75–99.
- Van Staal, C. R., Dewey, J. F., MacNiocaill, C. & McKerrow, W. S. (1998). The Cambrian–Silurian tectonic evolution of the Northern Appalachians and British Caledonides: History of a complex, west and southwest Pacific-type segment of Iapetus. In: Blundell, D. & Scott, A. C. (eds) *Lyell: The Past is the Key to the Present*. Geological Society, London, Special Publications **143**, 199–242.
- Van Staal, C. R., Whalen, J. B., Valverde-Vaquero, P., Zagorevski, A. & Rogers, N. (2009). Pre-Carboniferous, episodic accretion-related, orogenesis along the Laurentian margin of the northern Appalachians. In: Murphy, J. B., Keppie, J. D. & Hynes, A. J. (eds) *Ancient Orogens and Modern Analogues*. Geological Society, London, Special Publications **327**, 271–316.
- Verati, C., Bertrand, H. & Féraud, G. (2005). The farthest record of the Central Atlantic Magmatic Province into West Africa craton: Precise $^{40}\text{Ar}/^{39}\text{Ar}$ dating and geochemistry of Taoudenni basin intrusives (northern Mali). *Earth and Planetary Science Letters* **235**, 391–407.
- Verati, C., Rapaille, C., Féraud, G., Marzoli, A., Bertrand, H. & Youbi, N. (2007). $^{40}\text{Ar}/^{39}\text{Ar}$ ages and duration of the Central Atlantic Magmatic Province volcanism in Morocco and Portugal and its relation to the Triassic–Jurassic boundary. *Palaeogeography, Palaeoclimatology, Palaeoecology* **244**, 308–325.
- Walker, K. R. (1969). *The Palisades Sill, New Jersey: a Reinvestigation*. Geological Society of America, Special Papers **111**, 1–178.
- Webster, T. L., Murphy, J. B. & Gosse, J. C. (2006). Mapping subtle structures with light detection and ranging (LIDAR): flow units and phreatomagmatic rootless cones in the North Mountain Basalt, Nova Scotia. *Canadian Journal of Earth Sciences* **43**, 157–176.
- Weigand, P. W. & Ragland, P. C. (1970). Geochemistry of Mesozoic dolerite dykes from eastern North America. *Contributions to Mineralogy and Petrology* **29**, 195–214.
- Whalen, J. B., Jenner, G. A., Currie, K. L., Barr, S. M., Longstaffe, F. J. & Hegner, E. (1994). Geochemical and isotopic characteristics of granitoids of the Avalon Zone, southern New Brunswick: possible evidence for repeated delamination events. *Journal of Geology* **102**, 269–282.
- White, R. & McKenzie, D. (1989). Magmatism at rift zones: the generation of volcanic continental margins and flood basalts. *Journal of Geophysical Research* **94**, 7685–7729.
- White, R. & McKenzie, D. (1995). Mantle plumes and flood basalts. *Journal of Geophysical Research* **100**, 17543–17585.
- Widom, E. (1997). Sources of ocean island basalts: a review of the osmium isotope evidence. *Physica A* **244**, 484–496.
- Wilson, M. (1997). Thermal evolution of the Central Atlantic passive margins: continental break-up above a Mesozoic superplume. *Journal of Geological Society, London* **154**, 491–495.
- Woodhead, J. D., Herdt, J. M., Davidson, J. P. & Eggins, S. M. (2001). Hafnium isotope evidence for ‘conservative’ element mobility during subduction zone processes. *Earth and Planetary Science Letters* **192**, 331–346.
- Woodruff, L. G., Froelich, A. J., Belkin, H. E. & Gottfried, D. (1995). Evolution of tholeiitic diabase sheet systems in the eastern United States: examples from the Culpeper Basin, Virginia–Maryland, and the Gettysburg Basin, Pennsylvania. *Journal of Volcanology and Geothermal Research* **64**, 143–169.
- Workman, R. K., Hart, S. R., Jackson, M. G., Regelous, M., Farley, K. A., Bluszta, J., Kurz, M. D. & Staudigel, H. (2004). Recycled metasomatized lithosphere as the origin of the enriched mantle II (EM2) end-member: evidence from the Samoan volcanic chain. *Geochemistry, Geophysics, Geosystems*, 2003GC000623.
- Zartman, R. E. & Doe, B. R. (1981). Plumbotectonics—the model. *Tectonophysics* **75**, 135–162.
- Zindler, A. S. R. & Hart, S. (1986). Chemical geodynamics. *Annual Review of Earth and Planetary Sciences* **14**, 493–571.

Plume–Lithosphere Interaction during Migration of Cretaceous Alkaline Magmatism in SW Portugal: Evidence from U–Pb Ages and Pb–Sr–Hf Isotopes

M. GRANGE¹*, U. SCHÄRER¹, R. MERLE², J. GIRARDEAU³ AND G. CORNEN³

¹UNIVERSITE DE NICE–SOPHIA ANTIPOLIS, GEOAZUR (UMR 6526), PARC VALROSE, F-06108 NICE, FRANCE

²UNIVERSITY OF WESTERN AUSTRALIA, SCHOOL OF EARTH AND ENVIRONMENT, 35 STIRLING HIGHWAY, CRAWLEY, WA 6009, AUSTRALIA

³UNIVERSITE DE NANTES, LABORATOIRE DE PLANETOLOGIE ET GEODYNAMIQUE (UMR 6112), 2 RUE DE LA HOUSSINIÈRE, F-44322 NANTES CEDEX 3, FRANCE

RECEIVED JUNE 15, 2008; ACCEPTED MARCH 31, 2010

Large massifs of alkaline rocks are exposed along ~250 km of the Atlantic coast of Portugal. Their origin is still poorly understood, including the precise timing of their emplacement and their relationships with the well-constrained alkaline magmatic rocks that occur 200–1000 km offshore. To elucidate the precise timing and origin of the alkaline magmatism in this region, magmatic rocks from the three major alkaline massifs (Sintra, Sines, and Monchique) and an isolated diorite intrusion (Ribamar, north of Sintra) have been dated by the U–Pb method on titanite and zircon and characterized based on their Pb, Sr, and Hf isotopic compositions obtained on feldspar and zircon. From north to south, the resulting ages are: 88.3 ± 0.5 Ma (95% confidence level) for Ribamar, 83.4 ± 0.7, 82.0 ± 0.7, 81.7 ± 0.4, and 80.1 ± 1.0 Ma for the Sintra complex, 77.2 ± 0.6, 77.2 ± 0.4, and 76.1 ± 1.3 Ma for the Sines massif, and 70.0 ± 2.9 and 68.8 ± 1.0 Ma for the Monchique complex. Initial isotopic compositions of Pb in feldspars are in the range of 18.522–19.299 for $^{206}\text{Pb}/^{204}\text{Pb}$, 15.555–16.007 for $^{207}\text{Pb}/^{204}\text{Pb}$, and 38.480–39.330 for $^{208}\text{Pb}/^{204}\text{Pb}$. Initial $^{87}\text{Sr}/^{86}\text{Sr}$ of feldspars varies between 0.70274 and 0.70481 and initial Hf isotope ratios yield ϵHf_i values between +3.7 and +9.6. These results, together with major, trace, and rare earth element analyses, show that the ages, $(^{207}\text{Pb}/^{204}\text{Pb})_i$, and $(^{87}\text{Sr}/^{86}\text{Sr})_i$ increase northward, whereas the alkaline affinity, $(^{206}\text{Pb}/^{204}\text{Pb})_i$, and ϵHf_i increase southward, substantiating a north–south trend of geochemical and age variation.

The isotopic composition of the studied rocks can be explained by partial melting of a sub-lithospheric mantle source with an enriched DMM (Depleted MORB Mantle) signature and subsequent contamination by the metasomatized Iberian subcontinental lithospheric mantle (SCLM). The north–south age trend is in agreement with the motion of the Iberian plate between 88 and 60 Ma. The spatial and temporal variations in the isotopic signatures are explained by differences in the contribution of the two source components. The sub-lithospheric mantle-derived magmas are more contaminated by the SCLM in the northern part of the alignment, compared with the southern part of the studied region, where the rocks have isotopic signatures closer to those of enriched sub-lithospheric mantle. Our data are incorporated into a geodynamical model that explains the overall distribution of alkaline magmatism in this part of the eastern Central Atlantic, and provide new constraints on the occurrence of alkaline magmatism along the Iberian margin and the NW African plate. The spatial distribution of the magmatism is directly correlated with the motion of the Iberian plate above a deep-rooted thermal anomaly (mantle plume) that has caused magmatism since the Cretaceous.

KEY WORDS: alkaline magmatism; U–Pb geochronology; Pb–Sr–Hf isotopes; subcontinental lithospheric mantle (SCLM); Portugal

*Corresponding author. Present address: Department of Applied Geology, Curtin University of Technology, Level 2, Building 312, GPO Box U1987, Perth, WA 6845, Australia. Telephone: +61 8 9266 7969. Fax: +61 8 9266 3153. E-mail: m.grange@curtin.edu.au

INTRODUCTION

Recent geochronological and isotopic studies suggest that a plume-related thermal anomaly below the eastern Central Atlantic region has been the cause of widespread alkaline magmatic activity since the Cretaceous (e.g. Geldmacher *et al.*, 2006; Merle *et al.*, 2006, 2009). These manifestations occur in the oceanic lithosphere west of North Africa and Iberia (Fig. 1), along the SW–NE-trending Tore–Madeira Rise (TMR), which comprises a dozen seamounts extending from the Madeira Archipelago to the submarine Tore seamount, on the Gorringe Bank in the vicinity of the Azores–Gibraltar fracture zone (AGFZ), 200 km SE of Portugal, and two off-centre seamounts between the Gorringe Bank and the Madeira Archipelago (Ampere and Coral-Patch seamounts). Onshore, alkaline magmatic

rocks occur along the Iberian margin in Portugal, forming three main massifs and several isolated sills and plugs. However, a lack of age and isotopic constraints makes it difficult to establish reliable petrogenetic relationships between the continental and the oceanic alkaline magmatism, despite models that suggest the southernmost massif in Portugal (Monchique) and the eastern part of the Gorringe Bank (Mount Ormonde) were emplaced at the same time and originated from similar sources (Cornen, 1982; Bernard-Griffiths *et al.*, 1997). A recent study has also shown that the alkaline magmatism in this region (i.e. along the TMR and the seamounts between the TMR and the coast of the Portugal) can be geodynamically explained by the movement of the Iberian plate above a thermal anomaly, which has caused intermittent magmatism since the Cretaceous (Merle *et al.*, 2009).

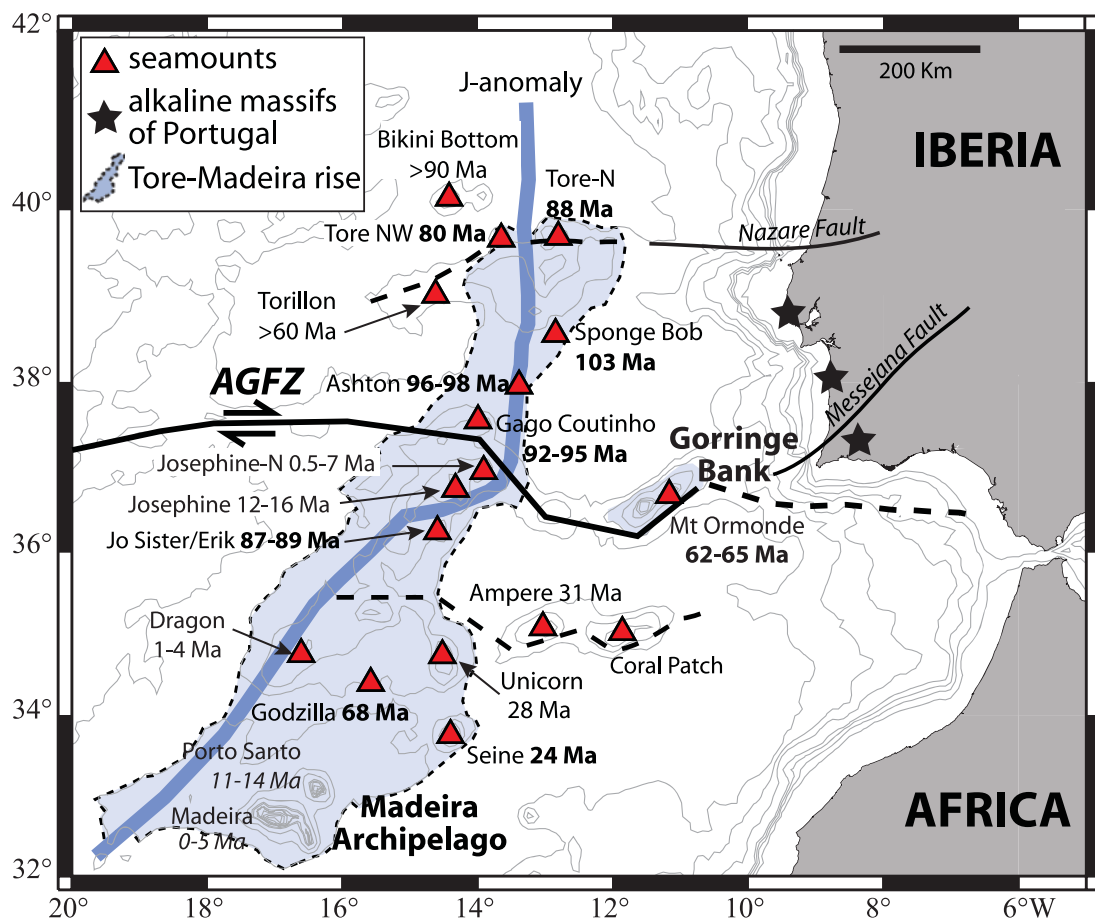


Fig. 1. Schematic bathymetric map of the eastern Central Atlantic (from Merle *et al.*, 2009). Faults are indicated by continuous lines and inferred faults by dashed lines; AGFZ, Azores–Gibraltar Fracture Zone. Seamount locations are indicated by triangles and their ages are those reported by Merle *et al.* (2009, and references therein); following their recommendations, ages in bold represent ages obtained on minerals ($U-Pb$ on titanite and zircon and $^{40}\text{Ar}-^{39}\text{Ar}$ on plagioclase, hornblende and biotite) and are considered to be the most reliable, whereas the other ages have to be considered with caution because they represent $^{40}\text{Ar}-^{39}\text{Ar}$ ages obtained on matrix samples. The ages from Porto Santo and Madeira (shown in italic) are undifferentiated ages obtained by $^{40}\text{Ar}-^{39}\text{Ar}$ on whole-rock and mineral separates (after Geldmacher *et al.*, 2000).

In this study, we investigate the precise timing of emplacement of the Portuguese alkaline massifs, based on U–Pb dating of zircon and titanite by isotope dilution thermal ionization mass spectrometry (ID-TIMS). We also characterize their magma sources using Pb–Sr and Hf isotope systematics on feldspar and zircon, and major and trace element analyses of whole-rock samples. We address questions about (1) the temporal and spatial extent of alkaline magmatism in Portugal, (2) the magma sources, including the possible involvement and interaction of both plume- and subcontinental lithospheric mantle (SCLM)-derived magmas, and (3) the relationships between the continental and oceanic alkaline magmatism in the context of eastern North Atlantic geodynamics.

GEOLOGICAL FRAMEWORK

General setting

The western Iberian margin was formed during the early Cretaceous when the Iberian microplate separated from Newfoundland. The 130–125 Ma magnetic anomaly (J-anomaly) was the first magnetic anomaly formed at the Mid-Atlantic Ridge north of the AGFZ and marks the western limit of the continent–ocean transition zone on the Iberian margin (Olivet, 1996). The continent–ocean transition is characterized by the unroofing of the subcontinental lithospheric mantle, which is made up of serpentized peridotites locally covered by thin sedimentary deposits (e.g. Boillot *et al.*, 1988; Beslier *et al.*, 1990; Girardeau *et al.*, 1998). Previous studies have shown that the Gorringe Bank is also a piece of unroofed SCLM, tilted during North Atlantic rifting and later capped by Cretaceous–Palaeocene alkaline magmatic rocks (e.g. Féraud *et al.*, 1986; Girardeau *et al.*, 1998; Schärer *et al.*, 2000). The SCLM of the western Iberian margin may be highly heterogeneous as a result of earlier Variscan orogenesis (400–250 Ma). During this orogenic cycle, the margin experienced subduction and associated mantle metasomatism, and the accretion of allochthonous terranes such as the Cabo Ortegal complex, which is a piece of metamorphosed and exhumed island arc (Girardeau & Gil Ibarguchi, 1991; Santos *et al.*, 1996, 2002).

The AGFZ is a major oceanic transform fault that has constituted the boundary between the African plate to the south and the European plate to the north since about 85 Ma, and formed in response to the northward motion of Africa (Sibuet *et al.*, 2004). Although this fault is a major tectonic boundary, strike-slip movements along it were limited between Early Jurassic and Oligocene times (Olivet, 1996). On the continent, the Messejana and Nazare faults are considered to be reactivated Hercynian structures connected to the AGFZ (Figs 1 and 2).

Widespread occurrences of alkaline rocks are found in the eastern North Atlantic and in Portugal, including the Madeira Archipelago, the TMR seamounts and the three

massifs of mainland Portugal studied here (Fig. 1). Various isotopic methods, such as U–Pb, K–Ar and ^{40}Ar – ^{39}Ar on minerals and whole-rock, have been used to determine the emplacement age of the oceanic rocks. Recently, Merle *et al.* (2009) produced a comprehensive geochronological review of the TMR seamounts and their surroundings. The interpretation of some ages is problematic because of the use of different isotopic systems, the unreliability of some dating methods, and the possible alteration of oceanic rocks. However, the ages reported in Fig. 1 are considered to be reliable estimates of the timing of magmatic events; readers are referred to Merle *et al.* (2009) for further discussion of these ages. The resulting age compilation generated for the TMR seamounts shows that these oceanic alkaline rocks were emplaced over an interval from the late Early Cretaceous (~103 Ma) until the present time. Merle *et al.* (2009) interpreted the emplacement of the alkaline magmatic rocks to be related to the motion of the Iberian plate above a mantle thermal anomaly. The northward motion of the Iberian plate would have been interrupted by the closure of the Neo-Tethys basin and the subsequent Pyrenean orogeny, and could explain the present-day distribution of the alkaline massifs and seamounts.

The Portugal alkaline massifs: previous petrological and geochemical data

The alkaline rocks occur in several massifs, several tens of square kilometres in extent, located along the Portugal coast from the Lisbon area to the Algarve province, 250 km to the south (Fig. 2a). The main magmatic complexes are, from north to south, Sintra, the Lisbon volcanic complex, Sines, and the Monchique massifs. Isolated bodies also occur, such as the Ribamar intrusion (50 km north of Sintra) and dikes in the Algarve region. The main massifs (Sintra, Sines and Monchique) comprise a variety of rocks with compositions ranging from granite to SiO_2 -undersaturated phonolite and nepheline syenite. Magnetic anomalies and susceptibilities confirm that the Sintra and Sines massifs extend far into the sea, which means that not all rock types potentially present could be sampled (Silva *et al.*, 2000).

Several attempts have been made over the past few decades to date the alkaline magmatism on the western coast of Portugal and a detailed review of this earlier work has been provided by Miranda *et al.* (2009). The ages reviewed in the study of Miranda *et al.* (2009) are K–Ar ages on whole-rock or separated minerals and Rb–Sr ages on whole-rock. These methods have proven to be unreliable for rocks older than a few million years (e.g. Baksi, 2007).

Some isolated intrusions occur north of Lisbon, including the Ribamar dioritic intrusion and the Paco d'Ilhas monzogabbroic–monzonitic sill (Miranda *et al.*, 2009). Miranda *et al.* (2009) proposed an age of 88.0 ± 2.7 Ma for the Paco d'Ilhas sill (K–Ar on biotite), whereas

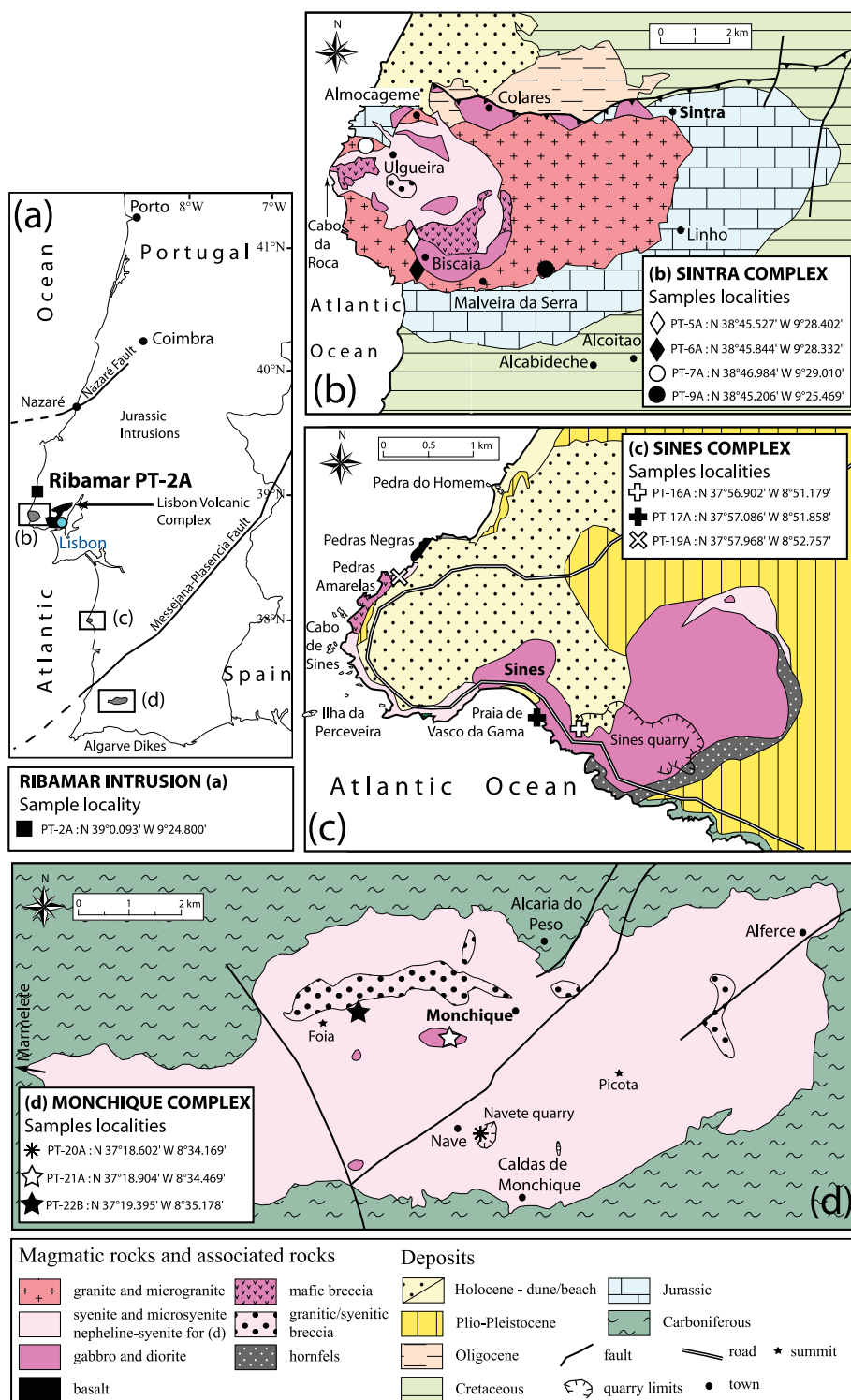


Fig. 2. Geological sketch maps of the alkaline complexes along the Portuguese coast (modified after Gonçalves, 1967; Canilho, 1972): (a) the full extent of the alkaline intrusions and in particular the Ribamar intrusion; (b) the Sintra complex; (c) the Sines complex; (d) the Monchique complex.

the Ribamar intrusion has not been investigated so far (Fig. 2a). Farther south, the Lisbon volcanic complex is composed of flows, plugs, sills and dikes comprising alkali basalt, gabbro, dolerite, trachyandesite, trachyte, and rhyolite (Palacios, 1985). A single attempt to date this magmatic activity has been made using the whole-rock K–Ar method, leading to an unreliable age (see details given by Miranda *et al.*, 2009).

The Sintra subvolcanic complex is located along the coast west of Lisbon, and has a semicircular structure (Fig. 2b). The core is composed of syenite surrounded by granite (e.g. Wright, 1969; Sparks & Wadge, 1975) and is intruded by mafic rocks. No reliable ages were available until the recent study by Miranda *et al.* (2009), who reported an age of 79.2 ± 0.8 Ma [95% confidence (conf.)] from the granite, obtained by the U–Pb method on zircon using laser ablation inductively coupled plasma mass spectrometry (LA-ICP-MS). The Foz da Fonte intrusion is a tephritic sill located between the Sintra massif and the Sines massif. This intrusion has been recently dated by the ^{40}Ar – ^{39}Ar step-heating method on amphibole separates (Miranda *et al.*, 2009). The weighted mean plateau gave an age of 93.6 ± 4.6 Ma (2σ) and the inverse isochron an age of 93.8 ± 7.8 Ma.

The Sines complex occurs about 100 km to the south of Lisbon along the coast. It displays a ring-shaped pattern comprising syenite, diorite–gabbro, basalt, and heterogeneous mafic breccias (Fig. 2c; Canilho, 1972; Rock, 1978). The syenite intrudes the gabbro and both are commonly cut by breccia dikes with basaltic to syenitic fragments. Several attempts to date the Sines complex have been made over the past three decades using the K–Ar technique. The results have been summarized by Miranda *et al.* (2009). A U–Pb age on zircon of 75.4 ± 0.6 Ma (95% conf.) obtained by LA-ICP-MS is the most reliable age constraining the emplacement of this massif (Miranda *et al.*, 2009).

The Monchique complex is the largest massif (63 km × 16 km), with an east–west elliptical shape (Fig. 2d), and has been described as a subvolcanic laccolith emplaced into Late Carboniferous marine sediments (Rock, 1978). It is mainly composed of nepheline syenite, alkali gabbro, and diorite, but also contains trachytic and syenitic breccias that host basalt, syenite, phonolite, and pelite fragments (Rock, 1978). This massif is intruded by phonolite plugs and lamprophyre dikes. Previous dating of the Monchique complex yielded K–Ar ages on minerals and whole-rock Rb–Sr isochron ages of ~ 72 Ma (Miranda *et al.*, 2009, and references therein). The nepheline syenite body was emplaced at 72.3 ± 8.4 Ma (2σ) based on a recent whole-rock Rb–Sr isochron age (Miranda *et al.*, 2009). The ultramafic components of the Monchique complex yield an age at 74.4 ± 4.0 Ma (2σ) showing that they were probably emplaced at the same

time (^{40}Ar – ^{39}Ar age on amphibole, Miranda *et al.*, 2009). At 72 Ma, whole-rock isotope analyses define initial $^{87}\text{Sr}/^{86}\text{Sr}$ (Sr_i) between 0.70312 and 0.70337, and initial epsilon Nd (ϵNd_i) values range between +4.3 and +5.6 (Rock, 1976; Bernard-Griffiths *et al.*, 1997; Miranda *et al.*, 2009). Initial Pb isotope ratios (Pb_i) of whole-rocks are 19.409–19.732 for $^{206}\text{Pb}/^{204}\text{Pb}$, 15.623–15.651 for $^{207}\text{Pb}/^{204}\text{Pb}$, and 39.38–39.80 for $^{208}\text{Pb}/^{204}\text{Pb}$ (Bernard-Griffiths *et al.*, 1997).

Rare basaltic dikes, between one and a few meters in width, occur in the Algarve region; they represent significantly smaller magmatic volumes compared with the three main massifs. Previous geochronological data for these dikes were obtained using the K–Ar technique on whole-rock, yielding ages between 77 ± 3 and 72 ± 2 Ma (no data published, cited by Martins, 1991). The age of these magmatic rocks was refined to 71.8 ± 3.8 Ma (2σ) by K–Ar dating of biotites extracted from a lamprophyre dike sampled in the Loulé area (Miranda *et al.*, 2009).

ANALYTICAL PROCEDURES

Major and trace element analyses were carried out using the SARM facilities (Service d'Analyses des Roches et Minéraux) at the CRPG (Centre de Recherches Pétrographiques et Géochimiques, Nancy, France), by inductively coupled plasma atomic emission spectrometry (ICP-AES) and ICP-MS, following the procedures described by Govindaraju & Mevelle (1987) and Carignan *et al.* (2001). The precision of the major element analyses is 1–5%, except for MnO, MgO, CaO, and P₂O₅ (10%). Trace element analyses have a precision of 5–10% for >50 ppm abundance, 5–15% for 10–50 ppm, 5–20% for 1–10 ppm, and 5–25% for <1 ppm.

Mineral separation was carried out using a Frantz isodynamic magnetic separator, heavy liquids (CHBr₃ and CH₂I₂), and hand-picking under a binocular microscope. All chemical procedures for isotope analyses and mass spectrometric measurements were performed at the University of Nice–Sophia Antipolis, except for the Hf measurements obtained on the MC-ICP-MS instruments at the Ecole Normale Supérieure (ENS-Lyon, France).

All grains used for isotope analyses (zircon, titanite, K-feldspar, and plagioclase) represent the most euhedral, transparent, and inclusion- and crack-free grains of the populations. To minimize the influence of surface alteration or weathering, selected grains were abraded (zircon and titanite) and then leached. Prior to hand-picking, zircons were mechanically abraded (Krogh, 1982), washed at 100°C for 1 h in 7N HNO₃, rinsed in triple distilled water and weighed. After transfer of 1–30 zircon grains to PTFE® pressure capsules, a ^{205}Pb – ^{233}U – ^{235}U isotope tracer solution was added and the sample dried on a hot plate. Dissolution and homogenization with the spike solution was achieved with 25N HF for 3 days at 215°C. After

drying, 3N HCl was added, and the capsules were closed and heated at 215°C for 1 day to dissolve the fluorides. This solution was then directly introduced onto AGW-IX8 200–400 mesh anion resin and chemical treatment was performed as described by Krogh (1973). This chemical procedure also separates U and Pb from Zr and Hf. Hafnium contained in the 3N HCl fraction was further processed through AGW-50X-12 cation resin® to eliminate ^{176}Yb interferences on ^{176}Hf (Patchett & Tatsumoto, 1980). Because Lu/Hf is very low in zircon (e.g. Patchett *et al.*, 1981; Schärer *et al.*, 1997), the present-day $^{176}\text{Hf}/^{177}\text{Hf}$ values directly reflect those of the magma sources at the time of melting. For details of the U–Pb–Hf systematics of zircons and associated chemical procedures we refer readers to Bodet & Schärer (2000).

For titanite, the abrasion, washing, weighing, and isotope tracer addition were identical to those for zircon but 2–20 grain titanite fractions were dissolved at 140°C for 15 h with 25N HF in 2 ml Savilex® beakers, followed by drying, and then addition of 6N HCl to dissolve the fluorides for 4 h at the same temperature as dissolution. The following chemical procedure used the same anion resin as for zircon but an HBr chemical procedure and an additional purification step for U (Manhès *et al.*, 1978). This latter chemical procedure was also used for K-feldspar and plagioclase, which were washed with 6N HCl and water, ground in an agate mortar and leached with a 1% HBr solution for 1–2 min (Schärer, 1991). After decanting the wash solution, additional washing was performed with triple distilled water and the ^{205}Pb – ^{233}U – ^{235}U tracer solution was added. After drying, about 1.5 ml of 25N HF was added in 2 ml Savilex® beakers and kept on the hot plate for 15 h at 140°C. It should be noted that one-third of the 3N HCl solution volume from the U–Pb chemistry was spiked with a ^{85}Rb – ^{84}Sr tracer solution so that the U–Pb and Rb–Sr isotope signatures could be measured on the same mineral fractions. For Rb–Sr concentration analyses on the spiked solution, Rb and Sr were separated using Eichrom Sr-Spec resin®. Isotopic composition measurements were performed on the remaining unspiked two-thirds of the original solution volume and Rb was separated from Sr using the Eichrom resin. Plagioclase and K-feldspar fractions extracted from the U–Pb dated samples and from an additional undated phonolite from the Monchique complex (PT-22B) were analysed for U–Pb and Rb–Sr (see Tables 4 and 5 below). Initial Pb_i and Sr_i ratios were obtained by correcting the measured ratios for the *in situ* decay of U and Rb, measured on the same fraction, to the time of formation defined by the U–Pb age of the rock.

Zircon fractions vary in weight between 0.061 and 0.101 mg and titanite between 0.170 and 0.360 mg, representing between 1 and 30 grains per fraction for zircon and between 2 and 20 grains for titanite. Grain sizes of

zircon were between 0.05 and 0.20 mm and those of titanite between 0.10 and 1.5 mm. Both minerals are essentially euhedral, transparent crystals, with zircon varying between colorless and slightly yellow, and titanite from yellow to brown. Opaque and transparent inclusions reach up to about 5 vol. % and were excluded from analyses when possible.

Overall analytical uncertainties of the zircon U–Pb dates are 1–3.5% for $^{206}\text{Pb}/^{238}\text{U}$ and 2–9% for $^{207}\text{Pb}/^{235}\text{U}$; correlation coefficients are between 0.3 and 0.7. For titanite, the corresponding errors and correlation coefficients are 2.5–3.5%, 4–20%, and 0.3–0.4, respectively. These uncertainties include in-run precisions, corrections for blanks and mass fractionation, and initial common Pb measured in the feldspar fractions. Lead blanks were 7–20 pg for zircon analyses and 30–60 pg for titanite. Concordia diagrams were plotted using the Isoplot Excel add-in (Ludwig, 2003); error ellipses in Figs 5–7 below take into consideration the above uncertainties and are plotted at the 2σ level. The age assigned to each sample corresponds to the weighted mean $^{206}\text{Pb}/^{238}\text{U}$ age of the different fractions, calculated with Isoplot and are reported at the 95% level confidence, unless otherwise specified.

All U–Pb and Pb isotope analyses were carried out on single degassed (2000°C) Re filaments (H_3PO_4 /Si-gel load) using a single secondary electron multiplier on a Thomson 206 mass spectrometer. Mass fractionation of $0.10 \pm 0.05\%$ per a.m.u. was monitored by repeated analysis of the NBS-981 standard, which yielded average ratios of 16.941 ± 0.044 (2σ) for $^{206}\text{Pb}/^{204}\text{Pb}$, 15.501 ± 0.044 for $^{207}\text{Pb}/^{204}\text{Pb}$, and 36.728 ± 0.078 for $^{208}\text{Pb}/^{204}\text{Pb}$. Strontium isotope compositions were measured on a VG-Sector instrument using single Re filaments with a $\text{H}_3\text{PO}_4/\text{TaF}_5$ load. The NBS-987 standard was regularly analysed to monitor the accuracy of the Sr measurement and yielded an average $(^{87}\text{Sr}/^{86}\text{Sr})_{\text{norm}}$ of 0.710289 ± 0.000082 (2σ). All Sr isotope measurements were normalized to $^{86}\text{Sr}/^{88}\text{Sr} = 0.1194$. Hafnium isotope measurements were performed on the Plasma VG-54 and the Nu plasma instruments at the ENS-Lyon using the JMC-475 Hf standard for calibration, run every fourth sample (Blichert-Toft *et al.*, 1997). This standard yielded a mean ratio of 0.282162 ± 0.000001 (2σ). All hafnium isotope measurements were normalized to $^{179}\text{Hf}/^{177}\text{Hf} = 0.7325$ (Patchett & Tatsumoto, 1980). Further comments on combined U–Pb–Hf isotope analyses of zircon have been given by Bodet & Schärer (2000). Decay constants of ^{238}U and ^{235}U are those determined by Jaffey *et al.* (1971), the constant for ^{87}Rb was taken from Steiger & Jäger (1977) and the ^{176}Lu decay constant is from Söderlund *et al.* (2004). Errors on isotopic ratios reported throughout the text and in Tables 4–6 (see below) correspond to analytical uncertainties (i.e. 2 standard error, internal measurement statistics).

RESULTS

Classification and petrology

Brief petrographic descriptions and petrological classifications of the studied samples are given in Table 1. Textural variability within a single outcrop is commonly observed. The rocks are generally fresh, with minimal alteration. However, some samples show some visible alteration of the plagioclase and/or K-feldspar. Altered minerals were not selected for analysis and the leaching procedures used allow us to establish that the isotope analyses are not biased by any form of alteration and therefore represent the primary isotopic composition of the magmas.

Major and trace element geochemistry

The analysed samples have a wide range of compositions as illustrated in the $\text{Na}_2\text{O} + \text{K}_2\text{O}$ vs SiO_2 diagram (TAS diagram, Fig. 3, Table 2). The Sintra samples plot in the alkali basalt to rhyolite fields, the Sines samples in the basalt to trachyte field, and the Monchique samples in the basanite to phonolite field. The Ribamar intrusion has basaltic trachy-andesitic composition. With the exception of the granite from the Sintra massif, all the rocks have an alkaline character, becoming more alkaline and SiO_2 -undersaturated from north to south (i.e. from Sintra to Monchique). Among the studied rocks, the alkali gabbro from Monchique (PT-21A) has the most primitive and SiO_2 -undersaturated composition, with MgO and CaO contents as high as 8.5 and 13.9 wt %, respectively, at ~41 wt % SiO_2 . The most mafic rocks are variably differentiated, as they have MgO contents ranging from 4 to 8.5 wt %. This is reflected in their compatible trace element contents ($\text{Ni} = 6\text{--}75 \text{ ppm}$, $\text{Co} = 22\text{--}50 \text{ ppm}$, $\text{Cr} = 5\text{--}190 \text{ ppm}$), which are lower than the range expected for magmas in equilibrium with mantle sources ($\text{Ni} = 200\text{--}500 \text{ ppm}$, $\text{Co} = 50\text{--}70 \text{ ppm}$, $\text{Cr} = 500\text{--}800 \text{ ppm}$, e.g. Allègre *et al.*, 1977).

Chondrite-normalized rare earth element (REE) patterns and primitive mantle normalized trace element patterns are shown in Fig. 4 for each studied massif, from Ribamar in the north to Monchique in the south. A common feature in the entire set of analysed rocks is their positive Pb anomaly. The Monchique alkali gabbro (PT-21A) is an exception with a slightly negative Pb anomaly, and represents the least differentiated and most mafic rock of this study. The Ribamar alkali diorite (PT-2A) shows a moderately steep REE pattern with $(\text{La/Yb})_{\text{N}} = 16$, and flat heavy REE (HREE) pattern. The trace element pattern is regular, showing no large anomalies (Fig. 4a and b).

Rocks from the Sintra massif have similar-shaped REE patterns (Fig. 4c). They are between 80 and 200 times enriched in the light REE (LREE) compared with chondrite, with $(\text{La/Yb})_{\text{N}}$ ranging from 5 to 19. The gabbro (PT-6A) does not have an Eu anomaly, and has a slightly convex

pattern in the middle REE (MREE). The three other samples have concave patterns and increasingly negative Eu anomalies, with (Eu/Eu^*) of 0.62 for the syenite (PT-7A), 0.28 for the alkali granite (PT-9A), and 0.12 for the micro-granite (PT-5A). Except for the gabbro (PT-6A), the incompatible trace element patterns of the Sintra rocks (Fig. 4d) show negative anomalies in Ba, Sr, P, and Ti (increasing in the same sense as the Eu anomaly), and similar positive anomalies in Pb. Both the syenite (PT-7A) and the alkali granite (PT-9A) have parallel incompatible trace element patterns, the syenite being the most enriched sample. Although the micro-granite appears to be the most differentiated rock type of the massif, with more than 77 wt % SiO_2 and only 0.06 wt % MgO (Table 2), it is also the least enriched rock in terms of its REE content compared with the three other samples, whereas the most primitive rock (alkali gabbro PT-6A) is the most enriched in REE. The more differentiated compositions, as indicated by their MgO contents, are less enriched in REE and have more negative Eu, Ba, Sr, and P anomalies. Moreover, the micro-granite (PT-5A) shows a flat pattern for the HREE with $(\text{Dy/Yb})_{\text{N}} = 0.90$.

The three analysed samples from the Sines complex are 200–400 times enriched in LREE compared with chondrites, with $(\text{La/Yb})_{\text{N}}$ between 9 and 19 (Fig. 4e). The two alkali gabbros (PT-16A and PT-17A) show parallel incompatible trace element patterns (Fig. 4f), although PT-17A has a more enriched REE pattern that is slightly convex in the MREE with a slight negative Eu anomaly ($\text{Eu/Eu}^* = 0.86$) compared with PT-16A. The syenite (PT-19A) is more enriched in LREE than the alkali gabbros, and has a pronounced concave shape in the MREE. This slight REE enrichment of the syenite compared with the alkali gabbros is also visible in the incompatible element pattern (Fig. 4f). All three samples show negative anomalies in Ba, P and Ti, and positive Pb anomalies, all being most pronounced for the syenite.

The REE patterns of the Monchique rocks are similar to those reported in previous studies (Bernard-Griffiths *et al.*, 1997) with up to 400 times LREE enrichment compared with chondrites, yielding $(\text{La/Yb})_{\text{N}}$ between 19 and 34 (Fig. 4g and h). The nepheline syenite (PT-20A) has a concave U-shaped REE pattern, similar to those reported for other samples from the same massif (Rock, 1976; Cornen, 1982; Bernard-Griffiths *et al.*, 1997). This feature is also present in the REE pattern of the phonolite (PT-22B). In contrast, the alkali gabbro (PT-21A) has a convex REE pattern. The nepheline syenite and phonolite have similar incompatible element patterns with negative anomalies in Ba and P, and to a lesser extent in Ti, and positive anomalies in Pb, all being more pronounced for the nepheline syenite (Fig. 4h). In contrast, the alkali gabbro has positive anomalies in Ba, Nb and Ti, and a negative anomaly in Pb.

Table 1: Petrographic descriptions of the studied samples from Portugal (from north to south)

Sample	Locality	Texture	Primary phases*	Alteration phases	Minor phases and accessories	Rock type
<i>Ribamar</i>						
PT-2A	quarry	fine-grained	plagioclase K-fsp clinopyroxene biotite	→ white micas → sericite → chlorite	oxides calcite	Alkali diorite
N 39°0'093' W 9°24'800'						
PT-5A	Biscaia village	micro-granular porphyric	quartz K-fsp plagioclase sparse muscovite		zircon oxides	Micro-granite
N 38°45'527' W 9°28'402'				→ sericite → white micas		
PT-6A	Biscaia quarry	medium-grained	plagioclase biotite clinopyroxene amphibole		apatite titanite zircon epidote	Alkali gabbro
N 38°45'844' W 9°28'332'				→ chlorite		
PT-7A	N Cabo da Roca	fine-grained	K-fsp biotite amphibole quartz sparse plagioclase	→ sericite → chlorite	zircon	Syenite
N 38°46'984' W 9°29'010'						
PT-9A	main granite intrusion	medium-grained	K-fsp quartz biotite plagioclase	→ sericite → chlorite → white micas	apatite zircon	Alkali granite
N 38°45'200' W 9°25'469'						
<i>Sines</i>						
PT-16A	quarry	coarse-grained	plagioclase clinopyroxene biotite sparse olivine		apatite sparse titanite oxides	Alkali gabbro
N 37°56'902' W 8°51'179'	S Sines			→ chlorite		
PT-17A	hill between harbor and beach	coarse-grained	plagioclase amphibole biotite clinopyroxene sparse quartz	→ white micas → amphibole	apatite titanite zircon oxides calcite	Alkali gabbro
N 37°57'086' W 8°51'858'						
PT-19A	Pedras Negras	fine-grained and tiny vesicles	K-fsp sparse plagioclase quartz amphibole biotite	→ sericite → white micas → chlorite	apatite titanite zircon oxides calcite epidote	Micro-syenite
N 37°57'968' W 8°52'757'						
<i>Monchique</i>						
PT-20A	Navete quarry	coarse-grained	alk. fsp nepheline clinopyroxene biotite	→ sericite → chlorite	titanite apatite oxides zeolite calcite	Nepheline syenite
N 37°18'602' W 8°34'169'						
PT-21A	east of Foia hill	coarse-grained porphyroid	amphibole (poikilitic) plagioclase (poikilitic) clinopyroxene nepheline biotite		apatite titanite oxides	Alkali gabbro
N 37°18'904' W 8°34'469'						
PT-22A	top of Foia hill	microlitic and porphyric	alk. fsp sparse plagioclase clinopyroxene (relics)	→ sericite → white micas	apatite calcite	Phonolite
N 37°19'395' W 8°35'178'						

*Most abundant primary phases are indicated at the top of the list.

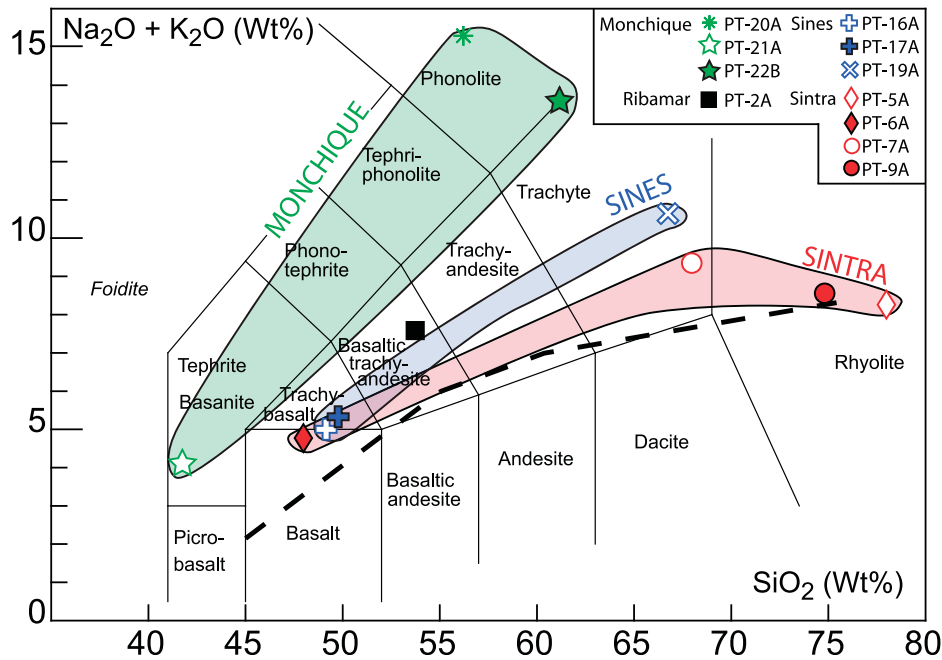


Fig. 3. Total alkalis vs SiO_2 diagram (Le Bas *et al.*, 1986) for the Portuguese samples. The dividing line (dashed) between alkaline and subalkaline series is from Miyashiro (1978).

U-Pb dating

Table 3 lists zircon and titanite U-Pb analytical results and Figs 5-7 show the corresponding concordia plots. All zircon and titanite ages were derived from $^{206}\text{Pb}/^{238}\text{U}$ because $^{207}\text{Pb}/^{235}\text{U}$ commonly has excessive scatter, especially for the titanite data. This scatter is a consequence of the low U contents in titanite and therefore low radiogenic Pb contents. Consequently, the $^{207}\text{Pb}/^{235}\text{U}$ ages are more sensitive to common Pb correction than $^{206}\text{Pb}/^{238}\text{U}$, and less precise. Specific features of the concordia diagrams for some samples are discussed below.

Six zircon fractions from the Ribamar diorite (PT-2A, Fig. 5a) yield identically concordant ages defining a weighted mean $^{206}\text{Pb}/^{238}\text{U}$ age of 88.3 ± 0.5 Ma (95% conf., MSWD = 0.90). These six zircon grains were not abraded because of their very fine acicular shape, which almost certainly would have been destroyed by abrasion. Nevertheless, the results are concordant and provide a very precise final age. The zircon ages obtained for the rocks of the Sintra massif are shown in Fig. 5b-e. Seven zircons from the micro-granite (PT-5A) give concordant ages with one grain having a slightly younger age than the bulk of the zircons. This grain (zircon 5) is unusually rich in U (>4570 ppm) and is most probably affected by recent Pb loss. Excluding this grain provides a weighted mean $^{206}\text{Pb}/^{238}\text{U}$ age of 82.0 ± 0.7 Ma (MSWD = 1.18) (Fig. 5b). For the alkali gabbro (PT-6A), 10 zircon fractions yield concordant ages, showing about 10% scatter along

the concordia curve. Using the six identically concordant fractions, an average $^{206}\text{Pb}/^{238}\text{U}$ age of 83.4 ± 0.7 Ma (95% conf., MSWD = 0.64) is defined (Fig. 5c). The four other zircons give younger ages between 74.9 and 81.3 Ma. For the micro-syenite (PT-7A), six zircon fractions give identically concordant ages and three fractions are discordant, one of them having a significantly older age at 142.1 ± 2.1 Ma (Fig. 5d). The weighted mean $^{206}\text{Pb}/^{238}\text{U}$ age of the six identically concordant ages is 80.1 ± 1.0 Ma (95% conf., MSWD = 2.0). Eight zircon fractions from the granite (PT-9A) yield concordant ages and one fraction (zircon 4) is about 5 Myr younger (Fig. 5e). The weighted mean $^{206}\text{Pb}/^{238}\text{U}$ age of the eight identical fractions is 81.7 ± 0.4 Ma (95% conf., MSWD = 0.96).

Concordia diagrams for zircon and titanite from the Sines massif are shown in Fig. 6. For one gabbro (PT-16A), five zircon fractions yield identical $^{206}\text{Pb}/^{238}\text{U}$ ages (including one fraction that is about 10% discordant; Fig. 6a) whereas one grain gives a significantly older concordant age of 131.2 ± 1.7 Ma (Table 3). The weighted mean $^{206}\text{Pb}/^{238}\text{U}$ age for the five identical fractions is 77.2 ± 0.6 Ma (95% conf., MSWD = 0.19). Nine fractions from the second gabbro (PT-17A) yield identically concordant $^{206}\text{Pb}/^{238}\text{U}$ ages (Fig. 6b), defining a weighted mean of 77.2 ± 0.4 Ma (95% conf., MSWD = 0.50). Seven zircon and five titanite fractions from the syenite (PT-19A) are mostly concordant and give a combined weighted mean $^{206}\text{Pb}/^{238}\text{U}$ age of 75.4 ± 1.2 Ma (95% conf.,

Table 2: Major and trace element concentrations of the Portuguese alkaline rocks

Massif:	Ribamar	Sintra				Sines			Monchique		
		2A	5A	6A	7A	9A	16A	17A	19A	20A	21A
SiO ₂ (wt %)	50.39	77.19	47.72	67.51	74.23	49.45	49.59	66.15	54.66	40.87	59.30
Al ₂ O ₃	16.44	12.37	17.46	15.68	13.31	15.08	17.84	16.71	21.38	11.75	17.83
FeO _T	8.29	0.92	11.25	3.31	1.95	12.01	10.45	2.81	3.00	13.54	2.93
MnO	0.19	0.00	0.18	0.08	0.04	0.17	0.18	0.10	0.10	0.19	0.14
MgO	2.55	0.06	4.00	0.89	0.23	6.18	4.51	0.59	0.66	8.51	0.73
CaO	6.14	0.19	9.99	1.78	0.69	9.09	8.59	1.49	1.72	13.88	1.85
Na ₂ O	4.12	3.54	3.47	4.52	3.74	3.38	3.63	5.37	8.27	2.43	7.37
K ₂ O	2.99	4.65	1.28	4.77	4.75	1.65	1.68	5.18	6.61	1.59	5.79
TiO ₂	1.98	0.07	2.83	0.63	0.23	3.00	2.53	0.58	0.73	4.62	0.84
P ₂ O ₅	0.63	<DL	1.27	0.16	0.05	0.59	0.64	0.12	0.11	0.53	0.17
LOI	6.84	0.63	0.69	0.71	0.91	0.15	0.97	1.05	2.24	1.10	2.01
Total	100.50	99.60	100.14	100.02	100.14	100.76	100.61	100.15	99.48	99.00	98.95
Na ₂ O + K ₂ O	7.11	8.18	4.74	9.29	8.49	5.03	5.31	10.55	14.88	4.01	13.16
V (ppm)	93.3	0.85	222	34.2	9.46	233	183	24.4	41.7	359	38.59
Co	8.69	0.24	22.5	4.49	1.45	37.7	25.4	3.61	3.40	49.71	3.14
Cr	5.87	7.14	5.33	13.1	7.53	176	56.6	6.07	13.8	190.3	5.14
Cu	5.66	<DL	12.0	4.97	<DL	49.7	32.1	3.99	4.46	61.1	<DL
Ni	4.92	3.20	6.11	7.90	4.13	75.5	37.4	4.60	6.77	58.3	<DL
Cs	1.33	4.14	1.53	8.35	4.78	1.20	1.57	2.13	4.37	0.45	1.12
Rb	77.4	213	35.4	189	172	46.7	48.3	218	215	32.1	102
Sr	1039	12.7	951	214	63.7	618	744	306	642	1166	431
Ba	766	25.3	424	606	280	430	376	629	369	870	578
Th	9.39	21.7	4.77	20.9	21.1	5.60	6.54	31.5	28.1	4.33	11.4
U	2.42	4.36	1.52	6.83	6.63	1.67	1.91	6.72	8.76	1.01	3.53
Nb	79.5	50.2	57.9	70.4	38.7	52.4	68.8	112	125	74.9	105
Pb	7.75	27.4	6.93	29.8	30.8	5.34	6.19	16.5	24.3	2.68	10.4
Zr	380	113	452	402	191	249	246	510	557	273	357
Hf	8.76	4.95	10.1	9.51	6.19	6.02	6.69	12.3	8.3	7.40	7.52
Y	33.7	17.3	35.4	25.5	32.2	26.0	49.6	31.6	11.0	29.3	24.3
La	64.8	16.9	56.8	64.3	45.9	41.6	50.2	86.1	61.9	55.2	91.3
Ce	137	35.9	123	120	94.0	87.2	118	158	90.1	122	181
Pr	16.3	4.43	15.3	12.3	10.5	10.5	15.9	15.8	7.69	15.3	20.0
Nd	63.9	15.6	63.4	41.1	37.1	42.1	70.2	51.2	22.3	61.3	68.4
Sm	12.2	3.43	12.8	7.08	7.74	8.45	15.8	8.22	3.08	11.9	10.4
Eu	3.60	0.11	3.65	1.24	0.65	2.63	4.18	1.96	0.90	3.66	2.57
Gd	9.64	2.67	10.8	5.29	6.48	7.36	14.1	6.01	2.19	9.44	6.95
Tb	1.32	0.48	1.48	0.84	1.05	1.03	2.00	0.93	0.33	1.26	0.98
Dy	6.99	3.11	7.60	4.67	5.99	5.54	10.9	5.38	1.85	6.53	5.24
Ho	1.21	0.62	1.31	0.85	1.12	0.97	1.90	1.01	0.35	1.06	0.89
Er	3.19	1.92	3.33	2.44	3.21	2.47	4.79	2.98	1.08	2.62	2.31
Tm	0.44	0.32	0.43	0.37	0.48	0.33	0.63	0.46	0.17	0.34	0.31
Yb	2.87	2.30	2.74	2.48	3.26	2.11	3.86	3.30	1.29	2.05	1.96
Lu	0.42	0.34	0.40	0.38	0.48	0.31	0.55	0.51	0.19	0.29	0.29
(La/Yb) _N	16.22	5.27	14.88	18.63	10.09	14.19	9.32	18.69	34.38	19.35	33.47
Eu/Eu*	1.02	0.12	0.95	0.62	0.28	1.02	0.86	0.85	1.05	1.06	0.92

LOI, loss on ignition; <DL, below detection limit; major and trace element analyses were carried out at the CRPG at Nancy (Govindaraju & Mevelle, 1987; Carignan *et al.*, 2001). The subscript N indicates the ratio normalized to the chondrite values (Sun & McDonough, 1989). Eu/Eu* = Eu_N/√(Sm_N × Gd_N).

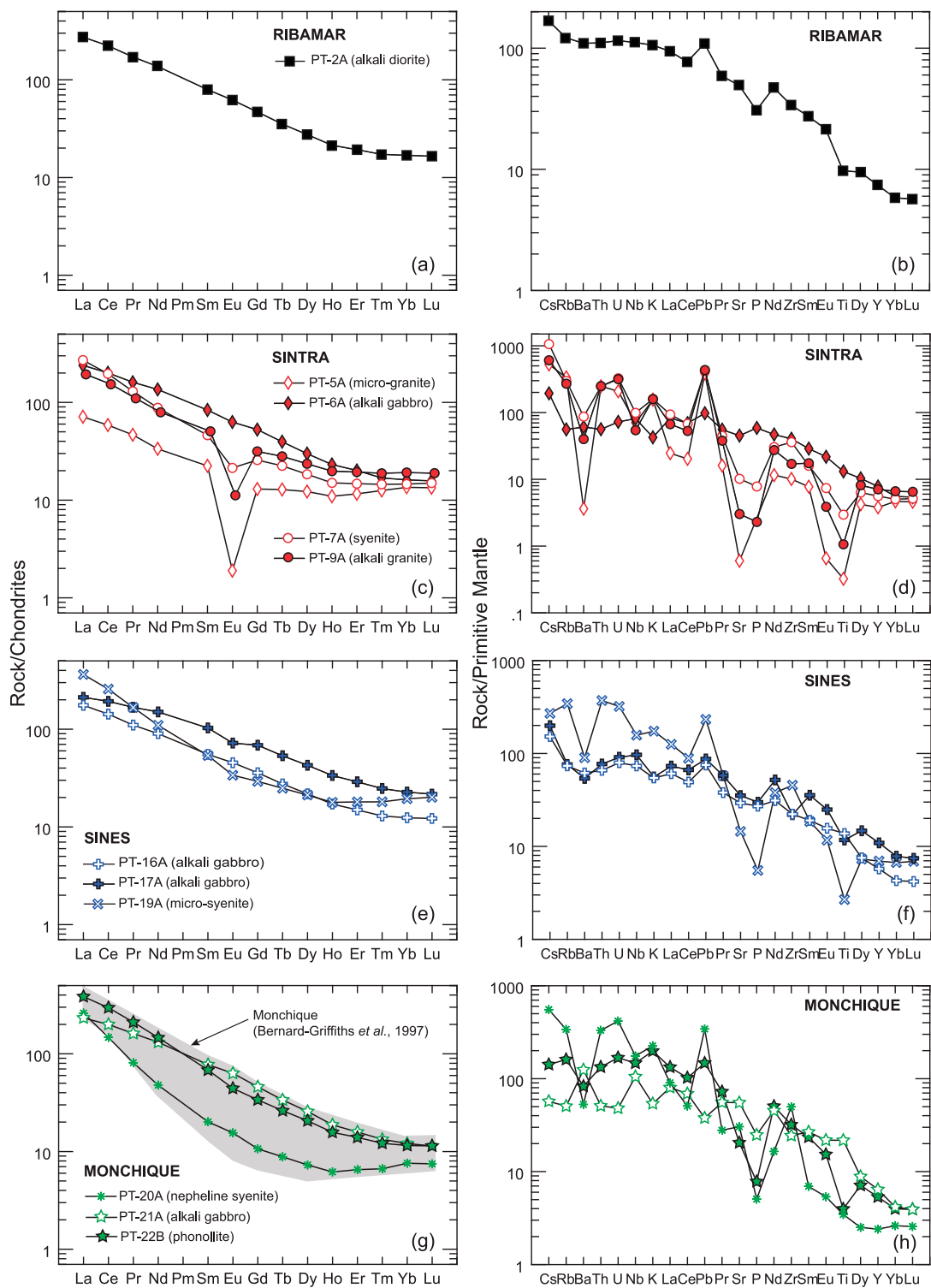


Fig. 4. REE and trace element patterns of the analyzed rocks, normalized to chondritic abundances for REE and to primitive mantle for all trace elements (Sun & McDonough, 1989).

Table 3: U-Pb analytical results for zircon and titanite from the Portuguese alkaline rocks

Location sample fraction ^a	Weight (mg)	Content		Measured ^c		Radiogenic Pb (at.%) ^d		Atomic ratios ^d		Apparent ages ^d (Ma)					
		U (ppm)	Pb ^b (pg)	$^{206}\text{Pb}/^{204}\text{Pb}$	^{206}Pb	^{207}Pb	^{208}Pb	$^{206}\text{Pb}/^{238}\text{U}$	$^{207}\text{Pb}/^{235}\text{U}$	$^{206}\text{Pb}/^{238}\text{U}$	$^{207}\text{Pb}/^{235}\text{U}$				
Ribamar															
<i>PT-2A (alkali diorite)</i>															
zircon 1 ^e	0.0935	810.0	41	1640	46.0	2.2	51.8	0.01382	0.09065	88.5 ± 1.0	88.1 ± 1.9				
zircon 2 ^e	0.0229	666.2	48	289	45.1	2.1	52.7	0.01357	0.08727	86.9 ± 1.4	85.0 ± 2.9				
zircon 3 ^e	0.0336	588.2	65	285	44.5	2.2	53.3	0.01378	0.09143	88.2 ± 1.9	88.8 ± 3.6				
zircon 4 ^e	0.0252	631.8	27	537	48.3	2.3	46.3	0.01382	0.09172	88.5 ± 1.3	89.1 ± 2.7				
zircon 5 ^e	0.0120	882.0	10	936	38.8	1.9	59.3	0.01381	0.09199	88.4 ± 1.0	89.4 ± 1.3				
zircon 6 ^e	0.0370	731.8	16	1459	43.8	2.1	54.1	0.01382	0.09137	88.5 ± 0.9	88.8 ± 1.8				
								Mean (95% conf.)		88.3 ± 0.5 Ma					
Sintra															
<i>PT-5A (micro-granite)</i>															
zircon 1	0.0453	972.3	126	305	87.7	4.1	8.2	0.01298	0.08283	83.1 ± 2.0	80.8 ± 3.2				
zircon 2	0.0427	1123	140	294	87.6	4.1	8.3	0.01277	0.08150	81.8 ± 2.2	79.6 ± 3.4				
zircon 3	0.0153	1291	64	266	84.9	4.0	11.1	0.01271	0.08202	81.4 ± 2.2	80.0 ± 3.6				
zircon 5 ^f	0.0213	4576	56	259	83.9	4.0	12.1	0.01209	0.07827	77.5 ± 2.1	76.5 ± 3.5				
zircon 6	0.0256	1803	82	474	86.7	4.1	9.2	0.01286	0.08427	82.4 ± 1.4	82.2 ± 2.3				
zircon 7	0.0209	1636	50	569	87.9	4.2	7.9	0.01282	0.08380	82.1 ± 1.4	81.7 ± 2.2				
zircon 8 ^f	0.0061	893.8	57	93	86.3	4.1	9.6	0.01239	0.08049	79.4 ± 2.6	78.4 ± 6.5				
								Mean (95% conf.)		82.0 ± 0.7 Ma					
<i>PT-6A (alkali diorite)</i>															
zircon 1	0.0622	299.7	100	182	72.3	3.5	24.2	0.01300	0.08609	83.3 ± 1.6	83.9 ± 3.4				
zircon 2 ^f	0.0311	401.8	87	132	79.2	3.6	17.2	0.01257	0.07766	80.5 ± 1.9	75.9 ± 4.5				
zircon 3 ^f	0.0201	453.1	58	136	77.3	3.8	18.9	0.01169	0.07931	74.9 ± 1.8	77.5 ± 4.5				
zircon 4	0.0255	174.9	31	140	75.3	3.7	21.0	0.01327	0.08899	85.0 ± 2.0	86.6 ± 4.6				
zircon 5 ^f	0.0559	468.6	74	307	70.4	3.2	26.4	0.01270	0.07847	81.3 ± 1.8	76.7 ± 3.3				
zircon 7	0.0711	368.0	27	805	72.4	3.5	24.1	0.01295	0.08665	83.0 ± 1.2	84.4 ± 1.7				
zircon 8 ^f	0.0848	438.8	161	198	75.1	3.4	21.4	0.01222	0.07695	78.3 ± 1.8	75.3 ± 3.4				
zircon 9	0.0630	366.1	56	357	72.3	3.4	24.3	0.01303	0.08350	83.4 ± 2.1	81.4 ± 2.6				
zircon 10	0.0644	444.3	59	417	70.4	3.3	26.3	0.01298	0.08352	83.1 ± 2.0	81.5 ± 2.5				
zircon 11	0.0820	391.9	61	454	70.8	3.4	25.8	0.01298	0.08426	83.1 ± 1.9	82.1 ± 2.6				
								Mean (95% conf.)		83.4 ± 0.7 Ma					
<i>PT-7A (micro-syenite)</i>															
zircon 1	0.0201	270.2	88	67	79.3	4.4	16.3	0.01231	0.09331	78.9 ± 2.4	90.6 ± 8.0				
zircon 4	0.0287	132.8	19	176	82.1	3.9	14.0	0.01274	0.08313	81.6 ± 1.9	81.1 ± 5.0				
zircon 5	0.0256	340.7	29	261	95.4	4.4	0.2	0.01274	0.08034	81.6 ± 1.4	78.5 ± 3.2				
zircon 6	0.0408	267.5	56	171	91.8	4.4	3.8	0.01244	0.08243	79.7 ± 1.3	80.4 ± 3.2				
zircon 7 ^f	0.0867	295.3	83	456	85.4	4.6	10.0	0.02229	0.16523	142.1 ± 2.0	155.3 ± 3.4				
zircon 8	0.0347	323.0	16	578	89.0	4.3	6.7	0.01244	0.08256	79.7 ± 1.1	80.5 ± 1.7				
zircon 9	0.0424	394.2	22	612	85.3	4.1	10.6	0.01241	0.08191	79.5 ± 1.2	79.9 ± 1.7				
								Mean (95% conf.)		80.1 ± 1.0 Ma					
<i>PT-9A (granite)</i>															
zircon 1	0.0985	581.0	155	320	83.7	4.0	12.3	0.01286	0.08400	82.4 ± 1.3	81.9 ± 2.6				
zircon 3	0.0941	708.7	66	827	85.7	4.1	10.2	0.01266	0.08288	81.1 ± 1.2	80.8 ± 2.1				
zircon 4 ^f	0.0802	443.7	54	528	85.2	4.2	10.6	0.01200	0.08102	76.9 ± 1.3	79.1 ± 2.1				
zircon 5	0.0671	444.1	32	762	85.5	4.0	10.4	0.01268	0.08232	81.3 ± 1.2	80.3 ± 2.0				
zircon 6	0.0883	505.9	228	174	83.8	3.9	12.3	0.01256	0.08051	80.4 ± 1.9	78.6 ± 3.2				
zircon 7	0.0770	589.1	148	270	85.0	4.1	10.9	0.01290	0.08477	82.7 ± 1.5	82.6 ± 3.2				

(continued)

Table 3: *Continued*

Location sample fraction ^a	Weight (mg)	Content		Measured ^c		Radiogenic Pb (at.%) ^d		Atomic ratios ^d		Apparent ages ^d (Ma)					
		U (ppm)	Pb ^b (pg)	²⁰⁶ Pb/ ²⁰⁴ Pb	²⁰⁶ Pb	²⁰⁷ Pb	²⁰⁸ Pb	²⁰⁶ Pb/ ²³⁸ U	²⁰⁷ Pb/ ²³⁵ U	²⁰⁶ Pb/ ²³⁸ U	²⁰⁷ Pb/ ²³⁵ U				
zircon 8	0.0504	768.6	97	342	86.0	4.1	9.9	0.01277	0.08336	81.8 ± 1.3	81.3 ± 2.3				
zircon 9	0.0643	473.2	64	399	89.4	4.3	6.3	0.01274	0.08433	81.6 ± 1.2	82.2 ± 2.5				
zircon 10	0.0642	774.5	33	1246	86.1	4.2	9.8	0.01280	0.08470	82.0 ± 0.9	82.6 ± 1.6				
								Mean (95% conf.)		81.7 ± 0.4 Ma					
Sines															
<i>PT-16A (alkali gabbro)</i>															
zircon 2 ^f	0.0255	205.5	22	313	76.6	3.7	19.7	0.02057	0.13646	131.2 ± 1.7	129.9 ± 2.6				
zircon 3	0.0244	666.3	20	642	76.0	3.7	20.3	0.01207	0.08041	77.3 ± 1.4	78.5 ± 2.2				
zircon 4	0.0285	673.2	53	301	78.3	4.2	17.5	0.01204	0.08895	77.1 ± 1.8	86.5 ± 3.5				
zircon 7	0.0275	396.5	27	321	84.4	4.1	11.5	0.01201	0.07967	77.0 ± 1.5	77.8 ± 2.5				
zircon 8	0.0369	640.7	32	576	81.0	3.9	15.1	0.01198	0.07914	76.8 ± 1.3	77.3 ± 2.3				
zircon 9	0.0628	410.9	27	750	78.5	3.8	17.7	0.01210	0.07934	77.5 ± 1.1	77.5 ± 1.7				
								Mean (95% conf.)		77.2 ± 0.6 Ma					
<i>PT-17A (alkali gabbro)</i>															
zircon 1	0.0930	278.6	258	95	80.9	4.0	15.2	0.01208	0.08118	77.4 ± 2.7	79.2 ± 6.9				
zircon 2	0.0154	197.1	60	57	79.5	4.2	16.3	0.01207	0.08423	77.4 ± 3.2	82.1 ± 9.5				
zircon 3	0.0831	240.7	37	430	83.0	4.0	13.0	0.01219	0.07962	78.1 ± 1.5	77.8 ± 2.3				
zircon 4	0.0971	287.6	16	1359	78.7	3.8	17.5	0.01200	0.07849	76.9 ± 0.9	76.7 ± 1.6				
zircon 5	0.0948	230.1	25	677	80.9	3.7	15.4	0.01211	0.07592	77.6 ± 1.7	74.3 ± 2.2				
zircon 7	0.0818	282.4	20	883	81.4	3.8	14.8	0.01196	0.07598	76.7 ± 1.0	74.4 ± 1.7				
zircon 8	0.1008	370.0	25	1156	77.4	3.7	18.9	0.01210	0.07934	77.5 ± 1.0	77.5 ± 1.6				
zircon 9	0.0738	301.6	13	1305	81.2	3.9	14.9	0.01209	0.07950	77.4 ± 0.9	77.7 ± 1.6				
zircon 10	0.0847	333.3	13	1722	80.2	3.8	16.0	0.01202	0.07828	77.0 ± 0.8	76.5 ± 1.5				
								Mean (95% conf.)		77.2 ± 0.4 Ma					
<i>PT-19A (micro-syenite)</i>															
titanite 1	0.2991	187.5	364	131	59.3	3.7	37.0	0.01153	0.09973	73.9 ± 1.8	96.5 ± 4.2				
titanite 2	0.1728	222.6	383	94	63.1	2.9	34.0	0.01190	0.07495	76.3 ± 1.7	73.4 ± 4.7				
titanite 4	0.2552	207.0	623	82	63.4	2.9	33.6	0.01162	0.07412	74.5 ± 2.1	72.6 ± 5.0				
titanite 5	0.3555	197.1	1602	50	58.8	2.7	38.5	0.01122	0.07184	71.9 ± 2.3	70.4 ± 9.0				
titanite 6	0.2922	215.9	940	67	61.0	2.8	36.2	0.01116	0.07071	71.5 ± 2.3	69.4 ± 8.8				
								Titanite mean (95% conf.)		74.0 ± 2.4					
zircon 1	0.0966	117.7	479	37	85.7	4.4	9.9	0.01195	0.08455	76.6 ± 2.0	82.4 ± 16.0				
zircon 2	0.0221	138.2	20	130	73.8	3.8	22.4	0.01184	0.08244	75.9 ± 2.0	80.6 ± 4.5				
zircon 5	0.0245	199.4	23	178	73.9	4.2	21.8	0.01214	0.09429	77.8 ± 1.6	91.5 ± 3.9				
zircon 7	0.0977	168.9	77	178	77.1	3.7	19.2	0.01182	0.07872	75.8 ± 1.8	76.9 ± 3.7				
zircon 8	0.0894	130.8	133	83	79.8	4.1	16.1	0.01149	0.08087	73.6 ± 2.1	79.0 ± 6.6				
zircon 9	0.0583	119.2	60	104	75.8	3.6	20.5	0.01156	0.07383	74.1 ± 1.8	72.3 ± 2.7				
zircon 11	0.0850	114.8	13	591	84.7	4.1	11.2	0.01195	0.07932	76.6 ± 1.1	77.5 ± 1.6				
								Zircon mean (95% conf.)		76.1 ± 1.3					
								Mean (95% conf.)		75.4 ± 1.2 Ma					
Monchique															
<i>PT-20A (nepheline syenite)</i>															
titanite 1	0.3496	30.22	546	33	35.0	2.4	62.6	0.01098	0.10352	70.4 ± 1.8	100.0 ± 19.6				
titanite 2	0.2675	28.52	423	32	36.5	2.4	61.1	0.01066	0.09578	68.4 ± 2.1	92.9 ± 19.7				
titanite 4	0.3327	30.27	582	31	35.0	2.3	62.7	0.01065	0.09495	68.3 ± 2.3	92.1 ± 19.0				
titanite 7	0.2920	28.94	537	31	34.4	3.0	62.6	0.01136	0.13673	72.8 ± 2.0	130.1 ± 25.9				
titanite 8	0.2632	27.73	545	30	37.7	1.8	60.5	0.01056	0.06871	67.7 ± 2.4	67.5 ± 14.4				
titanite 9	0.3210	29.48	494	33	35.8	2.0	62.2	0.01060	0.08032	68.0 ± 1.7	78.4 ± 14.8				

(continued)

Table 3: Continued

Location sample fraction ^a	Weight (mg)	Content		Measured ^c			Radiogenic Pb (at.%) ^d		Atomic ratios ^d		Apparent ages ^d (Ma)	
		U (ppm)	Pb ^b (pg)	206Pb/204Pb	206Pb	207Pb	208Pb	206Pb/238U	207Pb/235U	206Pb/238U	207Pb/235U	
titanite 10	0.1937	28.43	292	31	37.1	1.4	61.6	0.01043	0.05286	66.9±2.1	—	
titanite 11	0.3298	29.08	564	31	33.3	2.0	64.7	0.01050	0.08674	67.3±2.1	84.5±17.9	
titanite 13	0.2316	27.52	492	28	40.8	1.6	57.6	0.01061	0.05654	68.0±2.2	—	
titanite 14	0.3593	27.40	678	29	35.5	1.2	63.4	0.01086	0.04928	69.6±2.1	—	
titanite 17	0.2856	29.53	813	26	35.1	2.1	62.8	0.01058	0.08838	67.8±1.9	86.0±18.3	
titanite 18	0.3240	27.20	470	32	36.8	1.9	61.2	0.01087	0.07884	69.7±1.7	77.1±14.3	
Mean (95% conf.)											68.8±1.0 Ma	
<i>PT-21A (alkali gabbro)</i>												
titanite 1	0.3193	11.58	225	30	30.2	2.1	67.7	0.01047	0.09944	67.1±2.8	96.3±18.0	
titanite 2	0.2995	16.66	188	37	32.4	1.8	65.8	0.01077	0.08293	69.0±2.5	80.9±15.1	
titanite 3	0.2796	14.55	297	28	34.7	2.3	63.0	0.01034	0.09356	66.3±2.5	90.8±19.5	
titanite 4	0.2650	13.97	105	44	35.7	1.9	62.4	0.01144	0.08133	73.3±2.3	79.4±10.0	
titanite 5	0.2168	11.35	71	43	30.6	1.8	67.5	0.01121	0.09101	71.9±2.5	88.4±10.3	
titanite 6	0.2453	12.65	89	43	35.4	2.1	62.6	0.01105	0.08821	70.8±2.3	85.8±10.4	
Mean (95% conf.)											70.0±2.9 Ma	

^aAnalyses were performed on crack-free and euhedral zircons and titanites.

^bTotal amount of blank + initial Pb.

^cRatios corrected for mass-discrimination and isotope tracer contribution.

^dRatios corrected for mass-discrimination, isotope tracer contribution, blank, and initial common Pb determined in feldspars of the same rock (Table 4). Single errors are given at 2σ level. The mean age is the weighted mean average of the entire set of fractions, excluding some indexed †, given at 95% confidence level.

^eNot abraded fractions.

^fFractions not used for age calculation (see text for further details).

(For further details, see 'Analytical procedures'.)

MSWD = 4.2). The average $^{206}\text{Pb}/^{238}\text{U}$ age of the titanite is 74.0 ± 2.4 Ma (95% conf., MSWD = 3.9) and that of zircon is 76.1 ± 1.3 Ma (95% conf., MSWD = 2.7), suggesting that the time of crystallization for both minerals is the same within error (Fig. 6c). Nevertheless, we consider the age derived from the zircon analyses to date the formation of the rock, as there is more consistency in the zircon data from this rock. The entire range of calculated ages is between 71.5 ± 2.3 Ma (titanite 6) and 77.8 ± 1.6 Ma (zircon 5).

For the nepheline syenite from the Monchique complex (PT-20A), the 12 titanite fractions have identical $^{206}\text{Pb}/^{238}\text{U}$ ages, whereas they show scatter in $^{207}\text{Pb}/^{235}\text{U}$, reaching up to 20% discordance (Fig. 7a and b). The weighted mean $^{206}\text{Pb}/^{238}\text{U}$ age is 68.8 ± 1.0 Ma (95% conf., MSWD = 2.7). The six titanite fractions from the alkali gabbro (PT-21A) are slightly discordant, plotting to the right of the concordia curve and giving a weighted mean $^{206}\text{Pb}/^{238}\text{U}$ age of 70.0 ± 2.9 Ma (95% conf., MSWD = 4.9).

Pb, Sr and Hf isotope data

Isotopic compositions of Pb and Sr are presented in Tables 4 and 5. Initial Pb isotope ratios (Pb_i) of the rocks

are $18.522\text{--}19.299$ for $(^{206}\text{Pb})/^{204}\text{Pb}_i$, $15.555\text{--}16.007$ for $(^{207}\text{Pb})/^{204}\text{Pb}_i$ and $38.480\text{--}39.330$ for $(^{208}\text{Pb})/^{204}\text{Pb}_i$. Initial $^{87}\text{Sr}/^{86}\text{Sr}$ (Sr_i) of the feldspars lie between 0.70274 and 0.70481. Initial Hf isotope ratios of 18 zircon fractions yield ϵHf_i ranging between +3.7 and +9.6 (Table 6). Correlation diagrams between these initial isotope signatures are given in Figs 8 and 9.

In the Sintra massif, the most primitive rock (the alkali gabbro PT-6A) exhibits the highest $(^{207}\text{Pb})/^{204}\text{Pb}_i$ ratio (Fig. 8a), whereas the most differentiated rocks have much lower ratios, with compositions similar to mid-ocean ridge basalt (MORB) for syenite (PT-7A). This trend is less obvious for $(^{87}\text{Sr})/^{86}\text{Sr}_i$ but still valid (Fig. 8b), with three samples having similar elevated ratios whereas the most differentiated rock (micro-granite PT-5A) has a $(^{87}\text{Sr})/^{86}\text{Sr}_i$ in the field of the MORB. The same trend is observed in the rocks from the Sines and Monchique massifs: the most primitive rocks (PT-16A, -17A and -21A) have the highest $(^{87}\text{Sr})/^{86}\text{Sr}_i$, whereas the most differentiated rocks have low ratios down to the MORB field, with the Monchique rocks plotting in the lowest part of the MORB field. However, the Sines rocks all have similar $(^{207}\text{Pb})/^{204}\text{Pb}_i$ signatures.

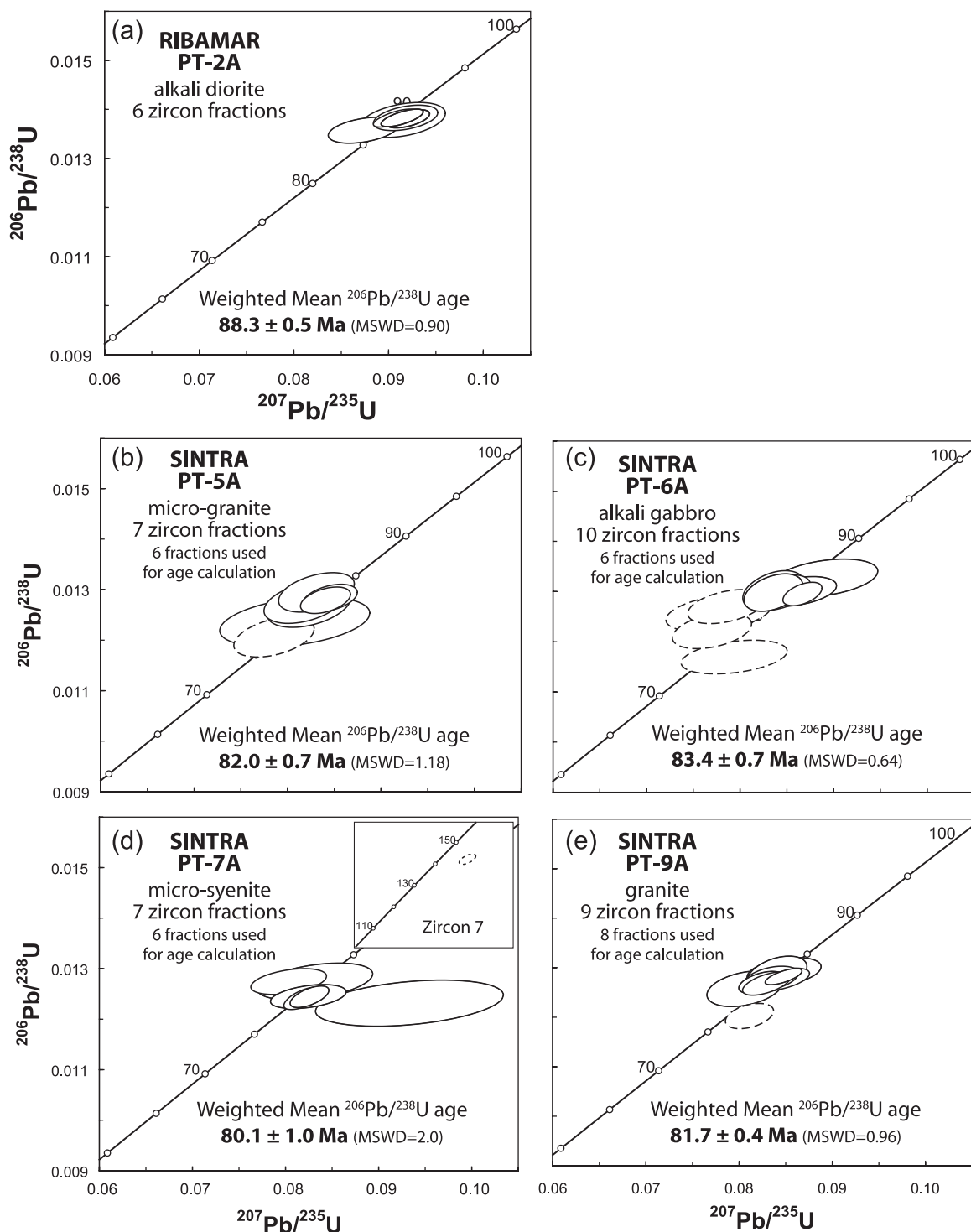


Fig. 5. Concordia diagrams showing U-Pb analytical data for zircons from the Ribamar alkali diorite (a) and for the Sintra massif: (b) micro-granite, (c) alkali gabbro, (d) syenite and (e) granite. Ellipses correspond to analytical uncertainties. Dashed ellipses correspond to analyses not taken into account for the age calculation (see text for further details).

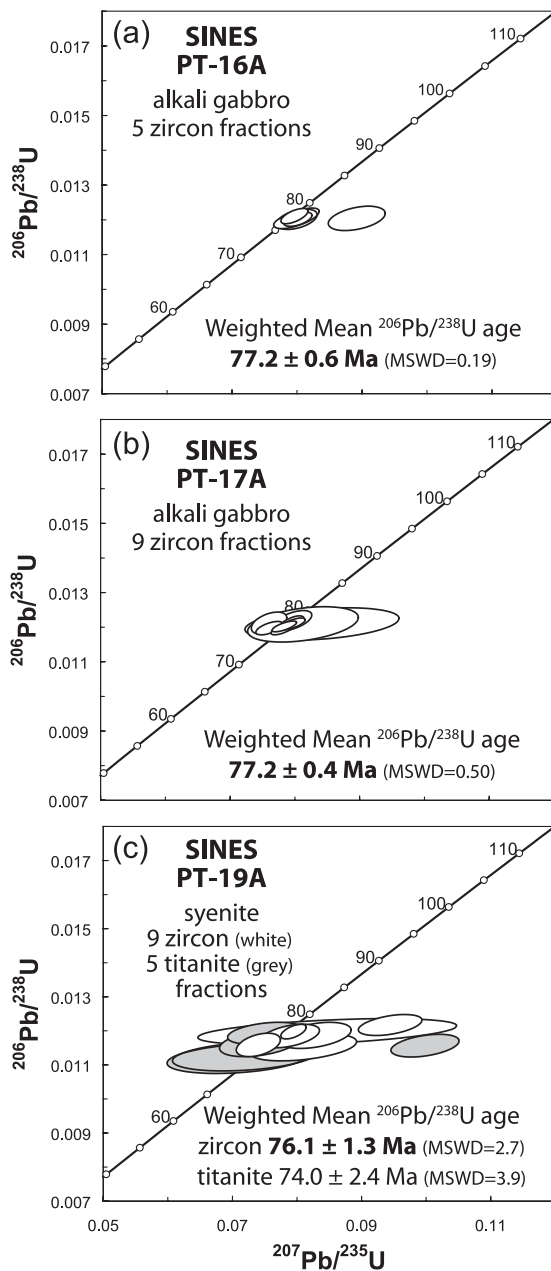


Fig. 6. Concordia diagrams showing U–Pb analytical data for zircons and titanites from: (a, b) two alkali gabbros and (c) the syenite of the Sines massif. Ellipses correspond to analytical uncertainties. Grey shaded ellipses correspond to analyses on titanites.

In addition to the intra-massif isotopic variation, there are also important variations in Pb_i and Sr_i between massifs (inter-massifs). From Sintra to Sines and then to Monchique, the rocks have progressively lower $(^{207}\text{Pb}/^{204}\text{Pb})_i$ and $(^{87}\text{Sr}/^{86}\text{Sr})_i$ and higher $(^{206}\text{Pb}/^{204}\text{Pb})_i$. The Monchique rocks exhibit both the highest

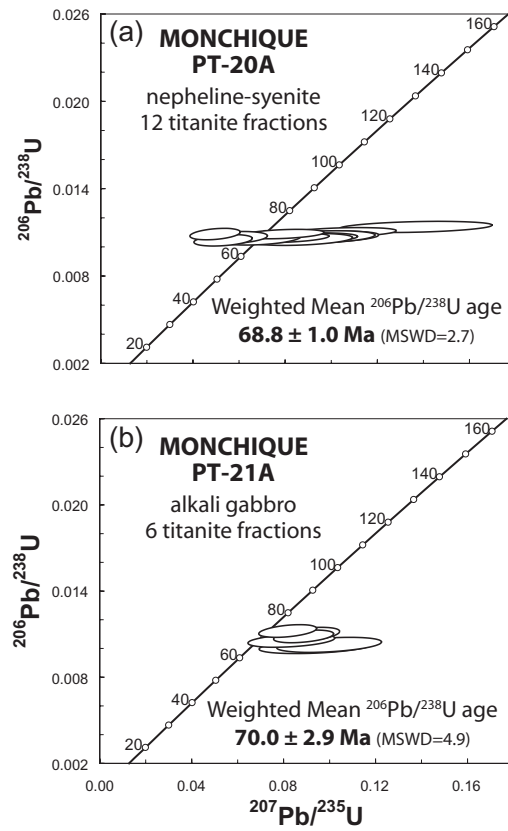


Fig. 7. Concordia diagrams showing U–Pb analytical data for titanites from (a) the nepheline syenite and (b) the alkali gabbro of the Monchique massif. Ellipses correspond to analytical uncertainties.

$(^{206}\text{Pb}/^{204}\text{Pb})_i$ (PT-20A at ~ 19.30) and the lowest $(^{207}\text{Pb}/^{204}\text{Pb})_i$ and $(^{87}\text{Sr}/^{86}\text{Sr})_i$ values (respectively PT-21A at 15.55 and PT-22B at 0.70274). They plot within the North Atlantic MORB field, similar to previous data obtained from Monchique rocks (Bernard-Griffiths *et al.*, 1997) and from the Tore seamounts (NW Tore, Merle *et al.*, 2006). Following this general trend of isotopic variation, the Sines rocks have less radiogenic $(^{206}\text{Pb}/^{204}\text{Pb})_i$ and more radiogenic $(^{207}\text{Pb}/^{204}\text{Pb})_i$ and $(^{87}\text{Sr}/^{86}\text{Sr})_i$ compared with the Monchique rocks. They are similar to the North Atlantic MORB field in $(^{207}\text{Pb}/^{204}\text{Pb})_i$ (Fig. 8). The isotopic compositions of the Ribamar sample (PT-2A) plot between the Sines and Sintra samples. The Sintra rocks have the highest $(^{207}\text{Pb}/^{204}\text{Pb})_i$ and $(^{87}\text{Sr}/^{86}\text{Sr})_i$ and the lowest $(^{206}\text{Pb}/^{204}\text{Pb})_i$. Figure 8 also shows the field of Cabo Ortegal ultramafic rocks (Santos *et al.*, 2002), recalculated at 80 Ma, as a proxy for the Iberian SCLM, and data from Jurassic alkaline rocks, emplaced during the Atlantic Ocean pre-rift period and interpreted to originate

Table 4: Initial Pb isotope ratios of feldspars from the Portuguese alkaline rocks

Location sample	Weight (mg)	Concentration ^a		μ ^b	Initial isotope ratios ^c			Source ^d signatures		
		U (ppm)	Pb (ppm)		$(^{206}\text{Pb}/^{204}\text{Pb})_i$	$(^{207}\text{Pb}/^{204}\text{Pb})_i$	$(^{208}\text{Pb}/^{204}\text{Pb})_i$	μ	ω	κ
<i>Ribamar</i>										
PT-2A	10.5	0.068	6.47	0.675	18.861 ± 0.010	15.639 ± 0.007	38.920 ± 0.019	9.41	38.0	4.03
<i>Sintra</i>										
PT-5A	9.88	0.156	22.8	0.436	18.522 ± 0.092	15.818 ± 0.045	38.669 ± 0.121	9.07	36.9	4.07
PT-6A	10.9	0.050	4.18	0.778	19.237 ± 0.087	16.007 ± 0.053	39.330 ± 0.125	9.78	39.6	4.05
PT-7A	16.7	0.968	7.93	7.858	18.906 ± 0.008	15.628 ± 0.005	38.629 ± 0.013	9.45	36.7	3.89
PT-9A	9.98	0.034	23.4	0.093	18.664 ± 0.008	15.668 ± 0.004	38.480 ± 0.008	9.21	36.2	3.93
<i>Sines</i>										
PT-16A	12.6	0.450	5.12	5.661	18.953 ± 0.018	15.628 ± 0.010	38.849 ± 0.019	9.49	37.6	3.96
PT-17A	10.7	0.023	2.83	0.510	18.801 ± 0.014	15.627 ± 0.013	38.653 ± 0.030	9.34	36.8	3.94
PT-19A	7.30	0.100	7.60	0.845	19.052 ± 0.008	15.623 ± 0.007	38.768 ± 0.015	9.58	37.3	3.89
<i>Monchique</i>										
PT-20A	10.9	0.018	7.37	0.155	19.299 ± 0.016	15.589 ± 0.014	39.153 ± 0.034	9.82	38.8	3.95
PT-21A	6.84	0.005	3.73	0.089	19.237 ± 0.014	15.555 ± 0.014	38.918 ± 0.025	9.76	37.8	3.88
PT-22B*	9.93	0.056	4.25	0.856	19.113 ± 0.014	15.660 ± 0.012	38.857 ± 0.027	9.64	37.6	3.90

^aCorrected for mass-discrimination, blank and isotope tracer contribution.

^b $\mu = ^{238}\text{U}/^{204}\text{Pb}$, used for correction of *in situ* decay of U.

^cRatios corrected for mass-discrimination, blank, isotope tracer contribution, and *in situ* decay of U using the U-Pb ages (Table 3); $(^{208}\text{Pb}/^{204}\text{Pb})_i$ is corrected for *in situ* decay of ^{232}Th estimated from μ and from $^{208}\text{Pb}/^{206}\text{Pb}$ measured in feldspars.

^d $\mu = (^{238}\text{U}/^{204}\text{Pb})$, $\omega = (^{232}\text{Th}/^{204}\text{Pb})$, $\kappa = (^{232}\text{Th}/^{238}\text{U})$ were calculated using the single-stage evolution model of the Earth mantle (Holmes, 1946) with an age of 4.56 Ga (Allègre *et al.*, 1995). Primordial Pb isotopic compositions are taken from Tatsumoto *et al.* (1973).

*Not dated, age taken from PT-20A.

(For further details see 'Analytical procedures').

from the metasomatized SCLM (Grange *et al.*, 2008). The new data from this study are similar in $(^{206}\text{Pb}/^{204}\text{Pb})_i$ to the Cabo Ortegal field, but some rocks from the Sintra massif are substantially higher in $(^{207}\text{Pb}/^{204}\text{Pb})_i$, similar to the trend defined by the Jurassic rocks (JRS, Fig. 8); whereas all the massifs contain some rocks lower in $(^{87}\text{Sr}/^{86}\text{Sr})_i$ than the Cabo Ortegal field.

Hafnium isotopic data, correlated with age of emplacement and Pb_i , are shown in Fig. 9, using the epsilon (ϵ) notation relative to chondritic uniform reservoir (CHUR), calculated for the time of crystallization of the rocks (ϵHf_i). Figure 9a also shows the evolution of the Depleted Mantle (DM) through time, which represents the evolution of the depleted asthenospheric mantle. The Hf isotope data were acquired on the zircon fractions used for U-Pb geochronology, although the samples from the Monchique massif did not contain any zircons and therefore no Hf data are available for these rocks. All the ϵHf_i values are positive (Fig. 9), ranging between +3.7 and +9.6, and plot between the CHUR and the DM evolution lines. These

data indicate that the magma source(s) is (are) more enriched than the asthenosphere. The ϵHf_i signatures increase progressively from the Ribamar intrusion to the Sines massif (i.e. from north to south). The variations in ϵHf_i vs $(^{206}\text{Pb}/^{204}\text{Pb})_i$, $(^{207}\text{Pb}/^{204}\text{Pb})_i$ and $(^{208}\text{Pb}/^{204}\text{Pb})_i$ (Fig. 9b-d) show that the studied samples have significantly lower ϵHf_i than the fields of Atlantic MORB and the Tore Madeira Rise rocks. Our data plot in the field of worldwide ocean island basalt (OIB) and they show the same initial Hf signatures as the Mbui-Mayi kimberlites from Zaire (Weis & Demaiffe, 1985; Schärer *et al.* 1997). As there are very few data with combined Pb and Hf isotopic analyses for rocks representing the SCLM (such as mantle xenoliths), this kimberlite field is taken as a proxy for the composition of the SCLM. An important characteristic of the Hf data is the large variation within the same sample of up to 4 epsilon units for Sintra sample PT-9A. These variations are well outside the single analytical uncertainties and are therefore considered to be significant.

Table 5: Rb–Sr compositions of feldspars from the Portuguese alkaline rocks

Location sample	Weight (mg)	Concentrations		$^{87}\text{Rb}/^{86}\text{Sr}$	Age (Ma) $^{206}\text{Pb}/^{238}\text{U}$	Isotope ratios ^a	
		Sr (ppm)	Rb(ppm)			$(^{87}\text{Sr}/^{86}\text{Sr})_{\text{norm}}$	$(^{87}\text{Sr}/^{86}\text{Sr})_i$
<i>Ribamar</i>							
PT-2A	10.5	435	35	0.235	88.3	0.70433 ± 3	0.70404
<i>Sintra</i>							
PT-5A	9.88	13.7	79	16.77	82.0	0.72286 ± 11	0.70329
PT-6A	10.9	724	2.4	0.010	83.4	0.70455 ± 4	0.70454
PT-7A	11.0	204	14	0.194	80.1	0.70479 ± 10	0.70457
PT-9A	10.0	42.6	77	5.275	81.7	0.71094 ± 7	0.70481
<i>Sines</i>							
PT-16A	12.6	595	12	0.060	77.2	0.70378 ± 3	0.70371
PT-17A	10.7	727	1.5	0.006	77.2	0.70392 ± 9	0.70391
PT-19A	7.30	348	28	0.236	76.1	0.70364 ± 7	0.70339
<i>Monchique</i>							
PT-20A	10.9	500	101	0.592	68.8	0.70391 ± 6	0.70333
PT-21A	6.84	1350	14	0.031	70.0	0.70359 ± 10	0.70356
PT-22B*	9.93	44.2	69	4.580	68.8	0.70722 ± 8	0.70274

^aRatios corrected for isotope tracer contribution and for *in situ* decay of Rb using the U–Pb ages (Table 3).

*Not dated, age taken from PT-20A.

(For further details see 'Analytical procedures'.)

DISCUSSION

Geochronological data

The U–Pb ages of the magmatic zircon and titanite can be considered to date the crystallization of these minerals from the magmas (e.g. Krogh, 1973; Zhang & Schärer, 1996). Our new ages significantly refine the intrusion ages along the western coast of Portugal; they are in the same range as those obtained by Miranda *et al.* (2009), but are more precise. The 10 new ages clearly substantiate alkaline magma emplacement between 88.2 ± 0.5 and 68.9 ± 1.1 Ma, covering a period of about 20 Myr in the Late Cretaceous, during Coniacian–Maastrichtian times (Gradstein *et al.*, 2004).

Some zircon fractions yield slightly different ages compared with the bulk zircon fractions used for the mean age calculation of the rock (e.g. PT-5A, PT-6A, PT-7A, PT-9A, PT-16A and PT-19A). The reason for these differences is not clear; however, the presence of a small amount of inherited radiogenic Pb in zircon could account for the older ages given by some zircons (PT-7A and PT-16A). Another explanation could be a slight difference between the initial Pb isotope composition of the zircon (and titanite) and the feldspar. As the zircon (and titanite) ages have been corrected with the initial Pb measured in

the feldspar, a difference could result in minor discordance. This interpretation is the most likely explanation for the $^{207}\text{Pb}/^{235}\text{U}$ discordance in titanite from sample PT-21A. Lastly, a recent loss of Pb from some of the grains could lead to a younger fraction of zircons (e.g. PT-5A, PT-6A and PT-9A).

Our new U–Pb ages for the alkaline massifs define a clear north–south age trend (Fig. 10a), from the Ribamar intrusion at ~ 88 Ma to the Monchique complex emplaced around 69 Ma. The four massifs therefore constitute a distinct 200 km NNW–SSE alignment of alkaline rocks parallel to the Portuguese coast.

Alkaline magmatism of similar age and chemical composition is also present in the oceanic domain, westward of this alignment (Fig. 1). Within the Mount Ormonde massif (constituting the eastern part of the Gorriong Bank), some alkaline rocks intrude SCLM peridotites and have been dated at 65 – 62 Ma (^{40}Ar – ^{39}Ar on amphiboles from diorites, Féraud *et al.*, 1982, 1986; see discussion by Merle *et al.*, 2009). Widespread occurrences of alkaline magmatic rocks have also been documented along the TMR, ranging in age from ~ 103 Ma to Pleistocene (Geldmacher *et al.*, 2006; Merle *et al.*, 2006, 2009). In particular, the trachytic magmatic rocks of the Tore sea-mounts, located about 500 km WNW of the Ribamar

Table 6: Initial Hf isotopic composition of zircons from the Portuguese alkaline rocks

Location sample fraction	$(^{176}\text{Hf}/^{177}\text{Hf})_{\text{norm}}^{\text{a}}$	$(^{206}\text{Pb}/^{238}\text{U})$ age (Ma)	$\varepsilon\text{Hf}_i^{\text{b}}$
Ribamar			
<i>PT-2A</i>			
zircon 2	0.282837 ± 3	88.3	4.1 ± 0.1
zircon 3	0.282885 ± 10	88.3	5.8 ± 0.4
Sintra			
<i>PT-5A</i>			
zircon 8	0.282859 ± 4	82.0	4.9 ± 0.1
zircon 9	0.282880 ± 3	82.0	5.6 ± 0.1
<i>PT-6A</i>			
zircon 1	0.282921 ± 7	83.4	7.1 ± 0.3
zircon 11	0.282940 ± 4	83.4	7.8 ± 0.1
<i>PT-7A</i>			
zircon 1	0.282910 ± 7	80.1	6.7 ± 0.2
zircon 2	0.282899 ± 10	80.1	6.3 ± 0.4
<i>PT-9A</i>			
zircon 1	0.282941 ± 4	81.7	7.8 ± 0.2
zircon 2	0.282823 ± 5	81.7	3.6 ± 0.2
zircon 10	0.282874 ± 3	81.7	5.4 ± 0.1
Sines			
<i>PT-16A</i>			
zircon 1	0.282922 ± 8	77.2	7.1 ± 0.3
zircon 9	0.282941 ± 5	77.2	7.8 ± 0.2
<i>PT-17A</i>			
zircon 1	0.282966 ± 5	77.2	8.7 ± 0.2
zircon 2	0.282918 ± 7	77.2	7.0 ± 0.2
zircon 10	0.282974 ± 5	77.2	9.0 ± 0.2
<i>PT-19A</i>			
zircon 1	0.282994 ± 9	76.1	9.7 ± 0.3
zircon 12	0.282982 ± 6	76.1	9.3 ± 0.2

^aUncertainties for $(^{176}\text{Hf}/^{177}\text{Hf})_{\text{norm}}$ are given relative to the last digits.

^bTo calculate εHf_i from $(^{176}\text{Hf}/^{177}\text{Hf})_{\text{norm}}$ the following constants were used: age of the Earth = 4.56 Ga; present-day $(^{176}\text{Lu}/^{177}\text{Hf})_{\text{CHUR}}^0 = 0.0332 \pm 2$; present-day $(^{176}\text{Hf}/^{177}\text{Hf})_{\text{CHUR}}^0 = 0.282772 \pm 29$ (Blichert-Toft & Albarède, 1997); $(\varepsilon\text{Hf})_{\text{sample}}^T = [(^{176}\text{Hf}/^{177}\text{Hf})_{\text{sample}}^T / (^{176}\text{Hf}/^{177}\text{Hf})_{\text{CHUR}}^T - 1] \times 10^4$, with $(^{176}\text{Hf}/^{177}\text{Hf})_{\text{CHUR}}^T = (^{176}\text{Hf}/^{177}\text{Hf})_{\text{CHUR}}^0 - (^{176}\text{Lu}/^{177}\text{Hf})_{\text{CHUR}}^0 \times (e^{\lambda_T} - 1)$ (Patchett *et al.*, 1981); $\lambda_{\text{Lu}} = 1.867 \times 10^{-11} \text{ a}^{-1}$ (Söderlund *et al.*, 2004), with T being the U-Pb age of the zircon. (For further details see 'Analytical procedures').

intrusion (Fig. 1), have been dated by the U-Pb method at 88.3 ± 3.8 Ma (Merle *et al.*, 2006), which is similar to our oldest age obtained from the Ribamar intrusion. Our new ages suggest that the period of magmatic activity on the

western coast of Portugal overlaps with that of the northern part of the TMR. The combined geochronological data from the alkaline magmatic rocks of the TMR, the Ormonde seamount and our new U-Pb ages from the alkaline massifs in western Portugal bracket the timing of an important alkaline magmatic event in the eastern part of the North Atlantic Ocean over ~ 26 Myr, between 88 and 62 Ma.

Magmatic differentiation

The analysed samples show large variations in whole-rock chemistry, with SiO_2 and MgO varying from 40.9 to 77.2 wt % and 0.06 to 8.5 wt % respectively. The most evolved rocks (phonolite, trachyte and granite) were probably produced by a fractional crystallization process as shown by the negative anomalies in the incompatible element patterns (Fig. 4). The negative anomalies in Ba, Sr and Eu can be explained by the fractionation of plagioclase, whereas those for P and Ti may be related to the fractionation of apatite and ilmenite, and/or titanite respectively. In the most mafic rocks ($\text{MgO} > 4$ wt %, PT-6A, PT-16A, PT-17A and PT-21A), the concentrations of compatible trace elements (Ni, Cr and Co) preclude the possibility that these rocks are representative of primitive magmas. Moreover, some of the rocks display convex MREE patterns that could be explained by amphibole and titanite accumulation (samples PT-6A, PT-17A, PT-21A). This feature has already been noted by Rock (1976) and Cornen (1982) in explaining the petrogenesis of the Serra de Monchique rocks. The U-shaped MREE patterns observed in the most evolved samples (PT-5A, PT-19A, PT-20A and PT-22B) are probably explained by amphibole fractionation as already documented for the Serra de Monchique samples (Cornen, 1982).

All these observations suggest that the chemical compositions of the studied samples reflect fractional crystallization–accumulation processes. Considering the relatively limited dataset for each massif and the absence of intermediate members of the differentiation series (i.e. granodiorite–trachyandesite), it is difficult to constrain the possible petrogenetic linkage between the mafic rocks and the most evolved samples through a fractional crystallization process. Moreover, as the mafic samples themselves show evidence for crystal accumulation, it is unlikely that they represent the parental magma. This precludes modelling of fractional crystallization processes using these samples to simulate the composition of the evolved rocks. Nevertheless, significant crystal fractionation must have occurred to produce the most evolved rocks. The characteristics of the REE patterns from the Sintra massif (i.e. the most evolved composition has the lowest enrichment in REE, Fig. 4c) can be explained by significant crystal fractionation. This process was sufficiently important that the incompatible REE were incorporated into the solid phases (such as zircon, which fractionates REE) before

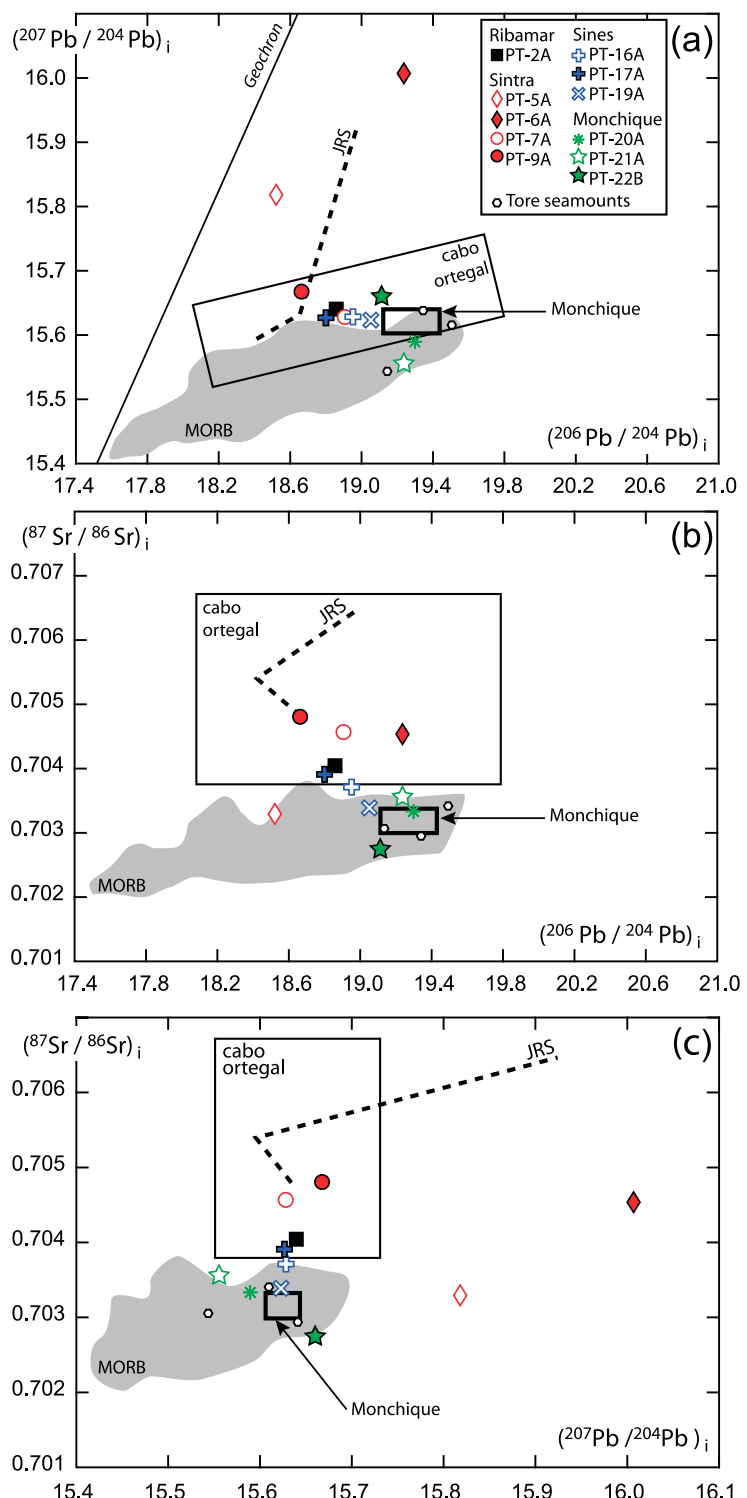


Fig. 8. (a) Variation of $(^{207}\text{Pb} / ^{204}\text{Pb})_i$ vs $(^{206}\text{Pb} / ^{204}\text{Pb})_i$; (b) $(^{87}\text{Sr} / ^{86}\text{Sr})_i$ vs $(^{206}\text{Pb} / ^{204}\text{Pb})_i$ and (c) $(^{87}\text{Sr} / ^{86}\text{Sr})_i$ vs $(^{207}\text{Pb} / ^{204}\text{Pb})_i$ for primary magmatic feldspars. Data from Table 3. Symbols are larger than the analytical uncertainties. For comparison the following fields are shown: (1) initial isotopic compositions of Atlantic N-MORB (GEOROC and PetDB databases); (2) previously published data for Monchique rocks (Bernard-Griffiths *et al.*, 1997); (3) north Tore and NW Tore seamounts (Merle *et al.*, 2006); (4) field for the subcontinental lithospheric mantle (SCLM) at Cabo Ortegal (Santos *et al.*, 2002) recalculated at 80 Ma using the decay constants from Steiger & Jäger (1977). The isotopic compositions of Jurassic igneous rocks (JRS) that originated from the SCLM of Portugal are also shown (three data points linked by a dashed line; Grange *et al.*, 2008). The geochron is the model of Holmes (1946) using a 4.56 Ga age for the Earth and primordial Pb measured in the Canyon Diablo troilite (Tatsumoto *et al.*, 1973).

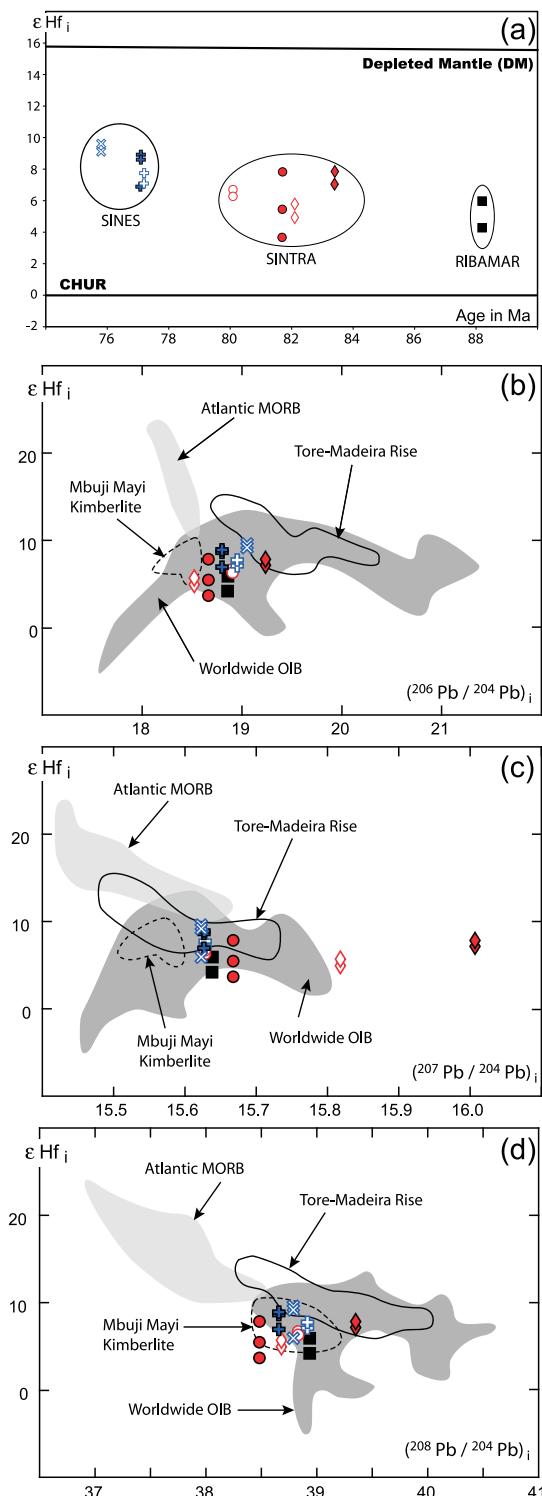


Fig. 9. Initial Hf isotopic compositions ($\epsilon_{\text{Hf}}^{\text{i}}$) measured in zircons. (a) $\epsilon_{\text{Hf}}^{\text{i}}$ as a function of age compared with the evolution of the chondritic uniform reservoir (CHUR) and the continuously LILE-HFSE-depleted mantle (DM). (b–d) correlation diagrams between $\epsilon_{\text{Hf}}^{\text{i}}$ and Pb initial isotopic compositions measured in feldspars. For

final solidification of the melts, leading to the most evolved liquid (represented by the granite PT-5A) being the least enriched in REE but highly differentiated, as indicated by its relative enrichment in the most incompatible elements such as U, Th and Rb. However, the rocks from the Sines massif may be linked through fractional crystallization. The REE patterns of both alkali gabbros (PT-16A and PT-17A) are consistent with their petrological types and major element compositions; that is, PT-16A is the least evolved rock, with olivine relics and ~ 6.2 wt % MgO, whereas PT-17A is more differentiated, containing quartz and only 4.5 wt % MgO. The parallel trace element patterns of these two samples may indicate that PT-17A is derived from a magma similar to PT-16A by fractional crystallization.

Magma sources

Constraints from the most primitive rocks

To constrain the source(s) of the Portuguese magmatic rocks, we focus on the most primitive mafic rocks for each massif (i.e. PT-6A for Sintra, PT-16A and 17A for Sines, and PT-21A for Monchique). Within each massif, these rocks have the highest MgO and lowest SiO₂ contents (Table 2) and are also the oldest (i.e. the first to be emplaced; Table 3). These rocks also appear to have undergone the least amount of crystal fractionation, as indicated by their REE and incompatible trace element patterns (Fig. 4). These features suggest that the magmas that formed these rocks had minimal interaction with any contaminant, such as the continental lithosphere (the SCLM and/or the crust) and therefore their isotopic characteristics are probably the closest to those of the source of the magmas. Consequently, we investigate these rocks first, from Sintra and Sines and then to Monchique.

The most primitive rocks from Sintra, and to a lesser extent from Sines, have the highest $(^{207}\text{Pb} / ^{204}\text{Pb})^{\text{i}}$ within their respective massifs, moderate $(^{206}\text{Pb} / ^{204}\text{Pb})^{\text{i}}$ and moderate to low Sr_i (with a maximum at 0.70454 for PT-6A). Moreover, their initial Hf signatures are all positive and are consistent with a derivation from a mantle source slightly less depleted than the source of MORB (i.e. the asthenosphere). The association of moderate to low Sr_i together with high $(^{207}\text{Pb} / ^{204}\text{Pb})^{\text{i}}$ is inconsistent with a model of mantle-derived magmas contaminated by the upper continental crust, as this interaction would produce

comparison are shown the fields of initial compositions of (1) Atlantic MORB (GEOROC database; Salters & White, 1998), (2) worldwide OIB (Salters & White, 1998; Lassiter *et al.*, 2003), (3) the Mbuji Mayi kimberlite, representing the only combined Pb–Hf data available for the subcontinental mantle (Weis & Demaiffe, 1985; Schärer *et al.*, 1997), and (4) the Tore–Madeira Rise, including the Cretaceous seamounts in its northern sector (Merle *et al.*, 2006) and younger seamounts of the southern part (Geldmacher *et al.*, 2006). The symbols are larger than analytical uncertainties and are defined in Fig. 8.

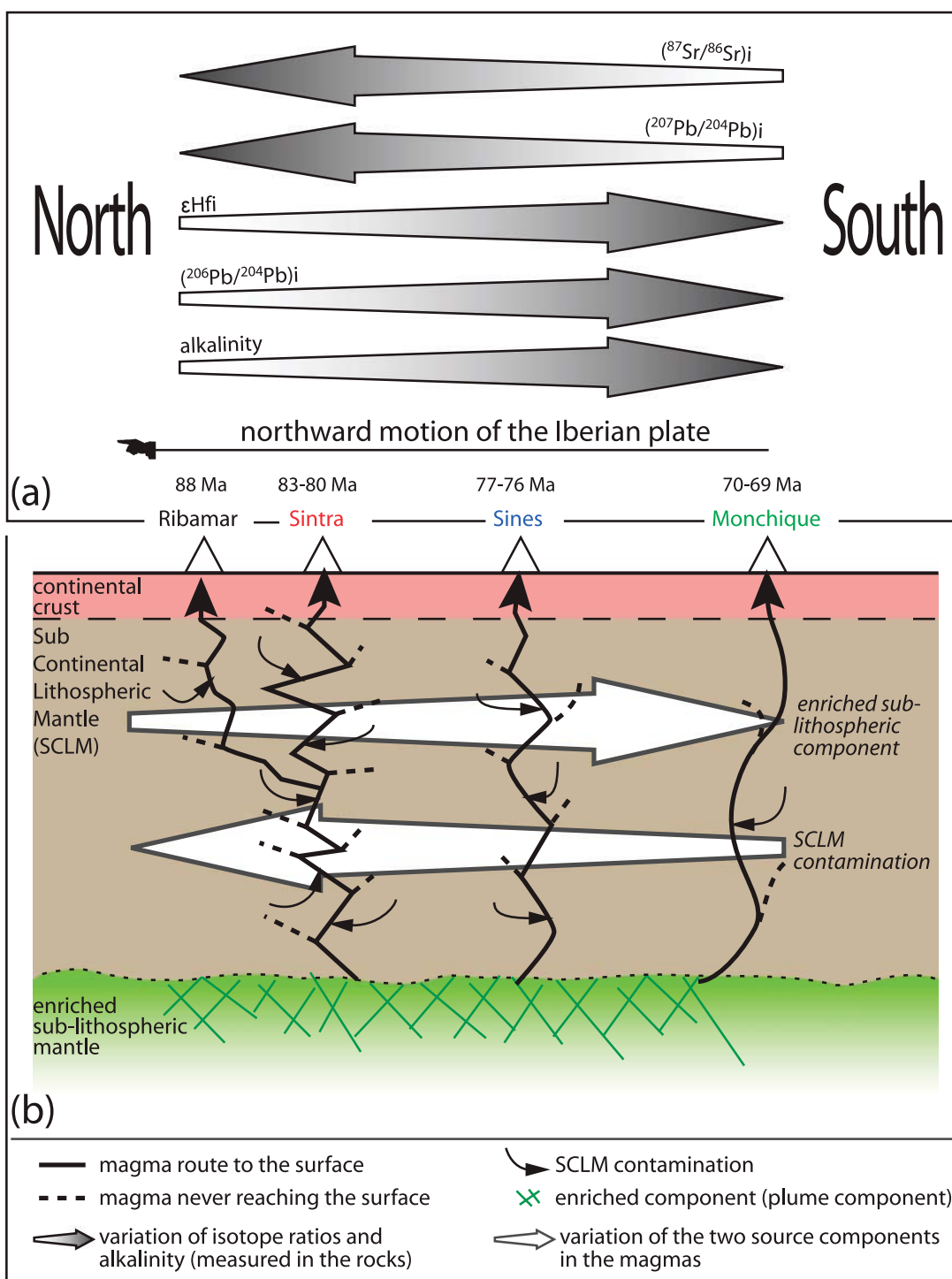


Fig. 10. (a) Synthesis of the data obtained in this study, showing the variations in the ages, alkalinity and isotopic signatures with the location of the samples. The arrows point in the direction of increasing isotope ratios and alkalinity. (b) Sketch of a geodynamic model consistent with the observed results: the north-south geochemical variations are explained by the involvement of two source components (enriched sub-lithospheric mantle + SCLM), with SCLM contamination of melts derived from the deep mantle source becoming less significant through time; that is, from north to south (see text for details). The white arrows point towards increasing influence of enriched sub-lithospheric and SCLM components.

both high ($^{207}\text{Pb}/^{204}\text{Pb}$)_i and high Sr_i. Moreover, significant contamination by the continental crust would be required to produce such high ($^{207}\text{Pb}/^{204}\text{Pb}$)_i leading to negative ϵHf_i . Our samples all display positive ϵHf_i up to +9·6. Indeed, contamination by the continental crust would also lead to high initial ($^{87}\text{Sr}/^{86}\text{Sr}$)_i, especially for those rocks with the highest ($^{207}\text{Pb}/^{204}\text{Pb}$)_i (16·007 ± 0·053 for PT-6A for only 0·70454 Sr_i).

Alkaline rocks with high ($^{207}\text{Pb}/^{204}\text{Pb}$)_i associated with relatively low ($^{206}\text{Pb}/^{204}\text{Pb}$)_i and moderate to low Sr_i are observed amongst the rocks from the Ormonde–Ampere and TMR seamounts, as well as in the Jurassic alkaline magmatic rocks occurring on the continental margin contemporaneous with Central Atlantic continental rifting (Bernard-Griffith *et al.*, 1997; Geldmacher & Hoernle, 2000; Merle *et al.*, 2006; Grange *et al.*, 2008). It is worth noting that an increase in ($^{207}\text{Pb}/^{204}\text{Pb}$)_i is observed from the Madeira Archipelago toward the continental alkaline massif of Monchique through the Ampere and Ormonde seamounts (Geldmacher & Hoernle, 2000). Merle *et al.* (2006) also reported highly radiogenic ($^{207}\text{Pb}/^{204}\text{Pb}$)_i from trachytes sampled on the Sponge Bob seamount (TMD4-3 at 15·714 ± 0·020 and TMD4-8 at 15·828 ± 0·040) associated with Sr_i as low as 0·70231. The highest ($^{207}\text{Pb}/^{204}\text{Pb}$)_i in the region has been identified in Jurassic continental alkaline rocks (syn-rift magmatism) with a value of 15·925 ± 0·013 (Grange *et al.*, 2008; sample PT-35B, Soure). Considering that these isotopic characteristics cannot be explained by contamination of mantle-derived magmas by the continental crust for the reasons explained above, and because the continental crust is not a likely contaminant for the rocks emplaced in the oceanic domain (TMR, Ormonde), we propose that these isotopic signatures are induced by interaction with the SCLM, which is characterized by low Rb/Sr and high $^{207}\text{Pb}/^{204}\text{Pb}$ at moderate $^{206}\text{Pb}/^{204}\text{Pb}$. Geldmacher & Hoernle (2000) explained the trend of increasing ($^{207}\text{Pb}/^{204}\text{Pb}$)_i towards the continent in terms of progressive contamination by the SCLM of magmas derived from an OIB-type mantle source. Merle *et al.* (2006) also invoked the interaction of magmas from an OIB-type source (deep mantle plume component) with material from the SCLM of the Iberian margin, as the SCLM peridotites from the Galicia Bank have Sr_i as low as 0·70210 (Chazot *et al.*, 2005). Grange *et al.* (2008) were unable to identify a significant crustal component and deduced that the high ($^{207}\text{Pb}/^{204}\text{Pb}$)_i signature was produced by partial melting of the SCLM. However, we note here that the positive Pb anomaly characterizing the incompatible elements patterns of the most primitive rocks from Portugal could be a feature induced by the contamination of the magmas by the continental crust. Nevertheless, the isotopic data allow us to rule out any contamination from this source. Therefore, we suggest that interaction with the SCLM

created this positive Pb anomaly, as suggested for the basaltic rocks erupted as part of the Central Atlantic Magmatic Province (CAMP) activity in southern Portugal (Marzoli *et al.*, 2006, and unpublished data). However, although the origin of this anomaly can be explained by the source itself, it is also possible that it is created or enhanced by crystal fractionation processes as the rocks considered here are not the crystallization products of primitive magmas and do not reflect the parental magma composition.

We conclude that an isotopic signature with high ($^{207}\text{Pb}/^{204}\text{Pb}$)_i, moderate ($^{206}\text{Pb}/^{204}\text{Pb}$)_i, low to moderate Sr_i and positive ϵHf_i in the igneous rocks from Sintra and Sines can be explained by a large contribution of the SCLM in the source of these rocks. The most primitive rock from Monchique (PT-21A), however, must have a different petrogenesis because it has the lowest ($^{207}\text{Pb}/^{204}\text{Pb}$)_i but the highest Sr_i among the samples from the massif, within the range of MORB and the Tore seamounts (Merle *et al.*, 2006). In addition, all the rocks from the Monchique massif have ($^{206}\text{Pb}/^{204}\text{Pb}$)_i higher than 19·1, plotting in the most enriched part of the MORB field. The mean value for enriched Depleted MORB Mantle (i.e. enriched DMM) in ($^{206}\text{Pb}/^{204}\text{Pb}$)_i is 18·977, for a ($^{207}\text{Pb}/^{204}\text{Pb}$)_i of 15·568 and a ($^{87}\text{Sr}/^{86}\text{Sr}$)_i of 0·70307 (Workman & Hart, 2005). Those MORB (Fig. 8) that display higher Pb_i signatures than those of the average enriched DMM may represent either an extremely enriched DMM or a mixture between a DMM-type source and an OIB-type component, such as the rocks in the North Atlantic region sampled in the vicinity of some hotspots (e.g. Dosso *et al.*, 1999). The primitive alkali gabbro PT-21A from Monchique has high ($^{206}\text{Pb}/^{204}\text{Pb}$)_i, with a low ($^{207}\text{Pb}/^{204}\text{Pb}$)_i and low Sr_i signature, similar to that expected for the most enriched MORB. This rock is also the only one displaying a negative Pb anomaly. Following the same arguments as above for the Sintra and Sines rocks, this anomaly could reflect a lesser contribution from the SCLM in the magma source. However, as already noted above for the Sintra and Sines rocks, this feature could reflect crystal fractionation processes and not source characteristics. Regardless of this anomaly, and considering the low ($^{207}\text{Pb}/^{204}\text{Pb}$)_i, similar to the low ($^{207}\text{Pb}/^{204}\text{Pb}$)_i observed in MORB, for such a high ($^{206}\text{Pb}/^{204}\text{Pb}$)_i (Fig. 8a), the component with radiogenic ($^{207}\text{Pb}/^{204}\text{Pb}$)_i identified in the Sintra massif is not present in the isotopic signature of this alkali gabbro from Monchique. As a consequence, the Monchique rocks are more likely to be produced from a source displaying enriched DMM-like features. The isotopic characteristics of this source, ($^{206}\text{Pb}/^{204}\text{Pb}$)_i > 19·1 and Sr_i ~ 0·7031, are very similar to the source for the Monchique and Ormonde massifs identified by Bernard-Griffiths *et al.* (1997) as a sub-lithospheric deep mantle source (OIB-type source). This source was

also identified in the isotopic signatures of the NW Tore seamount, which plot in the field of the Madeira Archipelago rocks, inferred to be plume-related (Merle *et al.*, 2006).

Several studies have suggested that this region of the eastern Central Atlantic is affected by a deep thermal anomaly (e.g. Montelli *et al.*, 2004) that could have sustained the alkaline volcanic activity in the oceanic domain for more than 100 Myr; this anomaly is interpreted to be related to the Madeira hotspot (e.g. Geldmacher & Hoernle, 2000; Geldmacher *et al.*, 2006; Merle *et al.*, 2006, 2009). Therefore, the enriched DMM-like component that we identify in the source of the Monchique rocks could either be a mantle plume with an enriched DMM signature or the ambient sub-lithospheric mantle (asthenosphere) enriched by a deep mantle plume. Both possibilities can account for the relatively high $(^{206}\text{Pb}/^{204}\text{Pb})_i$ observed in the rocks. However, in both cases, the involvement of a deep-rooted heat source (deep mantle plume) is required to produce such widespread magmatism since 100 Ma.

Constraints from the evolved rocks

The study of the most primitive rocks from each massif shows that there are two components involved in the genesis of the rocks. The first component is the SCLM, which dominates the isotopic signatures of the samples from Sintra (i.e. earlier in time and at the northern extent of the magmatic alignment); it is responsible for the highest $(^{207}\text{Pb}/^{204}\text{Pb})_i$ signatures. The second is a sub-lithospheric component with an enriched DMM isotopic signature [i.e. relatively high $(^{206}\text{Pb}/^{204}\text{Pb})_i$ at low $(^{207}\text{Pb}/^{204}\text{Pb})_i$]. This latter component is clearly identified in the samples from Monchique (i.e. later in the emplacement of the intrusive rocks and at the southern extent of the magmatic alignment).

The presence of an SCLM component in the source is further documented by the evolved rocks from the Sintra and Sines massifs. These massifs are the only locations where zircons having ages older than the mean emplacement age of the rocks (PT-7A and PT-16A, Table 3) and showing maximum variations in Hf signature of 4 and 2 epsilon units (PT-9A and PT-17A, respectively; Table 6) are found. However, these heterogeneities are not observed within the same rocks. An obvious explanation is that the oldest zircon fractions (zircon 7 for PT-7A and zircon 2 for PT-16A, Table 3) were not selected for Hf analysis (Table 6) and some U–Pb age measurements failed, resulting in fractions used for Hf tracing having no U–Pb ages. The only rock for which there is a complete dataset is PT-17A (alkali gabbro from Sines), for which all the zircon fractions selected for Hf analysis were also successfully dated. This rock shows that the zircon fractions with ϵHf_i varying within a range of 2 units have the same U–Pb age within error. However, as zircon grains with

visible inherited cores or xenocrysts were either discarded during hand-picking or not observed, and as most of the fractions showing outlier ages have not been analysed for Hf and vice versa, the mechanism producing these heterogeneities is difficult to explain. Nevertheless, we consider that such heterogeneities within the zircon population from the same rock most probably reflect heterogeneity within the source, as they cannot be produced by any crystallization–fractionation processes.

Zircon must have crystallized from magmas with heterogeneous Lu/Hf and U/Pb, resulting, in particular, in variable $^{176}\text{Hf}/^{177}\text{Hf}$ that would be incorporated into the zircon grains. These heterogeneities in Hf and Pb are most probably explained by heterogeneities in the SCLM component, resulting from pervasive infiltration of fluids (metasomatism) over time and modification of the mantle composition by re-enrichment in the most incompatible elements. These periods of metasomatism of the Iberian SCLM can be associated with orogeny–subduction cycles identified in the latest Archean (~2.3 Ga), Paleo–Neoproterozoic (~1.9 and 0.6 Ga) and Hercynian (0.4–0.3 Ga) times (e.g. Kuijper *et al.*, 1982; Peucat *et al.*, 1990; Santos *et al.*, 1996), and possibly by percolating magmas associated with the Atlantic pre- and syn-rift period (Charpentier *et al.*, 1998; Chazot *et al.*, 2005). These successive phases of metasomatism would enrich the SCLM in large ion lithophile elements (LILE) and high field strength elements (HFSE) as the enriched magmatic fluids percolated through the lithosphere. As a result, polyphase enrichment of the SCLM is likely to have produced varying time-integrated Rb/Sr, Sm/Nd, Lu/Hf, U/Pb and Th/Pb values. Therefore, the inherited radiogenic Pb and heterogeneous ϵHf_i in the alkaline massifs probably result from contamination of the alkaline parental magmas generated in the sub-lithospheric mantle during their ascent through the SCLM. This interpretation is supported by the observation that the oldest zircon fraction from the Sintra syenite (PT-7A) yields an age of 142 Ma, which is the same age as the pre-rift alkaline magmatism that originated from the SCLM (Grange *et al.*, 2008).

The data also indicate that the relative proportion of the SCLM and the sub-lithospheric mantle components vary from the Sintra to the Monchique massifs (i.e. from north to south) and also vary through time. The rocks from Sintra have the highest $(^{207}\text{Pb}/^{204}\text{Pb})_i$, inherited Pb, and ϵHf_i varying by up to 4 units; features all attributed to involvement of the SCLM. The rocks from Sines have lower $(^{207}\text{Pb}/^{204}\text{Pb})_i$, ϵHf_i variation of only 2 units and no obvious inherited Pb. Although no Hf data are available for the rocks from Monchique, they show the smallest SCLM component with the lowest $(^{207}\text{Pb}/^{204}\text{Pb})_i$ for the highest $(^{206}\text{Pb}/^{204}\text{Pb})_i$ and no inherited Pb. Therefore, these isotope characteristics suggest that the contribution of the SCLM within the source decreases from north to south,

and also through time. Indeed, the average signatures in $(^{206}\text{Pb}/^{204}\text{Pb})_i$ and ϵHf_i increase from Sintra (18.832 and +6.1, respectively) to Sines (18.935 and +8.4, respectively) and then to Monchique (19.216). The Sr_i ratios also decrease from north to south to reach an average value of 0.70321 for the Monchique rocks, which is close to the value proposed by Bernard-Griffiths *et al.* (1997) for their deep sub-lithospheric mantle source (~ 0.7031).

GEODYNAMIC IMPLICATIONS

Origin of the north–south age trend

The magmatic intrusions along the Portuguese continental margin were emplaced during a period of about 20 Myr along a north–south trend, with the oldest rocks, dated at 88 Ma, occurring to the north and the youngest rocks (69 Ma) emplaced in the south. Such age-related trends have been described for a number of seamount chains (e.g. Hawaii–Emperor chain, Walvis Ridge) and have been related to fixed, deep-rooted mantle plumes (hot-spots) above which the lithospheric plates move, tracking the record of hotspot activity through time. In this case, if the observed age progression is ascribed to plate motion, it would require that the Iberian Peninsula moved about 200 km toward the NNW between ~ 88 and 69 Ma. According to the geodynamic model proposed by Sibuet *et al.* (2004), the motion of the Iberian plate was toward the NE prior to 88 Ma, at which time its kinematics changed owing to the closure of the oceanic domain between Iberia and Europe. This event resulted in a period of quiescence in Iberian plate motion from 88 Ma until ~ 81 –80 Ma. At this time, subduction of the Iberian plate under Europe was initiated, resulting in NNW motion of the plate that continues today (Sibuet *et al.*, 2004). Our age data are consistent with the plate kinematics between 88–80 Ma and 68–60 Ma, when the Iberian plate was moving towards the NNW. The plate motion model proposed by Sibuet *et al.* (2004) has already been shown to be in accordance with the overall distribution of alkaline magmatism in the region, including the occurrences of alkaline magmatism on the continent. Indeed, the distribution of the magmatism has been interpreted to be a result of the interaction between a mantle plume emitting pulses of magma and the complex motion of the Iberian plate (Merle *et al.*, 2009). Our data agree with this geodynamic model and therefore confirm the preliminary data of Grange *et al.* (2007) used by Merle *et al.* (2009).

The emplacement of the alkaline complexes in Portugal along a NNW–SSE trend may have occurred along major lithospheric discontinuities, as the magmatic rocks both onshore and offshore are located close to such structures. These major faults, such as the Messejana and Nazare faults (Fig. 1), are Late Hercynian structures reactivated during the extensional rifting phases of the continent during the Jurassic and are connected to the AGFZ system

(Fig. 1). The role of these faults has already been invoked to explain the emplacement of the alkaline Jurassic magmas (syn-rift magmatism) in Portugal (Grange *et al.*, 2008) and the Cretaceous alkaline rocks of the Gorringe Bank and of the Tore seamounts (Féraud *et al.*, 1986; Geldmacher *et al.*, 2006; Merle *et al.*, 2006).

Origin of the north–south isotopic trend

A model to explain the spatial and temporal variations in the proportion of the SCLM and the sub-lithospheric mantle in the petrogenesis of the magmas is schematically shown in Fig. 10a, in which data from this study are summarized and the isotopic and age variation with latitude is shown. In Fig. 10b, a schematic illustration of the sources and emplacement mechanism of the alkaline rocks is provided and can be described as follows. During the initial stage (Ribamar and Sintra massif), slow ascent rates of magmas derived from the sub-lithospheric mantle through the less permeable SCLM resulted in significant chemical interaction between those two components. Consequently, the magmas inherited Pb and Hf components from the SCLM, as evidenced by some zircon fractions from the Sintra massif. Over time, magmas that originated from the sub-lithospheric mantle thermally ‘erode’ the SCLM and follow a more direct path towards the surface. This model implies that magmas coming from the deep mantle have a shorter residence time in the SCLM, and thus acquire a weaker isotopic fingerprint of the SCLM component (e.g. Sines rocks). Therefore, the isotopic signatures of the rocks change towards compositions closer to the sub-lithospheric component (Monchique massif). These variations are induced by the northward motion of the Iberian plate, resulting in the southward migration of the alkaline magmatism. The pathways of the deep magmas toward the surface become better developed through time, reducing the contamination by the SCLM.

An alternative way to explain the observed isotopic variations is to invoke a progressive variation in the composition of the sub-lithospheric component with time instead of variable contamination by the SCLM. Regardless of the composition of the enriched DMM-like component (deep mantle plume or a mixture of the asthenosphere with an OIB-like mantle plume), this explanation would probably imply variable degrees of melting, magma production and, therefore, variations in heat production within the plume for which we have no evidence. The contamination of parental magmas derived from a sub-lithospheric mantle source by various amount of SCLM is the most straightforward way in our opinion to explain the data, although we cannot exclude the possibility of coeval variation within the deep mantle source component.

SUMMARY AND CONCLUSIONS

The alkaline massifs located along the Atlantic coast of Portugal originated from magmas that were generated from a sub-lithospheric mantle source with an enriched DMM-like isotopic signature and were contaminated on their way to the surface by the SCLM. An important finding of this study is the correlation between ages, initial isotope signatures and spatial location of the studied intrusions, which probably reflects variations in the amount of contamination by the SCLM of the magmas from the sub-lithospheric source. This deep mantle source involved in the genesis of the alkaline continental rocks is most probably the same as that required to produce the magmatic rocks from the TMR and surrounding seamounts. Several geodynamical models have been proposed to explain the origin of this alkaline magmatism (e.g. Geldmacher *et al.*, 2000, 2001) but only the model proposed by Merle *et al.* (2009) takes into account the petrogenesis of the alkaline magmatism occurring on both oceanic and continental lithosphere and the complex motion of the Iberian plate. This model has been further constrained by the results of the present study; in particular, we have established the age of the onshore alkaline magmatism and confirmed that the period of alkaline magmatism extends almost continuously from the Cretaceous to the present day, from the north of the TMR to the active Madeira Archipelago. Our study shows that the alkaline magmatism of westernmost Portugal belongs to the same alkaline province as that described in the neighbouring oceanic domain west of the continent and thus provides important constraints in the reconstruction of the geodynamic history of the Central Atlantic Ocean.

ACKNOWLEDGEMENTS

The Ministry of Education and Research is acknowledged for the Ph.D. grant of M. Grange. We are grateful to A. Ribeiro and L. Pinheiro for field assistance and documents, and to M. Manetti and J. P. Goudour for technical help. Comments from K. Hoernle, two anonymous reviewers and Editor G. Wörner greatly helped to improve successive versions of this manuscript and achieve the publication of this work; the time and effort they spent on it is much appreciated. The authors also want to thank F. Korhonen for improving the English of the last version of the manuscript.

REFERENCES

- Allègre, C. J., Treuil, M., Minster, J. F., Minster, B. & Albarède, F. (1977). Systematic use of trace elements in igneous processes: part I. *Fractional crystallisation processes in volcanic suites*. Contributions to Mineralogy and Petrology **60**, 57–75.
- Allègre, C. J., Manhès, G. & Göpel, C. (1995). The age of the Earth. *Geochimica et Cosmochimica Acta* **59**, 1445–1456.
- Baksi, A. K. (2007). A quantitative tool for detecting alteration in undisturbed rocks and minerals—I: Water, chemical weathering, and atmospheric argon. In: Foulger, G. R. & Jurdy, D. M. (eds) *Plates, Plumes and Planetary Processes*. Geological Society of America, Special Papers **430**, 285–303.
- Bernard-Griffiths, J., Gruau, G., Cornen, G., Azambre, B. & Macé, J. (1997). Continental lithospheric contribution to alkaline magmatism: isotopic (Nd, Sr, Pb) and geochemical (REE) evidence from Serra de Monchique and Mount Ormonde complexes. *Journal of Petrology* **38**(1), 115–132.
- Beslier, M.-O., Girardeau, J. & Boillot, G. (1990). Kinematics of peridotite emplacement during North Atlantic continental rifting, Galicia, northwestern Spain. *Tectonophysics* **184**, 321–343.
- Blichert-Toft, J. & Albarède, F. (1997). The Lu–Hf isotope geochemistry of chondrites and the evolution of the mantle–crust system. *Earth and Planetary Science Letters* **148**, 243–258.
- Blichert-Toft, J., Chauvel, C. & Albarède, F. (1997). Separation of Hf and Lu for high-precision isotope analysis of rock samples by magnetic sector-multiple collector ICP-MS. *Contribution to Mineralogy and Petrology* **127**, 248–260.
- Bodet, F. & Schärer, U. (2000). Evolution of the SE-Asian continent from U–Pb and Hf isotopes in single grains of zircon and baddeleyite from large rivers. *Geochimica et Cosmochimica Acta* **64**, 2067–2091.
- Boillot, G., Girardeau, J. & Kornprobst, J. (1988). The rifting of the Galicia margin: crustal thinning and emplacement of mantle rocks on the sea floor. In: Boillot, G., Winterer, J. *et al.* (eds) *Proceeding of the Ocean Drilling Program, Scientific Results, 103*. College Station, TX: Ocean Drilling Program, pp. 741–746.
- Canilho, M. H. (1972). Estudo geológico-petrográfico do maciço eruptivo de Sines. *Boletim Museu Laboratorio Mineralogia-Geologia Faculdade de Ciencias, Universidade de Lisboa* **12**(2), 77–161.
- Carignan, J., Hild, P., Mevelle, G., Morel, J. & Yeghicheyan, D. (2001). Routine analyses of trace element in geological samples using flow injection and low-pressure on-line liquid chromatography coupled to ICP-MS: a study of geochemical reference materials BR, DR-N, UB-N, AN-G and GH. *Geostandard Newsletter* **25**, 187–198.
- Charpentier, S., Kornprobst, J., Chazot, G., Cornen, G. & Boillot, G. (1998). Interaction entre lithosphère et asthénosphère au cours de l'ouverture océanique: données isotopiques préliminaires sur la Marge passive de Galice (Atlantique Nord). *Comptes Rendus de l'Académie des Sciences* **326**, 757–762.
- Chazot, G., Charpentier, S., Kornprobst, J., Vannucci, R. & Luais, B. (2005). Lithospheric mantle evolution during continental break-up: the West Iberia non-volcanic passive margin. *Journal of Petrology* **46**(12), 2527–2568.
- Cornen, G. (1982). Petrology of the alkaline volcanism of Gorringe Bank (Southwest Portugal). *Marine Geology* **47**, 101–130.
- Dosso, L., Bougault, H., Langmuir, C., Bollinger, C., Bonnier, O. & Etoubleau, J. (1999). The age and distribution of mantle heterogeneity along the Mid-Atlantic Ridge (31–41°N). *Earth and Planetary Science Letters* **170**, 269–286.
- Féraud, G., Gastaud, G., Auzende, J.-M., Olivet, J.-L. & Cornen, G. (1982). $^{40}\text{Ar}/^{39}\text{Ar}$ ages for the alkaline volcanism and basement of Gorringe Bank, North Atlantic Ocean. *Earth and Planetary Science Letters* **57**, 211–226.
- Féraud, G., York, D., Mével, C., Cornen, G., Hall, C. M. & Auzende, J.-M. (1986). Additional $^{40}\text{Ar}/^{39}\text{Ar}$ dating of the basement and the alkaline volcanism of Gorringe Bank (Atlantic Ocean). *Earth and Planetary Science Letters* **79**, 255–269.
- Geldmacher, J. & Hoernle, K. (2000). The 72 Ma geochemical evolution of the Madeira hotspot (eastern North Atlantic): recycling of

- Paleozoic (= 500 Ma) oceanic lithosphere. *Earth and Planetary Science Letters* **183**, 73–92.
- Geldmacher, J., Van den Bogaard, P., Hoernle, K. & Schmincke, H. U. (2000). The $^{40}\text{Ar}/^{39}\text{Ar}$ age dating of the Madeira Archipelago and hotspot track (eastern North Atlantic). *Geochemistry, Geophysics, Geosystems* **1**, 1999GC000018.
- Geldmacher, J., Hoernle, K., Van den Bogaard, P., Zankl, G. & Garbe-Schönberg, D. (2001). Earlier history of the Canary hotspot based on the temporal and geochemical evolution of the Selvagen archipelago and neighboring seamounts in the eastern North Atlantic. *Journal of Volcanology and Geothermal Research* **110**, 55–87.
- Geldmacher, J., Hoernle, K., Klügel, A., Van den Bogaard, P., Wombacher, F. & Berning, B. (2006). Origin and geochemical evolution of the Madeira–Tore Rise (eastern North Atlantic). *Journal of Geophysical Research* **111**, B09206.
- GEOROC database (Geochemistry of rocks of the oceans and continents), Max-Planck Institut für Chemie. World Wide Web Address: <http://georoc.mpcn-mainz.gwdg.de/georoc/Start.asp>.
- Girardeau, J. & Gil Ibarguchi, J. I. (1991). Pyroxene-rich peridotites of the Cabo Ortegal Complex (northwestern Spain): evidence for large-scale upper mantle heterogeneity. *Journal of Petrology, Lherzolites Special Issue* 135–154.
- Girardeau, J., Cornen, G., Beslier, M.-O., Le Gall, B., Monnier, C., Agrinier, P., Dubuisson, G., Pinheiro, L., Ribeiro, A. & Whitechurch, H. (1998). Extensional tectonics in the Gorringe Bank rocks, Eastern Atlantic Ocean: evidence of an oceanic ultra-slow mantelllic accreting centre. *Terra Nova* **10**, 330–336.
- Gonçalves, F. (1967). Subsídios para o conhecimento geológico do maciço eruptivo de Monchique. Comunicações dos Serviços Geológicos de Portugal, Lisboa **LII**, 169–184.
- Govindaraju, K. & Mevelle, G. (1987). Fully automated dissolution and separation method for inductively coupled plasma atomic emission spectrometry rock analysis; Application to the determination of rare earth elements. *Journal of Analytical Atomic Spectrometry* **2**, 615–621.
- Gradstein, F. M., Ogg, J. G. & Smith, A. G. (2004). *A Geological Time Scale*. Cambridge: Cambridge University Press.
- Grange, M., Schärer, U., Cornen, G. & Girardeau, J. (2007). Time-space migration of melting within the East Atlantic plume and magmatism of Portugal: U–Pb ages and Pb–Sr–Hf isotopes. *Geochimica et Cosmochimica Acta* **71** (Suppl. 1) A351.
- Grange, M., Schärer, U., Cornen, G. & Girardeau, J. (2008). First alkaline magmatism during Iberia–Newfoundland rifting. *Terra Nova* **20**, 494–503.
- Holmes, A. (1946). An estimate of the age of the Earth. *Nature* **157** (3995), 680–684.
- Jaffey, H., Flynn, K. F., Glendenin, L. E., Bentley, W. C. & Essling, A. M. (1971). Precision measurements of half-lives and specific activities of ^{235}U and ^{238}U . *Physical Reviews* **C4**, 1889–1906.
- Krogh, T. E. (1973). A low contamination method for hydrothermal decomposition of zircon and extraction of U and Pb for isotopic ages determination. *Geochimica et Cosmochimica Acta* **37**, 485–494.
- Krogh, T. E. (1982). Improved accuracy of U–Pb zircon ages by the creation of more concordant systems using air abrasion technique. *Geochimica et Cosmochimica Acta* **46**, 637–649.
- Kuijper, R. P., Priem, H. N. A. & den Tex, E. (1982). Late Archean–Early Proterozoic source ages of zircons in rocks from the Paleozoic orogen of Western Galicia, NW Spain. *Precambrian Research* **19**, 1–29.
- Lassiter, J. C., Blachert-Toft, J., Hauri, E. H. & Barsczus, H. G. (2003). Isotope and trace element variations in lavas from Raivavae and Rapa, Cook Austral islands: constraints on the nature of the HIMU- and EM-mantle and the origin of mid-plate volcanism in French Polynesia. *Chemical Geology* **202**, 115–138.
- Le Bas, M. J., Le Maitre, R. W., Streckeisen, A. & Zanettin, B. (1986). A chemical classification of volcanic rocks based on the total alkali–silica diagram. *Journal of Petrology* **27**, 745–750.
- Ludwig, K. R. (2003). *User's Manual for Isoplot 3.00. Berkeley Geochronology Center Special Publication* **4**, 71.
- Manhès, G., Minster, J. F. & Allègre, C. J. (1978). Comparative U–Th–Pb and Rb–Sr study of the Saint Séverin amphoterite: consequence for early solar system chronology. *Earth and Planetary Science Letters* **39**, 14–24.
- Martins, L. T. (1991). *Actividade ígnea Mesozóica em Portugal (Contribuição petrológica e geoquímica)* Ph.D. thesis, University of Lisbon, 418 p.
- Marzoli, A., Rapaille, C., Reisberg, L. & Bertrand, H. (2006). Trace element and Sr–Nd–Pb–Os evidence for a lithospheric mantle source for the European CAMP basalts. *Geochimica et Cosmochimica Acta* **70** (18), Supplement 1, A397.
- Merle, R., Schärer, U., Girardeau, J. & Cornen, G. (2006). Cretaceous seamounts along the continent–ocean transition of the Iberian margin: U–Pb ages and Pb–Sr–Hf isotopes. *Geochimica et Cosmochimica Acta* **70**, 4950–4976.
- Merle, R., Jourdan, F., Marzoli, A., Renne, P. R., Grange, M. & Girardeau, J. (2009). Evidence of multi-phase Cretaceous to Quaternary alkaline magmatism on Tore–Madeira Rise and neighbouring seamounts from $^{40}\text{Ar}/^{39}\text{Ar}$ ages. *Journal of the Geological Society, London* **166**, 879–894.
- Miranda, R., Valadares, V., Terrinha, P., Mata, J., do Rosario Azevedo, M., Gaspara, M., Kullberg, J. C. & Ribeiro, C. (2009). Age constraints on the Late Cretaceous alkaline magmatism on the West Iberian Margin. *Cretaceous Research* **30**, 575–586.
- Miyashiro, A. (1978). Nature of alkaline volcanic rock series. *Contributions to Mineralogy and Petrology* **66**, 91–104.
- Montelli, R., Nolet, G., Dahlen, F. A., Masters, G., Engdahl, E. R. & Hung, S. H. (2004). Finite-frequency tomography reveals a variety of plume in the mantle. *Nature* **303**, 338–343.
- Olivet, J. L. (1996). La cinématique de la plaque ibérique—Kinematics of the Iberian plate. *Bulletin des Centres de Recherches Exploration–Production Elf Aquitaine* **20** (I), 131–195.
- Palacios, T. P. (1985). *Petrologia do Complexo Vulcanico de Lisboa. Tese de Doutoramento*. Universidade de Lisboa, 260 p.
- Patchett, P. J. & Tatsumoto, M. (1980). A routine high-precision method for Lu–Hf isotope geochemistry and chronology. *Contributions to Mineralogy and Petrology* **75**, 263–267.
- Patchett, P. J., Kouvo, O., Edge, C. E. & Tatsumoto, M. (1981). Evolution of continental crust and mantle heterogeneity: Evidence from Hf isotopes. *Contributions to Mineralogy and Petrology* **78**, 279–297.
- PetDB database (Petrological database of the Ocean Floor). World Wide Web Address: <http://www.petdb.org/>.
- Peucat, J. J., Bernard-Griffiths, J., Gil Ibarguchi, J. I., Dallmeyer, R., Menot, D., Cornichet, P. & Iglesias Ponce de León, M. (1990). Geochemical and geochronological cross-section of the deep Variscan crust: the Cabo Ortegal high pressure nappe (Northwestern Spain). *Tectonophysics* **177**, 263–292.
- Rock, N. M. S. (1976). The comparative strontium isotopic composition of alkaline rocks: new data from southern Portugal and east Africa. *Contributions to Mineralogy and Petrology* **56**, 205–228.
- Rock, N. M. S. (1978). Petrology and petrogenesis of the Monchique alkaline complex, southern Portugal. *Journal of Petrology* **19**, 171–214.
- Salters, V. J. M. & White, W. M. (1998). Hf isotopes constraints on mantle evolution. *Chemical Geology* **145**, 447–460.
- Santos, J. F., Schärer, U., Gil Ibarguchi, J. I. & Girardeau, J. (1996). Evolution of the Cabo Ortegal ultramafic–mafic complex:

- U–Pb, Rb–Sr and Pb–Pb isotope data. *Chemical Geology* **129**, 281–306.
- Santos, J. F., Schärer, U., Gil Ibarguchi, J. I. & Girardeau, J. (2002). Genesis of a pyroxenite-rich peridotite at Cabo Ortegal (NW Spain): Geochemical and Pb–Sr–Nd isotope data. *Journal of Petrology* **43**, 17–43.
- Schärer, U. (1991). Rapid continental crust formation at 1.7 Ga from a reservoir with chondritic isotope signatures, eastern Labrador. *Earth and Planetary Science Letters* **102**, 110–133.
- Schärer, U., Corfu, F. & Demaiffe, D. (1997). U–Pb and Lu–Hf isotopes in baddeleyite and zircon megacrysts from the Mbui Mayi kimberlite: constraints on the subcontinental mantle. *Chemical Geology* **143**, 1–16.
- Schärer, U., Girardeau, J., Cornen, G. & Boillot, G. (2000). 1.21 Ma asthenospheric magmatism prior to continental break-up in the North Atlantic and geodynamic implications. *Earth and Planetary Science Letters* **181**, 555–572.
- Sibuet, J. C., Srivastava, S. & Spakman, W. (2004). Pyrenean orogeny and plate kinematics. *Journal of Geophysical Research* **109**, B08104, doi:10.1029/2003JB002514.
- Silva, E. A., Miranda, J. M., Luis, J. F. & Galdeano, A. (2000). Correlation between the Paleozoic structures from West Iberian and Grand Banks margins using inversion of magnetic anomalies. *Tectonophysics* **321**, 57–71.
- Söderlund, U., Patchett, P. J., Vervoort, J. D. & Isachsen, C. E. (2004). The ^{176}Lu decay constant determined by Lu–Hf and U–Pb isotope systematics of Precambrian mafic intrusions. *Earth and Planetary Science Letters* **219**, 311–324.
- Sparks, R. S. J. & Wadge, G. (1975). Geological and geochemical studies of the Sintra alkaline igneous complex, Portugal. *Bulletin of Volcanology* **39**(3), 385–406.
- Steiger, R. H. & Jäger, E. (1977). Subcommission on geochronology convention on the use of decay constants in geo- and cosmochronology. *Earth and Planetary Science Letters* **36**, 359–362.
- Sun, S. S. & McDonough, W. F. (1989). Chemical and isotopic systematics of oceanic basalts: implication for mantle composition and processes. In: Saunders, A. D. & Norry, M. J. (eds) *Magmatism in the Ocean Basins*. Geological Society, London, Special Publications **42**, 313–345.
- Tatsumoto, M., Knight, R. J. & Allègre, C. J. (1973). Time differences in the formation of meteorites as determined from the ratio of 207-lead to 206-lead. *Science* **180**, 1279–1283.
- Weis, D. & Demaiffe, D. (1985). A depleted mantle source for kimberlites from Zaire: Nd, Sr and Pb isotopic evidence. *Earth and Planetary Science Letters* **73**, 269–277.
- Workman, R. K. & Hart, S. R. (2005). Major and trace element composition of the depleted MORB mantle (DMM). *Earth and Planetary Science Letters* **231**, 53–72.
- Wright, J. B. (1969). Re-interpretation of a mixed petrographic province—The Sintra intrusive complex (Portugal) and related rocks. *Geologische Rundschau* **58**, 538–564.
- Zhang, L.-S. & Schärer, U. (1996). Inherited Pb components in magmatic titanite and their consequence for the interpretation of U–Pb ages. *Earth and Planetary Science Letters* **138**, 57–65.

Evidence of multi-phase Cretaceous to Quaternary alkaline magmatism on Tore–Madeira Rise and neighbouring seamounts from $^{40}\text{Ar}/^{39}\text{Ar}$ ages

RENAUD MERLE^{1,2*}, FRED JOURDAN^{3,4}, ANDREA MARZOLI¹, PAUL R. RENNE^{3,5},
MARION GRANGE⁶ & JACQUES GIRARDEAU⁷

¹*Dipartimento de Geoscienze, Università di Padova, Via Giotto 1, 35137 Padova, Italy*

²*Present address: University of Western Australia, School of Earth and Geographical Sciences, 35 Stirling Highway, Crawley, WA 6009, Australia*

³*Berkeley Geochronology Center, 2455 Ridge Road, Berkeley, CA 94709, USA*

⁴*Western Australian Argon Isotope Facility, Department of Applied Geology and JdL-CMS, Curtin University of Technology, GPO Box U1987, Perth, WA 6845, Australia*

⁵*Department of Earth and Planetary Science, University of California, Berkeley, CA 94720, USA*

⁶*Department of Applied Geology, Curtin University of Technology, GPO Box U1987, Perth, WA 6845, Australia*

⁷*Laboratoire de Planétologie et Géodynamique, UMR-CNRS 6112, Université de Nantes, 2 rue de la Houssinière, 44322 Nantes cedex 3, France*

*Corresponding author (e-mail: rmerle@cyllene.uwa.edu.au)

Abstract: The Tore–Madeira Rise is a seamount chain located 300 km off the Portugal and Morocco coasts attributed to hotspot activity. U–Pb ages of lavas from the northern and central Tore–Madeira Rise range between 103 and 80.5 Ma whereas $^{40}\text{Ar}/^{39}\text{Ar}$ ages from the central and southern Tore–Madeira Rise yield ages ranging from 94.5 to 0.5 Ma. We performed new $^{40}\text{Ar}/^{39}\text{Ar}$ measurements to better understand the geodynamic history of the Tore–Madeira Rise. Plagioclase ages from the Bikini Bottom and Torillon seamounts suggest ages of >90 Ma and ≥ 60 Ma, respectively. Amphiboles from the Seine seamount yield an age of 24.0 ± 0.8 Ma. Biotites from lavas of the Ashton seamount give ages of 97.4 ± 1.1 Ma and 97.8 ± 1.1 Ma. The geochronological database available on the Tore–Madeira Rise has been filtered on statistical criteria to eliminate unreliable ages. The resulting database reveals three pulses of alkaline magmatism on the Tore–Madeira Rise at 103–80.5 Ma, at c. 68 Ma and between 30 Ma and the present. The magmatism was continuous from 103 Ma until c. 68 Ma and from c. 30 Ma until the present on the Tore–Madeira Rise, the surrounding seamounts and the Portugal coast. We suggest that the space–time distribution of this magmatism results from the interaction between a wide thermal anomaly emitting magmatic pulses and the complex motion of the Iberian plate.

Supplementary material: A detailed Ar measurements dataset is available at <http://www.geolsoc.org.uk/SUP18359>.

The Tore–Madeira Rise is a 1000 km long by 50 km wide seamount chain, oriented NNE–SSW along the Atlantic coast of Portugal and Morocco (Fig. 1a). It includes a dozen seamounts extending from the Tore seamount, located 300 km west of Lisbon, to the Madeira archipelago. For several decades, the nature of the rocks forming this aseismic ridge was almost unknown, and only very few samples were available. Two dredging campaigns were carried out in 2001 (R.V. *Meteor* expedition M51/1; Tore–Madeira Rise cruise, R.V. *Atalante*) to constrain the age and the main chemical characteristics of the rocks constituting the rise and to decipher the geodynamical process leading to its construction. Abundant alkaline lavas displaying similar chemical characteristics were dredged along the whole rise and at surrounding alkaline magmatism occurrences (Fig. 1). Two sets of contrasting ages were obtained on lavas from seamounts along the rise. Titanite and zircon U–Pb ages from differentiated lavas of the northern and central part of the rise ranged between c. 104 and c. 80 Ma (Merle *et al.* 2006); $^{40}\text{Ar}/^{39}\text{Ar}$ measurements carried out on groundmass and mineral separates from central and southern Tore–Madeira Rise

seamounts yielded Cretaceous (94 Ma) to Pleistocene ages (Geldmacher *et al.* 2005, 2006, 2008). These studies argued for a hotspot as the source of the Tore–Madeira Rise but it is still unclear if the Tore–Madeira Rise magmatism was related to the Madeira and/or Canary plumes (Geldmacher *et al.* 2006) or to a deep-rooted thermal anomaly feeding the Azores, Madeira and Canaries hotspots (Merle *et al.* 2006). Alternative hypotheses are accretion-related off-axis magmatic activity (Jagoutz *et al.* 2007) or shallow mantle upwelling (Geldmacher *et al.* 2008). These hypotheses are, however, strongly dependent on the reliability of the ages of the various seamounts. Moreover, no ages are available for some seamounts, in particular those located slightly off the main Tore–Madeira Rise alignment. As a consequence, the geodynamic process that triggered the magmatism on the Tore–Madeira Rise and in the surrounding area is still debated and additional geochronological data are required for the entire area.

The aim of this work is to document new $^{40}\text{Ar}/^{39}\text{Ar}$ dating performed on plagioclase, biotite and amphibole separates from lavas of four seamounts to improve the reliability of the two

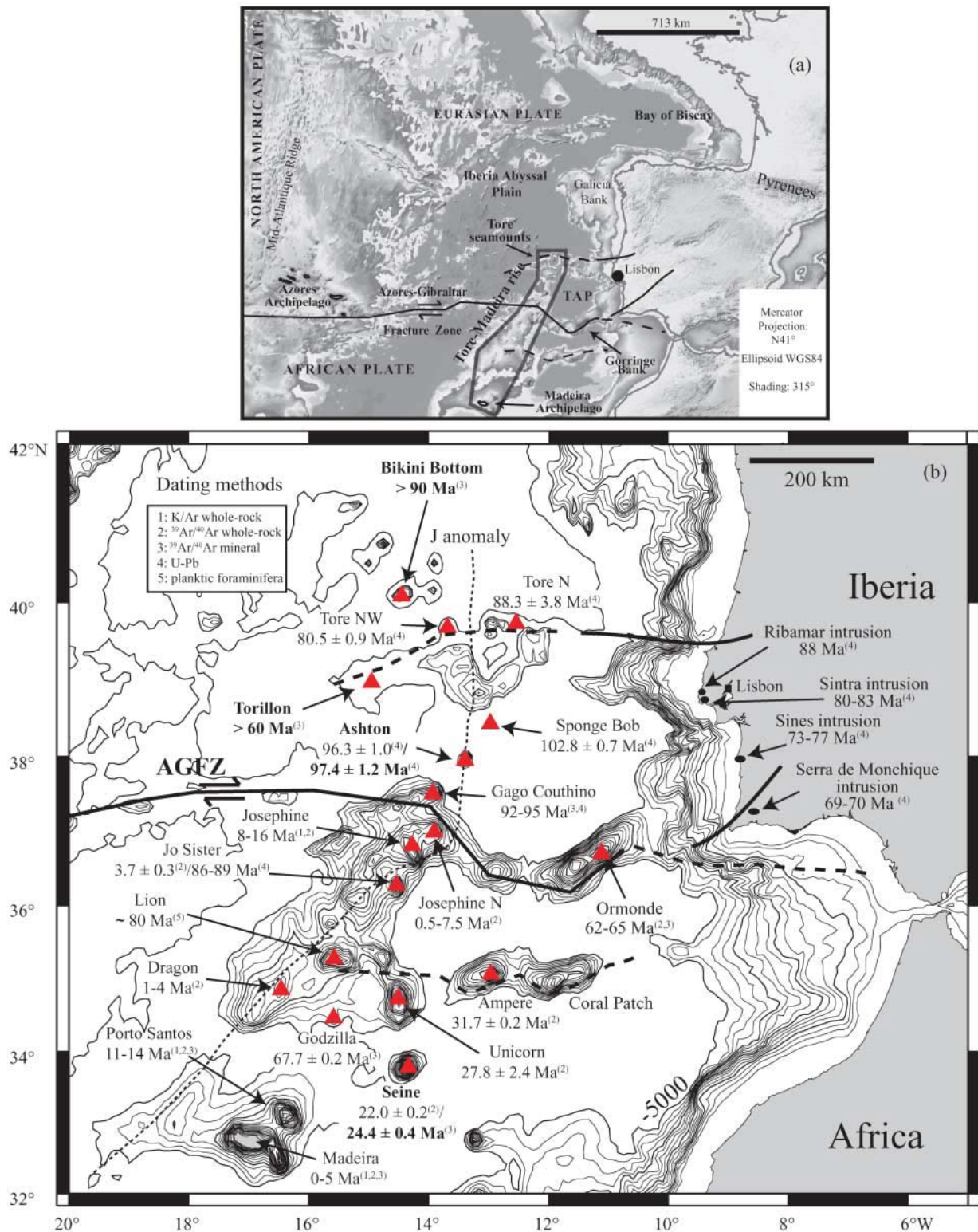


Fig. 1. (a) Bathymetric map of the eastern part of the northern central Atlantic (From Sibuet *et al.* 2004a). TAP, Tagus Abyssal Plain. (b) Bathymetric map of the study region showing the main structural units. Continuous lines represent faults, and dashed lines inferred faults. AGFZ, Azores–Gibraltar Fracture Zone. Triangles indicate seamounts where dating has been performed. Ages of Ormonde THR, Monchique, Madeira, Porto Santo, Ampère, Josephine, Unicorn and Seine are from Wendt *et al.* (1976), Féraud *et al.* (1982, 1986), Bernard-Griffiths *et al.* (1997), Geldmacher *et al.* (2000, 2005, 2006, 2008) and Merle *et al.* (2006). The geochronological data from this study are indicated in bold. Location of the J anomaly after Olivet (1996).

contrasting age sets mentioned above. New and carefully selected published ages, and geochemical and isotopic data are discussed and combined to obtain a more complete overview of the construction of the Tore-Madeira Rise. We give a new geodynamic interpretation of the Tore-Madeira Rise and the magmatic occurrences of this part of the Atlantic Ocean.

Geological setting

The Tore-Madeira Rise ranges roughly from 40°20'N to 32°30'N and from 11°30'W to 17°40'W. It displays a NNE-SSW-trending alignment of mounts, which is surrounded by scattered seamounts (Fig. 1a). The northern limit of the rise is the c. 2500 m high Tore seamount, which rims an elliptical (120 km × 90 km) depression lying at 5000 m below sea level. The scattered seamounts occurring in the vicinity of the main alignment are the Bikini Bottom seamount, located to the NNW of Tore; Torillon, around 100 km to the WSW of Tore; and the Unicorn and Seine seamounts (Fig. 1b). Most of the seamounts are at least 30 km in diameter (Seine reaches 48 km) with a height of over 3000 m above the sea floor. Considering the dimensions of the Tore-Madeira Rise (1000 km long by 50 km wide, and 2 km high), the estimated volume of magma emitted could reach 10⁵ km³. The Tore-Madeira Rise has been considered as one of the main structures in the northern central Atlantic Ocean.

The Azores-Gibraltar Fracture Zone, separating the Eurasian and African plates, is an important Atlantic transform fault, which splits into three branches towards the Tore seamounts, Gorringe Bank, and Ampère-Coral Patch seamounts (e.g. Laughton *et al.* 1975; Jiménez-Munt *et al.* 2001; Fig. 1). Since Oligocene times, movements along the branches of the Azores-Gibraltar Fracture Zone seem to be transpressive, with a slight dextral component (Le Gall *et al.* 1997; J. Malod, pers. comm.), whereas movements were very limited from Early Jurassic to Oligocene times (Olivet 1996).

Seamounts to the north of the Azores-Gibraltar Fracture Zone lie along the J anomaly, which is the first magnetic anomaly created by the Atlantic spreading centre along the Iberia margin (M0 to M3 magnetic anomalies, 125–130 Ma; Gradstein *et al.* 2004; Fig. 1b). This anomaly corresponds to the boundary between true oceanic crust and a transitional domain composed of continental lithosphere peridotites exhumed during rifting and stretching of the Iberian margin (Boillot *et al.* 1989; Beslier *et al.* 1993; Girardeau *et al.* 1998). To the south beyond the central branch of the Azores-Gibraltar Fracture Zone, magnetic anomalies older than J seem to be present in the Seine Abyssal Plain (Roest *et al.* 1992), implying that some seamounts of the Tore-Madeira Rise could be emplaced onto oceanic lithosphere.

The geodynamical process leading to the construction of the Tore-Madeira Rise is still debated. Several explanations have been put forward, such as a hotspot probably active coevally with spreading (Tucholke & Ludwig 1982; Pierce & Barton 1991; Geldmacher *et al.* 2006; Merle *et al.* 2006), accretion-related off-axis magmatic activity (Jagoutz *et al.* 2007) or shallow mantle upwelling (Geldmacher *et al.* 2008). It has been proposed that the Tore-Madeira Rise was built up by two magmatic phases, the earliest during Cretaceous times (Merle *et al.* 2006) forming the basement of the rise, capped by late Tertiary to recent magmas (Geldmacher *et al.* 2006). The magmas may have been focused along the lithospheric discontinuities, which facilitated magma ascent through the lithosphere (van der Linden 1979; Geldmacher *et al.* 2006; Merle *et al.* 2006).

In the neighbouring region of the Tore-Madeira Rise (within

<1000 km; Fig. 1b), widespread alkaline magmatism occurs on the Ormonde seamount (62–68 Ma, ⁴⁰Ar/³⁹Ar ages on both matrix and minerals; Féraud *et al.* 1982, 1986), the Ampère-Coral Patch seamounts (c. 31 Ma, ⁴⁰Ar/³⁹Ar ages on whole-rock samples; Geldmacher *et al.* 2000) and on the continent (Serra de Monchique complex: 69–70 Ma; Sines complex: 73–77 Ma; Sintra complex: 80–83 Ma; Ribamar intrusion: c. 88 Ma; U-Pb ages on titanite and zircon; Grange *et al.* 2007). All these magmatic occurrences as well as Tore-Madeira Rise samples display ocean island basalt (OIB)-like geochemical characteristics; in particular, a positive Nb anomaly (Bernard-Griffiths *et al.* 1997; Geldmacher *et al.* 2006, 2008; Merle 2006). The isotopic characteristics of the Tore-Madeira Rise rocks and the surrounding alkaline occurrences are interpreted to be derived from the same OIB-type (mantle plume-like) source (Geldmacher & Hoernle 2000; Geldmacher *et al.* 2006; Merle *et al.* 2006). However, isotopic heterogeneities exist both between the seamounts and within a single edifice. The isotopic compositions of the lavas from the Godzilla seamount (Fig. 1) are clearly distinct from those of the other seamounts of the Tore-Madeira Rise (see Geldmacher *et al.* 2006, 2008). The Cretaceous lavas display different isotopic characteristics from the Late Cenozoic volcanic rocks (Geldmacher *et al.* 2006) and a significant variation of the isotopic signature is observed among the Seine seamount samples (Geldmacher *et al.* 2005).

Previous geochronological data from the Tore-Madeira Rise seamounts

As already emphasized, two datasets of contrasting ages were obtained on lavas along the whole rise (see Fig. 1b). All the previous ⁴⁰Ar/³⁹Ar measurements were performed using the Taylor Creek Rhyolite sanidine standard (TCRs), for which the researchers adopted an age of 27.92 Ma (Dalrymple & Duffield 1988; Duffield & Dalrymple 1990). All the previous geochronological data from the Tore-Madeira Rise are given in the supplementary material, together with analytical methods, rock types, material dated, ages with errors and standards used.

The lavas from the northern seamounts (Tore, Sponge Bob and Ashton) have been dated by the U-Pb method on titanite and zircon from 80.5 ± 0.9 Ma to 104.4 ± 1.4 Ma (Merle *et al.* 2006).

In the central part of the rise, evolved lavas from Gago Coutinho seamount (also named Teresa by Geldmacher *et al.* 2006) have been dated between 92.3 ± 3.8 Ma and 94.5 ± 0.4 Ma (Geldmacher *et al.* 2006; Merle *et al.* 2006). Basic rocks dredged on Josephine North (Fig. 1) have been dated by ⁴⁰Ar/³⁹Ar on whole-rock between 0.5 ± 0.1 Ma and 7.4 ± 0.5 Ma (Geldmacher *et al.* 2006) and those from the Josephine seamount have yielded ages between 8.2 ± 0.2 Ma and 15.8 ± 0.9 Ma (Wendt *et al.* 1976; Geldmacher *et al.* 2006). The basaltic rocks dredged on the Jo Sister seamount (also named Erik by Geldmacher *et al.* 2006), dated by ⁴⁰Ar/³⁹Ar on matrix, have yielded an age of 3.62 ± 0.32 Ma (Geldmacher *et al.* 2006) whereas the dredged evolved lavas have been dated between 86.5 ± 3.4 Ma and 89.3 ± 2.3 Ma by U-Pb on titanite (Merle *et al.* 2006).

Seamounts in the southern part of the Tore-Madeira Rise have been dated by ⁴⁰Ar/³⁹Ar, except the altered basaltic samples dredged on the Lion seamount, estimated by a foraminifera fauna at c. 80 Ma (Geldmacher *et al.* 2006). The basaltic lavas dredged on the Dragon seamount are dated between 3.9 ± 0.3 Ma and 1.18 ± 0.18 Ma (Geldmacher *et al.* 2006), and those dredged on the Seine, Unicorn and Godzilla seamounts have yielded

$^{40}\text{Ar}/^{39}\text{Ar}$ ages of 21.7 ± 0.2 Ma, 27.4 ± 2.4 Ma and around 66 Ma, respectively (Geldmacher *et al.* 2005, 2008).

The $^{40}\text{Ar}/^{39}\text{Ar}$ ages of whole-rock and separated plagioclase grains from the Madeira archipelago lavas range from 14.3 ± 0.2 Ma to 0.2 ± 0.1 Ma (Geldmacher *et al.* 2000, and references therein).

Analytical procedures

Mineral and whole-rock analyses

Electron microprobe analysis (EMPA) of magmatic phases was performed with a Cameca SX50 automated electron microprobe (Microsonde Ouest, Brest), using an acceleration voltage of 15 kV, a beam current of 15 nA, a counting time of 6 s and correction by the ZAF method. Concentrations of <0.3 wt% are considered qualitative. Major and trace element analyses were carried out by inductively coupled plasma atomic emission spectrometry (ICP-AES) and inductively coupled plasma mass spectrometry (ICP-MS) at the University of Brest and the CRPG at Nancy (following analytical procedures of Govindaraju & Mevelle (1987) and Carignan *et al.* (2001)). For the samples analysed at the University of Brest, details of the analytical methods and sample preparation have been given by Cotten *et al.* (1995).

$^{40}\text{Ar}/^{39}\text{Ar}$ geochronology

Plagioclase grains were separated from either the 100–200 μm or the 200–315 μm fraction using a Frantz isodynamic magnetic separator. The plagioclase grains recovered in the 2 A non-magnetic fraction were selected by hand-picking under a binocular microscope. The amphibole and biotite grains were separated using heavy liquids (CH_3Br_3 and CH_2I_2 , respectively) and were hand-picked using a binocular microscope. Plagioclase and amphibole were further leached using diluted HF (2N) for 5 min and thoroughly rinsed in distilled water. The samples were loaded into aluminium discs along with the Fish Canyon sanidine standard (FCs = 28.03 ± 0.08 Ma; Jourdan & Renne 2007) and irradiated for 10 h in the CLICIT facility at the TRIGA reactor, Oregon.

$^{40}\text{Ar}/^{39}\text{Ar}$ analyses were performed at the Berkeley Geochronology Center. Both single-grain and multi-grain aliquots were degassed by step heating using a CO_2 laser with focused lenses and beam-integrator lens, respectively. Ar isotopes were measured in static mode using a MAP 215-50 mass spectrometer. Mass discrimination was monitored several times a day and yielded a mean D-value of 1.00633 ± 0.00175 per a.m.u. based on a power-law correction. Blank measurements were generally obtained after every three sample runs. J-values were calculated as the mean and standard deviation of the wells bracketing the samples (see, e.g. Jourdan & Renne 2007) and yielded a value of 0.002630 ± 0.000014 (0.54%). Ages were calculated using the

decay constants recommended by Steiger & Jäger (1977), and step-heating details, together with Ar isotopic data corrected for blank, mass discrimination and radioactive decay, are given in the supplementary material (errors are given at 1σ level).

Our criteria for the determination of plateau ages are as follows: plateaus must include at least 70% of the ^{39}Ar released; they should be distributed over a minimum of three consecutive steps indistinguishable at 95% confidence level; they should satisfy a probability of fit of at least 0.05. Plateau ages are given at the 2σ level and are calculated using the mean of all the plateau steps, each weighted by the inverse variance of its analytical error. Integrated ages (2σ) are calculated using the total gas released for each Ar isotope. Inverse isochrons include the maximum number of consecutive steps with a probability of fit ≥ 0.05 . The uncertainties on the $^{40}\text{Ar}^*/^{39}\text{Ar}^*$ ratios of the monitor are included in the calculation of the plateau age uncertainties but not the errors on the age of the monitor and on the decay constants (internal errors only).

Results

This paper presents new ages for four samples dredged during the Tore–Madeira Rise cruise. They come from the Bikini Bottom, Torillon and Seine seamounts, located off the main trend of the Tore–Madeira Rise. In addition, biotites from a trachyte dredged on the Ashton seamount have also been dated to test a previous U–Pb age obtained on possibly inherited zircon grains (Merle *et al.* 2006) given that the Ashton seamount is located on the very edge of the continental lithosphere (Fig. 1b). Coordinates and water depths of sampling sites are given in Table 1.

Petrological notes

The EMPA data for mineral phases from the Tore–Madeira Rise samples are available in the supplementary material. All but one sample (Ashton trachyte; TMD 14-9) display evidence of seawater interaction occurring as carbonate, Fe–Mn hydroxides, brown–green clays and rare zeolites (K-zeolites: phillipsite and erionite) invading the groundmass and filling cracks and vesicles. However, it is worth noting that the phenocrysts are usually well preserved. The sample from Bikini Bottom (TMD 2-1) is a slightly altered basaltic trachyandesite containing well-preserved phenocrysts of abundant (30% modal) plagioclase (2–8 mm in size), rare clinopyroxene (<1 mm), Fe–Ti oxides and iddingsitized olivine (1–2 mm in size). The groundmass is composed of feldspar laths and grains of Fe–Ti oxides. The basic sample from the Torillon seamount (TMD 12b-1) contains phenocrysts of iddingsitized olivine and scarce well-preserved plagioclase (>10 mm size). The groundmass is composed of feldspar laths, grains of Fe–Ti oxides and altered rare olivine grains. The TMD 14-9 sample is a fresh highly porphyritic trachyte containing K-feldspars, subordinate biotite, and sparse clinopyroxene and Fe–Ti oxide grains. The groundmass is composed of the same

Table 1. Sampling sites and dredging operations parameters

Seamount	Dredge	Beginning	End	Maximum depth (m)	Minimum depth (m)	Distance covered (m)	Height covered (m)
Bikini Bottom	TMD 2	40°03.74'N, 14°24.50'W	40°07.90'N, 13°39.31'W	3514	2234	4074	1280
Torillon	TMD 12b	39°10.63'N, 15°12.81'W	39°11.75'N, 15°10.51'W	3884	3126	2960	758
Ashton	TMD 14	38°01.29'N, 13°23.71'W	38°01.54'N, 13°22.66'W	2803	2395	3900	408
Seine	TMD 21	33°50.83'N, 14°15.71'W	33°51.18'N, 14°17.22'W	1975	1677	1020	298

minerals (Merle *et al.* 2006). A detailed description of this sample has been given by Merle *et al.* (2006). Sample TMD 21-2 from the Seine seamount is a basanite containing phenocrysts of clinopyroxene (*c.* 5% modal), iddingsitized olivine (*c.* 5% modal), microphenocrysts of Fe-Ti oxides and subordinate brown amphibole (*c.* 1% modal) up to 4 mm in size. The groundmass is composed of feldspar laths, clinopyroxene, Fe-Ti oxide grains and olivine.

Major and trace elements

The whole-rock analyses of samples TMD 2-1, TMD 12b-1 and TMD 21-2 are given in Table 2. Sample TMD 14-9 has been described by Merle *et al.* (2006). It is a very well-preserved trachyte (loss on ignition (LOI): 2 wt%) whose incompatible element patterns display Ba, Sr and Ti negative anomalies as a

result of feldspar and Fe-Ti oxide fractionation. Apart from this sample, the others show moderate to high loss on ignition (LOI = 3.0–11.0 wt%). Samples TMD 2-1 and TMD 21-2, with LOI <4.5 wt%, can be more confidently plotted in the total alkalis–silica (TAS) diagram (not shown) and plot in the field of basaltic trachyandesite and basanite, respectively. However, this result should be considered with caution, as seawater alteration has probably modified the chemistry of the rocks, especially the potassium content (see discussion below). All the samples described here display steep multi-element patterns with significant enrichment in the most incompatible elements (light rare earth elements, large ion lithophile elements, Th, Nb), typical of OIB-type lavas (Fig. 2). In particular, sample TMD 21-2 displays a positive Nb anomaly and its pattern shows similarities to the previously described Seine samples (Geldmacher *et al.* 2005; Fig. 2). Generally, positive K and P anomalies such as observed in the pattern of sample TMD 12b-1 (Fig. 2) could correspond to feldspar and apatite mineral accumulation, but as neither of these minerals is observed these anomalies are more probably related to seawater interaction. The data points from the studied samples plot in the field of the previously analysed Tore-Madeira Rise volcanic rocks in the Zr/Y v. Th/Nb diagram (Fig. 3), suggesting that these rocks belong to the same magmatic events as those described by Geldmacher *et al.* (2005, 2006).

Table 2. Major and trace element analyses of Tore-Madeira Rise samples

Sample:	TMD 2-1	TMD 12b-1	TMD 21-2
Petrographic type:	Basaltic trachyandesite	Basalt	Basanite
<i>wt%</i>			
SiO ₂	48.50	40.22	41.10
TiO ₂	3.09	3.22	3.84
Al ₂ O ₃	19.20	18.21	13.50
Fe ₂ O ₃ *	10.86	13.38	14.10
MnO	0.20	0.16	0.15
MgO	0.93	1.29	5.75
CaO	6.40	5.58	11.25
NaO	3.79	2.66	2.62
K ₂ O	2.84	2.81	1.78
P ₂ O ₅	0.81	1.35	1.02
LOI	3.03	11.04	4.39
Total	99.65	99.92	99.50
<i>ppm</i>			
Rb	34.0	22.3	36.0
Sr	770	503	645
Ba	295	300	425
Sc	15.8	—	26.0
V	220.0	276	368.0
Cr	17.0	93.8	272.0
Co	17.00	33.4	34.50
Ni	9.5	66	112.0
Y	34.5	35.9	40.0
Zr	372	298	322
Nb	53.5	56.9	68.0
La	40.5	46	58.5
Ce	92.0	93.6	110.0
Nd	52.0	46.6	61.0
Sm	11.3	9.92	11.6
Eu	3.60	3.02	3.33
Gd	9.50	8.7	10.40
Dy	7.20	6.24	7.25
Er	3.10	2.88	3.40
Yb	2.41	2.61	2.36
Th	4.30	5.51	6.90

Major and trace elements of samples TMD 2-1 and TMD 21-2 were obtained by ICP-AES at Brest (Université de Bretagne Occidentale) following the method described by Cotten *et al.* (1995). Relative standard deviations are <2% for major elements, Rb and Sr, and <5% for other trace elements. Analyses of sample TMD 12b-1 were performed at Nancy (SARM, CRPG-CNRS). Major elements were obtained by ICP-AES following the method described by Govindaraju & Mevelle (1987) and trace elements by ICP-MS following the method of Carignan *et al.* (2001). Analytical precision is 1–5% for major elements, except for MnO, MgO, Ca₂O and P₂O₅ (10%). For trace elements, analytical precision is in the range 5–10% for abundances >50 ppm, 5–15% between 50 and 10 ppm, 5–20% between 10 and 1 ppm, and 5–25% for abundances <1 ppm. LOI, loss on ignition. BE-N, AC-E, PM-S and WS-E were used as standards.

*Total iron expressed as Fe₂O₃.

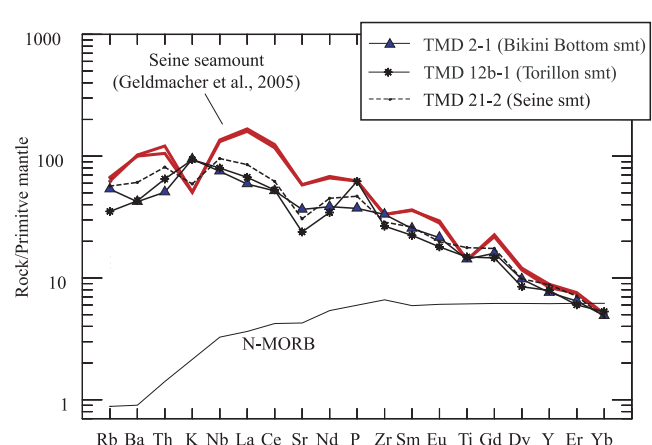


Fig. 2. Primitive mantle-normalized trace elements patterns. Normalization values from Sun & McDonough (1989). Average N-MORB pattern from Sun & McDonough (1989). Pattern of previously studied samples from the Seine seamount after Geldmacher *et al.* (2005).

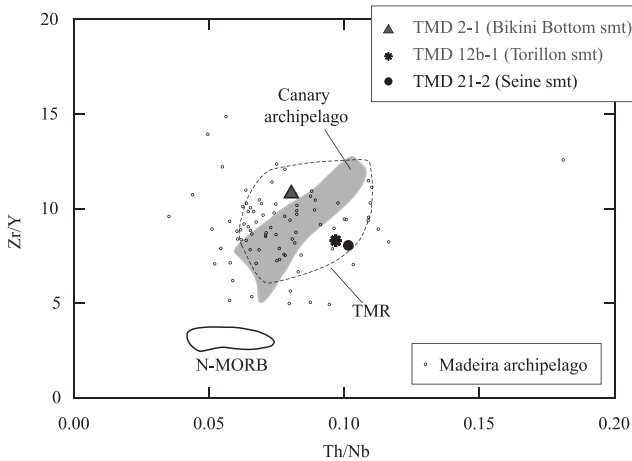


Fig. 3. Zr/Y v. Th/Nb plot for the data points of the Tore–Madeira Rise samples. Fields of Canary archipelago and Madeira archipelago basalts and Atlantic N-MORBs from Georoc and PetDB databases. Field of previously studied Tore–Madeira Rise samples from Geldmacher *et al.* (2005, 2006, 2008).

but displays only slight perturbation (Fig. 4b). EMPA yielded a mean Ca/K value well within error of the Ca/K ratio derived from the Ar experiments and suggested only negligible perturbation. Nevertheless, sample TMD 12b-1 failed to provide a plateau age, and based on steps associated with the highest Ca/K ratio can be interpreted only as a minimum age of c. 60 Ma (Fig. 4b).

Two statistically indistinguishable biotite plateau ages have been obtained for sample TMD 14-9 (Ashton). We obtained an age of 97.4 ± 1.1 Ma (MSWD = 1.07; $P = 0.38$) on a single biotite grain and 97.8 ± 1.1 Ma (MSWD = 0.8; $P = 0.78$) on a multi-grain aliquot (Fig. 4c and d). These two $^{40}\text{Ar}/^{39}\text{Ar}$ ages are indistinguishable from the U–Pb age at 96.30 ± 1 Ma obtained by Merle *et al.* (2006) on titanite and zircon fractions from the same sample. $^{40}\text{Ar}/^{39}\text{Ar}$ dating of amphibole crystals from sample TMD 21-1 from the Seine seamount yielded three indistinguishable plateau ages at 24.4 ± 0.4 Ma (MSWD = 0.23; $P = 1.0$) and 24.4 ± 0.5 Ma (MSWD = 1.24; $P = 0.26$) for the single-grain measurements (Fig. 4e and f) and 24.8 ± 0.3 Ma (MSWD = 1.72; $P = 0.13$) for the multi-grain aliquot measurements (Fig. 4g). These ages are slightly older than the previous age at 22.0 ± 0.2 Ma (recalculated using an age of 28.34 Ma for the TCs standard; Renne *et al.* 1998) obtained on groundmass by Geldmacher *et al.* (2005). For the two first aliquots, the $^{40}\text{Ar}/^{36}\text{Ar}$ intercept values on the inverse isochron diagrams are similar to the atmospheric ratio. The third aliquot displays a value higher than the atmospheric ratio and a much greater scatter of the data, suggesting that some heterogeneously distributed excess $^{40}\text{Ar}^*$ might be present (Figs 4 and 5). The third aliquot is therefore not included in the mean age calculation of TMD 21-1 (Table 4).

Discussion

Significance of the new $^{40}\text{Ar}/^{39}\text{Ar}$ ages

The activity on the northernmost Bikini Bottom seamount estimated at >90 Ma may be related to the Cretaceous phase already indicated by previous studies (Geldmacher *et al.* 2006; Merle *et al.* 2006) but the poor quality of the age data prevents us from further speculation. Similar poor data quality for the Torillon seamount suggests magmatic activity at ≥ 60 Ma in this

General characteristics	Mineral	Laboratory number	Plateau characteristics			Isochron characteristics							
			Integrated age (Ma, $\pm 2\sigma$)	Plateau age (Ma, $\pm 2\sigma$)	Total ^{39}Ar released (%)	MSWD	P	Mean age* (Ma, $\pm 2\sigma$)	n	$^{40}\text{Ar}/^{36}\text{Ar}$ intercept ($\pm 1\sigma$)	P		
TMD 14-9	Biotite	58375-02	97.5 \pm 1.2	97.4 \pm 1.2	100	1.2	0.28	97.7 \pm 1.2	—	98.0 \pm 1.2	20	294.2 \pm 1.7	0.82
		58375-04	97.7 \pm 1.7	97.8 \pm 1.1	100	0.80	0.71	—	—	—	—	—	—
TMD 12b-1	Plagioclase	58376-01	51.9 \pm 0.7	—	—	—	—	—	—	—	—	—	—
TMD 2-1	Plagioclase	58372-01	60.0 \pm 0.7	—	—	—	—	—	—	—	—	—	—
TMD 2-1		58373-01	23.9 \pm 0.9	24.4 \pm 0.4	100	0.3	0.98	24.4 \pm 0.4	16	24.4 \pm 0.4	16	292 \pm 3	0.35
TMD 21-2	Amphibole	58375-02	25.3 \pm 0.8	24.4 \pm 0.5	100	1.2	0.26	—	(excess $^{40}\text{Ar}^*$)?	23.4 \pm 0.4	13	551 \pm 19	1.7
		58373-03	25.6 \pm 0.3	24.8 \pm 0.3	71	1.7	0.13	—	—	—	—	—	—

* Mini-plateau ages. Summary table indicating integrated, plateau or mini-plateau and isochron ages for the TMR samples. MSWD for plateau and isochron, percentage of ^{39}Ar degassed used in the plateau calculation, number of analyses included in the isochron, and $^{40}\text{Ar}/^{36}\text{Ar}$ intercept are indicated. Plateau age calculated using trapped $^{40}\text{Ar}/^{36}\text{Ar}$ is indicated. Analytical uncertainties on the ages are quoted at 2σ confidence levels and at 1σ for the $^{40}\text{Ar}/^{36}\text{Ar}$ intercept. Bold data indicate the accepted age for a given sample.

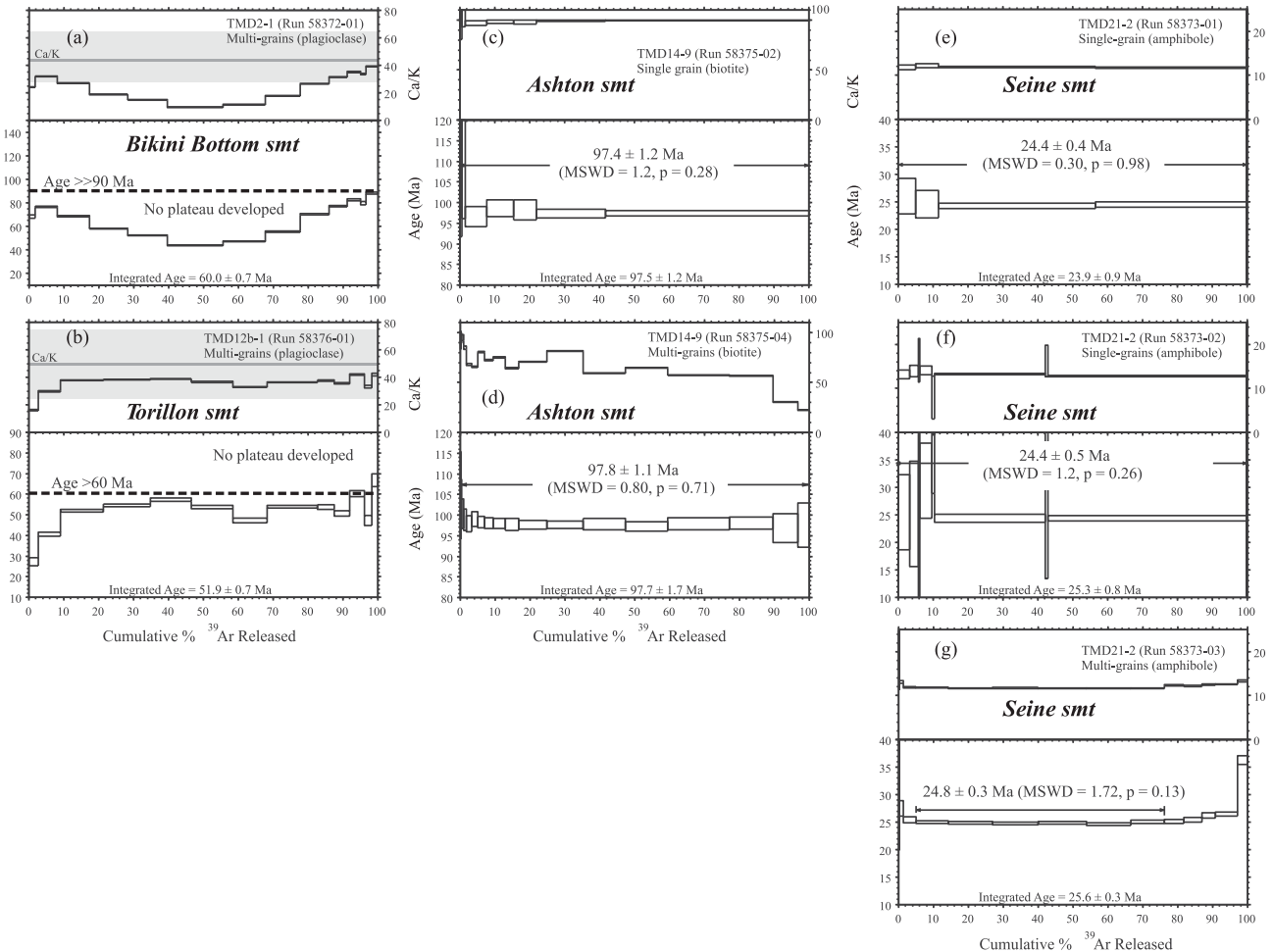


Fig. 4. Plagioclase, biotite and amphibole $^{40}\text{Ar}/^{39}\text{Ar}$ apparent age and related Ca/K ratio spectra of the plagioclase separates v. cumulative percentage of ^{39}Ar released. Errors on plateau ($>70\% \text{ }^{39}\text{Ar}$ released) and mini-plateau (50–70% ^{39}Ar released) ages are quoted at 2σ and do not include systematic errors (i.e. uncertainties on the age of the monitor and on the decay constant). MSWD and probability are indicated. Ages in bold represent the most reliable ages for each sample.

locality. The $^{40}\text{Ar}/^{39}\text{Ar}$ biotite ages obtained from the trachyte TMD 14-9 sampled on the Ashton seamount are indistinguishable from the U–Pb age (96.3 ± 1.0 Ma, Merle *et al.* 2006) yielded by titanite and zircon fractions extracted from the same rock. This implies that the zircon grains extracted from this alkaline lava have a magmatic origin as proposed by Merle *et al.* (2006) and are not inherited from the continental lithosphere. Nevertheless, this does not exclude the occurrence of the continental lithosphere beneath the seamount, as Ashton is located at its very edge (Fig. 1b). Considering that the $^{40}\text{Ar}/^{39}\text{Ar}$ ages only marginally allow the expected *c.* 1% intercalibration bias with U–Pb ages within errors (Min *et al.* 2000; Mundil *et al.* 2006), the data also seem to indicate minimal pre-eruptive magma residence times (e.g. Simon *et al.* 2008). Our new ages obtained on the lavas from the Seine seamount (24.4 ± 0.5 Ma) are reliable for sub-million year high-precision geochronology and confirm the occurrence of magmatic activity during the Late Oligocene.

Tore-Madeira Rise and surroundings age reliability

Precise and accurate radio-isotopic data play a critical role in obtaining the timing, duration, and rates of magmatic processes

occurring on the Tore-Madeira Rise. The new data given here confirm a long-lasting and geographically extended magmatic activity during the Cretaceous and the early Palaeocene. However, any geodynamical discussion must be based on a reliable age database and must exclude statistically and geologically untrustworthy measurements. It was not possible to calculate the alteration index (AI, Baksi 2007) to test the accuracy of the $^{40}\text{Ar}/^{39}\text{Ar}$ measurements, as the detailed $^{40}\text{Ar}/^{39}\text{Ar}$ dataset (% ^{39}Ar released, $^{40}\text{Ar}^*/^{39}\text{Ar}_K$, apparent age for each step) of the previously dated samples (Geldmacher *et al.* 2005, 2006, 2008) was not published.

$^{40}\text{Ar}/^{39}\text{Ar}$ geochronology performed on whole-rock and groundmass may be an interesting alternative when K-rich phenocryst phases are absent, provided that whole-rock acid etching is performed before measurements. This technique can in some cases yield good results (e.g. Pringle *et al.* 1991). Nevertheless, it becomes increasingly clear that K–Ar and $^{40}\text{Ar}/^{39}\text{Ar}$ measurement on groundmass displays technical limitations for high-precision and accuracy geochronology (except when rocks are only a couple of million years old; e.g. Hofmann *et al.* 2000; Baksi 2007; Jourdan *et al.* 2007a). These limitations are as follows.

- (1) The freshness of the samples is untestable using the Ca/K

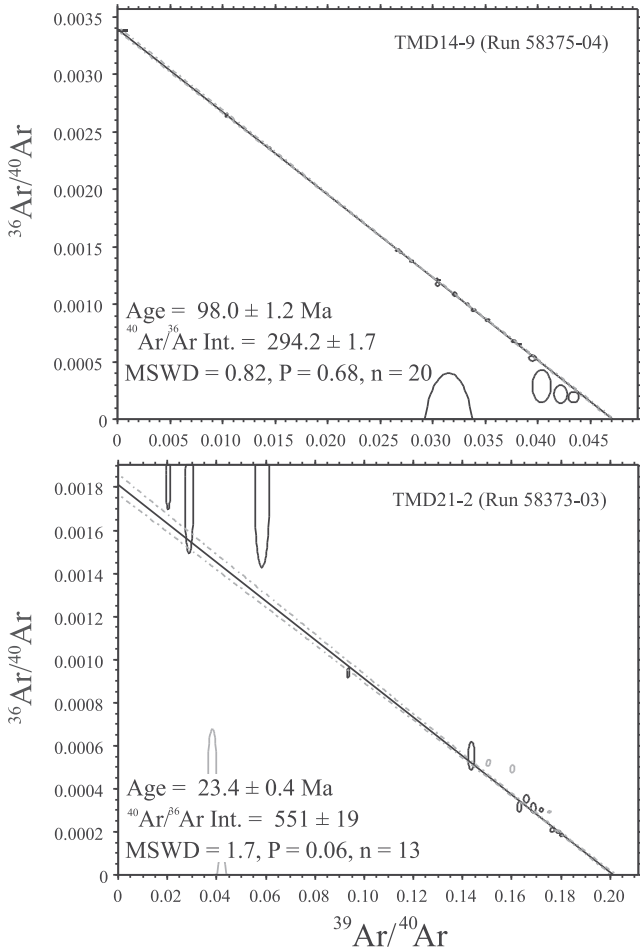


Fig. 5. Inverse correlation isochron plot of $^{36}\text{Ar}/^{40}\text{Ar}$ v. $^{39}\text{Ar}/^{40}\text{Ar}$ for two step-heated samples. MSWD and probability, and $^{40}\text{Ar}/^{36}\text{Ar}$ intercept are indicated. Excluded steps are indicated in grey.

ratio, because different minerals with different chemical compositions and activation energies will degas their Ar at various temperatures yielding complex Ca/K spectra.

(2) $^{40}\text{Ar}/^{36}\text{Ar}$ fractionation in the extraction line and sample chamber is known to yield older apparent ages (McDougall & Harrison 1999).

(3) The existence of fast neutron activation-induced ^{39}Ar and ^{37}Ar recoil and possible ejection (Turner & Cadogan 1974) creates significant ^{39}Ar and ^{37}Ar loss at the edge of a grain. In most cases, this will result in apparent older age because of the dominant effect of the ^{39}Ar loss (e.g. Onstott *et al.* 1995; Paine *et al.* 2006; Jourdan *et al.* 2007b), but for samples with high Ca/K and significant atmospheric contamination the recoil of ^{37}Ar may produce younger apparent ages because of recoil fractionation of Ca-derived ^{37}Ar and ^{36}Ar (e.g. Jourdan *et al.* 2007b). The recoil phenomenon may also involve a complex redistribution of the daughter atoms in different lattice sites.

Basaltic groundmass samples are generally enriched in potassium relative to the high Ca/K plagioclase phases, yielding age with better precision compared with mineral separates (as a result of low Ca interference correction and the larger Ar-ion beam). This is evidenced by our amphibole age (24.4 ± 0.4 Ma) from the Seine seamount (Figs 1 and 4), which is less precise than the earlier matrix age (22.0 ± 0.2 Ma; Geldmacher *et al.*

2005). However, it has been shown that in most cases for rocks older than a couple of million years, the accuracy of the age obtained on the groundmass may be questionable (e.g. Hofmann *et al.* 2000; Jourdan *et al.* 2007a). Here, we suggest that the age of c. 22 Ma obtained by Geldmacher *et al.* (2005) is c. 2 Ma younger because of the occurrence of cryptic alteration phases in the groundmass.

Furthermore, in basaltic rocks, the fine-grained groundmass carries most of the potassium (Mankinen & Dalrymple 1972) and thus renders the K–Ar and $^{40}\text{Ar}/^{39}\text{Ar}$ measurements largely dependent on the mobility of potassium during any geological event. This limitation is exacerbated for dredged rocks because they are strongly suspected to have undergone severe and pervasive rock–seawater interaction for millions of years, which has led to systematic chemical effects on the rock chemistry. These effects are illustrated by the geochemical composition of the Tore–Madeira Rise samples, in which the pervasive seawater–rock interaction led to crystallization of potassium-rich secondary phases such as zeolites (erionites, phillipsites), clay minerals (celadonite–dioctahedral clays mixture) and carbonates in voids and groundmass of the rocks (Fig. 6; Merle 2006). The crystallization of these alteration phases (brownstone facies, Cann 1979) implies an overall hydration of the samples and the mobility of alkaline elements such as potassium (e.g. Honnorez 1981). The potassium behaviour can be monitored in the Tore–Madeira Rise samples by a K_2O v. LOI diagram in which the LOI values can be used as a proxy for the alteration index. For a LOI value higher than 4.5%, the K_2O content of the Tore–Madeira Rise rocks displays a positive co-variation with increasing LOI (Fig. 7). This co-variation trend has already been found in submarine samples and interpreted as a potassium accumulation from seawater in the samples (e.g. Honnorez 1981). Therefore, the potassium content of the groundmass of Tore–Madeira Rise samples might reflect both magmatic composition and seawater interaction. The potassium mobility in basaltic rocks related to seawater interaction might occur even for LOI values lower than 2% (Caroff *et al.* 1995). As illustrated by the Tore–Madeira Rise samples, the most careful selection of fresh rock fragments based on optical methods is inadequate because alteration phases are almost inevitably present (see Fig. 6). Pervasive seawater alteration may affect the chemistry of the rocks so deeply that its effects are unlikely to be removed by any acid etching, thus compromising groundmass K–Ar and $^{40}\text{Ar}/^{39}\text{Ar}$ analyses.

Filtered age database and standard recalibration

To produce a robust age database to support the geodynamical discussion, $^{40}\text{Ar}/^{39}\text{Ar}$ total fusion measurements as well as K–Ar ages are rejected, as there is no means to check the validity of the age with internal criteria (e.g. age spectrum). Because our new step-heating Ar–Ar amphibole age from the Seine seamount is close to the previously published step-heating Ar–Ar matrix age, we consider that the step-heating matrix $^{40}\text{Ar}/^{39}\text{Ar}$ ages, although unreliable for high-precision geochronology, might have a geological significance and they are taken into consideration. We take into account only the $^{40}\text{Ar}/^{39}\text{Ar}$ plateaux (>70% of ^{39}Ar released) and mini-plateaux (between 50 and 70% of ^{39}Ar released). $^{40}\text{Ar}/^{39}\text{Ar}$ step-heating measurements having less than 50% of ^{39}Ar are considered as invalid (e.g. Baksi 1999; McDougall & Harrison 1999) and are rejected.

U–Pb and $^{40}\text{Ar}/^{39}\text{Ar}$ age data were tested using goodness of fit parameters such as the mean squared weighted deviation (MSWD) and probability of fit (P). These parameters were

Table 4. Filtered geochronological data from Tore-Madeira Rise and surrounding area

Reference	Sample name	Location	Phase analysed	Age (Ma)	Error (2σ) (Ma)	MSWD	P
This study	TMD 2-1	Bikini Bottom	plag	c. 90			
Merle <i>et al.</i> 2006	TMD 10c-1	Tore N	titanite	88.30	3.30	0.34	0.89
Merle <i>et al.</i> 2006	TMD 10c-2	Tore N	titanite	88.30	3.80	1.01	0.39
Merle <i>et al.</i> 2006	TMD 3b-2	Tore NW	titanite + zrc	80.48	0.90	0.86	0.54
This study	TMD 12b-1	Torillon	plag	c. 60			
Merle <i>et al.</i> 2006	TMD 4-3	Sponge Bob	titanite + zrc	102.77	0.71	0.38	0.91
Merle <i>et al.</i> 2006	TMD 14-9	Ashton	titanite + zrc	96.30	1.00	0.60	0.81
This study	TMD 14-9	Ashton	biot	97.40	1.20	1.20	0.28
This study	TMD 14-9	Ashton	biot	97.80	1.10	0.80	0.71
Merle <i>et al.</i> 2006	TMD 15-5	Gago Coutinho	titanite	92.30	3.70	0.25	0.91
Geldmacher <i>et al.</i> 2006	403 DR-5	Gago Coutinho	hbl	94.90	0.44	2.00	0.05
Geldmacher <i>et al.</i> 2006	399 DR-1	Josephine N (Pico Pia)	matrix	0.53	0.45	0.60	0.83
Geldmacher <i>et al.</i> 2006	406 DR-7	Josephine N (Toblerone Ridge)	gls	1.42	0.61	0.70	0.74
Geldmacher <i>et al.</i> 2006	406 DR-7	Josephine N (Toblerone Ridge)	matrix	0.47	0.13	1.50	0.07
Geldmacher <i>et al.</i> 2006	407 DR-4	Josephine N (Pico Julia)	matrix	7.09	0.72	0.70	0.74
Geldmacher <i>et al.</i> 2006	407 DR-4	Josephine N (Pico Julia)	matrix	7.50	0.47	0.60	0.80
Geldmacher <i>et al.</i> 2006	408 DR-2	Josephine	matrix	16.08	0.87	1.00	0.45
Geldmacher <i>et al.</i> 2006	408 DR-2	Josephine	matrix	13.83	0.65	1.40	0.14
Geldmacher <i>et al.</i> 2006	409 DR-1	Josephine	matrix	11.75	0.73	1.30	0.22
Geldmacher <i>et al.</i> 2006	409 DR-1	Josephine	matrix	11.59	0.65	0.50	0.89
Geldmacher <i>et al.</i> 2006	410 DR-4	Josephine	matrix	13.35	0.63	0.70	0.78
Geldmacher <i>et al.</i> 2006	410 DR-4	Josephine	matrix	13.14	0.30	1.60	0.07
Merle <i>et al.</i> 2006	TMD 16-1	Jo Sister	titanite	86.50	3.40	0.13	0.97
Merle <i>et al.</i> 2006	TMD 16-2	Jo Sister	titanite	89.30	2.30	0.76	0.64
Geldmacher <i>et al.</i> 2006	412 DR-2	Jo Sister	matrix	3.67	0.32	1.70	0.07
Geldmacher <i>et al.</i> 2006	429 DR-1	Dragon	matrix	1.45	0.43	0.90	0.57
Geldmacher <i>et al.</i> 2006	429 DR-1	Dragon	matrix	1.14	0.20	0.60	0.73
Geldmacher <i>et al.</i> 2006	431 DR-1	Dragon	matrix	4.00	0.30	1.30	0.19
Geldmacher <i>et al.</i> 2008	428 DR-1	Godzilla	biot	67.68	0.17	2.10	0.05
Geldmacher <i>et al.</i> 2005	423 DR-1	Unicorn	matrix	27.81	2.44	0.70	0.73
Geldmacher <i>et al.</i> 2005	426 DR-1	Seine	matrix	22.03	0.20	1.20	0.29
This study	TMD 21-1	Seine	plag	24.40	0.40	0.30	0.98
This study	TMD 21-1	Seine	plag	24.40	0.50	1.20	0.26
Geldmacher <i>et al.</i> 2000	DS-797-1	Ampère	matrix	31.67	0.20	1.33	0.19
Féraud <i>et al.</i> 1982	DR-06-03	Ormonde	biot	64.30	1.10	0.65	0.74
Féraud <i>et al.</i> 1982	DR-06-18	Ormonde	matrix	61.60	2.40	0.26	0.91
Féraud <i>et al.</i> 1986	CY14-2	Ormonde	biot	65.07	0.65	1.30	0.25

Bold type indicates age results reliable for sub-million year high-precision geochronology. zrc, zircon; biot, biotite; hbl, hornblende; gls, glass; plag, plagioclase.

calculated when lacking and are reported in Table 4 along with the filtered database. Interestingly, all the groundmass $^{40}\text{Ar}/^{39}\text{Ar}$ measurements fit the statistical test; however, as stated above, they still have to be considered with caution. In the following geodynamical discussion, groundmass $^{40}\text{Ar}/^{39}\text{Ar}$ data will be considered as a good estimate, but care must be taken if these data need to be used for very high-precision geochronology. All the $^{40}\text{Ar}/^{39}\text{Ar}$ data reported in Table 4 are calculated for an age of 28.03 Ma for FCs (Jourdan & Renne 2007) corresponding to an age of 28.34 Ma for TCRs.

Age and duration of magmatic activity on the Tore-Madeira Rise and in the surrounding area

Considering the available filtered Tore-Madeira Rise age database, it seems that three pulses of alkaline magmatism occurred from the end of the Early Cretaceous until the Late Palaeogene (Fig. 8). The oldest magmatic phase occurred between 103 and 80.5 Ma (magmatic phase 1) in the northern and the central part of the Tore-Madeira Rise (Fig. 1). The activity on the northernmost Bikini Bottom seamount estimated at c. 90 Ma could be related to this phase. It is also possible that this magmatic phase occurred in the southern part of the Tore-Madeira Rise, as the age of the Lion seamount has been estimated at c. 80 Ma (Geldmacher *et al.* 2006).

A second pulse of magmatism occurred on the Tore-Madeira Rise during the Late Cretaceous–Early Palaeocene (magmatic phase 2) between c. 70 and c. 60 Ma (Fig. 8). This phase could be limited to the southern part of the Tore-Madeira Rise and on the Godzilla seamount, but it could also have occurred in the northern part of the Tore-Madeira Rise, as the age of magmatic activity on the Torillon seamount has been estimated to be ≥ 60 Ma (Fig. 1). However, the existence of this phase is based on relatively few data, and additional data are desirable to constrain the timing and duration of this phase as a significant magmatic event at the Tore-Madeira Rise scale. Considering the few samples collected, we do not exclude the possibility that continuous magmatism could have occurred from 103 to c. 60 Ma with a lack of sampling for the 80–60 Ma period.

The last magmatic phase on the Tore-Madeira Rise (magmatic phase 3) began around 28 Ma in the southern part of the Tore-Madeira Rise (Seine–Unicorn area, Figs 1 and 8). The duration of this magmatic pulse relies upon a number of groundmass $^{40}\text{Ar}/^{39}\text{Ar}$ analyses, and it seems to persist until the present in the central part (Josephine area, Fig. 1) and southern part of the rise, leading to the construction of the Madeira archipelago.

Considering the magmatic activity that occurred between 88 and 69 Ma ($n = 10$) on the coast of Portugal (Grange *et al.* 2007) and at 65–62 Ma ($n = 3$) on the Ormonde seamount (Féraud *et al.* 1982, 1986; Table 4), magmas were emitted continuously

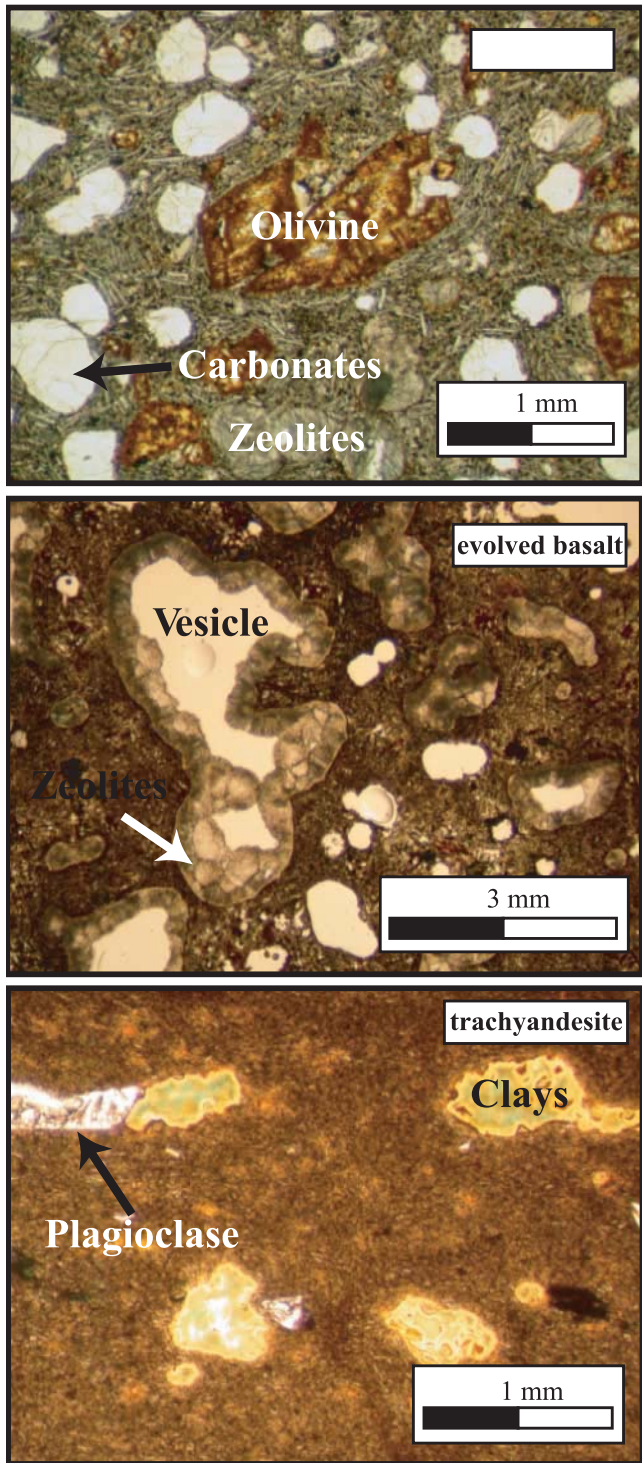


Fig. 6. Photographs of thin sections of basic and less evolved lavas dredged on the Tore–Madeira Rise. The vesicles are filled by clay minerals, zeolites and carbonates. The groundmass also shows overall oxidation as a result of seawater percolation.

from 103 to 62 Ma in the northern central Atlantic (Fig. 1). A U–Pb age of 77 Ma was obtained on a diorite from Ormonde (Schäfer *et al.* 2000), which is significantly older than the numerous previous $^{40}\text{Ar}/^{39}\text{Ar}$ ages (Féraud *et al.* 1982, 1986). This sample was collected on the top of the Ormonde seamount

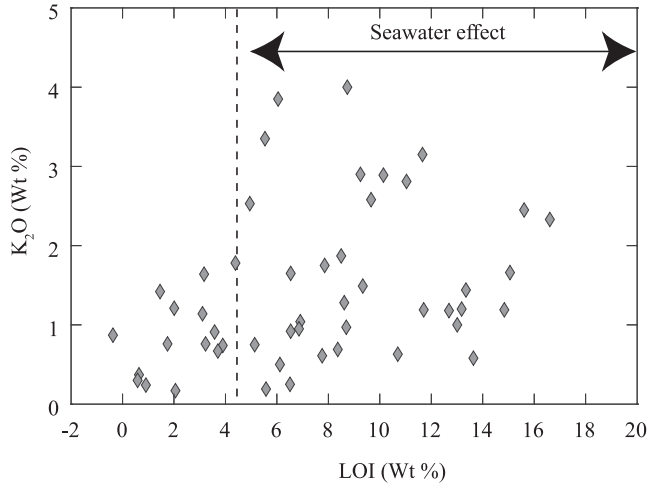


Fig. 7. Variation of potassium content as function of seawater alteration expressed as LOI (loss on ignition). The discrepancy observed for LOI higher than 4.5% is related to potassium mobility.

among dropstones of various continental petrographic types (Schäfer *et al.* 2000) and displays geochemical characteristics (similar REE and multi-element patterns, same initial Hf isotopic composition) and age (within uncertainties) similar to the diorites of the Sines complex described by Grange *et al.* (2007). As a consequence, this sample is most probably a dropstone from the Sines complex, not related to the alkaline activity on the Ormonde seamount. Magmatic activity might have occurred around 32 Ma on the Ampère–Coral Patch seamounts. However, this age was obtained on groundmass of a dredged sample (Geldmacher *et al.* 2000) and would require confirmation by $^{40}\text{Ar}/^{39}\text{Ar}$ on mineral separates. It emerges from this age compilation that a gap in magmatic activity occurred between around 60 and 32 Ma, at least considering the available dataset.

Refining the geodynamical model of the Tore–Madeira Rise origin

An OIB-type origin for the Tore–Madeira Rise

All the studied Tore–Madeira Rise lavas have unambiguous OIB-type geochemical characteristics. The enriched nature of the magmatism is likely to be inherited from the melting of enriched mantle domains (Geldmacher *et al.* 2005, 2006, 2008; Merle 2006). Such a geochemical signature argues for a hotspot-like nature for the origin of the Tore–Madeira Rise (Geldmacher *et al.* 2006; Merle *et al.* 2006). An OIB-type magmatism rules out any accretion-related off-axis magmatic activity (Jagoutz *et al.* 2007), as this model suggests the shallow melting of asthenosphere-like depleted mantle source. Moreover, the emplacement of the Tore–Madeira Rise seamounts postdates by at least 20 Ma the activity of the accreting centre in the region.

Considering that the Tore–Madeira Rise magmatism is volumetrically important ($c. 100 \times 10^3 \text{ km}^3$) and comparable with the Canary Archipelago magmatism ($150 \times 10^3 \text{ km}^3$), it is unlikely that it originates from shallow melting processes, such as edge-driven convection or adiabatic partial melting of magma occurring along transform faults. Furthermore, edge-driven convection would require thick cratonic lithosphere in the vicinity (King & Ritsema 2000), which has not been evidenced beneath Iberia and northwestern Africa.

During the Tore–Madeira Rise magmatic activity (103 Ma–

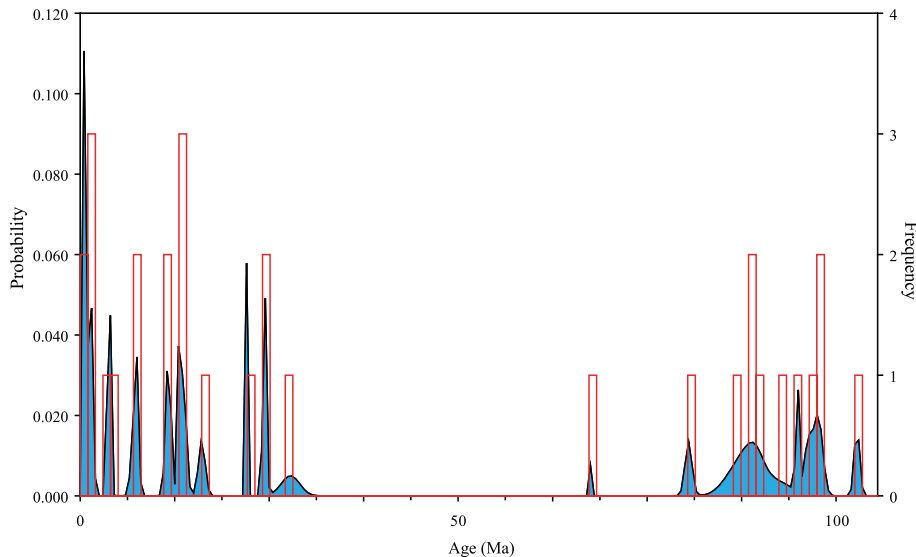


Fig. 8. Age frequency histogram (error bars not included) and probability density distribution diagram (PDD; error bars included in the curve calculation; PDD increment is 0.5 Ma) for the Tore-Madeira Rise lavas. Calculated using AgeDisplay Excel macro (Sircome 2004).

present), this part of the Iberian margin and the adjacent oceanic area underwent a major compression (e.g. Olivet 1996; Sibuet *et al.* 2004b). A strong heat source is then required to maintain a melting anomaly over the entire region for more than 100 Ma. In the case of a Hawaiian hotspot model, an increase of the ages along the seamounts chain is expected. In the Tore-Madeira Rise case, this simple feature is most probably complicated by the complex motion of the Iberian plate since the Early Cretaceous.

Problems of the previous models proposed for the Tore-Madeira Rise origin

The lack of a clear space-time correlation over the whole area (although local trends may exist) and the simultaneous magmatic activity observed at several places, such as on the Tore and Jo Sister seamounts and on the continent (Ribamar intrusion) at c. 88 Ma, seem to exclude a simple Hawaiian-type hotspot for the origin of the Tore-Madeira Rise. A recent study proposed that the Tore-Madeira Rise could have been built during two phases of magmatism, the older one of Cretaceous age being capped by a Miocene–Pleistocene phase (Geldmacher *et al.* 2006). The first phase would be due to the interaction between the Canary hotspot and the Mid-Atlantic Ridge, leading to the construction of an oceanic plateau, together with the J-Anomaly Ridge (located on the south of the Grand Banks of Newfoundland). The Tore-Madeira Rise and the J-Anomaly Ridge would constitute the basement of the second, Miocene–Pleistocene magmatic phase induced by the activity of the Madeira hotspot (Geldmacher *et al.* 2006). In spite of the advantage of providing an attractive geodynamical interpretation, this model presents some problems. (1) According to this model, the Cretaceous basement would correspond to the deepest part of the Tore-Madeira Rise and all the Miocene–Pleistocene rocks would be dredged from shallower depths. However, the dredging depth cannot be used to postulate any stratigraphic relations between Cretaceous and Miocene–Pleistocene rocks. Moreover, Cretaceous rocks were sometimes recovered at shallower depth than Miocene–Pleistocene rocks. For instance, the samples from Jo Sister (86–89 Ma) documented by Merle *et al.* (2006) were dredged between –2224 and –1960 m whereas the rocks from the eastern slope of the Josephine seamount (14–16 Ma) were dredged between –3600

and –3000 m. (2) The Tore-Madeira Rise and the J-Anomaly Ridge would be formed near the ridge axis around 125–130 Ma. Even if the possibility of an interaction with the Mid-Atlantic Ridge has been suspected for the oldest part of the Tore-Madeira Rise (Sponge Bob seamount, Merle *et al.* 2006), the magmatic activity exclusively younger than 103 Ma documented on the Tore-Madeira Rise post-dates the spreading of the Mid-Atlantic Ridge by at least 22 Ma. Moreover, the age of the emplacement of the J-Anomaly Ridge is not constrained by any isotopic age data. (3) The main problem of this model concerns the seamounts located to the north of the Azores–Gibraltar Fracture Zone, which are not taken into account in the proposed geodynamical interpretation of Geldmacher *et al.* (2006). If they are included in the proposed plate reconstruction, these seamounts would be in a position to originate from the Madeira hotspot and not from the Canary hotspot as proposed, thus contradicting the interpretation of the isotopic signatures (see Geldmacher *et al.* 2006, fig. 9 and discussion concerning the isotopic data). Therefore, if the magmatism of the northern part of the Tore-Madeira Rise is taken into account, it is necessary to consider the kinematics of the Iberian plate, which would necessarily influence the spatial distribution of the seamounts as they lie on the Iberian plate. (4) Finally, this model does not include the magmatic alkaline activity occurring on the Portugal coast between 88 and 69 Ma.

A wide, deep-rooted thermal anomaly located beneath the Azores, the Canaries and Madeira (Montelli *et al.* 2004) that could possibly have fed the Tore-Madeira Rise has also been proposed as a possible source of magmas leading to the construction of the Tore-Madeira Rise (Merle *et al.* 2006). This model, however, gives no details concerning the space-time-related emission of magmas.

New interpretation of the Tore-Madeira Rise geodynamics

Considering that three temporally and spatially distinct magmatic phases occurred on the Tore-Madeira Rise and display heterogeneous isotopic signatures (Geldmacher *et al.* 2005, 2006, 2008; this study), we suggest that short-lived, small-sized (less than 100 km in diameter) magma pulses were emitted from a thermal anomaly located under the Tore-Madeira Rise–Azores–

Madeira–Canary area. These magmatic pulses do not seem to be emitted randomly, as two local trends are observed between the Sponge Bob and Jo Sister seamounts (103–86 Ma) and between Ribamar and Serra de Monchique on the continent (88–69 Ma; Fig. 1b). The oceanic trend is oriented NE–SW, suggesting a northeastward motion of the Iberian plate. The continental trend is oriented NNW–SSE, suggesting a NNW motion of the Iberian plate. The movement of the Iberian plate since the Late Jurassic has been debated for three decades. However, a recent comprehensive geodynamical reconstruction of the Iberia plate motion and the Pyrenees orogenic formation (Sibuet *et al.* 2004b) suggests a plate motion toward the NE from 125 to around 83 Ma and toward the NNW from 83 Ma until the present (Fig. 9a). This model reconciles the onland data from the Pyrenees orogen formation and the offshore data from the Iberian margin and the Bay of Biscay. It suggests that a part of the Neo-Tethys Ocean was located between Iberia and Europe during the Late Jurassic–Early Cretaceous. This geodynamical reconstruction of the Iberian region (Sibuet *et al.* 2004b) together with our data allow us to propose a geodynamical model that involves an interaction between a thermal anomaly emitting magmatic pulses and the motion of the Iberia plate.

Stage 1, 103–88 Ma. The Iberia plate moved in a NE direction as a result of the subduction of the Neo-Tethys Ocean beneath Europe (Fig. 9a). During this period, Iberia behaved as a part of the African plate and the plate boundary was located in the Bay of Biscay and the Pyrenees. A magmatic pulse occurring during this period resulted in the age trend observed from Sponge Bob to Jo Sister (Fig. 9b), corresponding to the magmatic phase 1 on the Tore–Madeira Rise.

Stage 2, c. 88–81 Ma. The kinematics of the Iberian plate changed drastically around 83 Ma. Spreading of the Bay of Biscay ceased and subduction of the Neo-Tethys Ocean was completed (Fig. 9a). The motion of the Iberia plate shifted from SW–NE to SSE–NNE, leading to little or no movement during this stage. A period of several million years would be required for this change to take place, and it led to a heat accumulation in the mantle because of the blanketing effect of the lithosphere. As a consequence, the thermal anomaly became greater, and induced several magmatic pulses at various locations on the Tore–Madeira Rise as well as the Portugal coast. This may explain the occurrence of randomly located magmatism between 88 and 81 Ma, which ended the magmatic phase 1 on the Tore–Madeira Rise (Fig. 9b). It is possible that the lithospheric structures may have drained the ascending magmas.

Stage 3, 80–69 Ma. As the continental subduction of Iberia under Europe began, the Iberian plate started moving toward the NNW (Fig. 9a). The magmatic pulse already emitted during the previous stage along the Portugal coast produced an age trend from the Ribamar intrusion to the Serra de Monchique complex (Fig. 9b; Grange *et al.* 2007).

Stage 4, c. 68–60 Ma. A second period of randomly located magmatism occurred, corresponding to the magmatic phase 2 on the Tore–Madeira Rise (Fig. 9b). As for stage 2, this phase could be associated with a period of quiescence in the motion of the Iberia plate, leading again to the accumulation of heat under the lithosphere and the occurrence of several magmatic pulses. Such a motionless phase has not been described in the model proposed by Sibuet *et al.* (2004b; see Fig. 9a). However, considering the duration of the NNW motion phase in this model (*c.* 85 Ma to present), a brief motionless period may have occurred as identified between 69 and 56 Ma by Roest & Srivastava (1991).

Stage 5, 56–33 Ma. During this period, no magmatism is identified either on the continent or in the oceanic domain (Fig.

9b). This period corresponds to the main compression phase of the Pyrenees orogenesis (Olivet 1996; Sibuet *et al.* 2004b). During this period, a 90 km long slab of the oceanic lithosphere of the Bay of Biscay was subducted beneath the northern coast of the Iberian peninsula, along the North Iberian trough (Olivet 1996, and references therein). This subduction led to a thrust zone extending from the Pyrenees oceanward to the side of the Galicia Bank (e.g. Olivet 1996; Thimon *et al.* 2001). It is likely that an extensive and strong compression affected both the oceanic and continental lithosphere to the south of the Galicia Bank, as evidenced by the northward thrust of the Gorringe Bank on the Tagus Abyssal Plain in Early Tertiary times (Olivet 1996; Le Gall *et al.* 1997). This widespread compression, which affected both oceanic and continental lithosphere, may have prevented the ascent of the magmas toward the surface.

Stage 6, c. 32 Ma to the present. The Pyrenees orogen was built and the plate boundary between the European and African plates was at this stage the Azores–Gibraltar Fracture Zone (Fig. 9a). The Iberian plate now behaved as part of the European plate. The convergence between Europe and Africa, which involved an overall compression on the Iberia peninsula, was still continuing (Jiménez-Munt *et al.* 2001). This period is related to another phase of randomly located magmatic pulses. This magmatic activity corresponds to the magmatic phase 3 on the Tore–Madeira Rise. The compression on Iberia may have prevented the emission of magma at the surface and may explain the localization of magmatism on the African plate. The very slow motion of the African plate ($< 2 \text{ mm a}^{-1}$; Stich *et al.* 2006) may have favoured heat accumulation under the lithosphere by a blanketing effect and led to an increase of magmatic pulse emissions. The position of the magmatic occurrences close to the branches of the Azores–Gibraltar Fracture Zone (Fig. 9b) suggests that these lithospheric structures may have played the role of conduits to drain magmas to the surface.

Considering the geochronological, geochemical and isotopic data published on the Tore–Madeira Rise and the new $^{40}\text{Ar}/^{39}\text{Ar}$ data presented here, the magmatic phases on the Tore–Madeira Rise are mirrored by the interaction of a wide thermal anomaly beneath the lithosphere and the Iberia plate motion driven by orogenic and tectonic activity of the Pyrenees. This model satisfies the geodynamical constraints imposed by the kinematics of the Iberia plate.

A single magmatic province in the northern central Atlantic?

On the American plate, several seamount groups (Corner seamounts: 80–76 Ma; Newfoundland seamounts: 98 Ma; sills drilled on Ocean Drilling Program (ODP) Leg 210, Site 1276: 105–98 Ma; New England seamounts: 103–82 Ma) had magmatic activity contemporaneous with that of the Tore–Madeira Rise (Fig. 10) and were located at that time less than 1000 km from the Tore–Madeira Rise. Although most of these ages were obtained by either K–Ar or $^{40}\text{Ar}/^{39}\text{Ar}$ on groundmass, they suggest that a widespread magmatic activity occurred around 105 Ma in the northern central Atlantic. It is not excluded that the Azores Archipelago (from *c.* 85 Ma to present) and the Canary magmatic province (from 55 Ma and possibly 68 Ma to the present; Geldmacher *et al.* 2005) were also active at the same time as the Tore–Madeira Rise (Fig. 10). All these magmatic occurrences have previously been considered as independent magmatic provinces. They are relatively close in space to one another (less than 500 km) and seem to have been emplaced during the same period. It has been proposed in recent geochem-

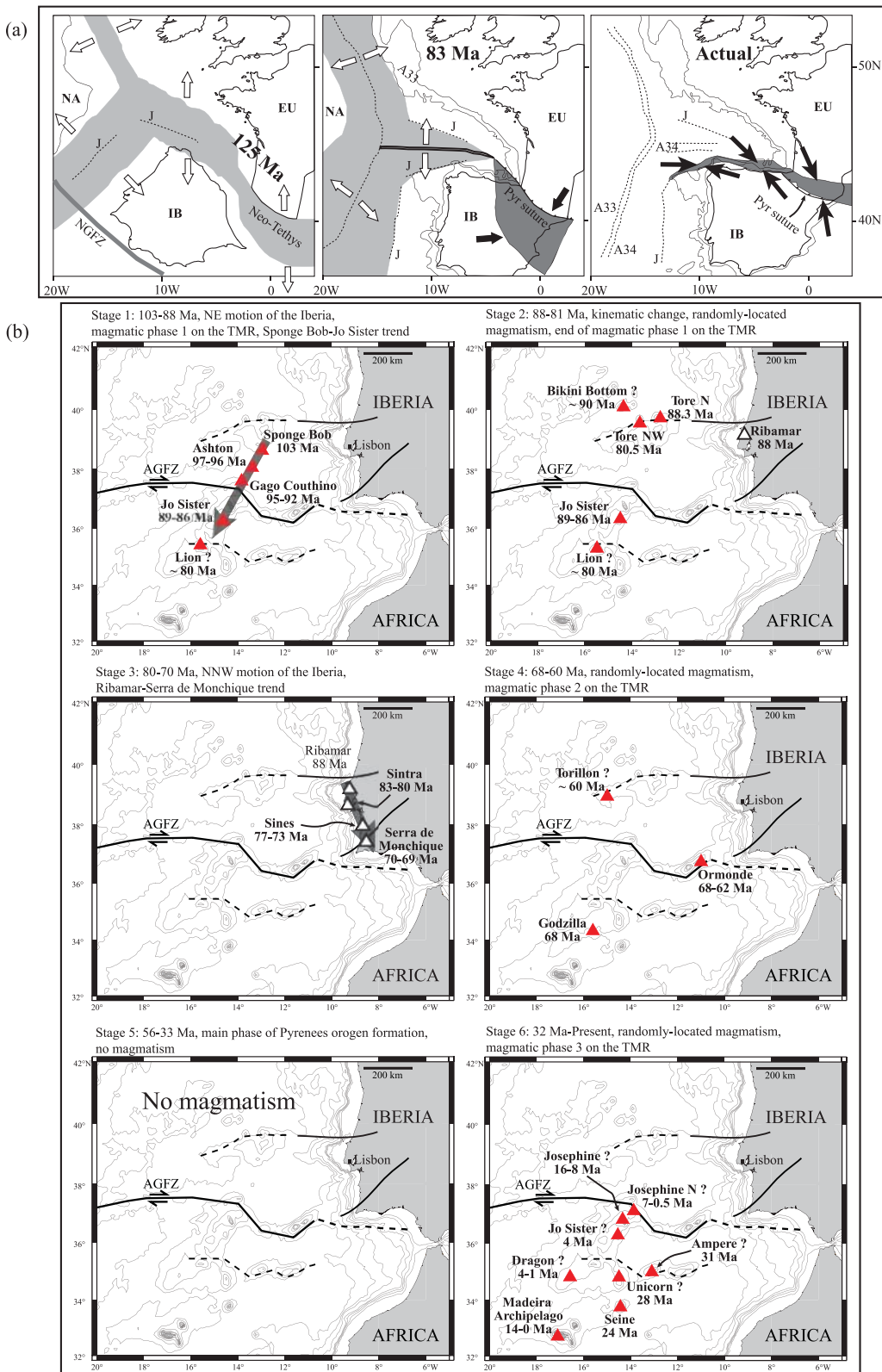


Fig. 9. Geodynamical model for the space–time distribution of magmatism on Tore–Madeira Rise and in the surrounding area. **(a)** Locations of the Iberian plate since 125 Ma relative to Europe considered to be fixed (adapted from Sibuet *et al.* 2004b). The light grey domains are areas in extension and dark grey domains are areas under compression. The double lines in the Bay of Biscay at 83 Ma indicate the proto-ridge. J, A33 and A34 are magnetic anomalies. The black arrows indicate the direction of convergence, and the white arrows the direction of extension. EU, Europe plate; IB, Iberian plate; NA, North America plate. Pyr suture, Pyrenees suture. NGFZ, Newfoundland–Gibraltar Fracture Zone. **(b)** Interpretation of magmatic activity on the Tore–Madeira Rise and in the surrounding area as different stages corresponding to the phases of the Iberian plate motion and Pyrenees orogenesis. Grey arrows indicate the magmatic trends.

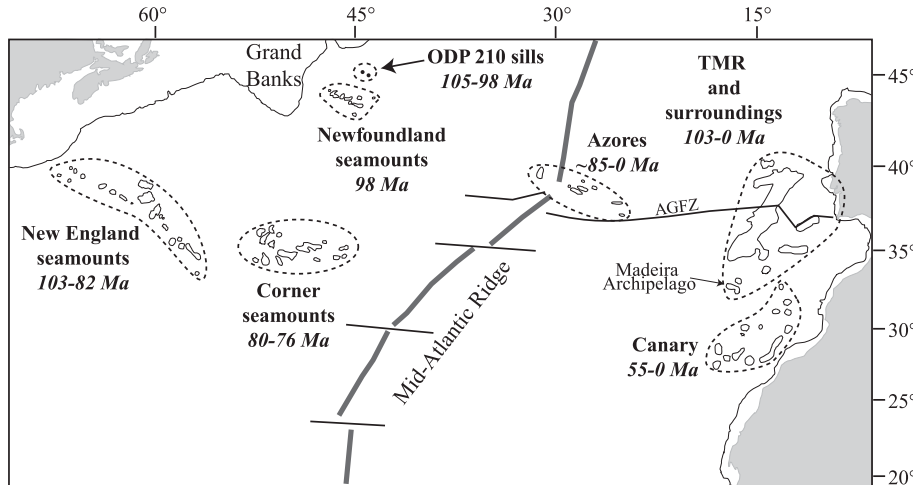


Fig. 10. Location of the various magmatic occurrences in the northern central Atlantic Ocean close to the Tore–Madeira Rise area at the time of its activity. Estimation of the volcanic activity of Azores from Gente *et al.* (2003); age of the ODP 210 sills from Hart & Blusztajn (2006); age of the New England seamounts from Duncan (1984); Newfoundland seamounts from Sullivan & Keen (1977). Range of the magmatic activity on the Canaries from Geldmacher *et al.* (2001).

ical studies that these provinces may share similar isotopic characteristics and thus, similar mantle source. For instance, the isotopic compositions of the Madeira and Canary archipelagos, New England seamounts and some Tore–Madeira Rise lavas tend to converge to a restricted composition corresponding to a HIMU-like mantle component (low-velocity component (LVC), defined by Hoernle *et al.* 1995; see also Taras & Hart 1987; Geldmacher & Hoernle 2000; Geldmacher *et al.* 2006). The similar source and coeval period of magmatic activity in the northern central Atlantic Ocean together with the thermal anomaly imaged by seismic tomography (Montelli *et al.* 2004) argue for a single magmatic province fed by a wide thermal anomaly as previously proposed for the SW Portugal–Canary–Madeira magmatism (Hoernle *et al.* 1995; Lustrino & Wilson 2007).

However, an isotopic heterogeneity is observed both between provinces and within a given province; for example, there is strong isotopic heterogeneity on São Miguel Island in the Azores (Widom *et al.* 1997); an EMI signature for Godzilla but HIMU for Josephine on the Tore–Madeira Rise (Geldmacher *et al.* 2006, 2008); and a clear EMII component in the ODP Leg 210 sills (Hart & Blusztajn 2006). A hypothesis to reconcile these data is to invoke a wide mantle plume or thermal anomaly that produced scattered magmatic pulses over a very large area that nevertheless formed a single large volcanic province.

Conclusions

Our new $^{40}\text{Ar}/^{39}\text{Ar}$ measurements of plagioclase, amphibole and biotite separates from the Bikini Bottom, Torillon, Ashton and Seine seamounts provide new constraints on the construction of the Tore–Madeira Rise. The filtered database argues for three magmatic phases on the Tore–Madeira Rise (103–80 Ma, c. 68 Ma and from c. 28 Ma until the present). Considering the magmatism that occurred on the Ampère–Coral Patch seamounts, Ormonde seamount and Portugal coast, the magmatic activity was continuous from 103 to c. 60 Ma and from c. 32 Ma to the present. Based on the space and time distribution of the magmatism on the Tore–Madeira Rise and in the surrounding area, we suggest that the Tore–Madeira Rise magmatism resulted from interaction between the complex motion of the Iberian plate as a result of the Pyrenees formation and a wide thermal anomaly located beneath the Canary–Madeira area. This thermal anomaly produced short-lived, small-scale (>100 km in diameter) magmatic pulses, which created seamount alignments

during the phases of motion of the Iberian plate between 103 and 80 Ma and between 80 and 70 Ma. During the periods of quiescence of the Iberian plate, the blanketing effect of the lithosphere (continental and/or oceanic) would cause an accumulation of heat in the mantle, leading to an increase of magma emissions. These periods correspond to the randomly located occurrence of magmatism between 88 and 81 Ma, 67 and 60 Ma and from 31 Ma to the present. During the main compression phase associated with the Pyrenees formation, between 56 and 33 Ma, no magmatism occurred. The overall compression that affected the Iberian plate would prevent magma emission at the surface.

The Tore–Madeira Rise magmatism could be related to the same geodynamic process that led to the genesis of several magmatic provinces in the northern central Atlantic such as the Newfoundland, Corner and New England seamounts, and the Azores and Canary Archipelagos, which were emplaced during the same period. All these magmatic occurrences could be the surface expressions of the thermal anomaly now located beneath the Canary–Azores area.

We thank the captain and the crew of the R.V. *Atalante*. For thin sections and technical assistance we thank E. Boeuf, B. De Quillac and H. Loyen. M. Bohn is thanked for assistance during electron-microprobe analyses. J. Cotten is acknowledged for providing ICP-AES analyses. Constructive comments by S. Kelley and I. Ukshtins-Peate helped to improve the manuscript. We also thank the editor S. Sherlock.

References

- BAKSI, A.K. 1999. Reevaluation of plate motion models based on hotspot tracks in the Atlantic and Indian Oceans. *Journal of Geology*, **107**, 13–26.
- BAKSI, A.K. 2007. A quantitative tool for detecting alteration in undisturbed rocks and minerals—I: Water, chemical weathering, and atmospheric argon. In: FOULGER, G.R. & JURDY, D.M. (eds) *Plates, Plumes and Planetary Processes*. Geological Society of America, Special Papers, **430**, 285–303.
- BERNARD-GRIFFITHS, J., GRUAU, G., CORNEN, G., AZAMBRE, B. & MACÉ, J. 1997. Continental lithospheric contribution to alkaline magmatism: isotopic (Nd, Sr, Pb) and geochemical (REE) evidence from Serra de Monchique and Mount Ormonde Complexes. *Journal of Petrology*, **38**, 115–132.
- BESLIER, M.-O., ASK, M. & BOILLOT, G. 1993. Ocean-continent boundary in the Iberia Abyssal Plain. *Tectonophysics*, **218**, 383–393.
- BOILLOT, G., FÉRAUD, G., REEQ, M. & GIRARDEAU, J. 1989. Undercrusting by serpentinite beneath rifted margins. *Nature*, **341**, 523–525.
- CANN, J.R. 1979. Metamorphism of oceanic crust. In: TALWANI, M., HARRISON, G.G. & HAYES, D.E. (eds) *Deep Drilling Results in the Atlantic Ocean: Ocean Crust*. American Geophysical Union, Maurice Ewing Series, **2**, 230–238.
- CARIGNAN, J., HILD, P., MEVELLE, G., MOREL, J. & YEGHICHEYAN, D. 2001.

- Routine analyses of trace element in geological samples using flow injection and low pressure on-line liquid chromatography coupled to ICP-MS: a study of geochemical reference materials BR, DR-N, UB-N, AN-G and GH. *Geostandards Newsletter*, **25**, 187–198.
- CAROFF, M., BELLON, H., CHAURIS, L., ET AL. 1995. Magmatisme fissural triasico-liaïsique dans l'ouest du Massif Armoricain (France): pétrologie, géochimie, âge, et modalités de la mise en place. *Canadian Journal of Earth Sciences*, **32**, 1921–1936.
- COTTEN, J., LE DEZ, A., BAU, M., ET AL. 1995. Origin of anomalous rare-earth elements and yttrium enrichments in subaerially exposed basalts: evidence from French Polynesia. *Chemical Geology*, **119**, 115–138.
- DALRYMPLE, G.B. & DUFFIELD, W.A. 1988. High precision $^{40}\text{Ar}/^{39}\text{Ar}$ dating of Oligocene tephra from the Mogollon–Datil volcanic field using a continuous laser system. *Geophysical Research Letters*, **15**, 463–466.
- DUFFIELD, W.A. & DALRYMPLE, G.B. 1990. Taylor Creek rhyolite of New Mexico, a rapidly emplaced field of domes and flows. *Bulletin of Volcanology*, **52**, 475–487.
- DUNCAN, R.A. 1984. Age progressive volcanism in the New England Seamounts and the opening of the central Atlantic Ocean. *Journal of Geophysical Research*, **89**, 9980–9990.
- FÉRAUD, G., GASTAUD, J., AUZENDE, J.M., OLIVET, J.L. & CORNEN, G. 1982. $^{40}\text{Ar}/^{39}\text{Ar}$ ages for the alkaline volcanism and basement of Gorringe Bank, North Atlantic Ocean. *Earth and Planetary Science Letters*, **57**, 211–226.
- FÉRAUD, G., YORK, D., MÉVEL, C., CORNEN, G. & AUZENDE, J.-M. 1986. Additional $^{40}\text{Ar}/^{39}\text{Ar}$ dating of the basement and alkaline volcanism of the Gorringe Bank (Atlantic Ocean). *Earth and Planetary Science Letters*, **79**, 255–269.
- GELDMACHER, J. & HOERNLE, K. 2000. The 72 Ma geochemical evolution of the Madeira hotspot (eastern North Atlantic): recycling of Paleozoic (≤ 500 Ma) oceanic lithosphere. *Earth and Planetary Science Letters*, **183**, 73–92.
- GELDMACHER, J., VAN DEN BOGAARD, P., HOERNLE, K. & SCHMINCKE, H.-U. 2000. The $^{40}\text{Ar}/^{39}\text{Ar}$ age dating of the Madeira Archipelago and hotspot track (eastern North Atlantic). *Geochemistry, Geophysics, Geosystems*, **1**, doi:10.1029/1999GC000018.
- GELDMACHER, J., HOERNLE, K., VAN DER BOGAARD, P., ZANKL, G. & GARBE-SCHÖNBERG, D. 2001. Earlier history of the ≥ 70 Ma old Canary hotspot based on the temporal and geochemical evolution of the Selvagen Archipelago and neighboring seamounts in the eastern North Atlantic. *Journal of Volcanology and Geothermal Research*, **111**, 55–87.
- GELDMACHER, J., HOERNLE, K., VAN DEN BOGAARD, P., DUGGEN, S. & WERNER, R. 2005. New $^{40}\text{Ar}/^{39}\text{Ar}$ age geochemical seamounts Canary and Madeira volcanic provinces: Support for the mantle plume hypothesis. *Earth and Planetary Science Letters*, **237**, 85–101.
- GELDMACHER, J., HOERNLE, K., KLÜGEL, A., VAN DEN BOGAARD, P., WOMBACHER, F. & BERNING, B. 2006. Origin and geochemical evolution of the Tore-Madeira Rise (eastern North Atlantic). *Journal of Geophysical Research*, **111**, B09206, doi:10.1029/2005JB003931.
- GELDMACHER, J., HOERNLE, K., KLÜGEL, A., VAN DEN BOGAARD, P. & BINDEMAN, I. 2008. Geochemistry of a new enriched mantle type locality in the northern hemisphere: Implications for the origin of the EM-I source. *Earth and Planetary Science Letters*, **265**, 167–182.
- GENTE, P., DYMENT, J., MAIA, M. & GOSLIN, J. 2003. Interaction between the Mid-Atlantic Ridge and the Azores hot-spot during the last 85 Myr: emplacement and rifting of the hot-spot-derived plateaus. *Geochemistry, Geophysics, Geosystems*, **4**, doi:10.1029/2003GC00052.
- GIRARDEAU, J., CORNEN, G., BESLIER, M.-O., ET AL. 1998. Extensional tectonics in the Gorringe Bank rocks, Eastern Atlantic Ocean: evidence of an oceanic ultra-slow mantellitic accreting centre. *Terra Nova*, **10**, 330–336.
- GOVINDARAJU, K. & MEVELLE, G. 1987. Fully automated dissolution and separation methods for inductively coupled plasma atomic emission spectroscopy rock analysis. Application to the determination of rare earth elements. *Journal of Analytical Atomic Spectrometry*, **2**, 615–621.
- GRADSTEIN, F.M., OGG, J.G. & SMITH, A.G. (eds) 2004. *A geological time scale*. Cambridge University Press, Cambridge.
- GRANGE, M., SCHÄRER, U., CORNEN, G. & GIRARDEAU, J. 2007. Time-space migration of melting within the East Atlantic plume and magmatism of Portugal: U–Pb ages and Pb–Sr–Hf isotopes. *Geochimica et Cosmochimica Acta*, **71**, supplement 1, A351.
- HART, S.R. & BLUSZTAJN, J. 2006. Age and geochemistry of the mafic sills, ODP site 1276, Newfoundland margin. *Chemical Geology*, **235**, 222–237.
- HOERNLE, K., ZHANG, Y.S. & GRAHAM, D. 1995. Seismic and geochemical evidence for large-scale mantle upwelling beneath the eastern Atlantic and western and central Europe. *Nature*, **374**, 34–39.
- HOFMANN, C., FÉRAUD, G. & COURTILOT, V. 2000. $^{40}\text{Ar}/^{39}\text{Ar}$ dating of mineral separates and whole rocks from the Western Ghats lava pile: further constraints on duration and age of the Deccan traps. *Earth and Planetary Science Letters*, **180**, 13–27.
- HONNOREZ, J. 1981. The aging of the oceanic crust at low temperature. In: EMILIANI, C. (ed.) *The Sea: the Oceanic Lithosphere*. Wiley, New York, 525–587.
- JAGOUTZ, O., MÜNTENER, O., MANATSCHAL, G., RUBATTO, D., PÉRON-PINVIDIC, G., TURRIN, B.D. & VILLA, I.M. 2007. The rift-to-drift transition in the North Atlantic: A stuttering start of the MORB machine? *Geology*, **35**, 1087–1090.
- JIMÉNEZ-MUNT, I., FERNANDEZ, M., TORNE, M. & BIRD, P. 2001. The transition from linear to diffuse plate boundary in the Azores–Gibraltar region: results from a thin-sheet model. *Earth and Planetary Science Letters*, **192**, 175–189.
- JOURDAN, F. & RENNE, P.R. 2007. Age calibration of the Fish Canyon sanidine $^{40}\text{Ar}/^{39}\text{Ar}$ dating standard using primary K–Ar standards. *Geochimica et Cosmochimica Acta*, **71**, 387–402.
- JOURDAN, F., FÉRAUD, G., BERTRAND, H., WATKEYS, M.K. & RENNE, P.R. 2007a. Distinct brief major events in the Karoo large igneous province clarified by new $^{40}\text{Ar}/^{39}\text{Ar}$ ages on the Lesotho basalts. *Lithos*, **98**, 195–209.
- JOURDAN, F., MATZEL, J.P. & RENNE, P.R. 2007b. ^{39}Ar and ^{37}Ar recoil loss during neutron irradiation of sanidine and plagioclase. *Geochimica et Cosmochimica Acta*, **71**, 2791–2808.
- KING, S.D. & RITSEMA, J. 2000. African hotspot volcanism: small-scale convection in the upper mantle beneath cratons. *Science*, **290**, 1137–1140.
- LAUGHTON, A.V., ROBERTS, D.G. & GRAVES, R. 1975. Bathymetry of the northeast Atlantic: mid-Atlantic ridge to southwest Europe. *Deep Sea Research*, **22**, 791–810.
- LE GALL, B., PIQUÉ, A., RÉHAULT, J.P., SPECHT, M. & MALOD, J. 1997. Structure et mise en place d'une ride océanique dans un contexte de limite de plaque convergente. *Comptes Rendus de l'Académie des Sciences*, **325**, 853–860.
- LUSTRINO, M. & WILSON, M. 2007. The circum-Mediterranean anorogenic Cenozoic igneous province. *Earth-Science Reviews*, **81**, 1–65.
- MANKINEN, E.A. & DALRYMPLE, G.B. 1972. Electron microprobe evaluation of terrestrial basalts for whole-rock K–Ar dating. *Earth and Planetary Science Letters*, **17**, 89–94.
- MCDOUGALL, I. & HARRISON, T.M. 1999. *Geochronology and Thermochronology by the $^{40}\text{Ar}/^{39}\text{Ar}$ Method*. Oxford University Press, Oxford.
- MERLE, R. 2006. *Age and origin of Tore-Madeira Rise: Beginning of Atlantic Ocean spreading or hotspot track. Petrology, geochemistry, U–Pb geochronology and Pb–Sr–Hf isotopes*. PhD thesis, University of Nantes.
- MERLE, R., SCHÄRER, U., GIRARDEAU, J. & CORNEN, G. 2006. Cretaceous seamounts along the ocean–continent of Iberian margin: U–Pb ages and Sr–Pb–Hf isotopes. *Geochimica et Cosmochimica Acta*, **70**, 4950–4976.
- MIN, K., MUNDIL, R., RENNE, P.R. & LUDWIG, K.R. 2000. A test for systematic errors in $^{40}\text{Ar}/^{39}\text{Ar}$ geochronology through comparison with U–Pb analysis of a 1.1 Ga rhyolite. *Geochimica et Cosmochimica Acta*, **64**, 73–98.
- MONTELLI, R., NOLET, G., DAHLEN, F.A., MASTERS, G., ENGDAHL, E.R. & HUNG, S.H. 2004. Finite-frequency tomography reveals a variety of plume in the mantle. *Nature*, **303**, 338–343.
- MUNDIL, R., RENNE, P.R., MIN, K.K. & LUDWIG, K.R. 2006. Resolvable miscalibration of the $^{40}\text{Ar}/^{39}\text{Ar}$ geochronometer. *EOS Transactions, American Geophysical Union*, **87**, Fall Meeting Supplement, Abstract V21A-0543.
- OLIVET, J.-L. 1996. La cinématique de la plaque Ibérique. *Bulletin des Centres de Recherches Exploration–Production Elf Aquitaine*, **20**, 131–195.
- ONSTOTT, T.C., MILLER, M.L., EWING, R.C. & WALSH, D. 1995. Recoil refinements: implications for the $^{40}\text{Ar}/^{39}\text{Ar}$ dating technique. *Geochimica et Cosmochimica Acta*, **59**, 1821–1834.
- PAIN, J.H., NOMADE, S. & RENNE, P.R. 2006. Quantification of ^{39}Ar recoil ejection from GA1550 biotite during neutron irradiation as a function of grain dimensions. *Geochimica et Cosmochimica Acta*, **70**, 1507–1517.
- PIERCE, C. & BARTON, P.J. 1991. Crustal structure of the Tore-Madeira Rise, Eastern North Atlantic—results of a DOBS wide-angle and normal incidence seismic experiment in the Josephine Seamount region. *Geophysical Journal International*, **106**, 357–378.
- PRINGLE, M.S., STAUDIGEL, H. & GEE, J. 1991. Jasper Seamount: Seven million years of volcanism. *Geology*, **19**, 364–368.
- RENNE, P.R., SWISHER, C.C., DEINO, A.L., KARNER, D.B., OWENS, T.L. & DEPAOLO, D.J. 1998. Intercalibration of standards, absolute ages and uncertainties in $^{40}\text{Ar}/^{39}\text{Ar}$ dating. *Chemical Geology*, **145**, 117–152.
- ROEST, W.R. & SRIVASTAVA, S.P. 1991. Kinematics of the plate boundaries between Eurasia, Iberia and Africa in the North Atlantic from the Late Cretaceous to the present. *Geology*, **19**, 613–616.
- ROEST, W.R., DANOBERTIA, J.J., VERHOEF, J. & COLETTE, B.J. 1992. Magnetic anomalies in the Canary basin and the Mesozoic evolution of the Central North Atlantic. *Marine Geophysical Researches*, **14**, 1–24.
- SCHÄRER, U., GIRARDEAU, J., CORNEN, G. & BOILLOT, G. 2000. 138–121 Ma asthenospheric magmatism prior to continental break-up in the North Atlantic and geodynamic implications. *Earth and Planetary Science Letters*, **181**, 555–572.
- SIBUET, J.-C., MONTI, S., LOUBRIE, B., MAZÉ, J.-P. & SRIVASTAVA, S. 2004a. Carte bathymétrique de l'Atlantique nord-est et du golfe de Gascogne: implications géodynamiques. *Bulletin de la Société Géologique de France*, **175**, 429–442.

- SIBUET, J.-C., SRIVASTAVA, S. & SPAKMAN, W. 2004b. Pyrenean orogeny and plate kinematics. *Journal of Geophysical Research*, **108**, B08104.
- SIMON, J.I., RENNE, P.R. & MUNDIL, R. 2008. Implications of pre-eruptive magmatic histories of zircons for U–Pb geochronology of silicic extrusions. *Earth and Planetary Science Letters*, **266**, 182–194.
- SIRCOMBE, K.N. 2004. AgeDisplay: An EXCEL workbook to evaluate and display univariate geochronological data using binned frequency histograms and probability density distributions. *Computers and Geosciences*, **30**, 21–31.
- STEIGER, R.H. & JÄGER, E. 1977. Subcommission on geochronology: convention on the use of decay constants in geo- and cosmochronology. *Earth and Planetary Science Letters*, **36**, 359–362.
- STICH, D., SERPELLONI, E., MANCILLA, F. DE L. & MORALES, J. 2006. Kinematics of the Iberia–Maghreb plate contact from seismic, moment tensors and GPS observations. *Tectonophysics*, **426**, 295–317.
- SULLIVAN, K.D. & KEEN, C.E. 1977. Newfoundland seamounts: Petrology and geochemistry. In: BARAGAR, W.R.A., COLEMAN, L.C. & HALL, J.M. (eds) *Volcanic Regimes in Canada*. Geological Association of Canada, Special Paper, **16**, 461–476.
- SUN, S.S. & McDONOUGH, W.F. 1989. Chemical and isotopic systematics of oceanic basalts: implication for mantle composition and processes. In: SAUNDERS, A.D. & NORRY, M.J. (eds) *Magmatism in the Ocean Basins*.
- Geological Society, London, Special Publications, **42**, 313–345.
- TARAS, B.D. & HART, S.R. 1987. Geochemical evolution of the New England seamount chain: isotopic and trace element constraints. *Chemical Geology*, **64**, 35–54.
- THINON, I., FIDALGO-GONZÁLEZ, L., RÉHAULT, J.-P. & OLIVET, J.-L. 2001. Déformations pyrénéennes dans le golfe de Gascogne. *Comptes Rendus de l'Académie des Sciences*, **332**, 561–568.
- TUCHOLKE, B.E. & LUDWIG, W.J. 1982. Structure and origin of the J Anomaly Ridge, Western North Atlantic Ocean. *Journal of Geophysical Research*, **87**, 9389–9407.
- TURNER, G. & CADOGAN, P. 1974. Possible effects of ^{39}Ar recoil in $^{40}\text{Ar}/^{39}\text{Ar}$ dating. *Proceeding of the 5th Lunar and Planetary Science Conference*, **2**, 1601–1615.
- VAN DER LINDEN, W.J.M. 1979. The Atlantic margin of Iberia and Morocco, a reinterpretation. *Tectonophysics*, **59**, 185–199.
- WENDT, I., KREUZER, H., MULLER, P., VON RAD, U. & RASCHKA, H. 1976. K–Ar age of basalts from Great Meteor and Josephine seamount (eastern North Atlantic). *Deep-Sea Research*, **23**, 849–862.
- WIDOM, E., CARLSON, R.W., GILL, J.B. & SCHMINCKE, H.-U. 1997. Th–Sr–Nd–Pb isotope and trace elements evidence for the origin of the São Miguel, Azores, enriched mantle source. *Chemical Geology*, **140**, 49–68.

Received 19 December 2008; revised typescript accepted 5 May 2009.
Scientific editing by Sarah Sherlock.



Cretaceous seamounts along the continent–ocean transition of the Iberian margin: U–Pb ages and Pb–Sr–Hf isotopes

Renaud Merle ^{a,b,*}, Urs Schärer ^a, Jacques Girardeau ^b, Guy Cornen ^b

^a Laboratoire de Géochronologie, Géosciences Azur UMR-CNRS 6526, parc Valrose, F-06108 Nice, France

^b Laboratoire de Planétologie et Géodynamique, UMR-CNRS 6112, Université de Nantes, 2 rue de la Houssinière, F-44322 Nantes cedex 3, France

Received 7 November 2005; accepted in revised form 5 July 2006

Abstract

To elucidate the age and origin of seamounts in the eastern North Atlantic, 54 titanite and 10 zircon fractions were dated by the U–Pb chronometer, and initial Pb, Sr, and Hf isotope ratios were measured in feldspars and zircon, respectively. Rocks analyzed are essentially trachy-andesites and trachytes dredged during the “Tore Madeira” cruise of the *Atalante* in 2001. The ages reveal different pulses of alkaline magmatism occurring at 104.4 ± 1.4 (2σ) Ma and 102.8 ± 0.7 Ma on the Sponge Bob seamount, at 96.3 ± 1.0 Ma on Ashton seamount, at 92.3 ± 3.8 Ma on the Gago Coutinho seamount, at 89.3 ± 2.3 Ma and 86.5 ± 3.4 Ma on the Jo Sister volcanic complex, and at 88.3 ± 3.3 Ma, 88.2 ± 3.9 , and 80.5 ± 0.9 Ma on the Tore locality. No space–time correlation is observed for alkaline volcanism in the northern section of the Tore-Madeira Rise, which occurred 20–30 m.y. after opening of the eastern North Atlantic. Initial isotope signatures are: 19.139 – 19.620 for $^{206}\text{Pb}/^{204}\text{Pb}$, 15.544 – 15.828 for $^{207}\text{Pb}/^{204}\text{Pb}$, 38.750 – 39.936 for $^{208}\text{Pb}/^{204}\text{Pb}$, 0.70231 – 0.70340 for $^{87}\text{Sr}/^{86}\text{Sr}$, and $+6.9$ to $+12.9$ for initial epsilon Hf. These signatures are different from Atlantic MORB, the Madeira Archipelago and the Azores, but they lie in the field of worldwide OIB. The Cretaceous seamounts therefore seem to be generated by melts from a OIB-type source that interact with continental lithospheric mantle lying formerly beneath Iberia and presently within the ocean–continent transition zone. Inheritance in zircon and high ^{207}Pb of initial Pb substantiate the presence of very minor amounts of continental material in the lithospheric mantle. A long-lived thermal anomaly is the most plausible explanation for alkaline magmatism since 104 Ma and it could well be that the same anomaly is still the driving force for tertiary and quaternary alkaline magmatism in the eastern North Atlantic region. This hypothesis is agreement with the plate-tectonic position of the region since Cretaceous time, including an about 30° anti-clockwise rotation of Iberia.

© 2006 Elsevier Inc. All rights reserved.

1. Introduction

The seamounts studied lie in the northern and central part of the Tore-Madeira Rise, which extends over about 1000 km in SW–NE direction, roughly matching the oldest, approximately 125–130 Ma old Atlantic magnetic anomaly of oceanic crust in this region (Fig. 1; J anomaly; Pitman and Talwani, 1972; Gradstein et al., 2004). Several hypothesis were put forward to explain the origin of the rise; however, none of them is sufficiently supported by geochronological and geochemical data. Earlier explanations are: (1) emplacement of late tertiary to recent magmas em-

placed along shear zones, related to N–S compression of the Iberian margin (Van der Linden, 1979; Geldmacher et al., in press), (2) volcanism occurring in relation to first oceanic lithosphere creation at 130–125 Ma, as suggested by its vicinity with the oldest Atlantic oceanic magnetic anomaly (Tucholke and Ludwig, 1982; Peirce and Barton, 1991; Olivet, 1996; Girardeau et al., 1998; Geldmacher et al., in press), (3) volcanism, ascribed to the accumulation of magmas underneath an unusually slow Atlantic ridge (Olivet, 1996; Girardeau et al., 1998), and (4) magmatism related to a “hot-spot-like” feature, active coevally with spreading (Tucholke and Ludwig, 1982; Peirce and Barton, 1991; Geldmacher et al., 2001; Geldmacher et al., in press).

Prior to this study, only a few geochronological or tracer isotope data were available for volcanoes emplaced

* Corresponding author. Fax: +33 4 92 07 68 16.

E-mail address: merle@chimie.univ-nantes.fr (R. Merle).

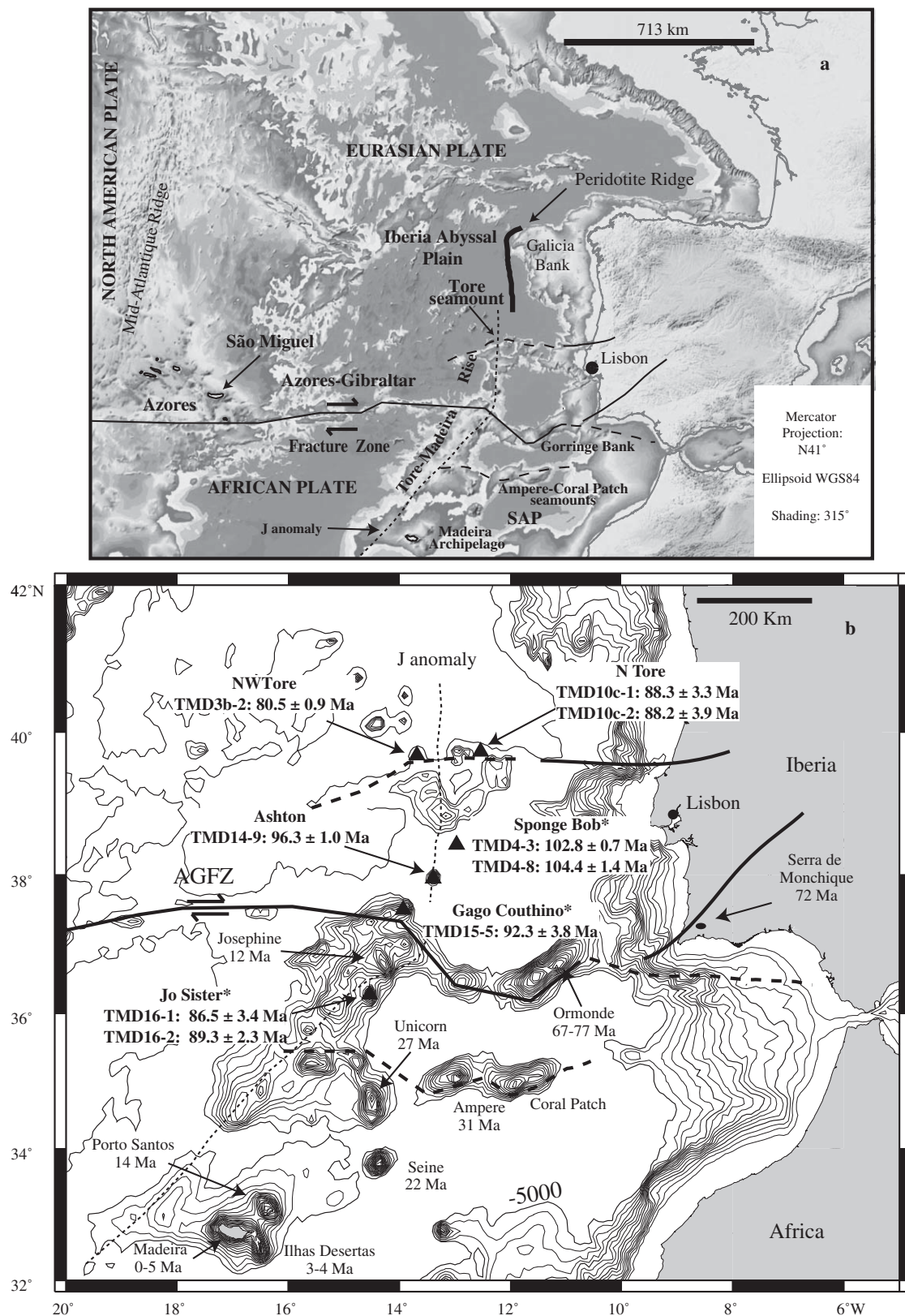


Fig. 1. (a) Map of the North Central Atlantic (modified after Sibuet et al., 2004a) distinguishing the main structural units. Solid lines represent faults, and dashed lines inferred faults. (b) Bathymetric map of the study region indicating the seamounts, sample locations and sample references. Seamount names for so far unnamed seamounts are marked (*). AGFZ, Azores-Gibraltar Fracture Zone. SAP, Seine Abyssal Plain. Ages of Ormonde, Monchique, Madeira, Porto Santo, Desertas Islands, Ampere, Josephine, Unicorn and Seine from Wendt et al. (1976); Féraud et al. (1981, 1982, 1986); Bernard-Griffiths et al. (1997); Schärer et al. (2000); Geldmacher et al. (2000, 2005). Location of the J anomaly after Olivet (1996).

between the Tore seamounts in the north, and Jo-Sister in the south (Fig. 1, Wendt et al., 1976; Geldmacher et al., in press). Rocks were collected by dredging during the 2001 “Tore-Madeira” cruise of the *Atalante*. Samples of kg-size were recovered, including basalts, trachy-andesites and trachytes with the latter two lithologies being as abundant as alkali basalts among the dredged rocks. The extent of seawater alteration is high in most rocks precluding systematic $^{40}\text{Ar}/^{39}\text{Ar}$ dating and isotope tracing of whole-rock samples. Given the strong degrees of alteration, only analyses of grain-by-grain selected mineral separates were possible, and as far as dating is concerned, the occurrence of primary magmatic titanite in most trachy-andesites and trachytes made it possible to use the U–Pb method. A few samples also contained very small amounts of zircon used for combined titanite–zircon dating and Hf isotope tracing on the same zircon grains. Fresh feldspar, either K-feldspar or plagioclase, was used for U–Pb (Pb–Pb) and Sr isotope analyses.

2. Geological framework

The Tore-Madeira Rise is a morphologically defined object. The Tore seamounts form a $\sim 120 \times 90$ km wide elliptic complex at its northern end having summits reaching ~ 2500 m over the -5000 m deep Tore depression (Fig. 1). The southernmost seamount studied here is Jo Sister lying at ~ 500 km distance from the Tore locality. It culminates at about 4000 m above sea floor. Other seamounts investigated here are, from North to South, Sponge Bob, Ashton and Gago Couthino, reaching 3000 m, 3500 m, and 3200 m above the -5000 m deep seafloor, respectively (Fig. 1). Jo Sister has also been named Erik and Gago Couthino, Teresa (Hoernle et al., 2003; Geldmacher et al., in press) but none of these names has been ratified so far. An important structure is the Azores-Gibraltar Fracture Zone (AGFZ) which is an Atlantic transform fault separating the Eurasian and African plates. Its eastern end appears to split into three branches towards the Tore, Gorringe, and Ampere-Coral Patch seamounts (e.g., Laughton et al., 1975; Jiménez-Munt et al., 2001). Dextral strike-slip movements along this fracture zone seem to be absent or very small on the plate scale since the J anomaly is not visibly displaced (Fig. 1). Since Oligocene times, movements along the main branch and the branches to the North and South of the AGFZ seem to be transpressive, with a slight dextral component along the main fracture due to extension in the Azores region evidenced by the modeling of focal mechanisms (Olivet, 1996; Malod, personal commun.).

Volcanoes to the North of the AGFZ lie along the first Atlantic magnetic anomaly (J anomaly, 125–130 Ma) in this region. This anomaly corresponds to the boundary between true oceanic crust and a transitional domain being composed of rifted and stretched Iberian continental margin, unroofed lithospheric peridotites (e.g., peridotite ridge; Fig. 1) detached from lowermost continental crust (Boillot

et al., 1989; Beslier et al., 1993). This transitional zone has locally been intruded by syn-rift basaltic dikes and gabbros (Beslier et al., 1988; Boillot et al., 1995; Schärer et al., 1995, 2000). North to $41^{\circ}30'N$ (Fig. 1), the J anomaly is not identified (south of Galicia Bank), implying that initial Atlantic opening along the Galicia Bank occurred later. To the South of the southern branch of the AGFZ, magnetic anomalies older than J seem to be present in the Seine Abyssal Plain (Roest et al., 1992) implying that some volcanoes to the South could be emplaced into oceanic lithosphere including the southern part of the Tore Madeira Rise.

Geophysical investigations show the rise substratum to be about 10 km thick, hypothetically containing some underplated magmas (Mauffret et al., 1989; Peirce and Barton, 1991; Pinheiro et al., 1992). It has also been suggested that formation of the rise represents a major event during opening of the Central and North Atlantic ocean (Olivet, 1996). This correlates with small-amplitude gravity anomalies suggesting that it is isostatically compensated on both the local and regional scale (Peirce and Barton, 1991).

A magmatic event distinct from ocean spreading is the emplacement of syn-rift related magmas prior or during the very early stages of Atlantic opening in the Iberia margin. Such gabbro and dolerite emplacement occurred at 121 Ma along the Galicia Bank (Féraud et al., 1988; Schärer et al., 1995, 2000) and at 138 Ma in the Gorringe Bank (Girardeau et al., 1998; Corneil et al., 1999; Schärer et al., 2000). These syn-rift subcontinental magmas have MORB source signatures and were most likely derived from the asthenosphere at that time.

Regionally important alkaline rocks, distinct from both syn-rift magmatism and 130–125 Ma Atlantic opening occur on the peridotitic–gabbroic Ormonde seamount, the Ampere-Coral Patch seamounts, as well as on the continent (Fig. 1). Rb–Sr, U–Pb and $^{40}\text{Ar}/^{39}\text{Ar}$ ages for these rocks range between 67–77 and 31 Ma (Rock, 1976; Féraud et al., 1982, 1986; McIntyre and Berger, 1982; Bernard-Griffiths et al., 1997; Geldmacher et al., 2000; Schärer et al., 2000). We will show that such alkaline magmatism is also a major component of the northern Tore-Madeira Rise, where differentiated alkaline rocks have been recognized.

3. Alkaline magmatism: previous studies

3.1. The Madeira archipelago

The 14 Ma to recent Madeira Archipelago is composed of volcanic and intrusive rocks of mostly alkaline affinity, where basalts range from tholeiites to basanites. $^{40}\text{Ar}/^{39}\text{Ar}$ ages on whole-rocks (total fusion) and plagioclase range from 4.63 ± 0.10 Ma to 0.18 ± 0.08 Ma (Geldmacher et al., 2000). The Desertas Islands of the archipelago are considered to be the N–S arm of the Madeira rift system for which $^{40}\text{Ar}/^{39}\text{Ar}$ whole-rock ages of basaltic lithologies range from 3.62 ± 0.24 to 3.25 ± 0.08 Ma (Geldmacher

et al., 2000). For Porto Santo Island located 45 km to the north-east of Madeira, alkali basalts to trachytic rocks (Geldmacher and Hoernle, 2000) have Ar whole-rock ages of 13.1 ± 0.4 and 12.3 ± 0.4 Ma (Féraud et al., 1981) and 14.31 ± 0.22 and 11.07 ± 0.10 Ma for plagioclase (Geldmacher et al., 2000). To explain source characteristics of Madeira volcanism contrasting hypothesis were proposed, (1) interaction of a high- $^{238}\text{U}/^{204}\text{Pb}$ (HIMU) plume component with N-MORB-like asthenosphere and oceanic lithosphere (Hoernle et al., 1991, 1995), (2) interaction of MORB source mantle with a mixture of HIMU and EMI-type mantle plume material (Mata et al., 1998), (3) recycling of relatively young oceanic crust (Thirlwall, 1997), (4) mixing of plume material containing a relatively young (~ 1.2 Ga) recycled oceanic crust and shallow MORB sources with a component of Paleozoic oceanic crust (Widom et al., 1999), (5) progressive melting of plume material containing relatively young (<1 Ga) recycled oceanic lithosphere from which enriched altered oceanic crust and depleted lower crust and lithospheric mantle were derived (Geldmacher and Hoernle, 2000, 2001), and (6) melting of metamorphosed oceanic lithosphere shortly after its formation (Halliday et al., 1992, 1993, 1995).

3.2. The Josephine, Seine, Unicorn, and Ampere-Coral Patch seamounts

Based on geochemical analyses and K-Ar whole-rock dating (12.6 ± 0.4 Ma; 8.2 ± 0.2 Ma) of the Josephine seamount it was originally suggested that the volcanoes building up the submarine mountain range between Josephine and the Tore localities reflect a Miocene magmatic event (Wendt et al., 1976). Further chemical analyses of Josephine lavas confirm its alkaline character (Merle et al., 2005).

Previous studies of three other volcanic complexes at Seine, Unicorn, and Ampere-Coral Patch (Fig. 1) yield whole-rock $^{40}\text{Ar}/^{39}\text{Ar}$ ages of 21.7 ± 0.2 Ma, 27.4 ± 2.4 Ma, and 31.20 ± 0.20 Ma, respectively (Geldmacher et al., 2000, 2005). It is important to note that they all lie significantly to the East of the Tore-Madeira Rise. The samples analyzed for these seamounts are olivine-phyric basanites and nephelinites with incompatible element characteristics similar to the volcanic rocks of the Madeira Archipelago. Initial Pb, Sr and Nd isotopic compositions of the Seine, Unicorn and Ampere-Coral Patch seamounts are interpreted as the result of interaction of Madeira plume melts with the overlying lithosphere, which contains continental lithospheric components (Geldmacher and Hoernle, 2000; Geldmacher et al., 2005).

3.3. The Ormonde seamount

This seamount marks the eastern summit of the Gorringe Bank. It is composed of peridotites that are intruded by 138 ± 1 and 136 ± 1 Ma old gabbros, and $67-77$ Ma old alkaline lavas on top of the bank (Féraud

et al., 1982, 1986; Cornen, 1982; Cornen et al., 1999; Schärer et al., 2000). The alkaline lavas show two magmatic trends (1) highly alkalic, silica-undersaturated rocks, ranging from nephelinites to phonolites and (2) mildly alkaline, silica-saturated volcanics ranging from alkali basalt and basanites to trachytes (Cornen, 1982). The alkaline rocks from the Ormonde seamount are interpreted on the basis of initial Pb, Sr, Nd and Hf (on zircon) isotopic compositions to be derived from sub-lithospheric mantle melts (OIB-like source) contaminated by ancient Rb-depleted and LREE-enriched lithospheric mantle detached during passive continental rifting (Bernard-Griffiths et al., 1997; Schärer et al., 2000).

3.4. Continental Serra de Monchique

This complex (Fig. 1) is a sub-volcanic nepheline syenite body interpreted as belonging to the Late Cretaceous Iberian Alkaline Igneous Province, related to late stages of opening of the Bay of Biscay (McIntyre, 1977; Cornen, 1982; McIntyre and Berger, 1982; Rock, 1982; Whitmarsh et al., 1986). Dominant lithologies are nepheline syenites and micro-syenites with minor gabbros and lamprophyres, having incompatible elements patterns similar to the alkali lavas on the Ormonde seamount. These rocks do not exhibit any chemical or isotope signatures for the assimilation of continental crust (Bernard-Griffiths et al., 1997). A whole rock-mineral Rb-Sr age for Serra de Monchique, and K-Ar mineral measurements yield an age of 72 ± 2 Ma (Rock, 1976; McIntyre and Berger, 1982; Bernard-Griffiths et al., 1997). Similar model for magma genesis are proposed for Ormonde and Monchique (Bernard-Griffiths et al., 1997).

4. Samples descriptions

4.1. Overview

Samples collected during the “Tore-Madeira Rise” cruise represent 40 different dredge sites located along the flanks of the different seamounts. Magmatic rocks were recovered in 22 dredges with exclusively basaltic lithologies to the south of the Jo-Sister locality, and significantly differentiated lithologies to the north (Fig. 1). Individual dredge depth of our samples are given in Table 1, ranging from -5007 to -1560 m representing seamount flank sections between about 1 and 6 km, taking into account individual seamount slopes measured at the sample localities. Although the depth of sections are different among the seamounts, the sampled rocks cover basal sections, intermediate levels, and top sections of the 3000–4000 m high seamounts. We therefore consider that sampling is representative for lithologies constituting the different seamounts, even if not all mounts could be sampled from the bottom to the top.

Since most magmatic rocks have suffered significant low-temperature alteration by seawater, dating accessory minerals by the U-Pb chronometers was potentially the

Table 1
Petrological and mineralogical descriptions of rock samples from the different seamounts

Samples	Location	Dredging depth (m) max–min	Rock type	Alteration (%)	Texture	Phenocrystals	Groundmass
Tore Smt (NW) TMD3b-2	39°41.66N, 13°41.66W	4930–3350	Trachyte	5–10	Almost aphyric, micro-vesicular, microlitic fluidal	Rare mm-size An ₃₇ to anorth (An ₆ ; Or ₂₁), diop (microphenocrysts): Wo _{47–49} ; En _{27–36} ; Fs _{23–24} , Fe–Ti ox	Lath of Anorth (An _{7–9} ; Or _{19–23}), pyroxene, Fe–Ti ox
Tore Smt (N) TMD10c-1	39°45.33N, 12°23.36W	5007–4589	Trachy-andesite	10–15	Slightly porphyritic, micro-vesicular, microlitic fluidal	Plag An _{40–44} , Mg-hastings, diop (rare) Wo _{48–49} ; En _{29–35} ; Fs _{19–22}	Feldspar lath, Fe–Ti ox, diop, Mg-hastings (sparse)
			Trachy-andesite	15	Slightly porphyritic, micro-vesicular, microlitic fluidal	Plag (oscillatory zoned) An _{38–47} , microphenocrysts of Mg-hastings (minor), diop Wo _{46–48} ; En _{27–36} ; Fs _{21–27} , titanite (very rare)	Laths of plag An _{18–41} , Fe–Ti ox, diop, Mg-hastings (rare)
Sponge Bob Smt TMD4-3	38°27.50N, 12°54.00W	3811–3243	Trachyte	5	Slightly porphyritic, microlitic fluidal	3–4 mm-size euhedral sanidine Or _{36–42} ; Ab _{56–62} (sparse), biotite, titanite, Fe–Ti ox	Feldspar laths, Fe–Ti ox, patchy biotite
			Trachyte	5–10	Porphyritic, microlitic fluidal	3–4 mm-size euhedral K-feld An _{1–8} ; Or _{25–48} (\approx 3% modal), biotite, titanite, Fe–Ti ox (microphenocrysts)	Feldspar laths, Fe–Ti ox, patchy biotite
Ashton Smt TMD14-9	38°01.54N, 13°22.66W	2803–2395	Trachyte	<5	Highly porphyritic, microlitic fluidal	6 mm–10 mm-size zoned K-fsp An _{2–11} ; Or _{18–40} (\approx 5% modal), subordinate mm-size biotites, diop Wo _{45–46} ; En _{38–39} ; Fs _{15–16} (sparse), Fe–Ti ox, apatite	Feldspar lath, Fe–Ti ox, biotite, needles of pyroxene
Gago Coutinho Smt TMD15-5	37°30.64N, 13°55.46W	2846–1560	Trachyte	5–10	Almost aphyric, microlitic fluidal	Euhedral zoned feldspar: An ₆ to anorth (An ₆ ; Or ₃₄), Mg-hastings, diop Wo _{45–46} ; En _{31–32} ; Fs _{22–23} (minor), Fe–Ti ox, titanite	Lath of anorth (An _{8–9} ; Or _{18–20}), Fe–Ti ox, pyroxene
Jo-Sister Smt TMD16-1	36°21.33N, 14°26.84W	2224–1960	Trachy-andesite	35	Almost aphyric, microlitic fluidal	Clino-amphibole (hastingsite, kaersutite), core-altered plag An _{35–58} (rare), titanite, Fe–Ti Ox	K-fsp laths (Or _{22–46} ; An _{2–15}), Fe–Ti ox
			Trachy-phonolite	25	Almost aphyric, microlitic fluidal	Clino-amphibole (hastingsite, kaersutite), diop Wo _{47–49} ; En _{29–38} ; Fs _{13–24} (microphenocrysts), titanite, Fe–Ti ox	K-fsp laths (Or _{22–46} ; An _{2–15}), Fe–Ti ox

An, anorthite; Or, orthoclase; anorth, anorthoclase; diop, diopside; ox, oxides; Mg-hastings, magnesio-hastingsite; plag, plagioclase; K-fsp, K-feldspar. Microprobe analyses (EMMA) were performed with a Cameca instrument (Microsonde Ouest, Brest). Analytical conditions were 15 kV, 15 nA, counting time 6 s, and correction by the ZAF method. Concentrations of <0.3% are considered qualitative.

most promising method to avoid alteration-induced bias on the ages. Seawater alteration partly transformed the crypto-crystalline groundmass to clay minerals, and facilitated Fe–Mn hydroxide in-filling of cracks and vesicles. In examining all differentiated rocks, only 5 trachytes and 4 trachy-andesites contained primary magmatic titanite and in consequence, our investigation was limited to these samples representing six seamounts (Fig. 1). Zircon was recovered from three of the titanite-bearing alkaline volcanics allowing combined U–Pb zircon–titanite dating and Hf isotope measurements on zircon.

4.2. Detailed sample description

The principal petrographical and mineralogical characteristics of the samples (thin sections and Electron Probe Microanalyses) are given in Table 1. The groundmasses of these samples show microlitic fluidal textures consisting of laths of feldspars. A trachyte (TMD3b-2, 0.5 kg in weight) dredged at NW-Tore is almost aphyric, displaying rare mm-size feldspar phenocrysts, euhedral titanites and few zircons. The matrix underwent alteration characterized by Fe–Mn hydroxides lining the inner walls of vesicles. The two samples from the northern part of Tore seamount (TMD10c-1; TMD10c-2, 1.4 and 0.2 kg in weight, respectively) are trachy-andesites, being slightly plagioclase-phyric and carrying sparse brown amphiboles. Alteration is characterized by Fe–Mn hydroxides, coating inner walls of vesicles. Titanite is less abundant in TMD10c-2 than in TMD10c-1 and no zircon could be seen.

The two Sponge Bob trachyte samples (TMD4-3, 1 kg in weight; TMD4-8, 2.5 kg in weight) are porphyritic in mm-size K-feldspar phenocrysts containing abundant titanite. TMD4-3 contains also a few zircons. The Ashton sample (TMD14-9, 1 kg in weight) is a fresh highly porphyritic trachyte yielding abundant titanite and large zircons reaching more than 1 mm in length. Zircon and titanite contain frequent inclusions of apatite and oxides. The trachyte dredged on the Gago Coutinho seamount (TMD15-5, 1 kg in weight) is almost aphyric containing rare euhedral phenocrysts of zoned feldspars. Alteration is characterized by Fe–Mn hydroxides along cracks. Titanite is abundant and typically contains oxide inclusions; but zircon was absent.

The trachy-andesite samples from the Jo Sister seamount (TMD16-1; TMD16-2, 4 and 1.5 kg in weight respectively) are the most altered of all our samples. Borders of all TMD16-1 fragments are yellow-orange colored, due to palagonization of the groundmass, whereas the interior is light grey. Sample TMD16-2 contains rare hastingsite–kaersutite phenocryst and abundant grains of titanite but no zircon. Alteration phases are hydroxides and clay minerals partly replacing the groundmass.

Fifty-four abraded and non-abraded titanite and 10 zircon fractions were selected from nine different trachy-andesites and trachytes for U–Pb geochronology. To search for heterogeneities, overgrowths, and inclusions, all populations were examined by optical microscopy, back-scattered

electrons (BSE), and cathodoluminescence (CL) as displayed in Fig. 2. Grain-by-grain selection of the essentially transparent titanites and zircons covers the full range of habits constituting the populations (Figs. 2a–e). Titanites are pale to dark yellow and occasionally light brown reflecting pleochroism. Opaque inclusions are abundant and most fractions analyzed contained such inclusions (Figs. 2f, g and i), as well as some transparent colorless euhedral crystals (probably apatites). Zircons are colorless and also contain transparent and opaque inclusions (Figs. 2d and e). No significant growth heterogeneities, overgrowth or old cores could be detected.

5. Analytical procedures

Mineral separation was carried out using Franz isodynamic magnetic separator, heavy liquids (CHBr_3 and CH_2I_2), and grain-by-grain hand-picking under the binocular microscope. Major and trace element analyses were carried out by ICP-AES and ICP-MS at the University of Brest (analytical procedures in Cotten et al., 1995) and the CRPG at Nancy (analytical procedures in Govindaraju and Mevelle, 1987 and Carignan et al., 2001). U–Pb and Pb isotope measurements were performed on a Thomson 206 mass-spectrometer using a SEM for U–Pb analyses, and a Faraday cage for Pb. Sr composition measurements were made on the VG-Sector mass-spectrometer. Lead and U isotopic ratios were corrected for $0.10 \pm 0.05\text{/amu}$ of mass-fractionation on the SEM, as determined from repeated runs of a mixed NBS-981 Pb/NBS-960 U standard, as well as the gravimetrically calibrated $^{233}\text{U}/^{235}\text{U}$ spike (NBS-995/NBS-993). For NBS-981 Pb our mean ratios ($n = 8$) corrected for mass-discrimination are: 16.941 ± 0.004 (2-sigma-STERR) for $^{206}\text{Pb}/^{204}\text{Pb}$, 15.501 ± 0.004 for $^{207}\text{Pb}/^{204}\text{Pb}$, and 36.728 ± 0.009 for $^{208}\text{Pb}/^{204}\text{Pb}$. For Faraday measurements, mass-fractionation on Pb is $0.10 \pm 0.03\text{/amu}$. Repeated measurements of total Pb blanks (2004–2005) yielded $60 \pm 30\text{ pg}$ for titanite and $20 \pm 60\text{ pg}$ for zircon, with less than 1 pg blank U for both procedures. Zircon and titanite grains were mechanically abraded to eliminate potentially altered crystal surfaces (Krogh, 1982). Prior to dissolution in pure >50% HF, titanite, zircon, and plagioclase were spiked with a mixed $^{205}\text{Pb}/^{235}\text{U}$ solution, whereas K-feldspar, devoid of U, was measured for composition only. Zircons were dissolved at 215°C for 3 days in Teflon bombs followed by anion exchange chemistry (modified from Krogh, 1973). Titanite and feldspar was dissolved in PFA Teflon beakers at 180°C (~ 18 h). An HBr procedure was used, for separation and purification of U and Pb from titanite and plagioclase, modified after Manhès et al. (1978). For U–Pb, Pb and Sr analyses, grain-by-grain selected feldspars were washed in HCl 6 N, ground in an agate mortar, and leached with 1% HF/HBr 1 N for a few minutes in the ultrasonic bath (e.g., Schärer, 1991) prior to dissolution.

Strontium composition measurements on size-fractions of grain-by-grain selected feldspars were done on unspiked

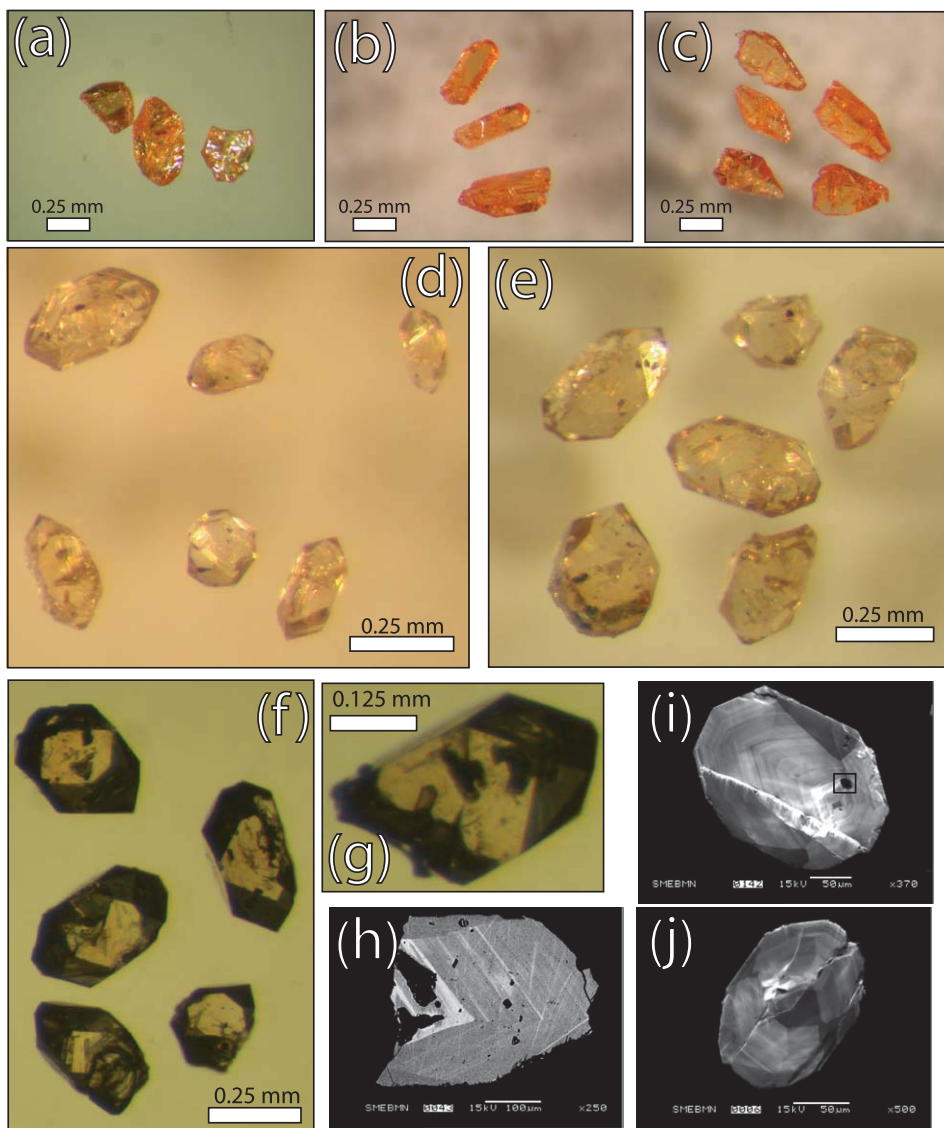


Fig. 2. Photomicrographs, CL and BSE images illustrating titanite and zircon grains. (a) prismatic fragments and a euhedral crystal of titanite; (b) and (c) two different types of euhedral crystals of titanites; (d) and (e) zircons with opaque and transparent inclusions; (f) (transmitted light) zircon with transparent inclusions; (g) zircon grain showing a well crystallized transparent inclusion, probably an apatite; (h) BSE image of a polished titanite grain showing regular oscillatory growth zoning; (i) cathodoluminescence (CL) image of a polished zircon grain showing well-developed regular oscillatory zoning, a well-crystallized inclusion is outlined; (j) CL image of a polished zircon grain showing well-developed regular oscillatory zoning.

aliquots on 2/3 of the total sample solution, reserving 1/3 of the parent solution for spiking with a mixed $^{85}\text{Rb}/^{84}\text{Sr}$ tracer for Rb–Sr concentration determination. For Sr chemical separation, we employed Eichrom Sr-Spec. resin while Rb separation was done with the AGW50-X12 cation resin. Sr measurement accuracy was monitored using NBS-987 standard yielding a mean ($n=8$) ratio of 0.71026 ± 0.00005 (2-sigma-STERR). Hafnium isotope measurements were performed on the Plasma-54 instrument at the Ecole Normale Supérieure at Lyon using the JMC-475 Hf standard for calibration after each sample (Blichert-Toft et al., 1997). All data were normalized to $^{176}\text{Hf}/^{177}\text{Hf} = 0.282161$ based on replicate analyses of JMC 475, run before and after each analysis. For Hf isotope analyses, the 3 N HCl fraction from the U–Pb proce-

dure was treated on the AGW50-X8 resin to avoid interferences from ^{176}Yb (e.g. Patchett and Tatsumoto, 1980; Bodet and Schäfer, 2000). Isochrons were calculated after Minster et al. (1979) and Ludwig (2003) with the latter also used for constructing concordia plots.

6. Major and trace element results

6.1. Major elements

Compositions range in SiO_2 from 56 to 63 wt% and between 0.21 and 0.67 wt% for MgO (Table 2), being consistent with trachy-andesites to trachytes. The wide range of alteration is reflected by their Loss On Ignition (LOI: 0.58–8.36 wt%). In the total-alkali vs. SiO_2 diagram

Table 2

Major and trace element analytical results of rock samples from the different seamounts

Sample: Seamount:	TMD3b-2 Tore (NW)	TMD10c-1 Tore (N)	TMD10c-2 Tore (N)	TMD4-3 Sponge Bob	TMD4-8 Sponge Bob	TMD14-9 Ashton	TMD15-5 Gago Coutinho	TMD16-1 Jo Sister	TMD16-2 Jo Sister
SiO ₂ (wt%)	62.00	58.18	58.45	62.98	63.40	60.25	62.20	56.40	56.67
TiO ₂	0.38	0.70	0.71	0.35	0.48	0.60	0.26	0.43	0.39
Al ₂ O ₃	18.75	19.64	19.30	18.06	18.60	17.84	19.35	19.55	18.25
Fe ₂ O ₃ *	2.86	3.94	3.87	2.33	2.11	2.53	2.08	3.10	2.96
MnO	0.23	0.22	0.29	0.10	0.06	0.11	0.12	0.28	0.20
MgO	0.38	0.59	0.58	0.31	0.21	0.41	0.28	0.67	0.55
CaO	2.43	2.69	2.65	0.39	0.35	3.66	1.09	0.93	2.11
Na ₂ O	6.75	6.18	6.20	6.61	6.45	6.10	6.75	4.95	5.37
K ₂ O	4.60	4.10	3.85	5.59	6.85	5.91	5.30	5.15	6.55
P ₂ O ₅	0.08	0.19	0.11	0.09	0.06	0.53	0.03	0.06	0.67
LOI	1.07	3.54	4.00	3.07	1.29	1.99	2.44	8.36	6.19
Total	99.53	99.97	100.02	99.88	99.86	99.93	99.90	99.88	99.90
Na ₂ O+K ₂ O	11.35	10.28	10.05	12.20	13.30	12.01	12.05	10.10	11.92
Q	0.05	—	—	1.89	—	—	—	4.21	—
Cor	—	0.62	0.40	0.66	0.08	—	0.62	4.69	0.10
Ne	—	—	—	—	1.34	3.12	—	—	4.10
Rb (ppm)	76.0	60.7	43.5	211.0	185.0	105.0	105.0	62.0	105.0
Sr	692	862	835	26	63	377	392	98	338
Ba	1200.0	987.0	1025.0	14.3	240.0	643.0	0240.0	265.0	240.0
V	19	18	20	36	32	19	12	15	15
Cr	5.5	—	2.0	—	4.0	—	2.5	2.0	—
Co	1.5	1.2	1.0	0.4	0.8	1.6	21.0	1.0	1.9
Ni	11.0	24.6	37.0	—	2.5	5.5	10.0	53.0	31.3
Y	11.0	22.5	12.8	86.8	57.0	31.2	5.2	20.5	25.0
Zr	355	387	502	1007	1235	637	262	955	899
Nb	81	114	122	173	261	129	48	227	188
La	97	59	39	187	180	110	33	117	112
Ce	213	186	190	283	290	182	136	213	183
Nd	40.0	50.1	30.5	106.0	72.0	68.1	18.0	50.0	46.0
Sm	5.10	8.09	5.15	16.20	9.60	11.00	2.10	6.65	6.28
Eu	1.55	2.94	2.12	3.30	2.18	2.76	0.74	1.43	1.19
Gd	3.10	6.20	3.85	12.80	8.50	7.16	1.40	4.80	4.32
Dy	2.10	4.68	2.85	13.80	8.20	6.84	0.90	3.95	4.49
Er	1.10	2.06	1.30	9.52	5.80	3.11	0.50	2.20	2.50
Yb	1.09	1.69	1.14	16.60	6.40	3.64	0.47	2.10	2.97
Th	13.7	13.8	13.2	49.5	29.0	14.1	19.3	29.0	25.4
Eu/Eu*	1.19	1.27	1.46	0.70	0.74	0.95	1.32	0.77	0.70

Major and trace elements of samples TMD 3b-2, TMD4-8, TMD10c-2, TMD15-5 and TMD16-1 were obtained by ICP-AES at Brest (Université de Bretagne Occidentale) following the method described in Cotten et al. (1995). Relative standard deviations are <2% for major elements, Rb and Sr, and <5% for other trace elements. Analyses of samples TMD4-3, TMD10c-1, TMD14-9 and TMD16-2 were performed at Nancy (CRPG-CNRS). Major elements were obtained by ICP-AES following the method described in Govindaraju and Mevelle (1987) and trace elements by ICP-MS following the method in Carignan et al. (2001). Analytical precision is at 1–5% for major elements, except for MnO, MgO, Ca₂O and P₂O₅ (10%). For trace elements, analytical precision is in the range 5–10% for abundances >50 ppm, 5–15% between 50 and 10 ppm, 5–20% between 10 and 1 ppm and 5–25% for abundances <1 ppm. Fe₂O₃*, total iron expressed as Fe₂O₃. LOI, loss on ignition. Eu/Eu* = Eu_N/√(Sm_N × Gd_N). CIPW norms calculated with adjusting Fe³⁺/Fe²⁺ ratio after Middlemost (1989). Q, normative quartz; Cor, normative corundum; Ne, normative nepheline.

(Fig. 3; TAS, Le Bas et al., 1986), all rocks lie either in the trachyte or trachy-andesite fields corroborating their alkaline affinity. One rock (TMD16-2) plots in the tephri-phono-lite field. This classification has to be considered to be influenced by the high degrees of seawater alteration. The freshest rocks are trachytes having less than 2 wt% of LOI, being devoid of CIPW normative corundum (Table 2, TMD3b-2; TMD4-8; TMD14-9). They are moderately alkaline (Na₂O + K₂O: 10–13 wt%), sodi-potassic, and slightly under-saturated or saturated in SiO₂ such as observed for trachytes on the Ormonde seamount (Bernard-Griffiths et al., 1997), where alkali magmatism was dated at 67–77 Ma (Féraud et al., 1982, 1986; Schärer et al.,

2000). The other rocks contain CIPW normative corundum (<5 wt%), associated in two rocks with significant CIPW normative quartz, which most likely is the direct result of seawater alteration.

6.2. Trace elements

Compatible trace element contents are low (Table 2; Ni < 53 ppm, Cr < 5.5 ppm, Co < 21 ppm, V < 36 ppm) which is in agreement with values expected for evolved lavas (Table 2). Cobalt content in the Gago Coutinho sample (TMD15-5) is high with respect to the other samples where compatible elements contents are low. This feature could

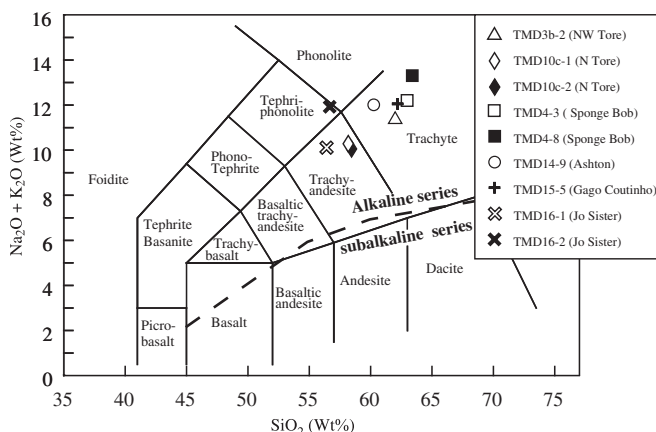


Fig. 3. Total-alkali vs. silica (Le Bas et al., 1986) discrimination diagram for our samples. The thick dashed line represents the boundary between the alkaline and the sub-alkaline domains (Miyashiro, 1978).

be related to seawater alteration of Fe–Mn hydroxides that incorporated Co. The incompatible element patterns of our samples (Fig. 4) are very similar to these of trachytes from Ormonde and Madeira which are interpreted to be produced by fractional crystallization from basaltic parental melts.

Five samples show negative anomalies in Sr and Ba (TMD4-3, TMD4-8, TMD14-9, TMD16-1 and TMD16-2). Although these rocks underwent various degrees of alteration the amplitude of trace element abundances do not seem to be correlated with alteration; they seem to be partly magmatic. Slightly negative Eu anomalies (Fig. 5) suggest fractionation of sodi-potassic feldspars during late stages of crystallization (Villemant et al., 1980). Rocks without Sr and Ba anomalies show weak positive Eu anomalies indicating that plagioclase is a cumulate phase in these rocks.

The concave shape of REE patterns is consistent with removal of amphibole and apatite from the magma (Fig. 5). The trachyte from Gago Coutinho (TMD15-5) displays significant depletion in moderately and slightly incompatible elements relative to trachytes from the Madeira Archipelago and Ormonde trachytes (Figs. 4 and 5). This suggests very evolved stages of crystallization including apatite fractionation causing magma depleted in middle REE and Y, and titanite producing depletion in middle REE and Nb. Fractionation of the latter phase is evidenced by Nb depletion. Such depletion also occurred in the TMD3b-2 lava (Tore NW). Three samples display Ce anomalies that could be related to the filling of vesicles and cracks by Fe–Mn hydroxides.

7. Geochronological and isotope results

7.1. General

The Tables 3 and 4 lists U–Pb analytical results of titanites and zircons, Table 5 gives initial Pb composition of

feldspars, Table 6 lists Rb–Sr analytical results for feldspars, and Table 7 shows initial Hf isotope compositions of zircon. For more analytical details we refer to the corresponding footnotes. Concordia and isochron diagrams for U–Pb analytical results are given in the Figs. 6–8. Initial Pb isotopic composition of feldspars are shown in Fig. 9, relative to the evolution of continental crust, the MORB-type mantle, and isotope signatures measured in magmatic rocks related to seamount formation in the Central Atlantic region (Fig. 10).

Given the fact that all titanites from the seamounts have significant amounts of initial common Pb, relative to radiogenic Pb, data are presented in both the Concordia ($^{207}\text{Pb}/^{235}\text{U}$ vs. $^{206}\text{Pb}/^{238}\text{U}$) and isochron diagrams ($^{238}\text{U}/^{204}\text{Pb}$ vs. $^{206}\text{Pb}/^{204}\text{Pb}$). The fundamental difference with this approach is that data of the Concordia plot are corrected for initial Pb, whereas the isochron data include initial Pb reflecting two different ways to derive ages. Since the titanite populations are young and poor in U, and consequently poor in radiogenic Pb, all ages are based on the $^{206}\text{Pb}/^{238}\text{U}$ chronometer because $^{207}\text{Pb}/^{235}\text{U}$ is not precise enough; however, the latter ratios serve to test whether the U–Pb chronometer behaved within analytical limits as a closed system since crystallization. Some of the ellipses (e.g., Figs. 6e and 8a) plot slightly to the left of the concordia curve, which can be explained by the uncertainty in common Pb correction due to real differences of initial Pb compositions in titanite, not identical to that measured in cogenetic feldspars.

7.2. U–Pb dating

7.2.1. Tore seamounts

From the northernmost expression of the volcanic range at Tore (Fig. 1) two samples were analyzed for titanite, and a third rock for titanite and zircon. In all populations, crystal surfaces are well developed and devoid of any corrosion features. From the TMD3b-2 trachyte from NW Tore, a series of 5 abraded and unabraded titanite and 4 zircon size fractions were analyzed. Titanites yield identically concordant data (Fig. 6a), defining an average $^{206}\text{Pb}/^{238}\text{U}$ age of 80.5 ± 0.9 Ma (2σ STERR). The same data produce together with initial Pb of cogenetic plagioclase an isochron age of 82.1 ± 2.4 Ma (Fig. 6b). The four zircon fractions yield one concordant and 2 very slightly discordant fractions with $^{206}\text{Pb}/^{238}\text{U}$ ages within error of the titanites. The fourth fraction plots about 10% discordant yielding a slightly older age around 99 Ma. These dates were not included in age calculation.

Six titanite fractions from the trachy-andesite (TMD10c-1) from north Tore yield identically concordant and very slightly discordant data defining a mean $^{206}\text{Pb}/^{238}\text{U}$ age of 88.3 ± 3.3 Ma (Fig. 6c). Plotted together with Pb data from plagioclase they yield a $^{238}\text{U}/^{204}\text{Pb}$ vs. $^{206}\text{Pb}/^{204}\text{Pb}$ isochron age of 87.8 ± 1.6 Ma (Fig. 6d). The third sample (TMD10c-2) is also a trachy-andesite from the same locality, for which four titanite fractions yield 3

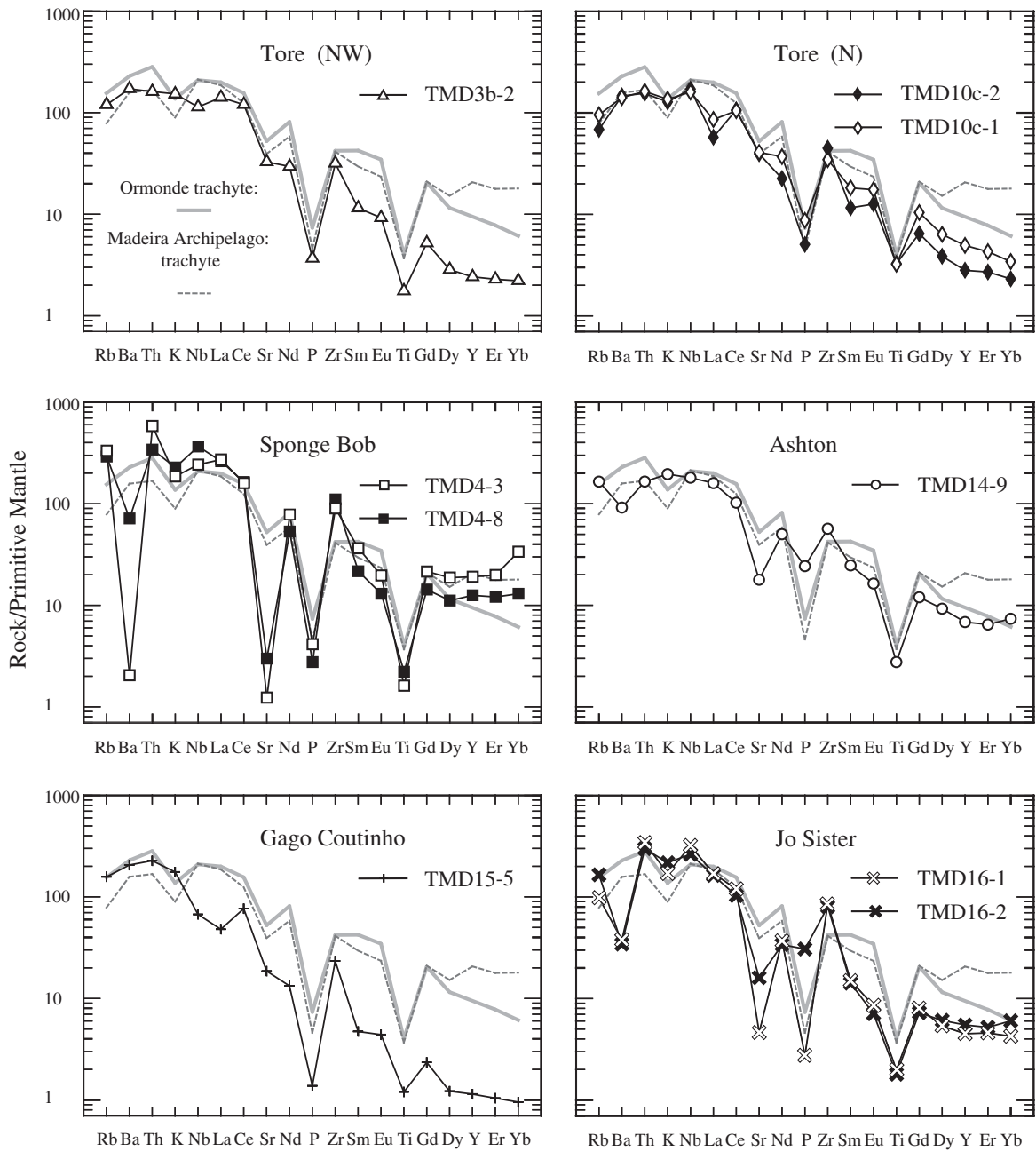


Fig. 4. Primitive mantle-normalized trace element patterns of the trachy-andesitic to trachytic samples studied here. For comparison are given a trachyte from the Ormonde seamount (Bernard-Griffiths et al., 1997) and a trachyte from the late Miocene-Quaternary Madeira Archipelago (Geldmacher and Hoernle, 2000). Normalization values from Sun and McDonough (1989).

identically concordant dates and a slightly discordant fraction defining together a mean age of 88.3 ± 3.9 Ma (Fig. 6e). Regressed with initial Pb of plagioclase they yield a $^{238}\text{U}/^{204}\text{Pb}$ - $^{206}\text{Pb}/^{204}\text{Pb}$ isochron age of 88.0 ± 4.5 Ma (Fig. 6f).

7.2.2. Sponge Bob seamount

Six titanite size-fractions from the Sponge Bob trachyte TMD4-3 yield identically concordant ages defining a mean age of 102.8 ± 0.7 Ma (Fig. 7a) and 3 zircon fractions give concordant to slightly discordant dates, with two fractions within error of the mean titanite age. The most discordant

fraction yields a slightly older age of about 111 Ma. Regressed together with K-fsp. the 6 titanite fractions give a isochron age of 102.7 ± 0.7 Ma (Fig. 7b). Six titanite fractions from the other trachyte (TMD4-8) yield equally concordant data defining a mean titanite age of 104.4 ± 1.4 Ma in the concordia plot (Fig. 7c) and 107.2 ± 3.4 Ma together with K-fsp. in the $^{238}\text{U}/^{204}\text{Pb}$ - $^{206}\text{Pb}/^{204}\text{Pb}$ isochron treatment (Fig. 7d).

7.2.3. Ashton seamount

Eight size-fractions of titanite from a trachyte (TMD 14-9) plot identically concordant defining an mean age of

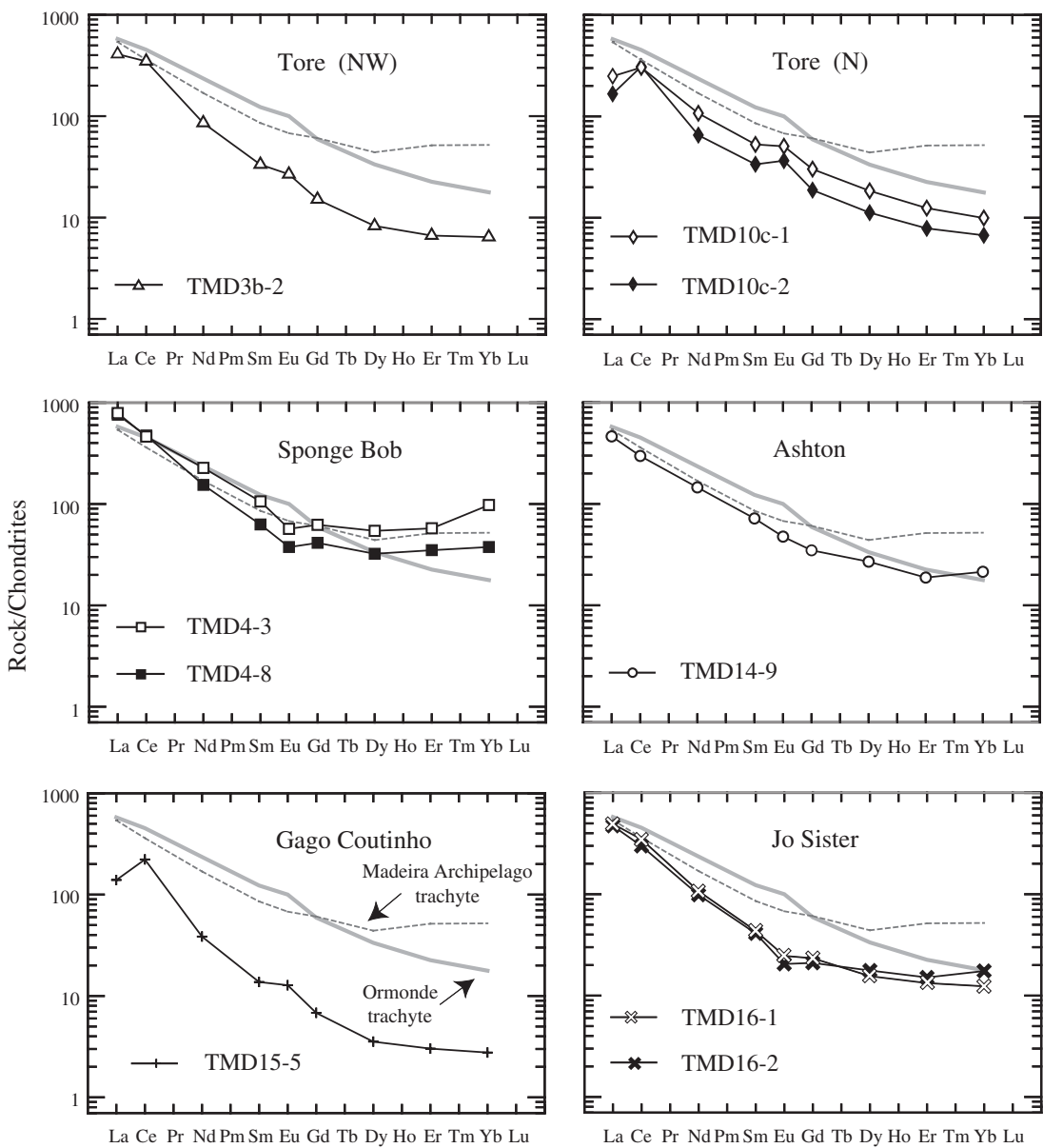


Fig. 5. Chondrite-normalized REE patterns of the samples studied here including the two reference rocks from Ormonde and Madeira seamount complexes. Normalization values from Sun and McDonough (1989).

94.3 ± 2.4 Ma, and two zircon fractions plot equally concordant (Fig. 7e). A third zircon analysis is about 2% discordant. The mean $^{206}\text{Pb}/^{238}\text{U}$ age of 96.8 ± 1.1 Ma for the three zircon fractions is identical to the titanite age. The full set of titanite and zircon data yields a mean age of 96.3 ± 1.0 Ma. The eight titanite fractions define together with K-fsp. a $^{238}\text{U}/^{204}\text{Pb}$ - $^{206}\text{Pb}/^{204}\text{Pb}$ isochron age of 93.7 ± 0.7 Ma (Fig. 7f).

7.2.4. Gago Coutinho seamount

Two of the five titanite fractions from a trachyte (TDM15-5) yield identically concordant ages, whereas the other three analyses plot by 2–4% discordant having slightly older $^{207}\text{Pb}/^{235}\text{U}$ ages (Fig. 8a). The mean $^{206}\text{Pb}/^{238}\text{U}$ age of all fractions is 92.3 ± 3.8 Ma. Their $^{238}\text{U}/^{204}\text{Pb}$ - $^{206}\text{Pb}/^{204}\text{Pb}$

isochron age including K-fsp. is 93.8 ± 1.5 Ma (Fig. 8b). These titanite ages agree within error with two new hornblende ages from other rocks of this seamount yielding 92.9 ± 0.6 and 94.5 ± 0.4 Ma obtained by the $^{40}\text{Ar}/^{39}\text{Ar}$ method (Geldmacher et al., in press).

7.2.5. Jo Sister seamount

Four titanite fractions from the trachy-andesite TMD16-1 plot identically concordant, whereas a fifth fraction lies about 2% discordant (Fig. 8c). Their mean $^{206}\text{Pb}/^{238}\text{U}$ age is 86.5 ± 3.4 Ma. All fractions regressed together with initial Pb measured in K-fsp. yield an isochron age of 86.7 ± 0.9 Ma (Fig. 8d). The tephri-phonolite sample (TMD16-2) yielded eight identically concordant titanite analyses, and a slightly discordant data defining a

Table 3

U-Pb analytical results (Concordia plot) for titanites and zircons from the different seamounts

Sample description ^a	Weight (mg)	Concentration (ppm)	^{206}Pb $\overline{^{204}\text{Pb}}$	^{206}Pb $\overline{^{207}\text{Pb}}$	^{206}Pb $\overline{^{208}\text{Pb}}$	Radiogenic Pb in atomic % ^c	^{206}Pb $\overline{^{238}\text{U}}$	^{207}Pb $\overline{^{235}\text{U}}$	Atomic ratios ^c	^{206}Pb $\overline{^{238}\text{U}}$	^{207}Pb $\overline{^{235}\text{U}}$	Apparent ages Ma ^c	Corr. Coef.	
<i>TMD 3b-2 (NW Tore)</i>														
Titanite														
(1) Titanite \approx 25 gr., NA, Ss, Pr, Frag., Gdn. to Lgt. Yw, opaq. incl.	0.2651	13.69	0.38	36.16	37.8	1.6	60.6	0.01222	8.5	0.0712	35.0	78.3	69.8	0.40
(2) Titanite 3 gr., Ls, sPr., Lgt. Yw, opaq. incl.	0.2990	13.66	0.44	44.10	35.8	2.1	62.1	0.01332	6.8	0.1073	16.3	85.3	103.5	0.51
(3) Titanite 12 gr., Ls, sPr., Lgt. Yw, opaq. incl.	0.3210	14.93	0.45	44.25	36.6	1.9	61.5	0.01263	7.5	0.0893	17.0	80.9	86.9	0.53
(4) Titanite 5 gr., Ls, sPr., Lgt. Yw	0.3455	15.61	0.48	50.48	36.3	2.1	61.6	0.01284	5.7	0.1003	14.1	82.3	97.1	0.51
(5) Titanite 6 gr., Ls, sPr., Lgt. Yw, opaq. incl.	0.2484	14.98	0.44	56.64	37.6	4.9	60.5	0.01275	9.9	0.0896	12.0	81.7	87.1	0.82
Zircon														
(6) Zircon 5 gr., Ss, sPr., Dk to Pl. Yw,	0.0900	117.29	2.01	135.54	62.7	3.0	34.3	0.01249	1.9	0.0832	4.2	80.0	81.2	0.54
(7) Zircon \approx 15 gr., Ss, sPr., Pl. Yw	0.0426	197.41	3.08	146.17	68.6	3.5	27.9	0.01242	2.4	0.0871	3.5	79.5	84.8	0.72
(8) Zircon \approx 12 gr., Ss, sPr., Pl. Yw	0.0787	232.75	4.66	305.98	54.7	2.9	42.4	0.01268	2.1	0.0932	4.2	81.2	90.5	0.58
(9) Zircon \approx 10 gr., Ss, sPr., opaq. incl.	0.0430	394.71	7.42	452.49	71.0	3.8	25.2	0.01549	1.3	0.1131	2.8	99.1	108.8	0.54
<i>TMD 10c-1 (N Tore)</i>														
Titanite														
(10) Titanite 8 gr., Ms to Ls, sPr., Gdn. to Lgt. Yw, opaq. incl.	0.2286	9.59	0.30	30.65	37.0	2.0	61.0	0.01326	9.5	0.0975	38.9	84.9	94.5	0.44
(11) Titanite 4 gr., Ls to VLs, sPr., Gdn. Yw	0.3191	9.75	0.34	48.98	34.6	2.1	63.3	0.01396	9.8	0.1162	17.4	89.4	111.6	0.62
(12) Titanite 14 gr., Ss to Ms, sPr., Gdn. Yw, opaq. incl.	0.2793	9.82	0.34	48.00	33.8	2.0	64.2	0.01360	11.7	0.1086	14.6	87.1	104.6	0.80
(13) Titanite 12 gr., Ms, sPr., Gdn. Yw, opaq. incl.	0.3727	9.07	0.35	44.70	32.2	2.1	65.7	0.01422	7.9	0.1254	16.5	91.0	119.9	0.58
(14) Titanite 8 gr., Ms, sPr., Lgt. Yw, opaq. incl.	0.2942	9.48	0.32	44.64	34.2	1.4	64.4	0.01349	10.7	0.0772	19.8	86.4	75.5	0.56
(15) Titanite 10 gr., Ms to Ls, sPr., Gdn. Yw, opaq. incl.	0.3658	10.62	0.40	51.02	32.4	1.7	65.9	0.01397	7.5	0.0988	12.8	89.4	95.6	0.63
<i>TMD 10c-2 (N Tore)</i>														
Titanite														
(16) Titanite \approx 10 gr., NA, Ss, Pr, Frag., Lgt. Yw, opaq. incl.	0.2417	9.20	0.27	27.80	43.0	3.1	53.9	0.01441	12.1	0.1452	32.9	92.3	137.7	0.52
(17) Titanite \approx 20 gr., NA, Ss, Pr, Frag., Lgt. Yw, opaq. incl.	0.3267	9.69	0.34	36.98	34.2	2.7	63.1	0.01393	7.4	0.1496	25.3	89.1	141.6	0.52
(18) Titanite \approx 25 gr., NA, Ss, Pr, Frag., Lgt. Yw, opaq. incl.	0.3960	10.63	0.37	26.74	32.8	2.6	64.6	0.01333	6.6	0.1455	42.0	85.4	137.9	0.64
(19) Titanite \approx 15 gr., NA, Ss, Pr, Frag., Lgt. Yw	0.2255	12.45	0.36	37.88	45.2	2.1	52.7	0.01515	15.5	0.0986	30.3	97.0	95.5	0.52
<i>TMD 4-3 (Sponge Bob)</i>														
Titanite														
(20) Titanite 7 gr., NA, Ls to VLs, sPr., Gdn. Yw	0.4524	9.16	0.45	28.58	28.9	1.5	69.6	0.01625	5.9	0.1164	53.4	103.9	111.8	0.58

(continued on next page)

Table 3 (continued)

Sample description ^a	Weight (mg)		Concentration (ppm)		206Pb 204Pb		Radiogenic Pb in atomic % ^c		Atomic ratios		Apparent ages Ma ^c		Corr. Coef.	
	U	Pb rad.	Meas. ^b	Pb	206Pb	207Pb	208Pb	238U	206Pb	235U	207Pb	238U		
(21) Titanite 7 gr., NA, Ls to Vls, Pr. Frag., Gdn. Yw	0.4502	11.73	0.54	31.97	30.5	1.2	68.3	0.01612	4.4	0.0904	39.6	103.1	87.9	0.49
(22) Titanite 12 gr., NA, Ls, Pr. Frag., Gdn. Yw, opaq. incl.	0.2302	11.90	0.53	30.31	31.1	1.3	67.5	0.01600	7.5	0.0942	38.4	102.3	91.4	0.39
(23) Titanite ≈12 gr., Ms to Ls, Pr. Frag., Gdn. Yw	0.2670	11.86	0.53	30.73	30.6	1.4	68.1	0.01590	7.0	0.0978	45.1	101.7	94.7	0.38
(24) Titanite 5 gr., NA, Ms, Pr. Frag., Gdn. Yw, opaq. incl.	0.2475	11.78	0.54	30.36	30.8	1.9	67.3	0.01639	8.6	0.1356	40.5	104.8	129.1	0.44
(25) Titanite 6 gr., NA, Ms to Ls, Lpt., Gdn. Yw	0.2007	12.13	0.55	28.48	30.6	1.1	68.3	0.01608	9.8	0.0796	65.8	102.8	77.8	0.31
Zircon														
(26) Zircon ≈12 gr., Ss, sPr., Nc, opaq. incl.	0.0632	312.74	8.11	440.97	53.7	2.7	43.6	0.01614	0.9	0.1124	1.7	103.2	108.1	0.62
(27) Zircon 5 gr., Ms, sPr., Nc, opaq. incl.	0.0701	237.05	5.80	316.11	56.3	2.7	41.0	0.01597	1.1	0.1060	2.0	102.1	102.3	0.62
(28) Zircon ≈14 gr., Ss, sPr., Nc, opaq./ap. incl.	0.0942	289.67	8.23	393.10	53.0	2.8	44.3	0.01745	3.7	0.1250	4.2	111.5	119.6	0.90
TMD 4-8 (Sponge Bob)														
Titanite														
(29) Titanite ≈10 gr., NA, Ms, Pr. Frag., Gdn. Yw, opaq. incl.	0.1822	11.60	0.49	22.67	33.3	1.7	65.0	0.01634	5.7	0.1144	74.2	104.5	110.0	0.74
(30) Titanite 6 gr., NA, Ms to Ls, Pr. Frag., Gdn. Yw	0.3526	12.48	0.61	22.73	27.5	1.4	71.1	0.01560	3.8	0.1065	61.6	99.8	102.8	0.87
(31) Titanite 4 gr., NA, Ls to Vls, Pr. Frag., Gdn. Yw	0.3684	12.95	0.66	22.21	27.0	0.1	71.9	0.01585	3.3	0.0895	59.5	101.4	87.0	0.75
(32) Titanite 8 gr., Ms to Ls, Pr. Frag., Gdn. Yw	0.3764	12.86	0.68	24.62	26.8	1.4	71.8	0.01634	3.5	0.1190	40.5	104.5	114.1	0.65
(33) Titanite 6 gr., Ls, Pr. Frag., Gdn. Yw	0.3674	12.27	0.64	28.62	27.1	1.0	71.9	0.01622	2.8	0.0834	30.6	103.7	81.3	0.47
(34) Titanite 8 gr., Ms to Ls, Pr. Frag., Gdn. Yw	0.3182	12.02	0.65	26.09	27.3	1.3	71.4	0.01701	2.4	0.1109	16.7	108.7	106.8	0.45
TMD 14-9 (Ashton)														
Titanite														
(35) Titanite 1 gr., Vls, sPr., Gdn. Yw	0.5448	9.99	0.47	34.32	26.8	1.2	72.0	0.01459	4.4	0.0876	43.2	93.4	85.3	0.53
(36) Titanite 11 gr., Ms, Pr. Frag., Gdn. Yw	0.1908	8.33	0.30	29.66	35.0	2.2	62.8	0.01454	11.9	0.1286	29.3	93.0	122.8	0.51
(37) Titanite 3 gr., NA, Ls, sPr., Gdn. Yw, opaq. incl.	0.1898	8.44	0.33	27.98	32.3	2.4	65.2	0.01454	9.7	0.1502	9.7	93.1	142.1	0.51
(38) Titanite 10 gr., Ms, Pr. Frag., Gdn. Yw, opaq. incl.	0.1165	8.96	0.28	27.20	40.2	2.2	57.6	0.01466	15.6	0.1120	15.6			
(39) Titanite ≈20 gr., Ss, Pr. Frag., Gdn. Yw, opaq. incl.	0.3374	8.79	0.38	30.64	29.3	1.4	69.3	0.01481	5.9	0.0974	46.9	94.8	94.4	0.51

(40) Titanite 1 gr., VLS, sPr., Gdn. Yw	0.3802	8.77	0.35	33.15	32.0	1.7	66.3	0.01479	6.0	0.1088	37.9	94.6	104.8	0.48
(41) Titanite 4 gr., NA, Ls to VLS, sPr., Gdn. Yw	0.3082	8.77	0.36	35.26	33.4	2.1	64.5	0.01593	14.0	0.1384	44.3	101.9	131.6	0.48
(42) Titanite 1 gr., VLS, sPr., Gdn. Yw	0.2570	8.47	0.34	29.90	32.5	1.8	65.7	0.01497	7.8	0.1142	44.4	95.8	109.8	0.49
Zircon														
(43) Zircon 4 gr., Ms, sPr., Nc	0.2142	56.06	1.05	323.70	69.2	3.3	27.5	0.01508	1.3	0.1000	2.2	96.5	96.8	0.66
(44) Zircon 6 gr., Ss, sPr., Nc, opaq./ap. incl.	0.0886	53.39	1.09	117.82	64.2	3.1	32.8	0.01525	4.0	0.1005	9.1	97.6	97.3	0.53
(45) Zircon 4 gr., Ms, sPr., Nc	0.0991	76.12	1.57	152.32	64.2	3.4	32.4	0.01531	3.1	0.1109	4.6	97.9	106.8	0.72

TMD 15-5 (Gago Coutinho)

Titanite														
(46) Titanite 8 gr., Ms, Pr. Frag., Gdn. to Dk Yw	0.1296	14.10	0.46	27.99	37.0	3.0	60.1	0.01402	8.7	0.1545	34.7	89.7	145.9	0.54
(47) Titanite 12 gr., Ms, Pr. Frag., Lgt. Yw, opaq. incl.	0.1350	13.16	4.7	0.37	44.9	2.7	52.4	0.01480	11.0	0.1221	17.3	94.7	117.0	0.65
(48) Titanite 15 gr., Ms, Pr. Frag., Lgt. to Dk Yw, opaq. incl.	0.1975	12.11	0.41	35.35	36.2	2.0	61.8	0.01425	9.4	0.1066	29.2	91.2	102.8	0.44
(49) Titanite 15 gr., Ms, Pr. Frag., Lgt. to Dk Yw, opaq. incl.	0.1854	14.47	0.50	36.17	36.8	2.7	60.5	0.01473	7.9	0.1483	18.4	94.2	140.4	0.56
(50) Titanite 20 gr., Ss, Pr. Frag., Lgt. Yw, opaq. incl.	0.2430	14.74	0.56	40.44	33.0	1.6	65.4	0.01440	9.3	0.0941	18.4	92.2	91.3	0.55

TMD 16-1 (Jo Sister)

Titanite														
(51) Titanite 10 gr., Ss, Pr. Frag., Lgt Gdn. Yw, opaq.incl.	0.2053	9.95	0.31	35.56	38.2	2.1	59.7	0.01394	12.0	0.1058	33.6	89.2	102.1	0.45
(52) Titanite 15 gr., NA, Ss, Pr. Frag., Lgt Gdn. Yw, opaq. incl.	0.2377	10.06	0.32	36.79	37.2	2.3	60.5	0.01359	10.4	0.1158	19.8	87.0	111.2	0.58
(53) Titanite 25 gr., Ss, Pr. Frag., Lgt Gdn. Yw, opaq.incl.	0.2567	10.07	0.34	30.64	35.5	2.1	62.5	0.01366	8.7	0.1106	22.8	87.5	106.5	0.50
(54) Titanite 9 gr., Ms, sPr., Lgt Gdn. Yw, opaq. incl.	0.2485	10.80	0.32	38.09	39.5	2.0	58.5	0.01336	9.6	0.0954	23.0	85.6	92.5	0.50
(55) Titanite 14 gr., Ms, sPr., Lgt Gdn. Yw, opaq. incl.	0.3621	10.86	0.35	39.58	36.0	1.8	62.2	0.01336	6.3	0.0918	23.8	85.6	89.2	0.44

(continued on next page)

Table 3 (continued)

Sample description ^a	Weight (mg)		Concentration (ppm) U	Radiogenic Pb in atomic % _e $\frac{^{206}\text{Pb}}{^{204}\text{Pb}}$		Atomic ratios ^c		Apparent ages Ma ^c	Corr. Coef.
	Pb rad.	Meas. ^b		$\frac{^{206}\text{Pb}}{^{207}\text{Pb}}$	$\frac{^{208}\text{Pb}}{^{238}\text{U}}$	$\frac{^{206}\text{Pb}}{^{235}\text{U}}$	$\frac{^{207}\text{Pb}}{^{235}\text{U}}$		
<i>TMD 16-2 (Jo Sister)</i>									
Titanite									
(56) Titanite \approx 10 gr., Ss to Ms, Pr, Frag., Gdn, Yw, opaq. incl.	0.2462	10.79	0.33	31.07	39.7	2.2	58.0	0.01402	6.9
(57) Titanite \approx 12 gr., Ss, Pr. Frag., Gdn, Yw, opaq. incl.	0.2716	10.80	0.38	28.75	40.1	1.9	63.0	0.01435	9.4
(58) Titanite 18 gr., NA, Ss, Pr. Frag., Lgt Gdn, Yw, opaq. incl.	0.3664	10.92	0.36	29.99	37.1	2.6	60.3	0.01423	5.2
(59) Titanite \approx 20 gr., NA, Ss, Pr. Frag., Gdn, Yw, opaq. incl.	0.3642	9.99	0.34	30.94	35.1	1.6	63.3	0.01372	5.2
(60) Titanite 6 gr., Ms to Ls, sPr., Gdn, Yw, opaq. incl.	0.2430	10.21	0.33	40.63	41.5	2.0	56.6	0.01548	11.8
(61) Titanite 8 gr., Ms, sPr., Gdn, Yw, opaq. incl.	0.1110	10.82	0.25	29.38	51.6	3.5	44.9	0.01354	18.3
(62) Titanite 10 gr., Ss, Pr. Frag., Gdn, Yw, opaq. incl.	0.2134	10.41	0.32	29.89	37.5	2.1	60.4	0.01315	11.9
(63) Titanite 10 gr., Ss to Ms, Pr. Frag., Gdn, Yw, opaq. incl.	0.2066	11.98	0.35	34.12	40.8	2.8	56.4	0.01365	12.9
(64) Titanite \approx 20 gr., NA, Ms, Pr. Frag., Lgt Yw, opaq. incl.	0.3099	10.47	0.32	36.27	37.8	2.3	59.9	0.01355	7.3

(a) Analyses were performed on transparent, euhedral titanites and zircons. NA, non-abraded (all other minerals mechanically abraded, following the technique described by Krogh (1982)). Gr., grains; Ss, small size (100–150 μm); Ms, middle size (150–200 μm); Ls, large size ($>250 \mu\text{m}$); Vls, very large size ($>250 \mu\text{m}$); Pr. Frag., prismatic fragment; sPr., short prismatic (length/width = 2 to 4); Yw, yellow; Dk., dark; Lgt., light, Gd., golden; Pl., pale; Ne, no color; opaq., incl., opaque inclusions, opaq./ap. incl., opaque and/or apatite inclusions. Mass discrimination is $0.10 \pm 0.05\%$ /amu for both Pb and U. Decay constants for ^{238}U and ^{235}U are those determined by Jaffey et al. (1971) and recommended by Steiger and Jäger (1977): $^{238}\text{U} = 1.55125 \times 10^{-10} \text{ y}^{-1} \pm 8.33 \times 10^{-14}$ (0.054%), $^{235}\text{U} = 9.84850 \times 10^{-10} \text{ y}^{-1} \pm 6.71 \times 10^{-13}$ (0.068%). Total Pb blanks are from 60 to 100 pg for titanite and from 20 to 34 pg for zircon. Total procedural U blanks are less than 1 pg in both procedures (see analytical procedures for details). (b) Ratios corrected for mass-discrimination and isotopic tracer. (c) Ratios corrected for mass-discrimination, isotopic tracer contribution, blank, and initial common Pb determined in leached K-fsp and Plag. from the same rock sample (Table 5).

Table 4

Isochron U-Pb data for the titanite fractions from the rock samples from the different seamounts

Samples	Concentration Pb comm. (ppm)	$^{206}\text{Pb}/^{204}\text{Pb}^{(a)}$ (α)	Error in % (2 σ -STERR)	238/204 ^(a) (μ)	Error in % (2 σ -STERR)
<i>TMD 3b-2 (NW Tore)</i>					
(1) Titanite	0.357	49.29	1.03	2467	1.11
(2) Titanite	0.257	64.66	0.65	3418	1.50
(3) Titanite	0.286	61.59	0.42	3360	4.74
(4) Titanite	0.231	74.94	0.87	4344	1.50
(5) Titanite	0.075	181.85	0.64	12761	1.82
(6) Plag.		19.14	0.07	—	—
<i>TMD 10c-1 (N Tore)</i>					
(7) Titanite	0.433	38.64	0.81	1443	0.96
(8) Titanite	0.099	109.01	1.47	6411	1.57
(9) Titanite	0.076	134.09	0.83	8425	0.50
(10) Titanite	0.158	72.72	1.14	3743	0.91
(11) Titanite	0.117	90.84	0.78	5287	0.54
(12) Titanite	0.134	91.67	0.59	5168	0.71
(13) Plag.		19.50	0.11	—	—
<i>TMD 10c-2 (N Tore)</i>					
(14) Titanite	0.543	35.22	0.57	1101	0.87
(15) Titanite	0.304	48.21	1.63	2072	1.47
(16) Titanite	0.938	29.17	0.35	737.1	0.62
(17) Plag.		19.34	0.08	—	—
<i>TMD 4-3 (Sponge Bob)</i>					
(18) Titanite	0.829	31.21	1.02	722.3	1.32
(19) Titanite	0.775	35.43	0.43	989.8	0.36
(20) Titanite	0.745	36.19	0.44	1045	0.50
(21) Titanite	0.736	36.23	0.74	1053	0.51
(22) Titanite	0.718	37.05	1.19	1072	1.32
(23) Titanite	0.842	34.63	0.71	942.6	1.33
(24) K-fsp		19.47	0.13	—	—
<i>TMD 4-8 (Sponge Bob)</i>					
(24) Titanite	3.43	23.27	0.66	223.3	0.98
(25) Titanite	3.83	22.98	0.52	215.3	1.13
(26) Titanite	4.32	22.75	0.32	197.7	1.13
(27) Titanite	2.49	25.19	0.55	340.6	0.88
(28) Titanite	1.26	30.00	0.54	640.2	0.51
(29) Titanite	1.85	26.93	0.17	429.9	0.50
(30) K-fsp		19.62	0.21	—	—
<i>TMD 14-9 (Ashton)</i>					
(31) Titanite	0.503	38.20	0.74	1291	0.48
(32) Titanite	0.394	39.35	0.42	1374	0.50
(33) Titanite	0.563	33.54	0.52	974.9	0.41
(34) Titanite	0.496	36.56	0.96	1172	0.61
(35) Titanite	0.556	34.59	0.54	1027	0.72
(36) Titanite	0.437	38.66	0.93	1305	1.15
(37) Titanite	0.516	35.32	0.94	1066	1.09
(38) K-fsp		19.36	0.04	—	—
<i>TMD 15-5 (Gago Coutinho)</i>					
(39) Titanite	0.977	32.63	0.65	941.3	0.38
(40) Titanite	0.309	60.50	0.24	2775	0.36
(41) Titanite	0.368	50.01	0.97	2145	1.17
(42) Titanite	0.482	48.27	0.55	1958	0.41
(43) Titanite	0.309	64.24	0.34	3110	0.91
(44) K-fsp		19.44	0.03	—	—
<i>TMD 16-1 (Jo Sister)</i>					
(45) Titanite	0.241	56.61	0.60	2730	0.50
(46) Titanite	0.316	47.97	0.51	2084	0.45
(47) Titanite	0.242	58.44	0.81	2914	0.97
(48) Titanite	0.288	52.45	0.78	2465	0.52
(49) K-fsp		19.50	0.05	—	—
<i>TMD 16-2 (Jo Sister)</i>					
(49) Titanite 9	0.572	36.81	0.42	1234	0.55

(continued on next page)

Table 4 (continued)

Samples	Concentration Pb comm. (ppm)	$^{206}\text{Pb}/^{204}\text{Pb}^{(a)}$ (α)	Error in % (2σ -STERR)	$^{238}/^{204}^{(a)}$ (μ)	Error in % (2σ -STERR)
(50) Titanite 10	0.661	34.85	0.88	1069	1.04
(51) Titanite 11	0.770	32.71	0.98	928.7	1.42
(52) Titanite 12	0.597	34.53	0.30	1095	0.33
(53) Titanite 17	0.349	46.96	0.82	2028	4.06
(54) Titanite 19	0.449	39.45	0.89	1517	1.29
(55) Titanite 20	0.311	53.93	0.99	2523	1.03
(56) Titanite 22	0.332	47.44	1.74	2062	0.95
(57) K-fsp		19.50	0.06	—	—

For each rock, initial Pb ratios were measured in plagioclases and K-fsp from the same rock (Table 5). ^(a) Ratio corrected for mass discrimination, isotopic tracer contribution, and Pb blank.

Table 5
Pb analytical results for feldspars of the different dated seamounts

Samples	Mineral	$(^{206}\text{Pb}/^{204}\text{Pb})_i$	$(^{207}\text{Pb}/^{204}\text{Pb})_i$	$(^{208}\text{Pb}/^{204}\text{Pb})_i$	Source		
		μ	ω	κ			
<i>Tore seamount</i>							
TMD3b-2	Plag	19.139 ± 0.013	15.544 ± 0.012	38.750 ± 0.030	9.68	37.23	3.85
TMD10c-1	Plag	19.496 ± 0.021	15.611 ± 0.021	39.281 ± 0.050	10.04	39.42	3.93
TMD10c-2	Plag	19.343 ± 0.016	15.642 ± 0.014	39.310 ± 0.025	9.89	39.54	4.00
<i>Sponge Bob seamount</i>							
TMD4-3	K-fsp	19.471 ± 0.025	15.714 ± 0.020	39.496 ± 0.049	10.04	40.41	4.03
TMD4-8	K-fsp	19.620 ± 0.042	15.828 ± 0.040	39.936 ± 0.109	10.19	42.19	4.14
<i>Ashton seamount</i>							
TMD14-9	K-fsp	19.363 ± 0.007	15.636 ± 0.006	39.179 ± 0.015	9.92	39.08	3.94
<i>Gago Coutinho seamount</i>							
TMD15-5	K-fsp	19.440 ± 0.006	15.661 ± 0.010	39.377 ± 0.028	9.99	39.84	3.99
<i>Jo Sister seamount</i>							
TMD16-1	K-fsp (microlite)	19.497 ± 0.009	15.652 ± 0.007	39.517 ± 0.016	10.04	40.36	4.02
TMD16-2	K-fsp (microlite)	19.496 ± 0.012	15.669 ± 0.009	39.552 ± 0.026	10.04	40.52	4.04

Plagioclases were spiked with the ^{233}U – ^{235}U – ^{205}Pb tracers to U/Pb. No significant amount of U was detected. Isotopic ratios were determined with a VG sector instrument using a Faraday cup and a Thomson 206 instrument using a Faraday cup and an electron multiplier system. For both instruments, the Faraday cups were used. All μ ($^{238}\text{U}/^{204}\text{Pb}$), ω ($^{232}\text{Th}/^{204}\text{Pb}$) and κ ($^{232}\text{Th}/^{238}\text{U}$) values were calculated for the U–Pb Concordia age of the same rock (Table 3) using a single-stage evolution model of the Earth mantle (Holmes, 1946). For these calculations, constants used are recommended by IUGS (Steiger and Jäger, 1977); an age of 4.56 Ga was used for the Earth (Allègre et al., 1995) and initial Pb composition measured in Canyon Diablo iron meteorite (Tatsumoto et al., 1973).

mean $^{206}\text{Pb}/^{238}\text{U}$ age of 89.3 ± 2.3 Ma (Fig. 8e). The titanite–K-fsp. $^{238}\text{U}/^{204}\text{Pb}$ – $^{206}\text{Pb}/^{204}\text{Pb}$ isochron age is 88.3 ± 1.3 Ma (Fig. 8f).

7.3. Pb–Sr–Hf isotope results

Pb, Sr, and Hf isotope data are summarized in the Tables 5–7, and plotted in the Figs. 9–12 together with data fields for Atlantic MORB, the latest Miocene to Quaternary São Miguel Island, the 14 Ma to recent Madeira Archipelago, and in particular, Ormonde and Monchique Cretaceous alkaline magmatism (Fig. 1). Where appropriate, data for worldwide OIB were also included as well as data from the Ampere, Seine, and Unicorn seamounts (Fig. 1). Initial Hf signatures are plotted vs. time in Fig. 11, together with evolution model curves for depleted MORB mantle (DM) and chondrite uniform mantle reservoir (CHUR).

8. Discussion

8.1. Geochronology

Since the U–Pb chronometer in zircon and titanite behave as closed systems at temperatures in excess to 700 °C (e.g., Krogh, 1973; Zhang and Schärer, 1996), all ages given in both the Concordia and isochron diagrams can be interpreted to date the crystallization of these minerals either in the magma chamber from where magmas were extracted or *in situ*, within the solidifying lava. Time intervals between chamber or lava crystallization can be considered to be short, compared to analytical uncertainties on the ages. Investigations of magma transfer kinetics show that these processes are very rapid occurring on the order of 100–200 ky (e.g. Condomines et al., 1982). Zircon data from two trachytes (Figs. 6a and 7a) substantiate the presence of very small amounts of older inherited zircon

Table 6
Rb-Sr analytical results for feldspars from the different seamount samples

Samples	Weight (mg)	Concentrations		$^{87}\text{Rb}/^{86}\text{Sr} \pm 2\%$	Concordia age (Ma)	$^{87}\text{Sr}/^{86}\text{Sr}$ measured	$(^{87}\text{Sr}/^{86}\text{Sr})_i$
		Sr (ppm)	Rb (ppm)				
<i>Tore seamount</i>							
TMD3b-2	9.95	459	2.39	0.0152	80.5	0.70308 ± 1	0.70306
TMD10c-1	9.34	630	0.51	0.0024	88.3	0.70341 ± 1	0.70340
TMD10c-2	8.03	705	0.53	0.0022	88.2	0.70294 ± 2	0.70294
<i>Sponge Bob seamount</i>							
TMD4-3	8.95	14.3	49.7	10.2	102.8	0.70869 ± 2	0.69396*
Duplicate	8.31	11.8	39.0	9.70	102.8	0.70928 ± 2	0.69528*
TMD4-8	8.46	72.7	23.6	0.951	104.4	0.70371 ± 3	0.70231
<i>Ashton seamount</i>							
TMD14-9	9.30	257	8.22	0.0935	96.3	0.70321 ± 1	0.70309
<i>Gago Coutinho seamount</i>							
TMD15-5	9.00	372	3.73	0.0294	92.3	0.70309 ± 1	0.70305
<i>Jo Sister seamount</i>							
TMD16-1	8.13	113	25.5	0.6596	86.5	0.70360 ± 4	0.70280
TMD16-2	9.20	69.4	29.9	1.26	89.3	0.70401 ± 3	0.70243

Measured $^{87}\text{Sr}/^{86}\text{Sr}$ ratios were normalized to $^{86}\text{Sr}/^{88}\text{Sr} = 0.1194$. Analytical uncertainties are $\pm 2\%$ for $^{87}\text{Rb}/^{86}\text{Sr}$. Uncertainties for measured $^{87}\text{Sr}/^{86}\text{Sr}$ are given in table relative to the last digits. The ^{87}Rb decay constant used to calculate $^{87}\text{Sr}/^{86}\text{Sr}_{(i)}$ is $1.42 \times 10^{-11}\text{y}^{-1}$ (Steiger and Jäger, 1977). Rb and Sr concentration were performed on a Thomson 206 mass-spectrometer using electron multiplier and a single Faraday cup. Isotopic compositions of Sr were performed on a VG sector mass-spectrometer using a single Faraday cup. *, overcorrection from high $^{87}\text{Rb}/^{86}\text{Sr}$.

Table 7
Hf isotope analytical results for the dated zircons of the different seamount samples

Samples	$^{176}\text{Hf}/^{177}\text{Hf}$ measured	Concordia age (Ma)	ϵHf_0 (present day)	ϵHf_i
<i>Tore seamount</i>				
TMD 3b-2 Z1	0.282983 ± 8	80.5	7.5	9.3 ± 0.3
TMD 3b-2 Z2	0.283084 ± 7	80.5	11.0	12.9 ± 0.2
TMD 3b-2 Z3	0.282996 ± 11	80.5	7.9	9.7 ± 0.4
<i>Sponge Bob seamount</i>				
TMD 4-3 Z1	0.282966 ± 8	102.8	6.9	9.2 ± 0.3
TMD 4-3 Z2	0.282901 ± 8	102.8	4.6	6.9 ± 0.3
<i>Ashton seamount</i>				
TMD 14-9 Z1	0.282965 ± 5	96.3	6.8	9.0 ± 0.2
TMD 14-9 Z2	0.282953 ± 8	96.3	6.4	8.6 ± 0.3
TMD 14-9 Z3	0.282942 ± 7	96.3	6.0	8.2 ± 0.2

Measured $^{176}\text{Hf}/^{177}\text{Hf}$ are corrected for mass-discrimination using $^{179}\text{Hf}/^{177}\text{Hf} = 0.7325$ (Patchett and Tatsumoto, 1980). JMC- 475 Hf standard: $^{176}\text{Hf}/^{177}\text{Hf} = 0.282163 \pm 9$ (Blichert-Toft et al., 1997). To calculate epsilon values (ϵHf_0 and ϵHf_i) the following constants were used: age of the Earth = 4.56 Ga; $(^{176}\text{Lu}/^{177}\text{Hf})_{\text{CHUR}}^0 = 0.0332 \pm 2$; $(^{176}\text{Hf}/^{177}\text{Hf})_{\text{CHUR}}$ today = 0.282772 ± 29 ; $(^{176}\text{Hf}/^{177}\text{Hf})_{\text{CHUR}}$ at 4.56 Ga = 0.279718 ± 29 (Blichert-Toft and Albarede, 1997); $\epsilon\text{Hf}_{\text{sample}}^T = [(^{176}\text{Hf}/^{177}\text{Hf})_{\text{sample}}^T / (^{176}\text{Hf}/^{177}\text{Hf})_{\text{CHUR}}^T - 1] \times 10^4$, with $(^{176}\text{Hf}/^{177}\text{Hf})_{\text{CHUR}}^T = (^{176}\text{Hf}/^{177}\text{Hf})_{\text{CHUR}}^0 - (^{176}\text{Lu}/^{177}\text{Hf})_{\text{CHUR}}^0 \times (e^{iT} - 1)$ (Patchett et al., 1981); $\lambda_{\text{Lu}} = 1.93 \times 10^{-2} \text{ Ga}^{-1}$ (Sguigna et al., 1982).

incorporated into the host magma. Such inheritance in mantle-derived rocks has also been observed for dikes intruding the ultramafic-mafic complex of the Ligurian Alps, where relic zircons appear to have been extracted from the subcontinental lithospheric mantle, tapped by asthenospheric magmas (Borsi et al., 1996). Alkali lavas (77 Ma) on top of the Ormonde seamount also shows zircon inheritance (Schärer et al., 2000).

The available U-Pb dates show that seamount genesis along the continent-ocean transition of the Iberian margin (Fig. 1) occurred over a period of at least 23.9 ± 1.2 m.y.

bracketed by the oldest seamount dated at 104.4 ± 1.4 Ma (107.2 ± 3.4 Ma for isochron), and 80.5 ± 0.9 Ma (82.0 ± 2.4 Ma for isochron) for the youngest. This implies that alkaline magmatism occurred roughly 21 m.y. after formation of the first Atlantic oceanic crust around 125–130 Ma (Gradstein et al., 2004). In consequence, construction of the seamounts cannot be attributed to Atlantic spreading as proposed earlier; they should be considered to reflect an exclusively intra-plate phenomena. An important time gap of about 70 m.y. exists between 104–81 Ma seamount emplacement along the northern segment of

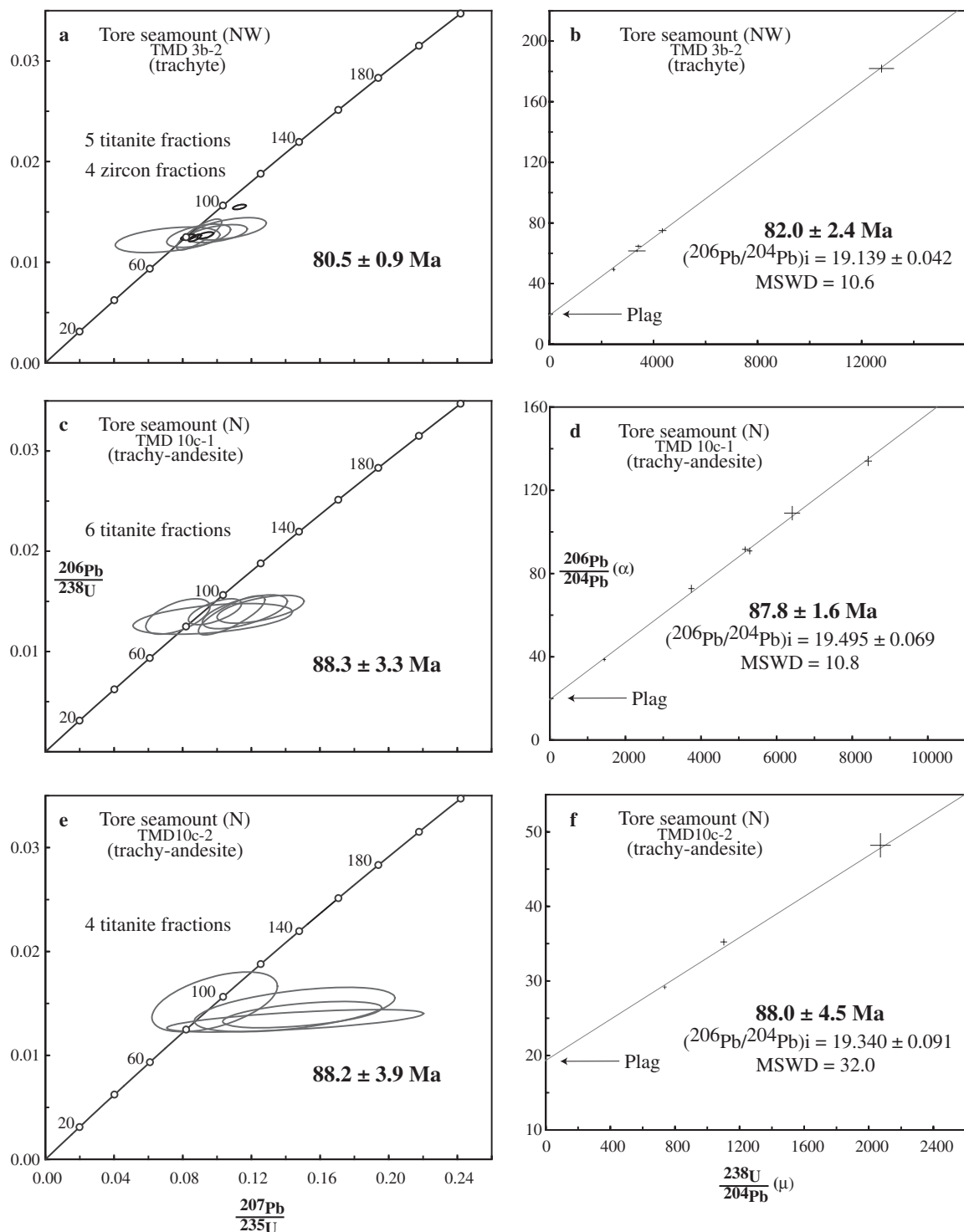


Fig. 6. Concordia and isochron plots of U-Pb dating results of titanite and zircon. Ellipses correspond to 2σ -STERR. Symbols in the isochron plots are two times larger than relative errors. Zircon fractions represented by thick ellipses.

the Tore-Madeira Rise, and the much younger, 14 Ma to recent formation of the Madeira Archipelago. The Cretaceous volcanic phases dated in this study could potentially be followed by Miocene to recent volcanism, as suggested by earlier K-Ar dating of Wendt et al. (1976) from the Josephine seamount. New $^{40}\text{Ar}/^{39}\text{Ar}$ data from this seamount and a further two seamounts south of Josephine

give ages between 0.5 and 16 Ma (Geldmacher et al., in press). These date corroborate the genesis of the Tore Madeira rise to be significantly more complex than previously thought. For instance, very contrasting ages of 86–89 Ma vs. 4 Ma indicate two very distinct phases of Jo Sister magmatic activity in Late Cretaceous and Pliocene times. Considering the sensitivity of whole-rock matrix to

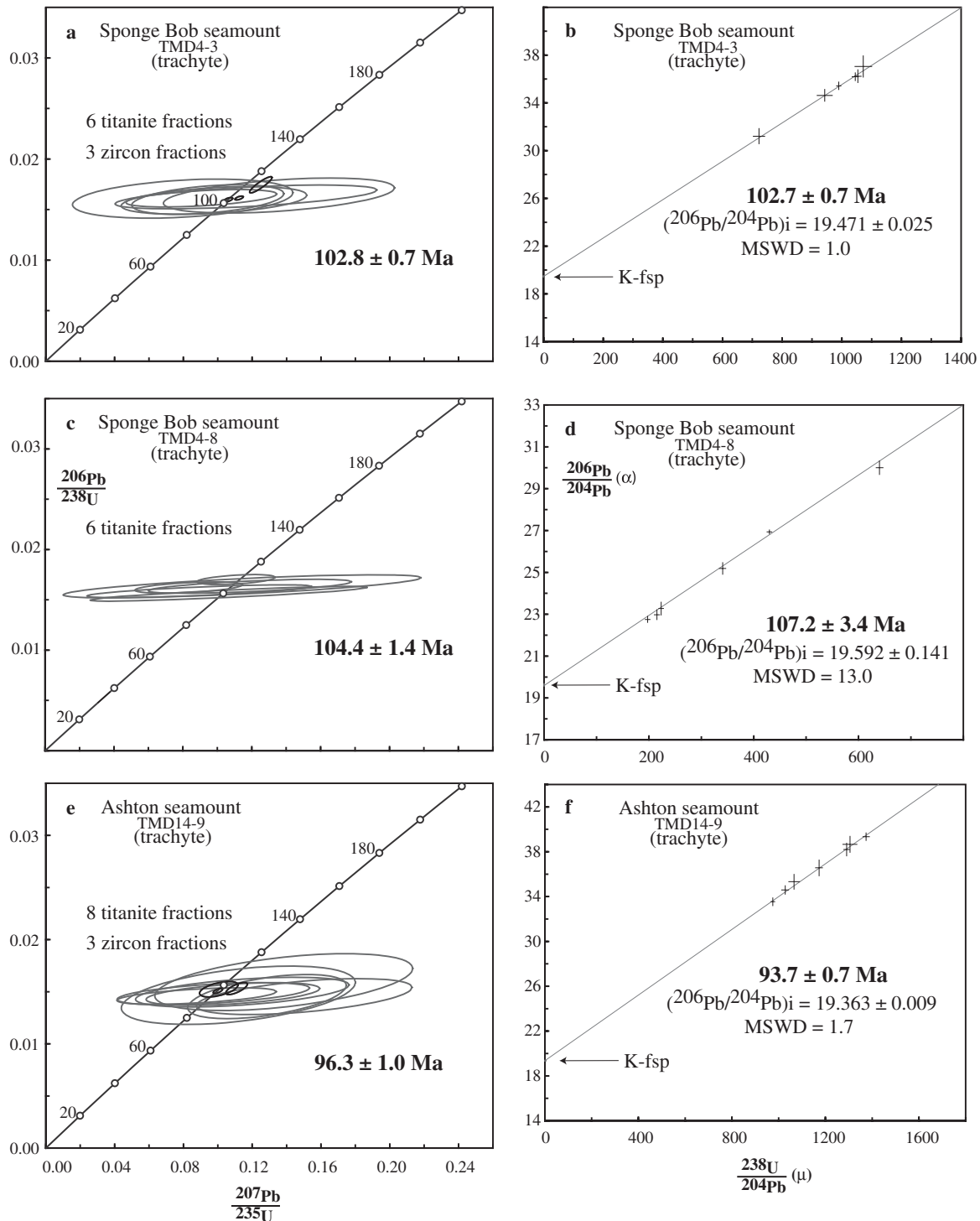


Fig. 7. Concordia and isochron plots of U-Pb dating results of titanite and zircon. Ellipses correspond to 2σ -STERR. Symbols in the isochron plots are two times larger than relative errors. Zircon fractions represented by thick ellipses.

seawater interactions, K-Ar and $^{40}\text{Ar}/^{39}\text{Ar}$ whole-rock ages from these seamounts require confirmation.

8.2. Petrogenesis of samples

All samples studied here are evolved alkaline lavas whose compositions range from trachy-andesite to tra-

chite, which cannot be derived by simple partial melting of peridotites. To explain their origin the following options have to be considered: (1) differentiation by crystal fractionation from an originally alkali-basaltic liquid, (2) small degrees of melting of non-peridotite sources, and (3) mixing of alkali-basaltic liquids with highly differentiated magmas having SiO_2 above 65 wt%. Note that the most evolved

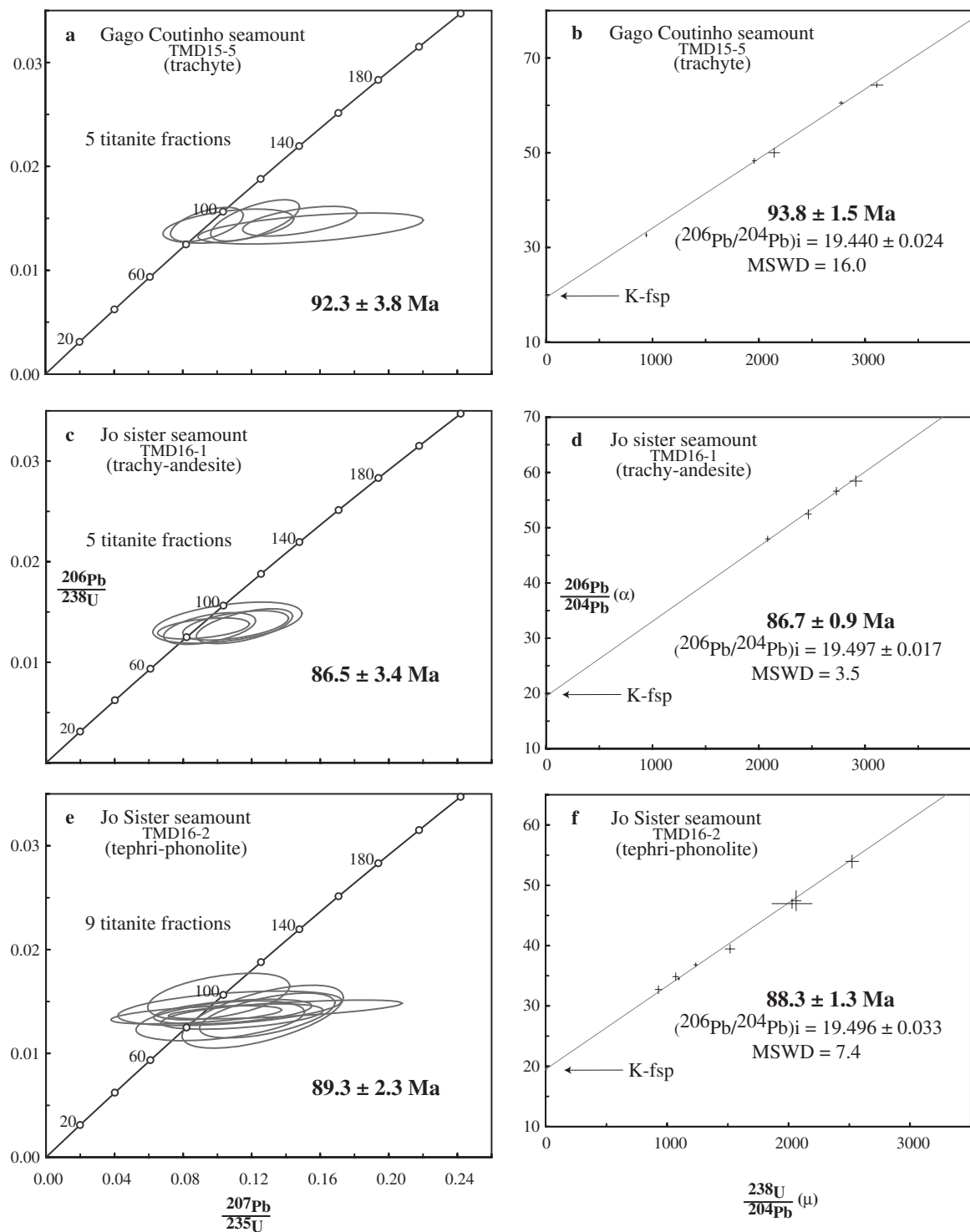


Fig. 8. Concordia and isochron plots of U-Pb analytical results of titanite and zircon. Ellipses correspond to 2σ -STERR. Symbols in the isochron plots are two times larger than relative errors.

rock analyzed here is a trachyte with 63.4 wt% SiO₂ (Table 2). To evaluate these possibilities it is useful to recall the following: (a) about half of the dredged samples are trachy-andesites and trachytes, whereas the remaining rocks are basanites and alkali-basalts; (b) the lavas studied here have experienced different degrees of crystal fractionation prior to extrusion, as indicated by anomalies in Ti, P, Sr

and Ba (Fig. 4). These anomalies can be ascribed to fractional crystallization of Fe-Ti oxides, apatite and feldspar. Plagioclase fractionation is corroborated by strong depletion in Sr and modestly negative Eu anomalies in some samples (Figs. 4 and 5). Some of the lavas are plagioclase cumulative as indicated by their slightly positive Eu anomalies.

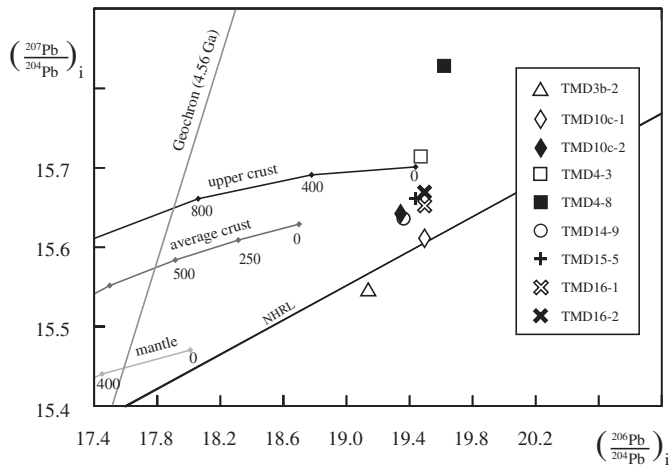


Fig. 9. $^{206}\text{Pb}/^{204}\text{Pb}$ vs. $^{207}\text{Pb}/^{204}\text{Pb}$ diagram of initial Pb isotopic composition measured in feldspars from the dated samples. Accuracy (2σ) of individual data are within the size of the symbols. The model curves for a single-stage evolution of the Earth (Geochron; Holmes, 1946), a multi-stage evolution of the Earth mantle, version II (Zartman and Doe, 1981), the evolution of the upper continental crust, version II (Zartman and Doe, 1981), and the model for average continental crust (Stacey and Kramers, 1975) are given for reference. The samples studied are represented with the same legend as in Fig. 3.

Storage for a considerable period of time of liquids in magma chambers may lead to wallrock assimilation, in particular the Iberian subcontinental mantle. Alternatively, “en route” contamination during magma ascent through this lithosphere could also occur. Arguments in favor of this are (1) the small components of inherited Pb present in a few zircons (Figs. 6a and 7a), (2) differences in initial Hf among zircons from a single rock (Fig. 11), and (3) relatively radiogenic common Pb, in particular ^{207}Pb which does not match any MORB or OIB mantle reservoir. Cases of high initial $^{207}\text{Pb}/^{204}\text{Pb}$ of subcontinental mantle are also reported for lherzolite xenoliths of recent volcanic rocks from Tanzania, E-Africa (Cohen et al., 1984).

8.3. Isotope characteristics

Initial Pb isotopic compositions (Fig. 9) are significantly more radiogenic than a single stage model (Geochron) and they roughly plot at the end or beyond the model evolution curve for upper continental crust (Zartman and Doe, 1981). Their variation is relatively limited in $^{206}\text{Pb}/^{204}\text{Pb}$ ranging from 19.139 to 19.620, whereas variations in $^{207}\text{Pb}/^{204}\text{Pb}$ are significantly larger lying between 15.544 and 15.828. Plotted in an $^{206}\text{Pb}/^{204}\text{Pb}$ - $^{207}\text{Pb}/^{204}\text{Pb}$ diagram (Fig. 10a) the data range from the Atlantic field for NW-Tore to significantly more radiogenic values. The same data trends are present in the $^{206}\text{Pb}/^{204}\text{Pb}$ - $^{208}\text{Pb}/^{204}\text{Pb}$ diagram (Fig. 10b) lying sub-parallel to data field from São Miguel Island of the Azores Archipelago (Widom et al., 1997; Moreira et al., 1999). A heterogeneous plume, containing in addition an old subcontinental lithospheric mantle was proposed for the origin of the São Miguel Island (Widom et al., 1997; Moreira et al., 1999). Lead of 3 sea-

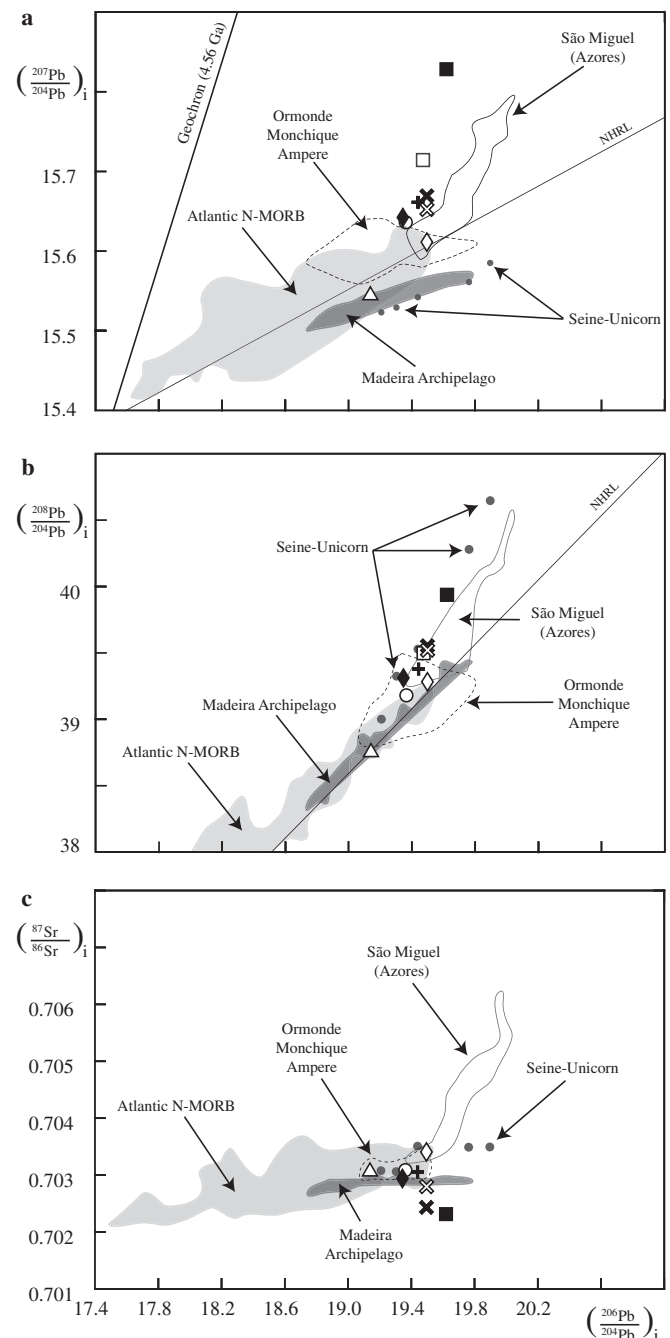


Fig. 10. Initial Pb-Pb and Pb-Sr isotopes diagrams. Data are shown relative to the present day data fields of Atlantic N-MORB, the Madeira Archipelago and São Miguel Island of the Azores Archipelago (PetDB and GEOROC databases). Also shown are data for the Monchique and Ormonde alkaline rocks (Bernard-Griffiths et al., 1997), as well for the seamounts at Ampere, Coral Patch, Seine, and Unicorn (Geldmacher and Hoernle, 2000; Geldmacher et al., 2005).

mounts (NW and N-Tore and Ashton) lies in the field of Atlantic MORB. Most initial $^{87}\text{Sr}/^{86}\text{Sr}$ values range from 0.70232 to 0.70340. A sample yields unreasonable low ratios below 0.70 (TMD4-3, Table 6). Since our single feldspars grains show very weak alteration features, it may be that apparent opening of the Rb-Sr system could be related to seawater alteration. In our case such alteration

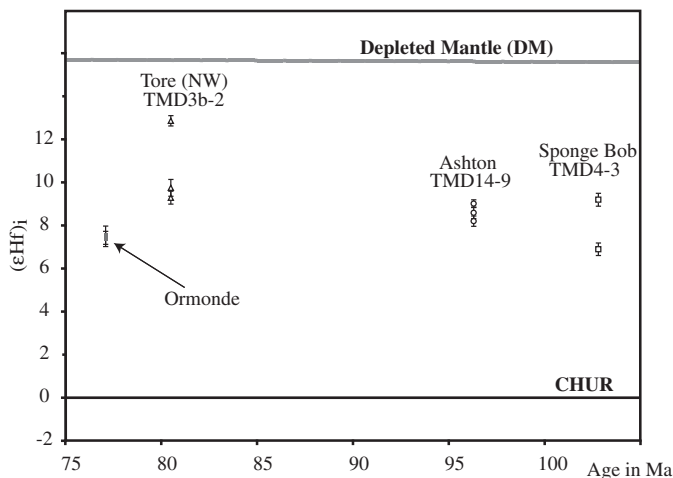


Fig. 11. Initial Hf isotopes signatures in relation to U–Pb ages of the different seamounts. For comparison, the evolution line of a chondritic mantle reservoir (CHUR) and an increasingly depleted mantle (DM) are plotted.

caused an increase in Rb/Sr leading to over-corrected initial ratio.

A plot of initial Sr and Pb isotope signatures reveals that three of our seamount samples (Jo Sister and Sponge Bob) are more radiogenic in ^{206}Pb than MORB, and two samples are less radiogenic in ^{87}Sr . These three rocks are a trachy-andesite (TMD16-1), a tephri-phonolite (TMD16-2), and a trachyte (TMD4-8). To evaluate the influence of potential bias by seawater alteration, we have calculated maximal shifts of initial $^{87}\text{Sr}/^{86}\text{Sr}$. We used 5–10% Rb/Sr fractionation that corresponds to the extent of maximal observed feldspar alteration. This test shows that the ratios are affected to a very low degree only. For example, sample TMD16-1 corrected for 10% Rb/Sr-fractionation yields a minimum $(^{87}\text{Sr}/^{86}\text{Sr})_i$ of 0.70271 and a maximum $(^{87}\text{Sr}/^{86}\text{Sr})_i$ of 0.70287, compared to the original value of 0.70280 (Table 6). The other five trachy-andesites and trachytes plot in the Atlantic MORB field as do Pb–Sr data from Ormonde and Serra de Monchique (Fig. 10c).

Zircons from three of the dated rocks were analyzed for their initial Hf isotope composition to help constrain potential magma sources. Three zircon fractions were measured for the trachyte samples TMD3b-2 and TMD14-9, and two for the TMD4-3 trachyte. Initial epsilon Hf values (ϵHf_i) ranging from +6.9 to +12.9 (Table 7; Fig. 11) lie between the CHUR evolution line and a MORB type reservoir (DM). It is important to note that differences exist in epsilon Hf between zircon fractions of a given sample that are much in excess of the analytical uncertainty. These differences could result from: (1) mixing of magma batches, each containing zircon crystals at the time of mixing, (2) incorporation of xenocrystic zircon by extraction from adjacent wallrocks in a magma already containing zircon, and (3) a successively adding relatively small volume of isotopically distinct melts to a large volume of magma with a uniform isotope composition, coupled with new zircon growth at, or shortly after the time of mixing. In any case,

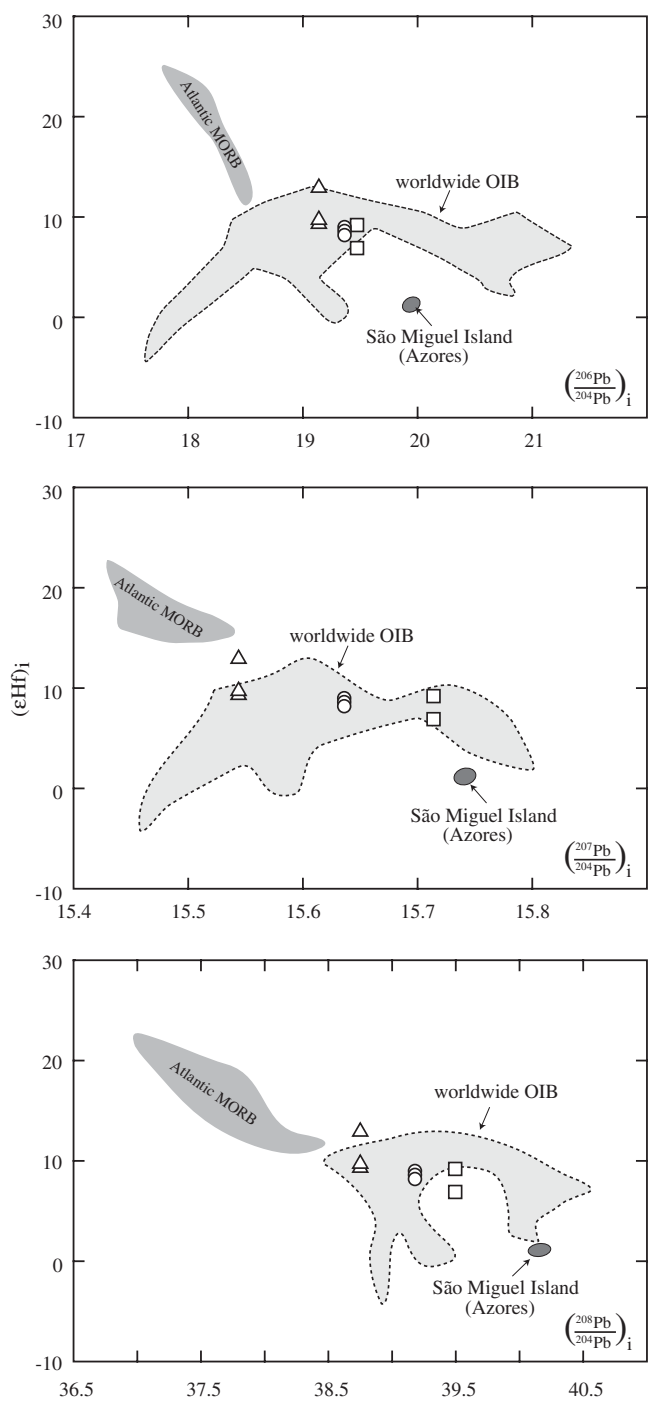


Fig. 12. Feldspar initial Pb vs. zircon initial Hf isotope signatures of the different seamount samples, compared to the present day data fields of Atlantic MORB (Salter and White, 1998; Nowell et al., 1998), worldwide OIB (Salter and White, 1998; Lassiter et al., 2003), and the São Miguel Island (Snyder et al., 2004).

this observation of differences in initial Hf signatures of zircon is consistent with the presence of small inherited radiogenic Pb components necessarily carried by relic zircons (Figs. 6a and 7a) that also requires extraction of grains from a different host. This host must have been significantly older than the magma, to explain inheritance in zircon, already observed in the 77 Ma old alkali rock on Ormonde (Fig. 11).

Fig. 12 shows correlations between initial Hf and Pb isotope signatures measured in the seamounts, plotted relative to the fields of Atlantic MORB, worldwide Ocean Island Basalts (OIB), and São Miguel Island. All our alkaline volcanic lavas are distinct from both Atlantic MORB and São Miguel volcanic rocks but they lie within the field of OIB sources.

8.4. Geodynamic context of magmatism

From a regional point of view, Cretaceous volcanoes roughly follow the significantly older J anomaly but also the different branches of the Azores-Gibraltar Fracture Zone (AGFZ; Fig. 1). This suggests these structures have played a major role for enabling magma ascent. An age difference of 7.8 ± 4.2 Ma observed for the two localities of the Tore seamount complex substantiates the hypothesis that its construction includes at least two distinct magmatic pulses. Since the two localities lie in the vicinity of the northern branch of the Azores-Gibraltar Fracture Zone (AGFZ in Fig. 1), magmatic activity could have been focused along the fault. It may also be that age gradients exist along faults such as suggested earlier by Féraud et al. (1977). Another useful observation is that formation of the seamounts between Tore and Jo Sister, and possibly up to the Madeira Archipelago, approximately follows the main direction of initial ocean spreading marked by the J anomaly (125–130 Ma) formed about 20 m.y. prior to first alkaline volcanism at 104 ± 1 Ma (Fig. 1). The boundary between the stretched continental lithosphere of Iberia and the oceanic lithosphere can be considered as a zone of weakness, and magmas can preferentially percolate through this zone, compared to normal oceanic or continental lithosphere. It is likely that this zone of weakness served as a guide for magma ascent and orientation of seamount emplacement. In extrapolating the actual spreading rate of 2.2 cm/y (DeMets et al., 1990) to Upper Cretaceous time, the Atlantic ridge would have been located about 460 km to the west at the time of volcanism at 104 Ma, using the 125–130 Ma initiation age for beginning Atlantic opening (Gradstein et al., 2004). On the other hand, if a very slow initial spreading rate of 0.67 cm/y is used (Srivastava et al., 2000) the distance would have been only 134 km.

From our new ages we cannot see any significant regional age trend along the seamount chain lying to the north of the Azores-Gibraltar-Fracture-Zone (AGFZ; Fig. 1). The same is true if we include the earlier dated 77 Ma old alkaline magmas on the Ormonde seamount and the 72 Ma old Serra de Monchique on the continent (Fig. 1). Given analytical uncertainties on these ages some minor regional age-trends may exist; however, they necessarily would lie within a few million years. An illustration for this are the three ages of the Tore seamounts (88.2 ± 3.9 ; 88.3 ± 3.3 ; 80.5 ± 0.9 Ma) where any age trend is necessarily limited to a few million years. Moreover, potential migration of

volcanism north of the AGFZ must be compatible with motions of the Iberian plate at that time. Different hypotheses were proposed for movements of Iberia between 120 and 80 Ma, converging toward an agreement that it moved in southeast direction by about 800 km (e.g., Malod, 1989; Olivet, 1996; Sibuet et al., 2004b). Since we cannot see the corresponding age trend in our volcanoes, i.e., the absence of ages becoming increasingly younger towards the northwest, a Hawaiian-type plume model can be ruled out. This excludes the northern part of the Tore-Madeira Rise to be the simple volcanic trace of Iberian motion over such a hot spot between 120 and 80 Ma. Concerning the Tore-Madeira Rise region to the south of the AGFZ, the Oligocene–Miocene Unicorn, Ampere, and Seine volcanoes do not match the axis of the rise, lying significantly to the east (Fig. 1). Their emplacement most likely reflects a particular geodynamic context, possibly in relation to lithospheric discontinuities such as expressed by the large E–W striking faults in this region (Fig. 1) as suggested previously by Geldmacher et al. (2005). An alternative hypothesis considers these seamounts to belong to the Madeira hot-spot track across the African plate, spanning the Madeira Archipelago through the Unicorn, Seine, Ampere and Ormonde seamounts to the Serra de Monchique alkaline complex (Geldmacher et al., 2000, 2005; Geldmacher and Hoernle, 2000).

To explain the large extent of alkaline magmatism in the eastern North Atlantic (Fig. 1) migration of melting within the head region of a long lived thermal anomaly seems to be the most likely model. Such activity since at least 104 Ma (oldest seamount) to recent times (Madeira Archipelago) would be consistent with the persistent existence of large plumes, reaching life times of 130 m.y. (e.g., Courtillot et al., 2003). This would mean that the same thermal anomaly was/is periodically active underneath the Atlantic oceanic crust, the transition zone, and the continental margin of Iberia. Finite-frequency tomography indicates the presence of a deep-rooted plume (>1000 km depth) having maxima P-wave anomalies at about 300 km depth, underneath the Azores, Canary, and Madeira complexes (Montelli et al., 2004). This assumption is also valid in space and time if the about 300 km W–E anti-clockwise rotation of the Iberian Peninsula is considered.

8.5. Origin of magmas

In considering the full set of new data it seems that 104–81 Ma alkaline magmas were derived from sources having a component with: (1) low Rb/Sr, (2) relatively high epsilon Hf and (3) relatively high $^{207}\text{Pb}/^{204}\text{Pb}$ at a given $^{206}\text{Pb}/^{204}\text{Pb}$ (Figs. 10–12). To acquire such isotopic signatures, the magma sources must have evolved in isolation for several hundred million years. In any model explaining the genesis of our alkaline magmas, a contribution of crustal material is required to explain radiogenic Pb, and in particular the presence of inherited old radiogenic Pb

discovered in zircon (Figs. 6a and 7a). The most likely explanation is the incorporation of very minor amounts of detrital sediments, assimilation of lower continental crust or lithospheric mantle containing relic detrital sediments. The observed decoupling of Hf–Sr from Pb signatures is entirely consistent with the fact that mantle melts can very easily be shifted in Pb by addition of even very small amounts (a few %) of continental material (e.g., Schärer, 1991). This is not the case for Hf and Sr for which mantle melts have a strong buffering effect.

Interaction of OIB-type magmas with material from the Iberian lithospheric mantle seems to be the most plausible interpretation, satisfying the presence of Rb-depleted lithospheric mantle, highly radiogenic Pb, and inherited Pb in zircon. Supporting evidence in favor of this hypothesis are Sr data from the peridotite ridge about 500 km off the coast of Iberia (Fig. 1) where $^{87}\text{Sr}/^{86}\text{Sr}$ as low as 0.7021 were observed in Cpx in lherzolites, representing potential contaminating material of our magmas (Chazot et al., 2005). It has been shown that isotopic heterogeneity of Iberian margin ultramafic rocks were already present at the time of rifting, reflecting a long and complex history of depletion and enrichment events affecting old mantle (Chazot et al., 2005). We emphasize that this model concerns alkaline volcanic activity investigated here, i.e., the northern section of the Tore-Madeira Rise north of the Azores-Gibraltar Fracture Zone (Fig. 1). It is also valid for the origin of the contemporaneous alkaline rocks on Ormonde and at continental Monchique, as well as the seamounts Ampere, Seine and Unicorn (Bernard-Griffiths et al., 1997; Geldmacher and Hoernle, 2000; Schärer et al., 2000; Geldmacher et al., 2005).

Given the geochemical and isotopic data for the northern part of Tore-Madeira Rise (Figs. 9, 10 and 12) we cannot reliably deduce mixing proportion between the OIB-type component, materials from the Iberian lithospheric mantle, and the necessarily very small amounts of crustal components present within or attached to the lithospheric mantle. This three components hypothesis applies to the seamounts composing the northern Tore Madeira rise volcanoes. On the other hand, sources of alkaline magmas to the South may vary, either along the rise or in neighbouring regions where alkaline volcanism occurs such as Seine, Ampere, and Ormonde (Fig. 1). Such differences were proposed for the origin of the latter seamounts as well as the Madeira Archipelago, where the involvement of a young high-U/Pb plume was proposed, interacting with enriched material present in the oceanic lithosphere possibly containing some continental material (Geldmacher and Hoernle, 2000; Geldmacher et al., 2005).

9. Major conclusions

- (1) U–Pb ages of six seamount complexes emplaced along an about 500 km long segment of the northern Tore-Madeira Rise yield ages between 104 and 81

Ma, being significantly different in age than previously assumed. Their origin is not related to 130–125 Ma initiation of opening of the Atlantic ocean.

- (2) A long-lived thermal anomaly, present underneath the continental plate margin since at least 104 Ma seems required to explain mantle melting and related volcanism. At the time of alkaline volcanism, the active Atlantic spreading center was located between 136 and 460 km to the West, corresponding to potential minimum and actually measured spreading rates of 0.67 and 2.2 cm/yr, respectively.
- (3) Magmas were probably generated in the head of a mantle plume (OIB-type magmas) with time–space migrating domains of melting under the oceanic lithosphere, the ocean–continent transition zone and the continent. Small portions of continental material have also been incorporated in the magmas.

Acknowledgment

We thank our colleagues of the Tore-Madeira cruise and the captain M. Houmar of the R/V *Atalante*. For microprobe, SEM analyses, thin sections and technical assistance we thank A. Barreau, E. Boeuf, M. Bohn, B. De Quillac, J.-P. Goudour, H. Loyen and M. Manetti. R. M. would like to thank Jo Cotten for ICP-AES analyses and M. Grange for help in zircon analyses. Constructive comments by Dr. K. Hoernle, Dr. S. Noble and an anonymous reviewer helped to considerably improve the manuscript. This work has also greatly benefited from the pertinent comments of Dr. F. Frey (associate editor) as well as J.-A. Barrat and J.-J. Peucat.

Associate editor: Frederick A. Frey

References

- Allègre, C.J., Manhès, G., Göpel, C., 1995. The age of the Earth. *Geochim. Cosmochim. Acta* **59**, 1445–1456.
- Bernard-Griffiths, J., Gruau, G., Cornen, G., Azambre, B., Macé, J., 1997. Continental lithospheric contribution to alkaline magmatism: isotopic (Nd, Sr, Pb) and geochemical (REE) evidence from Serra de Monchique and Mount Ormonde Complexes. *J. Petrol.* **38**, 115–132.
- Beslier, M.-O., Girardeau, J., Boillot, G., 1988. Lithologie et structures des péridotites à plagioclase bordant la marge continentale passive de la Galice (Espagne). *C.R. Acad. Sci. Paris* **306**, 373–380.
- Beslier, M.-O., Ask, M., Boillot, G., 1993. Ocean-continent boundary in the Iberia Abyssal Plain. *Tectonophysics* **218**, 383–393.
- Blichert-Toft, J., Albarède, F., 1997. Lu–Hf isotope geochemistry of chondrites and the evolution of mantle–crust system. *Earth Planet. Sci. Lett.* **148**, 243–258.
- Blichert-Toft, J., Chauvel, C., Albarède, F., 1997. Separation of Hf and Lu for high-precision isotope analysis of rock samples by magnetic sector-multiple collector ICP-MS. *Contrib. Mineral. Petrol.* **127**, 248–260.
- Bodet, F., Schärer, U., 2000. Evolution of the SE-Asian continent from U–Pb and Hf isotopes in single grains of zircon and baddeleyite from large rivers. *Geochim. Cosmochim. Acta* **64**, 2067–2091.
- Boillot, G., Feraud, G., Recq, M., Girardeau, J., 1989. Undercrusting by serpentinite beneath rifted margins. *Nature* **341**, 523–525.

- Boillot, G., Agrinier, P., Beslier, M.-O., Cornen, G., Froitzheim, N., Gardien, V., Girardeau, J., Gil Ibarguchi, J., Kornprobst, J., Moulade, M., Schärer, U., Vanney, J.-R., 1995. A lithospheric syn-rift shear zone at the ocean-continent transition preliminary results of the GALINAUTE II cruise (Nautilus dives on the Galicia Bank, Spain). *C.R. Acad. Sci. Paris* **321**, 1171–1178.
- Borsi, L., Schärer, U., Gaggero, L., Crispini, L., 1996. Age, origin and geodynamic significance of plagiogranite in lherzolithes and gabbros of the Piedmont-Ligurian ocean basin. *Earth Planet. Sci. Lett.* **140**, 227–241.
- Carignan, J., Hild, P., Mevelle, G., Morel, J., Yeghicheyan, D., 2001. Routine analyses of trace element in geological samples using flow injection and low pressure on-line liquid chromatography coupled to ICP-MS: a study of geochemical reference materials BR, DR-N, UB-N, AN-G and GH. *Geostand. Newsl.* **25**, 187–198.
- Chazot, G., Charpentier, S., Kornprobst, J., Vannucci, R., Luais, B., 2005. Lithospheric mantle evolution during continental break-up: the West Iberia non-volcanic passive margin. *J. Petrol.* **46**, 2527–2568.
- Cohen, R.S., O’Nions, R.K., Dawson, J.B., 1984. Isotope geochemistry of xenoliths from East Africa: implications for development of mantle reservoirs and their interaction. *Earth Planet. Sci. Lett.* **68**, 209–220.
- Condomines, M., Tanguy, J.C., Kieffer, G., Allègre, C.J., 1982. Magmatic evolution of a volcano using ^{230}Th - ^{238}U and trace elements systematics, the Etna case. *Geochim. Cosmochim. Acta* **46**, 1397–1416.
- Cornen, G., 1982. Petrology of the alkaline volcanism of Gorringe Bank (southwest Portugal). *Mar. Geol.* **47**, 101–130.
- Cornen, G., Girardeau, J., Monnier, C., 1999. Basalts, underplated gabbros and pyroxenites record the rifting process of the West Iberian margin. *Mineral. Petrol.* **67**, 111–142.
- Cotten, J., Le Dez, A., Bau, M., Caroff, M., Maury, R.C., Dulsky, P., Fourcade, S., Bohn, M., Brousse, R., 1995. Origin of anomalous rare-earth elements and yttrium enrichments in subaerially exposed basalts: evidence from French polynesia. *Chem. Geol.* **119**, 115–138.
- Courtillot, V., Davaille, A., Besse, J., Stock, J., 2003. Three distinct types of hotspots in the Earth’s mantle. *Earth Planet. Sci. Lett.* **205**, 295–308.
- DeMets, C., Gordon, R.G., Argus, D.F., Stein, S., 1990. Current plate motions. *Geophys. J. Int.* **101**, 425–478.
- Féraud, G., Bonnin, J., Olivet, J.-L., Auzende, J.-M., Bougault, H., 1977. Sur quelques datations du volcanisme alcalin de la ligne Açores-Gibraltar et leur contexte géodynamique. *C.R. Acad. Sci. Paris, Sér. D* **285**, 1203–1206.
- Féraud, G., Schmincke, H.U., Lietz, J., Gastaud, J., Pritchard, G., Bleil, U., 1981. New K-Ar ages, chemical analyses and magnetic data of rocks from the islands of Santa Maria (Azores), Porto Santo and Madeira (Madeira Archipelago) and Gran Canaria (Canary Islands). *Bull. Volcanol.* **44**, 359–375.
- Féraud, G., Gastaud, J., Auzende, J.-M., Olivet, J.-L., Cornen, G., 1982. $^{40}\text{Ar}/^{39}\text{Ar}$ ages for the alkaline volcanism and basement of Gorringe Bank, North Atlantic Ocean. *Earth Planet. Sci. Lett.* **57**, 211–226.
- Féraud, G., York, D., Mevel, C., Cornen, G., Hall, C.M., Auzende, J.M., 1986. Additional $^{40}\text{Ar}/^{39}\text{Ar}$ dating of the basement and the alkaline volcanism of Gorringe Bank (Atlantic Ocean). *Earth Planet. Sci. Lett.* **79**, 255–269.
- Féraud, G., Girardeau, J., Beslier, M.O., Boillot, G., 1988. Datation $^{40}\text{Ar}/^{39}\text{Ar}$ de la mise en place des peridotites bordant la marge de la Galice (Espagne). *C.R. Acad. Sci. Paris II* **307**, 49–55.
- Geldmacher, J., Van den Bogaard, P., Hoernle, K., Schmincke, H.U., 2000. The $^{40}\text{Ar}/^{39}\text{Ar}$ age dating of the Madeira Archipelago and hot spot track (eastern North Atlantic). *Geochim. Geophys. Geosyst.* **1**.
- Geldmacher, J., Hoernle, K., 2000. The 72 Ma geochemical evolution of the Madeira hot spot (eastern North Atlantic): recycling of Paleozoic (500 Ma) oceanic lithosphere. *Earth Planet. Sci. Lett.* **183**, 73–92.
- Geldmacher, J., Hoernle, K., 2001. Corrigendum to: The 72 Ma geochemical evolution of the Madeira hot spot (eastern North Atlantic): recycling of Paleozoic (500 Ma) oceanic lithosphere. *Earth Planet. Sci. Lett.* **186**, 333.
- Geldmacher, J., Hoernle, K., Bogaard, P.v.d., Zankl, G., Garbe-Schönberg, D., 2001. Earlier history of the ≥ 70 Ma old Canary hotspot based on the temporal and geochemical evolution of the Selvagens Archipelago and neighboring seamounts in the eastern North Atlantic. *J. Volcanol. Geotherm. Res.* **111**, 55–87.
- Geldmacher, J., Hoernle, K., Van den Bogaard, P., Duggen, S., Werner, R., 2005. New $^{40}\text{Ar}/^{39}\text{Ar}$ age geochemical seamounts Canary and Madeira volcanic provinces: Support for the mantle plume hypothesis. *Earth Planet. Sci. Lett.* **237**, 85–101.
- Geldmacher, J., Hoernle, K., Klügel, A., Van den Bogaard, P., Wombacher, F., Berning, B., Origin and geochemical evolution of the Tore-Madeira Rise (eastern North Atlantic), *J. Geophys. Res.* in press.
- Girardeau, J., Cornen, G., Beslier, M.O., Le Gall, B., Monnier, C., Agrinier, P., Dubuisson, G., Pinheiro, L., Ribeiro, A., Whitechurch, H., 1998. Extensional tectonics in the Gorringe Bank rocks, Eastern Atlantic Ocean: evidence of an oceanic ultra-slow mantellitic accreting center. *Terra Nova* **10**, 330–336.
- Govindaraju, K., Mevelle, G., 1987. Fully automated dissolution and separation methods for inductively coupled plasma atomic emission spectrometry rock analysis. Application to the determination of rare earth elements. *J. Anal. Atom. Spectrom.* **2**, 615–621.
- Gradstein, F.M., Ogg, J.G., Smith, A.G., 2004. *A geological time scale*. Cambridge University Press, Cambridge.
- Halliday, A.N., Davies, G.R., Lee, D.C., Tommasini, S., Paslick, C.R., Fitton, J.G., James, D.E., 1992. Lead isotopic evidence for young trace element enrichment in the oceanic upper mantle. *Nature* **359**, 623–627.
- Halliday, A.N., Davies, G.R., Lee, D.C., Tommasini, S., Paslick, C.R., Fitton, J.G., James, D.E., 1993. Correction to “Lead isotopic evidence for young trace element enrichment in the oceanic upper mantle”. *Nature* **362**, 184.
- Halliday, A.N., Lee, D.C., Tommasini, S., Davies, G.R., Paslick, C.R., Fitton, J.G., James, D.E., 1995. Incompatible trace elements in OIB and MORB and source enrichment in the sub-oceanic mantle. *Earth Planet. Sci. Lett.* **133**, 379–395.
- Hoernle, K., Schmincke, H.U., Tilton, G., 1991. Sr, Nd and Pb isotope geochemistry of volcanics from Madeira and Porto Santo Islands, North Atlantic Ocean. *EOS Trans. Am. Geophys. Union* **72**, 528.
- Hoernle, K., Zhang, Y.S., Graham, D., 1995. Seismic and geochemical evidence for large-scale mantle upwelling beneath the eastern Atlantic and western and central Europe. *Nature* **374**, 34–39.
- Hoernle, K., and scientific party (2003) Cruise report M51/1. In: C. Hemleben, K. Hoernle, B.B. Jörhensen, W. Roether. (Eds.), Meteor Berichte 03-1, Univ. Hamburg, Germany, 3–35.
- Holmes, A., 1946. An estimate of the age of the Earth. *Nature* **157**, 680–684.
- Jaffey, H., Flynn, K.F., Glendenin, L.E., Bentley, W.C., Essling, A.M., 1971. Precision measurements of half-lives and specific activities of ^{235}U and ^{238}U . *Phys. Rev.* **C4**, 1889–1906.
- Jiménez-Munt, I., Fernández, M., Torne, M., Bird, P., 2001. The transition from linear to diffuse plate boundary in the Azores-Gibraltar region: results from a thin-sheet model. *Earth Planet. Sci. Lett.* **192**, 175–189.
- Krogh, T.E., 1973. A low contamination method for hydrothermal decomposition of zircon and extraction of U and Pb for isotopic ages determination. *Geochim. Cosmochim. Acta* **37**, 485–494.
- Krogh, T.E., 1982. Improved accuracy of U-Pb zircon ages by the creation of more concordant systems using air abrasion technique. *Geochim. Cosmochim. Acta* **46**, 637–649.
- Lassiter, J.C., Blichert-Toft, J., Hauri, E.H., Barsczus, H.G., 2003. Isotope and trace elements variations in lavas from Raivavae and Rapa, Cook-Austral islands: constraints on the nature of the HIMU-and EM-mantle and the origin of mid-plate volcanism in French Polynesia. *Chem. Geol.* **202**, 115–138.
- Laughton, A.V., Roberts, D.G., Graves, R., 1975. Bathymetry of the northeast Atlantic: mid-Atlantic ridge to southwest Europe. *Deep Sea Res.* **22**, 791–810.
- Le Bas, M.J., Le Maitre, R.W., Streckeisen, A., Zanettin, B., 1986. A chemical classification of volcanic rocks based on the total alkali-silica diagram. *J. Petrol.* **27**, 745–750.

- Ludwig, K.R., 2003. User's Manual for Isoplot 3.00. Berkeley Geochronology Center Special Publication, 74pp.
- Malod, J.A., 1989. Ibérides et plaque ibérique. *Bull. Soc. Géol. France* **5**, 927–934.
- Manhès, G., Minster, J.F., Allègre, C.J., 1978. Comparative U–Th–Pb and Rb–Sr study of the Saint Séverin amphoterite: consequence for early solar system chronology. *Earth Planet. Sci. Lett.* **39**, 14–24.
- Mata, J., Kerrich, R., MacRae, N.D., Wu, T.W., 1998. Elemental and isotopic (Sr, Nd and Pb) characteristics of Madeira Island basalts: evidence for a composite HIMU-EMI plume fertilizing lithosphere. *Can. J. Earth Sci.* **35**, 980–997.
- Mauffret, A., Mougenot, D., Miles, P.R., Malod, J., 1989. Cenozoic deformation and Mesozoic abandoned spreading center in the Tagus Abyssal Plain (West of Portugal). *Can. J. Earth Sci.* **26**, 1101–1123.
- McIntyre, R.M., 1977. Anorogenic magmatism, plate motion and Atlantic evolution. *J. Geol. Soc. Lond.* **133**, 375–384.
- McIntyre, R.M., Berger, G.W., 1982. A note on the geochronology of the Iberian Alkaline Province. *Lithos* **15**, 133–136.
- Merle, R., Caroff, M., Girardeau, J., Cotten, J., Guivel, C., 2005. Segregation vesicles, cylinders, and sheets in vapor-differentiated pillow lavas: examples from Tore-Madeira Rise and Chile Triple Junction. *J. Volcanol. Geotherm. Res.* **141**, 109–122.
- Middlemost, A.E.K., 1989. Iron oxidation ratios, norms and the classification of the volcanic rocks. *Chem. Geol.* **77**, 19–26.
- Minster, J.F., Ricard, L.P., Allègre, C.J., 1979. ^{87}Rb – ^{87}Sr chronology of enstatite meteorites. *Earth Planet. Sci. Lett.* **44**, 420–440.
- Miyashiro, A., 1978. Nature of alkaline volcanic rock series. *Contrib. Mineral. Petro.* **66**, 91–104.
- Montelli, R., Nolet, G., Dahlen, F.A., Masters, G., Engdahl, E.R., Hung, S.H., 2004. Finite-frequency tomography reveals a variety of plume in the mantle. *Nature* **303**, 338–343.
- Moreira, M., Doucelance, R., Kurz, M.D., Dupré, B., Allègre, C.J., 1999. Helium and lead isotope geochemistry of the Azores Archipelago. *Earth Planet. Sci. Lett.* **169**, 189–205.
- Nowell, G.M., Kempton, P.D., Noble, S.R., Fitton, J.G., Saunders, A.D., Mahoney, J.J., Taylor, R.N., 1998. High-precision Hf isotope measurements of MORB and OIB by thermal ionization mass spectrometry: insight into the depleted mantle. *Chem. Geol.* **149**, 211–233.
- Olivet, J.-L., 1996. La cinématique de la plaque Ibérique. *Bull. Centres Rech. Explor.-Prod. Elf Aquitaine* **20**, 131–195.
- Patchett, P.J., Tatsumoto, M., 1980. A routine high-precision method for Lu–Hf isotope geochemistry and chronology. *Contrib. Mineral. Petro.* **75**, 263–267.
- Patchett, P.J., Kouvo, O., Edge, C.E., Tatsumoto, M., 1981. Evolution of continental crust and mantle heterogeneity: Evidence from Hf isotopes. *Contrib. Mineral. Petro.* **78**, 279–297.
- Pearce, C., Barton, P.J., 1991. Crustal structure of the Tore-Madeira Rise, Eastern North Atlantic—results of a DOBS wide-angle and normal incidence seismic experiment in the Josephine Seamount region. *Geophys. J. Int.* **106**, 357–378.
- Pinheiro, L.M., Whitmarsh, R.B., Miles, P.R., 1992. The Ocean-Continent boundary off the western continental margin of Iberia. II. Crustal structure in the Tagus Abyssal Plain. *Geophys. J. Int.* **109**, 106–124.
- Pitman III, W.C., Talwani, M., 1972. Sea-floor spreading in the North Atlantic. *Geol. Soc. Am. Bull.* **83**, 619–646.
- Rock, N.M.S., 1976. The comparative strontium isotopic composition of alkaline rocks: new data from southern Portugal and east Africa. *Contrib. Min. Petro.* **56**, 205–228.
- Rock, N.M.S., 1982. The late Cretaceous alkaline igneous province in the Iberian peninsula, and its tectonic significance. *Lithos* **15**, 111–131.
- Roest, W.R., Danobeitia, J.J., Verhoef, J., Colette, B.J., 1992. Magnetic anomalies in the Canary basin and the Mesozoic evolution of the Central North Atlantic. *Mar. Geophys. Res.* **14**, 1–24.
- Salters, V.J.M., White, W.M., 1998. Hf isotope constraints on mantle evolution. *Chem. Geol.* **145**, 447–460.
- Schärer, U., 1991. Rapid continental crust formation at 1.7 Ga from a reservoir with chondritic isotope signatures, eastern Labrador. *Earth Planet. Sci. Lett.* **102**, 110–133.
- Schärer, U., Kornprobst, J., Beslier, M.O., Boillot, G., Girardeau, J., 1995. Gabbro and related rocks emplacement beneath rifting continental crust: U–Pb geochronological and geochemical constraints for the Galicia passive margin (Spain). *Earth Planet. Sci. Lett.* **130**, 187–200.
- Schärer, U., Girardeau, J., Cornen, G., Boillot, G., 2000. 138–121 Ma asthenospheric magmatism prior to continental break-up in the North Atlantic and geodynamic implications. *Earth Planet. Sci. Lett.* **181**, 555–572.
- Sguigna, A.P., Larabee, A.J., Waddington, J.C., 1982. The half-life of ^{176}Hf by α - α coincidence measurements. *Can. J. Phys.* **60**, 361–364.
- Sibuet, J.C., Monti, S., Loubrieu, B., Mazé, J.P., Srivastava, S., 2004a. Carte bathymétrique de l'Atlantique nord-est et du golfe de Gascogne: implications géodynamiques. *Bull. Soc. Géol. France* **175**, 429–442.
- Sibuet, J.-C., Srivastava, S., Spakman, W., 2004b. Pyrenean orogeny and plate kinematics. *J. Geophys. Res.* **108**, B08104.
- Snyder, D.C., Widom, E., Pietruszka, A.J., Carlson, R.W., 2004. The role of open-system processes in the development of silicic magma chambers: a chemical and isotopic investigation of the Fogo A trachyte deposit, São Miguel, Azores. *J. Petrol.* **45**, 723–738.
- Srivastava, S.P., Sibuet, J.-C., Cande, S., Roest, W.R., Reid, I.D., 2000. Magnetic evidence for slow seafloor spreading during the formation of the Newfoundland and Iberian margins. *Earth Planet. Sci. Lett.* **182**, 61–76.
- Stacey, J.S., Kramers, J.D., 1975. Approximation of terrestrial lead isotope evolution by a two-stage model. *Earth Planet. Sci. Lett.* **26**, 207–221.
- Steiger, R.H., Jäger, E., 1977. Subcommission on geochronology: convention on the use of decay constants in geo- and cosmochronology. *Earth Planet. Sci. Lett.* **36**, 359–362.
- Sun, S.S., McDonough, W.F., 1989. Chemical and isotopic systematics of oceanic basalts: implication for mantle composition and processes. In: Saunders, A.D., Norry, M.J. (Eds.), *Magmatism in the ocean basins*, vol. 42. Geol. Soc. Spec. Publ., London, pp. 313–345.
- Tatsumoto, M., Knight, R.J., Allègre, C.J., 1973. Time differences in the formation of meteorites as determined from the ratio of 207-lead to 206-lead. *Science* **180**, 1279–1283.
- Thirlwall, M.F., 1997. Pb isotopic and elemental evidence for OIB derivation from young HIMU mantle. *Chem. Geol.* **139**, 51–74.
- Tucholke, B.E., Ludwig, W.J., 1982. Structure and origin of the J Anomaly Ridge, Western North Atlantic Ocean. *J. Geophys. Res.* **87**, 9389–9407.
- Van der Linden, W.J.M., 1979. The Atlantic margin of Iberia and Morocco, a reinterpretation. *Tectonophysics* **59**, 185–199.
- Villemant, B., Joron, J.-L., Jaffrezic, H., Treuil, M., Maury, R., Brousse, R., 1980. Cristallisation fractionnée d'un magma basaltique alcalin: la série de la chaîne des Puys (Massif Central, France) II: Géochimie. *Bull. Minéral.* **103**, 267–286.
- Wendt, I., Kreuzer, H., Müller, P., Von Rad, U., Raschka, H., 1976. K–Ar age of basalts from Great Meteor and Josephine seamount (eastern North Atlantic). *Deep Sea Res.* **23**, 849–862.
- Whitmarsh, R.B., Avedik, F., Saunders, M.R., 1986. The seismic structure of thinned continental crust in the northern Bay of Biscay. *Geo. J. Roy. Astr. Soc.* **86**, 589–602.
- Widom, E., Carlson, R.W., Gill, J.B., Schmincke, H.U., 1997. Th–Sr–Nd–Pb isotope and trace elements evidence for the origin of São Miguel, Azores, enriched mantle source. *Chem. Geol.* **140**, 49–68.
- Widom, E., Hoernle, K., Shirey, S.B., Schmincke, H.U., 1999. Os isotope systematics in the Canary Islands and Madeira: lithospheric contamination and mantle plume signature. *J. Petrol.* **40**, 279–296.
- Zartman, R.E., Doe, B.R., 1981. Plumbotectonics—the model. *Tectonophysics* **75**, 135–162.
- Zhang, L.S., Schärer, U., 1996. Inherited components in magmatic titanite and their consequence for the interpretation of U–Pb ages. *Earth Planet. Sci. Lett.* **138**, 57–65.